UNIVERSITÉ DE SHERBROOKE

Faculté de génie

Département de génie civil

Développement d'un nouveau dispositif piézoélectrique d'essai d'impulsion et caractérisation des sols avec les ondes de cisaillement

Thèse de doctorat es sciences appliquées

Spécialité: génie civil

Deyab GAMAL EL-DEAN

Sherbrooke (Québec), CANADA Décembre, 2007

Your file Votre référence
ISBN: 978-0-494-37971-4
Our file Notre référence
ISBN: 978-0-494-37971-4

UNIVERSITÉ DE
SHERBROOKE

Faculté de génie

Département de génie civil

DEVELOPMENT OF A NEW PIEZOELECTRIC PULSE TESTING DEVICE AND SOIL CHARACTERIZATION USING SHEAR WAVES

Deyab GAMAL EL-DEAN

Dissertation submitted in partial fulfillment
of the requirements for the degree of
Doctor of Philosophy
in
Civil Engineering

Sherbrooke (Québec), Canada **December, 2007**

ABSTRACT

The shear-wave velocity (V_s) is a fundamental parameter that correlates well to soil properties, and is important in many applications. Hence, there is an increasing interest in using shear-wave velocity to define soil state (void ratio, effective stresses, density, liquefaction potential, etc). The global idea of this research is to establish correlations between shear wave velocity and the basic soil parameters that can be used to evaluate soil properties and estimate its strength and deformation characteristics. These relationships will also allow the interpretation of in situ geophysical measurements in terms of the design parameters of soil. The needed reliable correlations should be based on accurate measurements.

In this research, it has been proven that the bender-elements method, which is widely used to measure shear wave velocity of soil in laboratory setups, suffers from fundamental and interpretative problems. Consequently, its results are controversial and might give highly erroneous values. After thorough numerical and laboratory investigations, a new piezoelectric pulse testing device (Ring Actuators Setup) was invented and developed in this research. This setup is composed of two units (emitter and receiver) and is capable of measuring shear and compression wave velocities of soil specimens. It is a completely new, versatile, advanced and accurate setup. With this device, many problems of pulse tests, which make interpretation of results difficult and ambiguous, were solved. The ring actuators setup overcomes wave reflections at boundaries (end-caps and sides), sample disturbance, weak shear coupling between soil and device (interaction) as well as the fixation problems, low resonant frequency and limited input voltage of the existing device. The development stages of this device were also useful in reaching important findings for building robust setups. This device was implemented in the top cap and pedestal of a large oedometer cell. This setup was also used with Proctor mold as well as other fabricated molds. Many pulse tests were carried out on different soil types using this device. Shear and compression wave velocities could be accurately measured at dry and partially saturated conditions under very low to high pressures. The compaction curves, in terms of V_s and water content, were drawn for two soil types using the new device. In addition, some correlations between V_s and soil parameters were obtained.

Numerical simulations and analytical studies were also carried out in this research in order to study the characteristics of elastic waves transmission through soil specimens in different laboratory setups. The bender-elements and the ring actuators models were studied. The interpretation problems of pulse tests were thoroughly investigated numerically and experimentally. In this research, the reason of 'near-field effect' in pulse tests, which causes significant errors in the interpretation process, could be discovered. The parameters that control this phenomenon could be stated and their effects on the test results were quantified. In light of these results, a new criterion for carrying out and interpreting pulse tests was established. Also, a simple interpretation method is introduced (Energy Rise-Time). Furthermore, the dispersive nature of pulse tests was proven numerically and experimentally. Moreover, it was concluded that the shear wave velocity from pulse tests should be interpreted in the frequency domain, which renders 'the simple methods of interpretation' inaccurate. Based on these findings, a new interpretation technique for pulse tests using Wigner-Ville transform was presented. It was successfully used to interpret the numerical and physical pulse test results in this study.

The last part of this research concerns soil characterization using shear wave velocity. Establishing correlations between V_s and soil parameters that can be used for soil characterization may be achieved in laboratory using piezoelectric devices, as mentioned above, or by deriving relationships between V_s and in situ test indices. In this research, the second approach was also examined for gravelly sands. Results of the comprehensive field testing program for the natural soil and the embankment materials (fill) at Péribonka dam site were used to achieve this goal. Thorough interpretations and analyses were carried out for these tests in order to derive correlations between each of CPTu and SPT indices and the in-situ V_s-measurements. Several important relationships and conclusions for soil characterization using shear waves could be reached. These correlations are useful for soil characterization not only at this site, but at other sites of similar soil composition.

RÉSUMÉ

La vitesse de l'onde de cisaillement (V_s) est un paramètre fondamental qui correspond bien aux propriétés de sol, et est important dans beaucoup d'applications. Par conséquent, il y a un intérêt croissant à l'emploi de la vitesse de l'onde de cisaillement pour définir l'état de sol (indice des vides, les contraintes effectives, la densité, le potentiel de liquéfaction, etc). L'idée globale de cette recherche est d'établir des corrélations entre la vitesse de l'onde de cisaillement et les paramètres de base de sol qui peuvent être employés pour évaluer les propriétés du sol et estimer ses caractéristiques de résistance et de déformation. Ces rapports permettront également d'interpréter des mesures géophysiques in situ en termes de paramètres de conception de sol. Les corrélations fiables nécessaires devraient être basées sur des mesures précises.

Dans cette recherche, on a prouvé que la méthode des languettes piézocéramiques (bender-elements), largement répandue pour mesurer la vitesse de l'onde de cisaillement du sol dans des installations de laboratoire, souffre de problèmes fondamentaux et interprétatifs. En conséquence, ses résultats sont controversés et pourraient donner des valeurs fortement incorrectes. Après des investigations numériques et expérimentales poussées, un nouveau dispositif piézoélectrique, installation des actuateurs d'anneau (Ring Actuators Setup), pour effectuez les essais d'impulsion a été inventé et développé dans cette recherche. Cette installation se compose de deux unités (émetteur et récepteur) et est capable de mesurer des vitesses de l'onde de cisaillement (V_s) et de compression (V_p) des spécimens de sol. C'est une installation complètement nouvelle, souple, avancée et précise. Avec ce dispositif, plusieurs problèmes d'essais d'impulsion, qui rendent l'interprétation des résultats difficile et ambiguë, ont été résolus. L'installation de Ring Actuators surmonte les réflexions de l'onde aux frontières (les extrémités et les côtés), la perturbation d'échantillon, la faible interaction de cisaillement entre le sol et le dispositif ainsi que les problèmes de fixation, la basse fréquence de résonance et la tension d'entrée limitée du dispositif existant. Les étapes de développement de ce dispositif sont également étaient utiles en obtenant des résultats importants afin de construire des installations robustes. Ce dispositif a été mis en application dans le cap et le piédestal d'une grande cellule d'oedomètre. Cette installation a été également employée avec le moule de Proctor comme d'autres moules fabriqués. Beaucoup d'essais d'impulsion ont été effectués sur différents types de sol à l'aide de ce dispositif. Des vitesses de l'onde de cisaillement et de compression ont pu être exactement mesurées à des conditions sèches et partiellement saturées, sous de très basses ou hautes pressions. Les courbes de compactage, en

termes de V_s et la teneur en eau, ont été dessinées pour deux types de sol à l'aide du nouveau dispositif. En plus, quelques corrélations entre V_s et les paramètres de sol ont été obtenus.

Des simulations numériques et des études analytiques ont également été effectuées dans mes travaux de recherche afin d'étudier les caractéristiques de la transmission de l'onde élastique à travers des spécimens de sol dans différentes installations de laboratoire. Des modèles des languettes piézocéramiques et des actuateurs d'anneau ont été étudiés. Les problèmes d'interprétation des essais d'impulsion ont été étudiés à fond, numériquement et expérimentalement. Dans cette recherche, les raisons du champ proche (near-field effects) en essais d'impulsion, qui causent des erreurs importantes dans le procédé d'interprétation, pourraient être découvertes. Les paramètres qui commandent ce phénomène pourraient être énoncés et leurs effets sur les résultats d'essai ont été mesurés. À la lumière de ces résultats, un nouveau critère pour effectuer et interpréter des essais d'impulsion a été établi. En outre, une méthode simple d'interprétation est présentée (temps de montée d'énergie). De plus, la nature dispersive des essais d'impulsion a été prouvée numériquement et expérimentalement. D'ailleurs, on a conclu que la vitesse de vague de cisaillement des essais d'impulsion devrait être interprétée dans le domaine de fréquence, qui rend les méthodes simples d'interprétation imprécises. Basée sur ces résultats, une nouvelle technique d'interprétation pour des essais d'impulsion employant Wigner-Ville Transforme a été présentée. Elle a été utilisée avec succès pour interpréter les résultats d'essai physiques et numériques d'impulsion.

La dernière partie de cette recherche concerne la caractérisation de sol en utilisant la vitesse de l'onde de cisaillement. L'établissement des corrélations entre V_s et les paramètres de sol, qui peuvent être employés pour la caractérisation de sol, peut être réalisé dans le laboratoire à l'aide de dispositifs piézoélectriques, comme mentionné ci-dessus, ou par dérivation des relations entre V_s et les paramètres d'essai in situ. Dans cette recherche, la deuxième approche a été également examinée pour les sables graveleux. Des résultats du programme complet d'essai sur le terrain, pour le sol naturel et les matériaux de barrage à l'emplacement du barrage de Péribonka, ont été employés pour réaliser ce but. Les interprétations et les analyses complètes ont été effectuées pour ces essais afin de dériver des corrélations entre chacune d'indice de CPTu et de SPT et des mesures de V_s in situ. Plusieurs relations et conclusions importantes pour la caractérisation du sol par les ondes de cisaillement ont pu être tirées. Ces corrélations sont utiles pour la caractérisation de sol non seulement à cet emplacement mais aux autres emplacements de composition de sol semblable.

DEDICATION

To the researchers and engineers who appreciate the value of science and knowledge.

To my beloved parents who favoured me over themselves and have given me all what they could. "My Lord! Bestow on them Your Mercy as they did bring me up when I was young."

To my wife who always supports me and understands my special circumstances as a researcher.

To my daughter Sarah and my son Abdo-Arrahman who came to life during my Ph.D. and have made a big difference in my life.

ACKNOWLEDGEMENT

First and foremost, praise and thanks go to my Creator and Provider (**Allah**) for his uncounted grace undeservingly bestowed upon me. "Glory be to You, we have no knowledge except what You have taught us. Verily, it is You, the All-Knower, the All-Wise."

I would like to express my greatest appreciation and thanks to my supervisor, **Prof. Guy Lefebvre**, for his guidance, helpful advice, and encouragement during this research. I had a lot of freedom in my work which I also appreciate in Mr. Lefebvre. I have learned a lot from his thorough knowledge and experience as well as from his nice and decent personality. I wish to express my sincere gratitude to him for his patience and understanding during the course of this research. I am proud to work with him and lucky to be his last Ph.D. student !

I am greatly indebted to **Dr. Mourad Karray**, for his cooperation, monitoring and friendship during the research. His unfailing guidance and continuous consulting effort were valuable to this research. He has written two codes (Wigner-Ville and RAKU) which were used in this study for signal interpretation. I also thank my colleague **Yannic Ethier** for his cooperation and for the fun we had during the difficult times of this research. The developement of ring actuators setup was in a collaborative work with him and Dr. Karray. I can not forget to acknowledge many friends whom I have gained during my study; my stay here at Sherbrooke was made enjoyable by them.

I also thank the professors of civil engineering department and all the faculty staff I have interacted with. Special thanks to Nicole Laverdière, the research secretary, for her prompt help and cooperation. Thanks are also extended to the department secretary, especially Marielle Beaudry. Appreciation is expressed to Jean-Guy Lemelin for his help in manufacturing a test setup and carrying out some complementary laboratory tests. Thanks are extended to Hydro-Quebec for their permission to analyze and publish the records of Peribonca dam.

I wish to express my greatest and profound gratitude to my parents, brothers and sisters, for their support and encouragement. Finally, I wish to thank my wife Nahed, for her love and the happiness she brought to me. My life here at Sherbrooke would not have been so full without my wife and my two kids.

Gamal El-Dean, Deyab

TABLE OF CONTENTS

LIST OF TABLES

LIST OF FIGURES

SYMBOLS AND NOTATIONS

ASF	age scaling factor for penetration-velocity equations
C	piezo actuator capacitance
$C.C$	cross-correlation function
C_c	coefficient of curvature
C_g	material constant in G_o empirical equations
C_N	overburden stress correction factor
C_p, C_s	compressional and shear wave velocities
CPT	cone penetration test
C_u	coefficient of uniformity
D	material damping ratio
D_{50}	median grain size
D_{10} , D_{30}, D_{60}	grain size of 10%, 30% and 40% passing, respectively
d_{31}	strain coefficient (displacement normal to polarization direction)
d_{33}	strain coefficient (displacement in polarization direction)
D_o , D_i	outer and inner diameter, respectively
D_r	relative density
E	modulus of elasticity (Young's modulus)
e	void ratio
e_i	initial void ratio
e_g	constant in void ratio function
e_{max} , e_{min}	maximum and minimum void ratio
F	cone friction ratio
FC	fines content
$F(e)$	void ratio function
f_n , f_o	resonant frequency
f, Fr	frequency
f_s	measured cone sleeve friction
G	shear modulus
g	gravity acceleration (g = 9.81 m/s^2)
G_{max} , G_o	small-strain shear modulus
G_s	specific gravity
H	height of ring
I	electrical current
I_c	soil behavior type index
k	the wave-number
k_{33} , k_{31}	electromechanical coupling factors for a piezoelectric element
K	soil bulk modulus
k_f	elastic frame bulk modulus
k_m	mineral bulk modulus
k_w	interstitial pore-fluid bulk modulus
K_o	coefficient of earth pressures at rest

L , L_s	sample length
L_b	bender length
L_{tt}	tip-to-tip distance in bender element test
m_1, m_2	material constants for V_s empirical equation
M, M_{max}	constrained modulus
M_G , M_M , M_C	modulus number
N	number of wave-lengths (2π-count)
N	measured blow count in SPT
n	porosity
n	an exponent used in normalizing cone tip resistance
n, n_g, n_a, n_b	an exponent of stress in G_o / V_s empirical equations
N_{60}	energy-corrected blow count
$(N_1)_{60}$	stress- and energy-corrected blow count
OCR	overconsolidation ratio
P'	mean effective pressure
P_a	a reference stress of 100 kPa
Q	material constant
Q	dimensionless cone tip resistance
Q_m	mechanical quality factor of a piezoceramic
q_c	measured cone tip resistance
q_{c1N}	normalized cone tip resistance
r	radius of ring actuator
S, S_r	degree of saturation
$S_{opt.}$	maximum suction degree of saturation
SPT	standard penetration test
T	period of a signal (1/Fr)
t	time
T_c	curie point of a piezoelectric element (°C)
t_s	shear wave arrival time
t_p	compression wave arrival time
$t_p^{ref.}$	arrival time of reflected compression wave
u	measured cone pore pressure
U_{pp}	peak-to-peak voltage
V	volume
V_{gr}	group velocity
V_p	compression wave velocity
V_{ph}	phase velocity
V_{pu}	unconstrained compression wave velocity
$V_p^{ref.}$	wave velocity of reflected compression wave
V_R	Rayleigh wave velocity
V_s	shear wave velocity
V_{s1} , V_{s0}	stress-normalized shear-wave velocity
w_c	water content
W_{comp}	compaction water content
Z	depth

γ	shear strain
γ , γ_{sat}	unit weight of soil
γ_d	dry unit weight of soil
λ	wavelength
λ	Lame's constant
ν	Poisson's ratio
ε	strain
φ	friction angle
φ	phase difference between two signals
$\Phi(f)$	phase of the cross-power spectrum
θ	the phase angle ($2\pi N$)
ρ	mass density
ω	angular frequency
σ'_h	horizontal effective pressure
σ'_m , σ'_o	mean effective confining pressure
σ'_v , σ'_{vo}	effective vertical or overburden stress

Chapter 1 INTRODUCTION

1.1 Introduction

A soil specimen generally undergoes irreversible deformation under loading such that the stress-strain relations for loading and subsequent reloading are quite different from that for first loading. However, if a given cycle of loading and unloading is repeated for a few cycles (about 10 to 20 cycles for sand and perhaps 100 or so for clay) the stress strain relation becomes a closed, long, narrow loop (hysteretic loop), whether the loading involves one-dimensional strain, one-dimensional stress, or torsional loading (Hardin and Black, 1968). Two parameters have been used to define this stress-strain relation (hysteretic loop), namely; the vibration (dynamic) modulus and the damping. The modulus is defined by the slope of a line from origin to the ends of the loop, and the area of the loop is a measure of the damping capacity of the soil. These parameters determine the characteristics of the corresponding (of same amplitude) wave propagation, the modulus being related to the velocity of propagation and the area of the loop to the attenuation. For problems involving small-amplitude steady-state vibration, the soil can often be assumed to be linearly elastic if damping can be neglected, or viscoelastic. The assumption of viscoelasticity should be a close approximation for all the small amplitude vibration problems.

The parameters defining the hysteretic loop stress-strain relation have been determined by measuring the force-displacement relation for a repeated loading test, such as cyclic torsional shear technique (ASTM 1987) or direct static stress-strain, or by the resonant-column technique. By the resonant-column technique the shear modulus (G_{max} or G_o) is determined from the resonant frequency of a column of soil and the damping capacity can be determined from the amplitude of vibration at resonance (Hardin, 1965) or by observation of the decay of free vibrations (Hall and Richard, 1963). Up till now, the damping capacity parameter has had little application. The most important soil parameter for the analysis of small-amplitude soil vibration problems is the modulus. Recently, soil moduli at very small strains are being easily determined by direct measurements of shear wave velocity (V_s) using piezoelectric transducers which can be mounted in many laboratory testing apparatuses. In the last two decades, different types of transducers have been used including shear plate, bender

element, compression transducer, and bender/extender element. The measurement simplicity, the immediacy of the results and the possibility of taking measurements during other mechanical tests make this piezoelectric testing technique very attractive. Bender-elements method is the most commonly used technique for these measurements although of its fundamental and interpretation problems that were reported by many researchers.

The piezoelectric pulse techniques have been used to measure the shear wave velocity of soil since Lawrence (1963). These methods have gained limited practical application in geotechnical laboratories although widely used. This is due to the perceived instrumental and interpretative problems. Identifying the exact time of arrival of shear wave is the most difficult and controversial part of a pulse test. In extreme cases, the errors in G_{max} values may be on the order of 50% (Viggiani and Atkinson, 1995). The basic research into the area of behaviour of piezoelectric devices is far behind the effort put forth in the study of soil behaviour using these sensors. Also, the study of the interpretation problems of piezoelectric pulse tests has been widespread, but no interpretation technique may claim preference. Bender-elements are the most commonly used devices for V_s-measurements at laboratory. The determination of G_{max} by resonant column method is sophisticated and involved inputs of the resonant frequency of the soil-equipment system, a variety of device dependent calibration constants and specimen dimensions and mass. The resonant column test can be used to evaluate the stiffness of soils at shearing strains ranging from 10^{-5} % to 1 %. However, analyses of the test data are strictly valid only in the region of very small strain (Isenhower, 1979) because analyses of resonant column tests are based on the assumption that the behaviour of soil is linear and elastic. Differences in shear modulus of more than 50% may appear when comparing measurement results from the cross-hole test and the resonant column test for the same subsoil (Roesler, 1979). Piezoelectric devices can measure the shear modulus of soil all over the strain range in a laboratory test; something behind the capability of a resonant column test with a fraction of its cost.

1.2 Importance of Shear Wave Velocity Measurements

For uncemented cohesionless soils, the shear-wave velocity (V_s) can be regarded as a fundamental engineering parameter. V_s can be an important tool in determining the physical properties of soil because of the direct relationship of shear wave velocity of soil to its physical properties. The measurement of the dynamic shear modulus is increasingly important

with regard to the investigation of the dynamic properties of the subsoil. The shear modulus at very small strains (G_{max} or G_o), which is directly related to shear wave velocity through soil bulk density,ρ, ($G_{max} = \rho V_s^2$), is a key parameter in predicting soil behaviour and soil-structure interaction in many applications. The shear-wave velocity of sand is also controlled primarily by the effective confining stresses and void ratio. Thus, there is an increasing interest in using shear-wave velocity to define the state of soil. The initial state of a sand, defined by the void ratio and effective mean normal stress relative to the steady/critical state at the same stress level, can be used to predict its large-strain response [Roscoe et al. (1958) and Been and Jefferies (1985)]. Robertson et al. (1992) suggested values of normalized shear-wave velocity to evaluate the in-situ state of cohesionless soils. They could identify the boundary between contractant or dilatant sands (loose or dense). The stiffness of soil at very small strain, G_{max}, is a useful parameter for characterizing the non-linear stress-strain behaviour of soil for monotonic loading and it is required for analyses of the dynamic and small strain cyclic loading of soils.

The small-strain shear modulus of soil, G_{max}, also termed elastic modulus, is a fundamental parameter in many kinds of static and dynamic analyses involving deformational calculations (Richart et al., 1970), or liquefaction analysis. Recently, G_{max} is used in conventional static loading problems applications. For example, using the modulus degradation hyperbolas for degrading the elastic modulus to strain levels relevant to deformation problems in geotechnical engineering such as foundation settlement and determining the stress-strain-strength curves for soil (Burland, 1989; Tatsuoka and Shibuya, 1991, Burns and Mayne, 1996; Mayne et al. 1999). G_{max} is also important in predicting soil behaviour during earthquakes, explosions, or machine and traffic vibrations. It can be equally important for small strain cyclic situations such as those caused by wind or wave loading. Knowledge of the dynamic shear modulus is necessary for the design of vibration isolation measures. G_{max} may also be used as an indirect indication of various soil parameters as it usually correlates well to other soil properties such as density, fabric, and liquefaction potential. It may also be used to indicate sample disturbance by comparing laboratory and field measurements. Besides providing information about the dynamic characteristics of soil, measurements of V_p and V_s with piezoelectric transducers in the triaxial test or in other

laboratory tests also provide complimentary information for data analysis and interpretation. For instance, measurement of V_p can be considered as an alternative method for verifying soil saturation. G_{max} measurements can be a useful guide during consolidation (i.e. to determine the rate of application of the drained deviator stress in an anisotropically consolidated triaxial test, or to investigate soil structure changes). The maximum stress direction can be evaluated by measurements of the shear wave velocity if the direction of S-wave propagation and polarization is varied (Roesler, 1979).

1.3 Research Objectives

In the field of soil mechanics, dynamic ground properties may be determined by a variety of in situ and laboratory tests, which yield various index values that are related to strength and deformation properties. The velocity of shear waves in the ground (V_s) as one of these indexes has come to be acknowledged as the most important geophysical property to be dealt with in seismic microzoning, earthquake engineering and many conventional geotechnical engineering applications. Nowadays, V_s measurement in the field is becoming easy and reliable, especially by non destructive methods such as surface waves. But these geophysical investigations methods to become routine tests, reliable correlations between V_s and each of the usual geotechnical parameters of soil and the in situ tests indices have to be developed. Two approaches are possible to obtain these correlations (in laboratory and in situ). Establishing these correlations should make the results of geophysical investigation methods readable in terms of conventional soil parameters, which will make geophysical investigation methods more attractive. This will reduce the need of conventional site investigation techniques, soil sampling, and finally reduce the cost of site investigations. Laboratory studies are important in establishing relationships between basic soil parameters and V_s. Therefore, a deep knowledge of pulse-tests and their interpretation methods are necessary for deriving reliable laboratory-based correlations. Research attention has to concentrate on understanding why a large scatter still exists in V_s-results obtained in laboratory.

In the beginning of this study, it was planned to derive some of these relationships in laboratory using bender elements measurements. After studying pulse tests and their interpretation problems as well as carrying out some numerical simulations and analyses, it was decided to look for a better sensor that can avoid the problems of benders. Hence, a new piezoelectric device is introduced and developed during this research (this is the core of this

study). Studying transmission of waves in laboratory specimens is another objective of this study in order to clear the ambiguity of pulse test results and interpretation. Numerical simulations are to be employed to investigate some aspects as well as for validating the findings. The third main objective of this study is to examine the usage of V_s for quality control of compaction works and characterization of partially saturated granular soils. Thus, the compaction curve in terms of V_s and water content is to be drawn for some soil types to examine the possibility of this application.

The second approach (in situ) was followed to derive some correlations between V_s and some in situ tests indices. The CPTu and SPT results with the in-situ V_s-measurements by MASW (Modal Analysis of Surface Waves) for the foundation soil and the lower embankment materials at Péribonka dam site are to be analyzed for deriving some correlations. The existing equations will be used for comparison with data of Péribonka dam.

1.4 Thesis Outline

This thesis is divided into eight chapters. This section introduces in brief the contents of each chapter.

Chapter 2 presents the currently existing piezoelectric sensors, literature of soil testing using these devices, the interpretation methods for pulse tests, and the existing equations for estimating shear wave velocity. It also presents the results of the existing studies for measuring shear wave velocity of compacted soil.

Chapter 3 presents some numerical simulations and analytical models for pulse tests and is divided into three parts. The first part is to numerically demonstrate the disadvantages of bender elements and their interpretation problems. The second part examines and analyzes new modes of shearing. The third section analyzes the problem of near-field effect and wave reflections, numerically and analytically. Some numerical simulations for developing the new device (ring actuator) which was invented and built in this study are introduced in this chapter.

Chapter 4 introduces a new criterion for carrying out and interpreting pulse tests. It also presents an advanced interpretation method for pulse velocity tests in frequency domain. This

method was developed throughout this research and is called Wigner-Ville Energy Analysis. It takes into account the dispersivity nature of pulse tests.

Chapter 5 details the design and manufacturing of a new piezoelectric device for elastic waves measurement (ring actuators setup) which was developed in this research. It presents and describes the different development stages of this device and the manufactured piezoelectric setups.

Chapter 6 introduces some pulse tests carried out on different soil types using the piezoelectric ring actuators setups. Many correlations, conclusions and findings are introduced based on the test results.

Chapter 7 presents some correlations between each of CPTu and SPT indices and the in-situ V_s measurements at Peribonca dam site. Several relationships are derived and presented based on this analysis.

Chapter 8 summarizes the conclusions and recommendations of this research and proposes some objectives for future research endeavors.

The dissertation is completed by three Appendices (A, B and C): A and B pertaining to Chapter 7 and the third to Chapter 6. The Appendices include the various equations that correlate V_s to the indices of SPT and CPT, the existing correlations for estimating the relative density of soil from SPT and CPT and some pulse test results.

Chapter 2 LITERATURE REVIEW

2.1 Introduction

This chapter introduces the findings of previous researches related to the topics of this thesis. It presents the different existing types of piezoelectric sensors, the interpretation methods for pulse tests, the interpretation difficulties, and the existing equations for estimating shear wave velocity or elastic shear modulus. This is to demonstrate the problems of pulse tests and to clarify the objectives of this research. This chapter also presents the results of the existing studies for measuring shear wave velocity of compacted soil. The various equations that correlate V_s to the indices of SPT and CPT tests are presented in Appendix A. Also, the different correlations for estimating the relative density of soil from SPT and CPT results are reported in Appendix B. These correlations will be used for comparison and analysis of Peribonca Dam data in Chapter 7.

2.2 Transducers for Laboratory Measurements of Shear Wave Velocity

Several laboratory techniques have been developed to measure the small-strain shear modulus, most notably the torsional resonant column and cyclic torsional shear technique (ASTM 2007). Also, direct static stress-strain measurements can be used. In these tests, shear moduli are measured at strains generally less than 10^{-3}%, where moduli are independent of strain amplitude. The terms 'elastic,' 'small-strain,' or 'dynamic' are typically used to describe the measurements and results. G_{max} is directly related to shear wave velocity, V_s, through bulk density, ρ, ($G_{max} = \rho V_s^2$). Beside these techniques, researchers have been using piezoelectric (acoustical) techniques utilizing direct-transmission measurements of V_s. Piezoelectric transducers have been used for this purpose since Lawrence (1963). The following sections introduce this technique and its varieties, its methods of interpretation and how V_s correlates to soil properties.

2.2.1 Piezoelectric Transducers

A piezoelectric material generates electrical output when subjected to mechanical deformation and vice versa it changes its shape when an electrical field is applied to it. The way a polarized

ceramic element deforms depends on ceramic shape and composition, direction of the polarization axis, and location of the applied electrical field. Generally, ceramics can be polarized to generate (or to sense) compression or shear waves. However, spurious motions always seem to be present. For instance, a ceramic element that mainly produces shear displacements will also generate small compressive displacements. This result is further amplified by the finite nature of the S-wave source, which also contributes to the creation of compression wave energy (Sanchez-Salinero 1986). Bender or shear-plate transducers can be used to generate and sense shear waves while compression transducer is used to generate and sense compressional waves.

The behaviour of ceramics is characterized by certain parameters. The piezoelectric constants d and g (d = piezoelectric charge constant and g = piezoelectric voltage constant) define ceramics quality for transmitter and receiver functions, respectively. The coupling coefficient k is an indicator of the efficiency in the conversion of energy from an electrical into a mechanical response and vice versa. An indication of the mechanical losses of energy can be obtained from the mechanical quality factor (Q_m). It is beneficial to select materials characterized with higher values of d, g, and k. The factor Q_m should be as low as possible for a rapid decay of transducer vibrations after the initial excitation.

The phase response of a piezo-actuator system can be approximated by a second order system [Physik Instrumente (PI), Germany] and is described by the following equation:

$$\theta = 2 \arctan \left(\frac{f}{f_o} \right) \tag{2.1}$$

where θ is the phase angle (deg.), f_o is the resonant frequency (Hz) and f is the operating frequency (Hz). The phase response is the delay between an input signal and deformation of the piezoceramic in terms of phase angle (phase-shift). Due to the importance of this phase-change on interpretation of pulse tests in the frequency domain, the previous equation is expressed graphically in Figure 2.1. It can be seen that a phase-shift (phase angle) of up to 90 degrees may be obtained when using piezoelectric sensors/actuators. This phase shift may slightly affect the interpretation methods that utilize the phase-angle in frequency domain analysis. The phase-shift increases by increasing the input frequency (Figure 2.1). Generally, fast response is one of the characteristic features of piezo-actuators. A rapid drive voltage causes a rapid position change.

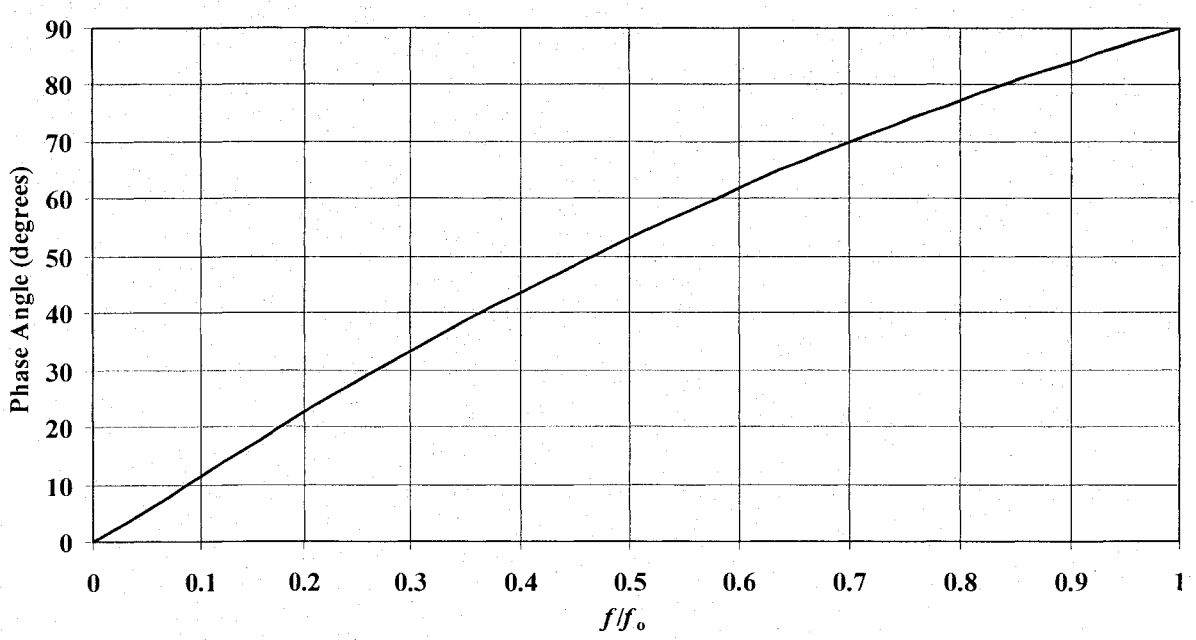

Figure 2.1 The Phase Response of a Piezo-Actuator System.

This property is necessary in dynamic applications such as shock-wave generation, vibration cancellation systems, scanning microscopy, etc.

2.2.2 Measurement Technique in Pulse Tests

Measurement of compression and shear wave velocities of soil specimens in the small-strain range can be suitably performed in the laboratory by means of piezoelectric transducers as follows. An elastic shear wave is generated by a piezoelectric transducer placed on one end of a soil specimen and is received at the other end of the specimen by another piezoelectric transducer. The distance between the two transducers, L, and the time required by the wave to cover this distance, t, are used to calculate the propagation velocity, V, defined by:

$$V = L/t \tag{2.2}$$

The pulse technique is mainly used to measure the shear wave velocity. A compression wave is simultaneously emitted during shear excitation. This wave may be monitored easily at the receiver. Brignoli, Goti, and Stokoe, II (1996) suggested that independent measurement of both P- and S-wave velocities significantly reinforces the interpretation process. The low cost of the electronic instrumentation, the measurement simplicity, the immediacy of the results and the possibility of taking measurements during other mechanical tests make this testing

technique very attractive. An advantage of using piezoceramic transducers is that the test procedures and computations of V_s (G_{max}) are much simpler and more direct than by using the resonant column test. The disadvantage of this technique is however the difficulty of test result interpretation. In addition, there is no direct or convenient method to determine the damping ratio (Dyvik and Madshus, 1985).

2.2.3 Elastic Waves Velocities and Soil Properties

The following equations, extrapolated from elastic continuum mechanics, explain the relationships between elastic soil properties and V_p and V_s:

$$G_{\max} = \rho V_s^2 \tag{2.3}$$

$$V_P^2 = \mathrm{K} + \frac{4}{3}\mathrm{G}_{\max}/\rho$$

(2.4)

$$\mathrm{K} = \mathrm{k}_m(\mathrm{k}_f + \mathrm{Q})/(\mathrm{k}_m + \mathrm{Q})$$

(2.5)

$$\mathrm{Q} = \mathrm{k}_w\left(\mathrm{k}_m - k_f\right)/n\left(\mathrm{k}_m - k_w\right) \tag{2.6}$$

where G_{max} is elastic shear modulus of the soil, V_s is shear wave velocity of the soil, V_p is compression wave velocity of the soil, ρ is bulk density of the soil, K is soil bulk modulus, k_w is interstitial pore-fluid bulk modulus, k_m is mineral bulk modulus, k_f is elastic frame bulk modulus, and n is porosity (in fraction of 1). All the above parameters can be determined independently but the most easily measured quantities are the compression and shear wave velocities and bulk density. Using the measurement of these three quantities, all the elastic parameters of a soil can be calculated. The following equations correlate the elastic soil parameters to each other.

$$K = \sigma / (\Delta V / V) = E / 3\,(1 - 2\nu) \tag{2.7}$$

$$G = E / 2\,(1 + \nu) \tag{2.8}$$

$$E = \sigma / \varepsilon = 2\,(1 + \nu)\,G \tag{2.9}$$

$$M = E / [(1 - \nu) / (1 + \nu)\,.\,(1-2\nu) \tag{2.10}$$

$$\lambda = E\,\nu / (1 + \nu).(1 - 2\nu) \tag{2.11}$$

$$\nu = (3K - 2G) / (6K + 2G) \quad (2.12)$$

where K is the bulk modulus (incompressibility = K^{-1}), σ is the stress on soil, E is Young's modulus (Elasticity), ν is Poisson's ratio, ε is the strain, G_{max} is the elastic shear modulus (rigidity), M is the constrained modulus, and λ is Lame's constant.

The constrained compression wave velocity, V_p, is related to the elastic constrained modulus, M_{max} as follows:

$$M_{\max} = \rho V_p^2 \quad (2.13)$$

On the other hand, if unconstrained compression waves are generated, this wave velocity is related to the small-strain Young's modulus, E_{max}, of the material by:

$$E_{\max} = \rho V_{pu}^2 \quad (2.14)$$

The arrangement of compression wave sources and receivers in the center of each end of the specimen results in measurement of constrained compression waves when the initial wave arrival is employed (Vaghela and Stokoe, 1995). However, Vaghela and Stokoe (1995) also have shown that this source-receiver arrangement can be used to measure unconstrained compression wave in the same specimen simply by exciting longitudinal resonance and accounting for added masses attached to the ends of the specimen.

2.2.4 Existing Measurement Devices

For measurement of shear waves, Lawrence (1963, 1965) described the first applications of piezoelectric transducers in shear wave testing of soil specimens. To generate and receive signals, he employed shear-plate transducers. A different transducer type was developed by Shirley and Anderson in 1975. They employed transducers consisting of two transverse-expansion mode piezoelectric crystals (benders) that were able to generate and detect shear waves. The bender transducers developed by Shirley and Anderson (1975) have been preferred to shear-plate transducers in recent studies. This preference seems to result from the ability of benders to develop relatively large deformations with low electrical excitation. Shear-plate transducers, have received little attention since Lawrence's work (1963, 1965), even though these transducers, when compared with bender elements, are more robust and easier to use with undisturbed specimens because of their non-invasive installation. The currently existing pulse testing devices are shear plates, bender elements, compression transducers and bender/extender elements. Despite its apparent simplicity, the pulse technique

using direct-transmission measurements has been used in few applications in geotechnical laboratories. This lack of application probably results from perceived instrumental and interpretative problems. In bender element tests the strains are not constant throughout the sample because of both material and geometric damping. However, the maximum shear strain generated in the soil is very small and was estimated to be less than 10^{-3} % (Dyvik and Madshus, 1985). The following subsections present the different existing piezo-electric devices as well as the literature of soil testing using these devices.

2.2.4.1 Shear-Plate Transducer

The shear-plate transducer is better suited than bender elements in testing undisturbed stiff soils and soils with large aggregate since shear-plate transducers do not to penetrate into the soil. Based on the work of Brignoli, Gotti, Stokoe II (1996), flat-plate shear transducers showed significant potential for future laboratory use because of their robustness and non-invasive nature. In the shear-plate transducer, the electrodes are applied to two faces that are parallel to the polarization direction as shown in Figure 2.2. A photo of shear plate (22mm diameter) and compression (14mm diameter) transducers (Ismail & Rammah, 2005) and another photo of a commercial shear plate setup are presented in Figure 2.3. Figure 2.4 displays the University of Western Australia shear plate (Ismail & Rammah, 2005) and a commercial shear plate. These figures depict the sizes of the currently existing shear plates.

The earliest work involving transducers to generate and receive shear waves in a soil specimen utilized shear plates of either quartz crystal or piezoelectric ceramic. There are several disadvantages with this type of transducer, the main problem being the large mismatch between the characteristic impedance (i.e. stiffness characteristics) of the element and that of a soil specimen. In other words, the mechanical motion that is transferred from the element to the soil is small because the element exhibits a small movement with a large force and the soil exhibits a large movement with a small force (Shirley and Hampton, 1978). Measurements of V_s by Brignoli, Goti and Stokoe, II (1996) demonstrate that the shear-plate transducer provides shear waveforms similar to those generated with the more widely used bender transducers. Shear-plate transducers give weak signals at low confining pressures that increase rapidly while increasing confining pressure. The strength of shear-plate signal overcomes those from bender transducers at confining pressures above 50 kPa.

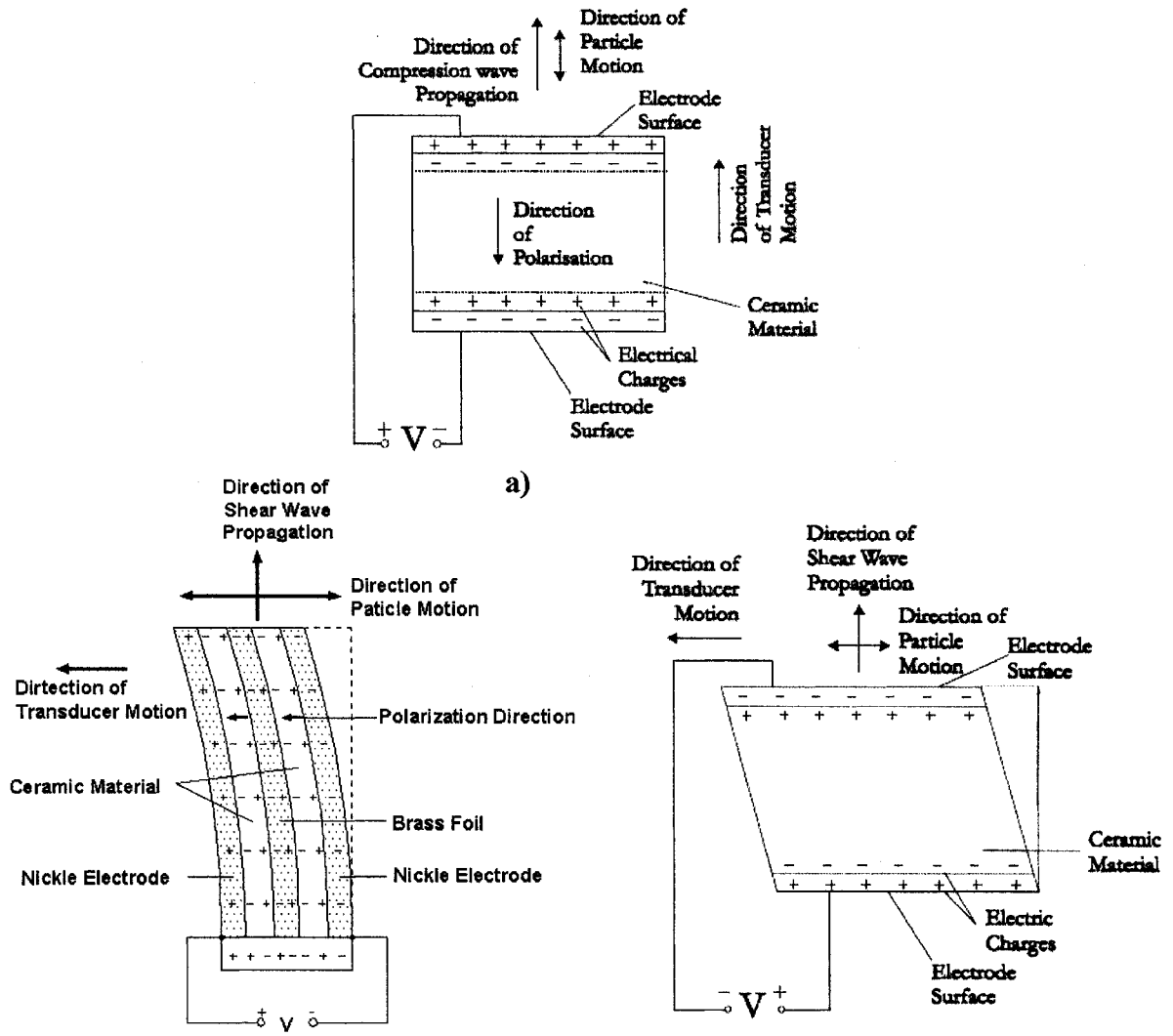

Figure 2.2 Wiring, Polarization and Displacement Details of Compression (a), Bender (b) and Shear-Plate (c) Transducers (after Brignoli, Goti and Stokoe II, 1996).

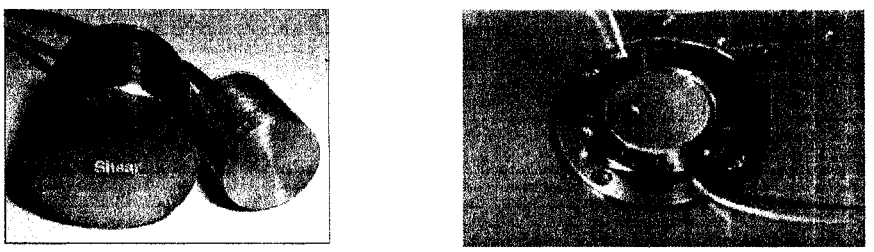

Figure 2.3 Shear-Plate and Compression Transducers by University of Western Australia (Ismail & Rammah, 2005) and a Commercial Shear Plate Setup.

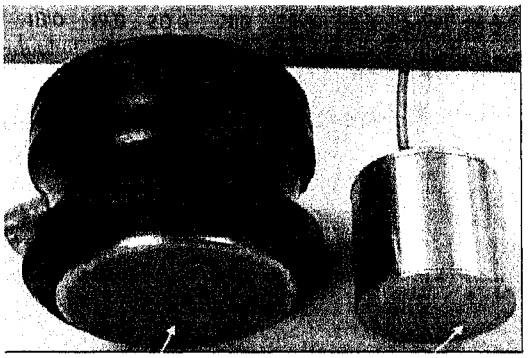

Figure 2.4 Two Sizes of Shear Plate Transducers (Commercial and UWA Plates).

Nakagawa, Soga and Mitchell (1996) used shear plates to create torsional excitations for measuring shear wave velocity of triaxial samples. Figure 2.5 displays the shear-plates arrangement and the setup design which included p-wave transducers as well. It can be realized that the s-wave transducers are behind the sample's end by a certain distance [Figure 2.5(b)]. Hence the transmitting wave from the emitter to the receiver travels through the two end caps during its direct travel path. Therefore, the additional travel time should be subtracted from the measured time.

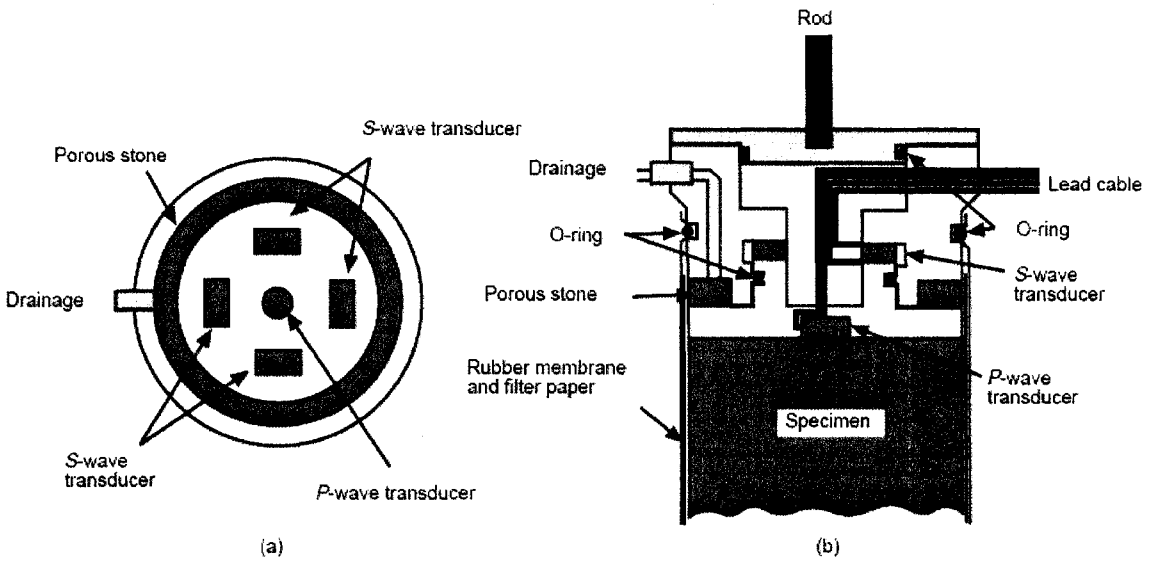

Figure 2.5 Shear-Plates for Torsional Pulse Test in a Triaxial Setup (Nakagawa, Soga and Mitchell (1996).

Nakagawa, Soga and Mitchell (1996) shear-plate transducers had a resonant frequency of 3 to 5 kHz and the p-transducers had 200 kHz. The authors have used an input voltage of

500V to test saturated kaolinite clay (e=1.36 and OCR=1.34) and this needed to amplify the output signal by more than 10^4 times (in two phases), and sometimes the output signal had to be filtered through high frequency pass or low frequency pass analog filters. Also, they have used output signals stacking operation (100 times) to increase the strength of the signal, even for p-wave measurements (Figure 2.6).

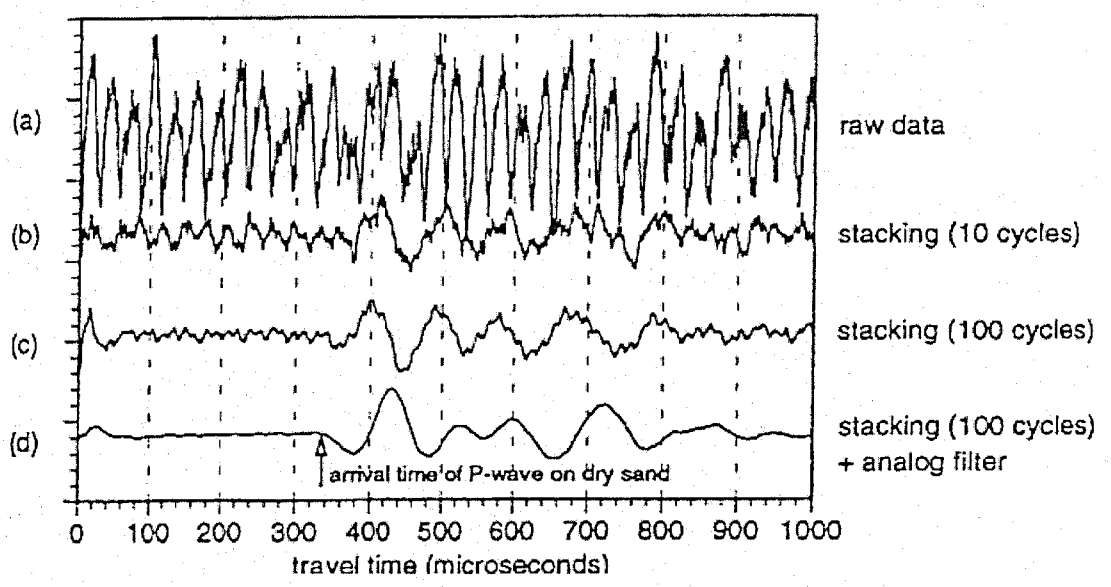

Figure 2.6 Effect of Stacking and Analog Filtering on Wave Signal Forms; Fine Sand Sample under σ'_c = 39.2 kPa (Nakagawa, Soga and Mitchell, 1996).

Some of the output signals obtained by Nakagawa, Soga and Mitchell (1996) on lightly over consolidated clay sample under a pressure of 49 kPa (e_0 = 1.36) are presented in Figure 2.7. On the output signal traces, they had several wave components which were considered by the authors as reflection of unknown waves or reflections of s-wave. Nakagawa, Soga and Mitchell (1996) measured the change in s-wave velocity during consolidation of Osaka-Bay clay using both the Pulse Transmission Method (PTM; torsional excitation by shear-plates), and the Resonant Column Method (RCM). Figure 2.8 displays the obtained results where it is seen that the pulse method gives higher values (about 30% difference) than the resonant column. The authors attributed this difference to the fundamental difference between the two tests, as the shear-plates measure V_s near the center of the sample where there is no or little disturbance due to sample preparation while the resonant column method measures the average rigidity of the whole sample (i.e. the disturbed peripheral part of the specimen affect the rigidity).

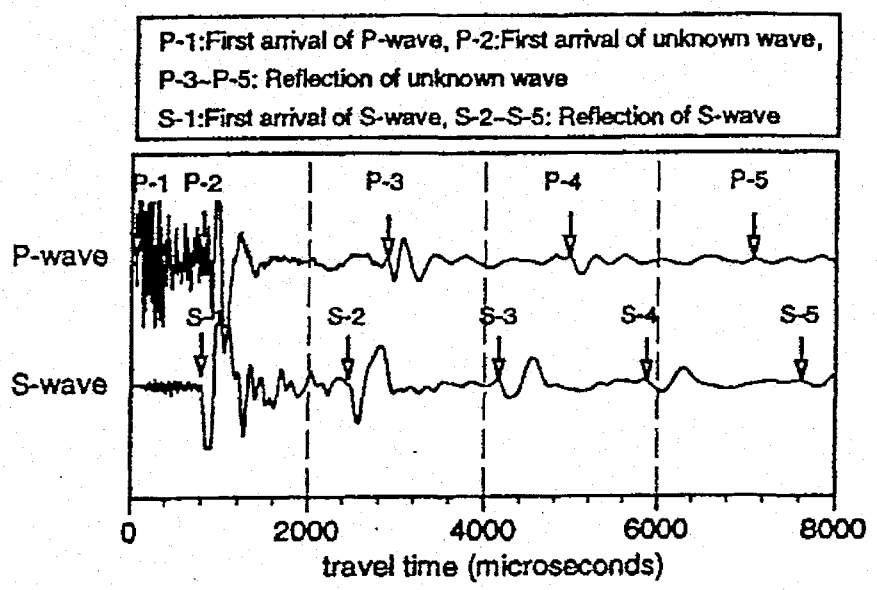

Figure 2.7 P- and S-waves Traces on Lightly Over Consolidated Clay Sample under a Pressure of 49 kPa (e_0 = 1.36) by Nakagawa, Soga and Mitchell (1996).

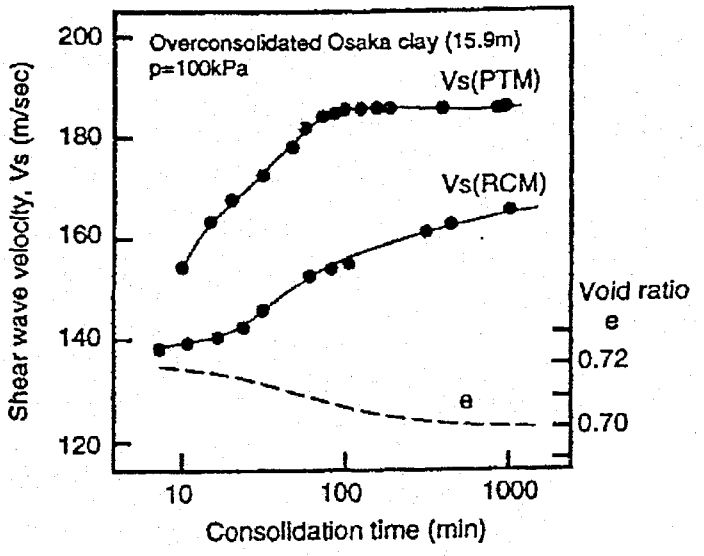

Figure 2.8 Change in S-Wave Velocity during Consolidation of Osaka-Bay Clay by Pulse Transmission and Resonant Column (Nakagawa, Soga and Mitchell, 1996).

Also, continuous increase in s-wave velocity after primary consolidation by the resonant column method was reported while it is nearly constant for the pulse method. This was explained by the very small change of structure of the undisturbed part of the clay sample

(where pulse test is measured) at secondary consolidation and the strength recovery of the disturbed peripheral part at secondary compression. These results show the fundamental differences between bender-elements and resonant column.

2.2.4.2 Bender Transducer

A bender element is an electro-mechanical transducer that either bends as an applied voltage is changed or generates a voltage as it bends [Figure 2.2(b)]. A bender element typically consists of two thin piezoceramic plates rigidly bonded to a central metallic plate. Two thin conductive layers (electrodes) are applied externally to the bender as shown in Figure 2.9. Another wiring for bender elements was introduced by Brignoli, Goti and Stokoe, II, (1996) in Figure 2.2(b). When a driving voltage is applied to the electrode, the polarization causes a bending displacement of the whole element. Benders are usually available in two types that differ simply in the electrical connection to the two polarized plates: a series or parallel connection. The series version is a better receiver, that is, higher output for a given distortion. This response occurs because the voltage is equal to the sum of the potentials available to the electrodes of each ceramic element.

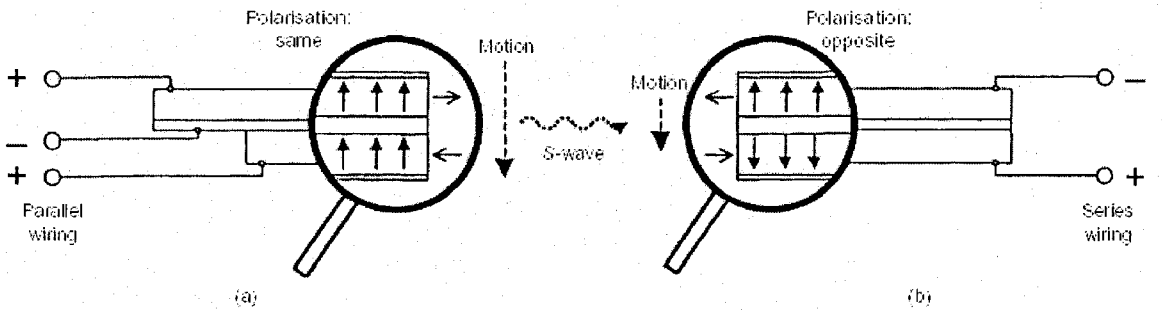

Figure 2.9 Typical Bender Elements Wiring, Polarization and Displacement Details: a) Transmitter; b) Receiver (Lings and Greening, 2001).

The parallel version is better used as a transmitter because it gives the largest distortion for a given input. With this connection, the available voltage is applied to each ceramic plate and is not divided between the two plates as in the series connection. A bender elements setup installed in a triaxial cell is shown in Figure 2.10. It is realized that bender-elements should penetrate into the soil sample which needs further sample preparation. Rough calculations of

the stiffness of the bender element mounted as a cantilever performed by Dyvik and Madshus (1985) indicate that it is in the same order of magnitude as the stiffness of the soil. A close match between the impedance of the transducer and soil makes the bender elements better suited for transmitting and receiving shear waves in a soil than the much stiffer shear plates.

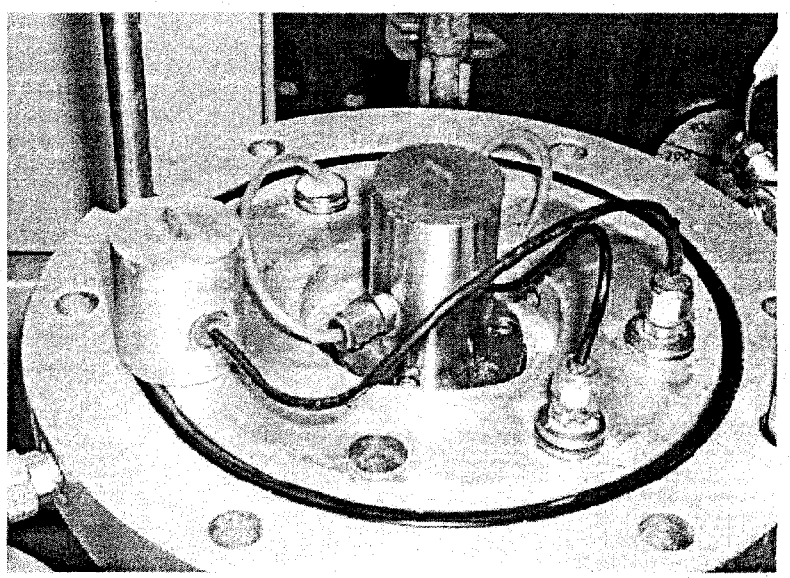

Figure 2.10 Bender Elements Setup in a Triaxial Cell (Nakagawa et al., 1997).

Special preparation of the transducers is required because of their high electrical impedance. It must be shielded from water intrusion at the contact points of the wires as well as grounded to minimize electromagnetic interference. An example of data collected from bender elements, with and without grounding is shown in Figure 2.11. The electromagnetic interference which is a capacitive discharge curve masks the output signal. Santamarina et al. (2001) recommend preparation techniques for piezoelectric transducers in geotechnical studies. In bender elements tests carried out by Wang et al. (2007), a stacking number of 512 was used to improve the signal-to-noise ratio as well as the resolution of output signal. In addition, filtering and amplification of the signal were necessary.

2.2.4.3 Compression Transducer

For the generation of P-waves, ceramic elements are polarized in the thickness direction, and electrodes are placed on the element faces normal to the polarization direction [Figure 2.2(a)]. This transducer is rarely used because p-wave velocity can be easily measured by the other devices which measure the s-wave velocity.

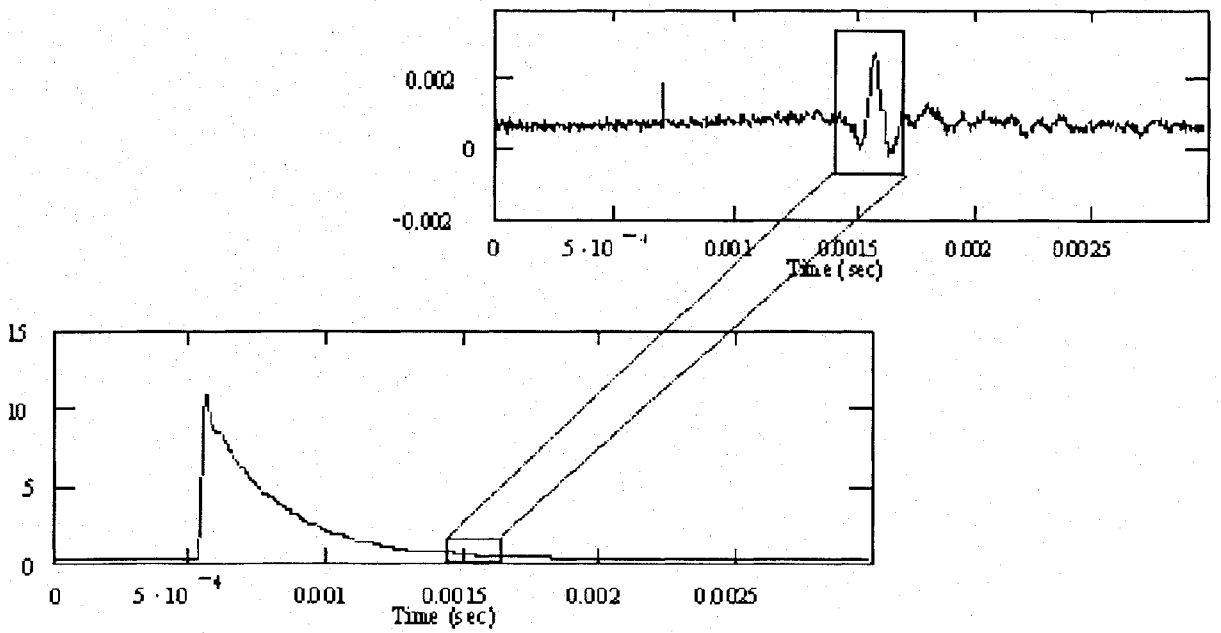

Figure 2.11 Very Large Electromagnetic Interference Masks the Arrival of the Mechanical Wave (Tanner, 2004).

2.2.4.4 Bender/Extender Element

Lings and Greening (2001) introduced a modification to a standard bender element design which resulted in a transducer capable of transmitting and receiving both P-waves and S-waves as shown in Figure 2.12. A control box has been developed to allow transducers to be quickly converted from bender to extender mode.

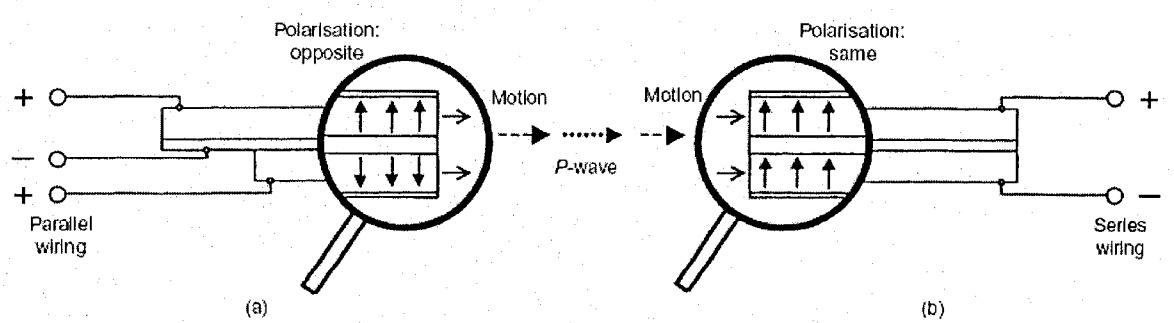

Figure 2.12 Typical Bender/Extender Elements Wiring, Polarization and Displacement Details: a) Transmitter; b) Receiver (Lings and Greening, 2001).

2.2.5 Disadvantages of Currently Existing Piezoelectric Devices

Bender-elements test has many disadvantages as it was reported by many authors. Ismail and Rammah (2005) reported the physical disadvantages of bender elements as follows:

a) The bender element should penetrate into the sample to transmit its bending deformation into shear strains in the surrounding soil. This process is invasive for undisturbed and cemented samples. Digging holes into a sample requires more work to refill the holes with a coupling material, usually epoxy or gypsum; further disturbance to the sample is possible during this handling.

b) The coated bimorph (cantilever bender that consists of two piezoelectric layers) is in direct contact with the soil, and this makes it prone to damage; failure of the epoxy coat will lead to a short circuit and hence loss of signal.

c) The bender element is affected by the stresses within the sample, most notably in the conical zone adjacent to the rough, conventional platens of the triaxial apparatus.

d) The bender element is not suitable for harsh environments, where electrolytes may penetrate through the epoxy, as in the case of electrokinetic treatment in laboratory experiments.

e) Because of its relatively small thickness (0.5 - 1.0 mm), the bender element is prone to depolarization at high voltage (maximum working voltage $\cong$ 100 V per 1-mm thickness). However, this depends on the number of working cycles and shape of the input signal. A higher voltage may be required in situations where signal attenuation is of concern, such as in the case of soft soils or stiff soils with a long travel distance.

f) Two different types of electrical connection are used for the transmitter and receiver for any pair of bender elements, to amplify both the transmitted and received signals: a parallel connection is required for the transmitter and a series connection for the receiver (Figure 2.9). This requires special care during manufacturing and testing.

For shear-plate, it needs high voltage to produce enough energy for a readable output signal. Ismail and Rammah (2005) found that the output signal amplitude of bender-elements is 10-times that of shear plates when testing soft clay sample, although the input voltages were 40 V and 200 V, respectively. The authors attributed this fact to the better coupling between the benders and soil. However, the shear plate performed better than bender elements for both a sandy sample and a cemented sand sample giving about 7 and 25 times, respectively, higher

amplitude than benders. These findings depict the importance of having good coupling between the piezoelectric device and soil. Also, they reflect the preference of shear plates because of their larger contact areas compared to benders.

2.3 Interpretation Methods for Pulse Tests

There are six known methods for the interpretation of pulse velocity tests. This section presents these methods and the commonly used numerical calculations for obtaining the time of flight of a transmitted signal. In order to subserve this analysis, the commonly used theoretical equations in the interpretation process are introduced followed by the used practice. The experiences gained from using these different methods are gathered herein to show the difficulty and ambiguity of signal interpretation.

When interpreting a pulse test in the frequency domain, the number of wave-lengths within the sample (2π-count; N) can be calculated as follows (Greening and Nash, 2002):

$$N = L / \lambda \tag{2.15}$$

where L equals the distance over which the wave is propagated and λ equals the wave length. The wave-number, k, is related to the wavelength, λ, as follows:

$$k = \frac{2\pi}{\lambda} = \frac{2\pi N}{L} \tag{2.16}$$

Hence, the phase velocity is generally given by

$$V_{ph} = \frac{\omega}{k} = \lambda f = \frac{2\pi f L}{\theta} \tag{2.17}$$

where ω is the angular frequency ($2\pi f$), f is the frequency and θ is the phase angle ($2\pi N$). Secondly, the group velocity is defined as

$$V_{gr} = \frac{\delta\omega}{\delta k} = V_{ph} + k\frac{\delta V_{ph}}{\delta k} \tag{2.18}$$

For a dispersive wave transmission, the phase velocity is a function of frequency (Greening and Nash, 2002). By using the N-Frequency relationship, the phase velocity at frequency f_i is found from

$$V_{ph}^{i} = \frac{Lf_i}{N_i} \tag{2.19}$$

which is related to the secant of the N-Frequency graph at point f_i. While, the group velocity is given by the tangent at the point f_i

$$V_{gr} = L\left(\frac{\delta f}{\delta N}\right)_i \tag{2.20}$$

For a non-dispersive system, V_{gr} and V_{ph} are equal (Greening and Nash, 2002). Also, the phase velocity is established from the unwrapped phase-frequency relationship by

$$V_{ph} = 2\pi L\frac{f}{\varphi} \tag{2.21}$$

where ϕ is the phase difference between two signals. Thus, the phase difference can be calculated as follows:

$$\varphi = \frac{2\pi L}{\lambda} \tag{2.22}$$

The group velocity is also calculated as follows:

$$V_{gr} = 2\pi L\frac{\delta f}{\delta \varphi} \tag{2.23}$$

The previous equations are used for pulse tests interpretation in the frequency domain. The following subsection presents the different existing interpretation methods for pulse tests.

2.3.1 Phase Velocity Method

The phase velocity technique depends on the fact that the input and output signals are composed of many frequencies. Using the phase of the cross-power spectrum $\Phi(f)$, it is possible to determine the phase velocity, $V_{ph}(f)$, for each frequency component as

$$V_{ph}(f) = \lambda/T = \lambda f = 2\pi f L/\Phi(f) \tag{2.24}$$

Consequently, if the input signal is a wave of certain frequency, the travel time for that frequency is determined using this technique for calculating the shear wave velocity.

2.3.2 Direct Arrival Method

Travel time of an impulse wave between two points in space may be taken as the time between the first direct arrival of the wave at each point. This method of interpretation

assumes plane wave fronts and the absence of any reflected or refracted waves [Arulnathan, Boulanger and Riemer (1998)]. In applying this approach to bender element tests, travel time has been estimated as the time between the start of the voltage pulse input to the transmitting bender and the first deflection in the output signal from the receiving bender. In other words, the time difference between the wave generation at emitter and the wave capture receive at the receiver is time-of-flight using this method (Figure 2.13). Different points have been suggested by several authors as the point of arrival of shear wave (points 0, 1, A, b, C, or D on Figure 2.13). The difficulty in identifying an unambiguous first (direct) arrival time is documented by many researchers. The time-of-flight method suffers from a major problem (Blewett, I. Blewett, Woodward, 1999). The group velocity dispersion (GVD) in the sample leads to different frequency components within the voltage-edge wave form arriving at different times, thus severely distorting the transmitted signal.

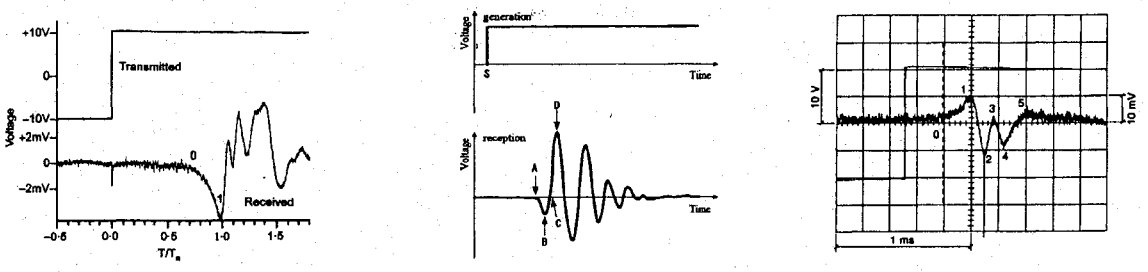

a) b) c)

Figure 2.13 Voltage Variation at Receiver for Step-Input Excitation [After: a) Jovicić, Coop and Simic (1996), b) Arulnathan, Boulanger & Riemer (1998) and c) Viggiani and Atkinson (1997)].

2.3.3 Second Arrival of the Output Signal Method

Output signals, such as the one shown in Figure 2.14(a), often show a clear second arrival of the input wave. This second arrival is just the input wave after it reflects from the receiver cap (first arrival), travels back to the transmitter cap where it reflects again, and then returns to the receiver cap a second time. Assuming plane wave propagation, the time between the first and second arrivals in the output signal is equal to twice the travel time of the wave from cap to cap (Boulanger et al. 1998). This travel time may be determined using either the characteristic peaks (e.g., points A' to A", B' to B", or C' to C" in Figure 2.14) or cross-correlation methods [Figure 2.17(a)].

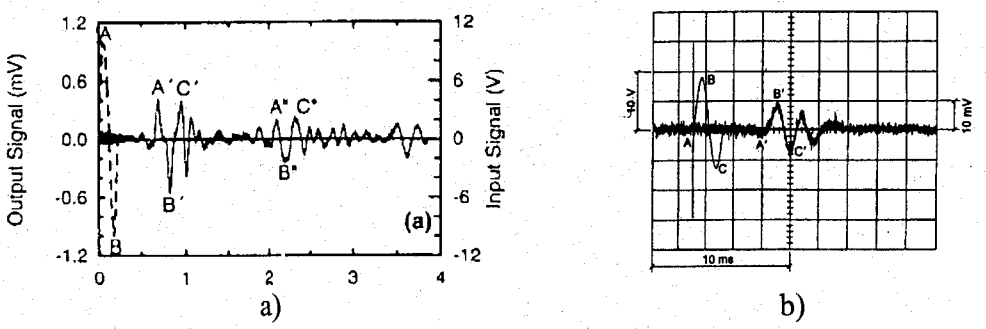

Figure 2.14 Bender Element test Results: input and output signals [After: a) Arulnathan, Boulanger and Riemer (1998) and b) Viggiani and Atkinson (1997)].

2.3.4 Characteristic Points Method

Travel time of an impulse wave between two points in space may be taken as the time between characteristic points in the signals recorded at these two points, again based on the assumption of plane wave fronts and the absence of any reflected or refracted waves. The most commonly used characteristic points are the first peak, first trough, or zero crossings of the input and output signals. For the bender element test in Figure 2.14, the travel time might be taken as the time between Points A and A' (t_a) or Points B and B' (t_b). The propagating wave always experiences a gentle spreading as it travelled through the sample (Viggiani and Atkinson, 1997). Because of this spreading, Jovicić, Coop and Simic (1996) expected that the travel time t_o, which is the beginning of transmitted wave to the first inversion of the received wave, would be the closest to the correct arrival of the shear wave. The first peak-to-peak, t_a, and trough-to-trough, t_b, time should only be used if t_o, t_a and t_b are all equal. Viggiani and Atkinson (1997) concluded that the use of characteristic points (usually the peaks) on the input and output signals to identify travel time is a simpler alternative provided that it is first shown to be consistent with the more rigorous cross-correlation analyses for a given set of test conditions. Kawaguchi, Mitachi and Shibuya (2001) mentioned that the peak-to-peak travel time between input and output pulses as suggested by Viggiani and Atkinson (1995) could essentially be incorrect. This definition may be practically acceptable only when the frequency of shear wave is high enough.

2.3.5 Cross-Correlation Method

Cross-correlation has often been suggested to determine the travel time between two signals, in laboratory and field testing. The cross-correlation function $CC_{xy}(t)$ is a measure of the degree of correlation of two signals X(t) and Y(t). The analytical expression of the cross-correlation function is as follows:

$$CC_{xy}(T_t) = \lim_{T \to \infty} \frac{1}{T} \int_T X(t) Y(t + T_t) dt \tag{2.25}$$

where T is the time record and T_t is the time shift between the signals.

It is usual to calculate the cross-correlation in the frequency domain using the following steps. A Fast Fourier Transform (FFT) transforms the time domain records to the frequency domain. The linear spectrum $L_x(f)$ of a signal X(t) is a function of frequency and is given by

$$L_x(f) = \text{FFT}[X(t)] \tag{2.26}$$

The linear spectrum is a vector in the complex field; its magnitude and phase are respectively the amplitude and the phase shift of each of the harmonic components of the signal. The linear spectra of the signals shown in Figure 2.14(b) are given in Figure 2.15. The cross-power spectrum $G_{xy}(f)$ of two signals X(t) and Y(t) is given in the following equation

$$G_{xy}(f) = L_x(f) \cdot L_y^*(f) \tag{2.27}$$

where $L_y^*(f)$ = the complex conjugate of the linear spectrum of Y(t).

For each frequency, the magnitude and phase of the cross-power spectrum are respectively the product of the amplitudes and the phase differences of the components of the two signals at that frequency. Figure 2.16 displays the cross-power spectrum phase diagram of the signals in Figure 2.14-b. From the magnitude it is possible to identify the range of frequencies that are common to both signals. The cross-correlation $CC_{xy}(t)$ is the inverse FFT of $G_{xy}(t)$ as follows:

$$CC_{xy}(t) = \text{IFFT}[G_{xy}(t)] \tag{2.28}$$

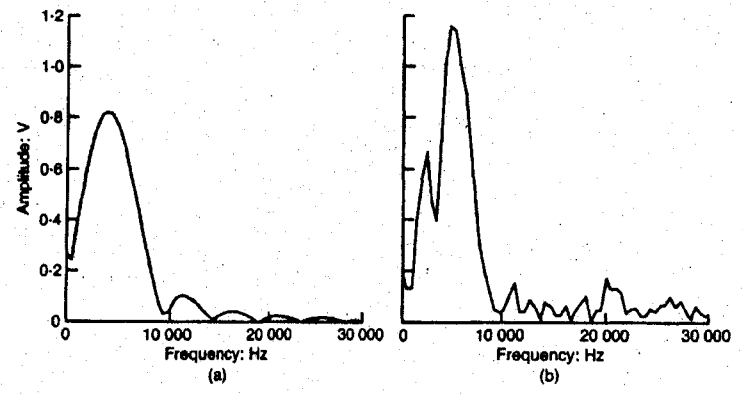

Figure 2.15 Linear Spectra of the Signals Shown in Figure 2.14-b: a) Transmitter b) Receiver (After Viggiani and Atkinson, 1997).

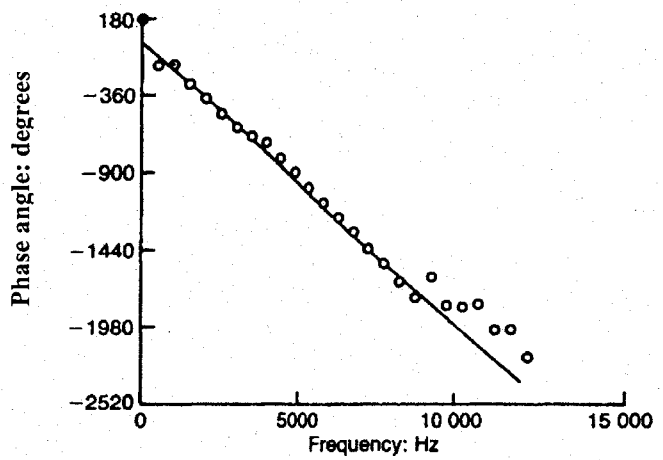

Figure 2.16 Cross-Power Spectrum Phase diagram of the Signals in Figure 2.14-b: (After Viggiani and Atkinson, 1997).

These calculations take only a few steps in a mathematics program and are no longer difficult task. The cross-correlation analysis is based on the assumption that the travel time is equal to the time shift T_{tcc} corresponding to the maximum of Equation (2.25), where X(t) is the signal at the receiver and Y(t) is the driving signal. Thus, T_{tcc} represents the travel time for the whole waveform. Figure 2.17 shows the cross-correlation of the signals in Figure 2.14 normalized with respect to the maximum absolute value, CC_{xymax}. Viggiani and Atkinson (1997) recognized that they were cross-correlating a signal input to one element with a signal output from another and that the input signal to the transmitter may not truly represent the motion of the element. However, using self-monitoring elements, they have found that with a

single sine pulse excitation the frequency spectrum of the input signal was similar to the frequency spectrum of the signal from the self-monitoring circuit. Consequently Viggiani and Atkinson (1997) did not believe that the cross-correlation analyses in their work were subject to significant error. This fact depicts the importance of investigating the actual deformation of a piezoelectric device.

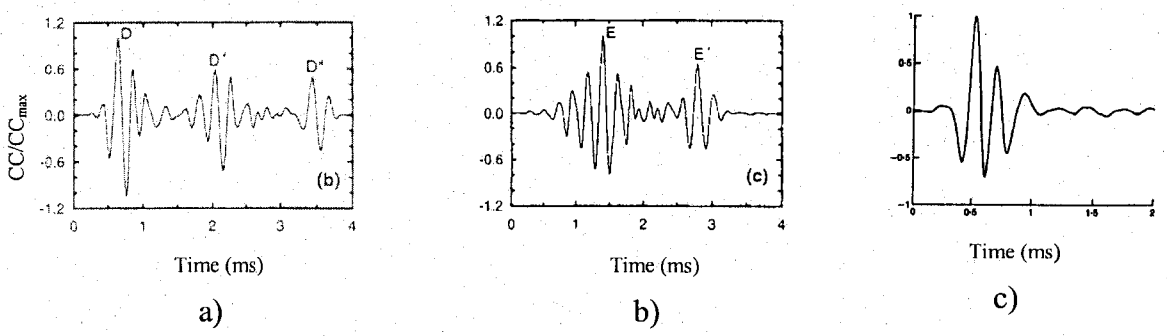

Figure 2.17 Bender Element Test Results: a) & c) C.C. of Output to Input Signals. b) C.C. of Output to Output Signals (Second Arrival Method) [after: a) & b) Arulnathan, Boulanger and Riemer (1998), c) Viggiani and Atkinson (1997)].

2.3.6 Group Velocity Method

A group travel time for a given range of frequencies, T_g, can be calculated by linearly interpolating the absolute cross-power spectrum phase diagram in that range of frequencies (Bodare & Massarsch, 1984). The cross-power spectra for the time records shown in Figure 2.14(b) are shown in Figure 2.18. The absolute cross-power spectrum phase diagram is shown in Figure 2.16 and the best-fit line slope, α, can be used to calculate the group travel time.

$$T_g = \alpha / 2\pi \qquad (2.29)$$

Viggiani and Atkinson (1995) results showed that the travel times calculated using the cross-correlation and phase velocity methods are almost identical.

2.4 Difficulty of Signals Interpretation

2.4.1 Introduction

In spite of the popularity of bender element test, the determination of correct shear wave arrival time is still an unsolved issue (Shibuya, 2000). This section further discusses the measurement and interpretation problems of pulse tests.

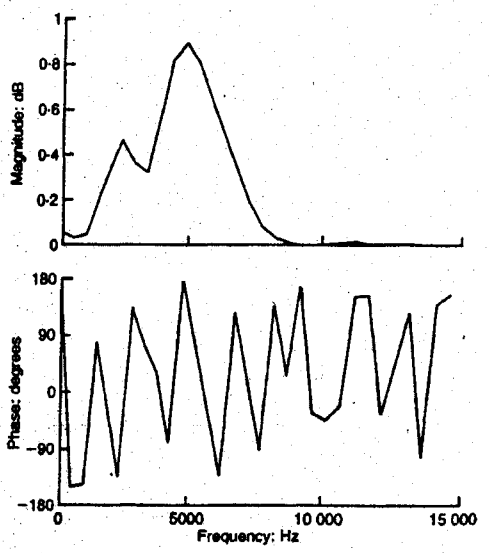

Figure 2.18 Cross-power Spectra of the Signals Shown in Figure 2.14-b (After Viggiani and Atkinson, 1997).

2.4.2 Signals Interpretation Problems

Following the recording of a piezoelectric test signals, the user has to decide which point on the received signal represents the correct arrival time. It is commonly taken that the first deflection of the received signal indicates the arrival of the wave. However, Dyvik and Madshus (1985) and Brignoli et al. (1996) suggested that the arrival of the shear wave is represented by the first maximum of the received signal. The potential error between these two interpretations is an overestimation of shear modulus of up to 14% (Viggiani and Atkinson, 1995). The determination of travel time by cross-correlation presumes that both signals are of the ''same nature'' (Santamarina & Fam, 1995). If this requirement is not fulfilled, cross-correlation may produce incorrect results. Jovicic et al. (1996) mentioned that the main problem of a pulse test interpretation is the subjectivity involved when determining an arrival. For example, cross-correlation is not warranted when one of the two signals is the result of multiple travel paths or diffraction effects. The peak of the cross-correlation or the cross-power spectrum analysis will strictly identify the travel time of the wave if the shape of the wave remains unchanged, so that the waves must be of predominantly one type, either compression or shear. If these techniques are to be applied more accurately, the near-field effect must therefore be minimized. Furthermore, the frequency of the received wave needs to be similar to that transmitted (Santamarina & Fam, 1995). Mancuso, Simonelli and Vinale

(1989) recommended that the time domain record to be decomposed into a group of harmonic waves of known frequency and amplitude. Cross correlation method yield physically impossible travel times (Tanner, 2004). This is probably due to the frequency shift between successive signals caused by the change in effective stresses in the soil specimen (Santamarina and Fratta, 1998).

Analytical solutions made by Sanchez-Salinero et al. (1986) for the body waves (P- & S-waves) generated by point sources in a 3-D elastic space were used to show that the wave fronts spread in a spherical manner. The travelling signal involved coupling between waves that exhibited the same particle motion but propagated at different velocities (compression and shear) and attenuated at different rates. The coupling of these waves at locations near the source was shown to obscure the first direct arrival of shear waves and to affect the travel times calculated using characteristic peaks, cross-correlation, or phase velocity methods. Sanchez-Salinero et al. (1986) have calculated the shear wave velocity between two receiver points, p1 & p2. In that study, the cross-correlation method was shown to be accurate for determining shear wave velocities for cases where the distance from the source to the first receiver (d_1) was greater than one shear wavelength (λ) and the distance from the source to the second receiver (d_2) was twice d_1. The phase velocity method was shown to develop significant errors, for a typical receiver spacing of $d_2/d_1 = 2$, when the ratio of d_1/λ was less than 1. These results illustrate the effect of the testing frequency on the shape of the received signal. It also highlights the difficulty of interpreting signals recorded near the source using conventional techniques due to P- and S- waves overlap.

Arulnathan, Boulanger and Riemer (1998) studied analytically and experimentally the errors in determining V_s from bender elements test by varying the frequency and the bender element length. They showed that the shape and magnitude of the output signal are significantly affected by the input frequency. They concluded that the errors in the travel time are a direct consequence of not accounting for the interference between incident and reflected waves at the receiving bender. The authors suggested that near-field effect is a primary source of error in pulse tests. Also, they concluded that the travel time errors from their bender element tests depend on the wave length to the bender element ratio (λ/L_b), the travel distance to wave length ratio (L_{tt}/λ), the method used to calculate the travel time, the relative stiffness of the soil and bender element and Poisson's ratio. Zeng and Ni (1998) have indicated that the

size of the bender element also affects the clarity of the shear wave first arrival. They concluded that if the stress levels are high enough, 300 kPa for their experiment, the motion of the bender will be inhibited. In order to correct this problem, the researchers optimized the size of the bender elements by experimentation taking into account stress levels, mounting techniques, sample size and tip-to-tip distance.

Also, numerical results conducted by Santamarina & Fam (1995) showed that the computed travel time generally differs from the true travel time. They stated that errors depend on the damping ratio between measurement device and tested soil, the natural period of "*the system*" ($1/F_n$) and the period of the input sine. Table 2.1 summarizes Santamarina and Fam (1995) numerical results; the error in computed travel time is normalized with respect to the natural period of the system. These results show that when cross-correlation method is used, the period of the input cycle T_{in} should be equal to or shorter than the natural period of the system (T_n) and that devices with higher damping ratio, D, are preferred. In general, travel times are a few T_n long; hence the percentage error with respect to travel time is smaller than the values shown in the table. The authors reported that the use of automated cross-correlation algorithms should be avoided in low-damping systems where the highest cross-correlation peak (the second peak) is approximately T_n away from the real value (first peak in the cross-correlation function). This means that the error depends on soil properties because it contributes to the natural period of the system. These results confirm the potential errors associated with cross correlation technique.

Table 2.1 Damping Ratio and Input Frequency Effect on the Error of Travel Time Using Cross-Correlation Method (Santamarina and Fam, 1995).

T_{in}/T_n	Fr_{in}/Fr_n	Damping (D)			
		10 %	20 %	30 %	40 %
0.5	2.0	+9.0	+8.0	+7.0	+6.0
0.8	1.25	+5.8	+5.1	+3.8	+3.3
1.0	1.0	0.0	0.0	0.0	0.0
1.25	0.8	-7.2	-6.8	-6.2	-5.8
2.0	0.5	-37.0	-32.0	-29.0	-26.0

* Error is a percentage of natural period of the system, T_n.

Hence, it is important to stress that the accuracy of V_s values obtained using bender element tests is not perfect [Salgado, Bandini and Karim (2000)]. Further investigations are necessary to clear the ambiguity of piezoelectric testing. Also, more advanced interpretation techniques are needed to overcome the interpretation difficulties. The role of frequency in signals interpretation should be further investigated. Moreover, the wave reflection at boundaries (sample sides and end caps) should be eliminated or separated from the received signal in order to get accurate and reliable interpretation results.

2.4.3 Sources of Errors in Transducer Elements Test

The error in calculating shear wave velocity may exist due to errors in calculating the sample length and/or the travel time. Therefore, Viggiani and Atkinson (1995) suggested following equation for the potential error in the shear modulus (ΔG_{max}).

$$\Delta G_{max} = \Delta\rho/\rho + 2\Delta L/L + 2\Delta t/t \qquad (2.30)$$

where $\Delta\rho$, ΔL and Δt are the errors in *density, Length* and *time* respectively.

There are some factors which contribute to the error in calculating travel time, namely, input frequency, near-field and waves interference. Those points are discussed in the following subsections.

2.4.3.1 Input Frequency

The optimum frequency of excitation depends on many factors such as soil rigidity and type of transducer (Brignoli, Goti, and Stokoe, II, 1996). Examining the signals at the receiver for increasing excitation frequencies of the transmitter is helpful during shear wave measurements when shear and compression waves strongly couple together in the output record. Since P- and S-waves travel at different speeds, they combine differently at different frequencies. Therefore, Brignoli, Goti, and Stokoe II, (1996) recommended that the velocity measurement is performed at a frequency for which a clear wave arrival is obtained. Additionally, in the case of V_s measurements, at least two wavelengths should be maintained between the transmitter and receiver ($L/\lambda \geq 2$) in order to perform the measurement in the far field (Sanchez-Salinero et al. 1986). In the case of a V_p measurement, the highest possible frequency should be used so that a constrained wave compression will be measured.

Shear wave measurements on specimens of 10-cm to 14-cm-height are usually carried out with frequencies ranging between 1 and 20 kHz, with the most interpretable waveforms

typically occurring in the 3 to 10-kHz range. For V_p measurements in similar saturated specimens, 100-kHz input frequency has always allowed excellent measurements. In case of V_p measurements on dry soils, the clearest wave arrivals have been obtained at lower frequencies, typically 40 to 80 kHz (Brignoli, Goti, and Stokoe, II, 1996). In contrast to P-waves, V_s measurements require more care in signal analysis. Care is necessary because the waveform at the receiver is not composed of only shear waves around the arrival time. The waveform is more complex. Therefore, to discriminate the arrival time of the shear wave in the waveform, one must understand the range in typical waveforms.

Brignoli, Goti, and Stokoe, II (1996) carried out a series of tests on saturated sand and soft clay samples and concluded that the initial S-wave peak tends to attenuate more rapidly than the remaining part of the signal as the height-to-diameter ratio of the sample increases. In case of the sand specimen with the greatest height (14-cm), the S-wave arrival is difficult to differentiate from the p-wave components in the waveform. In this case, examination of the signals at the receiver by varying the excitation frequency during the testing assisted in identifying the initial arrival. Kawaguchi, Mitachi and Shibuya (2001) studied the effect of form and frequency of input pulse at reception on NSF-clay and found that the amplitude of peaks at reception depends greatly on the initial movement velocity of the triggered bender or in other words depends greatly on the input frequency. They have suggested to perform bender element test with input pulse using various kinds of waveform over a wide rang of frequencies. Thus, it can be concluded that further investigations of piezoelectric test are needed in order to discover the role of frequency in signals interpretation.

2.4.3.2 Near-Field Phenomenon

The near-field effects in bender element tests have been recognized by previous investigators with references made to the findings of Sanchez-Salinero, Roesset & Stokoe (1986). Evidence for the existence of near-field components in bender element tests was found by Brignoli and Gotti (1992). Also, Jovicić, Coop. & Simić (1996) confirmed the existence and effect of near-field in their research results numerically and experimentally. Sanches-Salinero, Roesset & Stokoe (1986) developed an analytical solution for the time record at a monitoring point that would result from excitation with a transverse sine pulse of a point source within an infinite isotropic elastic medium. Their theoretical studies showed that the *first deflection* of the signal

may not correspond to the arrival of the shear wave but to the arrival of the so-called near-field component which travels with the velocity of a compression wave. The resulting wave was far from being a simple transversely polarized shear wave propagating in a longitudinal direction, as is assumed by the method. It was found to have coupled components, corresponding to the three terms as shown in Equation 2.31. All three terms represent transverse motion, but they propagate with different velocities; the first two (Γ_1 and Γ_2) with the velocity of a shear wave, and the third (Γ_3) with the velocity of a compression wave. For the three components the attenuation arising from the geometrical damping occurs at different rates, the second and third terms (Γ_2 and Γ_3) attenuating an order of magnitude faster than the first term (Γ_1), which represents the far field pure shear wave. The coupling of these waves was shown to obscure the first direct arrival of shear waves and to affect the travel times calculated using characteristic peaks, cross-correlation, or phase velocity methods at locations near the source.

$$\Gamma = \overbrace{\Gamma_1}^{\text{s-wave}} + \underbrace{\Gamma_2}_{\text{far field}} \overbrace{- \Gamma_3}^{\text{p-wave}} \quad \underbrace{\qquad}_{\text{near field term}} \tag{2.31}$$

Parametric studies of the propagation of elastic waves in an elastic medium by Mancuso and Vinale (1988) show that the near-field effect may mask the arrival of the shear wave when the distance between the source and the receiver is in the range 0.25-4.0 wavelengths, which can be estimated from $\lambda = V_s/f$ where f is the mean frequency of the received signal. Arulnathan, Boulanger and Riemer (1998) evaluated that "near-field" effects are potentially more complicated in a triaxial specimen than in the unbounded 3-D space considered by Sanchez-Salinero et al. (1986) because: (1) interpretation methods that use the input signal are similar to using a d_1/λ of zero (d_1 = distance from source to the first receiver), and so near-field waves will be stronger than were considered in many of their analyses; (2) the spherically spreading wave fronts that are generated by the transmitting bender can reflect from the boundaries and therefore travel between benders by indirect paths; and (3) the transmitting bender is not a point source. Consequently, the assumption of planar wave fronts moving one-dimensionally between the caps will introduce errors in addition to the near-field effects identified by Sanchez-Salinero et al. (1986).

Jovicić, Coop. and Simić (1996) confirmed the existence and effect of near-field in their research results numerically and experimentally. They have stated that the principal problem with the method has always been the subjectivity of the determination of the arrival time used to calculate V_s. They developed techniques for making measurements in stiffer materials, for which the potential error in stiffness through incorrect identification of the arrival time is greatly reduced. Jovicić, Coop. and Simić (1996) mentioned that the simplest way to obtain a bender element trace that may be interpreted objectively is to use a sinusoidal wave rather than the more usual square wave and to select a high enough frequency. Unfortunately, this cannot always be achieved, as at the high frequencies required for testing stiffer materials, overshooting of the transmitting element can occur. The limiting frequency at which overshooting starts to occur depends on the relative impedances of the soil and the element, and so overshooting becomes a more severe problem in stiffer materials. Therefore, in some circumstances, the measurements need to be made at lower frequencies in the presence of a near field effect. Two methods have been devised by Jovicić, Coop. & Simić (1996) to overcome this problem. The first is to distort the shape of the input wave using the function generator, so that the amplitude of the first upward cycle of the wave may be reduced so as to cancel out the near field effect, giving a distinct arrival of the shear wave as shown in Figure 2.19. Alternatively, the frequency of the input wave may be adjusted so as to give forced oscillation of the receiver at one of its natural frequencies, in which case resonance occurs. In this case the arrival time may be simply taken from one of the peaks or troughs of the input wave and the corresponding point on the output. For any measurement of G_{max}, and particularly if a new soil is being tested, several methods should be tried and the results compared, improving confidence in the data (Jovicić, Coop. and Simić, 1996). Kawaguchi, Mitachi and Shibuya (2001) found that the near-field effect was more significant at low pressures. Moreover, they concluded that the definition of travel time to make use of resonance conditions seems inappropriate, in particular when the frequency of shear wave is low. Brignoli, Goti, and Stokoe, II (1996) carried out a series of tests on saturated sand and soft clay samples. They concluded that the first peak, around the S-wave time of arrival, tends to attenuate more rapidly than the remaining part of the signal as the height-to-diameter ratio of the sample increases.

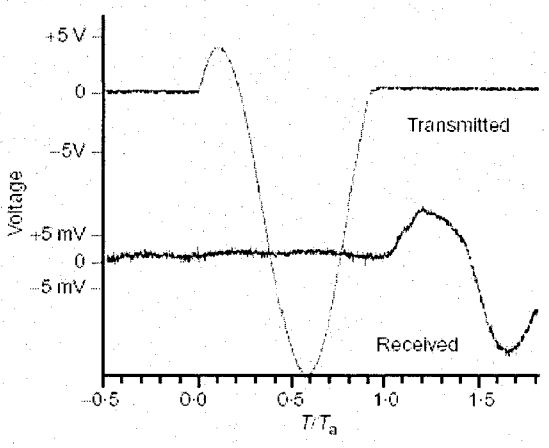

Figure 2.19 Cancelling the Near Field Effect with a Distorted Input Wave (Jovicić, Coop. & Simić, 1996)

Finally, many authors have reported the effect of near-field phenomenon on their laboratory and field tests result. Only two papers [Jovicić, Coop. & Simić (1996) and Blewett, Blewett, I., Woodward, (1999)] have suggested different ways to avoid it. But they have not introduce the cause of this phenomenon or why it is being cancelled using their techniques. Moreover, they have not showed whether the cancellation process results in giving accurate determination or not. Thus, it can be concluded that further investigation of piezoelectric pulse test is needed in order to put a criteria for objective results. Also, it is necessary to know how and at what conditions the reflection of waves at boundaries (sample sides and end caps) interrupts the interpretation. These interferences should be eliminated or separated from the received signal in order to obtain accurate and reliable results.

2.4.3.3 Wave Interference at the Rigid Boundaries

Arulnathan, Boulanger and Riemer (1998) investigated the interference of incident and reflected waves at the rigid boundaries (end caps) by performing a one-dimensional wave propagation analysis of cantilever type bender element tests. They found that interference can affect the interpretation of travel time. The main evidence of interference effect was that the input waves were sine-impulse (with two peaks) while the received waves were impulses with 4 peaks. The additional two peaks were an effect of reflected waves at end-caps. Furthermore, increasing input frequency, the amplitude of the received wave increased and the length of the received wave decreased. The cross-correlation gave the correct travel time when the ratio

λ/L_b (input wave length/bender element length) was less than or equal 4. As λ/L_b increases beyond this limit, the travel times are progressively underestimated, hence the V_s is overestimated.

Part of the difficulty in identifying the wave arrival arises from the fact that the wave which arrives first may not necessarily be the sought after shear wave. The reflected compression waves at sample sides can interfere with the positive identification of the direct shear wave. The results of the analysis conducted by Tanner (2004) for bender elements tests in an oedometer cell indicate that the first arrival will not be the shear wave but rather the compression wave that is reflected from the walls of their Plexiglass cell (H=76.6mm, D=63.2mm & L_b=7.5mm). A set of benders were mounted horizontally in the cell walls used by Tanner. Thus, the travel paths of the transmitted waves were in the horizontal plane. In order to avoid this complication, Tanner recommended that the geometry of the cell be designed such that the reflected compression wave will not reach the receiver before the direct shear wave. But Tanner (2004) has not considered the reflected p-wave which travels in the same direction of direct s-wave (i.e. cap reflection). This wave is reflected from the wall just behind the emitter and is recorded on the received signal before the other reflected wave which comes from the far walls of the cell.

2.4.4 Signal Dispersion

Viggiani and Atkinson (1995) mentioned that the shape of the received signal may be different according to the stiffness of the soil and the degree of fixity of the bender elements into the platens of the apparatus. Based on their bender element tests on over-consolidated boulder clay, they concluded that each of the cross-correlation and the group travel times, T_{cc} & T_g, can be regarded as the most accurate. These were always significantly larger than the time of the first deflection of the received signal (T_o). Greening and Nash (2002) noted that the causes of the nonlinear and, hence, dispersive behaviour in pulse tests may arise anywhere between generation of the input signal and the final measurement point. Blewett et al. (2000) showed that the relationship between phase and frequency contains nonlinearities indicating that the test setup causes *dispersion*. This phenomenon (e.g. Havelock 1914) is well known, especially in the physics literature, and can occur for a number of reasons (Sasche and Pao 1978), namely:

1. The presence of specimen boundaries;
2. Frequency dependence of material constitutive parameters;
3. Wave scattering by material inhomogeneities;
4. Dissipation of wave energy into heat; and
5. Amplitude dependence of wave speed.

Noting that the measured response includes the mechanical and electrical behaviour of the benders, as well as the characteristics of the material, Blewett et al. (2000) proposed a model for dispersion that includes a phase shift of π radians arising from the resonance of the bender element, as well as a frequency dependence of G_o of the material. The work alludes to the influence of specimen boundaries on the dispersion characteristics, but the effects are not quantified in their model (Greening and Nash, 2002).

Blewett, Blewett, I. and Woodward (2000) reported that the main problem associated with the use of square wave excitation is that group velocity dispersion (GVD) in the sample leads to the separation of different frequency components within the voltage-edge waveform. These components propagate at different speeds, arriving at different times, and producing a severely distorted received signal. It is recognized that, for a reduced number of frequency components in the driving voltage, the resulting distortion of the received pulse will also reduce. Therefore, the sine-input was preferred by many researchers. Other input-shapes that have smooth rise and end are more versatile because they reduce the frequency range of the input signal. Moreover, any practical pulse comprises a range of frequencies, giving rise to the possibility of distortion simply due to the natural propagation by and within physical subsystems possessing a non-uniform response to each of the frequency components (Santamarina and Fam 1997).

These findings reflect the dispersive nature of pulse tests in soil and the complexity of the test. Blewett, Blewett, I. and Woodward (2000) also reported that due to waves dispersion, a 'shear-modulus' should always be accompanied by a frequency range over which the parameter remains valid. Their bender-elements tests on Levenseat poorly graded fine sand employing continuous sinusoidal input wave at different frequencies gave indefinite trend between velocity and frequency (Figure 2.20). The change in this graph is around the resonance frequency of the bender ($\cong$ 5 kHz). Therefore it can be considered that this trend is not representative. The researchers concluded that the use of bender elements to measure

shear-wave velocity in the laboratory results in a frequency-dependent response that arises from contributions of the embedded bender elements and the medium rather than the test medium alone. This response causes significant distortion of received pulses where the choice of fundamental frequency lies within the resonant region of the system.

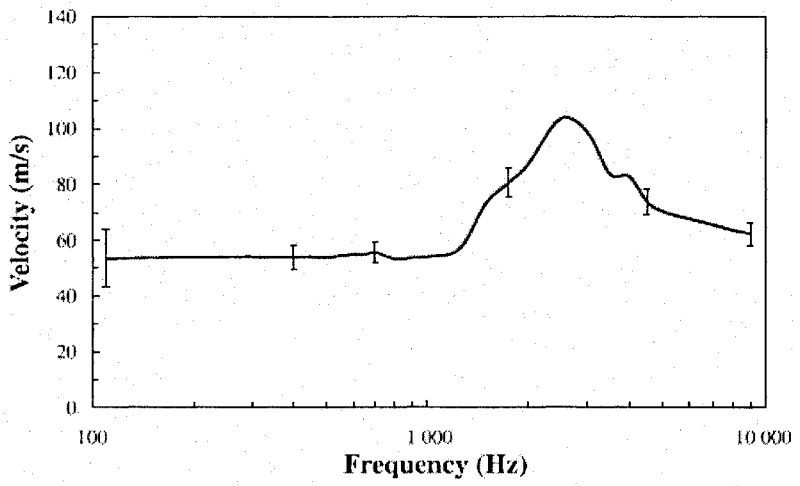

Figure 2.20 Dispersion Curve for Transmitter–Receiver Spacing of 75-mm (Blewett et al., 2000).

Greening and Nash (2002) carried out swept-sine pulse tests on a clay sample and showed a resonance of their bender elements and associated phase shift of 5 radians at around 1.1 kHz. They mentioned that 'while one would expect the transfer functions of the transmitter and receiver benders to cancel one another out, the net phase shift of around 2 radians might result from differences in the mounting arrangements of the benders'. However, Greening and Nash (2002) reported the lack of definition in the phase-velocity relationship at lower frequencies (<1.1 kHz), and alluded that this tends to obscure the dispersion resulting from near-field effect. They found improved definition of this relationship at lower frequencies by using a larger signal (input voltage varied from 0-10V). They attributed the poor definition in this range to high attenuation of the transmitted signal. Also, noise plays an important role in this frequency range. Finally, the authors' results indicate that time domain techniques significantly *underestimate* travel time, compared to their calculated V_{ph} and V_{gr}. They concluded that further work is clearly required to determine which estimates most closely match the true small strain shear stiffness of a soil.

2.4.5 Numerical Studies

The application of a voltage (V) across a free cantilever bender element causes a free deflection (X_f) at the tip that depends on the bender's dimensions and properties. If the bender is restrained against any deflection ($X = 0$), then it will instead develop a blocked force (F_b). A bender embedded in soil will develop some combination of force and deflection (F, X) that is intermediate to the free ($F = 0$, $X = X_f$) and fully restrained ($F = F_b$, $X = 0$) conditions and depends on the relative stiffness of the bender and the soil. In the FE analyses carried out by Arulnathan, Boulanger and Riemer (1998), the input voltage signal applied to the transmitting bender was modeled as an in-phase bending moment uniformly distributed along the length of the bender. A sine pulse input signal was used for all analyses. The output voltage signal from the receiving bender was taken as being proportional to the average bending moment along the length of the bender. The authors reported that the use of bending moments to represent input and output signals in the FE analyses only approximates the complex electro-mechanical behaviour of piezoceramics. Nevertheless, bending moments provide a more reasonable representation of piezoceramic behaviour than is provided by displacements (which were used by Jovicic et al. 1996).

Arulnathan, Boulanger and Riemer (1998) results showed that the cross-correlation calculated V_s values are less than the correct value, with the error being as large as 9% at $L_{tt}/\lambda = 0.50$ and decreasing to 2% or less for $L_{tt}/\lambda \geq 2$ (L_{tt} = travel distance). The cross-correlation gave the correct travel time when the ratio λ/L_b (input wave length/bender element length) was less than or equal 4. As λ/L_b increases beyond this limit, the travel times are progressively underestimated, hence the V_s is overestimated. The calculated V_s values computed by the second arrival method ranged from as much as 12% greater than the correct value at the lowest input signal frequency (giving λ/L_b= wave length/bender element length = 20 and $L_{tt}/\lambda = 0.5$) to 5% smaller than the correct value at a higher input signal frequency (giving $\lambda/L_b = 8$ and $L_{tt}/\lambda = 1.25$). The trend of increasing V_s with increasing λ/L_b ratio is consistent with the expected effects of wave interference at the end caps. Arulnathan, Boulanger and Riemer (1998) stated that the transfer functions, near-field and non one-dimensional wave travel effects can cause an underestimation or overestimation of V_s by significant amounts. Peelamedu et al. (2003) developed a computer code for determining the deformations of piezoelectric materials under static loading. Figure 2.21 shows the deformation of a

piezoelectric ring using four-node tetrahedron mesh. The results obtained from the investigation of multiple piezoelectric geometries including cuboids, cylinders, and *rings* using the developed computer codes were as predicted. No other information could be found in literature about numerical simulations of piezoelectric rings.

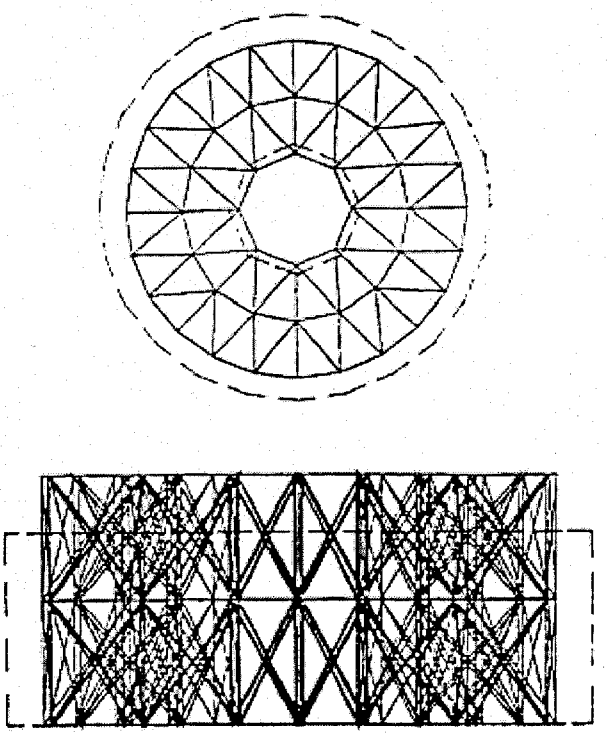

Figure 2.21 Deformation of a Piezoelectric Ring Using Four-Node Tetrahedron Mesh (Peelamedu et al., 2003).

2.5 Empirical Equations for Estimating Shear Wave Velocity

There are many empirical correlations for determining the elastic shear modulus of soil with two main variables (the mean effective stress and the voids ratio). These empirical equations can be used to estimate/evaluate V_s and G_{max} or inversely to determine the voids ratio or the mean effective stress from V_s. Also, the estimated G_{max} using these equations can be compared to field or laboratory measurements as a check of results accuracy or it can be used for estimating soil indices. Since 1960, many studies were conducted for measuring shear wave velocity or shear modulus of different soil types. Some of these investigations introduced empirical or semi-empirical equations for estimating V_s or shear modulus. Namely, Whitman (1960), Hardin and Richart (1963), Hardin and Black (1968), Iwasaki and Tatsuoka (1977),

Hardin (1978), Rosler (1979), Hardin (1980), Yu and Richart (1984), Wroth and Houlsby (1985), Ni (1987), Hryciw (1990), Jamiolkowski, Leroueil and Lo Presti (1991), Hryciw & Thomann (1993), Robertson et al. (1995), Jamiolkowski, Lancellotta and Lo Presti (1995) and Kokusho and Yoshida (1997). Some of these equations are introduced in the following subsections as these equations will be used for comparison with the results obtained in this study. The results of some researches that relate to these empirical equations are also summarized.

2.5.1 Hardin and Richart (1963)

Based on resonant column test results on isotropically consolidated round and angular sands, Hardin and Richart (1963) found that the small strain shear modulus (G_o) and the shear-wave velocity can be related to effective mean normal stress and void ratio as follows:

$$V_s = (m_1 - m_2\, e).(p')^n \tag{2.32}$$

Where Vs = shear wave velocity; e = void ratio; p' = effective mean normal stress; and m_1, m_2 and n are material constants.

Hardin and Richart (1963) found that n equals 0.25 and suggested that m_1 and m_2 have values of approximately 111 and 51 when stress is measured in kPa and shear wave velocity is measured in *m/s*. Hardin and Richart (1963) empirical equation relating G_o to σ'_o and void ratio has been widely used to determine the low-amplitude shear modulus of clean, cohesionless soils. Their empirical relation for G_0 at shear strain of less than 10^{-4} can be written as follows:

$$G_o = C_g P_A^{1-n_g} \frac{(e_g - e)^2}{1 + e} (\sigma'_m)^{n_g} \tag{2.33}$$

Where C_g, e_g, and n_g = regression constants that depend solely on the soil (soil intrinsic variables); σ'_m= mean effective stress; P_A = reference stress in the same units as σ'_m and e = void ratio.

2.5.2 Hardin and Black (1968)

Hardin and Black (1968) presented the following equations for dry sands based on their tests result as well as the test results of Hardin and Richart (1963):

For round grains (Ottawa sand):

$$G_o = \frac{(32.17 - 14.80\,e)^2}{(1+e)}(\sigma'_o)^{0.5} \quad \text{for } \sigma'_o \geq 2000 \text{ psf} \tag{2.34}$$

$$G_o = \frac{(22.52 - 11.60\,e)^2}{(1+e)}(\sigma'_o)^{0.6} \quad \text{for } \sigma'_o < 2000 \text{ psf} \tag{2.35}$$

For angular grains (crushed quartz):

$$G_o = \frac{(30.09 - 10.12\,e)^2}{(1+e)}(\sigma'_o)^{0.5} \tag{2.36}$$

where σ'_o is the mean effective principal stress in Ib/ft^2 and G_0 in Ib/in^2.

2.5.3 Jamiolkowski, Leroueil and Lo Presti (1991)

It is well known from theory of elasticity that maximum constrained modulus (M_o) can be calculated by

$$M_o = \rho V_p^2 \tag{2.37}$$

where V_p is the constrained compression wave velocity and ρ equals soil density.

This leads to the following empirical relationships between the above mentioned moduli and stresses (Jamiolkowski, Leroueil, and Lo Presti, 1991):

$$G_o = F(e)C_G P_a^{1-na-nb}\sigma_a'^{na}\sigma_b'^{nb} \tag{2.38}$$

$$M_o = F(e)C_M P_a^{1-4na}\sigma_a'^{4na} \tag{2.39}$$

$$E_o = F(e)C_E P_a^{1-4na}\sigma_a'^{4na} \tag{2.40}$$

where:

C_G, C_M and C_E are the material constants for shear modulus, constrained modulus and Young's modulus, respectively.

Intended primarily for clay soil, Jamiolkowski, Leroueil, and Lo Presti (1991) reported that in a given soil and for a given structure the maximum stiffness, G_o is linked to σ_m and e by means of the following empirical relationships:

$$G_o = M_G P_a^{1-n} \sigma_m^{'n} \tag{2.41}$$

Being: M_G = dimensionless *modulus number* depending on soil structure, void ratio function $F(e)$ and mineralogy where $M_G = C_G.F(e)$, C_G = the *material constant*, $F(e) = 1/(0.3 + 0.7\ e^2)$ according to Hardin (1978) or $1/e^{1.3}$ according to Lo Presti (1989), n = modulus exponent and P_a is the atmospheric pressure = 98.1 kPa (1 bar). Figure 2.22 presents the shear modulus number M_G versus void ratio for different types of soils. Also, typical values of modulus numbers and exponents for dense dry washed mortar sand, as obtained by Stokoe (1991) from the measured velocity of the body waves, are reported in Table 2.2.

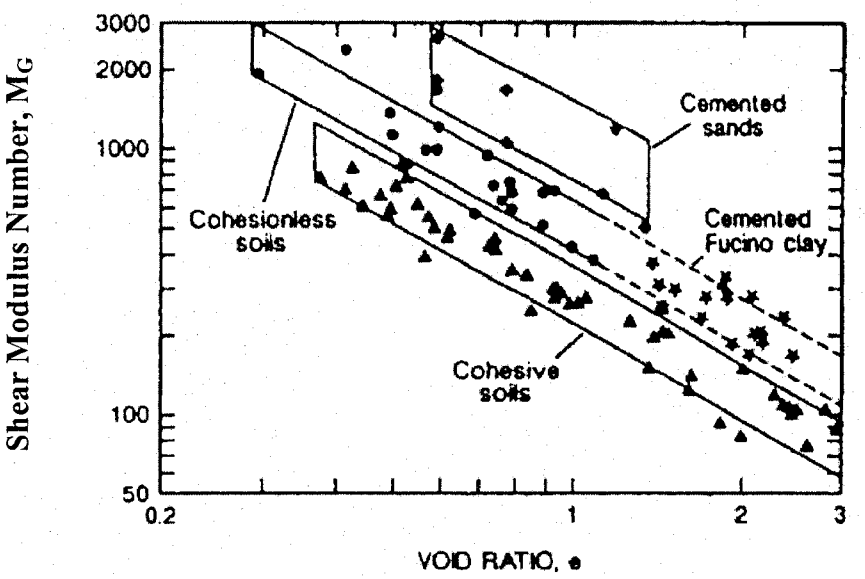

Figure 2.22 Shear Modulus Number M_G versus Void Ratio for Different Types of Soils (Jamiolkowski, Leroueil and Lo Presti, 1991).

Table 2.2 Stiffness Coefficients of Dry Washed Mortar sand from Seismic Body Waves (Stokoe, 1991)

Sand State	Modulus Number	Modulus Number	
Loose	$M_G = 658$	$n_a = 0.39$	$n_b = 0.15$
e = 0.760	$M_M = 1983$	4na = 0.53	-
	$M_c = 1758$	4na = 0.54	-
Dense	$M_G = 767$	$n_a = 0.28$	$n_b = 0.23$
e = 0.587	$M_M = 2020$	4na = 0.42	-
	$M_c = 1758$	4na = 0.44	-

Thus, Jamiolkowski, Leroueil, and Lo Presti equation can be written as follows:

$$G_o = M_G P_a^{1-n} e^{a_g} \sigma_m'^{n} \tag{2.42}$$

where a_g is a regression constant (an intrinsic variable of the soil).

2.5.4 Robertson et al. (1995)

During the consolidation stage in triaxial test, Robertson et al. (1995) carried out bender-elements pulse tests on Ottawa sand and has introduced the following relationship between shear wave velocity (V_s), void ratio (e), and mean effective stress (p'):

$$V_s = (381 - 259e)\,(P'/P_a)^{0.26} \tag{2.43}$$

The material constants 381 and 259 are in units of m/s and P_a is the atmospheric pressure (typically P_a = 100 kPa). The stress exponent 0.26 (n) was found to give the best fit to the data for Ottawa sand. This exponent is similar to that suggested by Hardin and Richart (1963) in Equation 2.32. The authors found that this relationship appears to fit the consolidation states as well as the ultimate steady state. They attributed that to the fabric of Ottawa sand that plays a minor role in this relationship. The normalized shear wave velocity for Ottawa sand with respect to applied stresses according to Robertson et al. (1995) can be written as follows:

$$V_{s1} = V_s\,(P_a / P')^{0.26} = (381 - 259e) \tag{2.44}$$

The authors used this normalized shear wave velocity for estimating the in situ state of sand (dilative or contractive) for assessing its potential to flow liquefaction.

2.5.5 Kokusho and Yoshida (1997)

Another important contribution in studying the effect of grain size and grading of soil on V_s was achieved by Kokusho and Yoshida (1997). Shear-wave velocities for sandy and gravelly soils with widely varying grain size distribution were measured in a large container. Figure 2.23 displays the grain size distribution of the tested soils. G25, G50 and G75 refer to three gravel soils of 1.13-mm, 2.28-mm and 7.30-mm mean diameter, respectively, while TS refers to sand of 0.34-mm mean diameter and 1.95 uniformity coefficient. V_s was formulated as functions of gradation, relative density and confining stresses. The normalized V_s has been found to be very sensitive to the difference in gradation. Figure 2.24 presents some of Kokusho and Yoshida (1997) results, using Roesler (1979) concept for normalizing V_s with respect to stresses ($V_{s1} = V_{s0}$). Kokusho and Yoshida (1997) derived four equations for estimating the normalized shear wave velocity (V_{s1}) of the soils they have tested (also written on Figure 2.24).

$V_{s1} = (480 - 382e)$ for TS (2.45)

$V_{s1} = (584 - 766e)$ for G25 (2.46)

$V_{s1} = (721 - 1395e)$ for G50 (2.47)

$V_{s1} = (668 - 1611e)$ for G75 (2.48)

It can be noticed that the normalized shear wave velocity versus void ratio relationships for different soils greatly differ to each other due to differences in gradation. Hardin and Richart (1963) relationships are also illustrated on Figure 2.24, indicating that their relationships are not applicable to other types of soil with different particle gradation. They found that well-graded gravel with much higher dry density than sand may actually be able to exhibit shear-wave velocity as low as that of poorly graded loose sand if it has a low enough relative density. Hence, they concluded that shear-wave velocity can not be uniquely determined by a function of void ratio as proposed by Hardin and Richart (1963) but is highly variable with difference in grain size distribution.

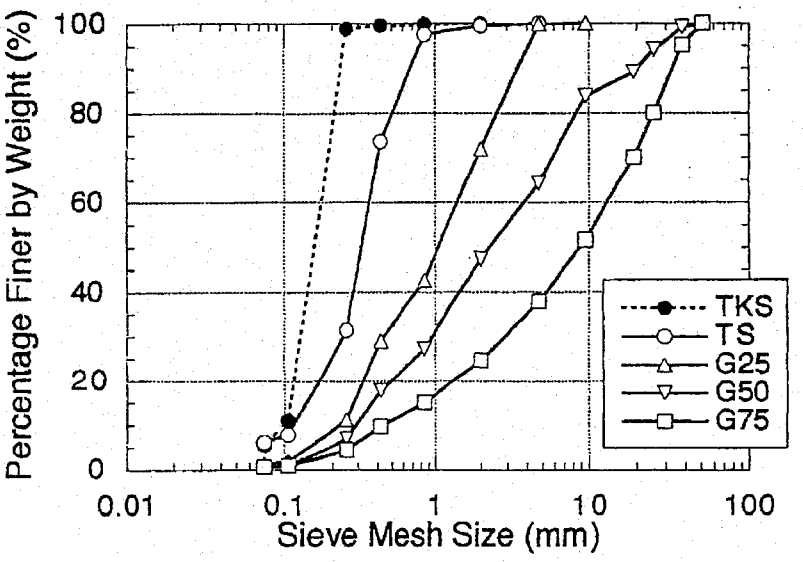

Figure 2.23 Grain Size Distribution of Five Types of Soils Tested by Kokusho and Yoshida (1997)

Also, the authors correlated the maximum and minimum normalized shear-wave velocity with respect to stress (V_{s1max} & V_{s1min}) to the uniformity coefficient of soil ($U_c = D_{60}/D_{10}$) as shown in Figure 2.25 where HC and LC shown in the figure refers to tests at high stresses and lower stresses, respectively. They inferred that minimum normalized shear-wave velocity do not differ so much for different soils at the loosest state, giving V_{s1min} a value of 120 m/s (Figure 2.25). The V_{s1max}, which corresponds to the minimum voids ratio, increases extensively with increasing the uniformity coefficient (U_c). The obtained relationship was fitted by Equation 2.49.

$$V_{s1\max} = 420\,U_c/(U_c+1) \tag{2.49}$$

Kokusho and Yoshida (1997) formulated V_s using relative density by

$$V_{s1} = V_{s1\min} + (V_{s1\max} - V_{s1\min})D_r \tag{2.50}$$

By substituting V_{s1max} & V_{s1min} in Equation 2.53, they derived the following equation for evaluating V_s of soil

$$V_{s1} = \left[120 + \{420U_c/(U_c+1) - 120\}D_r\right]\left(\sigma_h\sigma_v/P_a^2\right)^{0.125} \tag{2.51}$$

where V_s in m/sec and σ'_h, σ'_v and P_a are in the same units. It can be realized that the latter equation does not include a voids ratio function which was substituted by relative density.

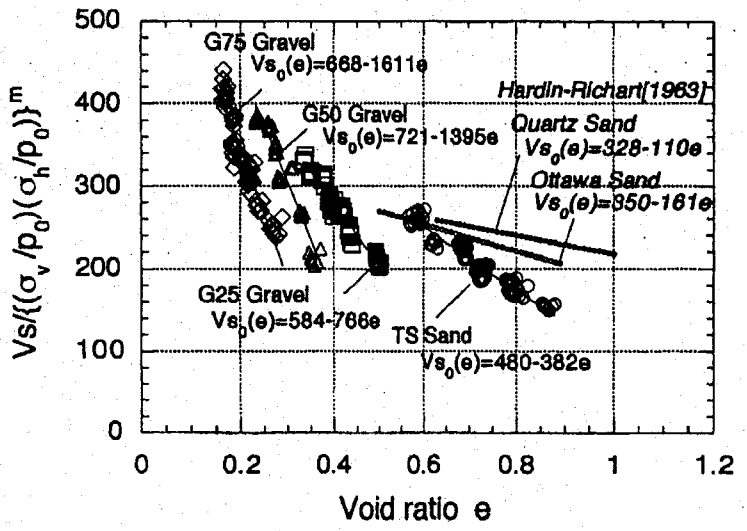

Figure 2.24 Relationship between Voids Ratio and Normalized Shear Wave Velocity (Kokusho and Yoshida, 1997).

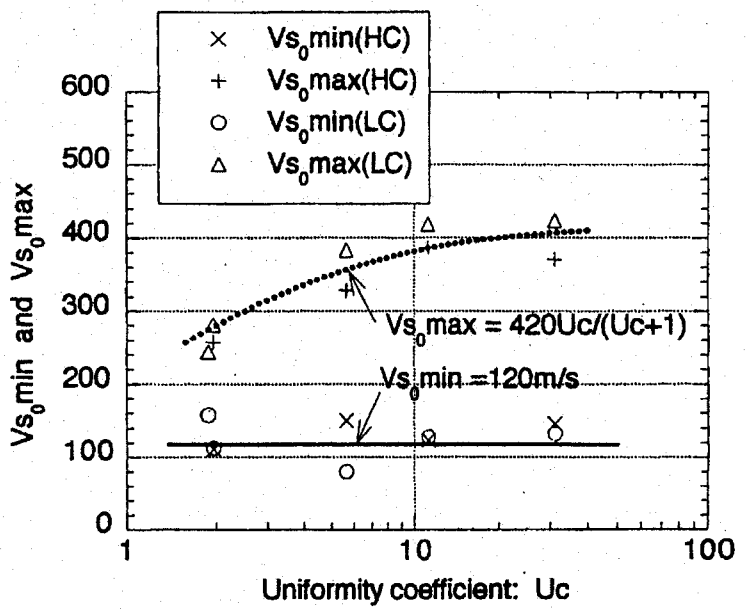

Figure 2.25 Relationship between Uniformity Coefficient and Each of Minimum and Maximum Normalized Shear Wave Velocity (Kokusho and Yoshida, 1997).

The weakness of Kokusho and Yoshida (1997) equations comes from giving V_{s1min} constant values depending on only five soil gradations whereas these parameters may vary from soil to another. However their study showed the need to consider soil gradation and the difference in maximum density of different soils in evaluating V_s. Also, the results indicated

that the voids ratio can not be used as a universal indicator for shear wave velocity determination, other parameters like relative density and uniformity coefficient may be important in these correlations.

2.5.6 Results of some Previous Studies

The results of Iwasaki and Tatsuoka (1977) indicate that G_o decreases with increasing fines content. Results of resonant column tests on Ticino sand by Lo Presti (1996) showed that the coefficient C_g of Hardin and Richart equation (2.32) is reduced by about 50% when the fines content increases from 0 to 25%, while n_g increases slightly. Randolph et al. (1994) also recognized a significant reduction in the small-strain stiffness of sand with addition of silt. According to those authors, the small-strain stiffness of silty sand with 5–10, 10–15, and 15–20% silt content ranges might be reduced by about 19, 25, and 50% of the G_o value of clean sand, respectively. Salgado, Bandini and Karim (2000) studied the effect of nonplastic fines content on the small strain stiffness and shear strength of Ottawa sand. A series of laboratory tests was performed on samples with fines content in the range of 0–20% by weight using triaxial tests equipped with bender elements. The results showed that the small-strain shear modulus depends on the power of mean effective stress, n, which increased from 0.4 to 0.8 with the increase of the silt content. Also, it was observed that the small-strain stiffness at a given relative density and confining stress level decreases dramatically with the addition of even small percentages of silt. This is an important result because the analyses of problems involving silty sand using stiffness properties of clean sand can be in serious error. The new concept in Salgado, Bandini and Karim (2000) approach is to determine the different constants of the V_s-empirical equations for each soil depending on its constituents (grain size and grading). These studies have clearly inferred the effect of grain size and grading on shear wave velocity of soil.

2.6 Correlations between V_s or G_o and Soil Parameters

This section presents the existing relationships between shear wave velocity or small-strain shear modulus and the usual soil parameters. These correlations are not targeted to include the factors that control G_o or V_s, but to investigate the relationship between basic soil parameters and its elastic properties (G_o, E_o, M_s, V_s, V_p). The direct correlations between soil parameters and G_{max} or V_s are very useful for soil characterization but are rare. Most of the existing

correlations were based on field tests result. Some studies were based on penetration tests carried out in calibration chambers. Some correlations were derived from theoretical calculations of (G_o) and/or V_s as opposed to a field-derived data base. These correlations have evolved because of the expense of direct measurement using conventional testing. Another reason is the development of in situ seismic investigation techniques which measure V_s and then the conventional in situ geotechnical indexes of soil are estimated from these correlations. The following subsections introduce the in-hand studies in this field up till now, namely Lade and Nelson (1987), Bellotti et al. (1997), Burns and Mayne (1996), Mayne, Martin and Schneider (1999) and Mayne (2001).

2.6.1 Lade and Nelson (1987)

The expression developed by Lade and Nelson (1987) for correlating the maximum shear modulus of soil, G_o, to other granular soil parameters takes the form of a power law. Their elastic model which was developed using dilatometer test (DMT) results is isotropic nonlinear and is written as follows:

$$G_o = M_G \left[\left(\frac{\sigma'_m}{P_a} \right)^2 + R \frac{J'_2}{P_a^2} \right]^{\lambda} \tag{2.52}$$

where M_G is a modulus number expressed using the relative density in percent as follows:

$$M_G = F(D_r) = 466.6 + 7.2 D_r (\%) \tag{2.53}$$

R is a function of Poisson's ratio [$R = 6(1+\upsilon)/(1-2\upsilon)$], J_2' is the second invariant of the deviator stress [$J_2' = (\sigma_v' - \sigma_h')^2/3$] and λ is a modulus exponent equals to 0.12 where σ_v' is the effective vertical stress, σ_h' is the effective horizontal stress, P_a is a reference pressure and σ_m' is the mean effective stress. The latter relationship is distinguished among others by using a relative density function $F(D_r)$ instead of the commonly used function for void ratio $F(e)$, and also by introducing the Poisson's ratio in evaluating G_o.

2.6.2 Bellotti et al. (1997)

Bellotti et al. (1997) carried out experimental tests in a calibration chamber (1.2-m in diameter and 1.5-m in height) using research dilatometer (RDMT) to study the stiffness of Toyoura sand (uniform angular to subangular quartz fine sand of D_{50} = 0.15-mm and C_u = 1.3). They confirmed the fact that the response of soils under monotonic loading is softer than under

cyclic loading. Bellotti et al. (1997) introduced Figure 2.26 which displays the relationship between relative density and the shear modulus from monotonic torsional shear test and research dilatometer test. This figure also displays the results of K_o-consolidated torsional shear tests conducted by Teachavorasinskun (1989) and Giunta (1993) on Toyoura uniform sand. The data show that the shear modulus increases with the increase of relative density. Also, it can be realized that the RDMT-shear-modulus (G_{dur}) values are much higher than monotonic torsional shear modulus values, G_o. The following relationships were drawn from the regression analyses of the data.

$$G_o = 0.921 D_r + 39.8 \quad (r^2=0.41) \quad \text{(Teachavorasinskun, 1989)} \quad (2.54)$$

$$G_o = 0.435 D_r + 49.5 \quad (r^2=0.73) \quad \text{(Giunta, 1993)} \quad (2.55)$$

$$G_{dur} = 2.97 D_r - 17.3 \quad (r^2=0.93) \quad \text{(Bellotti et al., 1997)} \quad (2.56)$$

where D_r is the relative density in percent (%), G_o is the shear modulus from torsion shear test in MPa and G_{dur} is the shear modulus from RDMT in MPa. G_{dur} was calculated from the dilatometer elastic modulus (E_{dur}) at cycles of unloading and reloading using elasticity theory equation relating shear modulus to Young's modulus through Poisson's ratio (ν) using the following equation. A Poisson's ratio (ν) value of 0.15 was used in these calculations.

$$G_{dur} = E_{dur} / 2(1-\upsilon) \quad (2.57)$$

Using the dilatometer modulus (E_d), Bellotti et al. (1997) presented a graph for the relationship between G_o/E_d and D_r (Figure 2.27). G_o values were computed using three empirical equations, namely Hardin (1963), Lade and Nelson (1987) and Hryciw (1990). A big scatter in the data can be realized, this could be explained considering that ratio G_o/E_d is for two parameters measured at different strain levels. G_o refers to quasi-elastic soil behaviour at small-strains while E_d is a measure of the elastic-plastic response of soil at high strains. Therefore, one can suggest that the ratio G_o/E_{dur} could be more suitable for this type of relationship.

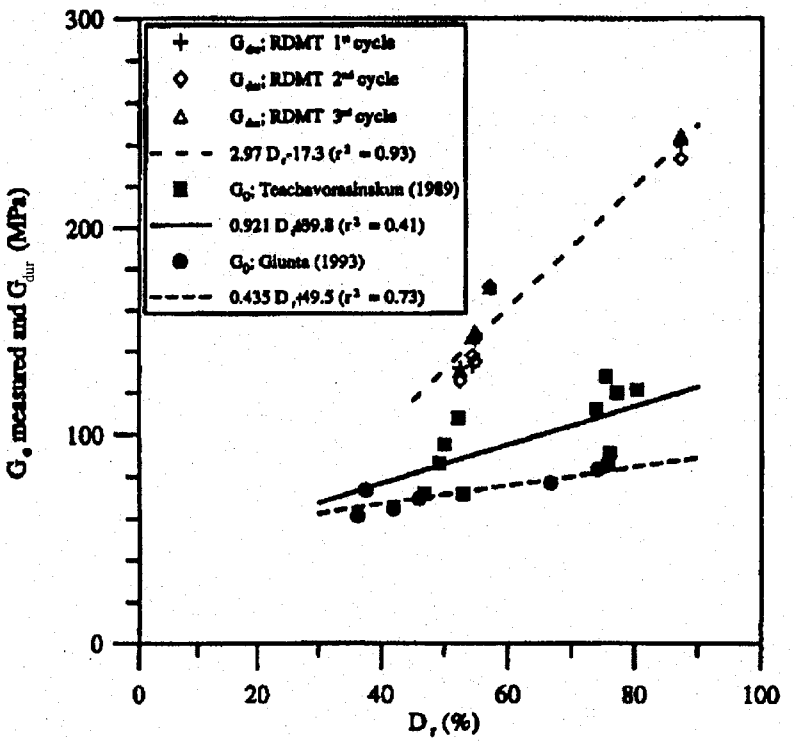

Figure 2.26 Shear Modulus as a Function of Relative Density for Toyoura Sand (Bellotti et al., 1997).

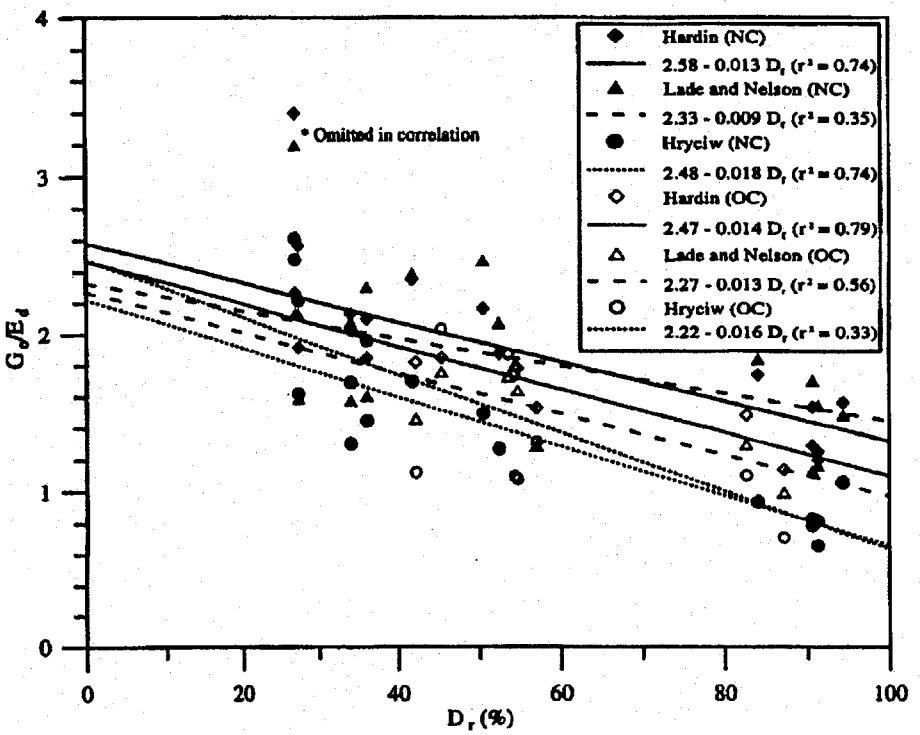

Figure 2.27 The G_o/E_d versus D_r for Normally and Over-Consolidated Toyoura Sand (Bellotti et al., 1997).

2.6.3 Burns and Mayne (1996)

A direct determination of soil mass density (ρ) is required in order to obtain G_{max} from in situ measurements of shear wave velocity. Therefore, a global correlation between mass density (ρ) and shear wave velocity (V_s) was developed by Burns and Mayne (1996). This type of correlations relay on the fact that V_s is mainly dependant on voids ratio and stress. When taking into account that the specific gravity (G_s) range of most soils is small (2.60 to 2.80), if G_s is considered a constant, the voids ratio can be an indicator for the soil density. A data base from all types of geomaterials (clays to sands to rocks) has been created by Burns and Mayne (1996) which facilitates the calculation of maximum shear modulus ($G_{max} = \rho V_s^2$). Seismic wave velocities for soils were determined from in situ methods (seismic cone, cross-hole, spectral analysis of surface waves, or suspension logging techniques). The unit weights (γ) and mass densities ($\rho = \gamma/g$) of these materials were determined from thin-wall tube samples. The data of rock materials were generally from laboratory testing on small specimens. A strong correlation was observed between the mass density and the measured shear wave velocity of the geomaterials. Figure 2.28 indicates the relationship trend from the regression analysis of the 438 data points. The regression equation for this relationship is given by

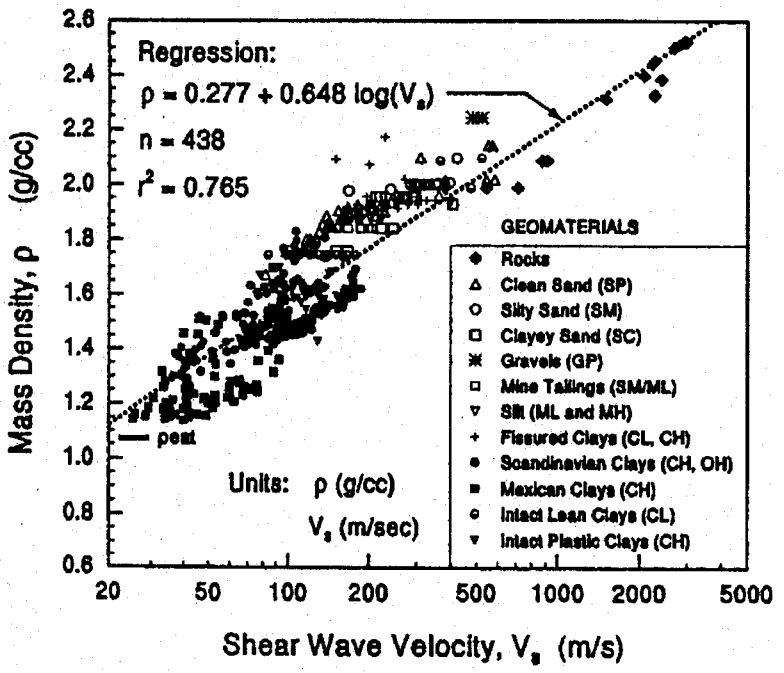

Figure 2.28 Mass Density versus Shear Wave Velocity for Different Geomaterials (Burns and Mayne, 1996).

$$\rho = 0.277 + 0.648(\log V_s) \qquad \text{(S.E.} = 0.126 \text{ \& } r^2 = 0.765) \qquad (2.58)$$

where: ρ = mass density (γ/g) in g/cm^3 (g = gravitational acceleration constant = 9.81 m/sec^2), V_s = shear wave velocity in m/sec, r^2 = coefficient of determination, n = number of data sets, and S.E. = standard error of the independent variable in the same units as ρ. Burns and Mayne (1996) also investigated a multiple regression analysis with two independent variables (actual and predicted unit weight of soil). The results are shown in Figure 2.29. The statistical analysis indicated an improved trend with the following equation:

$$\rho = 0.701(V_s)^{0.227} / (\sigma'_{vo})^{0.057} \qquad \text{(S.E.} = 0.118 \text{ \& } r^2 = 0.82) \qquad (2.59a)$$

or $$\gamma_T = 6.87(V_s)^{0.227} / (\sigma'_{vo})^{0.057} \qquad \text{(S.E.} = 0.118 \text{ \& } r^2 = 0.82) \qquad (2.59b)$$

where σ'_{vo} is effective vertical overburden stress in kN/m^2, V_s in m/sec., ρ in g/cm^3 and γ_T in kN/m^3. Considering that σ'_{vo} depends on knowing the mass density profile with depth before calculation, an iterative approach is required to solve Equation 2.59a or Equation 2.59b. Thus, Equation 2.59 may be of more practical use in routine explorations involving the need to convert V_s to G_{max}. These two equations are of immediate value to V_s surveys conducted using the spectral analysis of surface waves because no other information may be available before this test is conducted (Burns and Mayne, 1996).

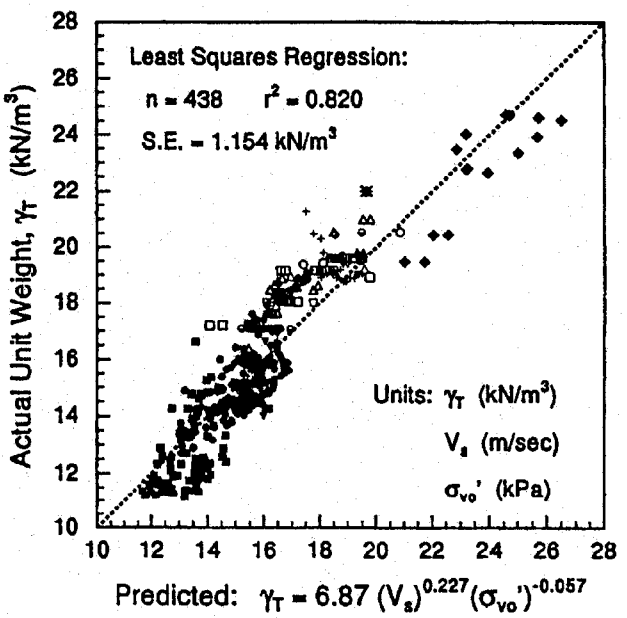

Figure 2.29 Multiple Regression Evaluation of Total Unit Weight for Different Geomaterials (Burns and Mayne, 1996).

2.6.4 Mayne, Schneider and Martin (1999)

Mayne, Schneider and Martin (1999) introduced an approximate equation for estimating the saturated mass density, ρ, from shear wave velocity knowing the sample depth. Their equation was extrapolated based on Burns and Mayne (1996) database of field and laboratory tests result on different soil types. Figure 2.30 depicts their regression equation which can be represented by

$$\rho = 1 + 1/[0.614 + 58.7(\log z + 1.095)/V_s] \tag{2.60}$$

where the depth z in meters and V_s in *m*/sec. This equation has a correlation coefficient (r^2) of 0.73.

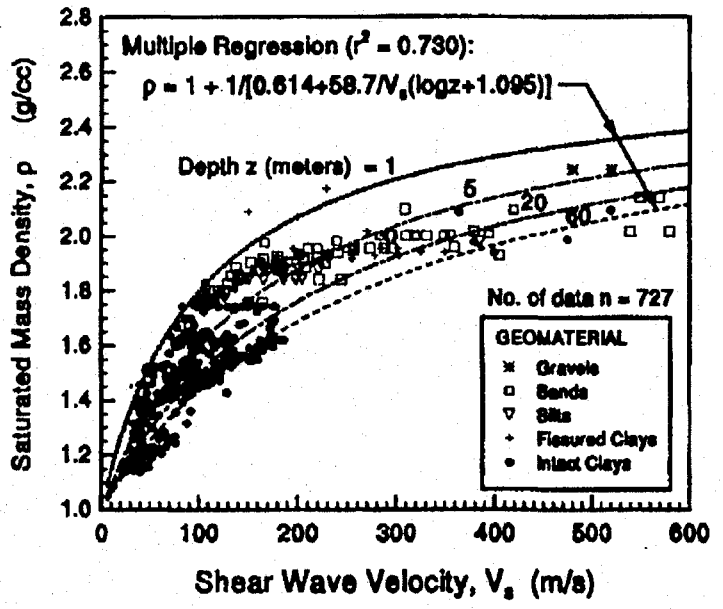

Figure 2.30 Relationship between Mass Density, Shear Wave Velocity and Depth of Overburden for Geomaterials (Mayne, Schneider and Martin, 1999).

2.6.5 Mayne (2001)

After compiling many data of unit weight and V_s for saturated geomaterials, Mayne (2001) introduced another equation for estimating the saturated mass density, γ_{sat}, based on shear wave velocity and depth, z. The equation is as follows:

$$\gamma_{sat} = 8.32 \log V_s - 1.61 \log z \qquad \text{(S.E.} = 0.118 \ \& \ r^2 = 0.82) \tag{2.61}$$

where γ_{sat} in kN/m^3, the depth z in meters and V_s in *m*/sec. This equation has a correlation coefficient (r^2) of 0.81 for 727 data points.

2.7 Compaction of Soil and Shear Modulus

Soil compaction is an important practice in soil stabilization as it increases soil strength, enhances its deformation characteristics, reduce permeability, mitigate liquefaction hazards, control swelling and shrinkage, and increase the overall durability of compacted earth works. Compaction specifications often require achievement of an in situ dry density of 90–95 % of the maximum value obtained from laboratory standard or modified Proctor test. However, the dry density itself is not a design parameter. It is rather used to infer other parameters such as strength and stiffness through some empirical equations. The small-strain shear stiffness is a more basic design parameter that may be examined for controlling compaction works. It can be calculated from shear wave velocity and bulk density of soil. Measuring the shear wave velocity of the compacted material during laboratory compaction by piezoelectric transducers enables investigating the compaction curve in terms of shear modulus or shear wave velocity and moisture content. Therefore it was planned in this research to investigate the possibility of drawing Proctor curve for some soils in terms of shear wave velocity and moisture content. Only two papers were published in this domain recently in 2006 and 2007. This section introduces resume of these two studies.

For unsaturated cohesive soils, the common equation for effective stress is not suitable because the degree of saturation and matric suction play a key role in soil stiffness and wave velocity. Fines content is also a fundamental variable. Thus, due to the difficulty in determining effective stresses, total stresses and matric suction (or degree of saturation) are used as stress state parameters. The effect of saturation on shear wave velocity of different soils has been studied by Cho and Santamarina (2001), Hardcastle and Sharma (1998), Qian et al. (1994), Rinaldi et al. (1998) and Wu et al. (1987). There is a general agreement among the various authors that wave velocity of unsaturated soils increases by decreasing void ratio and degree of saturation. In freshly remoulded soils, Qian et al. (1994) determined an optimum degree of saturation corresponding to a peak in shear wave velocity which was correlated with the D_{10} (grain size of 10% finer by weight) of the soil tested. The degree of saturation at maximum suction ($S_{opt.}$ %) depends on soil grains size and grading. For sands, it decreases by increasing the diameter for the finest 10% of the soil (D_{10}). The maximum-suction water

content of sands varies from 3% to 10%. The following empirical relation has been proposed by Wu et al. (1984) for natural subangular soils:

$$S_{opt.} = 1.5 - 6.5\log(D_{10}) \quad (2.62)$$

where D_{10} [mm] is the diameter for the finest 10% of the soil. For D_{10} = 1-mm the peak of suction stresses is reached at $S_{opt.}$ = 1.5%, and for D_{10} = 0.001-mm the peak is at $S_{opt.}$ = 21%.

Different stages have been recognized during the desaturation of the soil. The 'funicular stage' of saturation starts by air breaks in and the soil mass becomes unsaturated and water still forms a continuous phase (Figure 3.31). Negative pore pressure spreads in the soil mass by diffusion. As drying progresses, the suction pressure gradually increases, following a quasi-linear trend with decreasing saturation. The 'pendular stage' begins when water becomes disconnected, air is the continuous pore phase, and water rings form around particle contacts (menisci). An adsorbed film may be present on particle surfaces. The radii of menisci are small, thus the suction pressure increases significantly (Santamarina, Klein and Fam, 2001). Any change in suction within a meniscus is felt at other menisci through the corresponding change in vapour pressure. This is a slow homogenization process. The limit water content to pass from funicular to pendular stage was calculated for arrays of spherical particles by Cho and Santamarina (2001) in less than 3.2 and 6.3 % for tetrahedral and simple cubic packing, respectively. The development of water menisci at particle contacts generates strong capillary forces (tensile stresses), often referred to as matric suction, which stiffens the soil skeleton and increases wave velocity (Clariá Jr. and Rinaldi, 2007).

Ismail and Rammah (2006) built a setup that uses shear-plates for measuring shear wave velocity through the stabilized material (sand) during laboratory compaction (Figure 2.32). It enables measurement of the shear modulus in the horizontal direction with the possibility to change the polarization direction of the traveling signal from 0-90° (horizontal to vertical planes). Figure 2.33 shows a photo of the shear transducer with the rotation mechanism. The shear wave transducer was a commercial contact normal incidence type, with a free resonant frequency of 100 kHz and 25-mm diameter (Panametrics V1548). Some of the results obtained using this setup are shown in Figure 2.34. It can be realized that resonance exists on the output signal for the three used input frequency and there is no evidence of compression wave on the output signal. Ismail and Rammah (2006) draw the compaction curves for Perth subrounded to rounded medium sand. The results of the compaction test are

presented in Figure 2.35 in terms of variation of both $G_{o(ij)}$ and dry density with the moisture content, respectively. Figure 2.35 includes the shear modulus measurements in the vertical and horizontal planes. The compaction curve in Figure 2.35 has a bell shape similar to the familiar Proctor curve. The relationship between $G_{o(ij)}$ and γ_d is plotted separately in Figure 2.36. It appears from Figure 2.36 that significant reduction in $G_{o(ij)}$ occurred at moisture contents (MC) to the wet side of optimum. The magnitude of the reduction increases as the MC increases beyond the OMC.

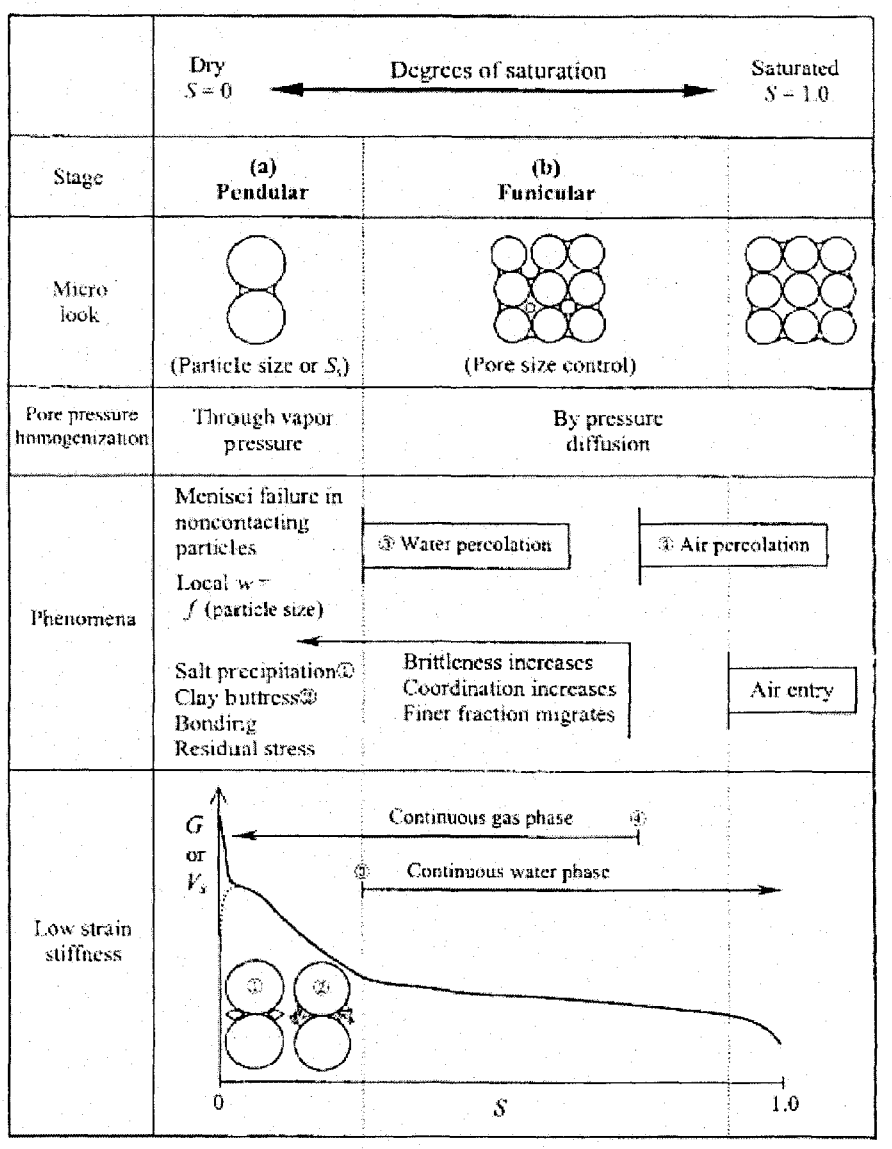

Figure 2.31 Stages of Unsaturated Conditions and Related Phenomena (Santamarina, Klein and Fam, 2001).

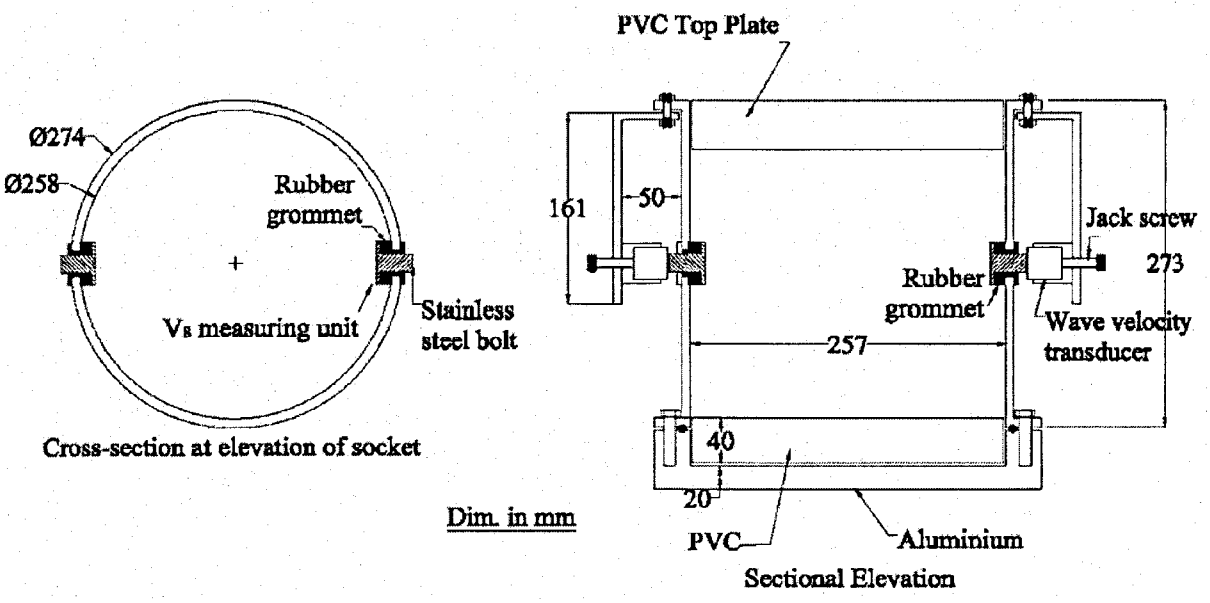

Figure 2.32 Details of a Seismic Compaction Mold (Ismail and Rammah, 2006).

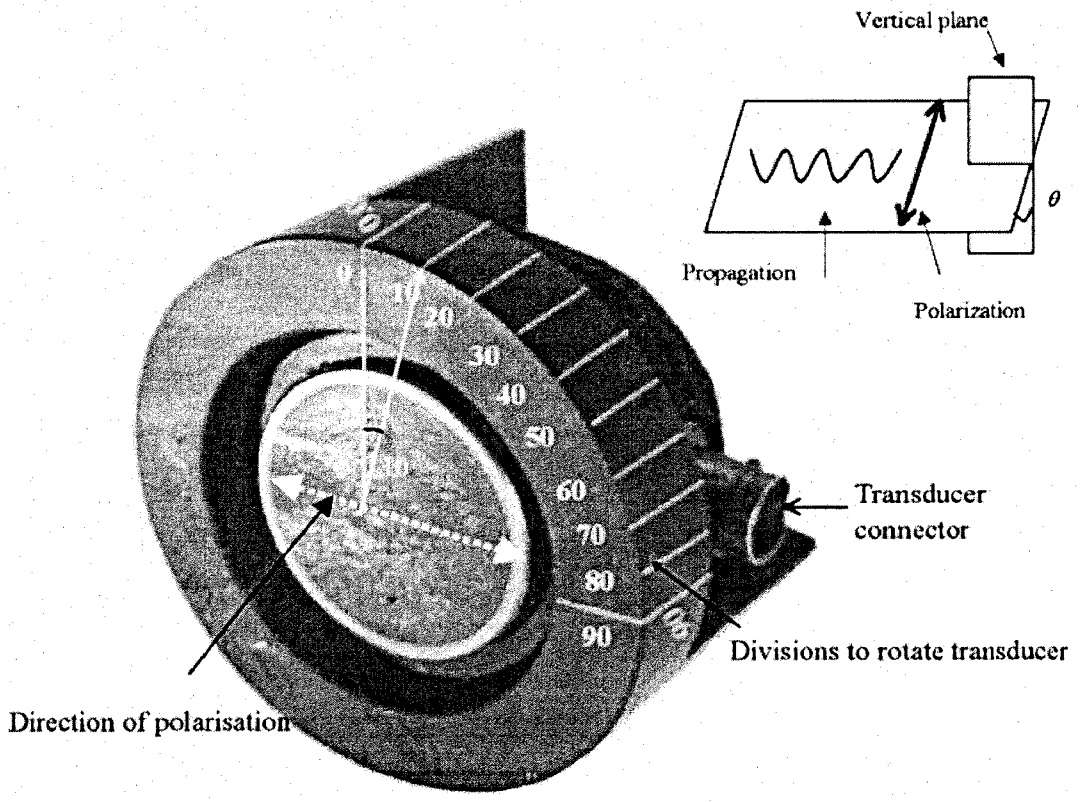

Figure 2.33 A Photo of the Shear Transducer with the Rotation Mechanism (Ismail and Rammah, 2006).

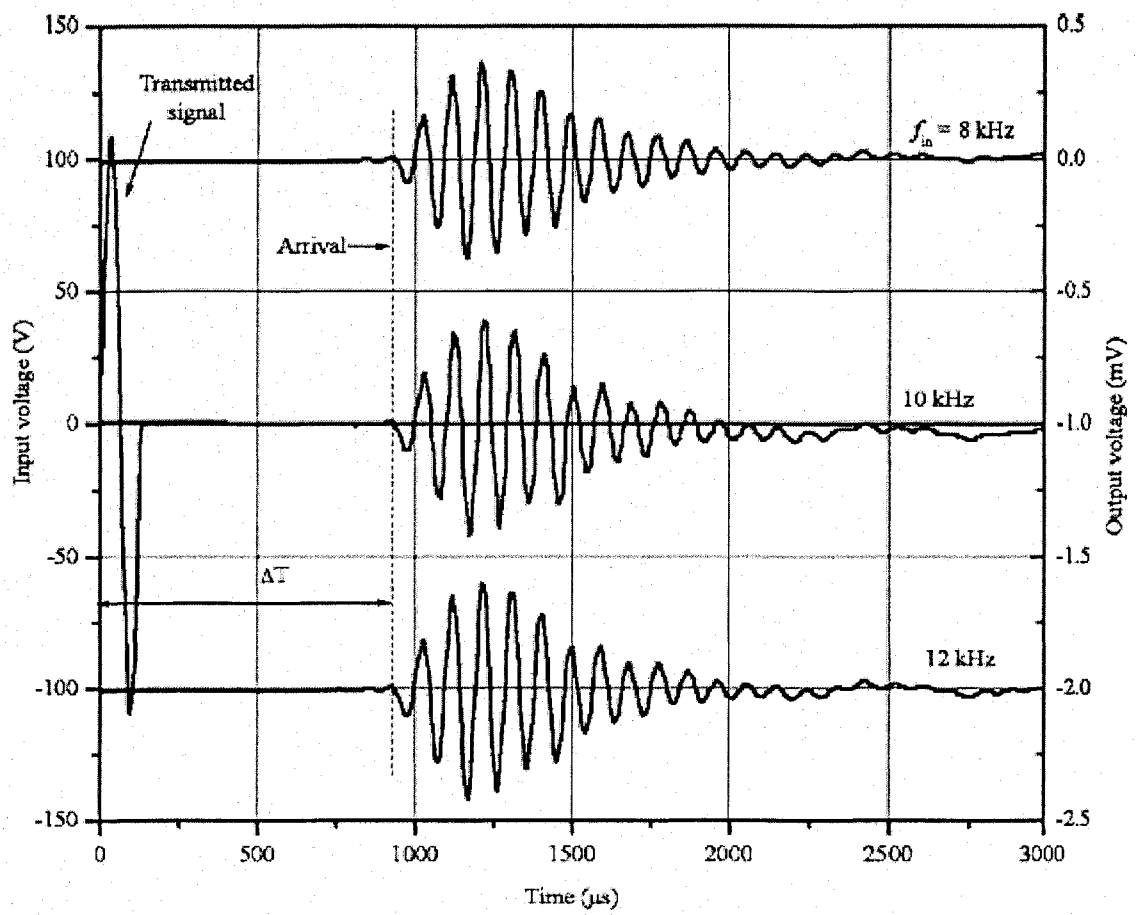

Figure 2.34 Determination of Arrival Time from Three Frequency Traces (Ismail and Rammah, 2006).

The influence of the degree of saturation on G_o of a silica sand with a mean grain size diameter of 0.36mm was investigated by Cho and Santamarina (2001). They reported a significant increase in G_o when the degree of saturation reduced below 10%, at about 2% moisture content, (Figure 2.37). Santamarina (2000) indicated that the effect of suction is a function of the degree of saturation, surface area, and particle shapes. Ismail and Rammah (2006) found similar trend when testing Perth sand by bender elements in the triaxial apparatus. The degree of saturation (S %) has a significant influence on G_o of Perth sand: a reduction of S from 100 % to 3.25 % increased G_{ohv} by about 30 % (Figure 2.38). The samples in the dry side of compaction experienced suction-induced increase in mean effective stress which increased the shear modulus. The shear modulus of the compacted Perth sand increased with increasing the vertical stress according to a power law relationship with an exponent n of

only 0.21–0.22 (Figure 2.39) compared to 0.5 for a dry sample of the same material. The authors attributed this difference between moist compacted and dry compacted sand to the presence of suction in the moist sand, which increased the area of contact between the particles and made them less sensitive to stress increase.

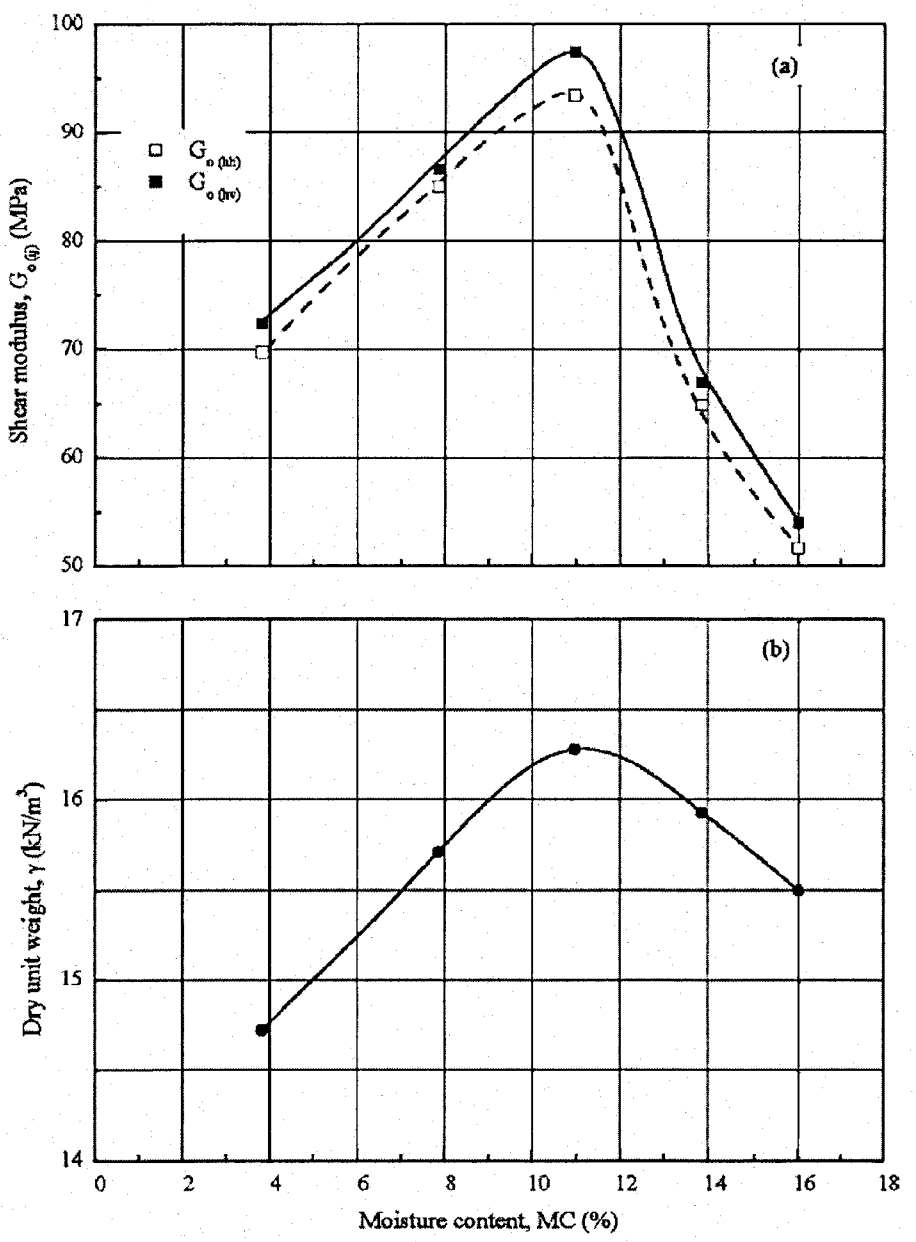

Figure 2.35 Relationship between Dry Unit Weight/Shear Modulus versus Moisture Content for Perth Sand (Ismail and Rammah, 2006).

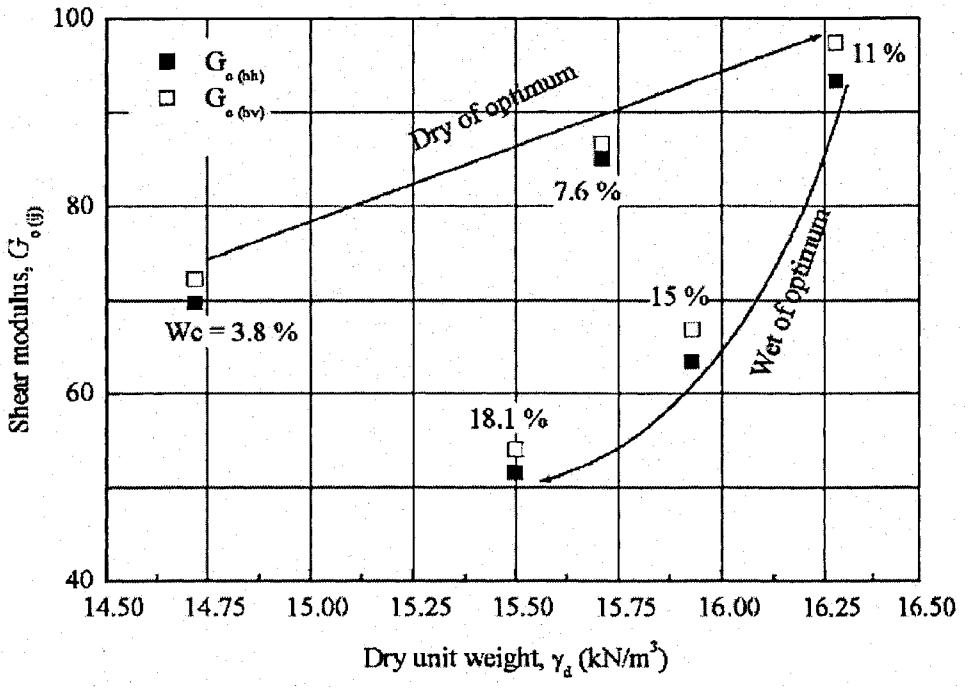

Figure 2.36 Variation of G_o with Dry Unit Weight and the Side of Optimum-w_c (Ismail and Rammah, 2006).

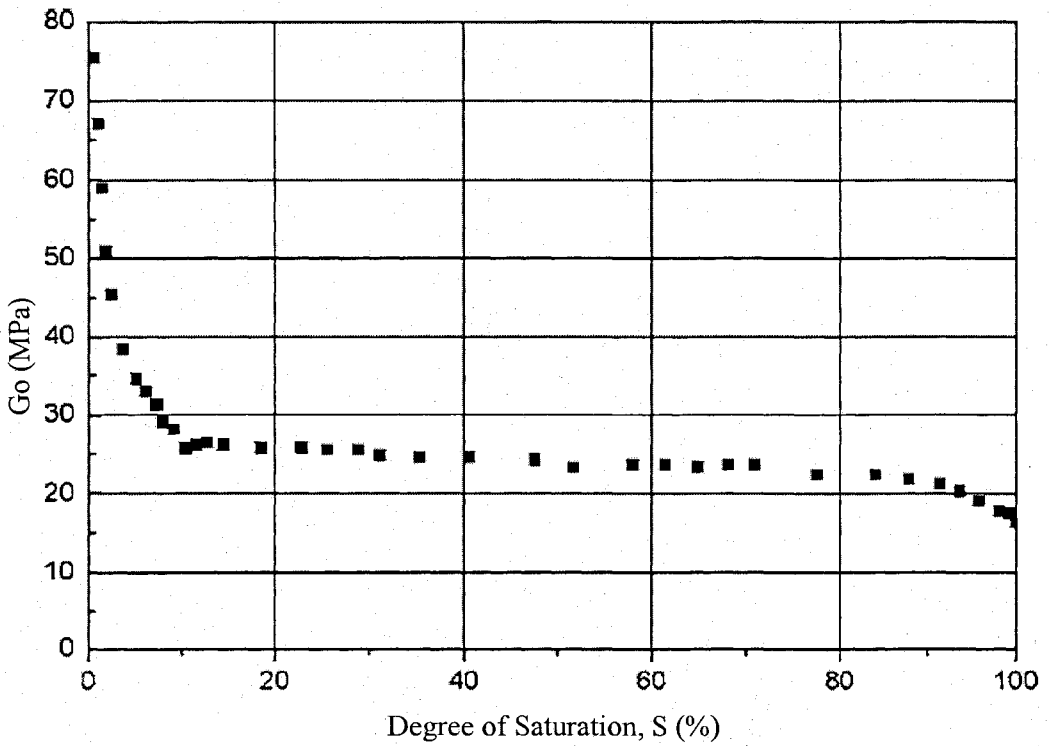

Figure 2.37 Variation of G_o with Degree of Saturation (Cho and Santamarina, 2001).

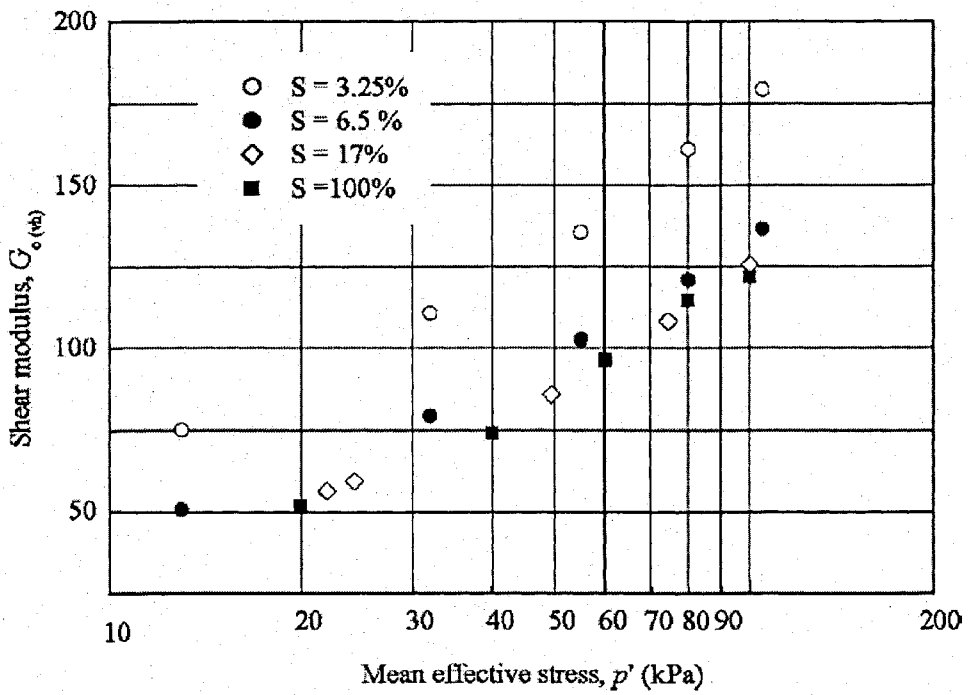

Figure 2.38 Influence of Degree of Saturation on $(G_o)_{hv}$ of Perth Sand (initial γ_d = 16 kN/m^3) during Isotropic Compression Test, (Ismail and Rammah, 2006).

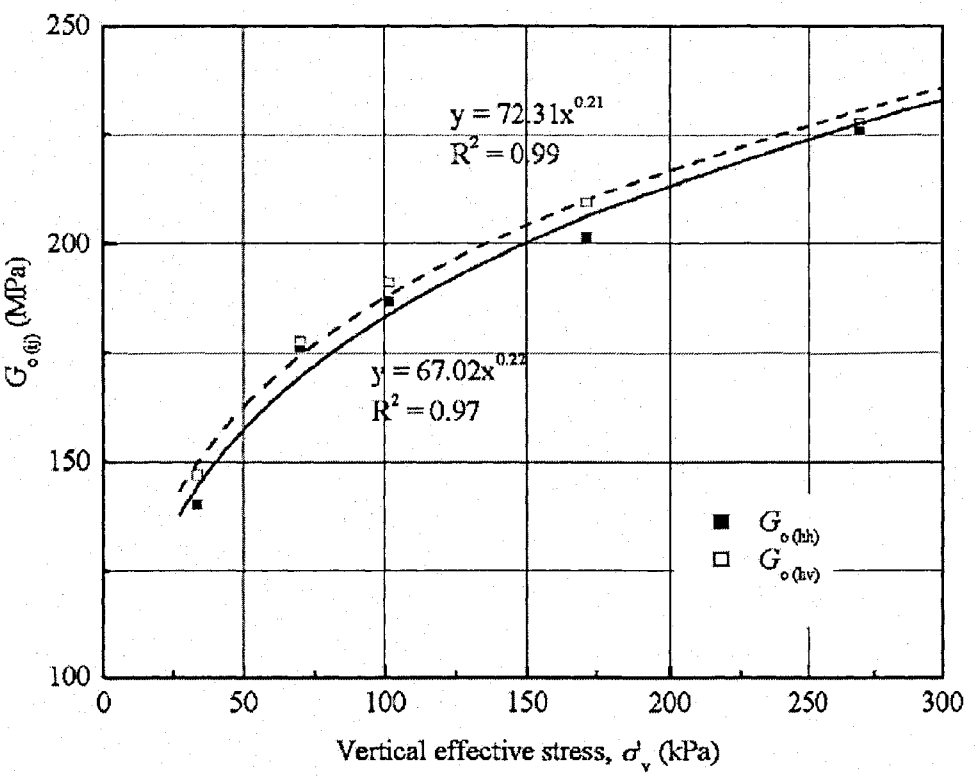

Figure 2.39 Variation of $(G_o)_{ij}$ with Vertical Stress for Compacted Moist Sand (Ismail and Rammah, 2006).

Clariá Jr. and Rinaldi (2007) carried out an experimental program to investigate the variation of shear stiffness with the moisture content of compacted clayey silt samples in a modified isotropic cell. Matric suction of the compacted specimens was measured by a tensiometer prior to testing in compression and V_s was measured by bender elements. They found that shear wave velocity for the compacted clayey silt is governed by a complex combination of four fundamental variables: confining pressure, soil structure developed during compaction, moisture content, and compaction density. The effect of soil fabric seems to affect shear wave velocity in specimens compacted and tested at the same density and water content. At zero applied confining pressure, unsaturated specimens show nonzero initial values of shear wave velocity, which decreases with increasing water content (Figure 2.40). The samples were tested at different compaction moisture contents; values between brackets show the dry unit weight of the specimens. All the curves show that wave velocity increases with confining pressure and decreases with water content, the rate of increment being more pronounced for samples tested with higher water content.

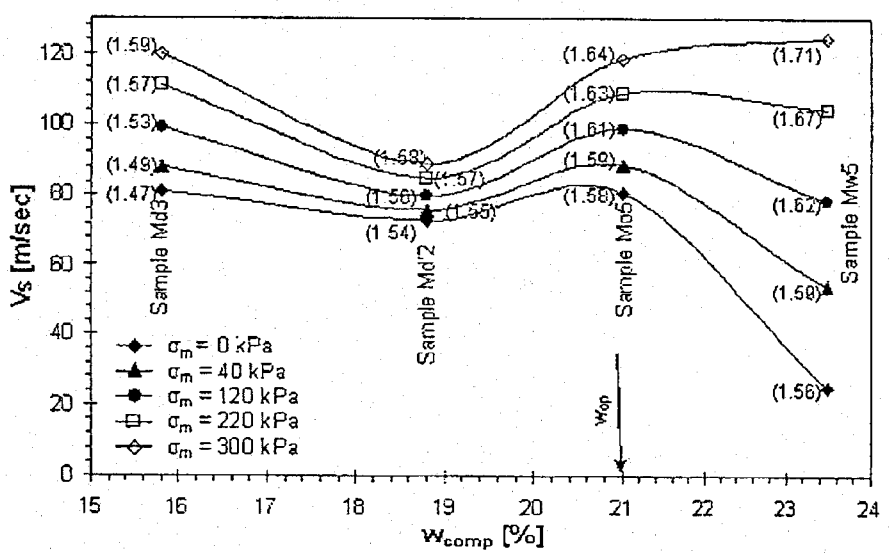

Figure 2.40 Variation of V_s with Compaction Water Content and Isotropic Confining Pressure (Clariá Jr. and Rinaldi, 2007).

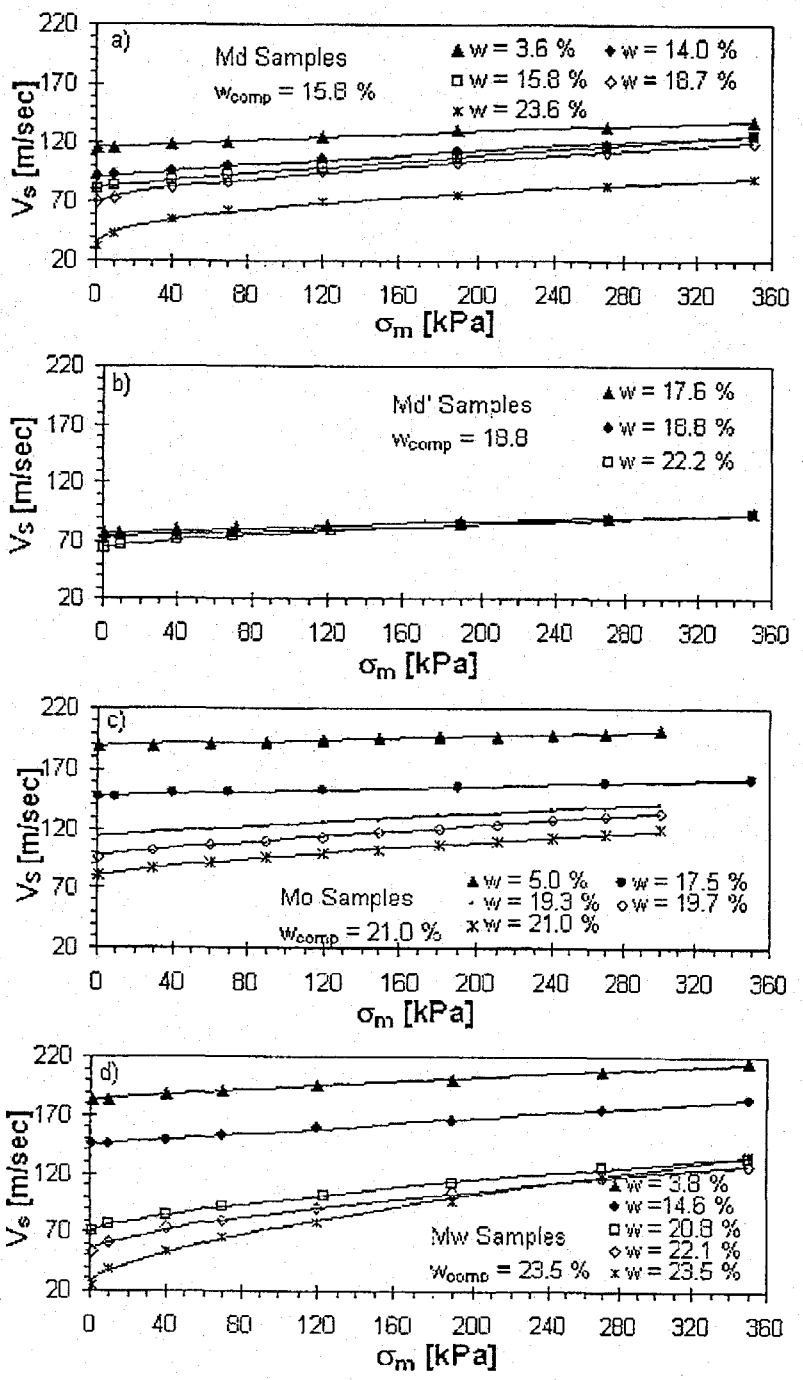

Figure 2.41 Variation V_s with σ_m and w_c: a) Samples Compacted Dry of Optimum (M_d), b) Samples Compacted Dry of Optimum (M_d'), c) Samples Compacted at the Optimum, d) Samples Compacted Wet of Optimum (M_w) [Clariá Jr. and Rinaldi, 2007].

Additionally the authors subjected the samples to drying/wetting after compaction. They found that by increasing the confining pressure, specimens compacted wet of optimum are

more compressible and therefore the rate of increment of wave velocity is higher as compared to the specimens compacted dry of optimum (Figure 2.42). The W_{comp} value on each graph is the compaction water content. As suction is decreased by addition of water, wave velocity decreases since interparticle contact forces are lowered. In contrast, as water content increases, the soil becomes more compressible and thus, wave velocity is more affected by confining pressure. At the optimum moisture content, the compressibility of the soil is low, and wave velocity is mainly affected by interparticle contact forces that increase with confining pressure.

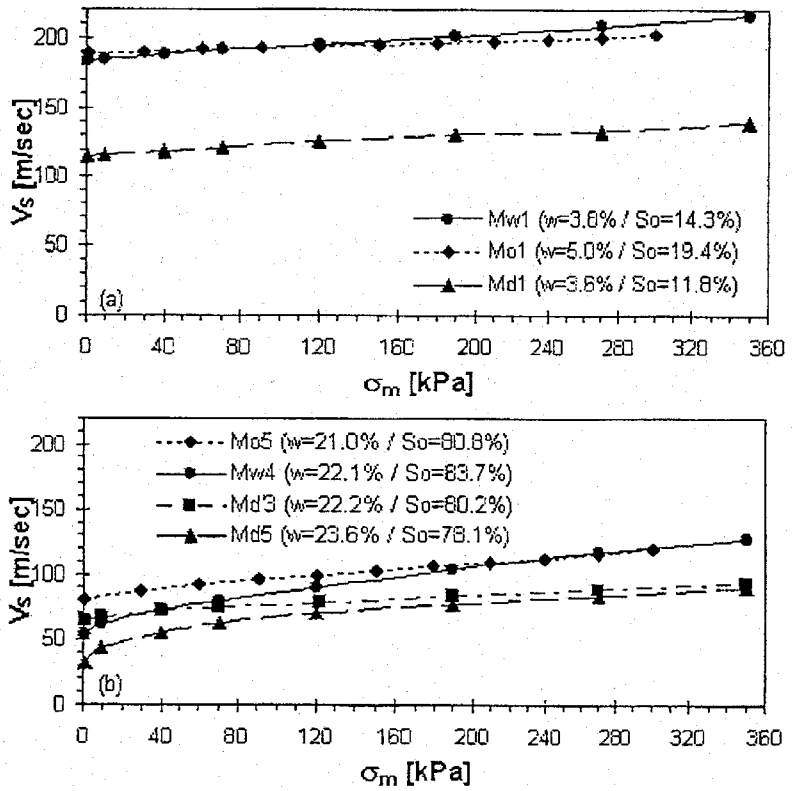

Figure 2.42 Variation of V_s with σ_m for Samples Compacted at Different Moisture Contents but Tested at a Similar Degree of Saturation (Clariá Jr. and Rinaldi, 2007).

Finally, Clariá Jr. and Rinaldi (2007) stated that control of compaction of low plasticity clayey silt by means of in-situ shear wave velocity measurements could be misleading. Certainly, the effect of drying or wetting before compaction may result in a complex interpretation of the measured shear velocities. Thus, the evaluation of compaction

by means of wave velocity must include at least knowledge of the compaction procedure as well as an additional determination of water content.

2.8 Conclusions

Shear wave velocity can be an important tool in determining the physical properties of soil because of its direct relationship with soil parameters. In this chapter, it has been shown that the bender-elements method, which is widely used to measure shear wave velocity of soil in laboratory setups, suffers from fundamental and interpretative problems. Interpretting bender elements test results is difficult and controversial. Some researchers have reported errors in elastic shear modulus, calculated by pulse tests, of up to 50%. Also, no interpretation method from the currently existing methods may claim preference. The near-field effect is a main source of errors in pulse tests. Further investigations are necessary to clear the ambiguity of piezoelectric testing and its interpretation difficulty. In addition, there are few correlations which relate shear wave velocity to usual soil parameters. Hence, accurate measurements are needed for establishing reliable correlations of this type at laboratory. Finally, the research in behaviour of piezoelectric devices is far behind the study of soil behaviour using these sensors.

Chapter 3 NUMERICAL SIMULATIONS AND ANALYTICAL MODELS FOR PULSE VELOCITY TESTS

3.1 Introduction

Numerical simulations for pulse velocity tests were carried out in this chapter using THE FLAC® software (Version 4.0) by Itasca (2003). FLAC employs the finite difference code in calculation. Three dimensional (3-D) axisymmetric modeling is configured for most of the simulations. This chapter consists of a fundamental concepts section and four primary parts. The first main part is to demonstrate the disadvantages of bender elements and their interpretation problems. The second part is for introducing new modes of shearing and their analysis using numerical simulations. The third part is for analyzing the problem of near-field effect and wave reflections. The last section introduces and studies some analytical models for wave reflections on sample sides and its effects on signal interpretations considering the different controlling parameters. Based on the findings in these four sections, a new V_s-measurement-device is designed and built in this study. Thus, some simulations were carried out to check and develop the performance of the new transducer and the special testing caps where this transducer was mounted. These simulations are spread out in the different parts of this chapter.

3.2 Fundamental Concepts in Numerical Simulations

This section is dedicated to explain some technical points in numerical simulations to serve the analysis of the carried out simulation in this study. It introduces some information about the model's mesh, boundaries and damping.

Kuhlemeyer and Lysmer (1973) showed that the wavelength (λ) determines the accuracy for wave propagation problems. They found that the maximum element length in the direction of propagation (L_{max}) must be smaller than one-tenth to one-eighth of the wave length (λ) associated with the highest frequency component of the input wave that contains appreciable energy (FLAC suggests one-tenth factor). This condition can be written as follows:

$$L_{max} \leq \lambda_{min}/8 \quad : L_{max} \leq V_{min}/(8f_{max}) \tag{3.1}$$

Also, the fastest possible wave should pass across the smallest element in no fewer than 10 times of the calculation time-step in order to preserve numerical stability and accuracy (Arroyo et al., 2006).

$$L_{min} \geq 10\Delta t\, V_{max} \tag{3.2}$$

These factors were considered during the carried out simulations (Chapter 3). The results of Lee and Santamarina (2005) for directivity measurements inferred that much of the energy is radiated from benders at angles less than 30° with the sample axis. During pulse wave velocity measurements on triaxial samples of Toyoura sand, Mohsin & Airey (2003) noticed that when varying the confining pressure, seemingly abrupt jumps in the velocity estimate occurred if the maximum peak of the cross-correlation function was always selected. They varied the cross-correlation peak subjectively in order to recover a reasonable trend. Increasing confinement increases soil stiffness and hence would increase the shear and bulk wave velocities of the material. Hence, the probing wave length in a sample of fixed dimensions would increase. This, in turn, would affect the interpretation of the signals.

Specifying boundaries to the numerical model in dynamic analyses may cause the applied propagating waves to reflect back into the model. Using a larger model may minimize this problem but, as a consequence, the computational time becomes large. An alternative is to use quiet (silent or viscous or absorbing) boundary to overcome the problem. Quiet boundary operates in the time domain and was based on the use of independent dashpots in the normal and shear directions applied at the model boundaries (Girsang, 2001). Quiet or absorbing boundaries are implemented in FLAC® to prevent wave reflections. A silent boundary is effective in absorbing the propagating waves for waves arriving at angles of incidence (with the boundary) larger than 30°. The formulation of a quiet boundary can be written as:

$$t_n = -\rho V_p V_{cn} \tag{3.3}$$

$$t_s = -\rho V_s V_{cs} \tag{3.4}$$

where t_n = the normal stress at the model boundary, t_s = the shear stress at the model boundary, ρ = mass density, V_p = the p-wave velocity, V_s = the s-wave velocity, V_{cn} = the normal component of the velocity at the model boundary, V_{cs} = the shear component of the velocity at the model boundary.

The lateral boundaries of an oedometer is a metallic interface while it is a rubber membrane in triaxial. The higher the impedance of the confining media relative to that of the soil the higher the portion of energy reflected back into specimen. This means that perfect reflection is attained in oedometer cells of metallic boundaries or when testing dry samples in triaxial apparatus. Saturated soil tested in a triaxial setup would be an intermediate case. Imperfections or asymmetric at the mechanical connections between transducers, soil and end platens will result in non-negligible phase shift (Arroyo et al., 2006). For a single input sin wave with apparent frequency F_{ap}, 99% of the signal energy lies below 2 F_{ap}. Arroyo et al. (2006) demonstrated the effect of side boundaries on the shape and interpretation of signals and stated that the errors that are incurred by disregarding the sample size effects may be very important. They concluded that these errors increase by increasing slender geometries, high wave lengths, reflecting boundaries, and low material attenuation. Arroyo et al. (2006) suggested including material damping, Poisson's ratio, wave length, and sample size in the propagation models for pulse tests interpretation. In addition they suggested enhancing the lateral boundary radiation (dissipation) of energy which would help the interpretation of bender tests.

Damping should be applied to a system subjected to dynamic loading, to count for geometric and material attenuation. FLAC® (version 4), which was used to perform the numerical simulations in this study, has three options of damping embedded in the code, namely Rayleigh damping, local damping, and artificial viscosity. This section discusses Rayleigh damping because it is best suited for this research. Local damping is embodied in the FLAC® static solution and may be used for dynamic analysis but it becomes unreliable for complex input time history (Girsang, C. H., 2001). Artificial viscosity is best used for waves with a sharp front. Rayleigh damping is frequency-dependent and has two components: mass-proportional and stiffness-proportional. FLAC® enables the users to define the first component only or the second component only or the sum of both components. At lower frequency of the system, the mass damping is more dominant, while at high frequency the stiffness damping is more dominant. Figure 3.1 shows that Rayleigh damping has a reasonably flat region that spans about 1/3 the frequency range.

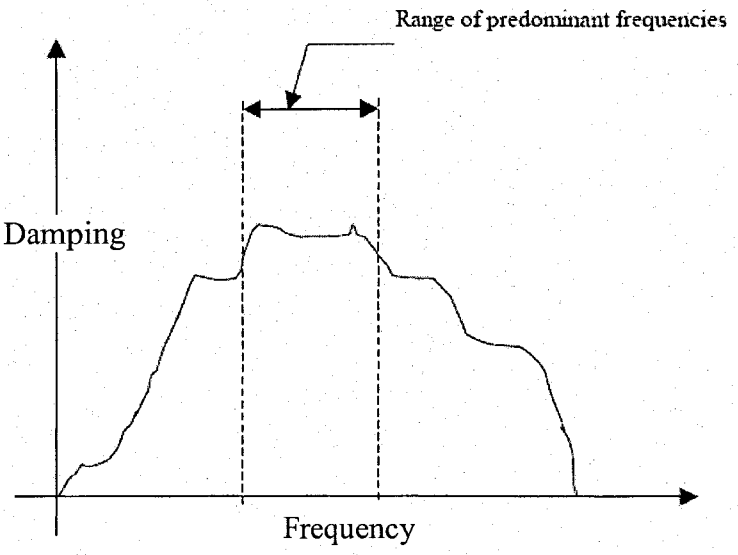

Figure 3.1 Rayleigh Damping versus Frequency (FLAC® Manual)

The idea in FLAC is to adjust the center frequency (f_{min}) of Rayleigh damping so it lies within the flat region, i.e. the range of predominant frequencies in the system. The center frequency (f_{min}) is the frequency at which the mass-proportional and stiffness proportional damping each contributes one-half of the total damping. For many cases, the predominant frequencies are related to the natural mode of oscillation of a system.

$$f = C/\lambda \tag{3.5}$$

where

f = the fundamental frequency related to the natural mode of oscillation of a system

C = the velocity of the wave related to the natural mode of oscillation of a system = C_S or C_P, depending on the problem analyzed

λ = the longest wavelength related to the natural mode of oscillation of a system.

3.3 Numerical Simulation of Elastic Waves Transmission through Laboratory Specimens by Bender Elements

3.3.1 Introduction

This section examines the interpretation problems related to elastic waves velocity measurements in laboratory by bender elements using numerical simulations. In addition, a new proposed method for the interpretation of shear wave pulse tests (Energy-Rise) are

introduced based on the numerical analyses. The currently used interpretation techniques were presented in Chapter 2. The purpose of these simulations is to investigate the propagation characteristics of elastic waves through soil, especially the effect of model dimensions, frequency of the input wave and soil properties on the interpreted velocity using the different existing techniques. Interference of waves and near-field phenomenon effects on the shape and interpretation process of the received signal are also considered.

3.3.2 Bender Element Models

Numerical analyses of bender elements pulse velocity test were carried out in this study. Thirty two numerical simulations were carried out for investigating the difficulties associated with signals interpretation (Table 3.1). The numerical model for bender elements is non axisymmetric due to the geometry of bender elements as well as the input signal which produces nonsymmetrical loading. Axisymetric models are 3-D models. Hence, the bender elements simulations were carried out using 2-D dynamic elastic modeling for simplicity. The system Rayleigh damping ratio is taken 1% at a frequency of 12 kHz. The soil mesh elements are 0.5mm squares. Each bender is 3mm long, 1mm thick and is located in the center of the sample (Figure 3.2). The bender-elements moduli were taken as 622 MPa for the bulk modulus (K) and 233 MPa for the shear modulus (G_o). The input signal is a sin-wave force applied to the tip of the bender element located at bottom of the sample. While, the received signal is the lateral (horizontal) displacement of the binder's tip located at top of the sample. Knowing the input soil parameters, the theoretical (actual) shear wave velocity (V_s) is calculated. The wavelength (λ) of the input signal is determined from the following equation provided that the input wave frequency (F) is known.

$$\lambda = V_s / F \qquad (3.6)$$

Consequently, the number of wave lengths within the sample's effective length is calculated (L_{tt}/λ). The input wave frequency is adjusted so that certain number of wave-lengths is obtained within the sample. This model is checked theoretically and found to be free of error. In other words, the calculated propagating-velocities of compression and shear waves between different receiver points inside the specimen were found equal to the input values. The sample length was varied in the different carried out simulations.

Table 3.1 The Carried out Numerical Simulations for Bender Elements Pulse Test.

Group No.	Soil Dimensions (mm)		Soil Density (Kg/m^3)	V_s (m/s)	V_p (m/s)	Poisson's Ratio	Input wave Frequency (kHz)
	D	H					
1	50	70	1800	200	400	0.333	3.125 – 25
2	50	70	2000	190	602.5	0.45	28.13 – 50
3	50	100	1800	200	400	0.333	2.12 – 17.02
4	50	140	1800	200	400	0.333	2.12 – 17.02

3.3.2.1 Signals Interpretation in Time Domain

The first group of simulations (no.1) represents a bender element setup installed in a triaxial apparatus (Figure 3.2). The simulated soil sample has a height of 70mm and a diameter of 50mm. The sample's boundary conditions are fixed in X and Y-directions at bottom and top ends of the soil sample while it is free at sides. The input frequency is varied from 3.125 kHz to 25 kHz, giving a range of sample's effective length to wave length ratio (L_{tt}/λ) of 1 to 8. Table 3.1 shows the input parameters for this group of simulations as well as for the other simulations carried out in this section. Figure 3.3 presents the output signals for two groups of simulations; each group is composed of 8 simulations with varying frequency. The horizontal axis is the time devided by the theoretical arrival time of shear wave (normalized time). Figure 3.3(a) shows the received signals for simulations of group no. 1. Two lines are drawn on this graph to show the theoretical arrival times of the P- and S-waves. The output signals for the simulations of group no.1 show that the arrival time by the direct arrival method varies from an input frequency to another. Choosing the point of arrival by direct arrival method depends on personal judgement. The arrival point is normally chosen depending on the shape of the received signal (first deflection, first peak or first trough, i.e. points A, B and C on Figure 3.3(a). Neither the first small peak, which can be considered as the first deflection (point A), nor the first trough (point B) nor the second peak (point C) represents the correct arrival time for all input frequencies of Simulation 1. If point C is chosen as the point of arrival, the s-wave arrival time is considerably overestimated. The closest point to the theoretical time is the

first trough (point B). The smallest error in travel time is 1.5% at the highest frequency (25 kHz). At low frequencies, less than 12.5 kHz which corresponds to $L_{tt}/\lambda \leq 4$, the shear wave arrival is not clear due to what is sometimes referred to as "near-field effect".

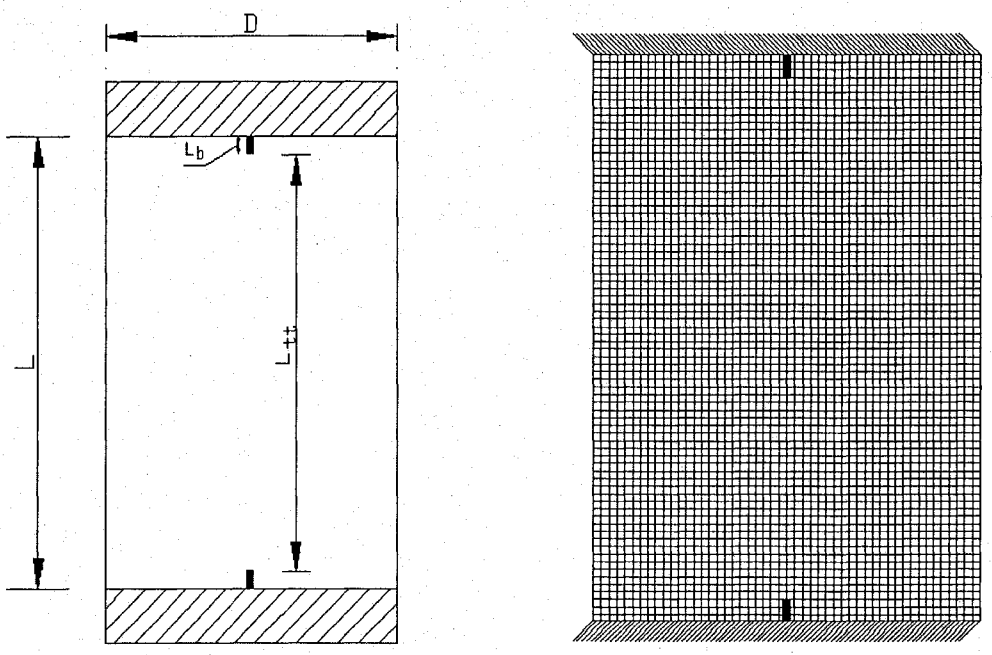

Figure 3.2 A Model for a Bender Element Setup Installed in a Triaxial Apparatus.

The second group of simulations (no. 2) is similar in geometry and end conditions to the previous simulation (no. 1) except that soil properties are different and the applied input wave frequencies are higher (Table 3.1). The specimen has a shear wave velocity of 190 m/s and P-wave velocity of 602.5 m/s (Poisson's ratio equals 0.45). The input frequency was varied from 28.13 to 50 kHz giving L_{tt}/λ ratio varies from 9 to 16. Figure 3.3(b) displays the results of these simulations. It can be realized that the P-wave arrival is more evident for soil of high Poisson's ratio. Also, increasing the input wave frequency increases the amplitude of compression wave. Other secondary waves are recorded on the received signal. They represent the reflected waves at the boundaries of the model, from either the sample's sides or the cap and base of the setup. These waves obscure the first arrival of the s-wave at some frequencies. This is evident for all input frequencies in group of simulations no. 2.

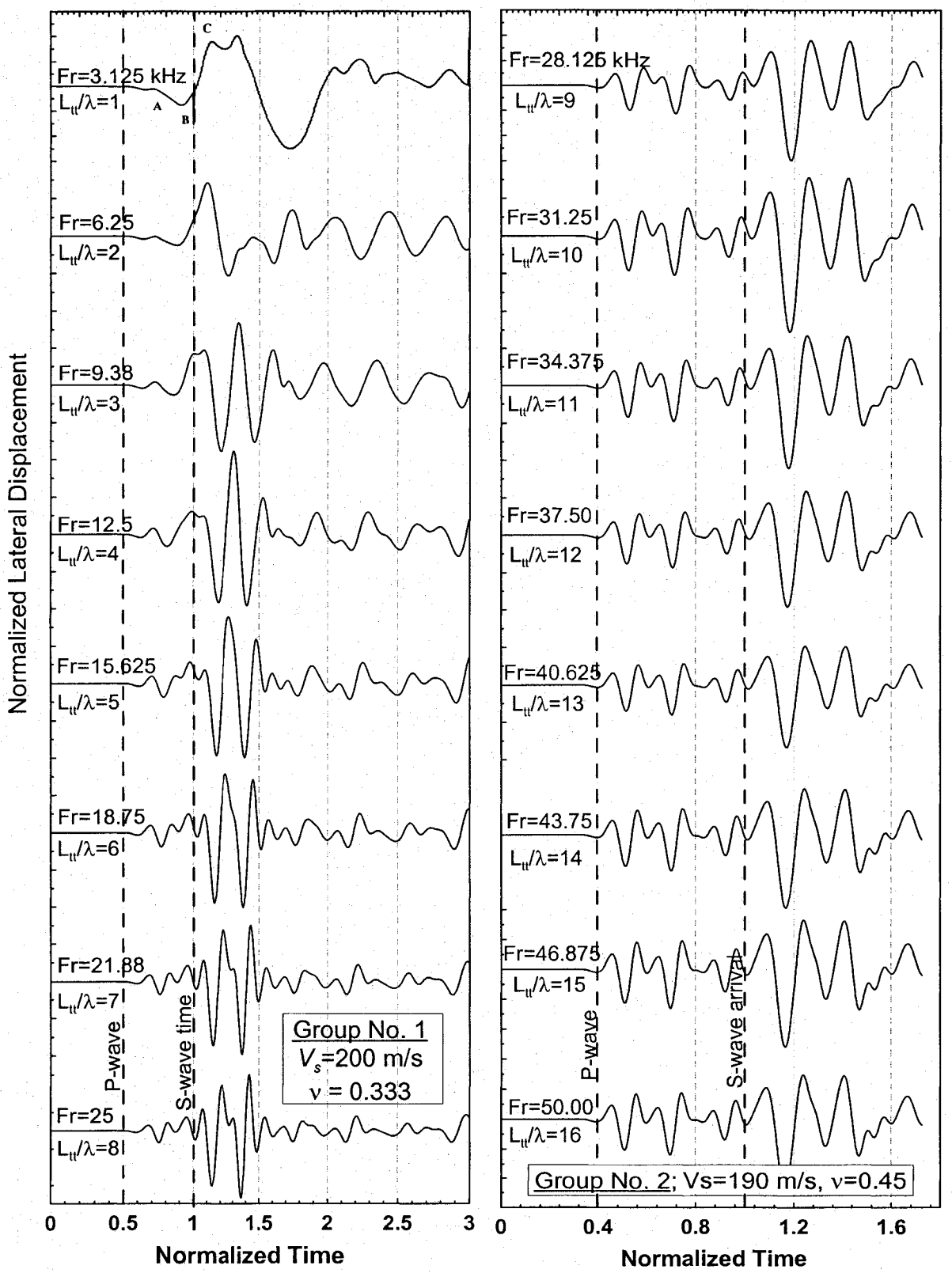

Figure 3.3 Output Signals of the Numerical Simulations for Bender Elements Pulse Test (Groups 1 & 2).

When using point C (first major peak), the error in direct arrival time varies from 8 % to 11% for this group of simulations (no. 2). The smallest error is about 1% at 50 kHz input frequency. The direct arrival time error ranges between 3.5% and 0.5% when considering the first trough as point of arrival. If the point of first-deflection is considered as the arrival point, the time error decreases from -1% to -4%. Thus, the shear wave velocity is over estimated. Figure 3.4 shows the variation of the normalized arrival time with frequency for the three proposed points of arrival (A, B & C) using results of the simulations in groups 1 and 2. The error in the direct arrival time varies from -13 % to +33 % and is higher at low input frequencies (up to 12.5 kHz) for the three chosen points of arrival. The errors are smaller at high input frequencies than at low frequencies. The error range becomes -5% to +11% when the input frequency is bigger than the threshold value for near-field effect ($L_{tt}/\lambda = 4$). The break in the curves of Figure 3.4 between frequencies 25 and 28.125 kHz suggests that soil properties have an influence on the interpreted V_s using the direct arrival interpretation method. The second important observation regarding the simulations of groups 1 & 2 concerns the Cross-Correlation technique. In some case, the absolute maximum of the cross-correlation function does not represent the correct point of arrival.

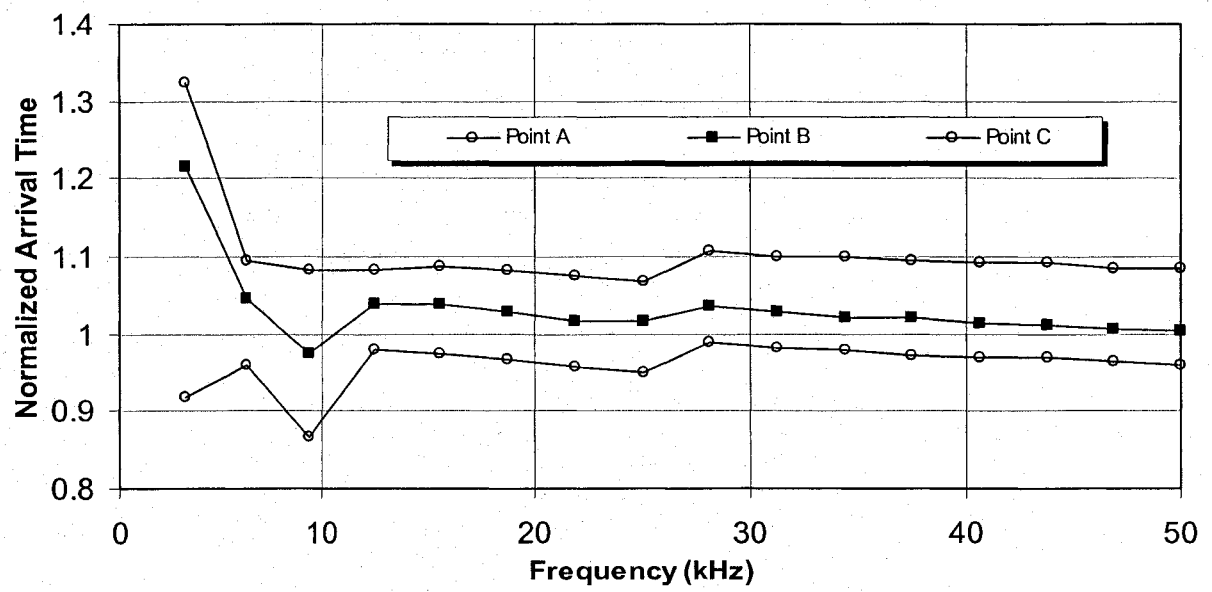

Figure 3.4 Variation of Direct Arrival Time with Input Frequency for points A, B and C Using Results of Simulations 1 and 2.

3.3.2.2 Cross-Correlation Method

Some automated algorisms/programs are being used to calculate the absolute maximum of the cross-correlation (C.C) function. Therefore, this type of C.C time is called "auto-C.C". For numerical simulations, the theoretical arrival time is known. Hence, the C.C peak that is close to this time is chosen, although it is smaller than the maximum peak. Figure 3.5 plots these two types of cross-correlations for simulations 1 & 2. The auto-C.C values are much higher than the most correct C.C values except at very high input frequencies where the two values are the same. For the two types of C.C., the arrival time is considerably over estimated. The error in cross correlation time varies between +8 % to +33% for these two groups of simulations when considering the first peak as the point of arrival. Thus, the maximum peak of C.C function is not always the correct choice. The cross-correlation method may produce erroneous results at some cases.

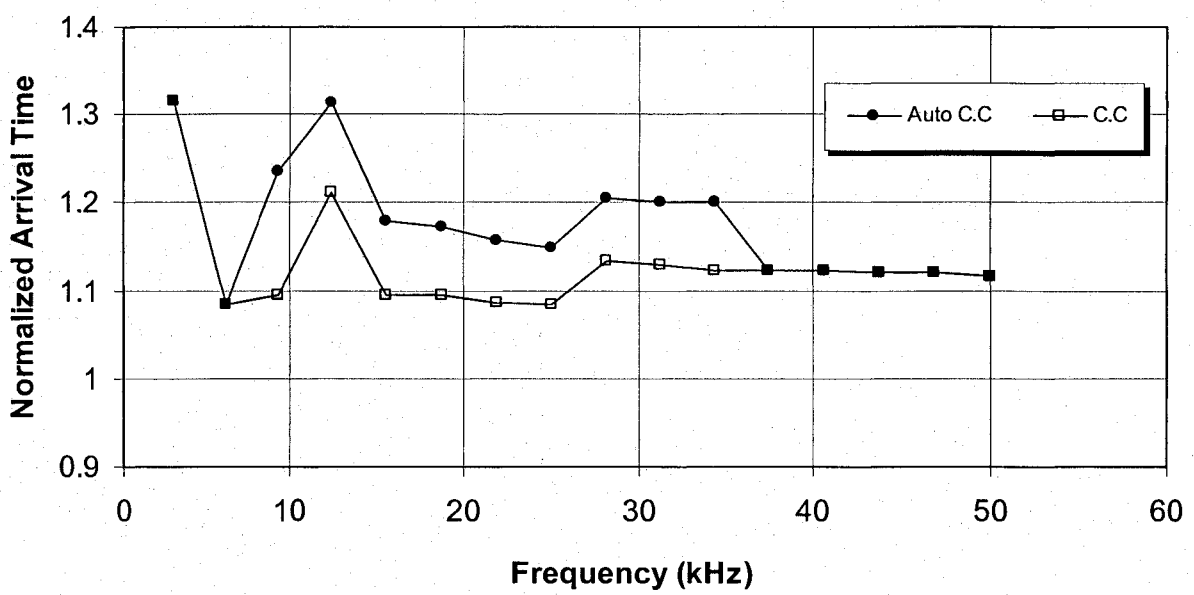

Figure 3.5 Cross-Correlation Arrival Times of Shear Wave for Results of Simulations No. 1 and No. 2.

Viggiani and Atkinson (1997) recognized that they were cross-correlating a signal *input* to one element with a signal *output* from another element and that the input signal to the transmitter may not truly represent the motion of the element. However, using self-monitoring elements, Schulteiss (1982) have found that with a single sine pulse excitation the frequency

spectrum of the input signal was similar to the frequency spectrum of the signal from the self-monitoring circuit. This may be correct for low input frequencies and as long as resonance does not occur. Figure 3.6 displays the relationship between cross-correlation time and input frequency for results of simulations 1 & 2 using two different input data sets. For the first curve, the cross-correlation time was calculated using the input force at emitter and the output deformation at receiver. The emitter deformation is used instead of the input force for the second curve. It can be seen that there are pronounced differences between the two methods. The deformation-to-deformation results give more accurate values at high frequencies. This proves that there is a small time delay taken by bender elements for converting the input force to displacement within soil. This delay depends on the rigidity of the bender. Also, these results prove that the cross-correlation method does not give accurate results at low input frequencies.

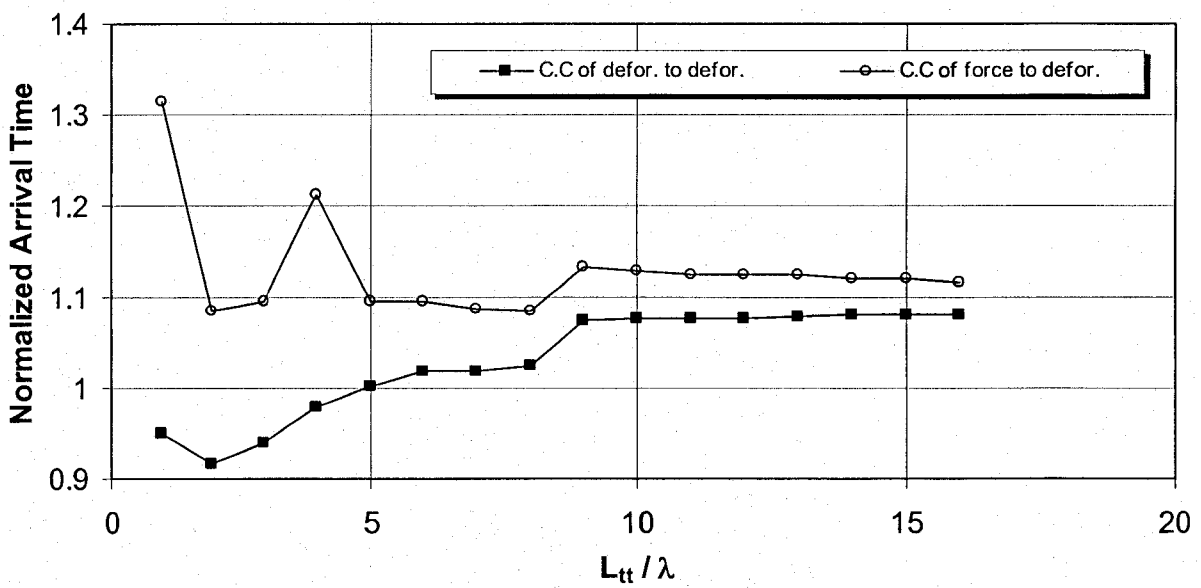

Figure 3.6 Cross-Correlation Based on both Input Force and Deformation at Emitter for Results of Simulations 1 and 2.

3.3.2.3 New Interpretation Method (Energy Rise)

The energy of the cross correlation function was explored in this study as a mean to calculate the time of arrival. The energy envelope was calculated after Goodman (1960). This envelope displays the energy of the cross correlation function versus time according to the following equation:

$$E = [f^2(t) + q^2(t)]^{0.5} \tag{3.7}$$

where $f(t)$ is the signal in the time (t) domain and q(t) is the conjugate function of $f(t)$.

Figure 3.7 shows the C.C function and its energy envelope for a simulation in group 1 (F_r = 12.5 kHz). It is realized that the C.C. time at the first peak is far from the true value. Two points are considered for examining the energy method; the energy rise time (point R) and the maximum energy time (point M). These two points are demonstrated on Figure 3.7 on the energy curve.

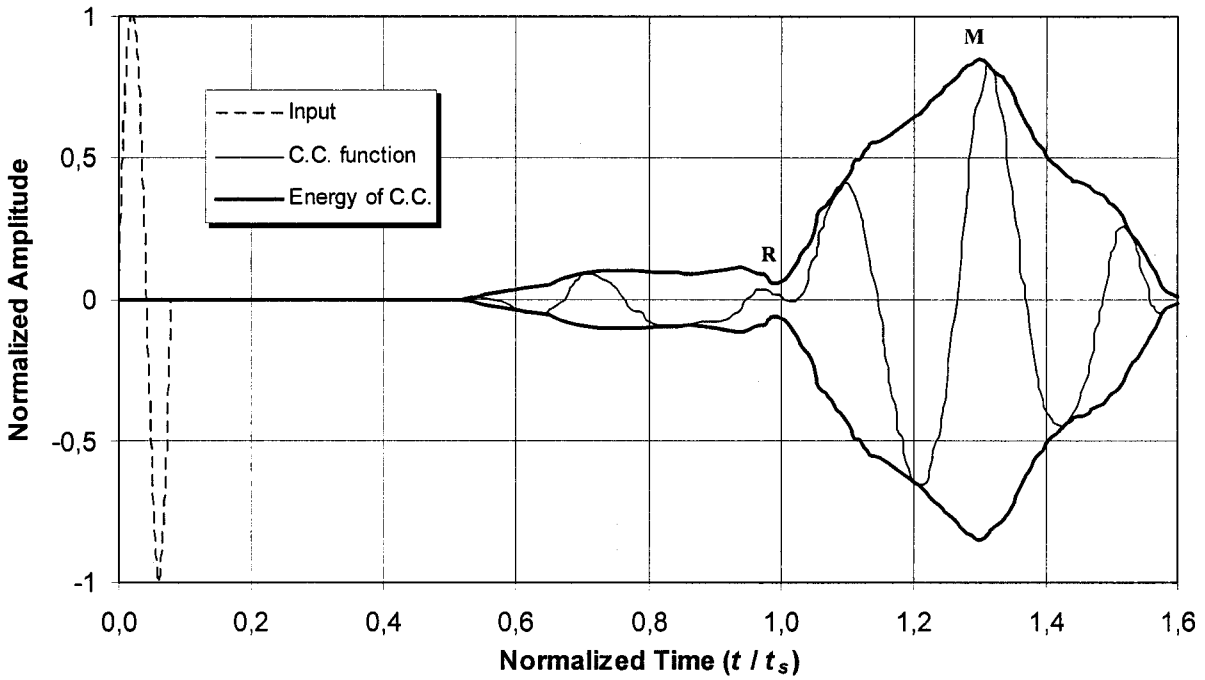

Figure 3.7 Input and Output Signals, their C.C Function and its Energy Envelope for Simulation No. 1 (Fr = 12.5 kHz).

Figure 3.8 displays the C.C function and the energy envelope versus time for a simulation of group no. 2 at frequency of 40.625 kHz. It can be seen that the energy rise time is more accurate than the maximum energy time. Figure 3.9 shows the relationship between

the normalized time of arrival and frequency for simulations 1 and 2 using five interpretation methods; the direct arrival, cross-correlation, peak-to-peak, the maximum energy and the energy rise. It can be seen that the maximum energy method gives higher values for the arrival time than the cross correlation values. Surprisingly, the energy rise time gives more accurate values than the cross correlation method. The error in computing travel time using the energy-rise method, at high frequencies behind the threshold for near-field effect, is less than 5% while it is up to 13 % for C.C method. The energy rise method is the most accurate for frequencies less than the 27 kHz. This range of frequencies is the most commonly used for testing soil in laboratory. Higher frequencies are rarely used for shear wave measurements but can be used for p-wave measurements. Even at the higher frequencies of group no. 2 simulations, the values of energy rise time are close to the values of direct arrival method, which is more accurate in this range. These findings are encouraging for further analyses of pulse tests employing the energy analysis technique.

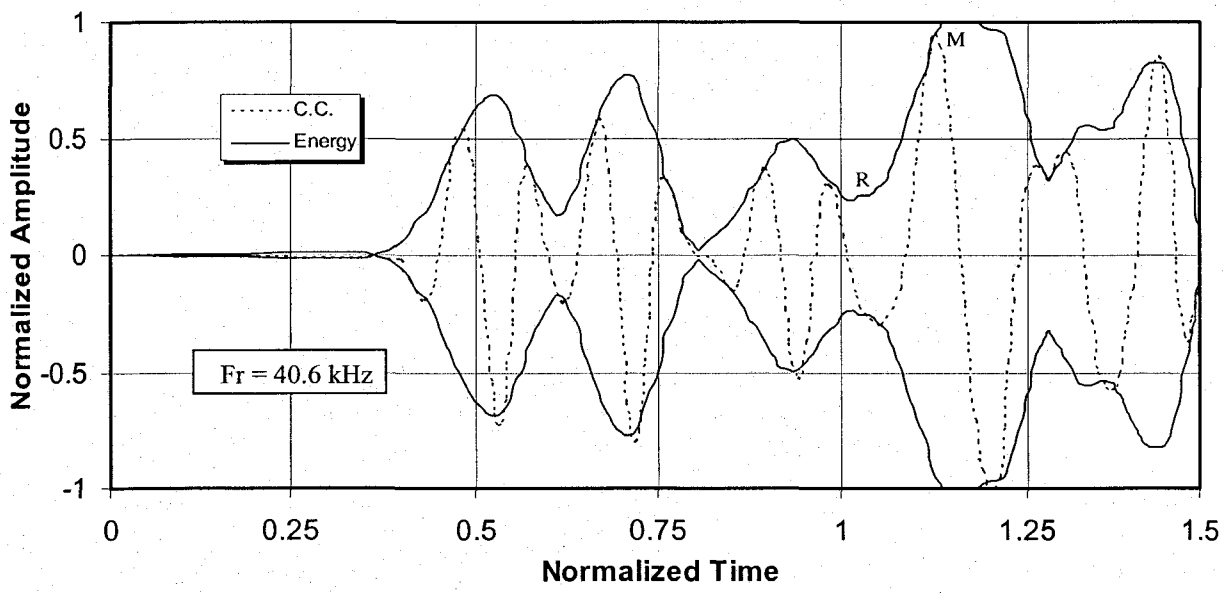

Figure 3.8 The Energy Envelop and C.C. Function for a Simulation of Group No. 2.

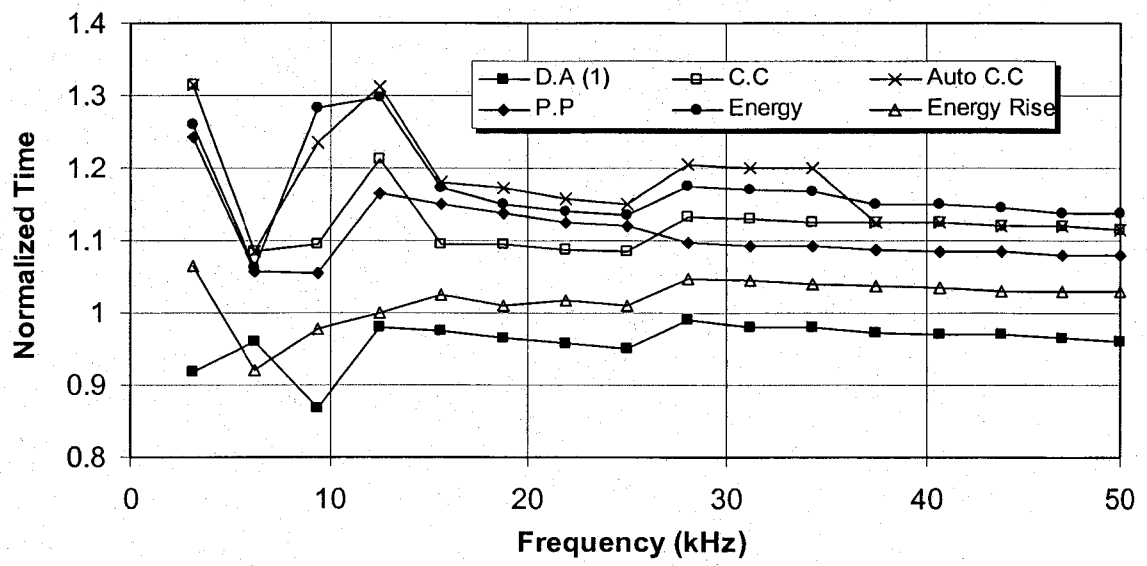

Figure 3.9 Different Arrival Times for Results of Simulations 1 and 2.

Kawaguchi, Mitachi and Shibuya (2001) mentioned that the peak-to-peak travel time between input and output pulses could essentially be incorrect; this definition may be practically acceptable only when the frequency of shear wave is high enough. These findings agree with the results of numerical simulations in this study. The peak to peak time approaches the correct time when increasing the input frequency.

3.3.2.4 Shape of Output Signal and Sample's Height

The height of the sample is increased to 100-mm for the third group of simulations (no.3) while all other parameters are the same like in simulation no.1. The L_{tt}/λ ratio for this simulation varied from 1 to 8. The output signals of this simulation are displayed on Figure 3.10(a). The direct arrival error in calculating the travel time for this simulation varies from 0 % to +15% when the first trough is considered as the time of arrival. This error range is less than that for the simulations of groups 1 and 2. Also, it can be realized that what is called near-field effect does not exist in this group of simulations at any frequency. Nevertheless, the ambiguity of choosing the point of arrival still exists at low frequencies. This is evident for frequencies up to 8.51 kHz, which corresponds to $Ltt/\lambda \leq 4$. These numerical results agree with the previous laboratory finding by Arulnathan et al. (2000).

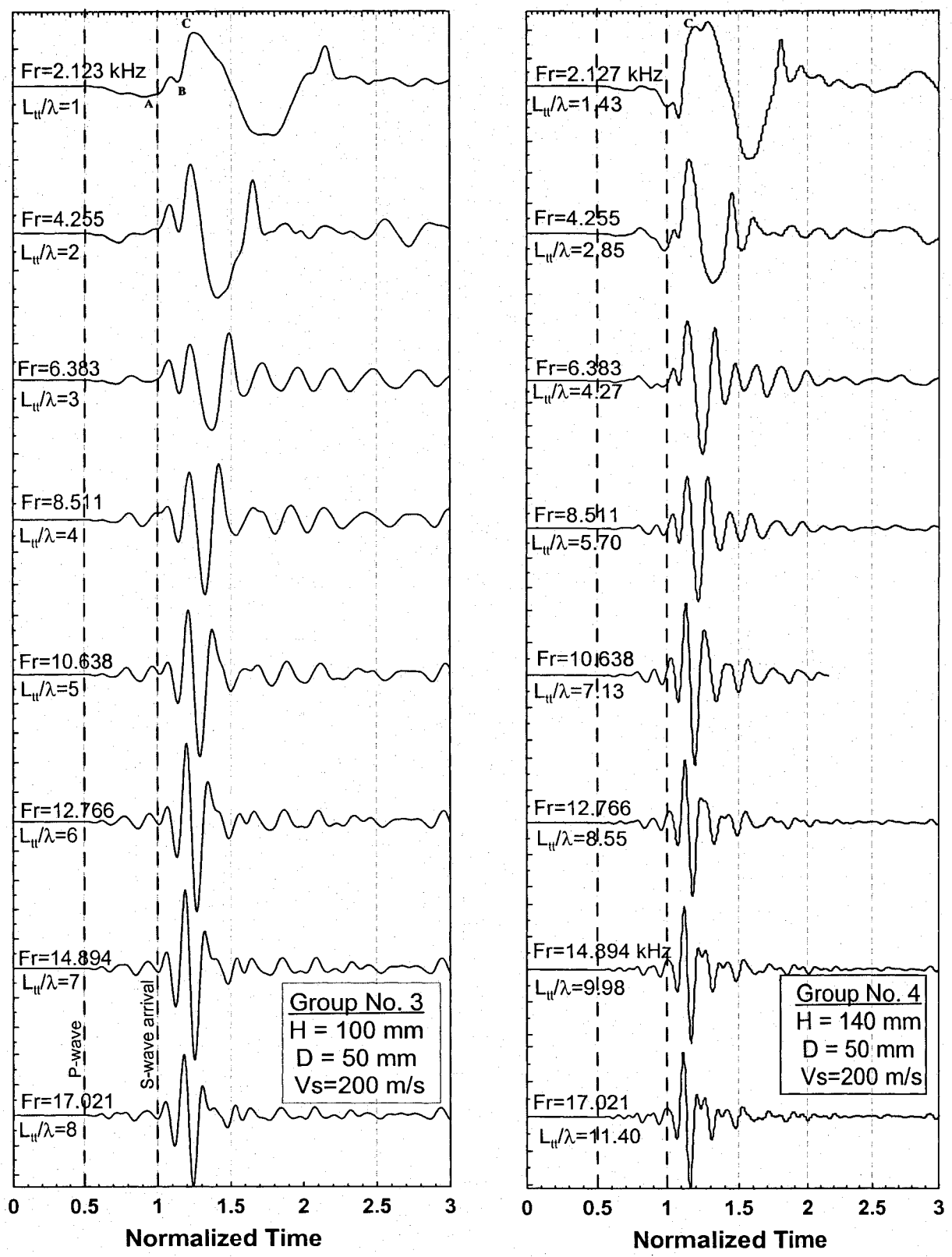

Figure 3.10 Output Signals of the Numerical Simulations for Bender Elements Pulse Test (Groups 3 and 4).

The height of the sample is increased to 140mm in the simulations of group no 4. The received signals are shown in Figure 3.10(b). The direct arrival time error for shear wave varies from -4 % to +9 % for the results of these simulations. The correct arrival time for this group of simulations is seen to be at or near the first peak of the received signals for frequencies 8.51 kHz to 17.021 kHz while it is at or near the first trough (near field effect) for the lower input frequencies where $L_{tt}/\lambda \leq 4$. On the other hand, in simulations of groups 2 & 3, the first trough is the nearest point to the correct arrival time at high input frequencies.

3.3.3 Conclusions

The previous results mean that neither the first peak nor the first trough is a characteristic point for the s-wave arrival. Therefore, the direct arrival method does not accurately give the correct arrival time because it depends on the shape of the received signal. Also, the personal judgment (subjectivity) influences choosing the arrival point on the time domain record. Generally, the shape of the received signal depends on the sample's dimensions and properties, the input waveform, frequency and voltage, the bender element length and rigidity, and its degree of fixation.

Thus, bender elements pulse tests suffer from many interpretation problems. The currently existing interpretation techniques are not accurate enough for precise measurements. Relying on one method of interpretation solely is not recommended. The time-domain methods should be used with caution or for situation where relative or approximate measurements are needed. Many input frequencies should be tried for each testing point in order to check the correct arrival time. At some conditions, the direct arrival technique may introduce minor error at some frequencies. But this is not guaranteed for all tests because there is no rule to definitely determine the correct arrival point using the time domain as it was shown previously.

The Energy-Rise interpretation method for pulse tests gave the most accurate interpretation results for the carried out simulations among the four other commonly used techniques.

3.4 New Modes of Shearing Excitation for Pulse Velocity Tests

Two new modes of excitation for carrying out pulse tests, which defer from bender element mode, are explored and analyzed herein. The first mode is radial shearing and the second is all-base simple shear. Three sizes of the excitations area were investigated for the first mode. Five groups of numerical simulations were carried out to study these new modes of shearing excitation.

3.4.1 The Numerical Model

Only the soil is simulated in these models for simplicity. The soil specimens have a length of 116mm and a diameter of 102mm. The soil properties were taken as 150 m/s for shear wave velocity and 0.333 for Poisson's ratio. The numerical model is chosen to be axisymmetric dynamic elastic. The end conditions are fixed in the y-direction at top and bottom ends of the specimen (all over the surface) and free in the x-direction where the excitation force is applied (D_e) [fixed in x-direction out of the excitation area]. The side boundaries of the model are free in X and Y directions. The soil elements are squares of 0.5mm side length. The damping ratio was taken as 0.5 % for this group of simulations. The input signal is a sin-wave force applied at the bottom end of the sample. The received signal is taken as the lateral (horizontal) displacement at the receiver. Figure 3.11 shows the model dimensions and its boundary conditions. The soil parameters and end conditions are also given in Table 3.2.

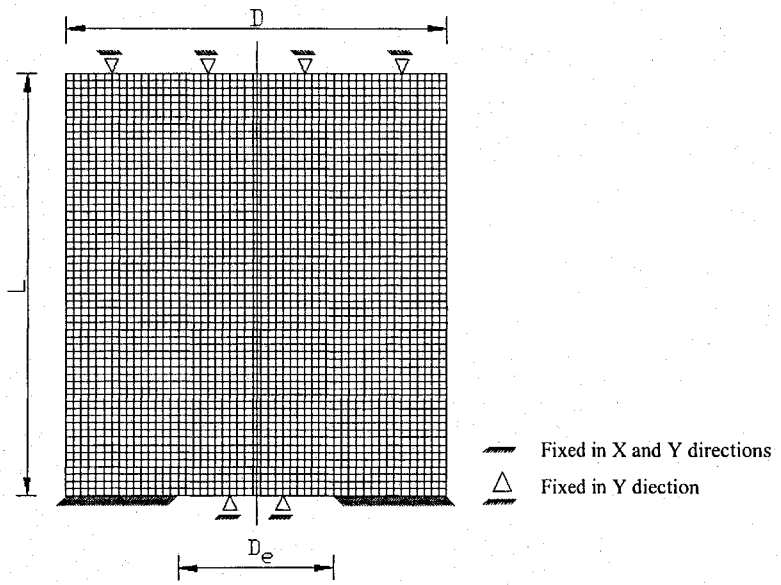

Figure 3.11 The Numerical Model and its Boundary Conditions.

Table 3.2 Numerical Simulations for the New Modes of Shearing Excitation.

Group No.	Geometry & end Conditions	Size of Emitter (D_e)	Soil Dimensions (mm)		Soil Density (Kg/m^3)	V_s (m/s)	V_p (m/s)	Poisson's Ratio	Input wave Freq. (kHz)
			D	H					
5	Proctor Sample, free sides	2mm base radial shear	102	116	1800	150	300	0.333	10 - 40
6	Proctor Sample, fixed mold sides	D/4 base radial shear	102	116	1800	150	300	0.333	10 - 40
7	Proctor Sample, free mold sides	D/4 base radial shear	102	116	1800	150	300	0.333	10 - 40
8	Proctor Sample, free sides	All base radial shear	102	116	1800	150	300	0.333	10 – 40
9	Proctor Sample, free sides, 2D-model	All base simple shear	102	116	1800	150	300	0.333	10 – 40

3.4.2 Excitation with 2mm-Diameter Radial Shearing

Simulation Group No 5 was performed to investigate the suitability of *radial* shear excitation by a plate of 2mm-diameter compared to other modes of excitation. The input wave is applied as a horizontal force in the radial direction, distributed all over the area of a 2mm-diameter circle (at each node). It is noticed that the diameter of the emitter and the receiver of this model are equal to the thickness of a bender element. The frequency of input sine-wave signal is varied for each group of simulation (10, 20, 30 & 40 kHz). The signal is applied in the horizontal direction at the sample's base. The horizontal deformation at the sample's axis (not shown here) is zero because the model is axisymmetric. Figure 3.12 shows the horizontal displacement of the receiver element which lies at 1-mm from the center of the sample at top.

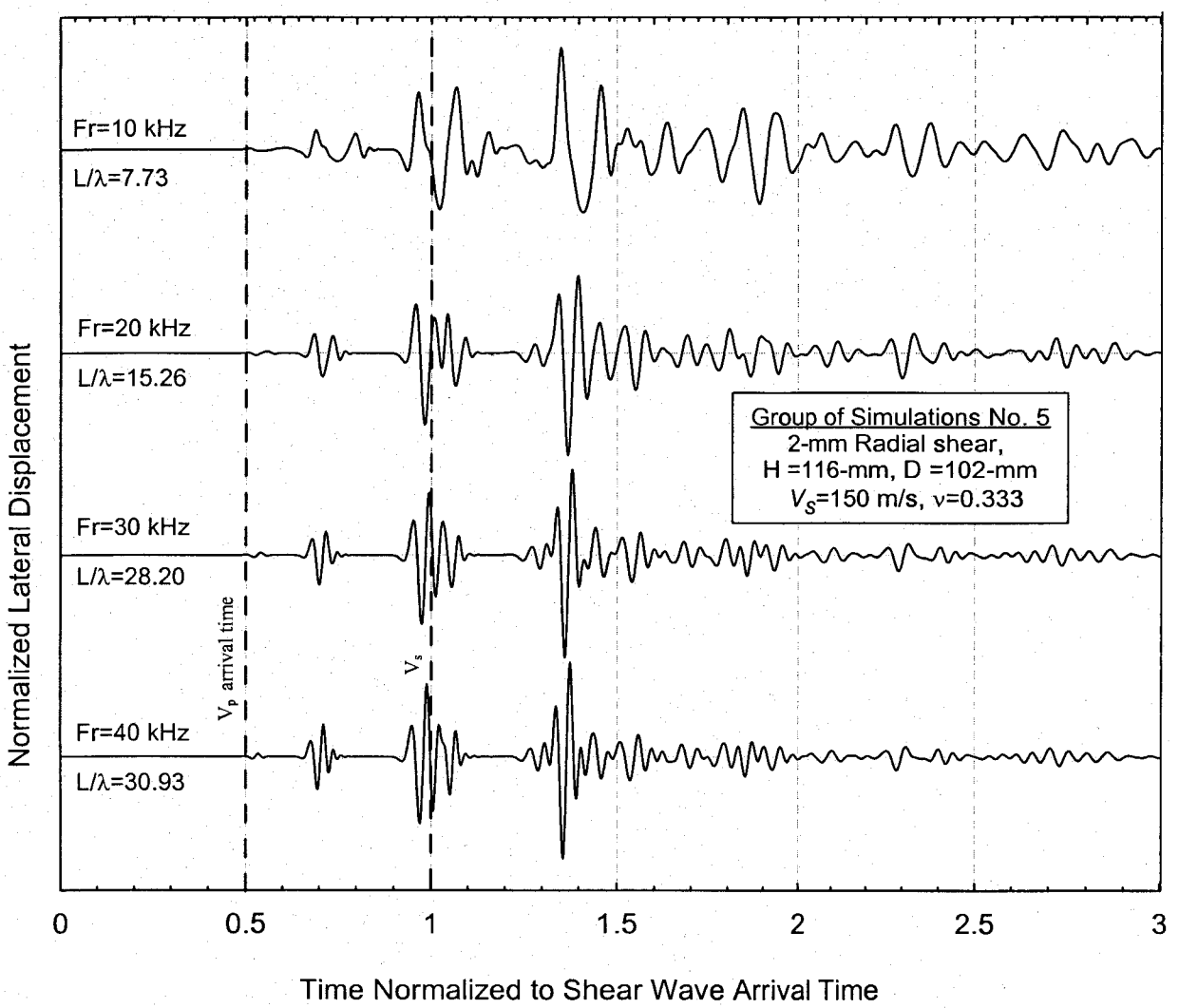

Figure 3.12 Output Signals of Simulation Group No. 5 (Excitation Area of 2-mm-Diameter).

For all input wave frequencies, the obvious S-wave arrival time differs from the correct arrival time while the P-wave arrival time is accurate. This can be explained by analyzing the vector displacement of the model's elements at different times during the wave transmission. Figure 3.13 shows nodes displacement of the model at eight different times (Only the right-half of the specimen is displayed). When the p-wave encounters the sample's sides, it emits two reflected waves that precede the base shear wave: a compression wave and a shear wave. The reflected compression wave is more energetic than the reflected s-wave. This p-wave obscures the shear wave front. It can be realized that the wave's fronts are curved. Hence, it hits the free surface of the sample at a certain angle of inclination resulting in creation of many reflected and re-reflected waves. Moreover, the reflected waves meet each other and produce other waves

which increase the complexity of the received signal. These reflected waves travel before and after the base shear wave. Hence, they obscure the first arrival of the main shear wave at certain conditions.

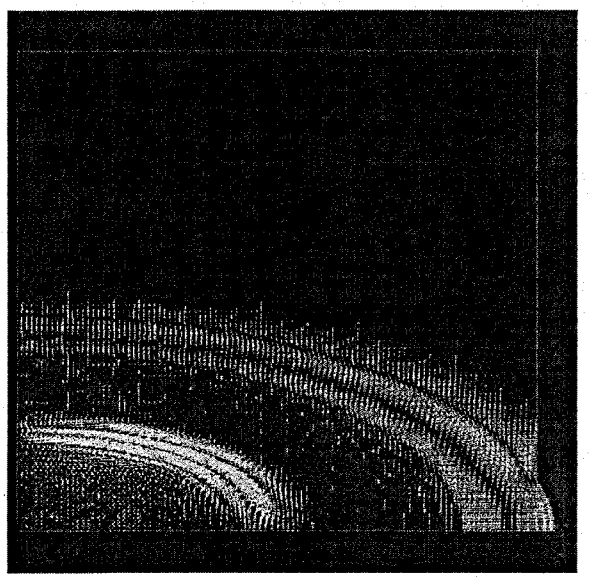

a) The compression and shear waves spread in a spherical manner.

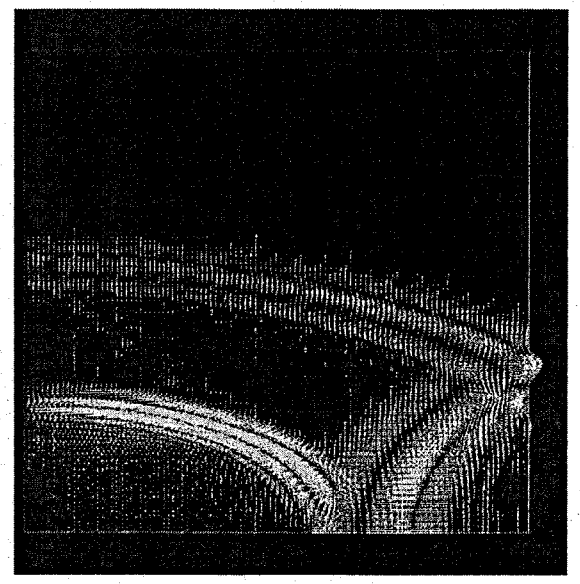

b) Creation of side reflected waves (compression and shear waves).

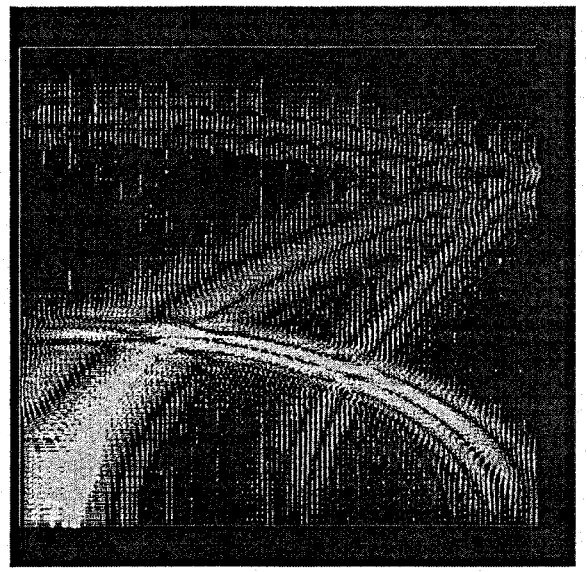

c) The reflected P-wave from both sides meet each other at the sample's centre behind the s-wave. The reflected shear wave due to p-wave is also seen.

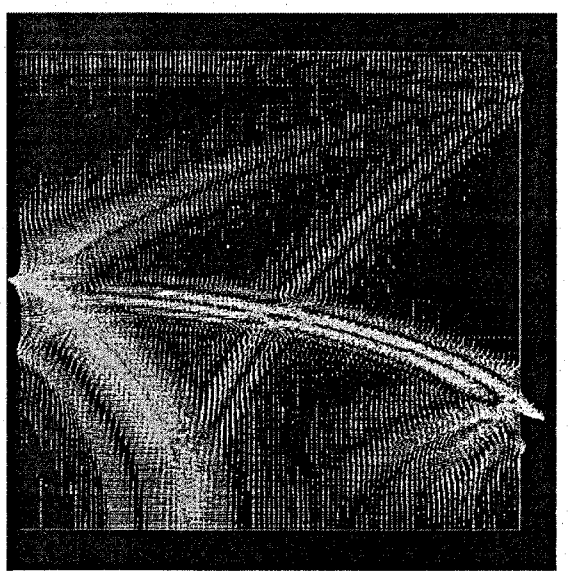

d) Creation of more reflected p-waves when the reflected waves coming from sides meet each other at center. Also, the base s-wave creates other reflections at sample's side.

Figure 3.13 Displacement Vectors for Simulation 5 at Different Times.

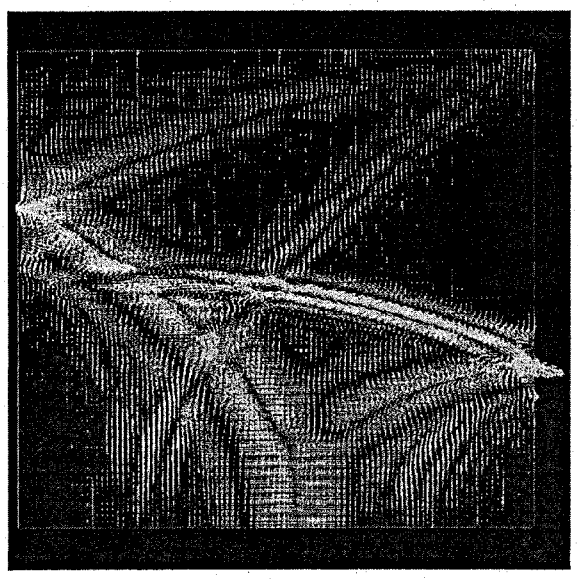

e) Progress of reflected waves. The s-wave energy is less than the energy of reflected waves.

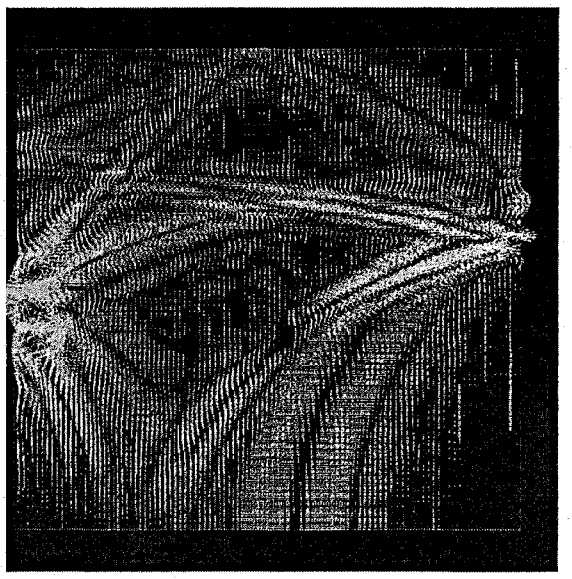

f) The reflected waves reach the upper cap and create other reflections.

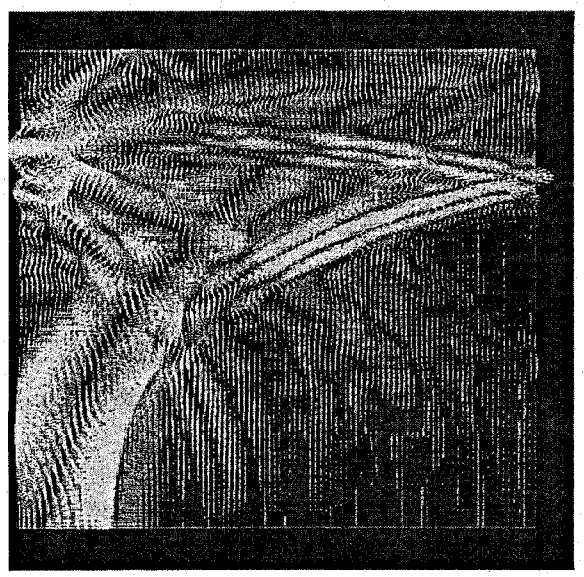

g) The reflected waves reach the receiver in front of the base-shear wave which has less amplitude.

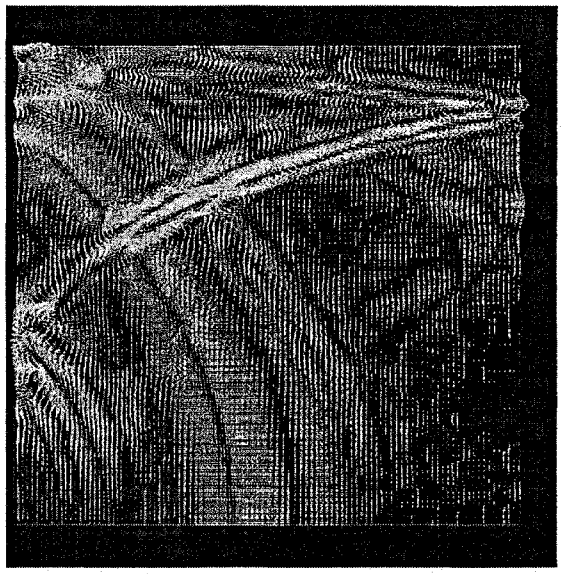

h) The s-wave reaches the receiver followed by reflected shear wave of high energy.

Figure 3.13 Displacement Vectors for Simulation 5 at Different Times (cont.).

3.4.3 Excitation with 26mm-Diameter Radial Shearing

The diameter of the emission area is increased to 26-mm in Group of Simulations No. 6. The sample's sides are chosen to be fixed while all the other parameters are the same as in Group

of Simulations No. 5. The input force is distributed all over the excitation area. The output signals of this simulation are shown in Figure 3.14 for a capturing point 20mm away from the centerline at top. Figure 3.14 reveals that the direct arrival method would either overestimate or underestimate the travel time depending on the input frequency. It can be seen that p-wave arrival time matches the theoretical time because no reflections precede the P-wave. The measured amplitude of the p-wave is relatively small compared to s-wave amplitude because the model is fixed in y-direction at top and bottom. In addition, the input wave is applied as a shear wave in the x-direction. These small deformations of the p-wave are due to the vertical elastic deformation of the soil elements according to theory of elasticity. The p-wave amplitude depends on the value of Poisson's ratio. Figure 3.15 shows the y-displacements at receiver for an input frequency of 30 kHz. It can be seen that the P-wave amplitude is bigger in the y-direction.

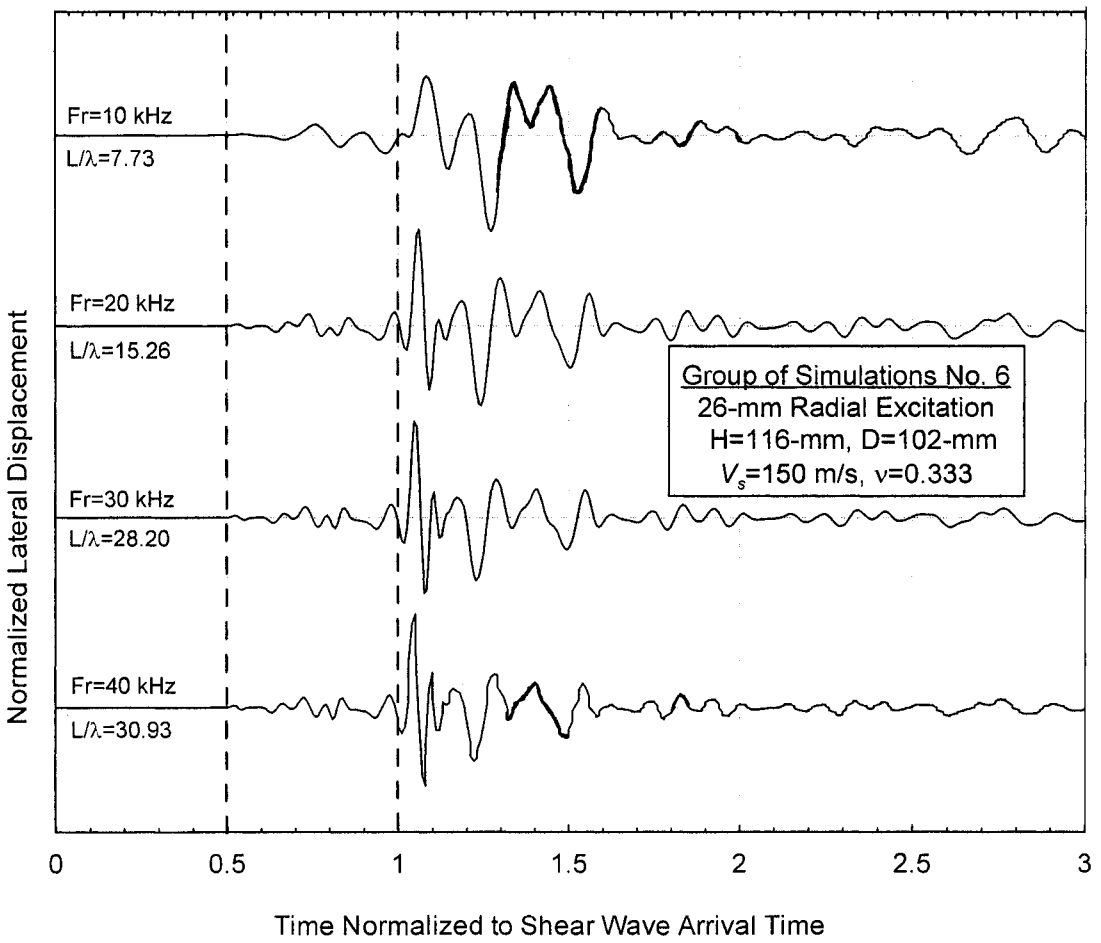

Figure 3.14 Lateral Displacements at Receiver for Simulation 6.

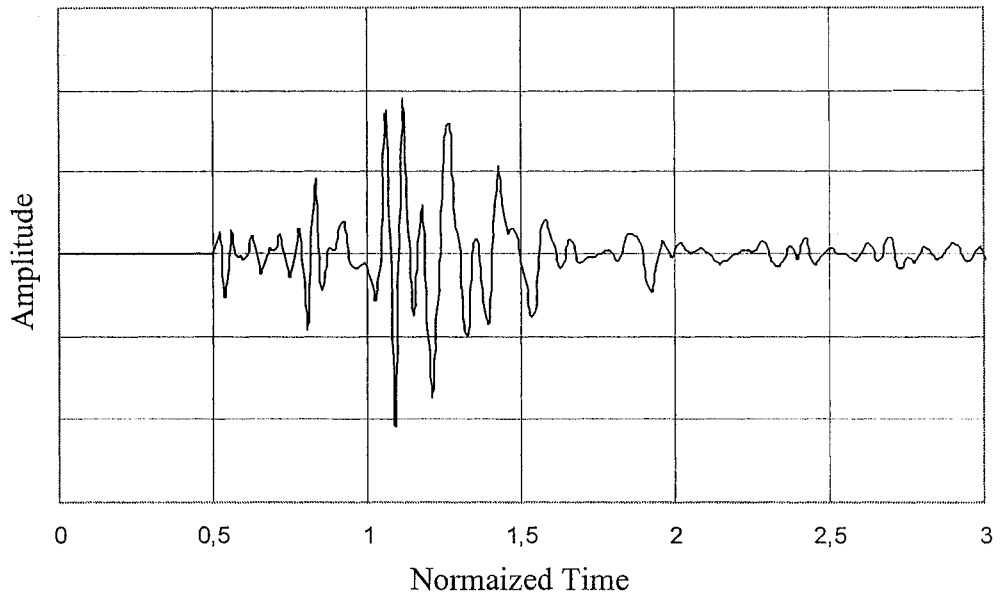

Figure 3.15 Vertical Displacements at Receiver for Simulation 6 (Fr=30 kHz).

Considering that the front of the propagating signal is curved, it can be concluded that the point source and receiver setup may be inaccurate measurement device when the emitter and receiver are not on the same axis which is parallel to the wave propagation direction. This is normally the case when more than one emitter are installed at one end of a specimen. The front of the traveling wave is curved, thus it arrives at different times at each point on the sample's end. Thus the bender element may miss the first arrival point of the transmitted wave or it may not capture it at all when the wave arrives away of the element. Figure 3.16 shows the received signals of Group of Simulations No. 6 at a receiver point located at a distance of 7.5mm from the centerline of the specimen. The received signal has some portions where no deformation is recorded. Also, the second major-wave on the output signal has higher energy than the shear wave. This dominant wave would be considered as the shear wave if measurements are made without understanding and analyzing the test setup. Therefore, an actuator that is capable to sense the movement all over a wide area is believed to be more precise for measurement because it will record the received waves all over its surface.

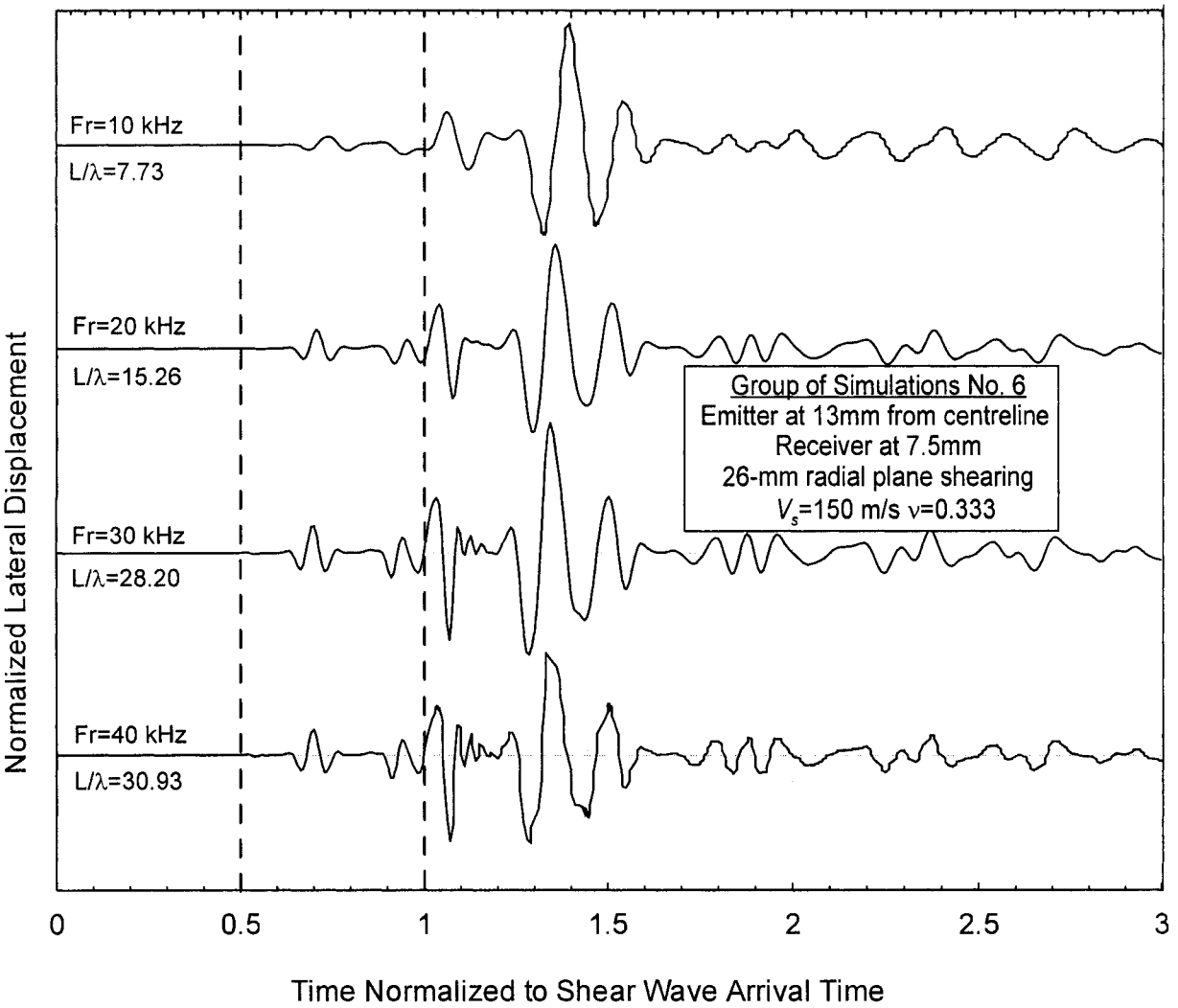

Figure 3.16 Lateral Displacement at a Different Reception Point for Simulation 6.

Another Group of Simulations (No. 7) was carried out with free mold-sides condition in order to investigate the boundary condition effect. All other parameters of these simulations are the same as in Group of Simulations No. 6. Figure 3.17 shows the results of these simulations for a capturing point 20-mm away from the centerline. Almost, the obtained signals have the same shapes as in Group of simulations No. 6. This means that a free boundary condition of the sides has nearly the same effect as a fixed boundary condition on the shape of the received signal. The wave is reflected from a free boundary like it does when it encounters a fixed or hard boundary. The p-wave reflection in this case is smaller than that in a fixed boundary case, and it attenuate quickly when it meets the base shear wave.

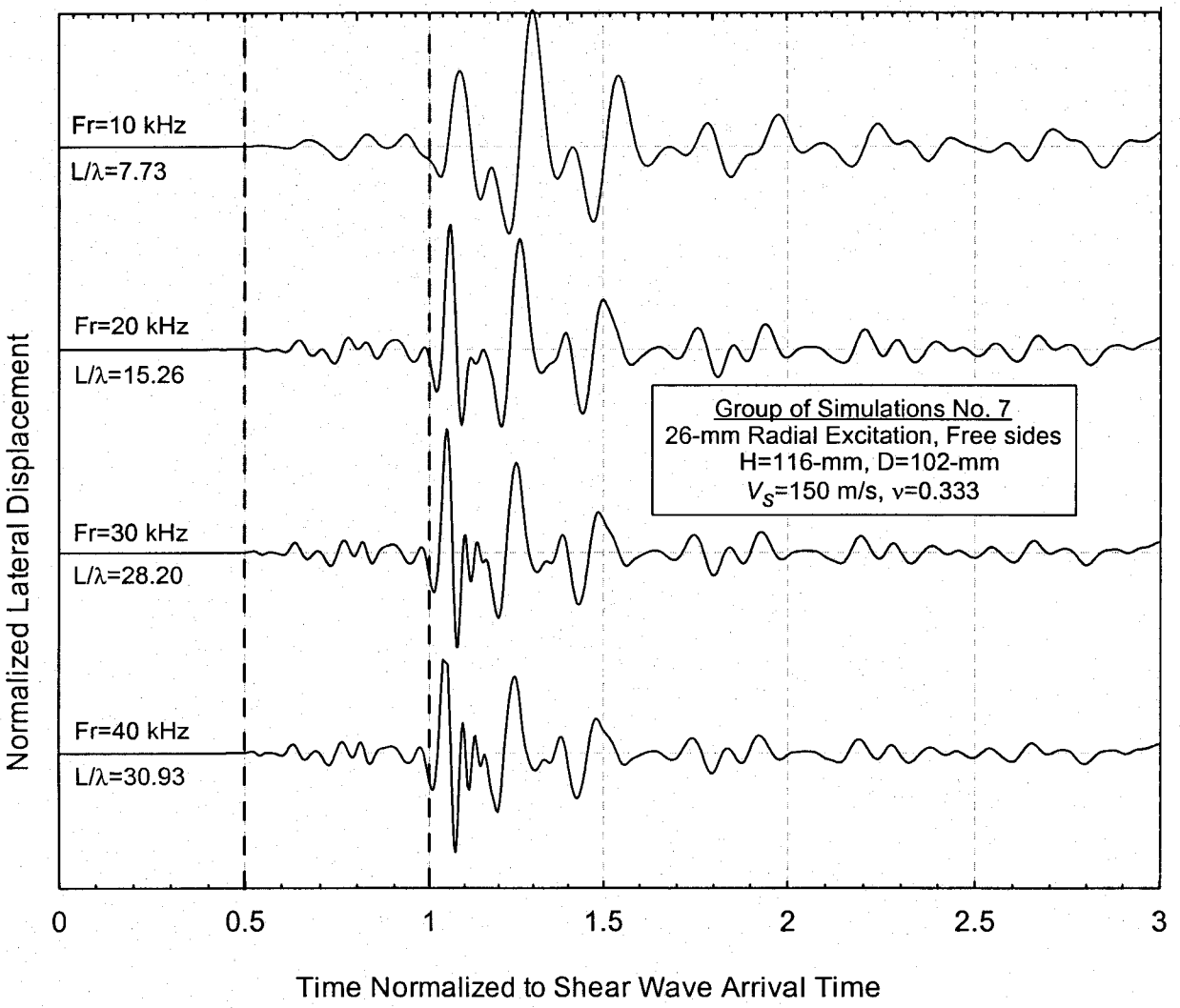

Figure 3.17 Lateral Displacements at Receiver for Simulation 7.

Figure 3.18 displays the horizontal displacement in the model at different times, in order to investigate the wave transmission characteristics. The s-wave reflection is bigger than that of p-wave. The reflected wave travels behind the base S-wave at an inclination with the horizontal direction. This wave is recorded as a secondary wave which comes behind the main shear wave. At low frequencies, the amplitude of this wave is bigger than the base shear wave (Figures 3.16 & 3.17). This secondary wave corresponds to the maximum of the cross correlation function. Thus, it might be falsely chosen as the shear wave. By increasing the input frequency at emitter, its amplitude becomes less and it separates well from the base shear wave (Figure 3.17). These results are clearly seen on Figure 3.18 which shows the displacement vectors of simulation 7 during wave propagation.

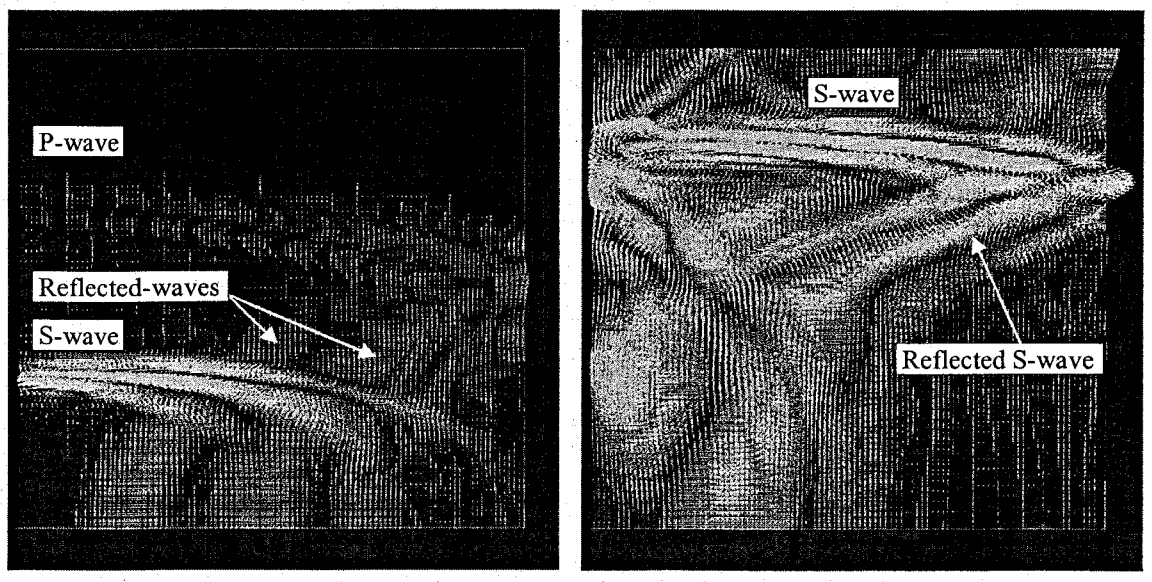

a) The s-wave is travelling clearly behind the p-wave.

b) The s-wave travels followed by a reflected shear wave which has high energy.

Figure 3.18 Displacement Vectors for Simulation 7 at Two Times (Fr = 30 kHz).

3.4.4 All Base Radial Shear Excitation

Group of Simulation No. 8 is configured so that excitation is made by a shearing wave applied all over the bottom of the sample. In other words, this case represents a whole base radial shearing. Figure 3.19 displays the received signals at the top end of the sample. The direct arrival time of the S-wave is clear without any preceding near-field effect. The first deflection in the signal is sharp and accurately represents the theoretical arrival time. The reflected waves from the sides of the sample are eliminated. The base shear wave is the only dominant wave within the received signal. Figure 3.20 shows the displacement of soil elements for simulation 8 while the shear wave is traveling inside the specimen. The all-base mode of excitation creates a neat horizontal wave front which is perpendicular to the sample's sides (mold sides). Hence, the reflected wave is also a horizontal wave in the opposite direction, i.e. in the same plane of the transmitted wave. Thus, it reduces the deformation's amplitude of the base shear wave and it does not create secondary waves near or away from the base-shear wave.

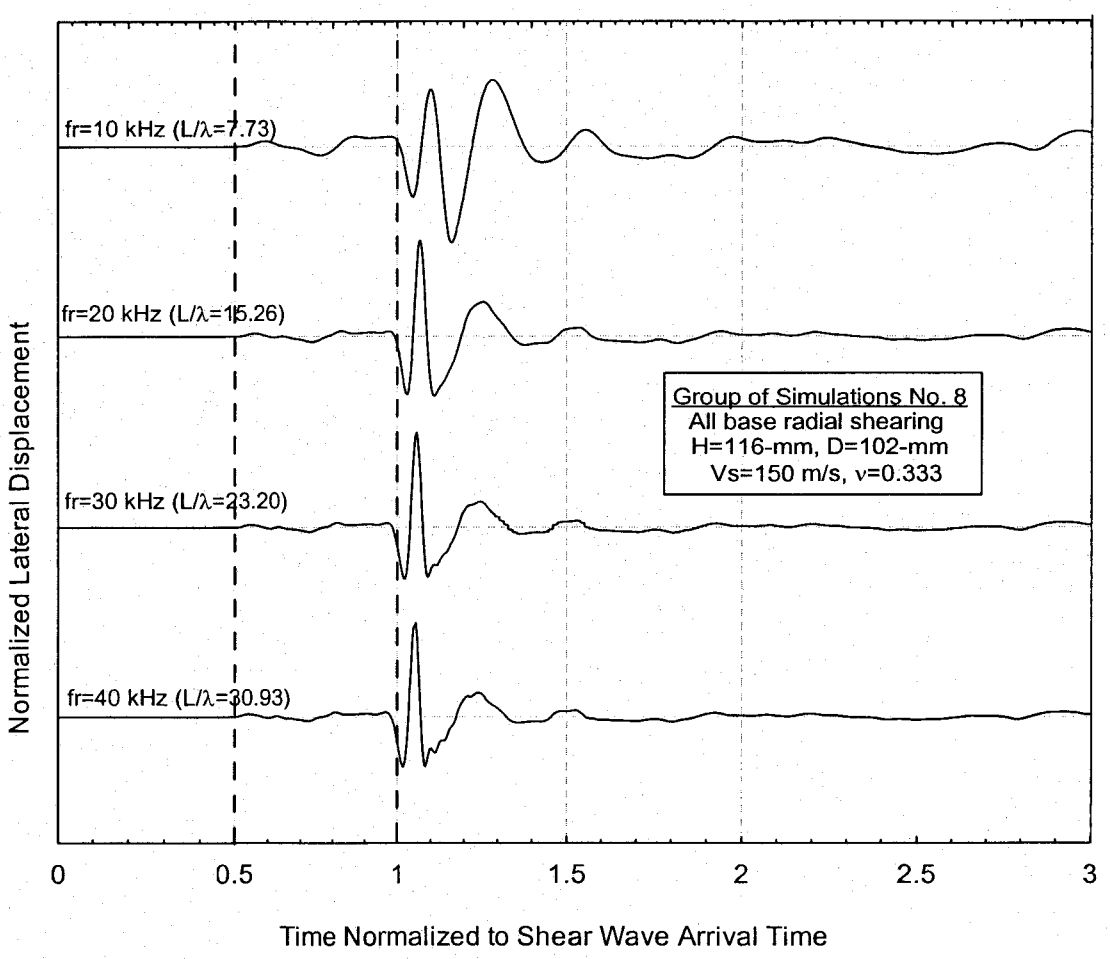

Figure 3.19 Lateral Displacements at the Receiver for Simulation 8.

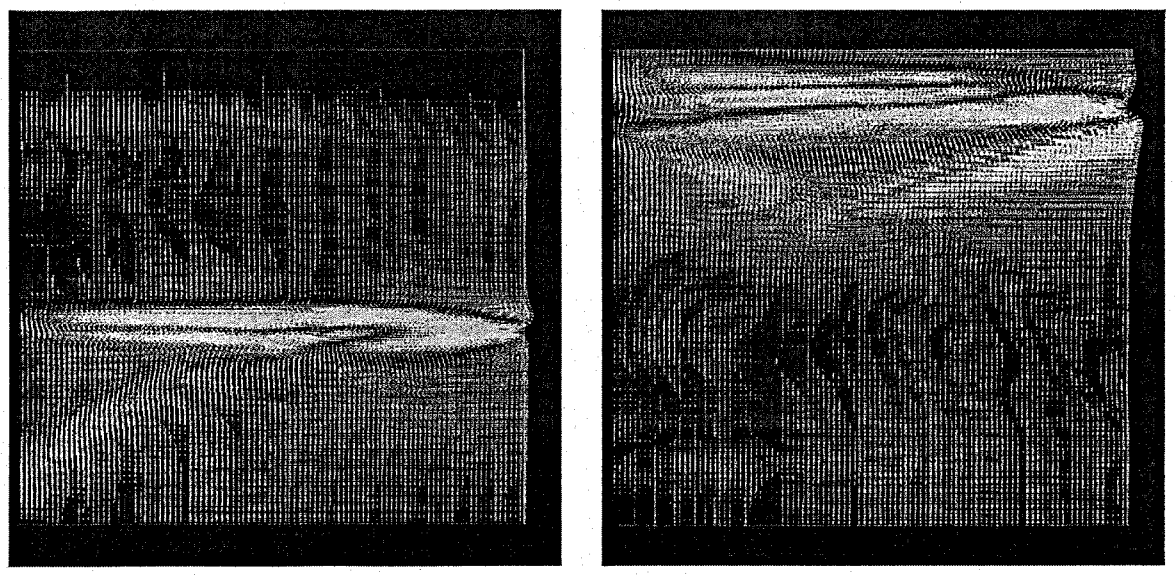

Figure 3.20 Victor Displacements for Simulation 8 during Waves Travel through the Sample (Fr = 20 kHz).

Figure 3.21 shows the normalized arrival time for Group of Simulation No. 8 using different interpretation methods. It can be realized that all these methods give quite accurate results for this type of shearing. The error in calculating the arrival time is within 5% for all methods except for maximum energy at 10 kHz. The relationship of direct arrival method shows a clear stable change in the arrival time with frequency. The measured direct arrival time approaches the correct value by decreasing the input frequency. Extrapolating the direct arrival curve at zero frequency almost gives the correct arrival time. This confirms that the input frequency affects the interpreted shear wave velocity. In other words, transmission of elastic waves in soil has a dispersive nature. Each frequency travels at a certain velocity. Therefore, the time-of-flight calculated by direct arrival method suffers from a major problem due to the velocity dispersion in the sample. This leads to different frequency components within the wave form arriving at different times near to the exact arrival time, thus severely distorting the transmitted signal. Therefore, the arrival time can be accurately calculated using frequency domain analysis. The characteristic velocity should be extrapolated at zero frequency (as demonstrated in Chapter 4). Further research is needed to study these finding for developing a new method of interpretation based on the analysis of both frequency domain and energy data. This issue is studied in detail in chapter 4.

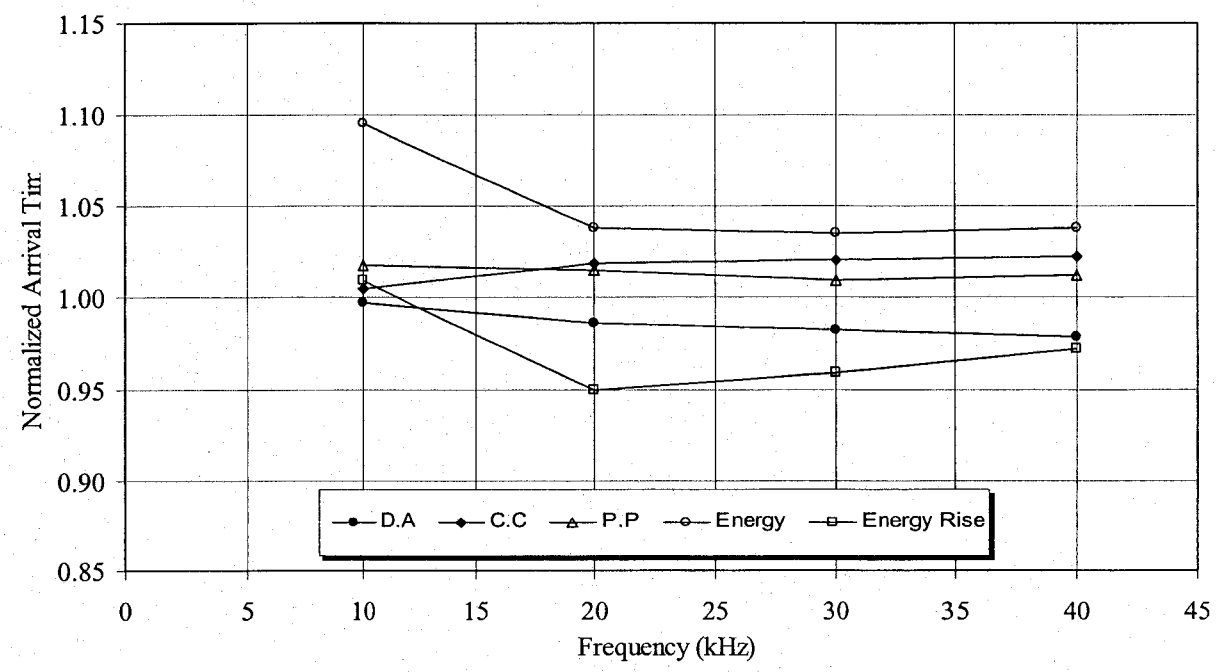

Figure 3.21 The Travel Time using Different Methods for Simulation 8.

3.4.5 All Base Simple Shear Excitation

A second mode of shearing was examined in this research. The soil is excited all over the whole surface with a simple shear (the excitation is not in the radial direction). The whole end is forced to deform in one direction at a time. For a sine wave input, the soil's end deforms laterally in one direction during the 1st half of the signal, then in the opposite direction in the second half. This mode represents a large circular shear plate of a diameter equals to the sample's diameter. This mode of shearing was simulated in 2-D model for simplicity (Group of Simulation No. 9). The results of this simulation are shown on Figure 3.22 at four input frequencies. It can be realized that the time of arrival is nearly at the first peak and it varies from frequency to another. These results are much better than bender elements results. Figure 3.23 shows the displacement vectors of the model's elements while the s-wave is about halfway to the receiver. It shows that the p-wave front emits a diagonal reflected wave with a small energy compared to the s-wave energy. The s-wave front is still horizontal.

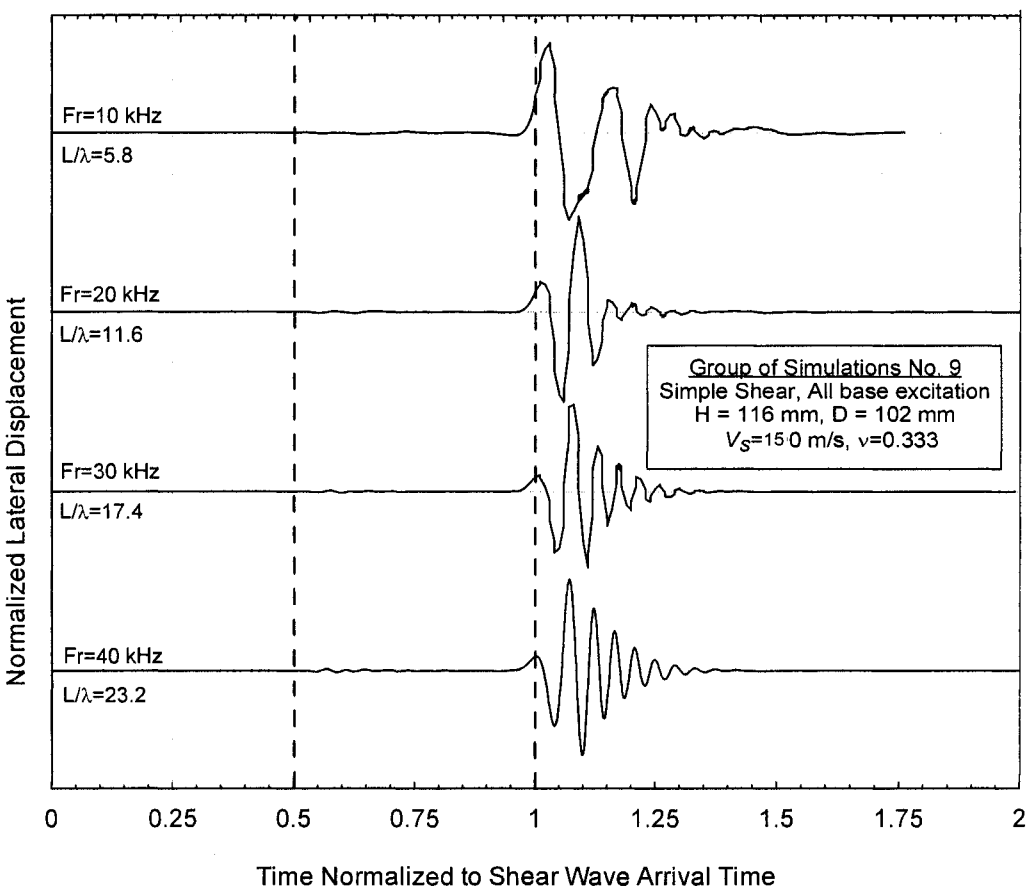

Figure 3.22 Lateral Displacements at Receiver for Simulation 9.

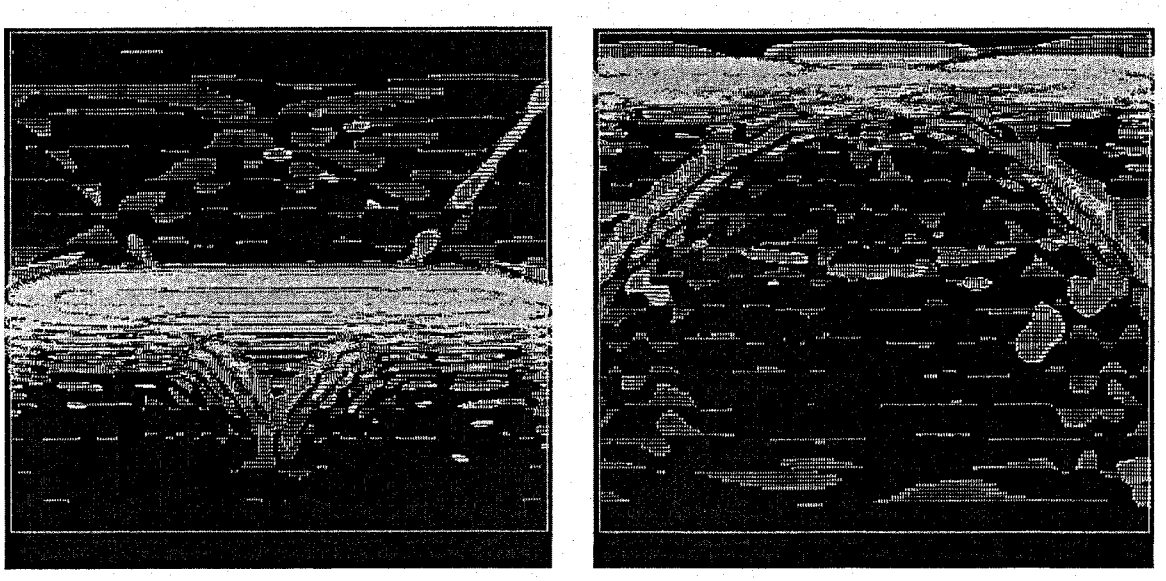

Figure 3.23 The Elements Displacements in Simulation 9 while the S-wave is Halfway and at Receiver (Fr = 30 kHz).

3.4.6 The Best Mode of Excitation

Based on the previous results, it is believed that the whole base radial shearing excitation is better than the other tried excitation types. Also, it is superior to bender elements mode because the travelling signal does not create secondary waves. A device for emitting and receiving signals that works in the whole base mode of excitation and does not penetrate into soil can be better than bender element. This device will eliminate wave reflections at end caps. It may be used to measure the shear wave velocity in the time domain without side reflections. In addition, it does not require penetration into soil which may cause disturbance to the sample. Also, it can be used for hard soils where the penetration of the testing device is difficult.

3.5 Reflected Waves and Near-Field Effect in Piezoelectric Pulse Tests

3.5.1 Introduction

A significant reason for difficulties associated with signals interpretation is the phenomenon that has been called near-field effect. Many interpretation methods are being used to determine the shear wave arrival time on the output signal of a pulse test. None of these methods has definite preference to others. These methods do not always give accurate results as revealed in previous researches. This is due to the ideal interpretation assumptions which in most cases do not coincide with reality (Chapter 2). In fact, most of bender element test results do not comply with these assumptions. Generally, any output signal can be used to obtain a value for the arrival time although it may be totally wrong. Consequently, huge numbers of uncertain results of pulse tests exist. Output signals of largely-different shapes have been recorded by numerous researchers. This suggests that there is one or more unconsidered variable that differs from a study to another which contributes to these differences. Also, a criterion of having good representative signals does not currently existing.

This section discusses and analyzes wave reflection during the measurement of elastic waves velocity at laboratory using bender element method, and how it affects the interpretation process. The near-field effect phenomenon is thoroughly investigated in the following sections. Different numerical simulations for the new mode of shearing excitation of the new proposed testing device were carried out for studying this phenomenon. Also, analytical models for pulse test in oedometer and triaxial setups were carried out for quantifying the extent of waves' interference due to variation of sample's dimensions and Poisson's ratio.

3.5.2 Numerical Simulations for Studying Near-Field Phenomenon

In this section, some numerical simulations for elastic waves propagation through laboratory specimens were carried out to investigate the near-field effect. This phenomenon could be explained by considering different factors. The propagation characteristics are studied considering the effect of model dimensions, input wave frequency, system damping ratio and soil properties on shape of the received signal.

Bender-elements pulse tests in triaxial setup were simulated for showing the near-field effect at different input frequencies (Section 3.2). Using these numerical simulations, it could be proved that the shape of output signal differs when changing the height of the sample while all other parameters being the same. This means that the sample dimensions play an important role in drawing the shape of the received signal. Also, the near-field effect does not exist for all input wave frequencies in group of simulations no. 3. However, in simulation no. 1 at low input frequencies (up to 12.5 kHz), the shear wave arrival is not clear due to the near-field effect. Looking to the results of these simulations, it can be seen that the direct (first) arrival time varies from an input frequency to another. The frequency of the input sine-wave affects the shape of the output signal. Many authors have reported this phenomenon and mentioned different ways to avoid it (Chapter 2). But they have not introduced neither the cause of this phenomenon nor the reason of its occurrence nor why it is cancelled using their cancellation methods. These points are considered herein.

Based on the numerical and experimental experience gained in this study, the uncertainty in determining a clear arrival time at *low* input frequencies due to near-field effect can be understood as follows. The emitter takes relatively long time to input a low frequency signal. The P-wave front arrives at receiver while the emitter still applying the input sine-wave. Therefore the shape of the received signal is not a sine-like, but a flat shape signal (i.e. not a well defined wave) at low input frequencies (Simulation No.1). The preceding downward shape (near-field effect) is due to reflected waves generated by the P-wave when it hits the free boundaries (sides) of the sample. Figure 3.24 presents the soil displacements for Simulation Group No. 1 at input frequency of 25 kHz. Descriptions of the different stages of waves transmission are written under each graph in the figure (please refer to these explanations). The images of this figure show waves reflection at sides and end caps at different times. The near-field downward shape on the received signals at low frequencies is reflected waves coming from the sample's boundaries. Two reflected waves are emitted; one from the right side and the other from the left side. These reflected waves would be emitted too due to any shield around the sample like the walls of an oedometer cell. These waves are compression deformations which travel just before the base shear wave. Thus, it travels with the compression wave velocity which let them forehead the s-wave. The reflected waves may

be due to a direct reflected path from the sample sides or due to multiple reflected paths between sample sides and end caps depending on sample dimensions. This also depends on the Poisson's ratio which determines the speed of p-wave compared to s-wave (i.e. how much the reflected compression wave is far away from the base shear wave and whether it is proceeding or following). In other words, how much is the difference between the correct arrival time of shear wave and that of the reflected waves (either direct or indirect reflection).

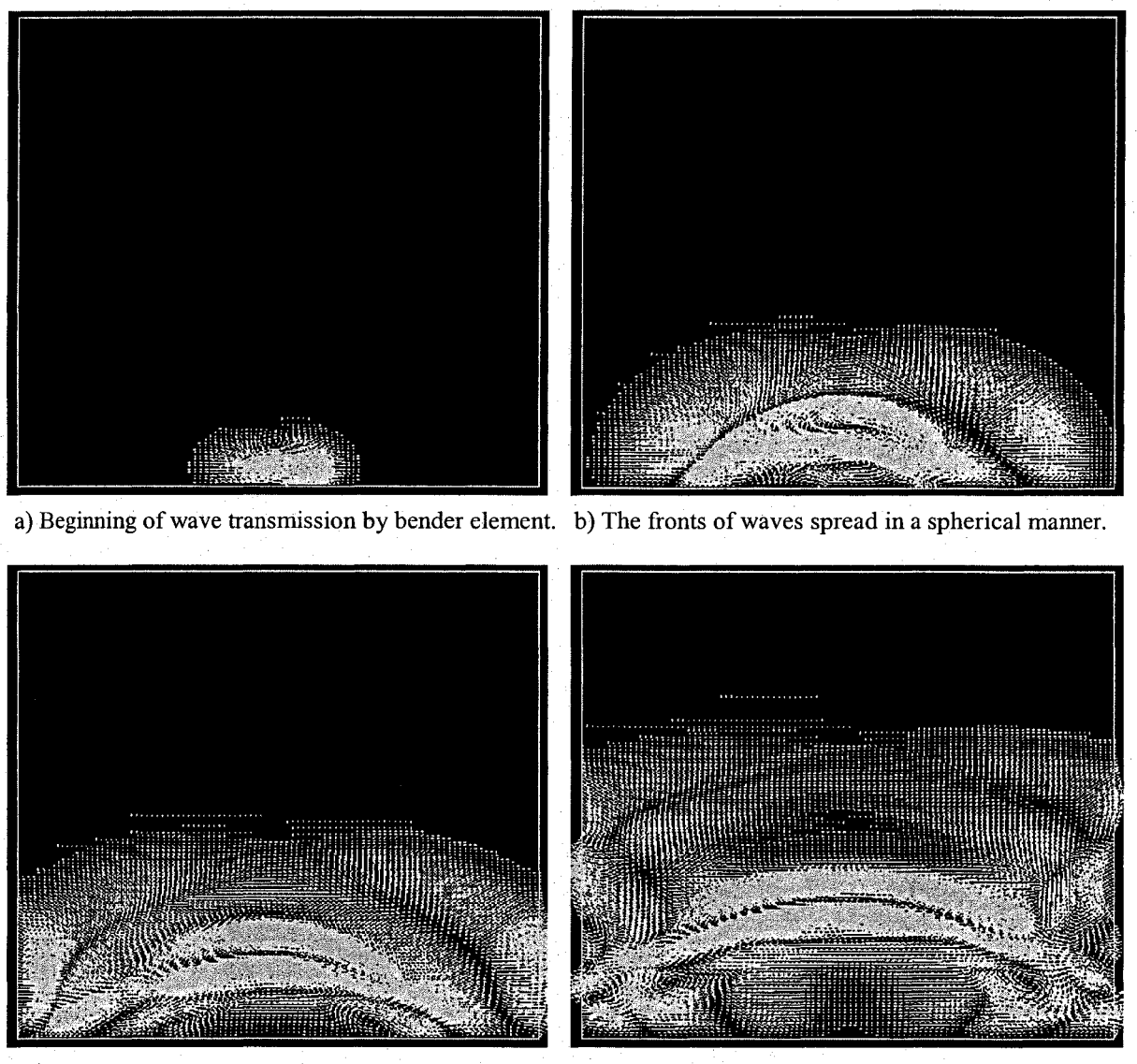

a) Beginning of wave transmission by bender element. b) The fronts of waves spread in a spherical manner.

c) Beginning of side reflected p-wave creation. d) Progression of reflections at both sides.

Figure 3.24 Displacement Vectors for Simulation No.1 (Fr. = 25 kHz).

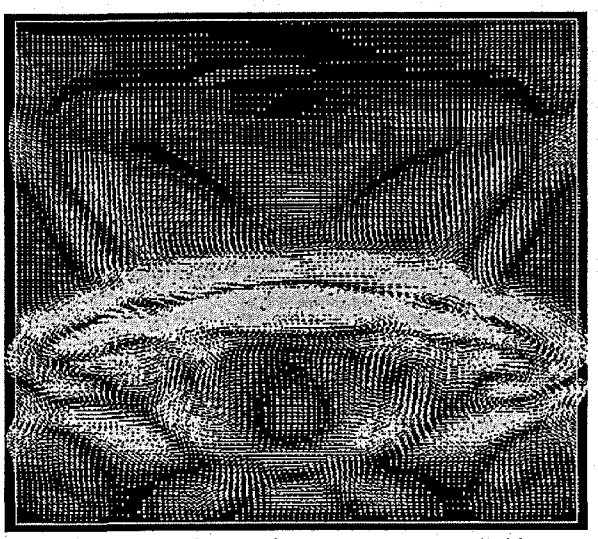

e) Progression of curved s-wave accompanied by wall-reflected p- & s-waves from both sides (time = p-wave arrival time).

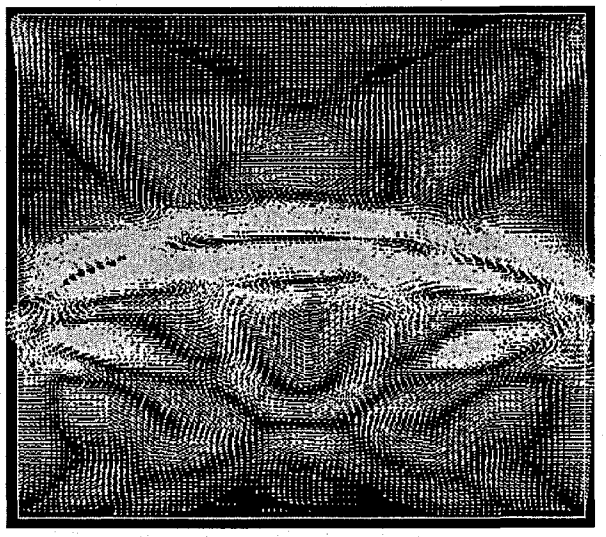

f) Curvature of s-wave decreases and wall-reflected p-waves reach sample's corner at top.

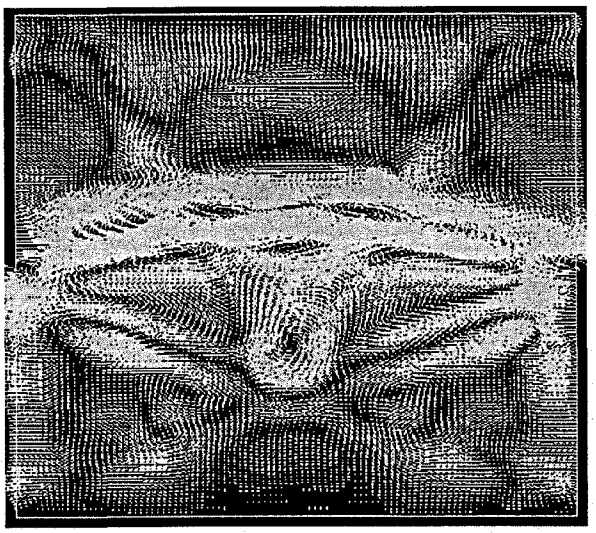

g) Wall-reflected p-wave is re-reflected at top cap while s-wave side-reflection follows the shear wave at some inclination with horizontal.

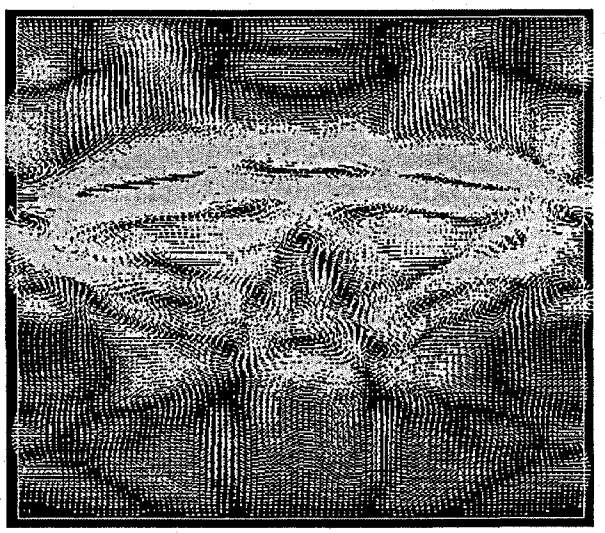

h) Wall-reflected p-wave from both sides travels to sample's centre and the cap reflects part of it along with the direct p-wave.

Figure 3.24 Displacement Vectors for Simulation No.1, Fr. = 25 kHz (cont.).

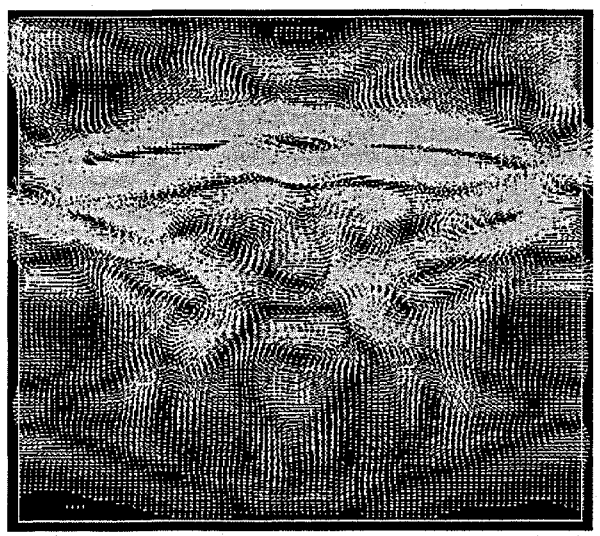

i) Wall-reflected p-wave from both sides meet each other at centre (at the receiver bender) while many other reflections follows the base shear wave.

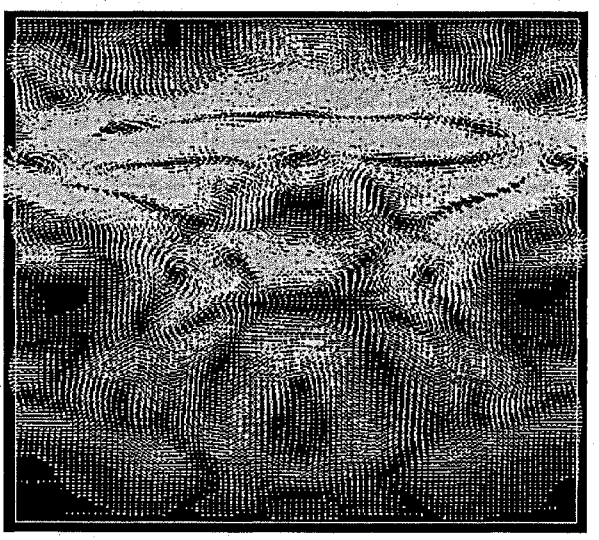

j) Wall-reflected and cap-reflected p-waves at centre proceed the s-wave with many other reflections every where in the sample while s-wave side-reflection still follows shear wave at some inclination.

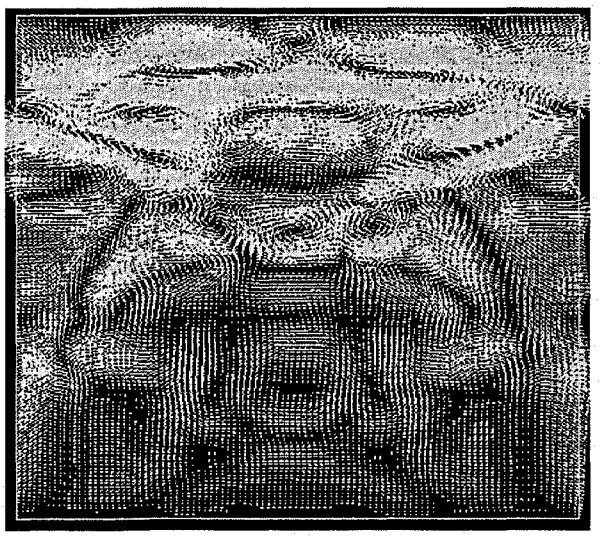

k) Time just before the s-wave arrival where the reflections still exist at centre.

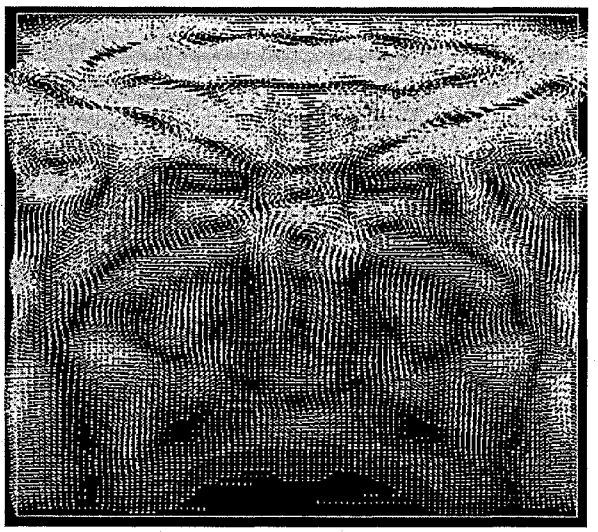

l) Time of shear wave arrival while s-wave side-reflection still follows shear wave at some inclination.

Figure 3.24 Displacement Vectors for Simulation No.1, Fr. = 25 kHz (cont.).

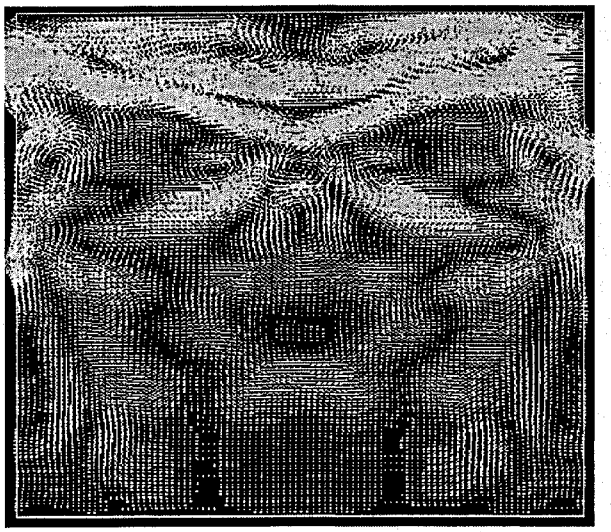

m) S-wave side-reflection waves reach the top corner of the sample.

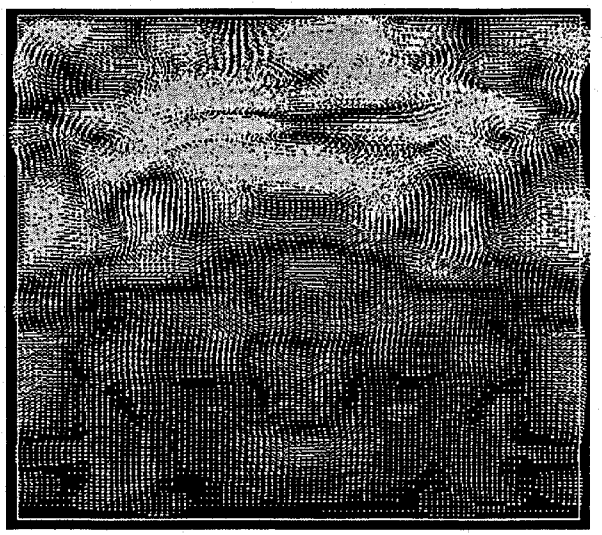

n) Time of side-reflect s-waves reach the receiver

Figure 3.24 Displacement Vectors for Simulation No.1, Fr. = 25 kHz (cont.).

These reflected waves are more attenuated at high input wave frequencies than at low input frequencies because they are composed of high frequencies. Thus, those waves are easily seen at low input frequencies rather than at high input frequencies. Nevertheless, they still exist at high input frequencies but with low energy that may not affect the interpretation process. The third parameter which controls this phenomenon is the system damping ratio which depends on each of soil damping, both emitter and receiver damping and boundary conditions. Increasing the system damping decreases the amplitude of the shear wave compared to the compression wave amplitude. This phenomenon is not realized in bender elements tests because the amplitude of the p-wave is already small. But when comparing the amplitudes of received signals at different input frequencies, it is easily determined that the s-wave amplitude decreases by increasing the input wave frequency. Figure 3.25 shows the received signals for three input frequencies in Simulation No. 2. For the Ring Actuators setup (Chapter 5), this phenomenon is so clear because the rings emit significantly higher amplitudes of both compression and shear waves.

Another way was followed to prove that the near-field effect is due to reflected waves. Group of Simulations No.1 was repeated adding a quiet boundary condition at the sample's sides (Group of Simulations No. 1Q). The quiet boundary condition is a software option which does not create a reflected wave due to an incident wave. The quiet boundary represents a high attenuating material installed around the sample (absorbing boundary). Table 3.3 introduces the carried out numerical simulations in this section. These simulations are also important as they represent a stage in developing the new piezoelectric device which is invented in this research (Chapter 5).

Table 3.3 Numerical Simulations for Studying Near-Field Effect.

Group No.	Sim. No.	Emitter's Geometry & end Conditions	Soil Dimensions (mm)		Soil Density (Kg/m^3)	V_s (m/s)	V_p (m/s)	Poisson's Ratio	Damping Ratio (%)	Input wave Freq. (kHz)
			D	H						
1Q	1-8	Triaxial sample, quiet sides, 2-D, fixed ends, bender elements	50	70	1800	200	400	0.333	1	3.125 - 25
10	c	Axi-symmetric, Quiet top and bottom, discs at top and bottom (D = 20mm & H = 3mm)	60	64	1800	200	333	0.218	1	25 (sine)
	d								0	25 (sine)
	e								4	25 (sine)
	f								1	25 (sine)
	g								0	25 (sine)
	h								2	25 (sine)
11	a	Axi-symmetric, Quiet top and bottom, discs at top and bottom (D = 20mm & H = 3mm)	60	64	1800	200	400	0.333	0	50 (sine)
	b								0	50 (half-sine)
	1-2-3-4-5								1	10-100 (sine)
12	6-7-8-9	Axi-symmetric, Quiet top and bottom, discs at top and bottom (D = 20mm & H = 3mm)	60	64	1800	100	200	0.333	1	10-100 (sine)

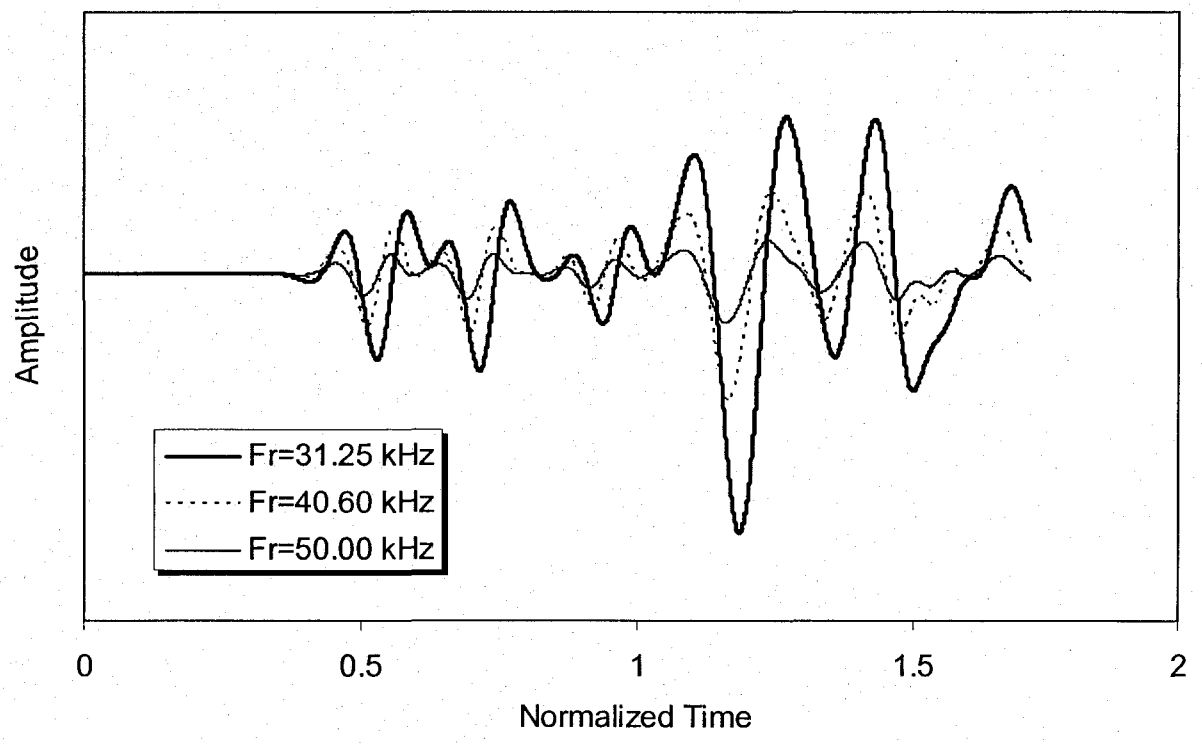

Figure 3.25 Amplitude Decrease with Increasing Input Wave Frequency.

The displacement vectors of this simulation at different times are shown in Figure 3.26. It is clear that there is no other wave except the base shear wave. Comparing these images to the similar images of Simulation No.1 shows major differences. There are many secondary waves travelling within the specimen for Simulation No.1 which do not exist in Simulation 1Q. Those are the sides-reflected waves which makes interpretation of received signals difficult. The received signals of Simulation 1Q are shown in Figure 3.27 with that of Simulation 1 for comparison. There is no downward-shape that precedes the s-wave (near-field effect) even at low input frequencies. Also, the shear wave arrival is so sharp and clear for all input frequencies. Moreover, the arrival time matches to high extent the theoretical time for all input wave frequencies. These results strongly prove that the near-field is due to reflected waves. In near-field measurements, the p- and s-waves are not well separated from each other. The setup geometry and properties besides the boundary conditions determine the shape of the received signal. Thus it controls the interpretation process.

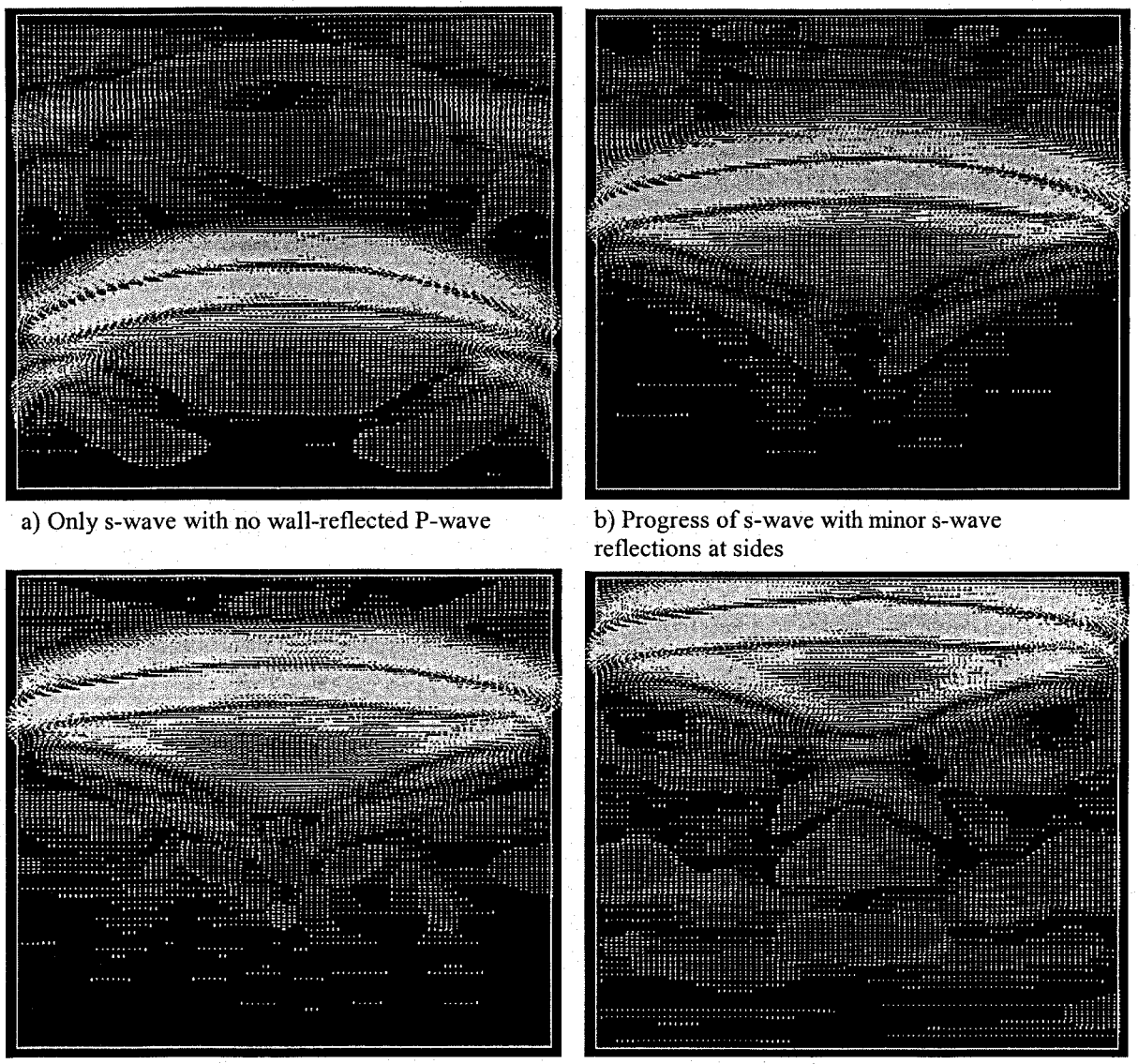

a) Only s-wave with no wall-reflected P-wave

b) Progress of s-wave with minor s-wave reflections at sides

c) Small s-wave side-reflections still follow the base shear wave at some inclination

d) Time of shear wave arrival; s-wave side-reflections still follow the base shear wave with the same velocity.

Figure 3.26 Displacement Vectors for Simulation No. 1Q.

If reflected waves are overlapping the shear wave, the interpretation may be affected. The degree of error depends on the extent of overlapping. If the arrival time of a reflected wave is near to the theoretical arrival time, the accuracy of interpretation is not guaranteed. When the reflected waves arrive after the base shear wave, the interpretation of arrival time using direct arrival method is expected to be accurate. This case is better than the case of a reflected wave arrives just before the shear wave. However, for these two cases the cross-correlation technique will give inaccurate result due to coupling of the two waves.

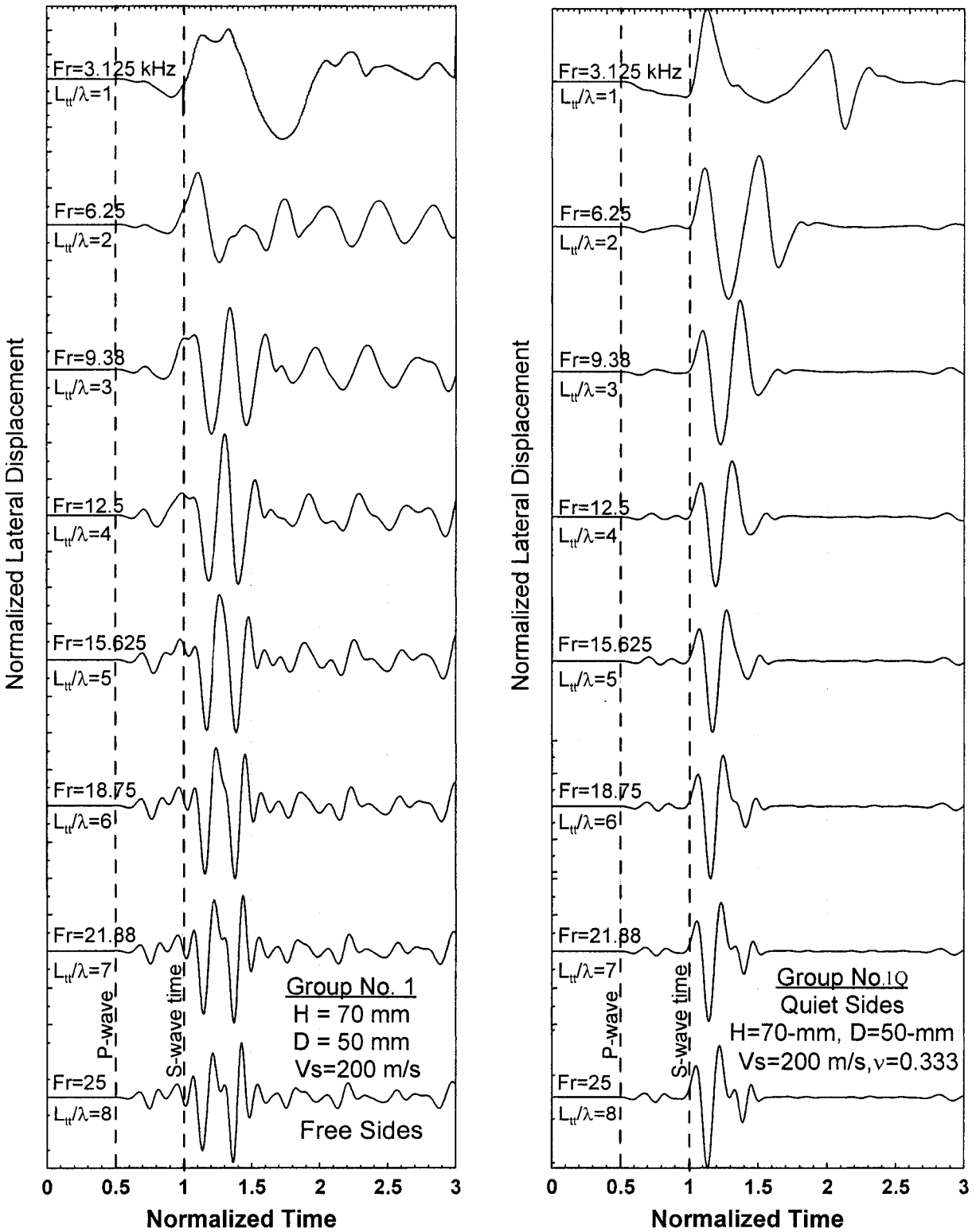

Figure 3.27 The Received Signals for Groups of Simulations No. 1 and 1Q.

In Group of Simulations No.3, the L_{tt}/λ ratio was varied from 1 to 8 (Figure 3.10). It can be realized that what is called near-field effect does not exist in this group of simulation at all. This can be explained based on the carried out simulation findings as follows. Increasing the sample height decreases the amplitude of all components of the received signal. This allows the weak reflected waves to be attenuated more than the base waves. The reflected waves vanish before reaching the receiver when the sample height is sufficient. Moreover, increasing the sample's length gives a space to the reflected waves so that they cancel each other before reaching the receiver. The reflected waves from the sample sides meet each other at sample's centre and thus severely attenuate each other (Figure 3.24).

Another piezoelectric setup with different configuration was numerically simulated to prove this fact (Figure 3.28). This setup uses another mode of shearing that defers from bender element mode. The emitted signal is made by a circular load applied, in the radial direction, on the perimeter of a 3mm-thickness disk of 20-mm diameter at the base of the sample. A null zone cylinder of 0.5-mm thickness surrounds the disk to eliminate wave transmission to the outer disk. The sample dimensions are 64mm-length and 60mm-diameter. Figure 3.28 shows the model and its dimensions for Group of Simulations No. 10. The input is a sine-wave that forces the sample's surface at emitter to vibrate (expands and shrinks) in the radial direction. This mode of shearing is better and more efficient than bender element mode (Chapter 3; Section 3). In order to avoid reflection of the waves at the end caps, quiet boundary condition is configured at top and bottom of the model. This option is chosen in order to focus on reflected waves being emitted at sample sides. Among the output signals of Simulation No. 10 shown on Figure 3.29, two signals are considered for comparison (the other output signals will be discussed later on in this section). The first signal (c) is for a free sides sample model while the second signal (f) is for a quiet sample sides. These two signals show the differences between an output without reflected waves and another normally received signal. Figure 3.29(f) shows that no waves precede the main base shear wave for a quiet boundary condition. This confirms that the wave which precedes the base shear wave is a reflected wave coming from sample's sides. The reflections at the sample sides due to s-wave come after the base s-wave [Figure 2.29(c)]. Therefore it does not affect the first arrival time. But it may affect the times calculated using the second arrival or peak-to-peak methods.

Group of Simulation No. 11 is similar in geometry to simulation 5 but the soil parameters are different (V_p = 400 m/s.). Also, the damping ratio is taken 0 or 1%. The input frequency is varied from 10 to 100 kHz (Figure 3.30). Increasing the input wave frequency in Group of Simulation No. 11 increases the amplitude of compression wave and reduces the amplitude of the shear wave as well. Decreasing the damping ratio up to zero increases the frequency content of the output signal. At very high frequencies, half-sine input has the same effect of a sine input. Other secondary waves are recorded on the received signal. They represent the reflected waves at the sample's sides. At input frequency of 10 kHz, the reflected wave amplitude is bigger than the shear wave amplitude which is not evidently seen. The amplitude of this wave decreases by increasing the input frequency until it is nearly vanishes at input frequency of 100 kHz.

Examining results of Group of Simulation No. 7 shows that the s-wave reflection is bigger than that of p-wave at low input frequencies (Figure 3.17; see also Figure 3.30). The reflected wave travels behind the base s-wave at an inclination with the horizontal direction (as shown in Figure 3.18). This wave is recorded as a secondary wave which comes after the main shear wave (Figure 3.17). At low input frequencies, the amplitude of this wave is bigger than the base shear wave. This wave corresponds to the maximum of the cross correlation function. Thus, it falsely determine the arrival time. By increasing the input frequency at the emitter, its amplitude becomes less and it separates well from the base shear wave (Figure 3.30). At these high frequencies, the reflected p-wave is small and it attenuates quickly. Increasing diameter to length (D/L) ratio of the sample is so efficient for eliminating the reflected waves. This will allow the s-wave to reach the receiver before the reflected waves do. Moreover, for the same sample dimensions and input frequency, pulse tests on a weak soil will be easier to interpret than on a hard soil. This is due to the well separation between the different components of the output signal (Group of Simulations No. 12: Figure 3.31).

The "system damping ratio" plays an important role in magnifying or reducing the effect of reflected waves (near-field waves) which overlap the base s-wave. Simulation Group No. 10 (c-d-e-f-g-h) shows the results of a soil model simulated with different damping ratios (Figure 3.29). The damping ratio was varied from 0 to 4%. It is clear that increasing the damping ratio increases the 'relative amplitude' of the reflected wave (the relative amplitude is the reflected wave amplitude to the shear wave amplitude). Although, increasing the

damping ratio decreases the amplitude of all components of the received signal. But, it attenuates the s-wave more than any other component. Therefore, the reflected wave amplitude continues to increase compared to the s-wave amplitude. At a damping ratio of 4%, the amplitude of the reflected wave is equal to the shear wave amplitude. Also, the p-wave relative amplitude increases by increasing the damping ratio. Moreover, the frequency domain of the received signal differs considerably when the damping ratio equals zero [Figure 3.29 (d) & (g) and Figure 3.30 (a) & (b)], i.e. more components exist on the output signal, but this does not change the relative amplitude of the different components in the signal. Thus, the difficulty of interpreting a signal increases by increasing the damping ratio. This is the case for a weak soil or at low-stresses condition where the damping ratio is high. It is useful to mention that the damping ratio for soils at very low strains is less than about 2 %.

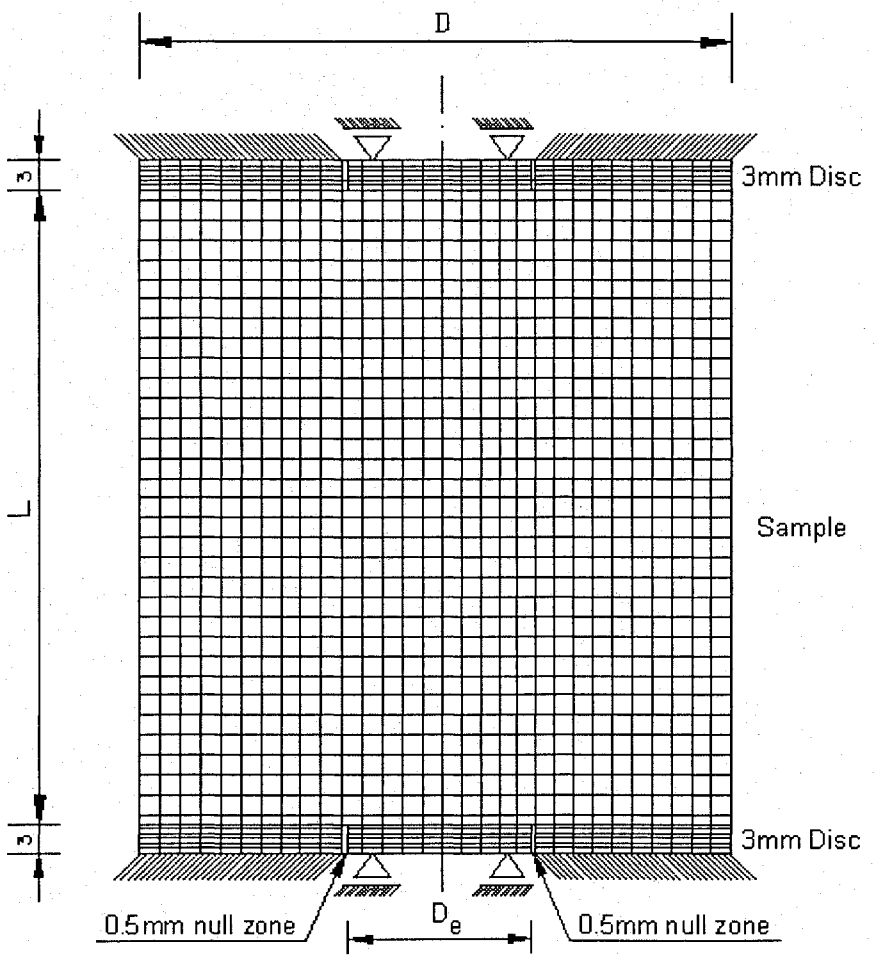

Figure 3.28 The Geometry of the Used Model for Simulations 10, 11 & 12 (the mesh of the model is 0.5mm squares).

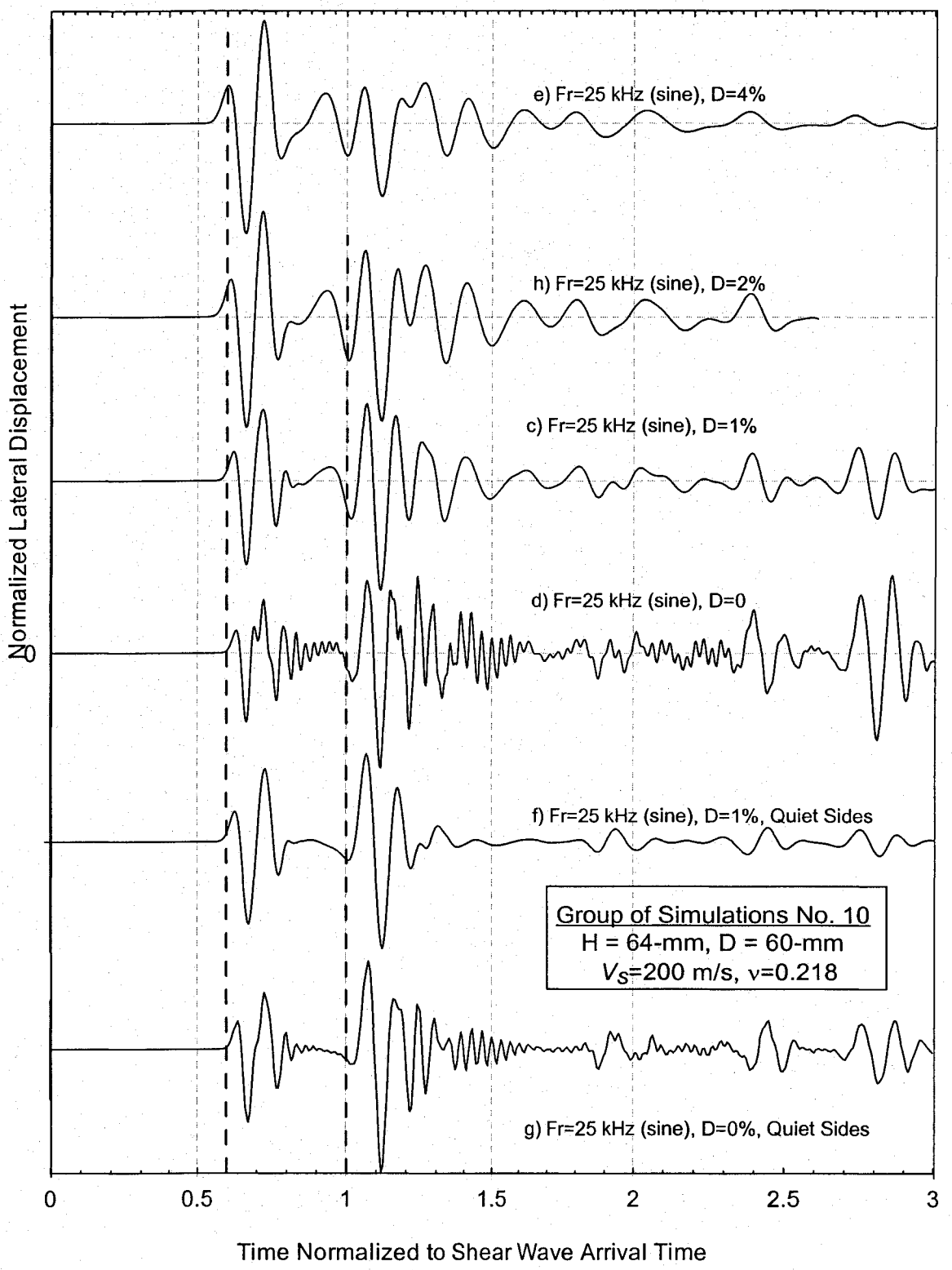

Figure 3.29 Output Signals for Group of Simulation No. 10 at Different Damping Ratios and Boundary Conditions.

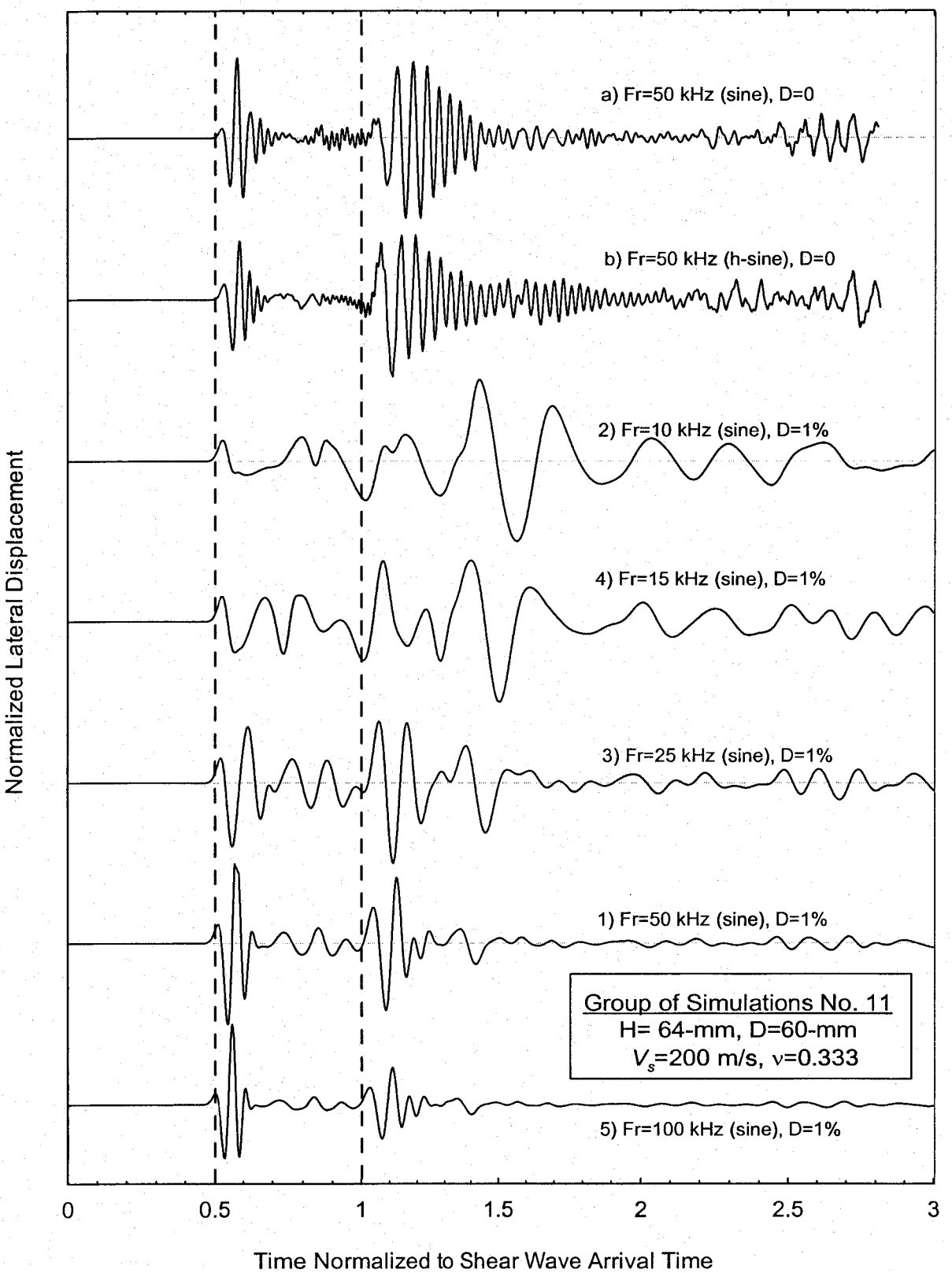

Figure 3.30 Output Signals for Group of Simulation No. 11 at Different Input Frequencies and Damping Ratios.

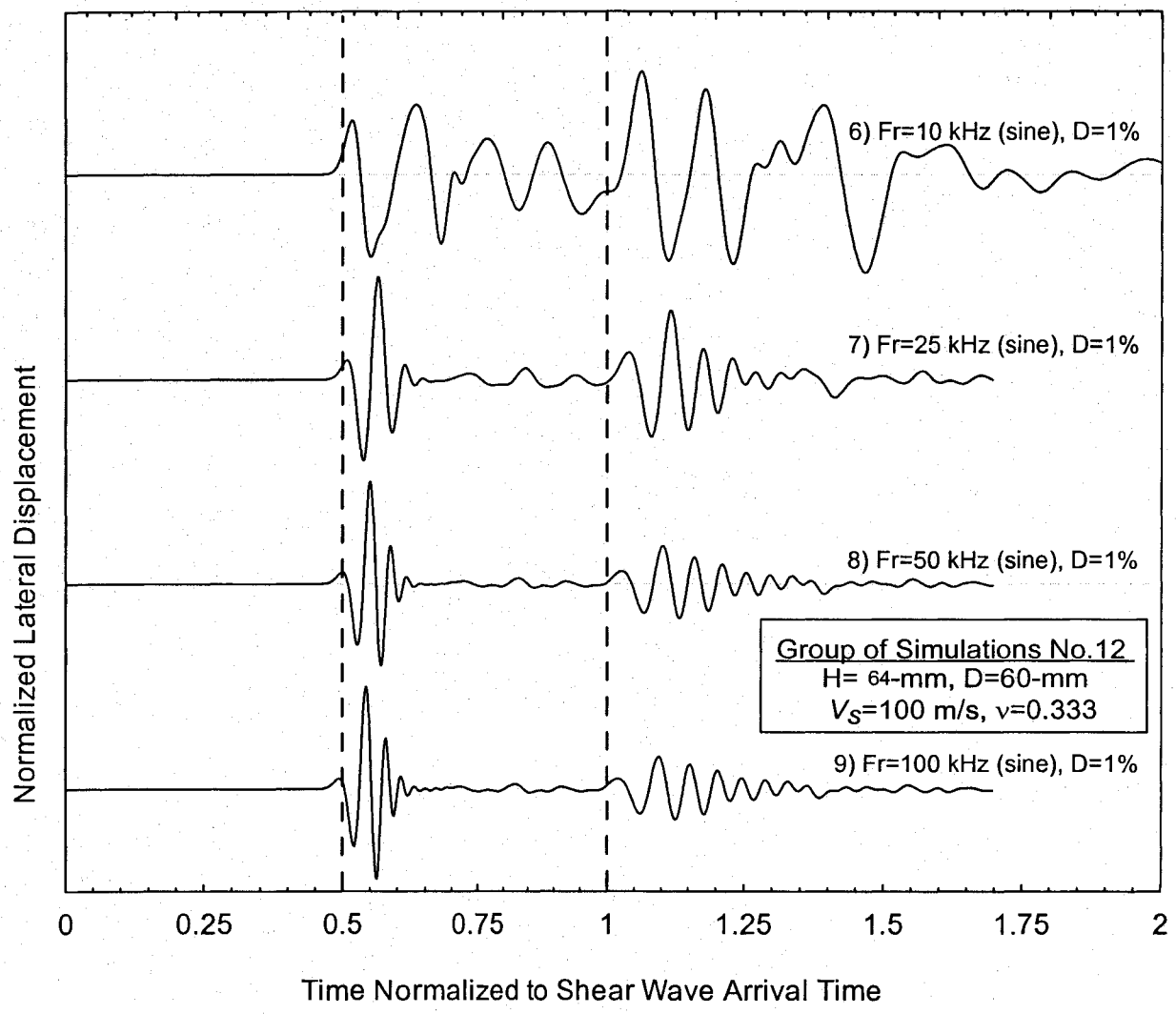

Figure 3.31 Results of Simulation Group No. 12 at Different Input Frequencies.

3.5.3 Analytical Models for Studying the Effect of Sample Dimensions

Some analytical calculations were carried out in this section in order to clearly show the effect of sample dimensions on reflection of waves and how this phenomenon can affect the shape of the received signal. Figure 3.32 shows two trajectories for the direct shear wave and the reflected compression wave at a sample's side. The front of the travelling waves are spherical in the case of bender elements, therefore other paths of different inclinations are possible. The drawn path for p-wave is the shortest possible trajectory. Thus it is the critical path that may interfere with the shear wave. Overlapping of waves depends on the sample's dimensions and the Poisson's Ratio of soil as it will be proved herein.

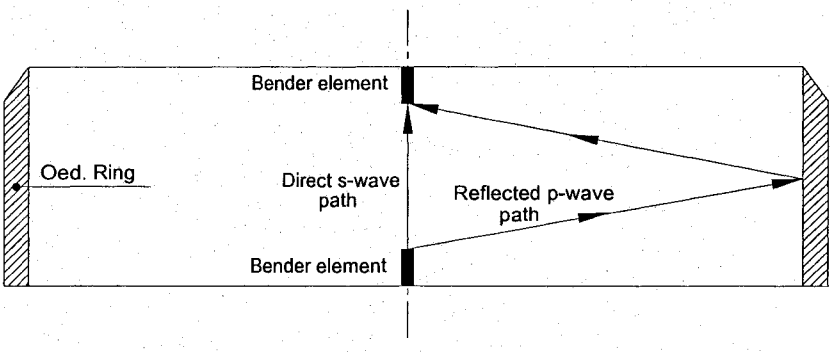

Figure 3.32 The Critical Path of a Reflected Compression Wave in an Oedometer Cell with Bender Elements Setup.

The following equation for elastic strains governs the ratio between the shear and compression wave velocities in any medium:

$$\frac{V_p^{ref.}}{V_s} = \sqrt{\frac{\nu - 1}{\nu - 0.5}} \tag{3.8}$$

where $V_p^{ref.}$ is the reflected compression wave.

Replacing the velocity terms by lengths and times (V=L/t), the following equation is obtained:

$$\frac{t_p^{ref.}}{t_s} = c\sqrt{\frac{\nu - 1}{\nu - 0.5}} \tag{3.9}$$

where c is a constant depends on the dimensions of the sample, the emitter and the receiver [for bender elements, $c = f(L, D, L_b)$]. Assuming different values for Poisson's ratio, the ratio between the reflected compression wave arrival time and shear wave arrival time ($t_p^{ref.}/t_s$) is obtained for any geometry configuration. Figure 3.33 displays $t_p^{ref.}/t_s$ with the variation of Poisson's ratio for bender-elements pulse tests in some triaxial samples of different length to diameter ratios (L/D). The length of bender elements is taken 3-mm for these analyses.

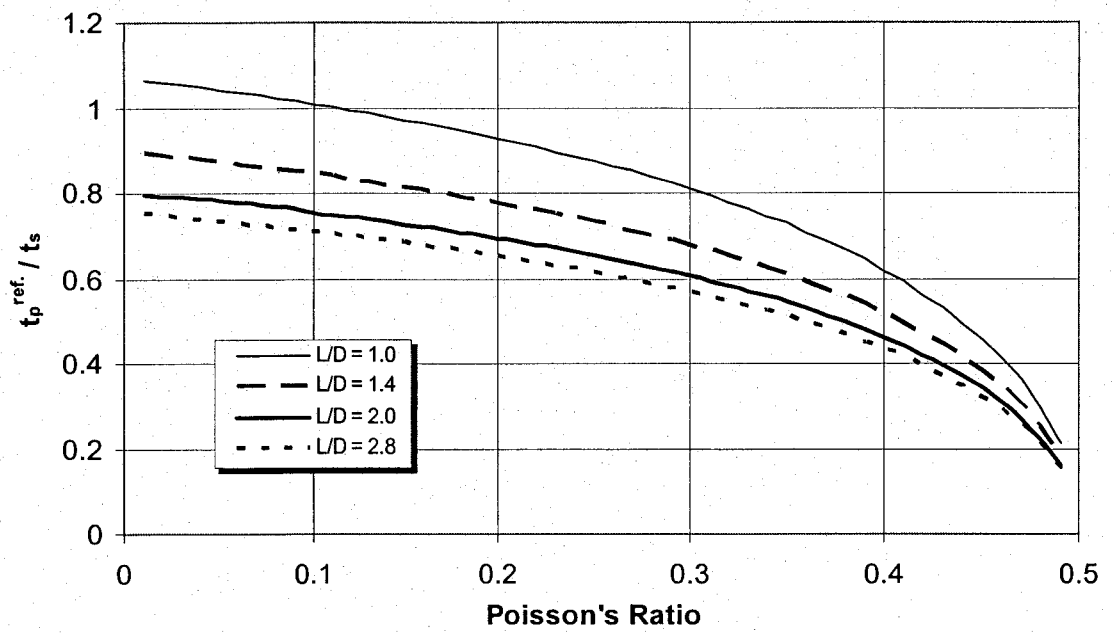

Figure 3.33 Reflected P-wave Arrival Time with Respect to S-wave Arrival versus Poisson's Ratio in Triaxial Cells with Bender-Elements Setup.

It can be realized that $t_p^{ref.}/t_s$ decreases by increasing the Poisson's ratio due the decrease of the arrival time of side-reflected compression wave. The graph shows that the reflected p-wave proceeds the shear wave by considerable time for all Poisson's ratio values except for the sample of L/D equals one at the low values of Poisson's ratio. For soil samples of similar geometry and Poisson's ratio, the reflected p-wave is relatively close to the arrival of shear wave. Poisson's ratio values obtained from compressional and shear wave velocities (seismic refraction measurements) for surface soils (unsaturated (or partially saturated) sediments, and totally saturated sediments) varied from 0.05 to 0.45 for soil porosity range of 0.20-0.65 (Salem, 2000). This means that this low range of Poisson's ratio is normal for small strain testing of soils. It is known that the Poisson's ratio decreases by increasing the applied stresses on soil. Thus, the interference of waves is critical at high stresses for short samples in the triaxial apparatus.

Figure 3.34 displays $t_p^{ref.}/t_s$ for samples inside some oedometer cells of different dimensions at different values of Poisson's ratio. It is clear in the figure that the side-reflected p-wave arrives at receiver behind the base shear wave in general, except at high Poisson's

ratio values. Increasing the height to diameter ratio of the soil sample lets the side-reflected compression wave arrival time more close to the shear wave arrival time. For the sample of L/D equals 0.87, the arrival time of the reflected wave precedes the base shear wave at Poisson's ratio values over 0.27. All mostly, the arrival time of the reflected p-wave is so close to shear wave arrival time for this sample at the normal range of Poisson's ratio of dry or partially saturated soil. Thus, oedometer cells of higher ratios of height to diameter will be a possible cause of wave interference. Misleading results may be obtained due to sides-reflected waves when overlapping occurs with the shear wave.

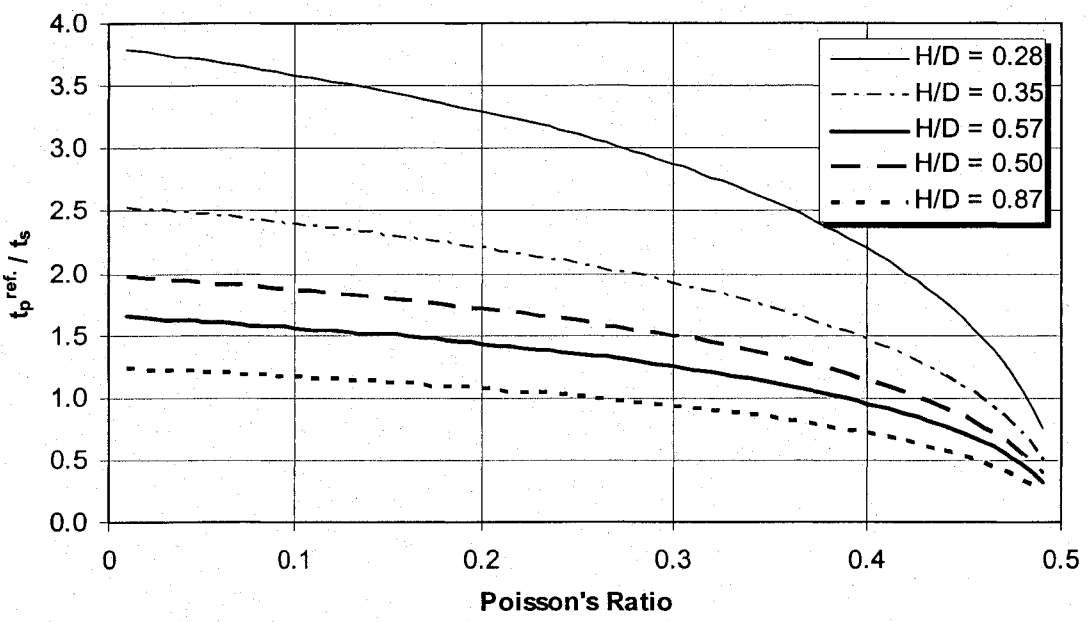

Figure 3.34 Reflected P-wave Arrival Time with Respect to S-wave Arrival versus Poisson's Ratio in some Oedometer Cells with Bender-Elements Setup.

Table 3.4 presents nominal values of elastic modulus and Poisson's ratio (Das, 1994) for soil. It can be seen that the Poisson's ratio varies from 0.15 to 0.45. These values may be roughly used for setup design or for checking the validity of test results. Another possibility may occur and results in difficulty of interpreting the output signal. The second arrival of the compression wave over the direct path between the emitter and receiver may obscure the first arrival of the shear wave. This case depends on soil properties and dimensions as the case for the reflected compression wave (Equation 3.9). Two examples are introduced here to demonstrate this case. Piezoelectric disc setups (emitters and receivers) installed in two

apparatuses (a large oedometer cell and a Proctor mold) are studied. Figures 3.35 and 3.37 display the configuration of the two setups while Figures 3.36 and 3.38 present the analytical results in a relationship between $t_p^{ref.}/t_s$ and Poisson's ratio. It can be realized that the interference in both setups may occurs at Poisson's ratio values between 0.3 and 0.5. Thus, this case of interference should be checked when performing pulse tests.

Table 3.4 Typical Values of Elastic Modulus and Poisson's Ratio (Das, 1994).

Soil Type	Elastic Modulus, E (MPa)	Poisson's Ratio, ν
Loose sand	10.35 – 26.60	0.2 – 0.4
Medium sand		0.25 – 0.4
Dense sand	34.50 – 69.00	0.3 – 0.45
Silty sand		0.2 – 0.4
Soft clay	1.38 – 3.45	0.15 – 0.25
Medium clay		0.2 – 0.5
Hard clay	5.865 – 13.80	

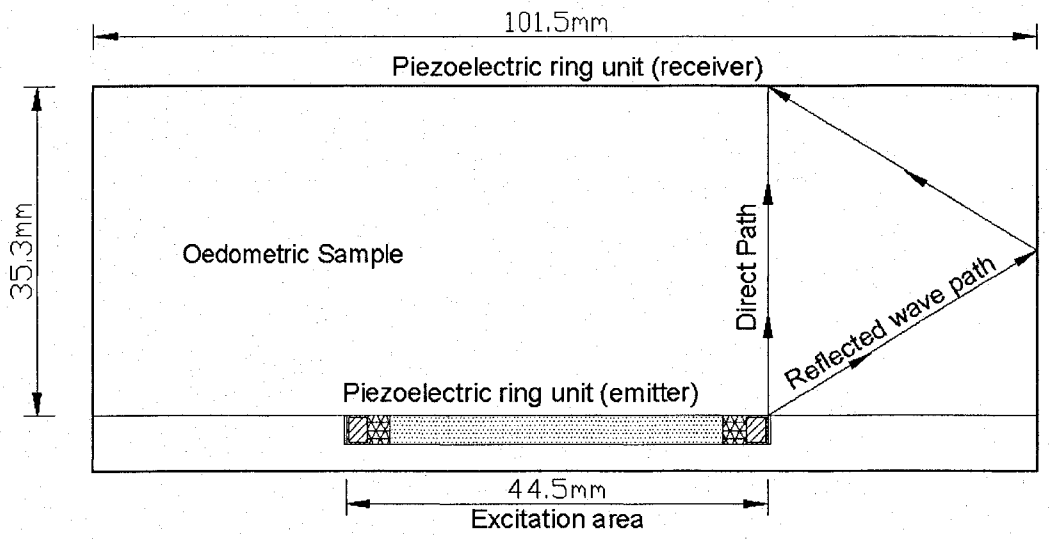

Figure 3.35 Direct and Side-Reflected Paths in an Oedometer Cell (Dim. in mm).

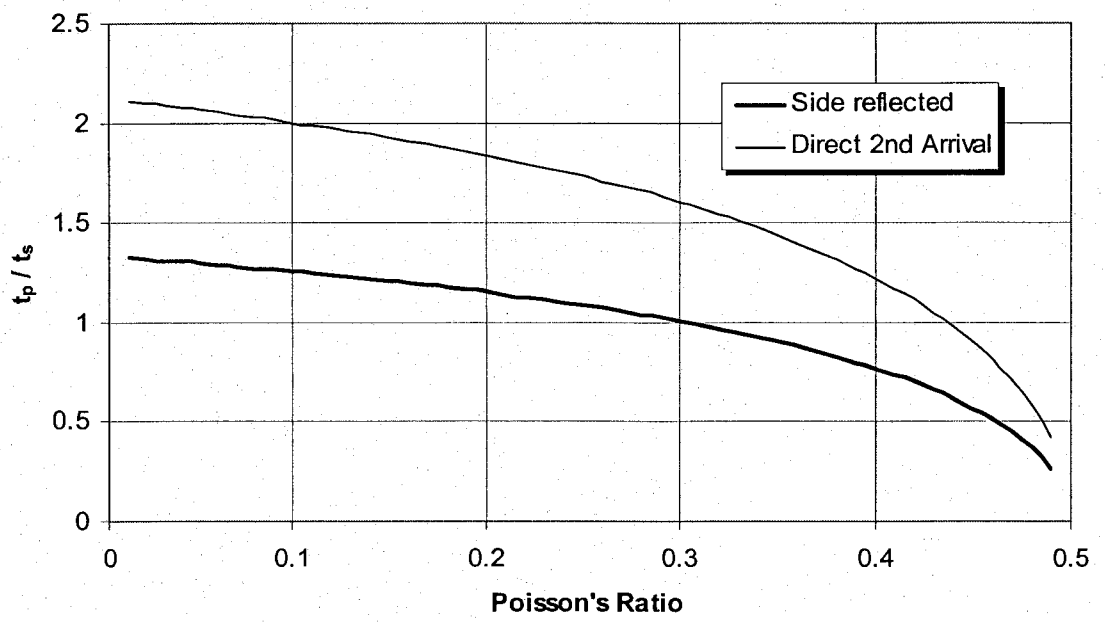

Figure 3.36 P-wave Arrival Times with Respect to S-wave Arrival versus Poisson's Ratio in a Large Oedometer Cell for a Pulse Test by Disks Setup.

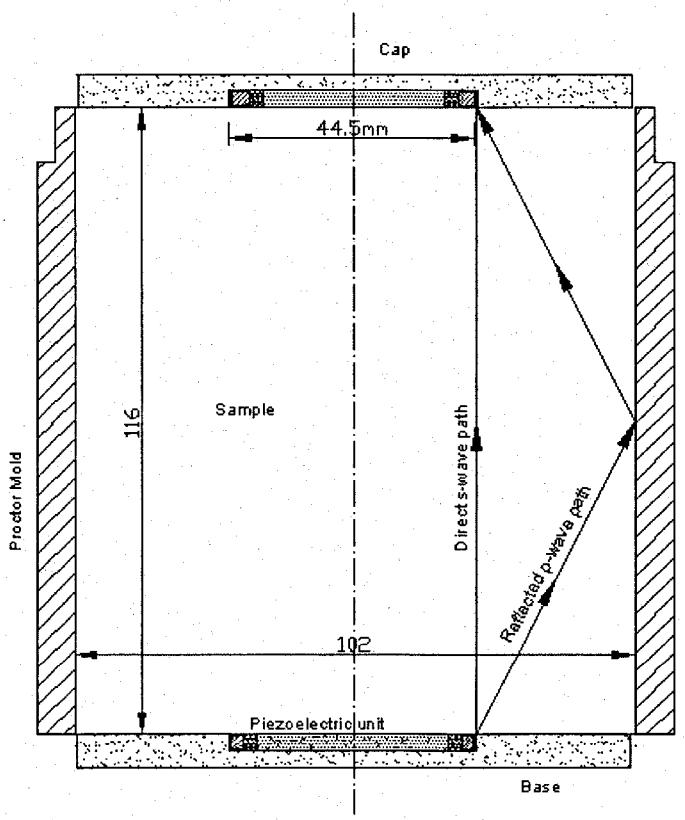

Figure 3.37 Direct and Side-Reflected Paths in a Proctor Mold.

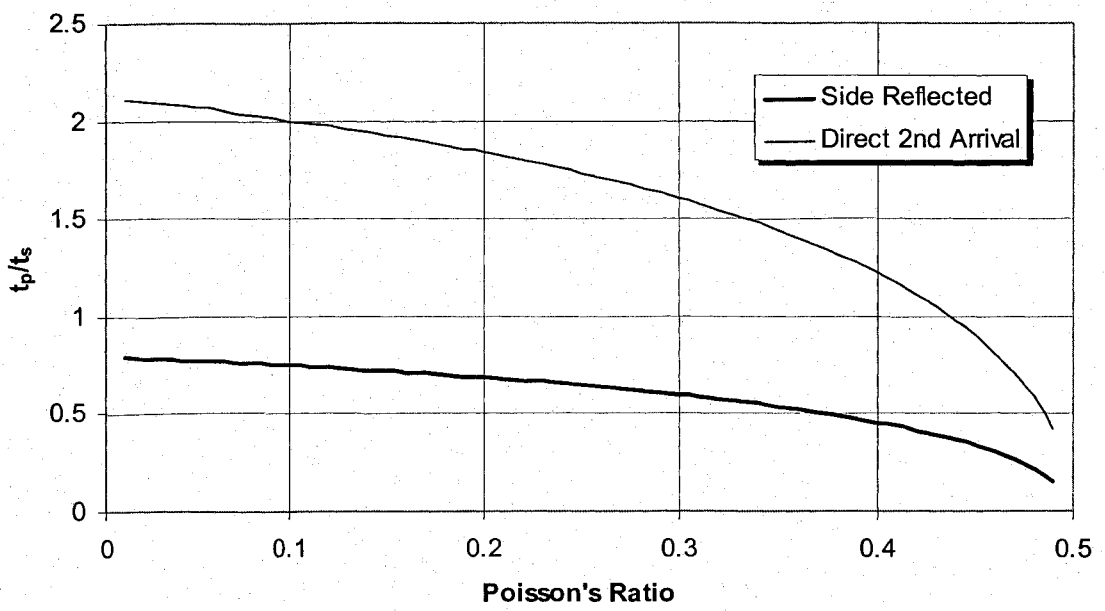

Figure 3.38 P-wave Arrival Times with Respect to S-wave Arrival versus Poisson's Ratio in Proctor Mold during a Pulse Test by Disks Setup.

Thus, the sample dimensions play an important role in drawing the shape of a received signal besides the Poisson's ratio. Much care should be given to the analysis of wave interference due to reflected waves at sample's sides. This phenomenon can severely affects the interpretation of recorded signals. In the other hand, recording of reflected waves may be useful in checking the accuracy of results when it is recorded away of the shear wave, especially when the shear wave arrival is suspicious. By computing the Poisson's ratio from direct measurements of shear and compression waves, then this value is used to compute the arrival time of the reflected p-wave. If this time matches a recorded wave on the signal record, this means that accurate assessment of shear wave arrival time has been made. Otherwise, the chosen point for the base shear wave arrival should be changed to adjust this criterion.

3.5.4 Application of Previous Equations to Laboratory Tests

This section demonstrates the existence of reflected waves on the time domain results of a carried out laboratory test using the simple calculations. Figure 3.39 shows a pulse test on an Ottawa sand sample in the large oedometer cell using the setup shown in Figure 3.35. The output results show that t_s equals 100ms, t_p equals 48ms. Hence, Poisson's ratio (ν) was

calculated and found equals 0.35. Entering this value in Figure 4.36 (or Equation 3.9), a $t_p^{ref.}/t_s$ value of 0.91 is obtained. Thus, the reflected p-wave time is calculated as 100×0.91 = 91ms.

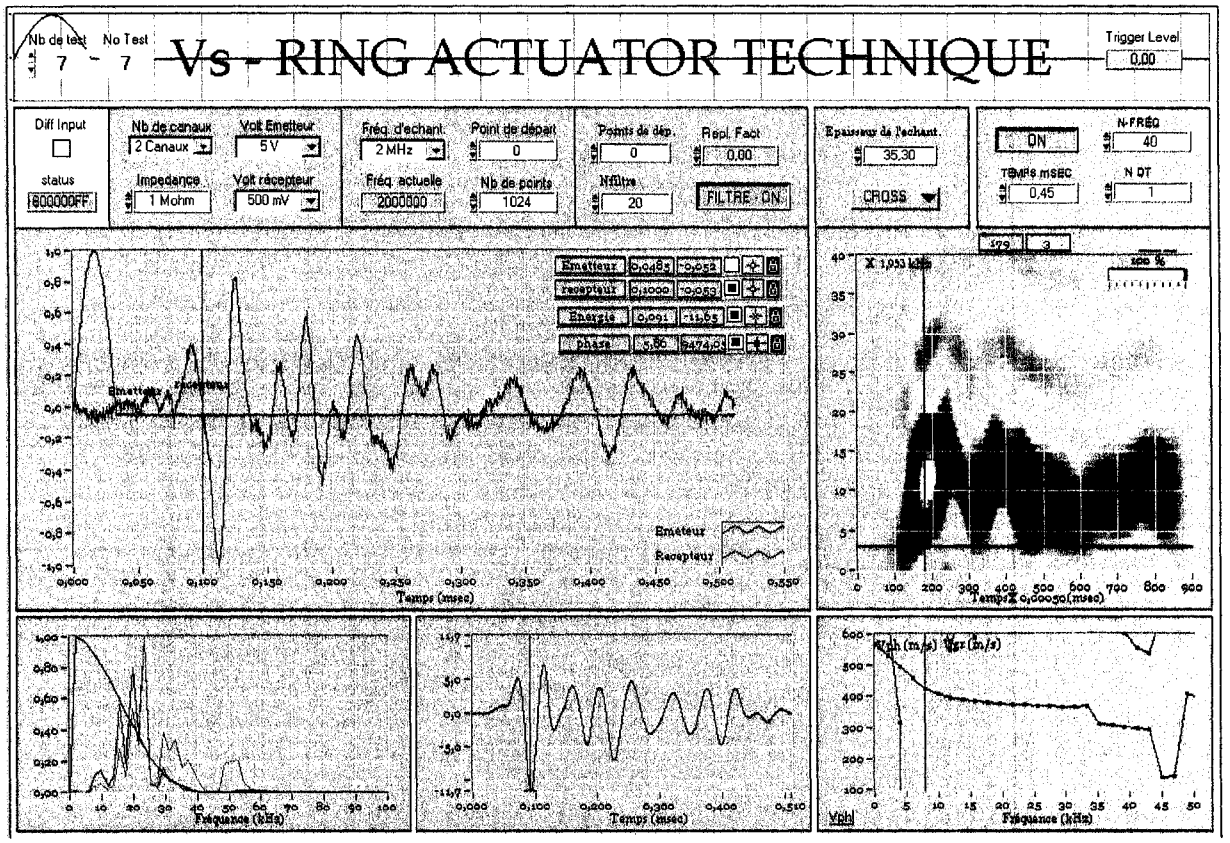

Figure 3.39 Pulse Test on an Ottawa Sand Sample in the Large Oedometer Cell that Proves the Reflection at Sides.

A peak at 91ms is seen in Figure 3.39 which corresponds to the reflected p-wave arrival time. It is clear that the frequency of this wave is higher than the base shear wave velocity. This also proves the interference of the two signals near to the shear wave arrival time. Other explanatory cases are introduced within the laboratory tests result in Chapter 5.

3.6 Summary

The disadvantages of bender elements and their interpretation problems were investigated. The reasons for difficulty of signal interpretation were explained. The shape of the output signal depends on the input frequency, soil rigidity, Poisson's ratio, method of interpretation

and sample's height. New modes of shearing excitations were studied and analyzed. The best mode of excitation was chosen as a basis for a pulse test device. Some numerical simulations for developing this device were carried out. The near-field effect and wave reflections at boundaries were analyzed, numerically and analytically. It was proven in this chapter that near-field effect depends on input frequrncy, damping ratio of soil, Poisson's ratio and sample dimensions. Reflected waves may interfere with the base shear wave according to these parameters.

Chapter 4 DISPERSIVITY AND INTERPRETATION OF PULSE VELOCITY TESTS

4.1 Introduction

This chapter is dedicated to introduce a method for pulse tests interpretation using time-frequency-energy analysis. The thorough investigations of pulse tests in this study (Chapters 2 & 3) have broaded our understanding of these tests and have guided us to develope this new technique. This method analyzes pulse test results using Pseudo-Wigner-Ville Tranform considering the dispersive nature of the tranmitted signals. Hence, it overcomes the effect of input frequency on shape of the output signal which affects the interpretation of shear wave velocity. The technique uses the Cross-Correlation (C.C.) function as the input data. Hence, the quality of the output results depends on the accuracy of the input C.C. function and how far signal interference exists in the test. In spite of this fact, this technique is capable of separating the different waves within the output signal Therefore, a new criterion for signal interpretation is introduced in this chapter to overcome this problem.

4.2 A New Criterion for Assessing the Shear Wave Arrival Time in Time Domain

Initially, some fundamental points regarding wave interpretation should be kept in mind when performing pulse tests on soil. Shear wave amplitude in the received signal is higher at low input frequencies than at high frequencies (Simulation No. 2). At very high frequencies, the shear wave component may be absent. On the other hand, the compression wave arrival is clearly evident at higher frequencies and represents the first deflection on the received signal. The amplitude of shear wave component is higher than the amplitude of the p-wave for the commonly used frequencies (normally up to 20 kHz). For a certain input frequency, the p-wave component (when it is evidently present) has the higher frequency domain within the received signal while the shear wave component has lower frequency domain.

The new criterion for pulse tests is established based on the laboratory and numerical findings of this research. The following practice is recommended for carrying out and obtaining representative output signal. High input frequencies may eliminate or mask the shear wave. Low input frequency signal should be used in order to obtain a signal of higher

shear-wave amplitude than that of the p-wave. Therefore, many input frequencies should be tried beginning at very low frequencies up to the resonant frequency of the system. Different input shapes should be tried. This gives more confidence to the interpretation because some smooth-edged input shapes can effectively reduce the p-wave amplitude within the received signal leaving dominant and clear s-wave component. In the mean while, these shapes give a smooth (flat) shear wave arrival of low amplitude. Usually, the highest input wave frequency that does not create resonance in the system gives the most reliable signal for interpretation. This can be explained considering that arrivals of the different components of a received signal are not sharp at low input frequencies. This is not favourable as it gives more room for guessing rather than obtaining a clear arrival. Moreover, at some frequencies, the p-wave deformations (pattern) on the received signal connect smoothly to the first arrival of the shear wave. This masks the point of arrival for shear wave. At other frequencies, a clear check point can be seen on the received signal representing the shear wave arrival. Thus, trying many input shapes and frequencies would clarify a characteristic point which represents the shear wave arrival where a clear wave arrival is obtained. A characteristic point of a constant time delay between input and output should be seen on most or all of the received wave logs. Finally, we have to conciliate between all available data whether direct measurements or data analyses. The cross correlation, energy envelope, Wegner-Ville energy pattern, phase and group velocities are helpful interpretation tools. Using this new criterion would give better (more accurate) results but may not give the characteristic velocity.

4.3 A New Interpretation Method for Pulse Tests (Wigner-Ville Energy Analysis)

The numerical simulations in this study have shown that the current methods for interpreting the shear wave velocity (V_s) from laboratory piezoelectric pulse tests are theoretically not accurate. Therefore another technique was developed in this study in order to compute the characteristic V_s of soil. This technique basically depends on Pseudo-Wigner-Ville technique for computing the group velocity in time and frequency domain. Applying this technique to 'emitted and received waves of some numerical simulation' was found to give a V_s value which is identical to the predefined input value in the simulation.

Wigner-Ville Distribution is a method to represent signals in the time/frequency domain. Originally this quasi-probability distribution was a representation of the wave-function in quantum physics. This distribution was introduced by Eugene Wigner in 1932 to study quantum corrections to classical statistical mechanics. It was re-derived later by J. Ville in 1948 as a quadratic (in signal) representation of the local time-frequency energy of a signal. Therefore, this form is called Wigner-Ville Distribution (Transform) and is written as follows:

$$WV(t,f) = \int_{-\infty}^{\infty} x(t+\tau/2)x^{*}(t-\tau/2).\exp(-2i\pi f\tau)d\tau \qquad (4.1)$$

where t is the time, f is the frequency, x(t) is the time-'finite-energy' function of the signal and x*(t) is its complex conjugate. More details about this technique can be found in Karray (1999).

As a pioneer application of this distribution, it is used here for the interpretation of pulse tests. A new interpretation technique is introduced herein and is called 'Wigner-Ville Energy Analysis Method'. It was developed in a team work in the geotechnical research group at University of Sherbrooke. The used code in the testing and analyzing software (LabVIEW; Ver. 6.1) was written by Dr. Mourad Karray. This new technique depends on analyzing the cross correlation function of the emitted and received waves in order to obtain its energy function [Equation 3.7] in time domain. The Wigner-Ville method is used to draw the time-frequency-energy graph (3-D plot). This plot distinguishes the different wave components which exist within the signal. Then, this plot is used to obtain the dispersion curves (velocity versus frequency) for the compression and shear waves of the output the signal.

Two codes were written in LabVIEW® media to analyze pulse tests using Wigner-Ville Energy Analysis Method. The first code is for analyzing numerical simulation output signals. Figure 4.1 shows the analysis of a numerical simulation result using this code. The simulation is for a proctor sample tested by radial shear all over its base [Simulation No. 9 at input frequency of 40 kHz; Chapter 3]. The material properties of soil are V_s = 150m/s, ν = 0.33 and γ_b = 1800 kg/m^3. The sample base is fixed in the vertical direction in order to eliminate the compression wave so that the analysis is easily demonstrated for one output component (shear wave). The graph in Figure 4.1 is the screen display of the used software (LabVIEW® 6.1) to carry out the analysis, and is divided into five graphs and two control

windows. The first plot (graph) in the upper right corner presents the input and output signals in the time domain. The amplitude of each signal is normalized to its maximum value. The second plot in the upper left part of the graph presents the cross-correlation function (C.C) and its energy function (in red). The mirror of the energy function across the horizontal axis is also plotted so that the energy envelope is obtained. The small plot on the left displays the frequency domain of the input and output signals (amplitude versus frequency). The lower plot to the left shows the time-frequency-energy distribution of the C.C function (Wigner-Ville Distribution). The horizontal scale is the time, the vertical scale represents the frequency and the energy is expressed in colour-scale (third dimension). The control of the energy colours is in the lower left corner of the graph. There is a scale factor for each axis. This graph shows that the frequency domain of the C.C. function varies from 3.5 to 28 kHz. In the graph to the lower right corner of the display, the dispersion curves for the shear wave velocity is plotted. The group velocity dispersion curve is shown in red, its best fit curve is shown by circles in blue, and the phase velocity dispersion is shown in continuous blue curve.

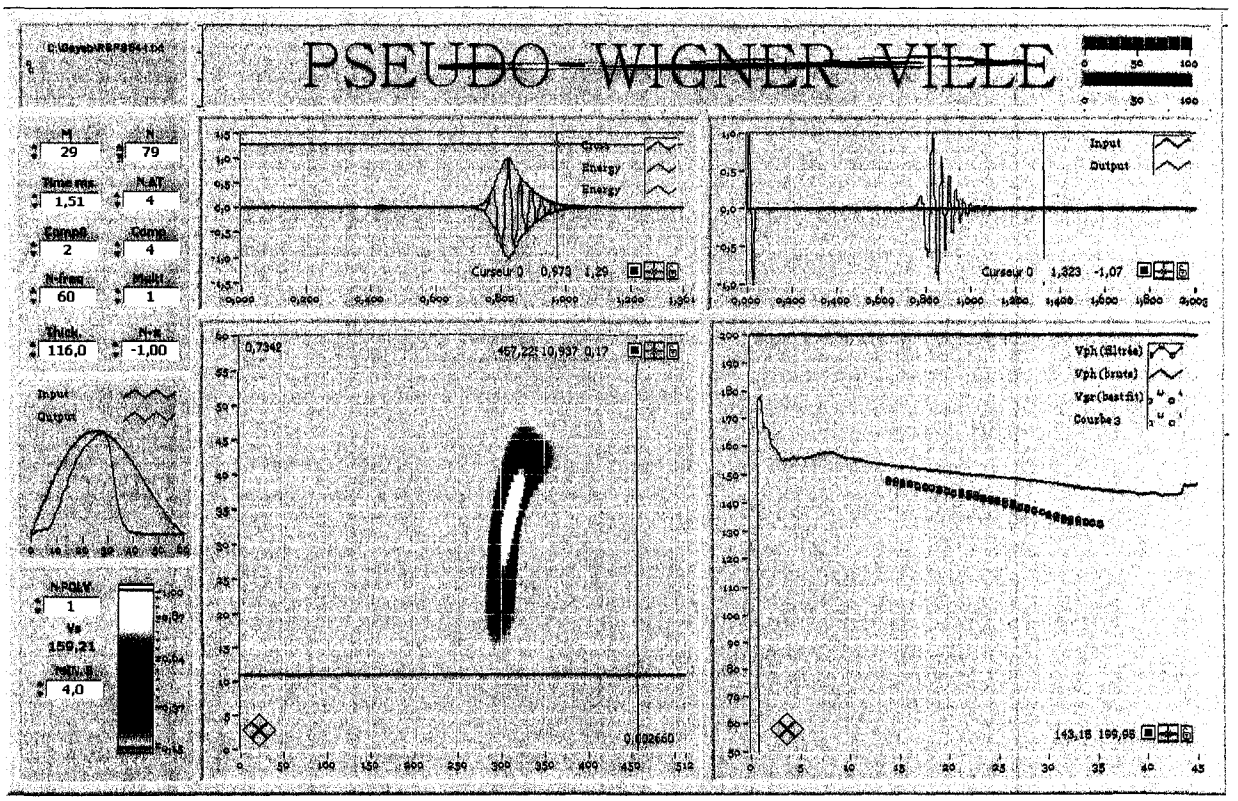

Figure 4.1 Wigner-Ville Energy Analysis for a Numerical Simulation Result.

In Figure 4.1, it can be seen that the phase and group velocities increase with deceasing the frequencies up to a threshold limit. The velocities dispersion curves at very low frequencies are not well defined. The group velocity is less than the phase velocity. Extrapolating the phase velocity curve at zero frequency gives a V_s velocity which coincides with the theoretical value (150m/s). Also, the arrival time of the shear wave velocity can be measured from the output signal, C.C, Energy envelope, and roughly from the time-frequency-energy plot. The second LabVIEW® code was written for carrying out laboratory pulse tests and interpreting their results. It is similar to the first code and is tailored to control the testing equipments and collects the test data. A common output of this code is shown in Figure 4.2 (a screen display of the used LabVIEW® software). Figure 4.2 presents a laboratory pulse test, on dry Ottawa sand sample in a Plexiglass mold of 76.2mm-height under a pressure of 248 kPa carried out using Setup 7 (Chapter 5), interpreted by Wigner-Ville Energy Analysis Method. The different graphs in this figure are presented on the same figure.

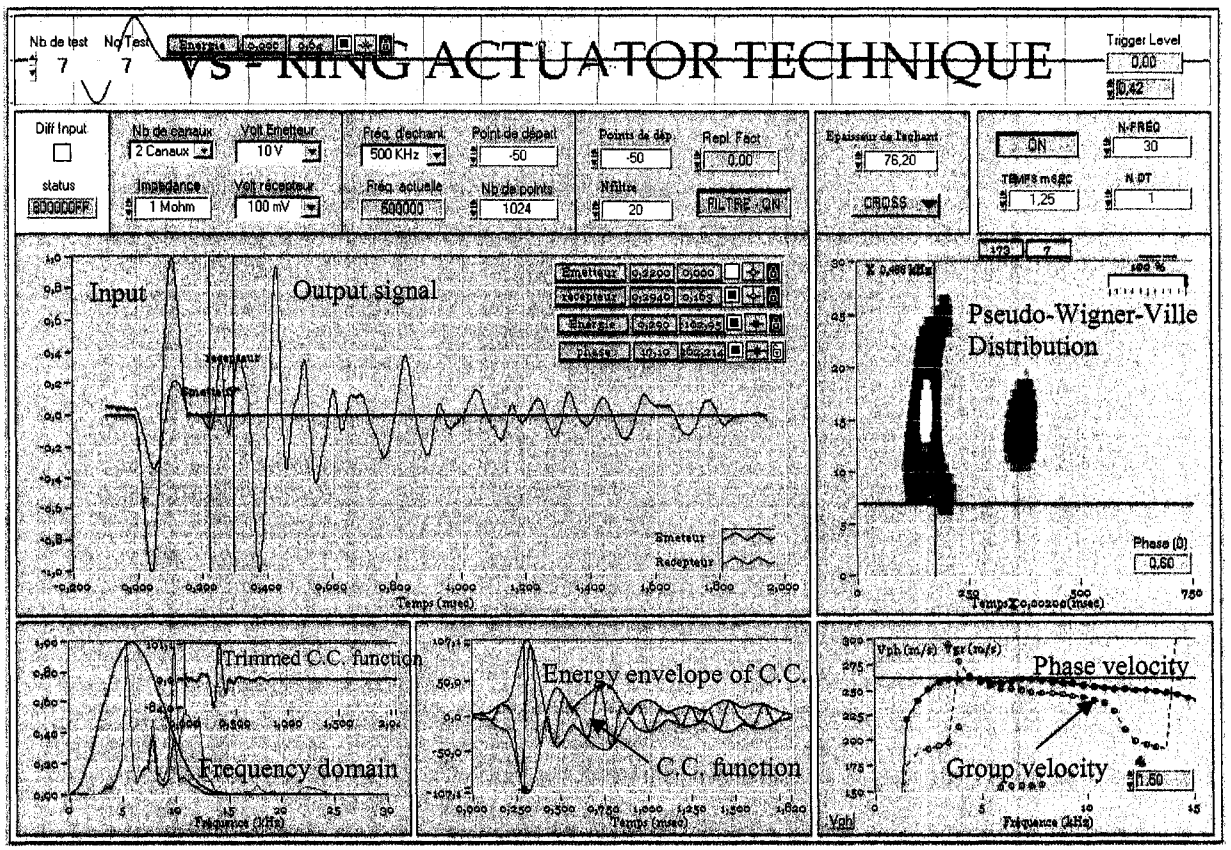

Figure 4.2 Wigner-Ville Energy Analysis for a Laboratory Pulse Test on Ottawa Sand.

4.4 Application of Wigner-Ville Energy Analysis on Numerical Simulation Results

The Wigner-Ville Energy Analysis technique was used to analyse many numerical simulations and laboratory tests (see Chapter 5). It was realized that there is a general trend for velocity dispersion. The phase and group velocities increase with decreasing the frequency (except at very low frequencies where the relationship is not clear; e.g. Figures 4.1 & 4.2). This dispersion pattern agrees with the findings reported in Chapter 3 regarding the "energy rise-time method". The correct velocity is at the energy rise-time and is neither at the energy peak nor at the peak of the C.C (i.e. the characteristic velocity is higher than the velocity determined from the energy-peak time). Using the Wigner-Ville Energy Analysis Method, the interpreted V_s values for the numerical simulations in this study were very close to the actual (theoretical) input values. This proves that the characteristic shear wave velocity should be interpreted in the frequency domain at zero frequency.

Some other numerical simulations were carried out in this chapter. The simulated soil sample (D = 50mm and H = 70mm) had a shear wave velocity of 200 m/s and a Poisson's ratio of 0.333. Figure 4.3 shows the analysis of these simulations in the frequency domain using Wigner-Ville Energy Analysis Method. These simulations introduce three modes of shearing excitation for pulse test. The first is plane-shear all over the sample base (Simulation No. 80). The second is point excitation at centre (Simulation no. 81) while the third mode is bender element with different bender length (Simulations No. 82-85). Six graphs are presented in Figure 4.3 for the relationship between frequency and group velocity. This Figure depicts the large interference in the received wave due to wave reflections when carrying out tests by bender elements. This can be realized from the different values of group velocity (V_g) at the same frequency (Simulations no. 82-85; graphs e & f). By increasing the length of bender element, the interference increase. This interference obscure the correct wave arrival time. The whole base and the point source shearing modes give no interference [Figure 4.3(a) & (b)]. In general, the velocity increases by decreasing frequency. The velocity tends to match the theoretical V_s value at zero frequency.

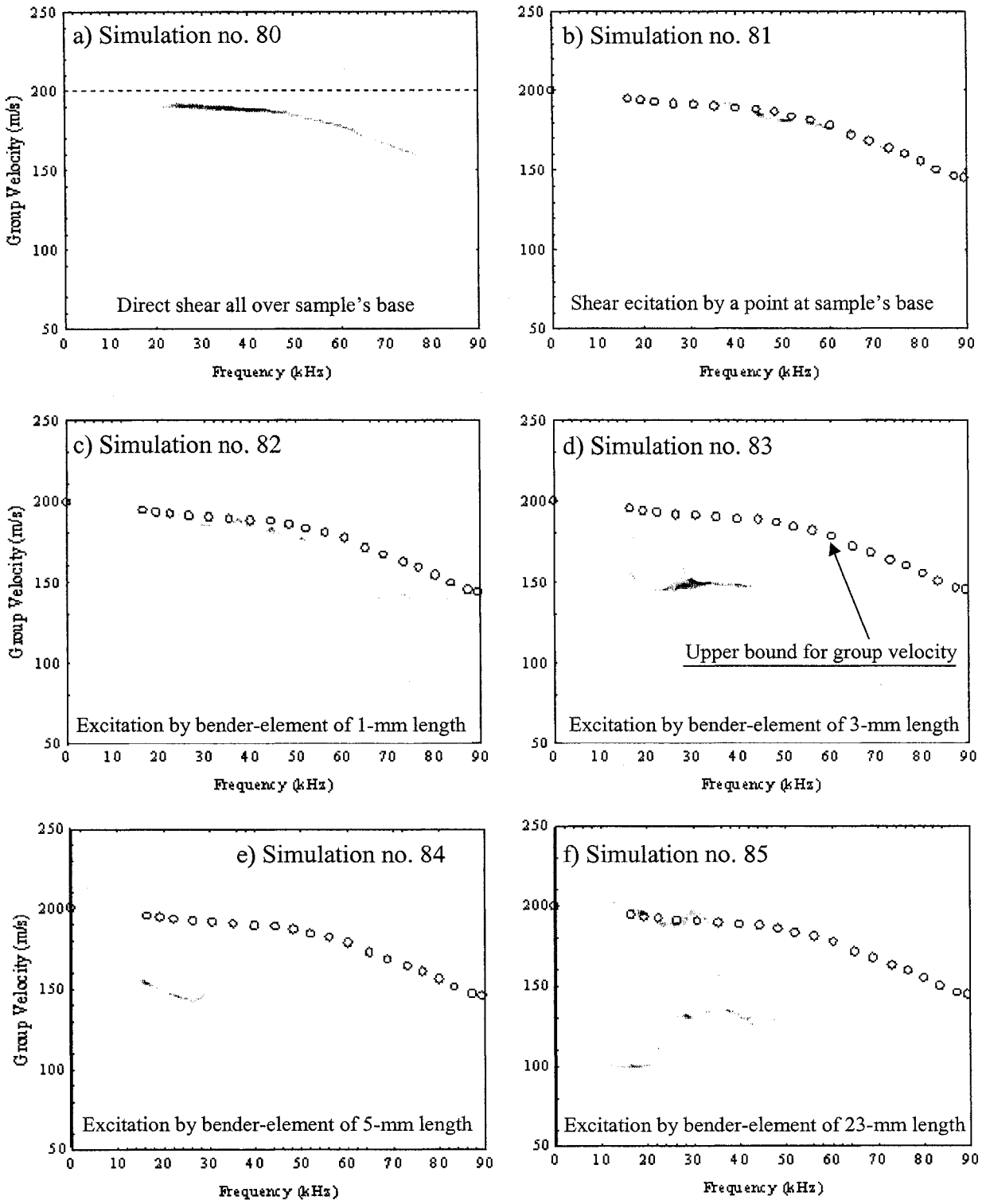

Figure 4.3 Analyses of some Numerical Simulations in the Frequency Domain Using Wigner-Ville Technique.

Another mode of shearing is simulated in order to prove this fact. The shearing is performed by 'a 3mm-thick disc of 20mm diameter' excited by horizontal radial forces on its perimeter (Simulations no. 86). The sample input compression and shear wave velocities are 400 and 200 m/s, respectively. The result of this simulation is shown in Figure 4.4. The velocity decreases with increasing frequency. The maximum value of the dispersion curve (at zero frequency) matches the theoretical wave velocity. Hence, elastic waves propagation in soil is dispersive. The inaccuracy of V_s measurements using common interpretation methods can be explained herein considering the dispersive nature of waves transmission in soil. Any wave propagating in a soil is composed of many frequencies. The soil disperses these frequencies making each frequency component travel at a certain velocity. The velocity of any frequency within the wave differs from the velocities of other frequencies. Also, it differs from velocity of the whole signal as a group of frequencies (group velocity).

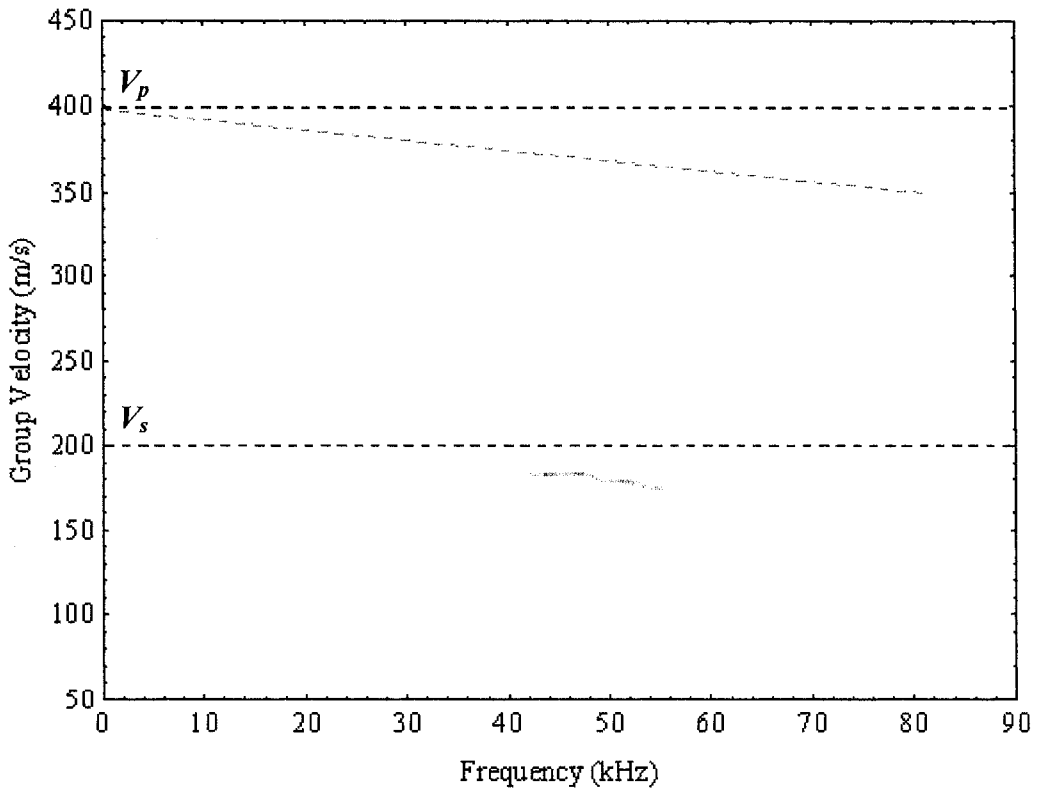

Figure 4.4 Numerical Simulation of a Pulse Test Using Ring Actuators Interpreted by Wigner-Ville Energy Analysis Method.

The characteristic shear or compression wave velocity of soil, at a certain condition, is constant and independent of frequency. Therefore, using time domain interpretation methods would not measure the characteristic property V_s of soil but would give another velocity which may accidentally be comparable to the intrinsic velocity in some cases. The measured velocity varies according to the technique used in interpreting the travel time of the wave (Chapter 2). Applying Wigner-Ville Energy Analysis is found to give a V_s value which is identical or very close to the predefined input value in a numerical simulation. Figure 4.5 introduce the interpretation of simulation no. 11(a) by Wigner-Ville Energy Analysis Method (the emitter is a 3-mm thick disc of 20mm diameter). The phase and group velocity curves tend to intersect on the velocity axis at a velocity of 198 m/s which almost equals the theoretical velocity (200 m/s).

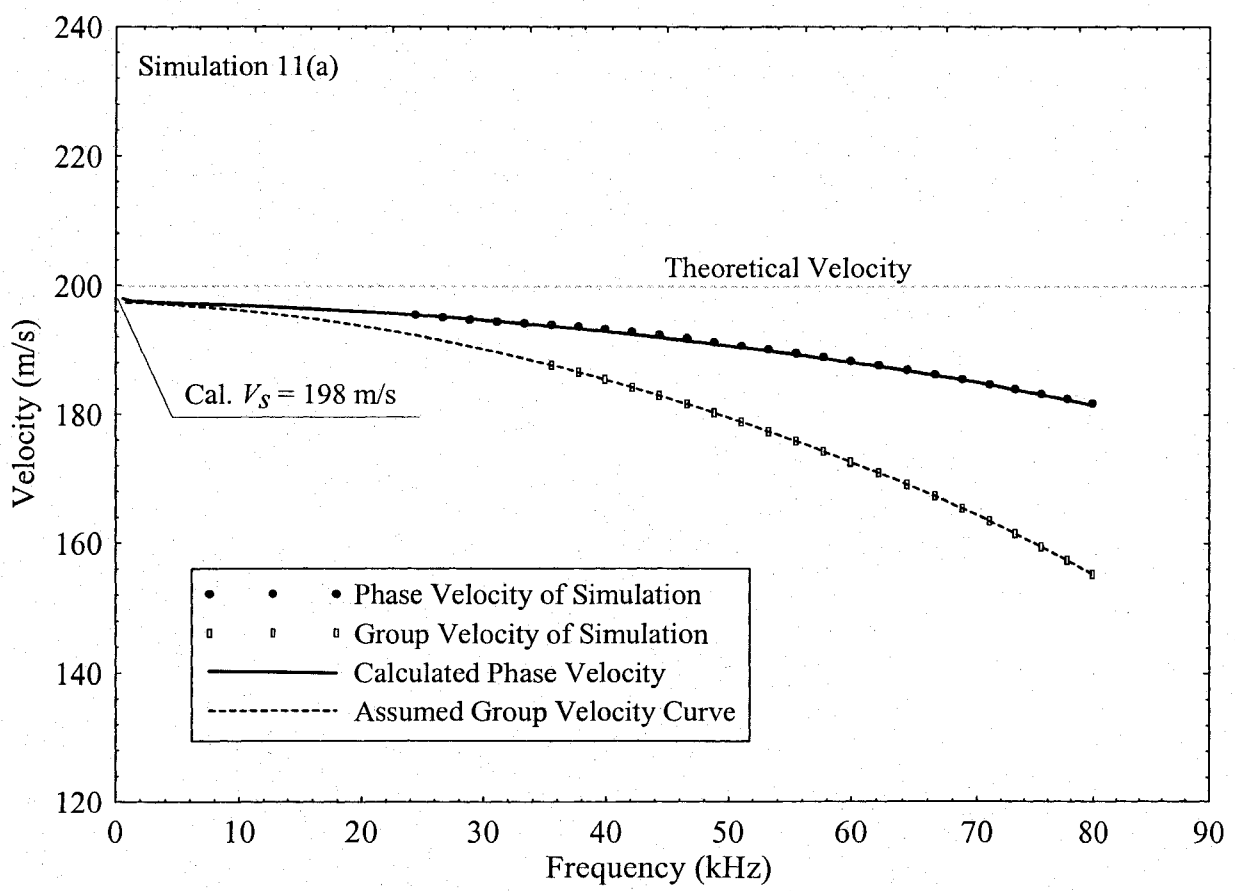

Figure 4.5 Simulation 11(a) Interpreted by Wigner-Ville Energy Analysis.

4.5 Integrating the Group Velocity Curve for Obtaining the Characteristic Velocity

In order to overcome the problem of the undefined Frequency-V_s relationship at low frequencies, a technique is developed in this study in order to calculate the velocity at zero frequency. Theoretically, the phase velocity (V_{ph}) curve can be obtained from the integration of the group velocity curve. Thus, a software is built to compute the velocity at zero frequency and is called RAKU. The two reliable (well defined curves at high frequencies) parts of group and phase velocity dispersion curves are used to achieve this goal. The group velocity curve at very low frequencies, beginning from zero, is assumed in the same trend of the existing portion of the curve at high frequencies. Then, the whole curve is integrated to calculate the phase velocity curve. If the calculated phase velocity curve matches the actual phase velocity curve, this means that the assumed dispersion is correct and the velocity at zero frequency is the characteristic velocity of shear wave. If not, a new fitting is assumed for the group velocity curve beginning at a different velocity value at zero frequency. This process is repeated until a complete match is achieved. Normally three iterations are sufficient. Figure 4.5 shows the assumed and calculated curves as well as the actual data points at high frequencies (phase and group velocities) for simulation no. 11(a). The calculated group and phase dispersion curves match the actual velocities at high frequencies. The two curves intersect with the vertical axis at the same point giving a shear wave velocity of 198 m/s. This value almost equals the input shear wave velocity (200 m/s). Then, the error in calculating V_s using this technique is 1% for this simulation. This shows that the characteristic velocity of a soil sample should be interpreted in frequency domain.

Group of Simulations No. 13 was carried out for pulse tests on a Proctor sample (L = 116-mm & D = 102-mm). The excitation is made by a pair of 6mm divided-discs at top and bottom. Each disk is divided into four equal parts. These simulations were carried out using a 2-D model. The soil had a V_s of 200 m/s and a V_p of 400 m/s (Poisson ratio = 0.333 and the damping ratio = 1%). The input frequency is taken as 10, 20, 30 and 40 kHz in the four simulations of this group. The output signals of these simulations are shown in Figure 4.6. It can be realized that the p-wave amplitude is small compared to shear wave amplitude. Also, the secondary waves on the output signals are minor. The integration process for the result of

a simulation of this group (Fr = 20 kHz) was carried out using the developed software. The result of this analysis is presented in Figure 4.7 in relationships between the velocity and frequency. The dispersion curves of the group and phase velocities were used to interpret the shear wave velocity. It can be seen that the phase velocity curve of the output signal is higher than expected. Theoretically, it should approach the velocity axis at a velocity of 200 m/s. Its trend gives a velocity of about 205 m/s instead of 200 m/s. This phenomenon was found in some simulations and laboratory tests. It is encountered at relatively high input frequencies. It can be understood considering the phase response of the emitter and receiver devices as it was reported in Chapter 2 (Figure 2.1). There is some phase-shift which depends on the input frequency. Therefore, the phase velocity curve is adjusted by changing the phase-angle (adding a phase shift) so that it intersects with the group velocity curve at the correct velocity (Figure 4.7). This treatment reduced the values of the phase velocity curve. Thus, the integrated velocity coincides with the phase velocity at zero frequency. This phenomenon has not been seen in pulse soil testing at low input frequencies which supports our explanation. Also, further analysis of this phenomenon is recommended for other devices of different dimensions under different conditions. These results depict the importance of studying piezoelectric devices before interpreting their results.

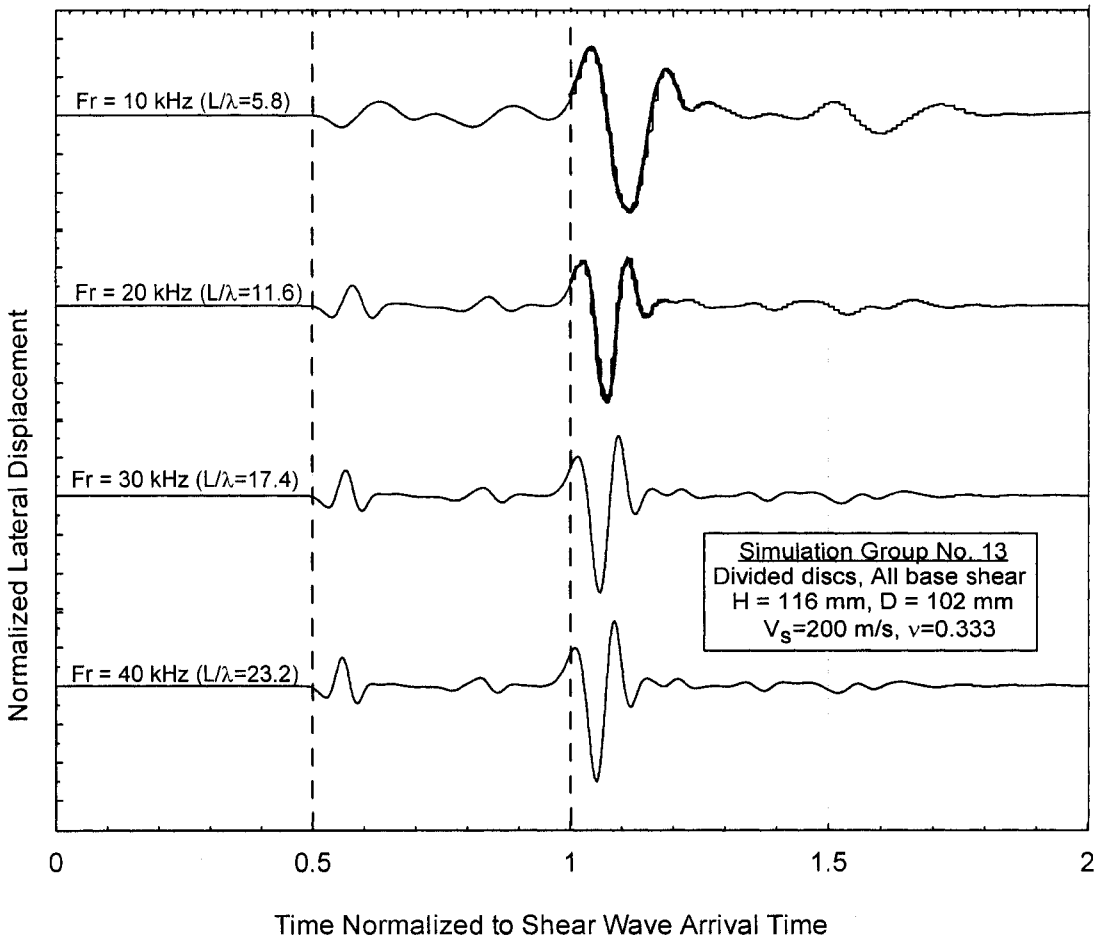

Figure 4.6 Output Signals for Group of Simulations No. 13.

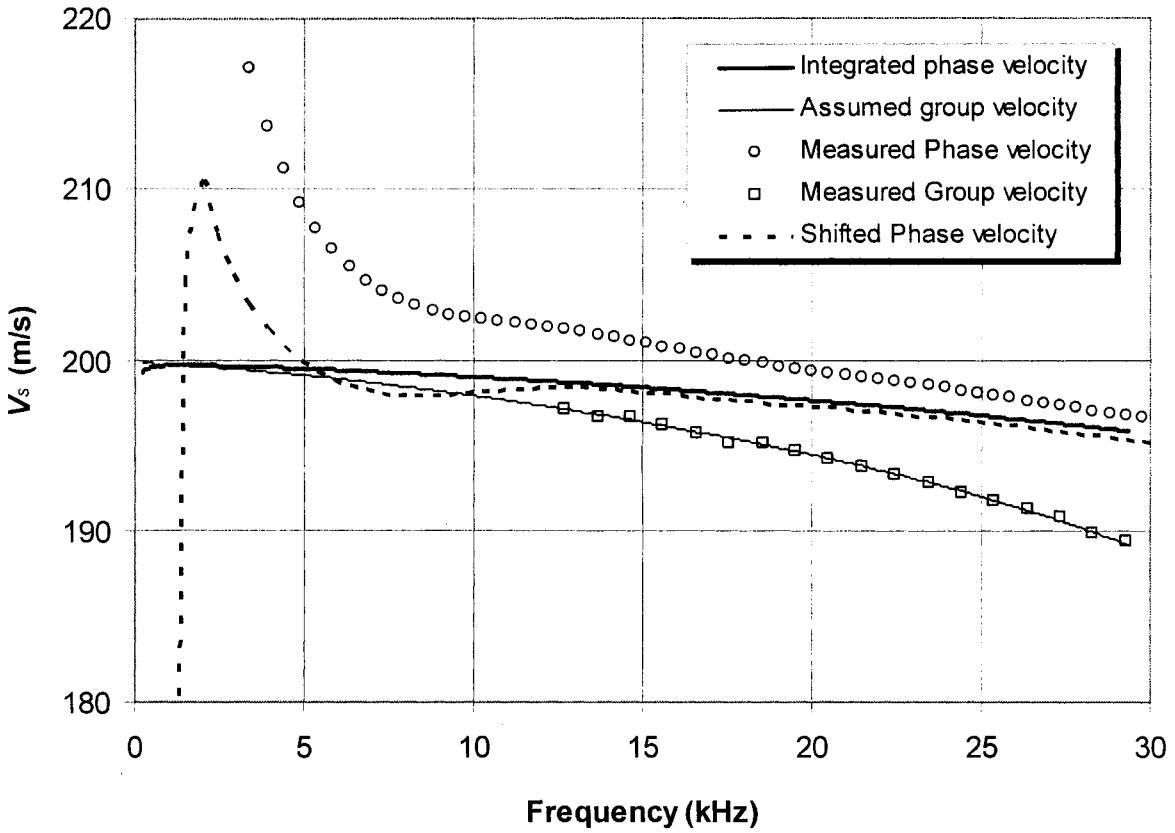

Figure 4.7 Integration of V_{gr} for Obtaining the Characteristic V_s for Simulation No. 13 (Fr = 20 kHz).

4.6 Conclusions

The numerical simulations of pulse tests have shown a velocity increase with the decrease of frequency. The characteristic shear wave velocity of soil should be interpreted considering the dispersive nature of pulse tests. This velocity is calculated from the velocity dispersion curves at zero frequency. The Wigner-Ville Energy Analysis Method gives an accurate and unique V_s value, regardless of the input wave frequency, without the need to make any personal judgement. The integration of the group velocity dispersion curve for obtaining the phase velocity curve was found useful in calculating the characteristic shear wave velocity in pulse tests. This technique will be used to interpret the pulse tests result of this study (Chapters 5 and 6). The existing interpretation methods are also used to double-check accuracy of the results.

(Blank)

Chapter 5 DEVELOPMENT OF A NEW PIEZOELECTRIC DEVICE FOR PULSE VELOCITY TESTS: RING ACTUATORS SETUP

5.1 Introduction

A new device for emitting and capturing small-strain waves is invented and developed in this study. The new setup (ring actuators) is designed to avoid reflection of waves at the top and bottom caps of the testing apparatus. Also, it does not need penetration into soil which makes it suitable for testing all types of soils without special preparations. This new system is a breakthrough which has improved wave interpretation and has gone many steps further. This chapter spread out the development stages for this new actuator.

According to previous findings in this research, it was planned in the beginning of this study to build a device to overcome some of the interpretation problems associated with previous devices and retains the advantages of currently existing devices. The practical and theoretical basis which has led to thinking in and suggesting this setup is introduced in Chapters 2 & 3. The developments of this new setup passed by many stages, most of them were so important in achieving the desired performance and building the final setup. Since using piezoelectric rings in geotechnical engineering is a pioneer application, this new application began by an idea and took enormous and unfading effort until it has become a reality. In this chapter, the development of this new system is introduced and some results are presented. The different development stages of this new setup are reported in detail as they show many important findings which are useful in understanding the performance of this setup, waves transmission characteristics, signal treatment and interpretation. In addition, this information is vital in building this new setup or similar devices. Also, the peripheral instruments required for operating this setup were also optimized during this research. Numerical simulations were carried out to overcome some encountered problems during the development process as well as for investigating some technical points.

5.2 Piezoelectric Ring-Actuators and their Preference

After studying and analysing the bender element pulse test as it is detailed in Chapters 2 & 3, many reasons have led to thinking in building another device that can avoid the disadvantages

of bender elements such as their applicability limitations, wave reflections at boundaries, and test interpretation difficulty (Figure 5.1). Numerical simulations also proved that devices which can emit and receive planner waves over large area are preferred to other sources which emit waves at a point or over a smaller area. Hence, the available piezoelectric material shapes were investigated for choosing an actuator that can be used to achieve the required goals. There were two possibilities to emit planner waves without penetration into soil; discs and rings (a short part of a tube). Both of them can vibrate in the radial direction to emit planner waves over large area. But piezoelectric discs are impervious and installing them at soil ends will not allow pore water flow from/to soil. Hence, rings were chosen so that porous plates can be installed inside them (Figure 5.2).

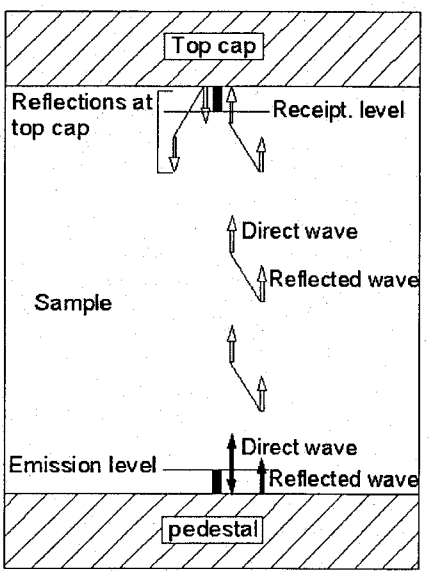

Figure 5.1 Interference of Waves at Receiver Due to Reflections on Pedestal and Top Cap for a Bender-Elements System.

The piezoelectric ring and the porous stone are glued together so that deformations of the ring are transmitted to the inner stone letting it vibrates in the same way as rings. Recalling that this setup does not require penetration into soil, roughness of the contact surface (at porous stone and rings) is important in transmitting the signal to soil sample. For fine grained soils, adhesion between the device and soil may achieve good interaction. Thus, excitation is made at sample's end through friction and/or adhesion between the inner porous plate and

soil. For bender elements, the shearing wave is generated inside the sample at the bender element's tip (at a distance from end of the sample). Therefore, wave's reflections at emitter's cap due to input wave do not exist for ring actuator setup. Signal interference in bender elements setup due to coupling of incident and reflected waves at end caps can affect the interpretation of travel time. This type of interference is illustrated in the Figure 5.1.

Other type of reflection is possible in ring actuator setup or in any other setup. The waves may travel inside the emitter's cap and then are reflected inside the cap back towards the emitter and soil. This type of reflections is handled here by providing a thin absorbing layer of rubber at the back of emitter. An absorbing layer is also introduced at back of the receiver. As a pioneer characteristic of ring actuators, their measurements take into account the soil anisotropy in the three dimensions (soil as a mass) rather than 1-plane measurements made by other devices. The soil deformations in ring actuators pulse test are all over a circular area (Figure 5.2) and propagate perpendicular to this plane. Therefore, a ring actuator test result is similar to the result of surface waves geophysical investigations which measure V_s of soil as a mass, partially; due to their interpretation procedures. Thus the results from field and laboratory measurements can be compared.

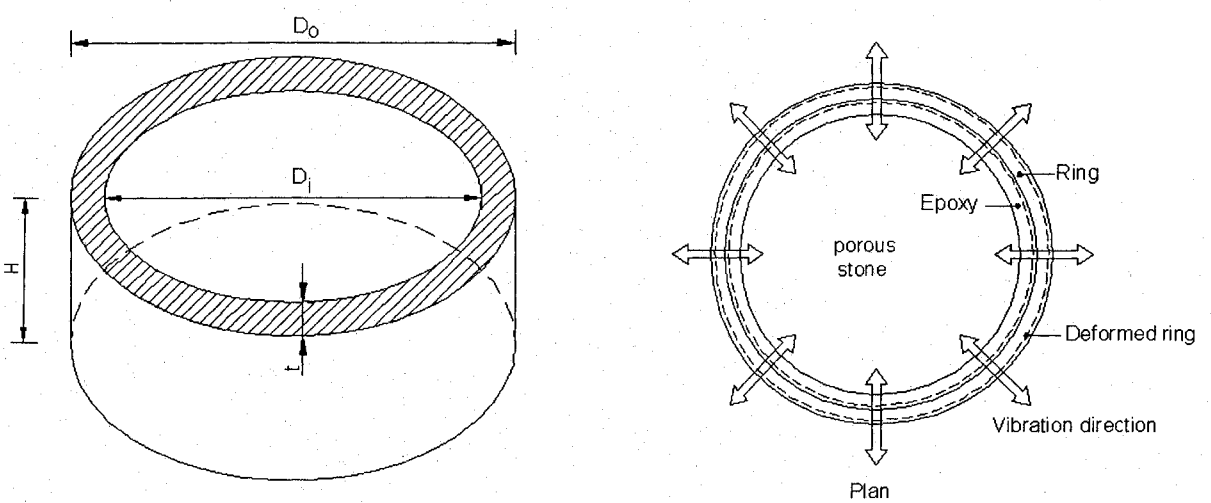

Piezoelectric ring — Piezoelectric ring glued to an inner stone

Figure 5.2 Dimensions and Deformations of a Piezoelectric Ring Actuator Polarized in the Radial Direction.

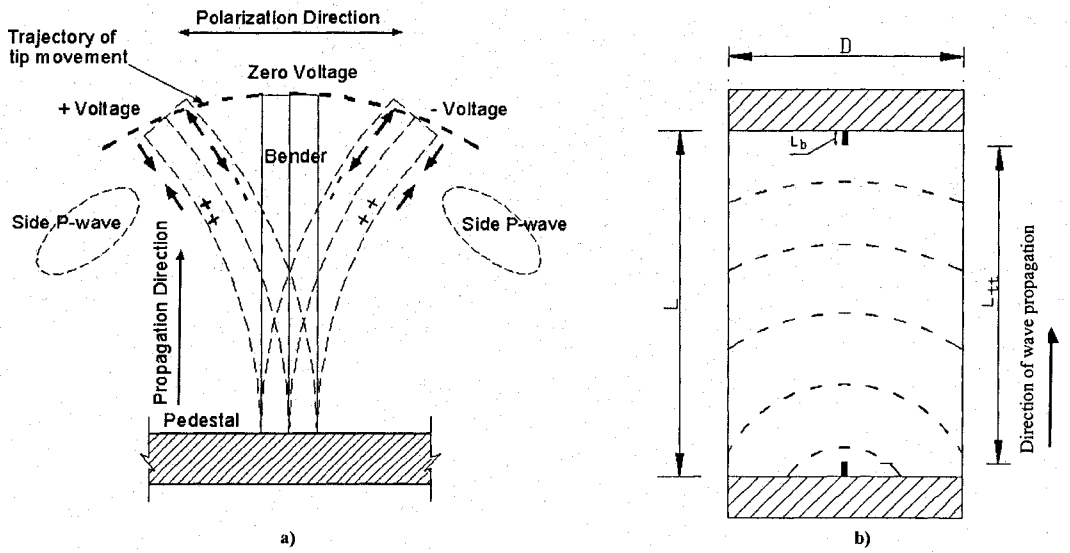

Figure 5.3 Bender Element Mode of Excitation.

Moreover, the mode of excitation for bender elements is bending. From this mode benders took their name. The bender-element bends to the left and right when being derived by a signal. Hence, the bender's tip moves in a curved path (a small part of circle). This type of excitation produces non plane waves; curved wave fronts (Figure 5.3). Also, it emits relatively strong compression waves perpendicular to the bender's plane. Also, the contact area of shear excitation is too small compared to that of side compression excitation. For ring actuators, the deformations transmitted to soil are shear excitation rather than bending. Also, the excitation is made over a large area. This eliminates the side compression waves and introduces high-energy shear wave.

5.3 Manufacturing the Ring Actuators Setup

Precise and careful manufacturing of the piezoelectric rings is crucial in order to have a device that can produce reliable results. The rings used in the different setups in this study were carefully cut by a mechanical saw to an appropriate size from bigger cylinders (tubes) having wall-electrodes and polarized in the radial direction (Figures 5.4 & 5.5). Tubes are coated with very thin film of silver from inside and outside to work as electrodes. They operate on the transversal piezo effect. When an electric voltage is applied between the outer and inner diameter of a thin-walled tube, it contracts/expands axially and radially. The rings used in this

study are made of "lead zirconate titanate – 850E" manufactured by APC International Ltd., USA. This material is used for low power devices giving high coupling and high charge sensitivity. It produces a clean, noise-free frequency response as reported by the manufacturer. Table 5.1 displays the properties of this material. The notations used in this table are described as follows:

K = Relative dielectric constant (at constant stress).

D.F = Dielectric Dissipation Factor at 1 kHz, low field (Dielectric Loss in percentage)

T_c = Curie point (°C).

d_{33} = Piezoelectric Charge Constant: induced polarization in direction 3 (parallel to direction in which ceramic element is polarized) per unit stress applied in direction 3 or induced strain in direction 3 per unit electric field applied in direction 3 (Figure 5.4).

d_{31} = Piezoelectric Charge Constant: induced polarization in direction 3 per unit stress applied in direction 1 (perpendicular to direction in which ceramic element is polarized) or induced strain in direction 1 per unit electric field applied in direction 3.

k_{33} = Electromechanical Coupling Factor (%): factor for electric field in direction 3 and longitudinal vibrations in direction (ceramic rod, length >10x diameter).

k_{31} = Electromechanical Coupling Factor (%): factor for electric field in direction 3 and longitudinal vibrations in direction 1.

Q_m = Mechanical quality factor.

Table 5.1 Properties of the Used Piezoelectric Material (850-E).

K	D.F	T_c [C°]	k_{31} (%)	d_{33} [pC/N or Pm/V]	d_{31} [pC/N or Pm/V]	Density [g/cc]	Q_m	Electrodes Thickness [μm]
1800	0.02	300	> 0.35	350	-175	7.5	85	6-12

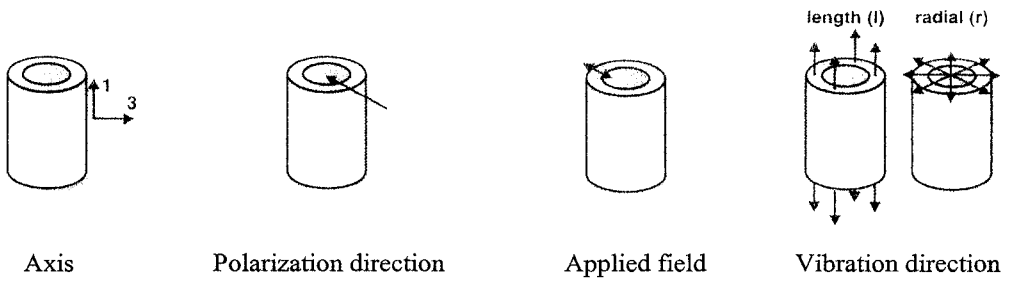

Figure 5.4 The Configurations of Piezoelectric Cylinders.

The configurations of piezoelectric cylinders are shown in Figure 5.4. The ring actuators used in this research are 44-mm in outer diameter. Two ring heights were chosen according to setup dimensions; 2.5mm and 3.0mm (Table 5.2). A special coaxial cable was connected to the wall-electrodes of each ring; one wire to each electrode. Figure 5.6 shows different sizes of piezoelectric ring transducers connected to the wires with a schematic drawing for their composition. The input voltage is applied to the ring in the thickness direction (horizontal). When a driving voltage is applied to the silver films on the inner and outer surfaces of the ring (wall-electrodes), it deforms in the radial direction depending on the shape and polarity of input signal. This will cause the soil to contract or expand laterally (shear waves). Other secondary deformations will occur within the soil in the vertical direction (compression waves). These deformations are due partially to the horizontal deformations (contraction/expansion) of the emitter. Also, these vertical deformations are due to soil elasticity which depends on Poisson's ratio. The wires were welded to the very thin silver electrodes using special welding silver (Kester© Solder) at a temperature below 530° F (277° C). The contact time between piezoelectric ring and the welding iron should not exceed 3 seconds. Otherwise, the rings would be exposed to high temperature that may weaken or cancel the polarization of the piezoelectric material. As explained latter in this chapter, for some setups that have metallic inner-stone, an additional wire is connected to the inner-stone to ground it.

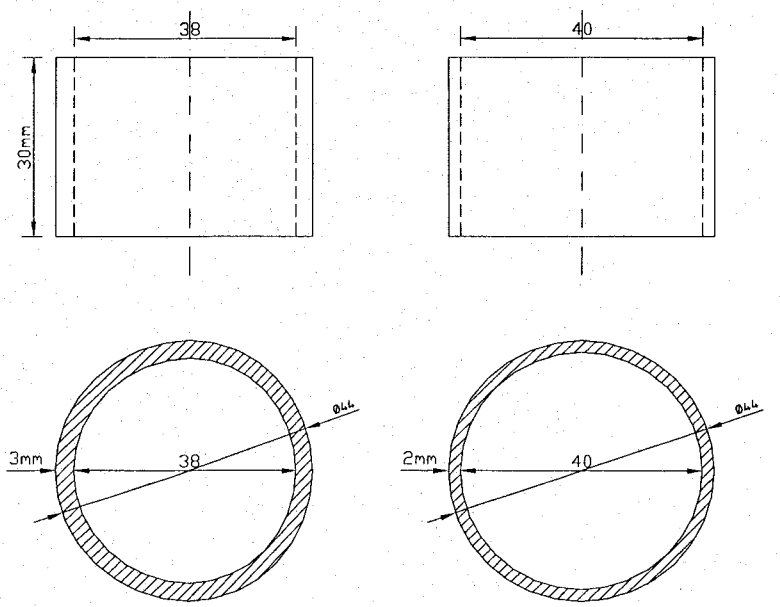

Figure 5.5 Dimensions of the Chosen Piezoelectric Tubes for Having Rings.

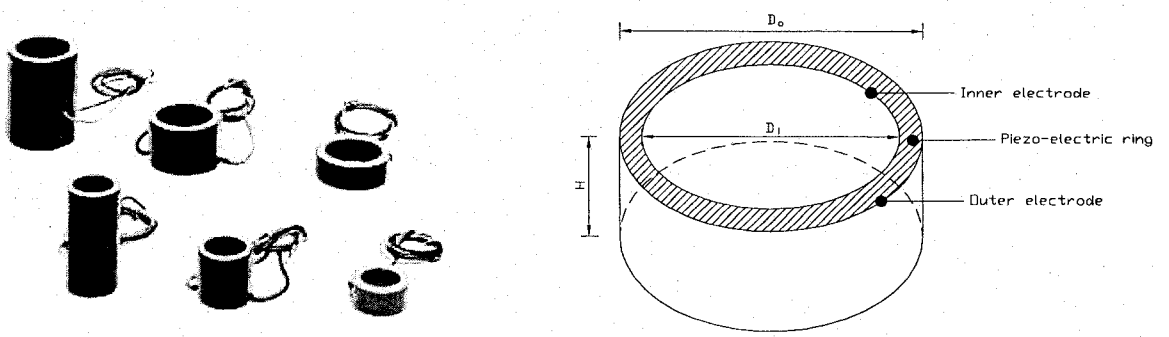

Figure 5.6 Piezoceramic Ring and Cylinder Transducers with Schismatic Drawing for their Composition.

Piezoelectric materials should not be exposed to water as this will electrically short the transducer. Therefore, the rings were cased (coated) by a waterproof epoxy material. Low viscosity, 30-minutes setting time, Loctite E-30CL epoxy adhesion, made by Hysol©, was used to cover the rings. Figure 5.7 shows the rings with their cables after the waterproof casing has been applied. Five to seven thin layers of coating were applied to prevent electrical shortcut. The final thickness of epoxy coat is about 1.25mm. Great care was necessary to obtain a casing free of open seams, cracks or air bubbles. Extra volume or irregularities of epoxy had to be gently removed by using smooth sandpaper in order to obtain even coating.

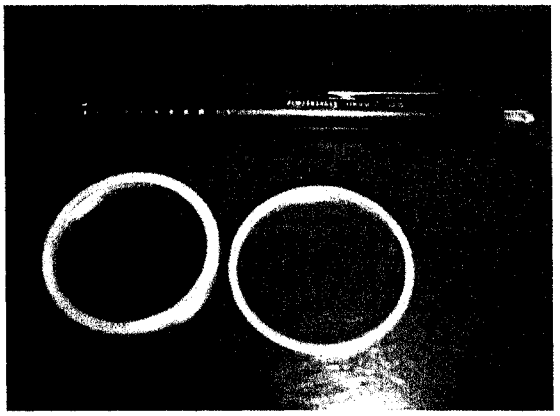

a) Emitter and receiver rings after cut from cylinders

b) Wiring and coating the rings with epoxy resin

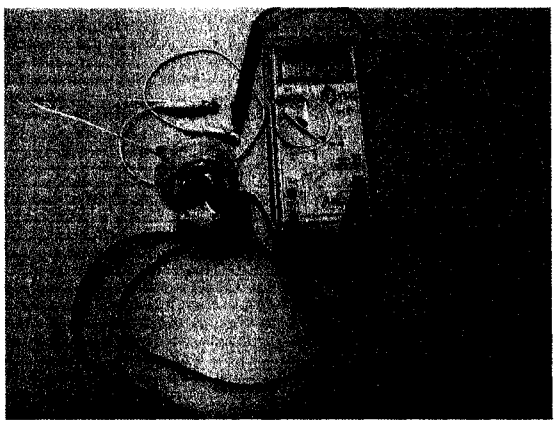

c) Shortcut checking by water solution and voltmeter

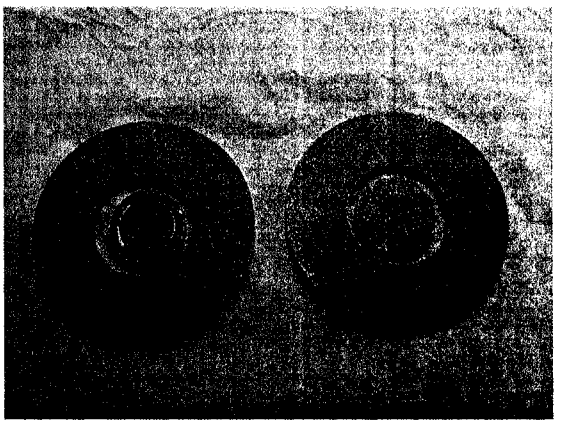

d) Outer and inner stones (at emitter & receiver)

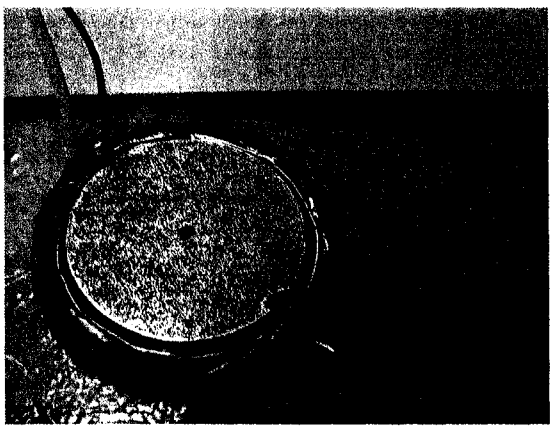

e) Gluing the porous stone to the ring and connecting the ground wire

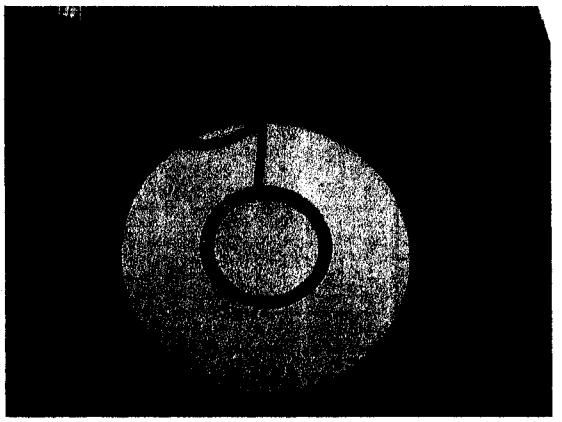

f) Ring actuators unit inside the outer porous stone

Figure 5.7 Manufacturing a Piezoelectric Ring Setup.

Even resin coating is important for proper fitting of the rings inside the setup as well as for producing uniform deformations in all radial directions. Also, sensitive handling of the rings is important due to the very fragile nature of the rings. Excess pressure would break the rings or depolarize it. Electrical shortcut is checked by immersing the rings in heavy salted water (severe environment). Then checking that there is no shortcut in the circuit is performed (no continuity of any possible circuit which includes one or both of the electrodes). Figure 5.7 shows the different stages for manufacturing a ring actuators setup. The next step in the manufacturing process is fixing the ring to the inner porous stone. The inner-stone should be accurately positioned (horizontally and vertically) and glued to the rings. Figure 5.8 presents a drawing for a ring actuator glued to porous-stone. Positioning and even glue is crucial for obtaining a setup that operates as required. The deformation of emitter should be radial axisymmetric, centered at the sample's axis. The displacement of each point on the emitter should be proportional to its distance from center. Irregularities in the vertical direction will lead to bad contact and/or load concentration. Also, inaccurate horizontal-positioning of the inner-stone with respect to ring actuator could cause distorted deformation. The vertical positioning depends on the height difference between the ring and the inner-stone. The mid-height of the ring should be vertically adjusted at mid-height of the inner-porous-stone (Figure 5.8).

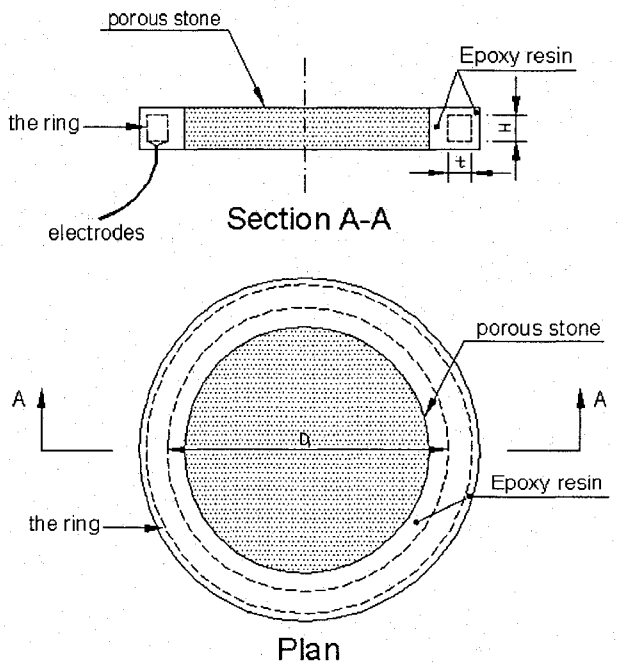

Figure 5.8 A Ring Actuator Glued to Porous Stone.

The cased ring and its inner stone becomes one piezoelectric unit that can be installed in a testing setup. Using the device as a transmitter or a receiver element was taken into consideration as it will be shown later on in this chapter. A disc-shape space is machined in "the porous stone of the cap" to accommodate the actuator device. The ring unit is fitted inside the outer porous stone of the testing setup and acts as part of the end cap (Figure 5.7). An absorbing material is installed behind the porous stone for attenuating any travelling waves though cap or pedestal. The coaxial wires which are connected to the electrodes of the rings exit through a vertical hole, passing through the different components of the base pedestal or the top cap.

5.4 Strains in Ring Actuators

Currently, to our knowledge, the equations for calculating the strains in short cylinders (rings) have not been yet derived. The cylinder equations will be used with some judgement to estimate the strains in ring actuators setup. The static displacement of a piezoelectric free cylinder can be computed as follows. The longitudinal 'extension/contraction' strain ($\Delta H/H$), depending on voltage direction, can be estimated from the following equation:

$$\frac{\Delta H}{H} = \frac{d_{31}V}{t} = \frac{d_{31}V}{(D_o - D_i)/2} \tag{5.1}$$

The change in wall-thickness can be computed as follows:

$$\Delta t = \Delta\left(\frac{D_o - D_i}{2}\right) = d_{33}V \tag{5.2}$$

The radial displacement is a result of the superposition of decrease/increase in wall thickness (Equation 5.2) and the tangential extension/contraction. Hence, the radial strain can be computed as follows:

$$\frac{\Delta r}{r} = \frac{d_{31}V}{t} \tag{5.3}$$

where:

d_{31} = strain coefficient (displacement normal to polarization direction) (m/V)

d_{33} = strain coefficient (displacement in polarization direction) (m/V)

H = length of the PZT ceramic tube, r = radius of the tube, V = applied voltage, D_o = outer diameter and D_i = inner diameter

These equations are valid for cylinder of H >> r (5 to 10X). The ring actuators prepared for this study had a height of 2.5mm or 3.5mm. They were cut from cylinders of an outer diameter of 44mm (Table 5.2). Thus, the ratio of h/r is less than 5. Therefore, further investigation is needed to derive the exact deformation equations for these rings. These equations are important for calculating the strain level in rings that will be transmitted to soil in order to make sure of carrying out pulse tests in the very small strain range (< 0.001 %).

Table 5.2 Dimensions and Properties of the Chosen Piezoelectric Cylinders (850-E).

The Function	Dimensions (mm)			Capacitance at 1kHz (p Farad)	Resonance Frequency (kHz)			Coupling Coefficient (K_{31}) %
	D_o (mm)	D_i (mm)	Length (mm)		Length	Planer	Thick-ness	
Emitter	44.0	38.0	30.0	20500	55	48	670	0.40
Receiver	44.0	40.0	30.0	30000	55	47	1005	0.45

The deformation of unrestrained ring can be roughly computed from the previous equations. In this research, the voltage used for carrying out the laboratory tests varied from 10 to 200 Volts. Table 5.3 introduces the computed strains in the radial and longitudinal direction as well as in the thickness of the piezoelectric tubes/rings made of Material 850-E (APC Inc. Catalogue). The thickness strain is the strain in the wall of the ring (horizontal), while the longitudinal strain is the strain in the height direction (vertical). As the previous equations shows, the longitudinal strain equals the radial strain. It can be realized that the radial and longitudinal strains of an unrestrained ring of 3mm-thickness are in the elastic range for input voltage of up to 200 Volts while the strains in the thickness direction are within the elastic range for input volt of up to 100. The thickness strains are always about double the radial/longitudinal strains. If a 2mm-wall-thickness ring is used as an emitter, the strains are much higher than those for a 3mm ring and the elastic stain limit is reached under lower input voltages.

Table 5.3 Computed Strains of Unrestrained Piezoelectric Cylinders/Rings.

Strain ($\times 10^{-5}$)	Wall Thickness (t)	Input Tension (Volt)				
		20	50	100	150	200
Radial ($\Delta r/r$) or Longitudinal ($\Delta H/H$)	3mm	0.12	0.29	0.58	0.88	1.17
Thickness ($\Delta t/t$)		0.23	0.58	1.17	1.75	2.33
Radial ($\Delta r/r$) or Longitudinal ($\Delta H/H$)	2mm	0.18	0.44	0.88	1.31	1.75
Thickness ($\Delta t/t$)		0.35	0.88	1.75	2.63	3.5

A parametric study was carried out to investigate the best dimensions for a piezoelectric ring as an emitter. Two cylinders of 3mm and 2mm wall-thickness were chosen from the available products of the manufacturing company. The cylinders were cut to rings of 2.5mm or 3.5mm height (length). Table 5.4 displays the computed deformations for four rings of different heights and wall-thicknesses under different input voltage. Table 5.4 indicates that decreasing the wall-thicknesses of the ring will increase the deformation in the horizontal direction (shear wave deformations). At the same time, this would increase the deformation in the vertical direction (compression wave deformations) with the same percentage, considering that the ratio of longitudinal to radial deformation, $\Delta H/\Delta r$, is always constant for the same ring height (3.5mm) and equals 0.08 [$\Delta r/r = \Delta H/H$ then $\Delta H/\Delta r = H/r$). Decreasing the wall-thicknesses of the ring also increases the ratio of radial to thickness deformation ($\Delta r/\Delta t$) which is desired for energetic (high amplitude) shearing over the whole inner-area of the ring. The Poisson's ratio of the rings ($\Delta t.H/\Delta H.t$) equals 0.49. The thickness deformations, Δt, do not change with thichness or height change because only the input volt controls them (Equation 5.2). Increasing the height of the ring increases both the radial and longitudinal deformations. Also, the radial to thickness deformation ($\Delta r/\Delta t$) increases while $\Delta t/\Delta H$ decreases. This would

make the shear wave more evident on the received signal than the compression wave, which is highly desired.

Table 5.4 Rough Estimation of Deformations for Unrestrained Piezoelectric Rings.

Wall Thickness (t)	Input Tension (Volt)	Deformation (nm)									
		Ring Height = 2.5mm					Ring Height = 3.5mm				
		Δr	Δt	ΔH	Δt/ΔH	Δr/Δt	Δr	Δt	ΔH	Δt/ΔH	Δr/Δt
3mm	20	36.7	7.0	2.9	2.40	5.2	51.3	7.0	4.1	1.71	7.3
	50	91.7	17.5	7.3	2.40	5.2	128.3	17.5	10.2	1.71	7.3
	100	183.3	35.0	14.6	2.40	5.2	256.7	35.0	20.4	1.71	7.3
	150	275.0	52.5	21.9	2.40	5.2	385.0	52.5	30.6	1.71	7.3
	200	366.7	70.0	29.2	2.40	5.2	513.3	70.0	40.8	1.71	7.3
2mm	20	77.0	7.0	6.1	1.60	7.9	55.0	7.0	4.4	1.14	11.0
	50	192.5	17.5	15.3	1.60	7.9	137.5	17.5	10.9	1.14	11.0
	100	385.0	35.0	30.6	1.60	7.9	275.0	35.0	21.9	1.14	11.0
	150	577.5	52.5	45.9	1.60	7.9	412.5	52.5	32.8	1.14	11.0
	200	770.0	70.0	61.3	1.60	7.9	550.0	70.0	43.8	1.14	11.0

Table 5.4 shows that the best emitter should have the longest height and the thinnest wall-thickness (ring of t=2mm & h=3.5mm). The actual deformations in the rings should be less than the computed values due to many factors. First, the stiffness of the actual setup is much higher than the unbounded rings due to the restraints made by the inner stone and the coating epoxy. Secondly, the applied stresses on the soil, which are transmitted to the rings, introduce additional restraints. Third, the friction at the upper and lower surfaces of the piezoelectric setup (the rings and inner-stone) and each of the soil and the cap participate in reducing the strain level.

5.5 Tested Soils

This section introduces the different soil types used in this study. Some pulse test results on these soils are introduced in this chapter. Five soil types were tested in the experimental program; four sand types and one till soil. The standard Ottawa sand (C-109) was one of these soils. The grain size distribution curves of these soils are shown in Figures 5.9 and 5.10. The characteristics of Ottawa sand used by Salgado et al. (2000) are also presented for comparison. Also, Table 5.5 presents the grain size characteristics of these soils. The tested soil types have different grading characteristics varies from silty sand to well graded sand. The average particle diameter (D_{50}) of these soils varies from 0.11 to 0.42 and the uniformity coefficient (C_u) range is 1.49 – 18.9. The minimum and maximum void ratios e_{min} and e_{max} were measured according to ASTM (D 4253 and D 4254) and found equals 0.49 and 0.73 for the standard Ottawa sand (C-109); 0.26 and 0.62 for the LG4 till, respectively.

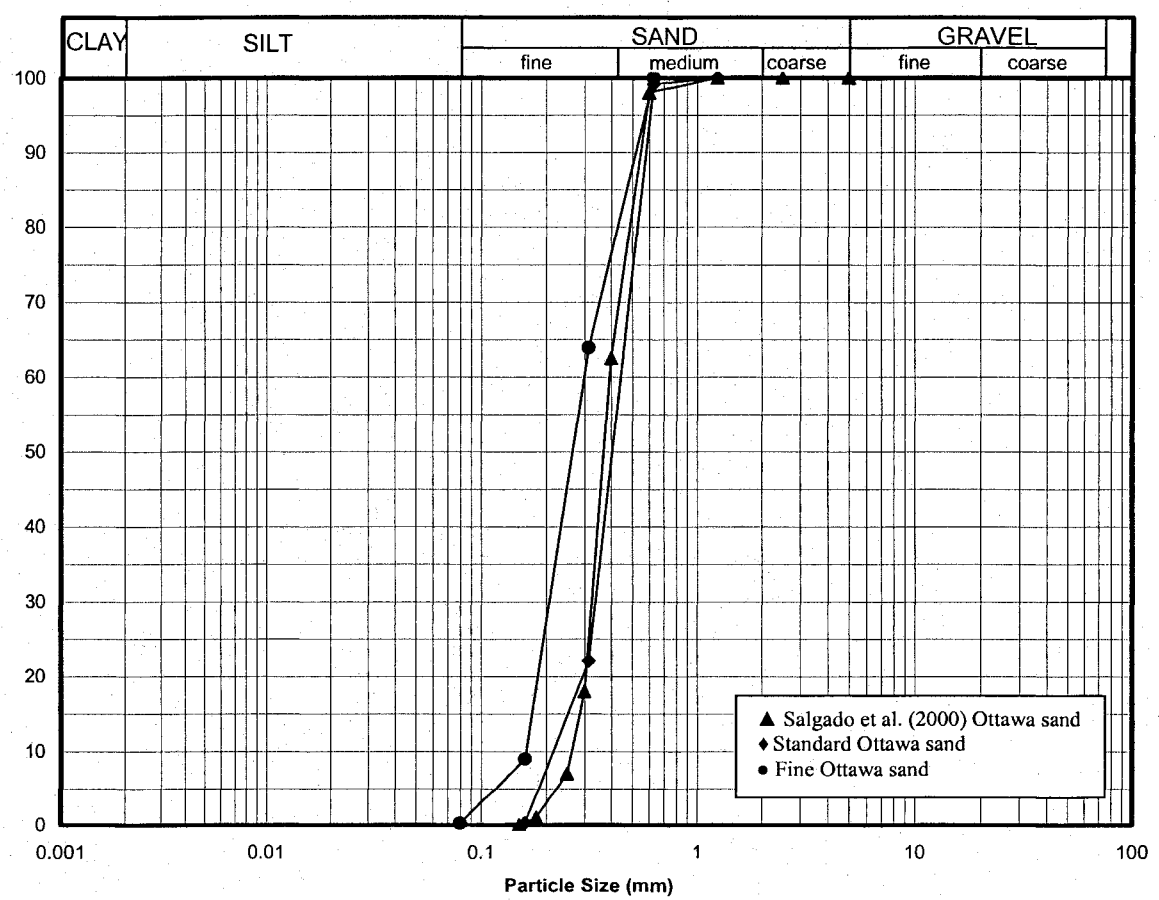

Figure 5.9 Grain Size Distribution of Ottawa Sand (C-109).

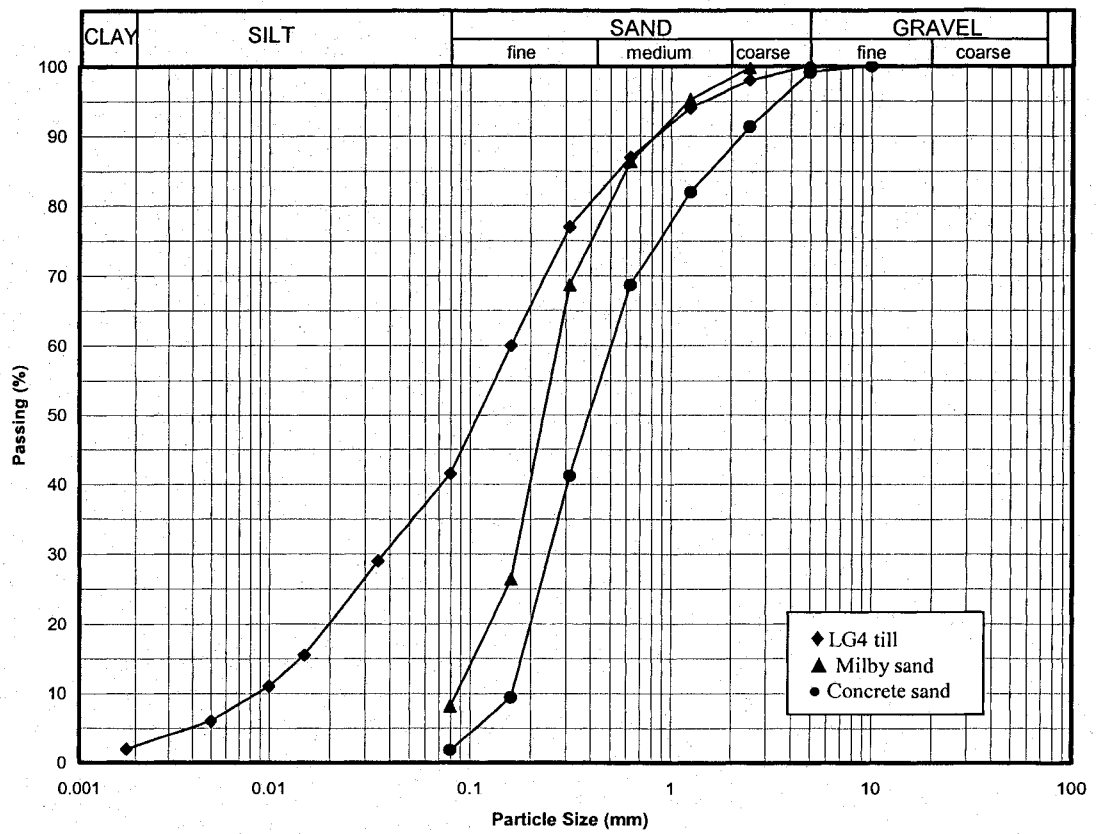

Figure 5.10 The Grain Size Distribution Curves for some Soil Types.

Table 5.5 Grain Size Characteristics of some Soil Types.

Sample	D_{50} (mm)	D_{60} (mm)	D_{30} (mm)	D_{10} (mm)	C_u	C_c
Salgado et al. Ottawa Sand	0.37	0.394	0.328	0.264	1.49	1.03
Standard Ottawa Sand (C-109)	0.37	0.397	0.314	0.202	1.96	1.23
Fine Ottawa Sand	0.28	0.304	0.219	0.163	1.87	0.97
Milby Sand	0.247	0.283	0.173	0.088	3.2	1.2
Concrete Sand	0.416	0.531	0.260	0.163	3.3	0.8
LG4 Till (Silty Sand)	0.11	0.17	0.04	0.009	18.9	1.06

5.6 The Used Laboratory Setups

A piezoelectric setup is composed of two units (emitter and receiver). The ring actuators were implemented in the top cap and the pedestal of a large oedometer cell. The equipped cap and

pedestal constitute a pulse test setup. The two ring actuator units were changed several times with each development after fabrication of new units (as it will be explained in the next section). This set was used to carry out pulse tests in each of the standard Proctor mold, a large oedometer cell and other fabricated molds. Table 5.6 introduces the dimensions of these laboratory setups. The majority of experimental tests were carried out in the Proctor mold and the large oedometer ring.

Table 5.6 Dimensions of the Used Laboratory Setups.

Setup	Description	H (mm)	D_i (mm)	D_o (mm)	Material type
A	**Large Oedometer Ring**	35.3	100.9	108.9	Brass
B	**Proctor Mold**	115.5	101.5	115.5	Steel
C	**Short Mold**	76.2	100.9	113.9	Plexiglass
D	**Medium Mold**	95	100.9	113.9	Plexiglass
E	**Long Mold**	101.7	100.9	113.9	Plexiglass

5.7 Development of the Ring Actuators Setup

Eight different setups were built in this study. Each setup had some improvements to its precedent. This section presents these setups considering their characteristics, components, advantages, behaviour in testing, and the ideas and conclusions taken from each setup.

5.7.1 Setup 1

In January 2003, the first setup that incorporated piezoelectric ring actuators for pulse testing of soil has been built in the geotechnical laboratory at Université de Sherbrooke. Figure 5.11 shows the drawings of this preliminary setup. It uses piezoelectric rings of D_o = 16mm, D_i = 11mm and H = 2.5mm. The specifications of all ring-actuator setups manufactured in this study are found in Table 5.7. Setup 1 was designed to eliminate reflected waves coming from the back of rings, from inside the caps, by introducing a rubber pad behind the rings and the porous stones. Figure 5.12 displays a photograph of rings and porous stones as similar to those used in Setup 1. The testing caps and the complete piezoelectric setup are shown in Figure 5.13. The rubber pad was a good energy-absorbent material but deforms under loading.

Therefore, when stress-strain relationship is required, the soil net settlements were calculated based on a calibration test in order to subtract deformations of the rubber band and the setup. The rings were excited by a step/rectangular input signal of 20 Volts amplitude using HP 35653A 50 kHz source module. The used equipments, the wiring and connections are shown in Figure 5.14.

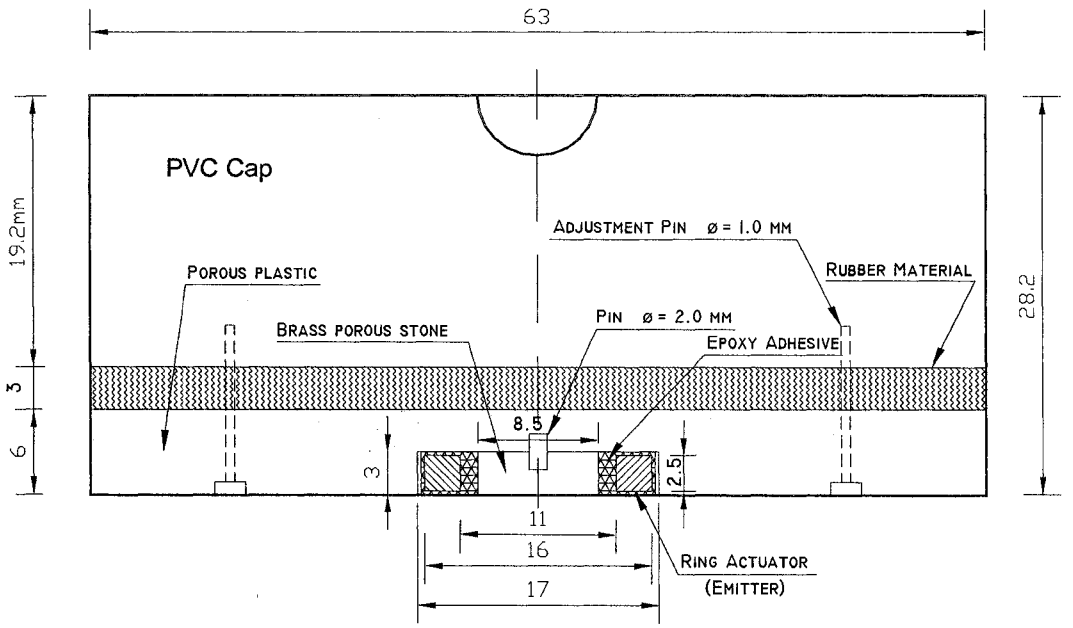

Figure 5.11 A Design for Cap Equipped with a Ring Actuator for Carrying out Pulse Tests at Laboratory (Setup 1).

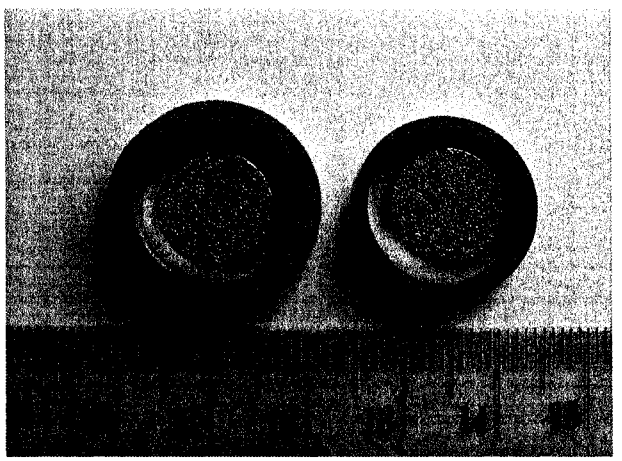

Figure 5.12: Small-Size Piezoelectric Rings and Porous Stones.

Figure 5.13 The First Setup that Incorporated Ring Actuators for Pulse Testing of Soil: Emitter & Receiver Units.

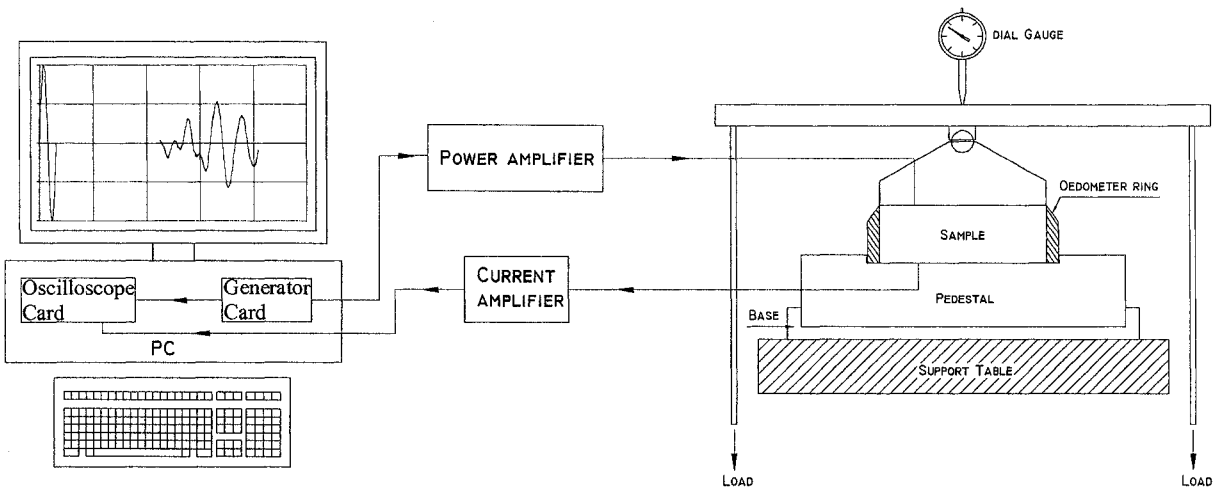

Figure 5.14 Pulse Test Equipments and Wiring, Connected to an Oedometric Sample Loaded by a Simple Frame.

In general, Setup No. 1 gave encouraging preliminary results. The obtained conclusions were consistent with previous findings. Using this setup, it could be realized that increasing the input voltage and frequency increases the clarity of output signal and make the interpretation easier. When using a rectangular input pulse, increasing the input-wave time (decreasing frequency) makes the shear wave component clearer on the output signal as it was found in simulations. While decreasing the input time results in a dominant component of the compression wave. Nevertheless, increasing the input time more than normal causes recording evident noise within the output signal, that confuses the interpretation. Therefore, an input frequency more than 1.5 kHz is preferred, so that pulse tests may be carried out in a noise-free condition. Also, at this stage it could be experimentally demonstrated that a sine- or half-sine-shape input is better than a step or a square input as it was reported in literature. Finally, it could be concluded that bigger ring dimensions would be more suitable for obtaining clearer output signals. Also, increasing the surface roughness of the inner stone was important for good coupling between porous stone and soil.

Table 5.7 Specifications of the Ring Actuator Setups Manufactured in this Study.

Setup No.	Date	Ring Dim. (mm)	Inner Stone	Outer Stone	Base & Cap	Attenuator	Resonant Frequency	Notes
1	April, 2003	D_{out} = 16 D_{in} = 11 t= 2.5	3mm porous brass + 3mm back porous plastic	6mm porous plastic	PVC, D=63mm t = 19.2mm	3mm rubber attenuator	---	Preliminary testing
2	Oct., 2003	D_{out} = 44 D_{in} (E)=38 D_{in} (R)=40 t_{ring} = 2.5	3mm porous brass + 3mm back porous plastic	6mm porous plastic	Steel top cap of D=101.5mm & t = 30mm PVC base of D=196.5mm & t = 30mm	3mm rubber attenuator	32 KHz	Chips porous stone
3	Dec., 2003	D_{out} = 44 D_{in} (E)=38 D_{in} (R)=40 t_{ring} = 2.5	3mm porous brass + 3mm back porous plastic	6mm porous plastic	Steel top cap of D=101.5mm & t = 30mm PVC base of D=196.5mm & t = 30mm	3mm rubber attenuator	33 kHz	Grounding wires installed + Epoxy is added to the back of the porous stone
4	June, 2004	D_{out} = 44 D_{in} (E)=38 D_{in} (R)=40 t_{ring} = 2.5	6mm porous brass	6mm porous brass	Steel top cap of D=101mm & t = 30mm PVC base of D=196.5mm & t = 30mm	3mm rubber attenuator	33 kHz	

Table 5.7 Specifications of the Ring Actuator Setups Manufactured in this Study (cont.).

Setup No.	Date	Ring Dim. (mm)	Inner Stone	Outer Stone	Base & Cap	Attenuator	Resonant Frequency	Notes
5	Dec., 2004	D_{out} = 44 D_{in} (E)=38 D_{in} (R)=40 t_{ring} = 3.5	6mm cemented sand	6mm porous brass	Steel top cap of D=101mm & t = 30mm PVC base of D=196.5mm & t = 30mm	Rubber lamina + 3mm PVC disc	43 kHz	
6	April., 2005	D_{out} = 44 D_{in} (E)=38 D_{in} (R)=40 t_{ring} = 3.5	6mm Aluminium	6mm porous brass	Steel top cap of D=101mm & t = 30mm PVC base of D=196.5mm & t = 30mm	Rubber lamina + 3mm PVC disc	112 kHz	sand grains glued to the Aluminium top surface by conductive epoxy
7	Aug. 2005	D_{out} = 44 D_{in} (E)=38 D_{in} (R)=40 t_{ring} = 3.5	6mm Aluminum cut into 4 pieces and glued by silicon	6mm porous brass	Steel top cap of D=101mm & t = 30mm PVC base of D=196.5mm & t = 30mm	Rubber lamina + 3mm PVC disc	17 kHz	Aluminum surfaces made rough by scratching in two directions
7c	Oct. 2005	D_{out} = 44 D_{in} (E)=38 D_{in} (R)=40 t_{ring} = 3.5	6mm Aluminum cut into 4 pieces and glued by silicon, surfaces roughed by scratching	6mm porous brass covered by 0.6mm Aluminum plate	Steel top cap of D=101mm & t = 30mm PVC base of D=196.5mm & t = 30mm	Rubber lamina + 3mm PVC disc	17 kHz	Aluminum plates extend over the rings
8	Oct. 2005	D_{out} = 44 D_{in} (E)=38 D_{in} (R)=40 t_{ring} = 3.5	6mm cemented sand cut into 4 pieces and glued by silicon + 0.6mm sand layer glued by epoxy at soil sides	6mm porous brass with 0.6mm Aluminum plate	Steel top cap of D=101mm & t = 30mm PVC base of D=196.5mm & t = 30mm	Rubber lamina + 3mm PVC disc	17 kHz	aluminium plates extend over the rings

5.7.2 Setup 2

The second piezoelectric setup (Setup No. 2) has been designed with bigger dimensions than the first setup in order to suit making tests on samples of higher lengths such as Proctor samples. Figure 5.15 shows the design drawing for this setup in an oedometer setup. This piezoelectric setup was also installed in a base platen and a top cap which were used to test samples in Proctor mold (Figure 5.16). Table 5.7 displays the dimensions and configurations of the pulse emitter and receiver devices in this setup.

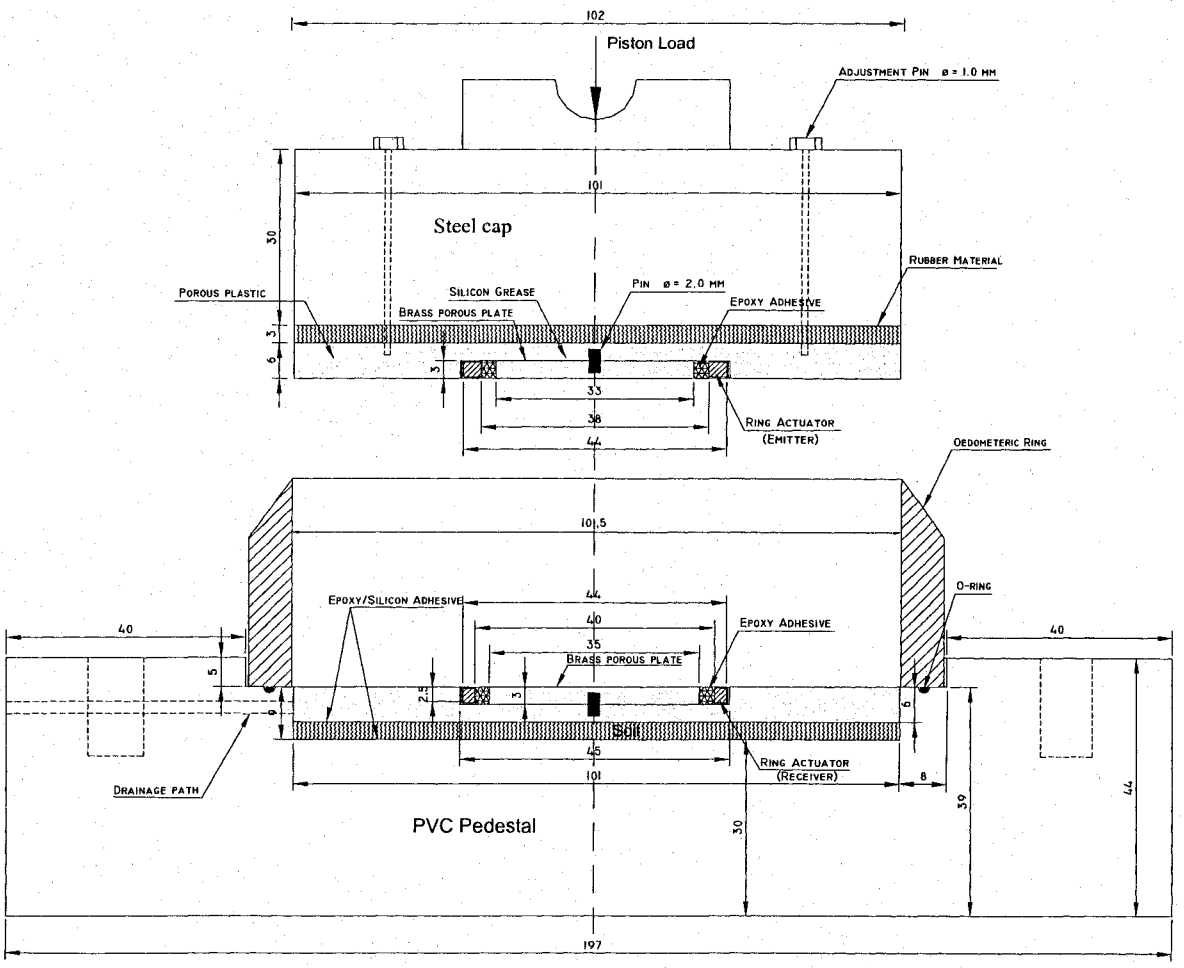

Figure 5.15 Design Drawings of the Ring Actuators Setup for Measuring V_p and V_s in an Oedometric Ring (Setup 2).

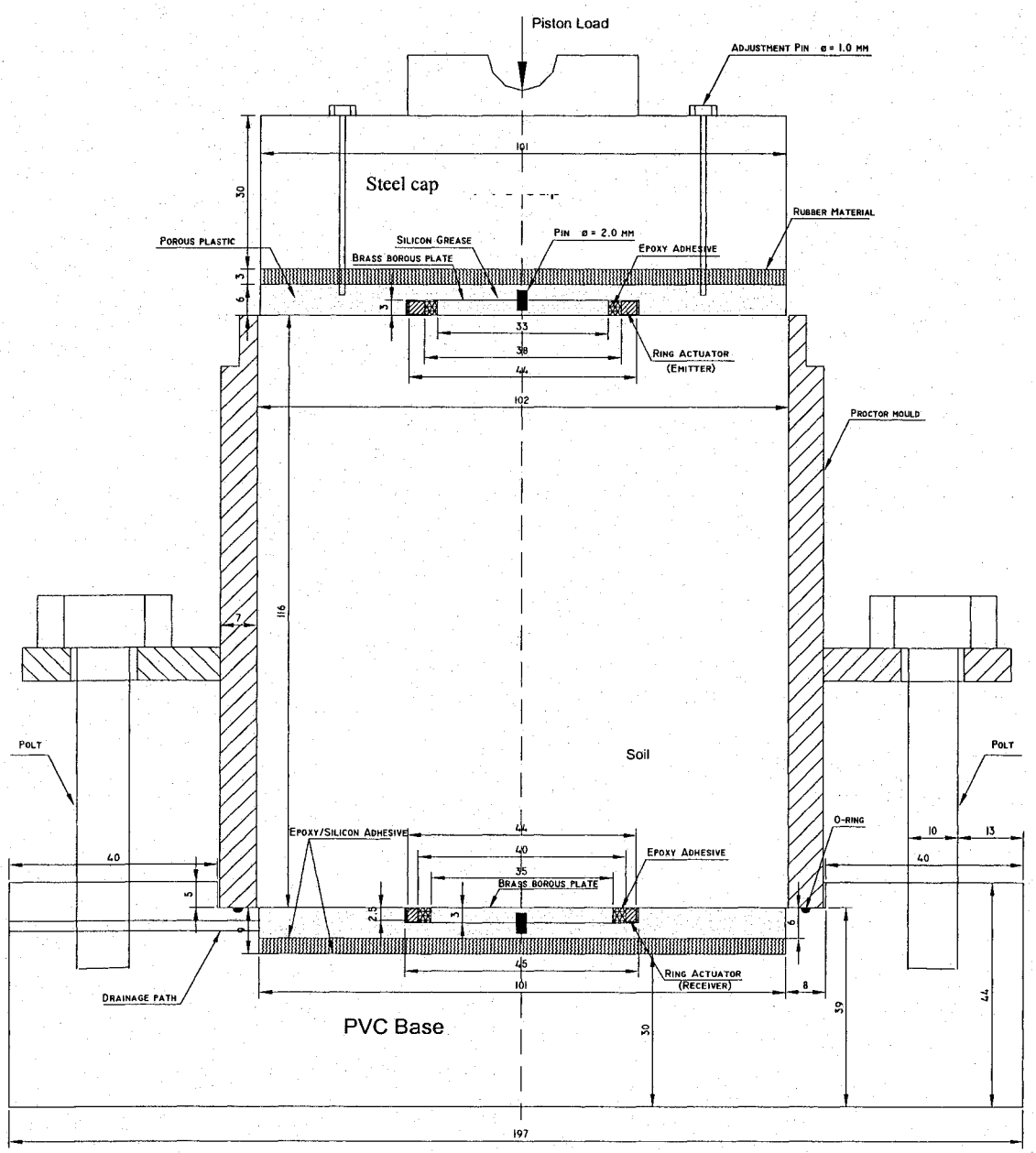

Figure 5.16 A Piezoelectric Ring Actuators Setup for Measuring Shear Wave Velocity of Soil in a Proctor Mold (Setup 2).

It was mentioned before that coating the rings with even and non permeative layer is very difficult. It was expected to put about 3-4 layers of epoxy to have a waterproof element. But due to the circular shape of the ring shape and its small dimensions, it took more layers (up to 7 layers). When coating the transmitter and receiver rings of setup 2 with epoxy, this needed many layers to isolate the rings from humidity and prevent short between electrodes. Hence, the final thickness of the rings including the casing becomes 4.0mm. The thickness of

inner porous stone is 3.0mm. Therefore, the inner stone was adjusted to have even surface at the soil side. Thus, the back surface of the coated ring was 1mm higher than the back of the stone (Figure 5.17). Figure 5.18 introduces a photo for Setup 2 where the thickness difference is seen. Consequently, the piezoelectric unit thickness has become 4.0mm while its prepared housing (settling grove) in the cap/pedestal is 3.0mm. This made each piezoelectric unit is extruded by 1mm ahead of the cap/pedestal surface (not even surface). Therefore, each soil sample tested by this setup had been shaped at its top and bottom surfaces by grooving a 1-mm-thick disk-shape at center to introduce a space for the piezoelectric units. Table 5.7 introduces the dimensions and components of all setups made during this study as well as the resonant frequency of the receiver unit (the ring actuator and inner porous plate). Figure 5.19 shows a simple loading frame used to apply vertical pressures on laboratory samples (Oedometric and Proctor). The top cap and base platen are equipped with a ring actuator setup to carry out pulse tests.

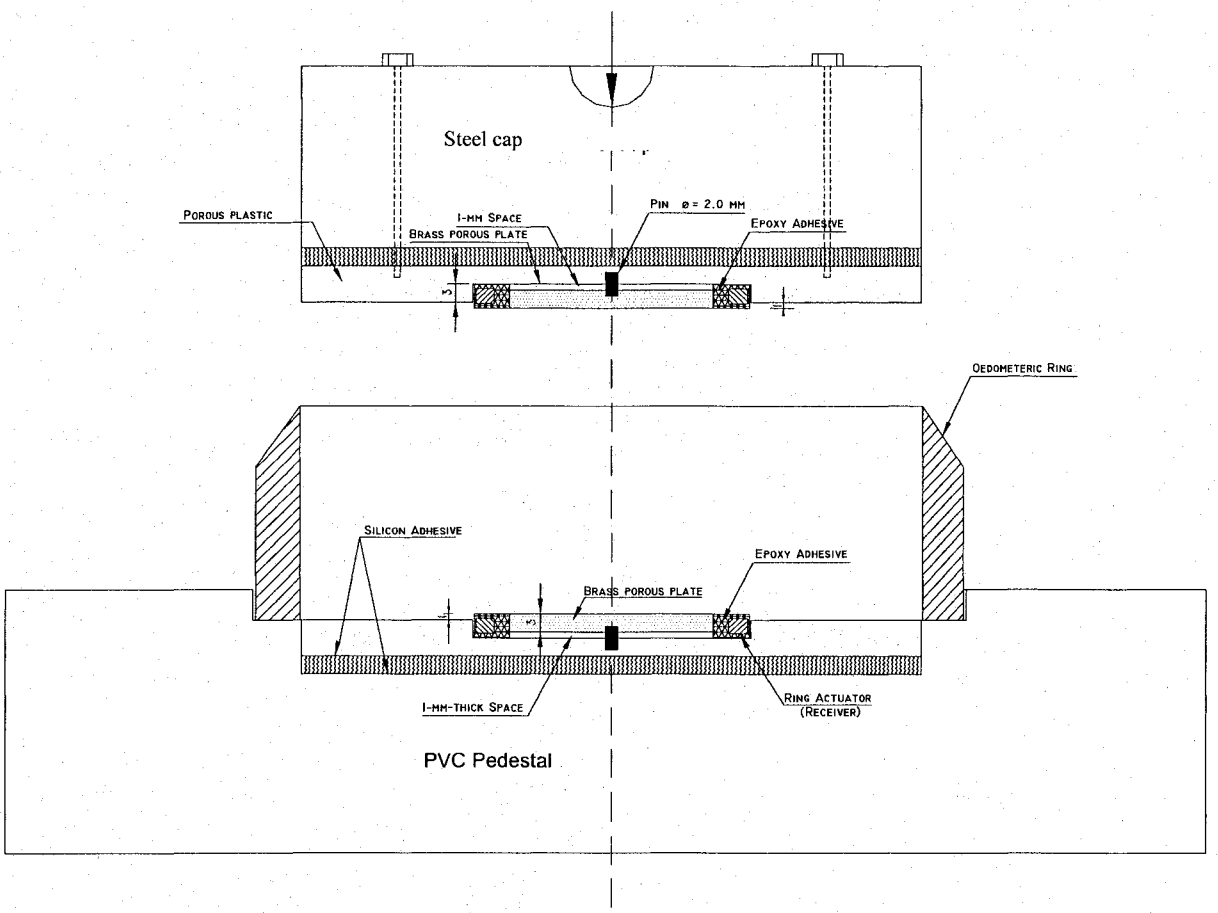

Figure 5.17 Large Oedometer Cell with Piezoelectric Ring Actuators (Setup 2).

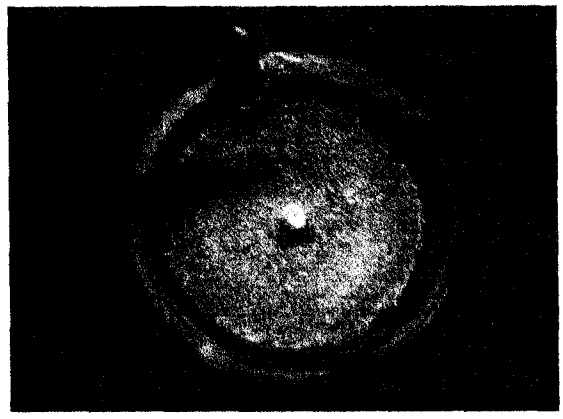

Figure 5.18 Transmitter of Setup 2 after Connecting the Grounding Wire.

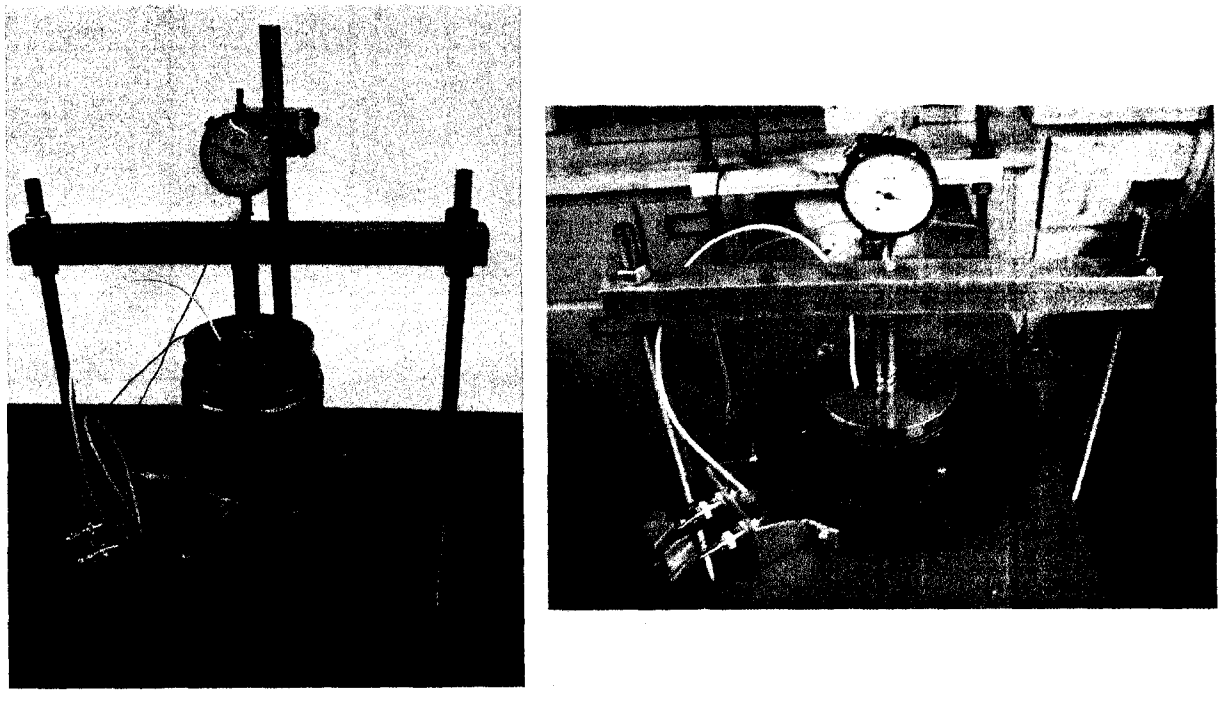

Figure 5.19 Ring Actuator Pulse Tests in an Oedometer Ring (Setup A) and in a Proctor Mold (Setup B) during One Dimensional Compression Tests.

Setup 2 has produced better results than the 1st setup even at very low pressures. The direct arrival times could be determined easier on the output signal, especially for compression wave. Also, many other secondary waves of relatively high amplitude were recorded on the received log. Figure 5.20 introduces a pulse test result on a LG4 till sample (w_c = 3.0 %) in a Proctor mold under a vertical pressure, σ_v, of 11.63 kPa. The sample was

tested with 20 Volts amplitude rectangular shape of 30μs input time. It is seen that there are many wave components in the output signal. The different soil types tested in this study are described in Section 5.5. Many energetic waves are recorded on the received log, which are also seen on C.C. function and the Wigner-Ville plot. Moreover, this affects the phase and group velocities dispersion curves (lower right graph). The researcher was curious to know the reason/source of these waves. It was a challenge to eliminate or reduce the energy of these waves. This issue was vital because these secondary waves interrupted the interpretation process (by Wigner-Ville method). Theoretically, one wave is sent into the soil (shear wave) and due to the finite nature of the source as well as of the soil, a compression wave is generated in the same time. Therefore, it is expected to see only two dominant signals on the received log (compression and shear waves) if there is no other waves due to any other reason.

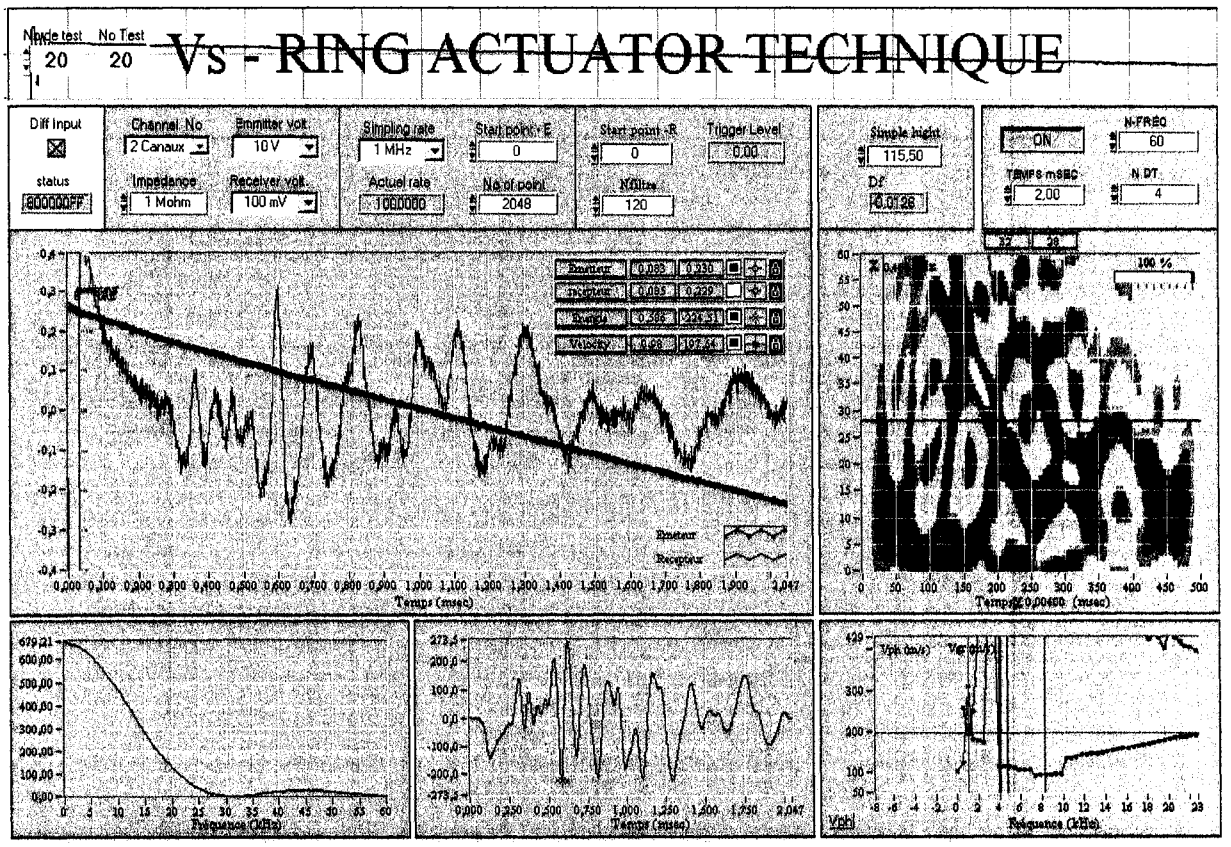

Figure 5.20 LG4 Till Proctor Sample Tested by Setup 2 Using a Rectangular Input Signal (t=30μs).

The geotechnical research team at University of Sherbrooke (Prof. Guy Lefebvre, Dr. Mourad Karray, Yannic Ethier & Deyab Gamal El-Dean) have used the laboratory test results in exploring and developing the Wigner-Ville Energy Analysis Method during this research. Each carried out laboratory test were interpreted using this new technique besides the conventional methods. If the phase and group velocities dispersion curves are not in good agreement with the theoretical trends, this means that the setup and/or equipments under investigation need more development to avoid these problems. Otherwise, we had to update/revise the Wigner-Ville execution software for more volunteer analysis in order to solve the difficulty of interpretation.

During this stage, several unexpected dispersion curves of different shapes were obtained indicating the existence of some problems in the test setup or difficulties in signals interpretation. For example, recording a high energy wave on the received log between the compression and shear waves arises many questions about its source/reason. Also, merging of compression and shear waves at low frequencies, on velocity versus frequency graph, is another frequent problem.

Some of the carried out tests using Setup 2 are presented in Figures 5.21 – 5.24. It can be realized that a clear shear wave arrival is seen even at very low pressures. Also, the compression wave is evidently recorded at high input frequencies. The cross-correlation function is better for a sine input than for a rectangular shape. In addition, the Wigner-Ville energy analysis is giving better results when using sine-shape input.

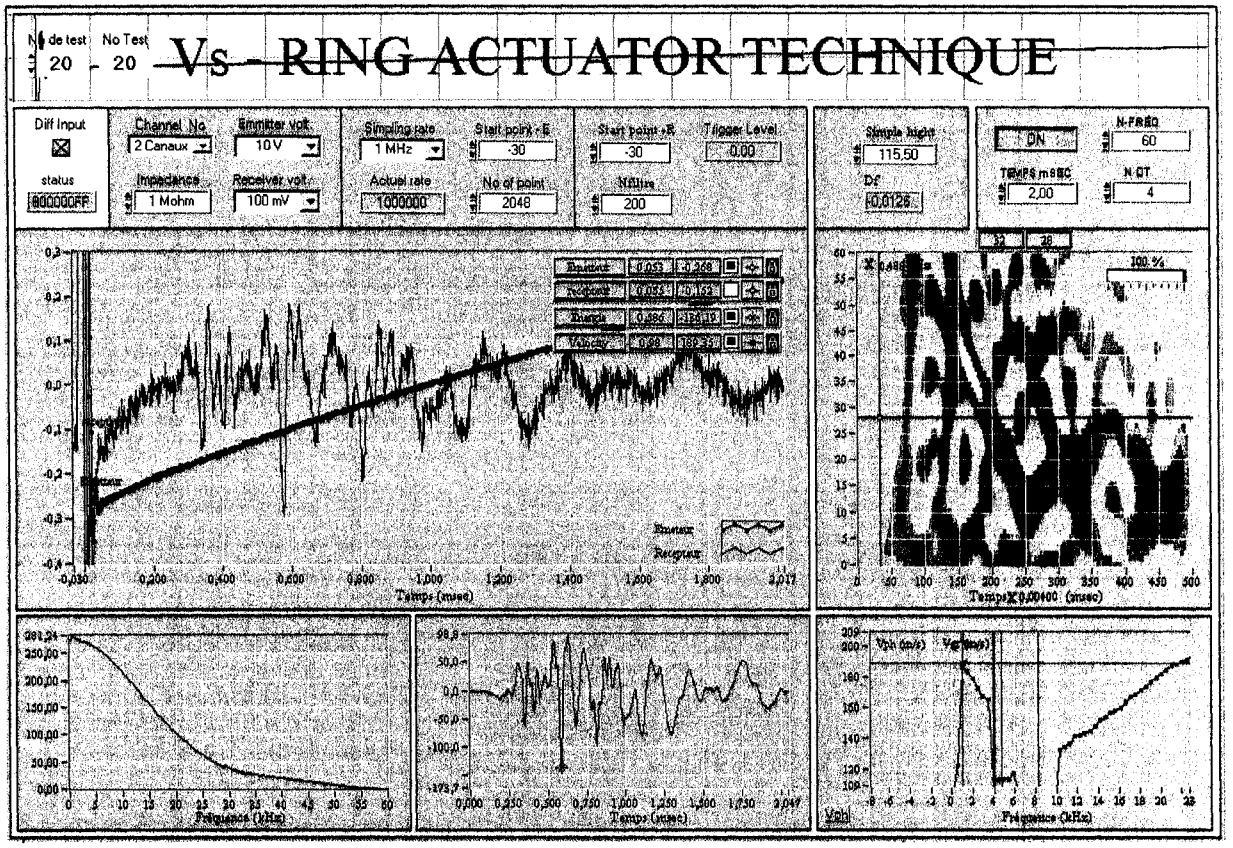

Figure 5.21 Proctor Sample of a LG4 Till Tested by Setup 2 Using a Rectangular Input Signal (t=15μs).

Increasing the input frequency by decreasing the input time clarified the p-wave component. However, very high input frequency reduces (or eliminate) the amplitude of the shear-wave giving dominant p-wave of higher energy than s-wave. Figure 5.21 presents a pulse test result on a LG4 till sample (W_c = 6.0 %, σ_v = 28 kPa). The input time (t) of this test is 15μs compared to 30μs for the test in Figure 5.20. It can be realized that the relative amplitude of the compression wave is bigger in Figure 5.21 than in Figure 5.20. Another pulse tests on partially saturated compacted LG4 sample (W_c = 6.0 %, σ_v = 28 kPa) was carried out using Setup 2 in Proctor mold (Figure 5.22). This sample was tested by sine-wave of 20 kHz input frequency. In Figure 5.20, the sample (W_c = 3.0 %, σ_v = 11.6 kPa) was tested by a rectangular shape of 30μs input time. The measured shear wave velocities for these two samples are about 225 m/s and 200 m/s, respectively, based on C.C. and direct arrival methods. These velocity values are compatible with the applied stresses on these two samples.

However, the dominant energy for the test in Figure 5.22 is giving a velocity of about 387 m/s, which is the compression wave velocity (i.e. the shear wave has lower energy than the p-wave). Also, the p-wave time is far away from the s-wave time for the Proctor samples which has a length of about 116mm. This criterion changes when testing shorter samples. Also, Setup 2 was used to test some oedometer samples. Figure 5.23 displays a pulse test results for air-dried medium-density Milby sand sample. This sample was under a vertical pressure (σ_v) of 33.6 kPa and tested by a rectangular shape of 15μs input time. It can be seen that coupling of compression and shear waves exists in this test.

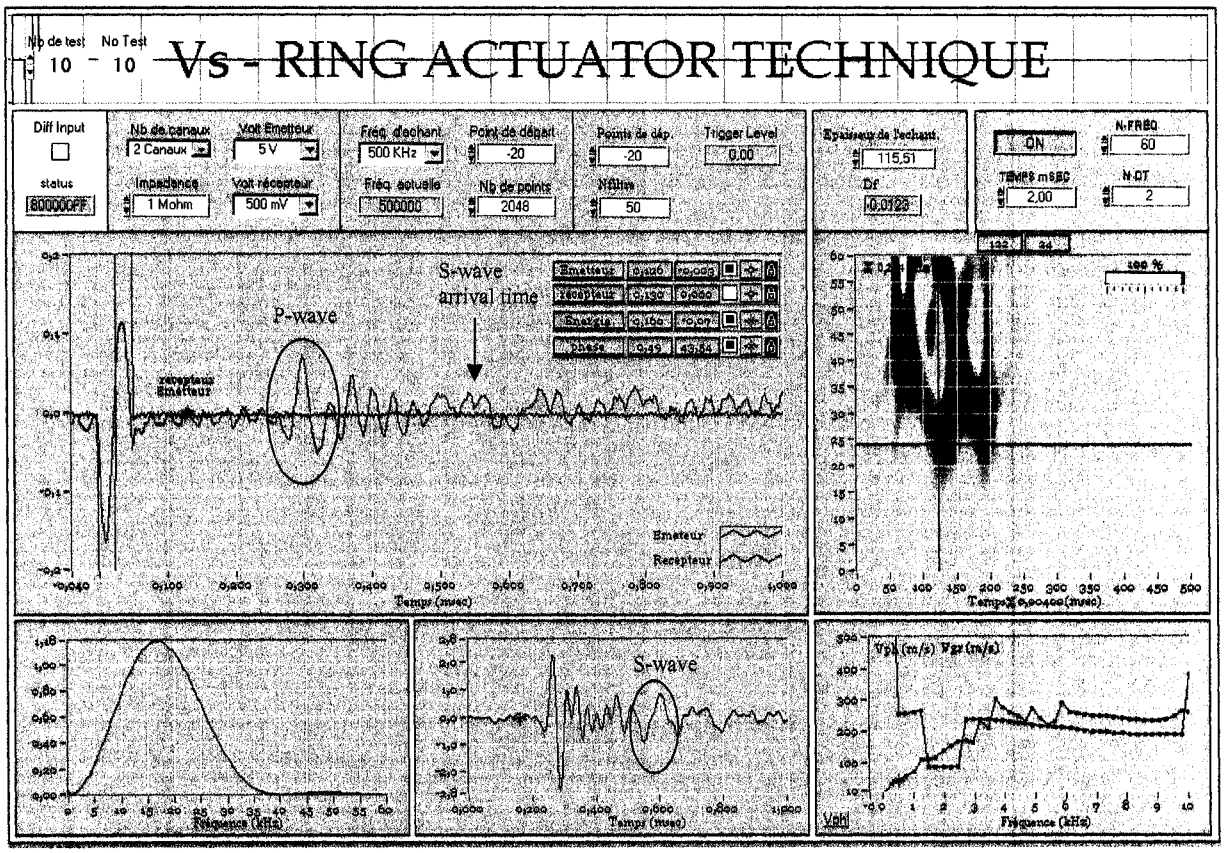

Figure 5.22 LG4 Proctor Sample Tested by Setup 2 Using Sine Wave of 20 kHz.

Another problem was encountered during initial testing; the duplicate of the input signal was captured on the output signal (e.g. the test in Figure 5.22). Many explanations were possible for this phenomenon. The first explanation suggests that an electrical wave is transmitted through the pore water inside the soil to the receiver element (short circuit). The

second suggests that this phenomenon is due to the electro-magnetic field of the transmitter, which affects the receiver piezoelectric ring. The third explanation suggests that this wave is due to interference between input and output signals somewhere else through the wires or setup components where magnetic fields are possible to transmit. At this stage, this problem was overcome by trimming the interference range from the output signal. This treatment is suitable (valid) as long as the compression wave component is not overlapping the duplicate wave. Figure 5.24 shows a pulse test result on Milby sand sample in the oedometer cell. In this test, the C.C. function for the unfiltered output-signal is plotted. It is clear that the duplicate of the input signal affects the C.C. function.

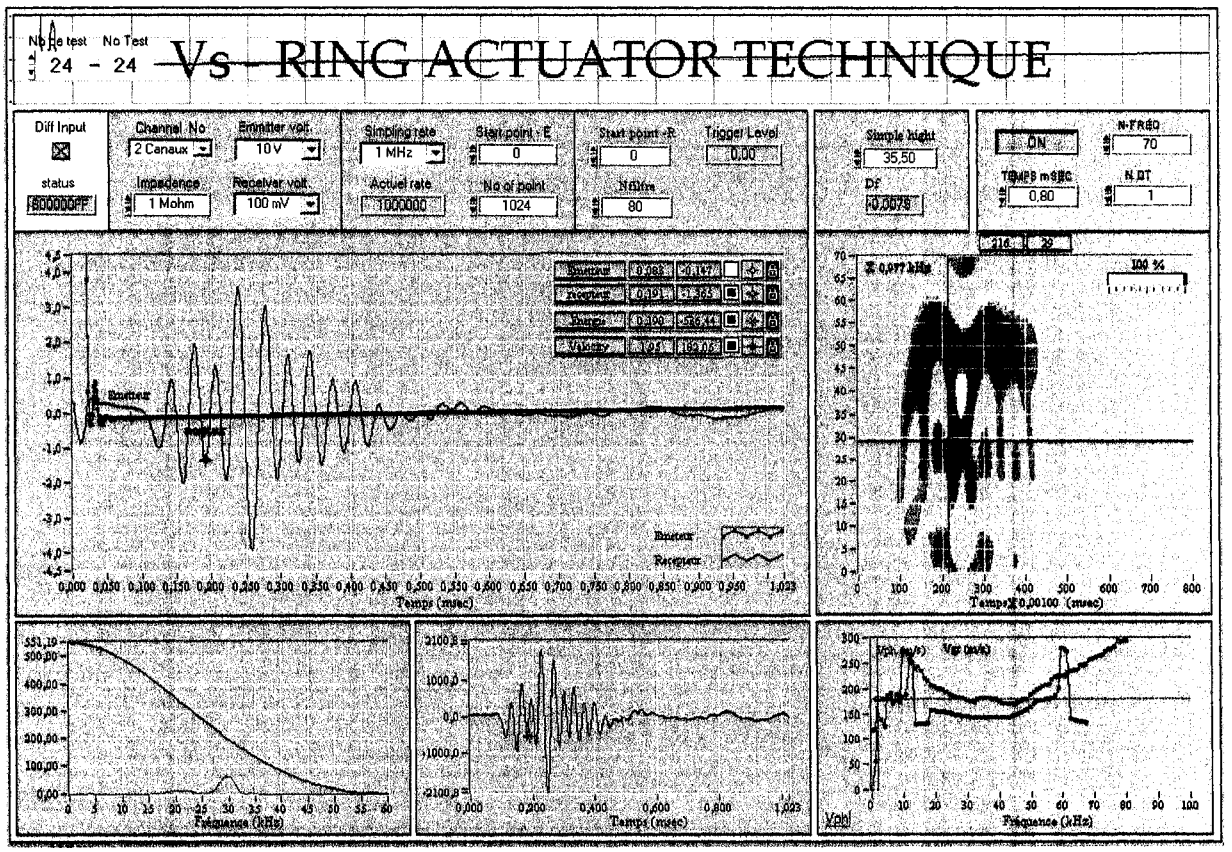

Figure 5.23 Coupling of Compression and Shear Waves on Output Signal in a Pulse Test on Medium-Density Milby Sand Sample Tested by Setup 2 in an Oedometer Cell.

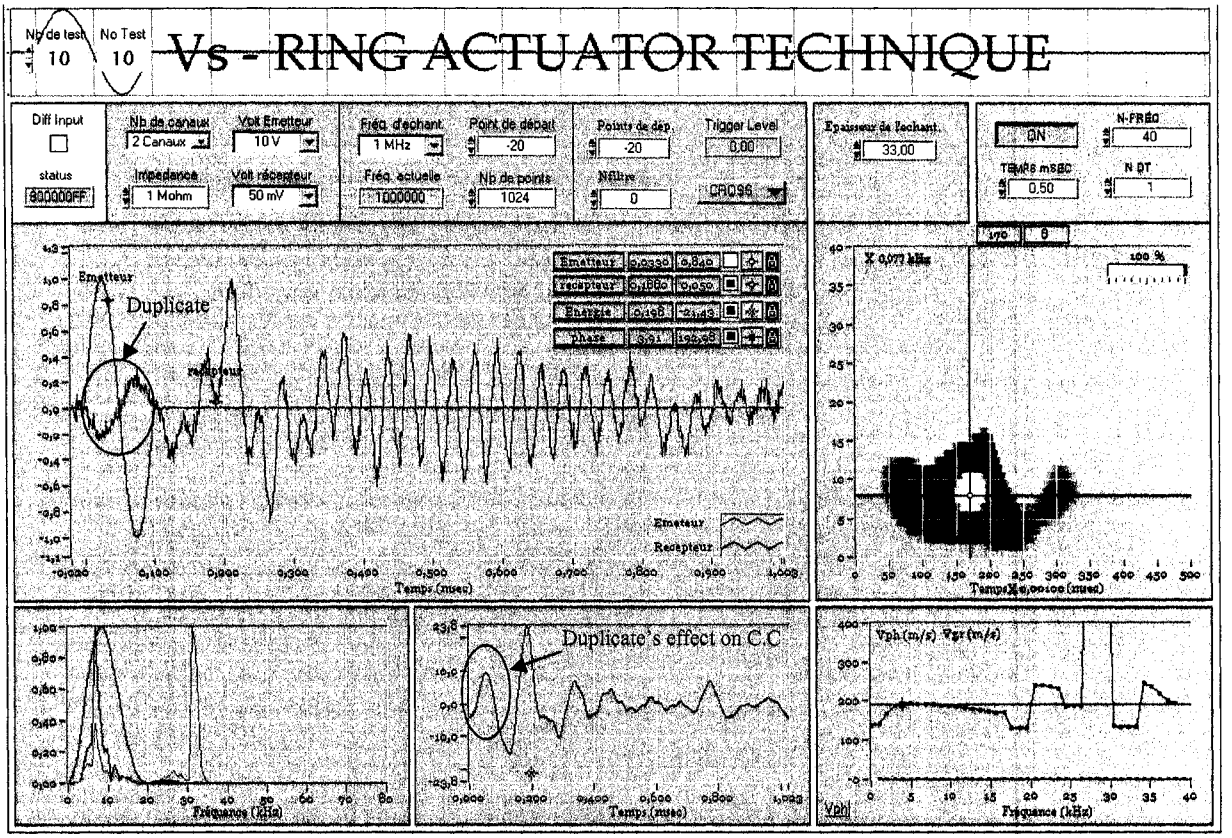

Figure 5.24 Pulse Test on Milby Sand Sample in Large Oedometer Cell.

Many laboratory tests were carried out using setup 2. The obtained results were sometimes difficult to interpret due to the shape of output signal. On the received signal, some small deflections at the beginning of the signal for considerable time followed by two or more dominant peaks were usually obtained (Figure 5.25). A pulse test on Milby sand sample in Proctor mold (W_c = 6.0 %, σ_v = 11.6 kPa) is presented on Figure 5.25. The input wave is half-sine of 25 kHz frequency and 10 Volts amplitude. The output results show that V_p= 350 m/s, but V_s is not clear whether it is 144 m/s or 215 m/s; 144 is most probably the true value. The other wave may be a reflected wave. This confusion makes us ask; which is which? If the first deflection is considered as the p-wave arrival, the s-wave should be the first major peak. In this case, a question arises; what the second peak is? Moreover, this interpretation choice gives high values for compression and shear waves velocities at these very low stresses. Therefore, another interpretation was sought. The early deflections were considered as secondary waves that pass through the body of mold and reach the receiver before the base signal. This is possible considering the very high rigidity of the mold's material (steel)

compared to the tested soil. Then, the first peak represents the p-wave and the second peak should be the s-wave. But this gives a very low value for the Poisson's ratio of soil (0.05). Hence, a third interpretation was sought. The first deflection is considered as the p-wave arrival and the second dominant peak is the s-wave. And the 1st dominant peak is considered as a reflected wave coming from the mold sides. This interpretation gives a very high Poisson's ratio for soil. Finally, it is believed that overlapping of minor waves creates major peaks on the output signal which hide the correct arrival time of the S-wave. Hence, the arrival times at the two peaks is considered inaccurate. These questionable interpretations were so useful for developing deeper thinking and analyses. This demands more development to the setup in order to have a volunteer device which can give clear and unsuspicious results.

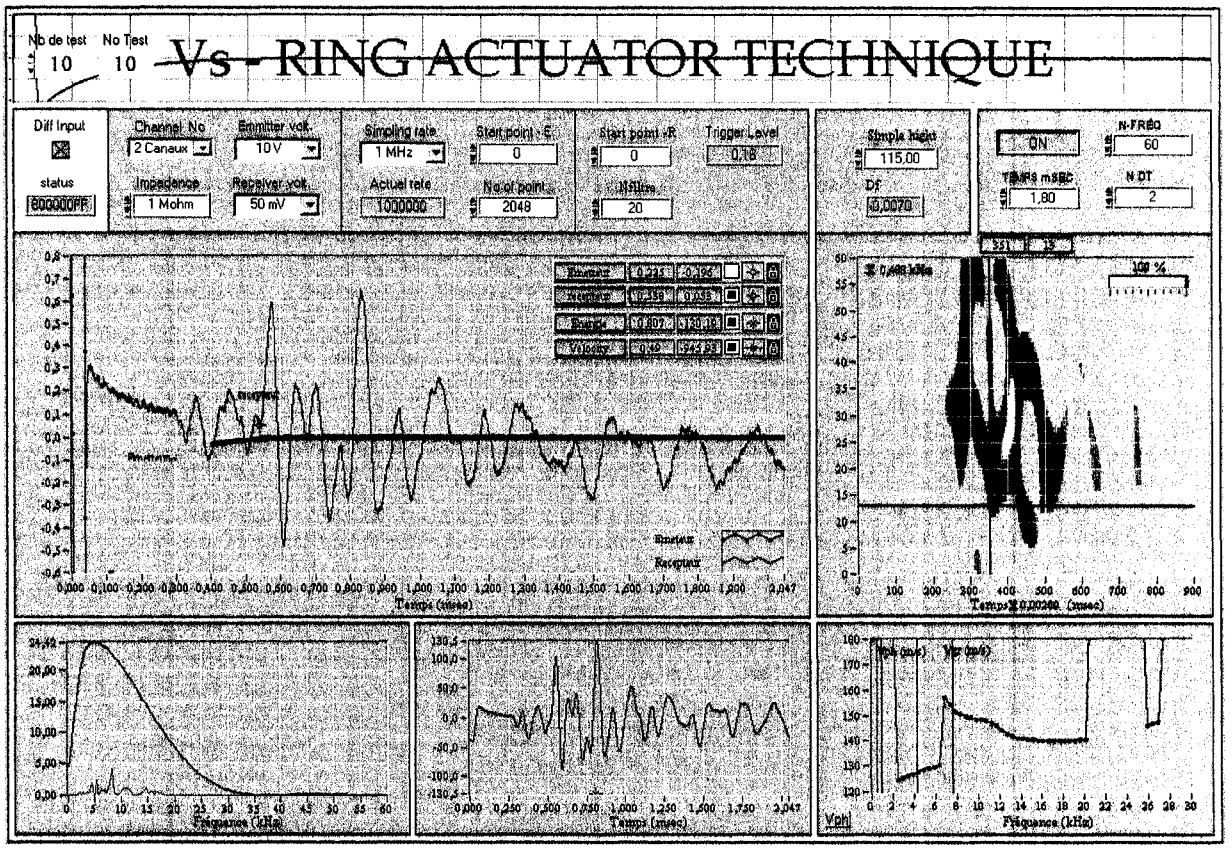

Figure 5.25 Proctor Sample of Milby Sand (w_c = 6.0 %, σ_v = 11.63 kPa) Tested with Setup 2.

5.7.3 Setup 3

Considering the fact that setup 2 is having different thicknesses for the inner porous stone and the coated rings, there was a space (1mm-thick) behind the inner stone. These configurations are suitable for testing soil under small to medium stresses. High stress may destroy the setup and affect its performance. For setup 2, the vertical stresses on the inner stone are transmitted to ring resulting in higher vertical and torsion stresses on the ring. These stresses cause static voltage in the circuits. The value of this voltage increases by increasing the applied stress. In addition, when surcharging a load on the soil, more time is needed to have equilibrium of this induced voltage. Moreover, the stress concentration may reduce the ability of the rings to vibrate laterally when the input voltage is applied. On the other hand, the receiver element will be partially restricted to react by the deformations in soil and would produce very low voltages. In spite of these facts, Setup 2 has functioned quite well at low stresses. Therefore, a new setup was sought to be more suitable. Setup 3 was built exactly as setup 2 (with ground wires connected to the inner porous stones) except that the gap behind the inner stone was filled with an epoxy material in order to have a full support at back. Figure 5.26 displays the drawing for Setup 3 and a photo for the ring actuator setup. This setup gave better results than setup 2. It enhanced the output signal to large extent. Figure 5.27 displays the results and interpretation of a pulse test on a partially saturated Milby sand sample (w_c = 6.0 %, σ_v = 33.6 kPa). The input wave is half-sine of 12.5 kHz frequency and 5 Volts amplitude.

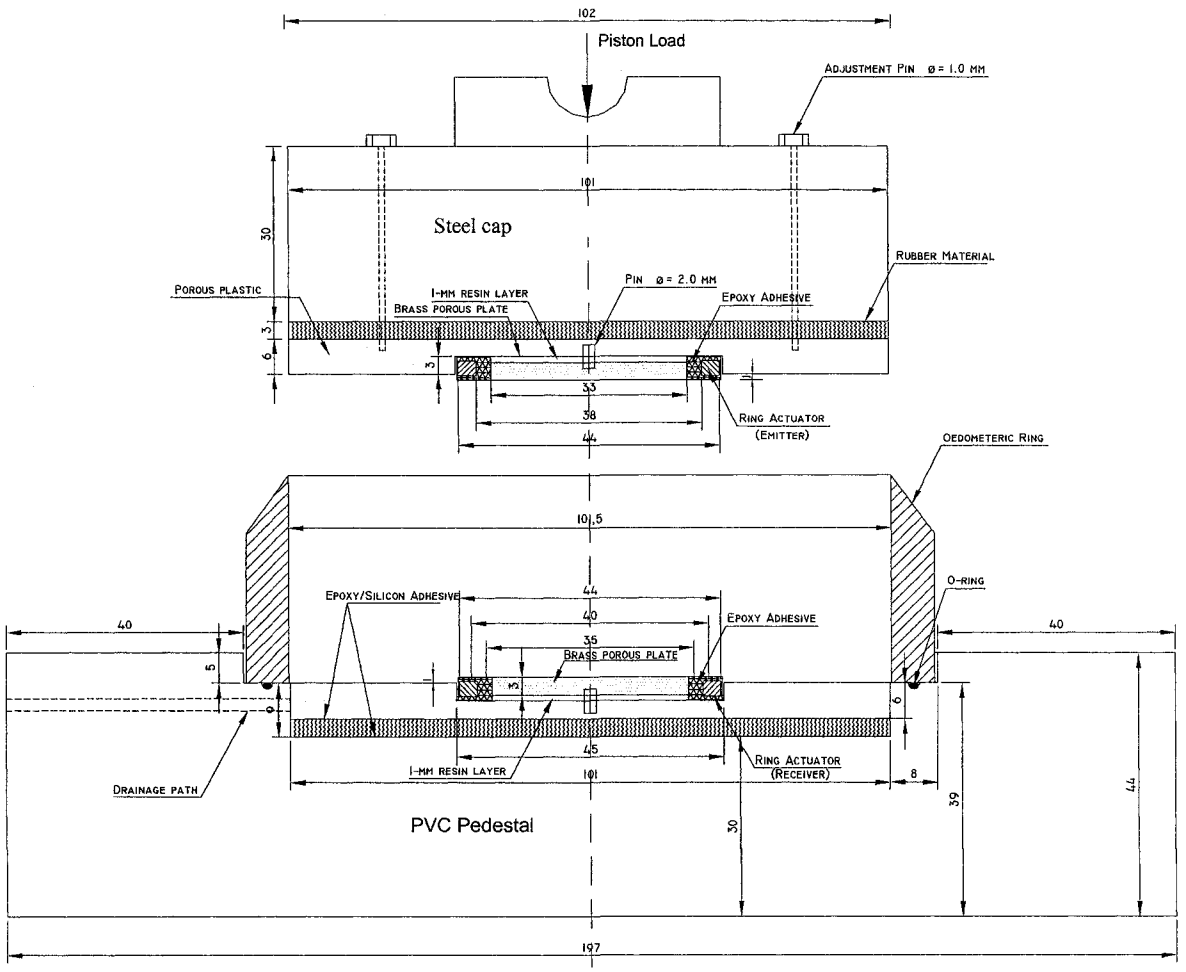

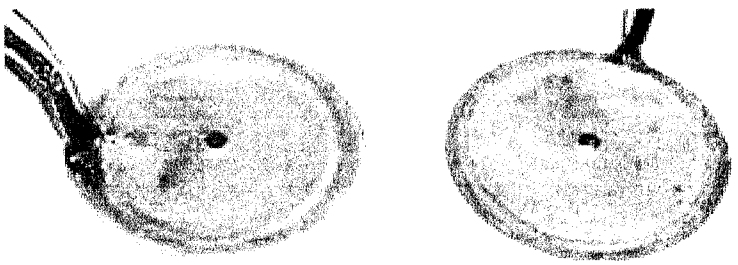

Figure 5.26 Drawing for Setup 3 in an Oedometeric Ring and a Picture for it Showing the Emitter and Receiver Units.

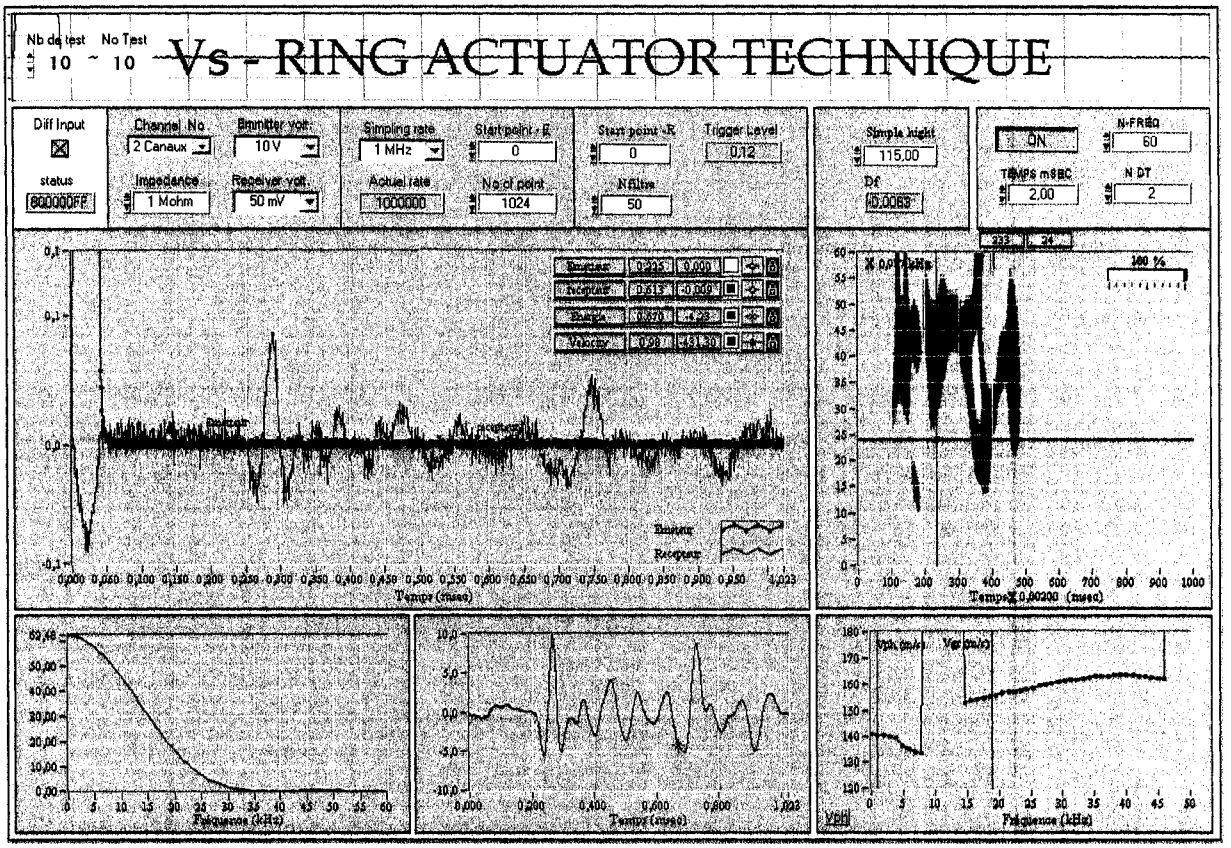

Figure 5.27 Milby Sand Proctor Sample Tested by Setup 3 Using Half-Sine Input (Fr = 12.5 kHz).

There is only one dominant wave on the received log at time of arrival (s-wave). Also, the second arrival of the s-wave is easily seen. There are no other major waves on the output signal. The Wigner-Ville energy analysis has become better too. The p-wave is not evident on the received log because the frequency of the input wave is low (12.5 kHz). This enhancement could be attributed to the ease of vibration of the rings after filling the space behind the inner stone. Also, this filling has prevented the inner-stone from making secondary deformations in the vertical direction which may be the reason for the secondary waves on the previous received logs. A rotation of the inner-plate in the vertical direction is possible under the induced torsion stresses on the rings. In addition, the center of gravities for the rings and inner-plate are at different elevations, this participates in increasing this action. As another enhancement to the setup, the back surface of hardened epoxy behind the inner-stone was

polished to have it smoother in order to ease the vibrations of the transmitter and receiver units. This enhanced the output signals as it is seen on Figure 5.28. This showed the importance to have a smooth contact surfaces at back of piezoelectric units. This issue has been carefully treated in the next setups.

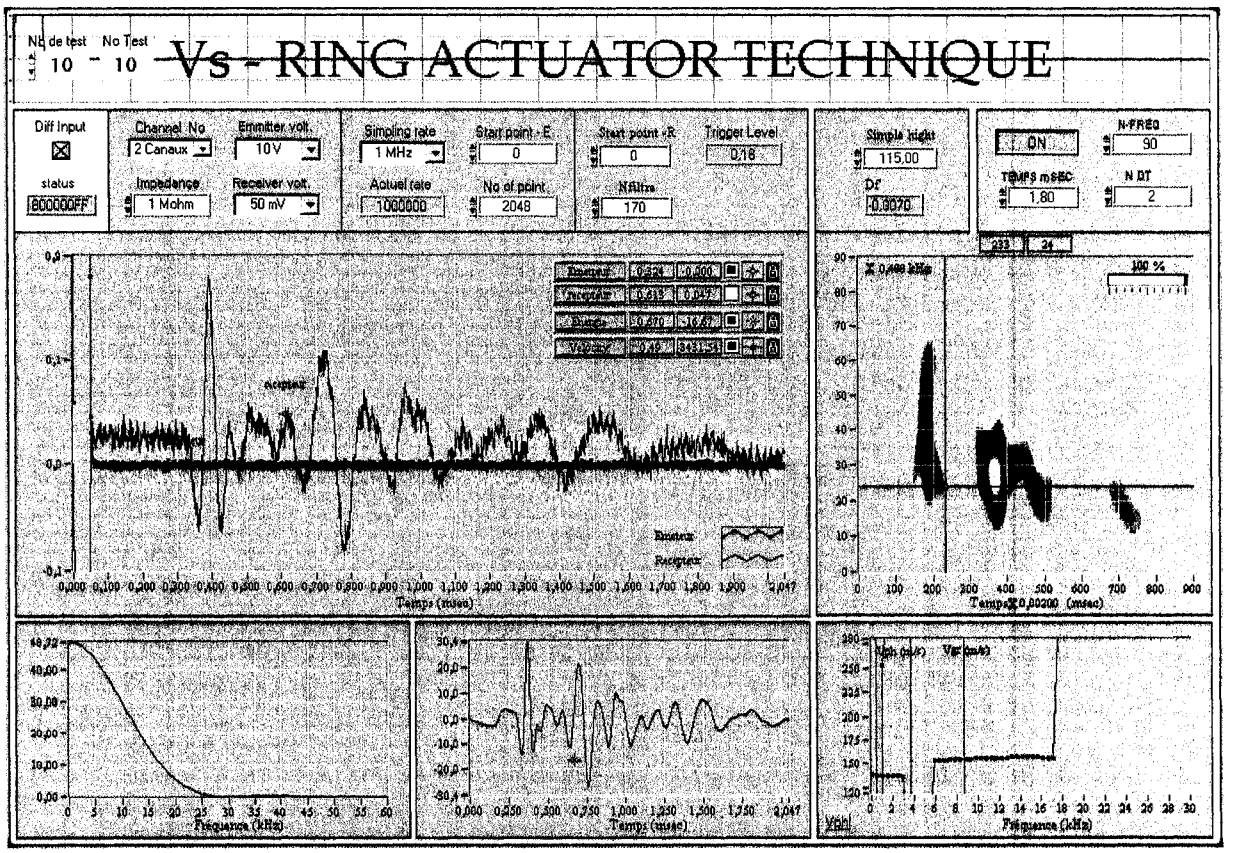

Figure 5.28 Milby Sand Proctor Sample Tested by Setup 3 Using half-Sine Input (Fr = 10 kHz).

5.7.4 Setup 4

This setup was designed considering the experience and conclusions gained from the previous setups. It was decided to increase the thickness of the inner-stone to 6mm instead of 3mm and to make the rings centered with the inner-stone in the vertical direction. Having the center of gravity of the ring and the inner-plate in the same elevation gives mainly shear-deformation in the inner-plate rather than bending/torsion deformations. Hence, it would transmit the desired

excitation to soil. Also, this setup is equipped with ground wires for the emitter and receiver. Figure 5.29 presents the drawing of this setup (see also Table 5.7). There is something to be realized in this setup; the final thickness of the coated piezoelectric ring is 3.5mm while the porous stone thickness is 6mm. Thus, the rings are not directly contacting soil surface. Only the surface of inner-porous-stone transmits the signal to soil and vice versa. For some tests where medium or high pressures would be applied on soil, the space over the ring was filled with a filling material in order to have even surface at the soil's side (Figure 5.30).

Carrying out tests using this setup confirmed that relatively high input frequencies are better than low input frequencies. This results in clear output signals and well defined arrivals. However, the input frequency is limited by the resonant frequency of the receiver unit. Normally, the maximum input frequency that can be applied without having resonance at receiver is about half the resonant frequency of the receiver unit. Thus, a system of higher resonant frequency is preferred than low resonant frequency systems especially for some conditions that require high input frequencies. The resonant frequency of setup 4 is 33 kHz. This allowed testing to be made using frequencies up to about 15 kHz without having resonance in most of the tests.

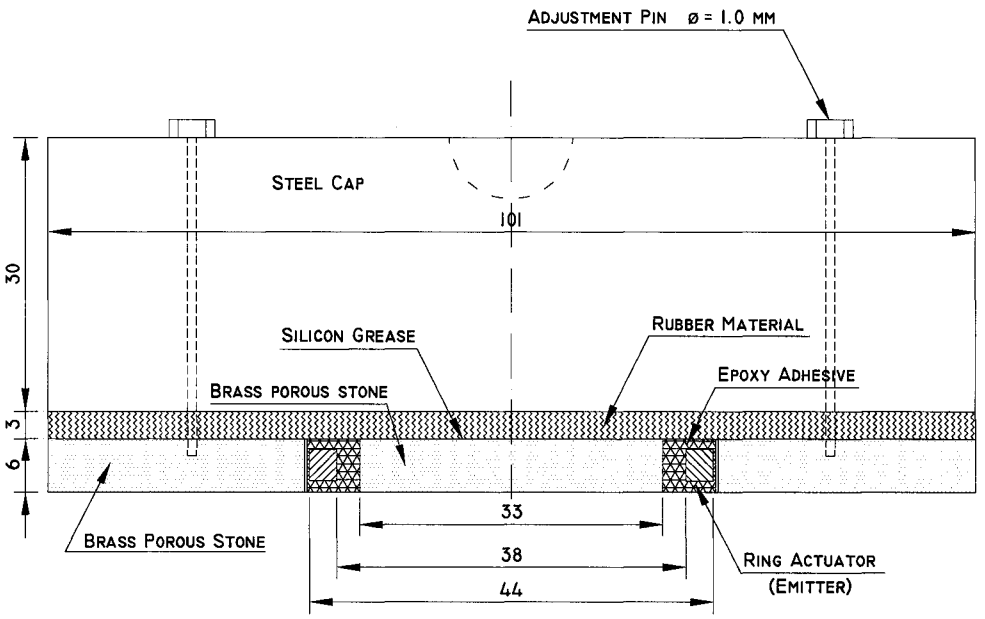

Figure 5.29 The Emitter Unit of Setup 4.

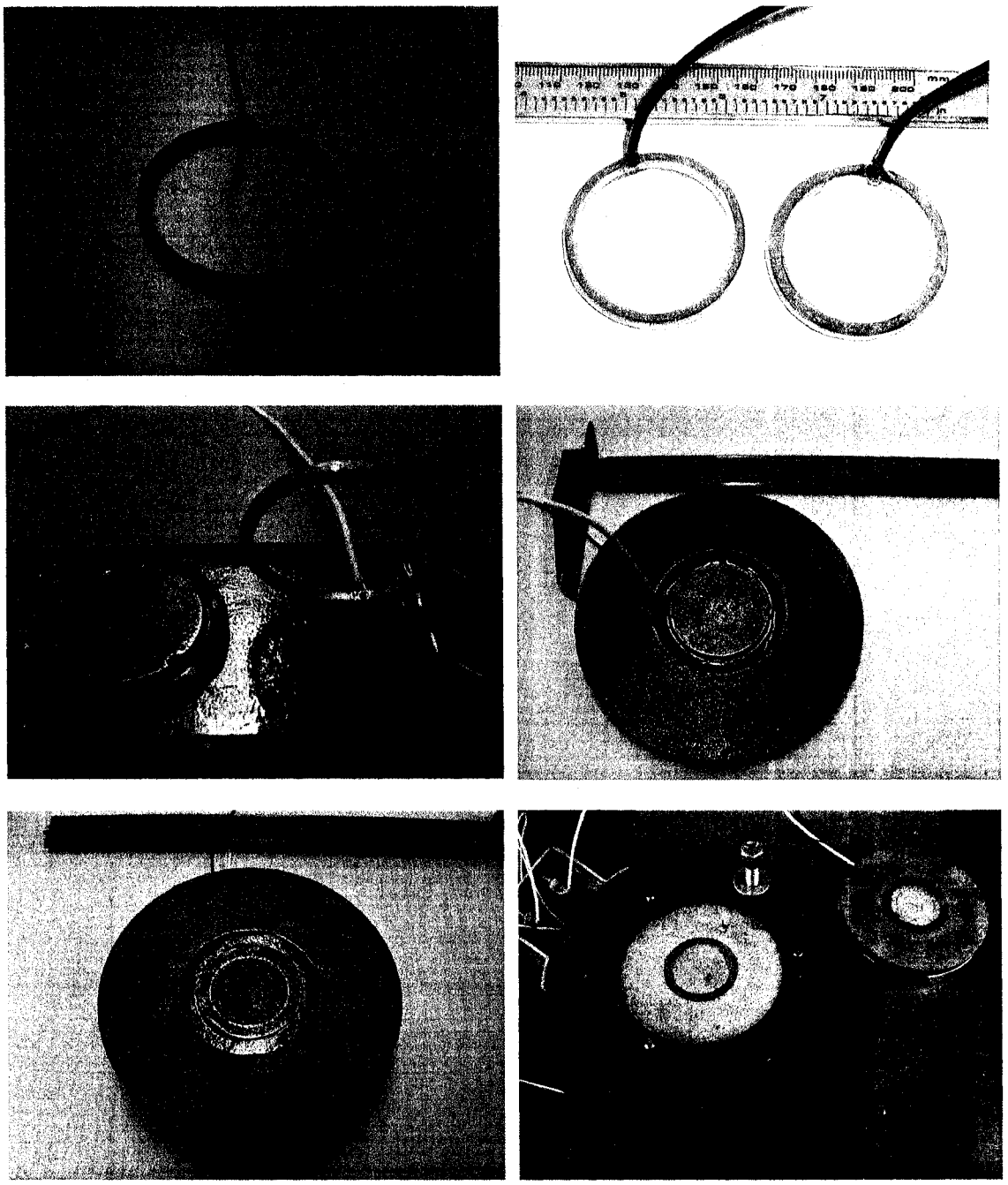

Figure 5.30 Steps of Manufacturing Setup 4 in Photos.

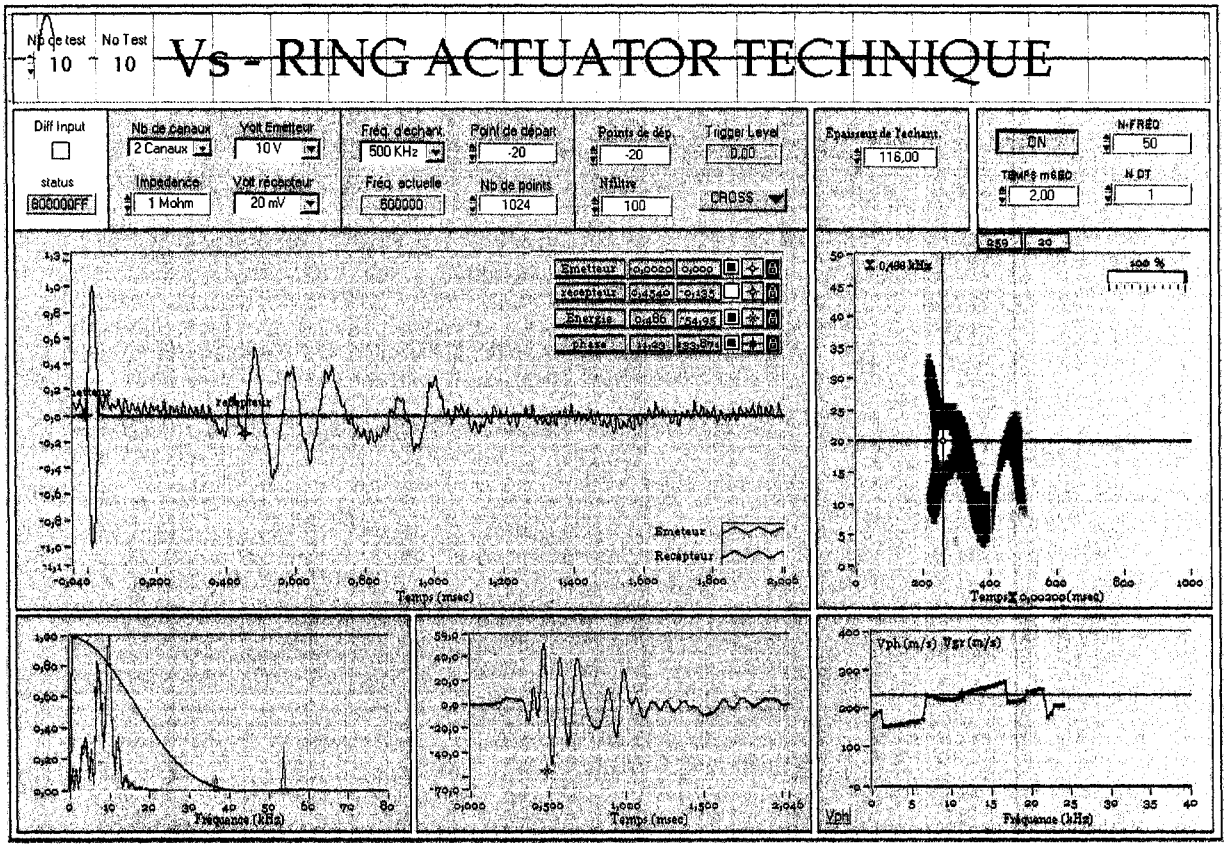

Figure 5.31 Pulse Test on Proctor Sample of Concrete Sand Using Setup 4.

For some Proctor-sample pulse tests, a third wave is recorded between the p- and s-waves. It is believed that this wave is due to the resonance of soil sample (Figure 5.31). The results in Figure 5.31 is for a concrete sand sample (H = 116-mm & W_c = 11 %), tested by a half-sine-wave of 15 kHz input frequency and 25 Volts amplitude. Another thing was tried to cancel the duplicate of the input signal. A circular lamina of aluminium foil with a diameter equals to the sample's diameter was installed between the transmitter and the sample. The same treatment is made at receiver. These two laminas were introduced at the emitter and receiver surfaces in order to work as a ground for preventing the electromagnetic waves from travelling into soil. They are connected to a ground source. Also, the body of the cell and the metal bracket of the cables' connections on the cell were grounded. This has eliminated the duplicate shape on the received signal. Thus, it could be easy to test the samples using relatively low input frequencies without interference due to the input-duplicate (Figure 5.32). The output signal could not be filtered from this duplicate when it overlaps the shear wave component.

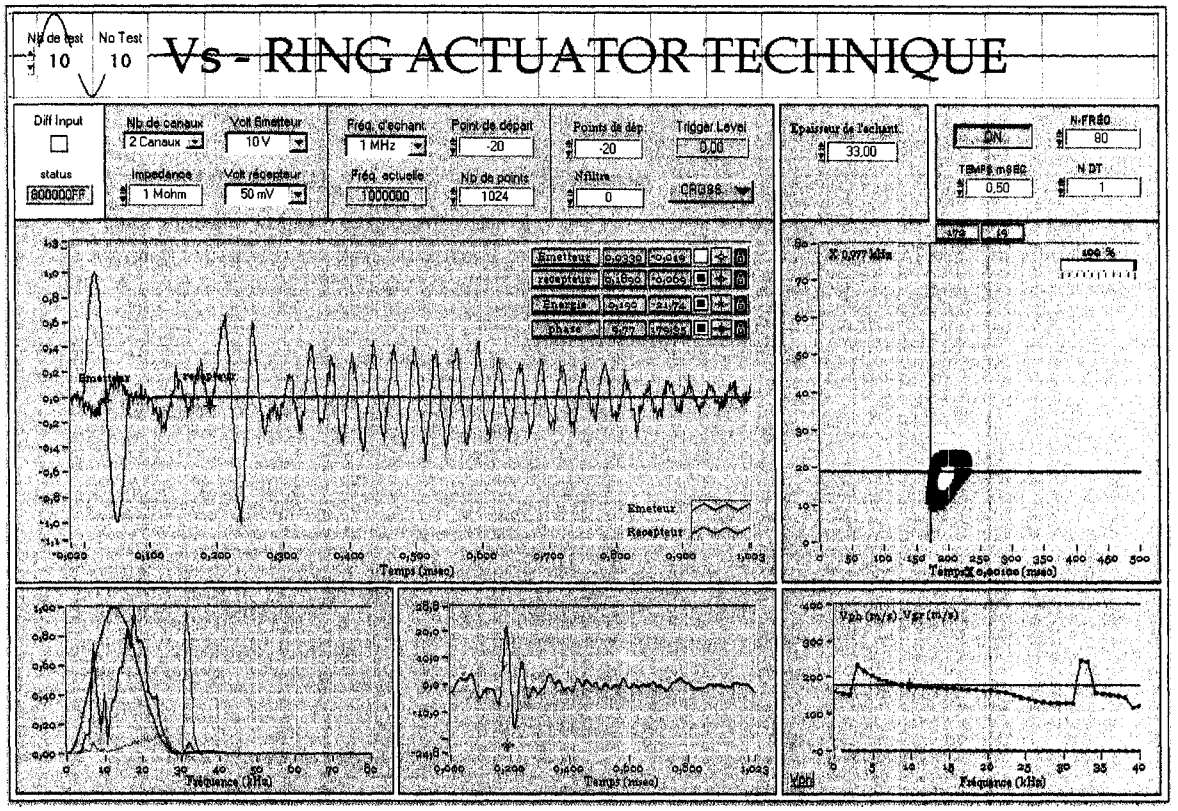

Figure 5.32 Pulse Test on Milby Sand by Setup 4 in Large Oedometer Cell.

At high frequencies this duplicate can be removed (filtered) because its time is short, and normally it does not interfere with the output signal components.

5.7.5 Setup 5

This setup was built to increase the resonant frequency of the transmitter and receiver units. For a certain piezoelectric ring, the resonant frequency of the transmitter/receiver unit depends on the rigidity of the inner-stone and its weight. This fact is theoretically demonstrated as follows. In general, the resonant frequency of a spring/mass system is a function of its stiffness and effective mass. The resonant frequency always refers to the unloaded actuators with one end fixed and ideally is given as follows:

$$f_o = \frac{1}{2\pi}\sqrt{\frac{k_T}{m_{eff}}} \tag{5.4}$$

where: f_o = resonant frequency (Hz), k_T = Actuator stiffness (N/m) and m_{eff} = effective mass (1/3 of the mass of the ceramic + overload) [kg].

Figure 5.33 shows the effective mass of a piezoelectric actuator fixed at one end.

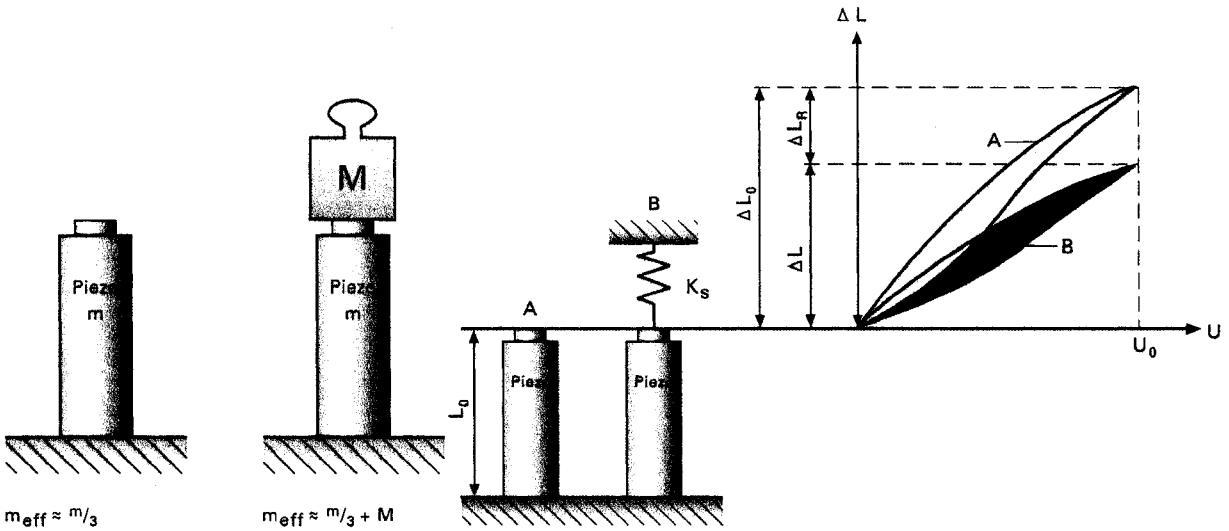

a) Effective mass of an actuator fixed at one end

b) Effective displacement of a piezo actuator acting against a spring load

Figure 5.33 Effective Mass and Displacement of a Piezo-Actuator (after PI Co.).

Due to the non-ideal spring behaviour of piezoceramics, the theoretical result from the above equation does not necessarily match the real-world behaviour of the piezo-actuator system under large signal conditions. When adding a mass M to the actuator, the resonant frequency drops according to the following equation:

$$f_o' = \sqrt{\frac{m_{eff}}{m_{eff}'}} \tag{5.5}$$

where:

$$m_{eff}' = m_{eff} + M \tag{5.6}$$

M is the additional mass (kg).

The above equations show that to double the resonant frequency of a spring-mass system, it is necessary to either increase the stiffness by a factor of 4 or decrease the effective mass to 25 % of its original value. Increasing the load on the actuator does not significantly affect its resonant frequency. When an unrestrained piezoelectric ceramic element is exposed to a high frequency alternating electric field, an impedance minimum, the planar or radial resonance

frequency, coincides with the series resonance frequency, f_s. The relationship between the radial mode resonance frequency constant, N_P, and the diameter of the ceramic element, D_ϕ, is expressed by:

$$N_P = f_s D_\phi \quad (5.7)$$

At higher resonance, another impedance (the resistance to vibration of the medium) minimum is encountered (i.e. the axial resonance frequency). The thickness mode frequency constant, N_T, is related to the thickness of the ceramic element, t, by:

$$N_T = f_s t \quad (5.8)$$

A third frequency constant, the longitudinal mode frequency constant, is related to the length of the element:

$$N_L = f_s L \quad (5.9)$$

For the piezoelectric material 850 of the rings used in this study, the frequency constants are presented in Table 5.8. Similarly, as a simple approach, the following equations estimate the resonant frequency of a free piezoelectric tube in the radial direction (APC International Ltd.):

$$f_o = \frac{1000 - 1100}{D_o} \quad (5.10)$$

where f_o = resonant frequency (kHz) and D_o = outer diameter of the ring (mm).

Therefore, it was decided to increase the resonant frequency of the piezoelectric units by using more rigid inner-stones. The inner-stone used in this setup is porous sandstone of a light unit weight (2.18 gm/cm^3). Also, it has a stiffness which is relatively closer to the soil stiffness compared to the brass inner-stone which was used in the previous setups. This match between soil and the piezoelectric device is desirable for good coupling between the soil and the transmitter/receiver units. The unit weight of the previously used brass-stone is 5.00 g/cm^3. This means that the resonant frequency of the setup under study (#5) should be about 50% [$(5.00/2.18)^{0.5} = 1.51$] higher than that of the previous setup if the rigidity of the two porous materials is considered the same (Equation 5.5). Actually, the stiffness of the porous brass material is believed to be higher than the porous sandstone. Therefore, a smaller increase in the resonant frequency was expected. Another improvement was made in this setup. The height of the piezoelectric ring is increased to 3.5mm so that more power can be applied to the soil, and the radial to thickness deformation ($\Delta r/\Delta t$) increases. This is useful in testing long

or/and high-attenuating samples. On the other hand, this height increase of the piezoelectric ring reduces the resonant frequency of the ring in the vertical direction due to its stiffness decrease. This does not practically affect the measurements as the resonant frequency in the vertical direction is high compared to the resonant frequency in the radial direction. However, this height change increases the stiffness in the horizontal direction which is desirable. Also, a 0.25mm thick rubber lamina was used to replace the 3-mm attenuating material at emitter while a rubber lamina and a PVC disc replaced the other attenuator at receiver. These new configuration for the attenuating materials were found sufficient for absorbing the reflected waves within the pedestal and the cap. Figure 5.34 shows a drawing for the emitter of this new setup.

Table 5.8 Frequency Constant of the Used Piezoelectric Material.

Material 850	Frequency Constant (Hz.m or m/s)
N_L (longitudinal)	1500
N_T (thickness)	2032
N_P (planar)	1980

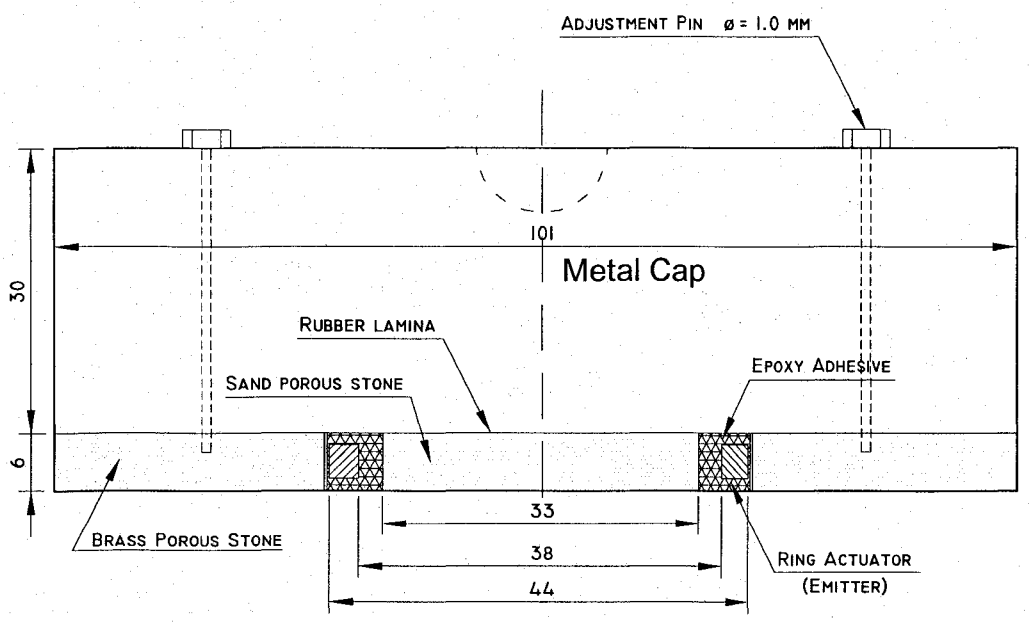

Figure 5.34 The Emitter Unit of Setup 5.

Based on the carried out pulse tests, Setup 5 has a resonant frequency of 43 kHz in the radial direction. This means that the radial resonant frequency has increased by about 30% compared to Setup 4. In other words, the available frequency domain that can be used for testing is increased by 30% compared to that of Setup 4. This setup has functioned well and allowed using relatively higher input-frequencies, which is helpful in signal interpretation of pulse tests as discussed in Chapter 4. This improvement is more desirable for testing Proctor samples due to its limiting boundary conditions. Figures 5.35, 5.36 & 5.37 show three test results performed using Setup 5.

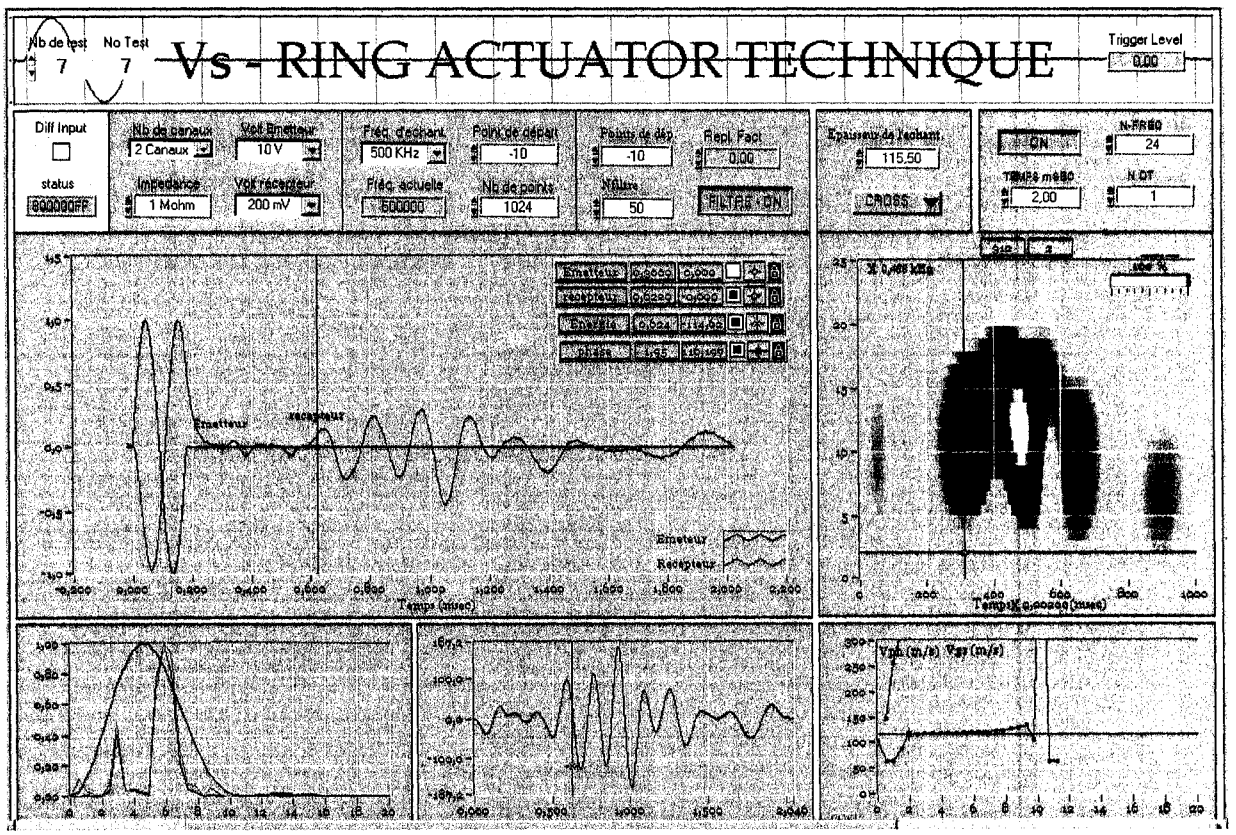

Figure 5.35 Pulse Test on Proctor Sample of Concrete Sand Using Setup 5.

The first Proctor sample is concrete sand under a pressure of 33.6 kPa (H = 116-mm & w_c = 8 %). It was tested by a sine-wave of 12.5 kHz input frequency and 20 Volts amplitude. The second sample is LG4 specimen tested in an oedometer cell under a pressure of 28.6 kPa (H = 35.5-mm & w_c = 6.5 %). It was tested by a half-sine-wave of 10 kHz input frequency and 10 Volts amplitude. The third sample is for concrete sand in Proctor mold under a pressure of 61.1 kPa (H = 116-mm & w_c = 0 %). It was tested by a sine-wave of 8 kHz input frequency

and 10 Volts amplitude. These figures show that carrying out pulse tests inside Proctor mold still a problematic issue. Two dominant waves exist on the received signal log letting the interpreter question which wave is the base shear wave (Figures 5.35 & 5.37). The shear wave arrival is however clear for the oedometer sample test (Figures 5.36).

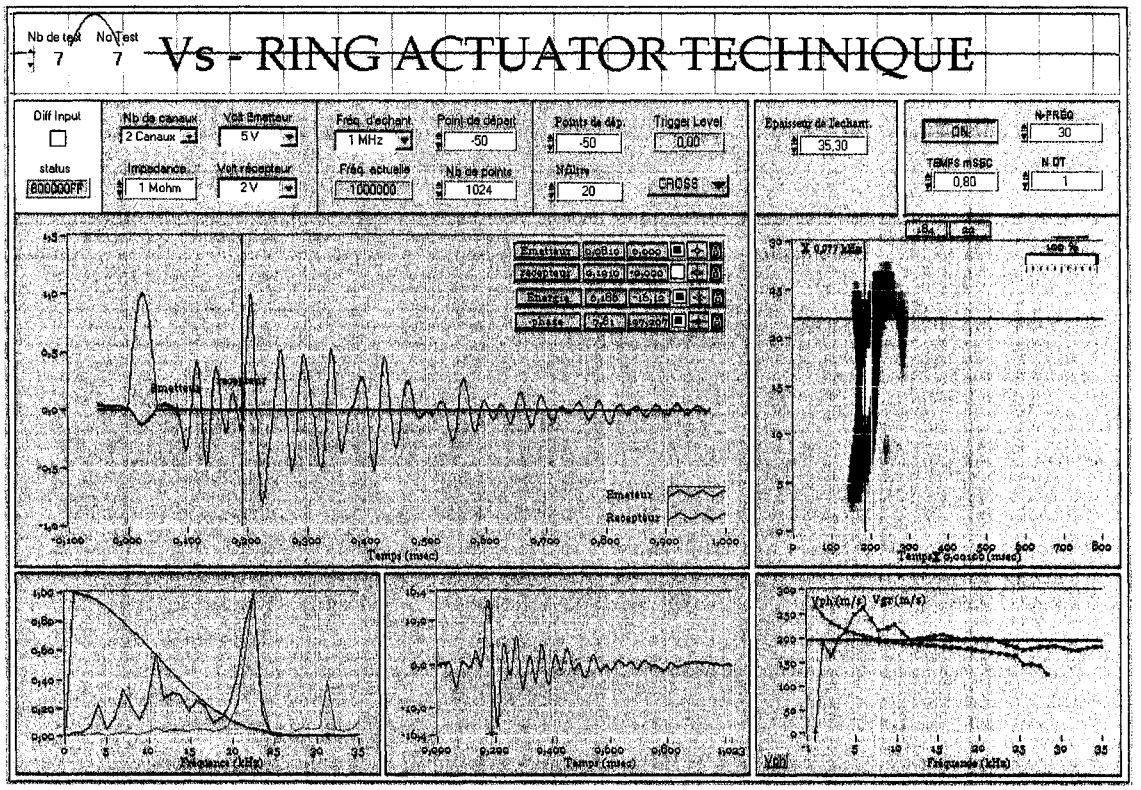

Figure 5.36 Pulse Test on Proctor Sample of LG4 Using Setup 5.

5.7.6 Setup 6

This setup was designed to further increase the resonant frequency of the transmitter and receiver. According to Equation 5.4, the resonant frequency of the piezoelectric unit increases by increasing the stiffness of the inner-disc. The resonant frequency is proportional to the ratio of $(E/\gamma)^{0.5}$. Hence, the unit weight and stiffness are the primary factors that control the natural frequency of a system. Table 5.9 shows the resonant frequency factor $[(E/\gamma)^{0.5}]$ for different materials. Aluminum is the best among these materials for obtaining higher resonant frequency. The stiffness of the Aluminum is much higher than porous sandstone which was used in previous setups. Therefore, a solid Aluminum inner-stone was installed inside the ring to increase the resonant frequency of the piezoelectric units. The surface of the Aluminium

inner-stone is smooth, and should be roughened to transmit the signals to soil. The surface was made rough by gluing a thin layer of siliceous sand grains to the surface which contacts the soil. A conductive epoxy resin was used as an adhesive material to enable grounding the setup.

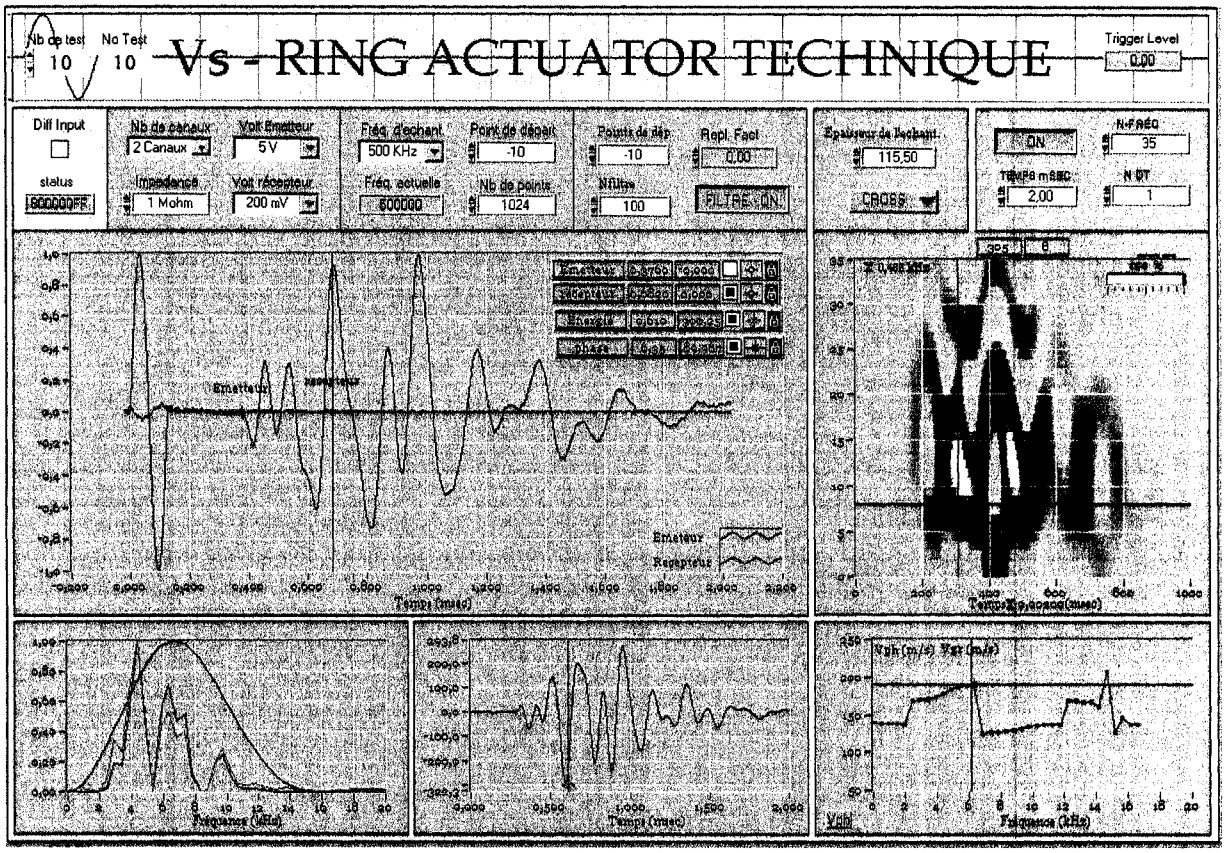

Figure 5.37 Pulse Test on Proctor Sample of Concrete Sand Using Setup 5 (Fr=8 kHz).

Table 5.9 Resonant Frequency Factor for Different Materials.

Material	γ (t/m^3)	E (MPa)	Resonant Frequency Factor $[(E/\gamma)^{0.5}]$
Steel	8.0	2.114E+5	158
Aluminium	2.0	0.747E+5	191
Polyethersulfone	1.36	0.028E+5	45
Plexiglass	1.19	0.031E+5	50
Al foam	1.0	0.140E+5	118

Table 5.7 displays the characteristics of Setup 6, and Figure 5.38 shows the setup and the process of increasing the roughness of its surfaces. This pulse-test setup had a resonant frequency of 112 kHz, which is about 3-times that of Setup 5.

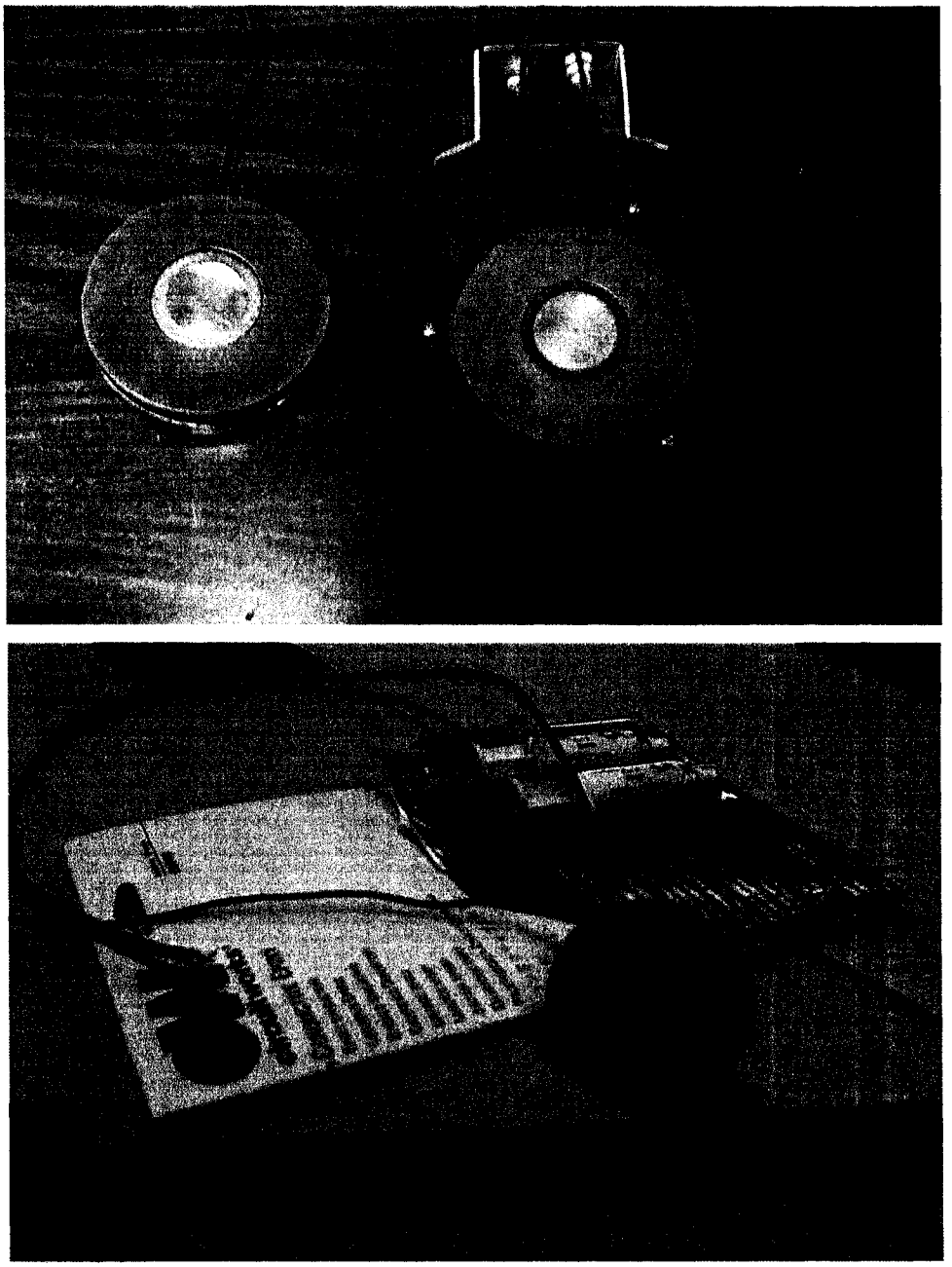

Figure 5.38 Setup 6 and its Modifications.

Figure 5.39 displays a pulse test result on a dry dense Ottawa sand oedometeric-sample under a pressure of 33.6 kPa (half-sine input of 15 kHz frequency). Figure 5.40 shows another

test result on a medium dense sample of the same soil (density = 1.742) under the same pressure (half-sine input of 8 kHz frequency). The shear wave increases by increasing soil density. Figure 5.41 shows the results of a third test on the same soil of the test in Figure 5.40 (fine Ottawa sand) at the same density but under a pressure of 116 kPa (the input wave is a half-sine of 33 kHz frequency). The velocity clearly increases by increasing the pressure on soil. It can be seen that good results were obtained using this setup. Some ambiguity of assessing the shear wave still exists however. Two dominant waves are present on the received log for most of the tests. It is difficult to differentiate the shear wave component. The amplitude of the shear wave becomes very small compared to the p-wave when increasing the pressure. At these high pressures, the p-wave is the dominant wave and the shear wave location is not clear. Using a better signal amplifier has helped in magnifying the signal and making the shear wave component more detectable. The weakness of the shear wave signal may be attributed to insufficient contact between the device and the soil. The high rigidity of the inner stone produces a weak s-wave. In other words, the compression wave does not need roughness to be well transmitted to the soil. Therefore, another development was sought to solve this problem.

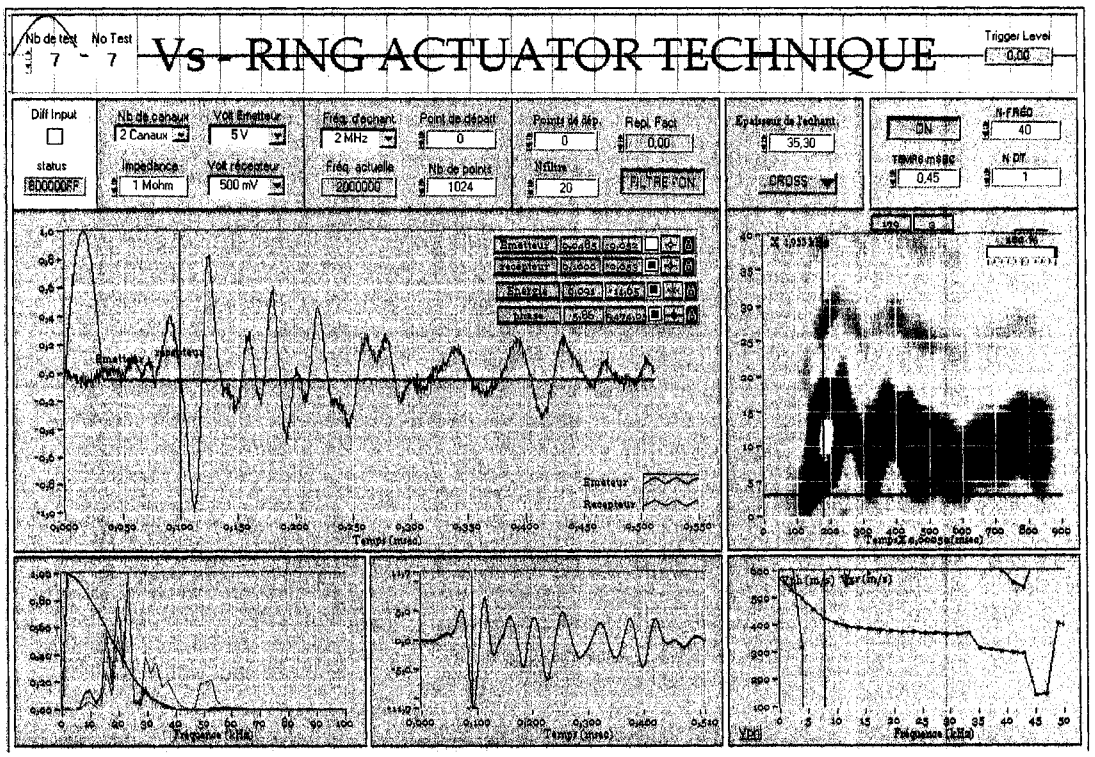

Figure 5.39 Pulse Test on Fine Ottawa Sand in a Large Oedometric Ring.

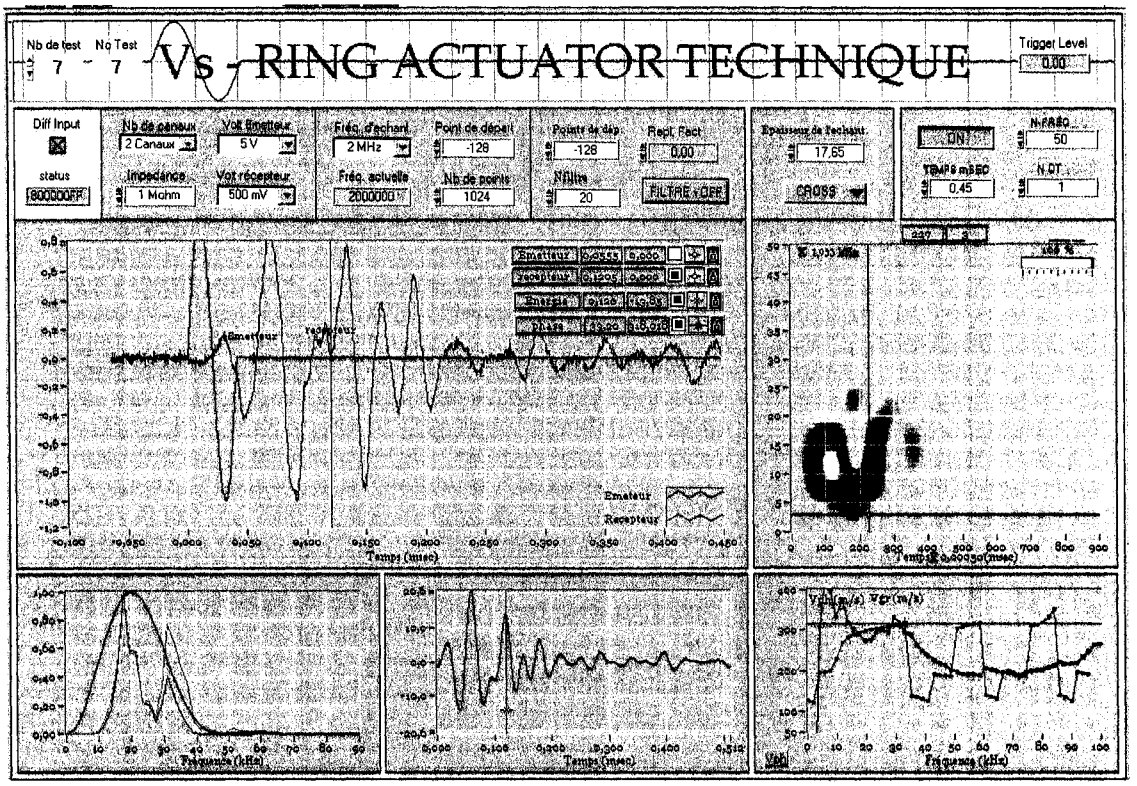

Figure 5.40 Pulse Test on Fine Ottawa Sand in a Large Oedometric Ring (L=17.65mm).

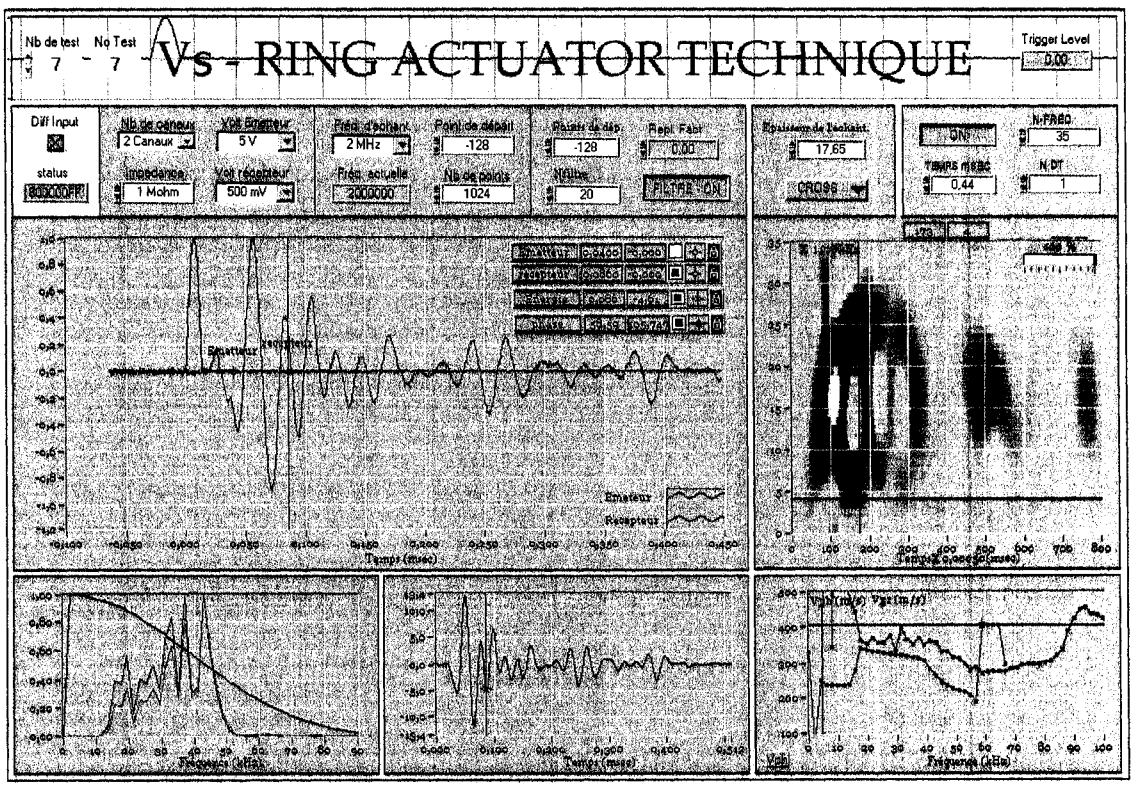

Figure 5.41 Pulse Test on Fine Ottawa Sand in a Large Oedometric Ring (Pr. =116 kPa).

5.7.7 Setup 7

For all previous setups, the shear deformations of the device vary along the radius. The maximum value of deformation is at the outer perimeter of the ring while it is zero at center. Figure 5.42 shows a schematic drawing for these deformations for a ring with a solid inner-stone. In order to have a clear shearing, a uniform or nearly uniform distribution of the shear deformations all over the surface of the device would be better. In addition, the simulation results have shown that decreasing the rigidity of the emitter decreases the amplitude of the compression wave. Therefore, it was decided to cut the inner-stone into four pieces and connect them by an elastic material. This would make the emitter-ring displaces the inner-stone pieces in and out easily without deforming them. This would apply uniform shear deformations to the soil. Also, the p-wave amplitude should be greatly reduced or eliminated. For this setup, the p-wave will be emitted only from the piezoelectric ring as long as the inner stone continues to be flexible and displaces with the deformations of the ring. Figure 5.43 displays a plan view of the emitter-ring and its 4-pieces-split inner-stone as well as the deformation pattern along the radius. The surface of the aluminium pieces, which contacts the soil, was made rough by scratching them in two directions. Figure 5.44 displays some photos for Setup 7c at some of its manufacturing stages.

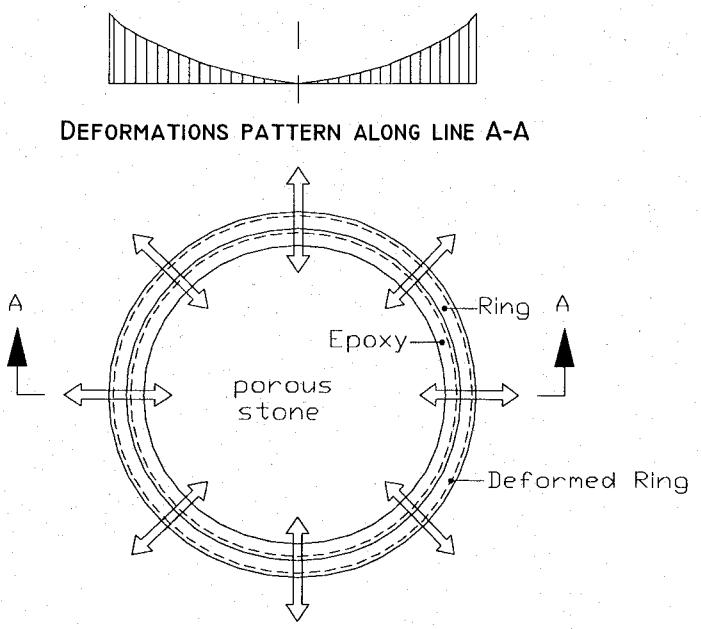

Figure 5.42 A Ring Setup with Solid Interior Stone and its Deformation Profile.

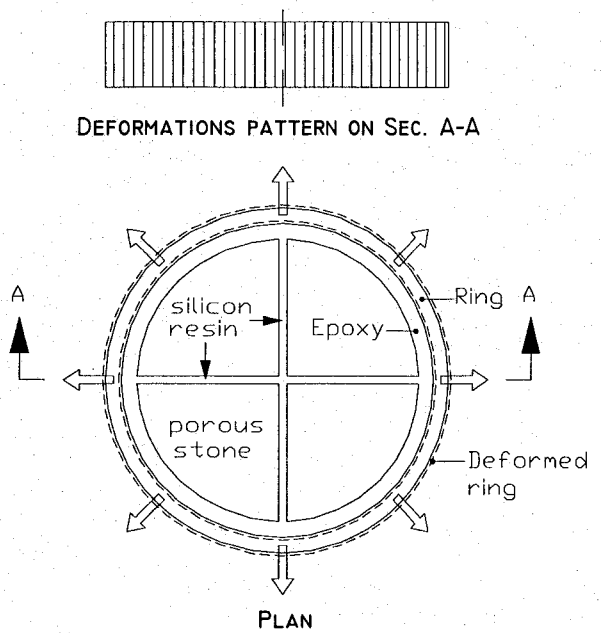

Figure 5.43 A Ring Setup with Divided Interior Stone and its Deformation Profile.

This setup made a drastic change in the quality of the output signals of pulse tests. A clear dominant shear wave arrival was obtained. The amplitude of the compression wave is much less than that of the shear wave. In addition, the second arrival of shear wave is clearly recorded. Moreover, the Wigner-Ville analysis has become much better so that the dispersion of the received signals approached the theoretical trend. This was achieved by trimming the received signal so that the analysis is made only for the shear wave component. The compression wave and other secondary waves are excluded. Figure 5.45 displays a pulse test on dry Ottawa sand in oedometer cell under a pressure of 22.6 kPa. The figure shows the C.C functions for the originally received signal and the trimmed signal. Figure 5.46 displays a pulse test on dry LG4 till sample in a Plexiglass mold of 76.2-mm height under a pressure of 798 kPa. The dispersion curves for phase and group velocities take the shape of the theoretical trends. The same effect for this treatment was also realized and confirmed in numerical simulation results.

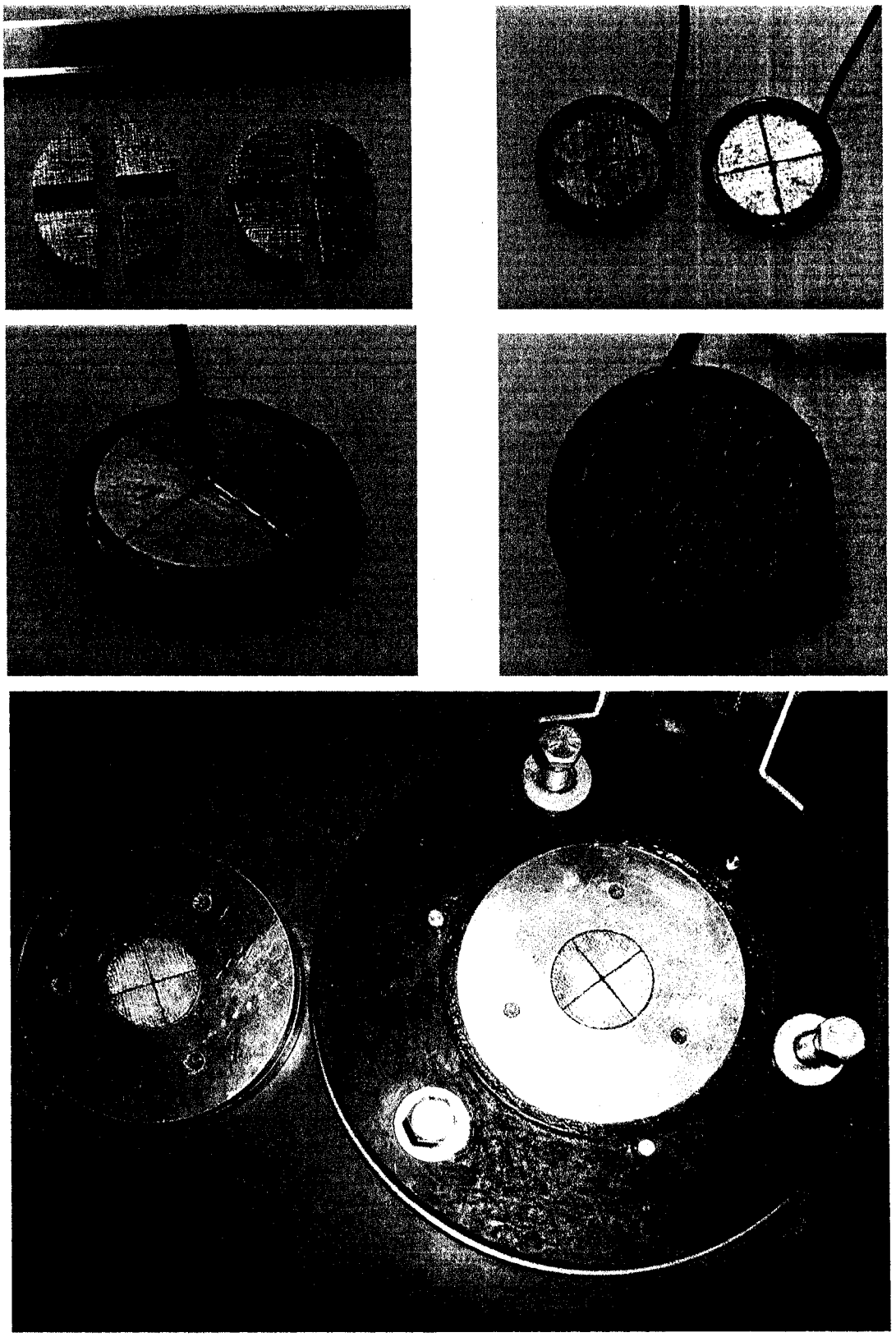

Figure 5.44 Some Photos for Setup 7c and its Manufacturing Processes.

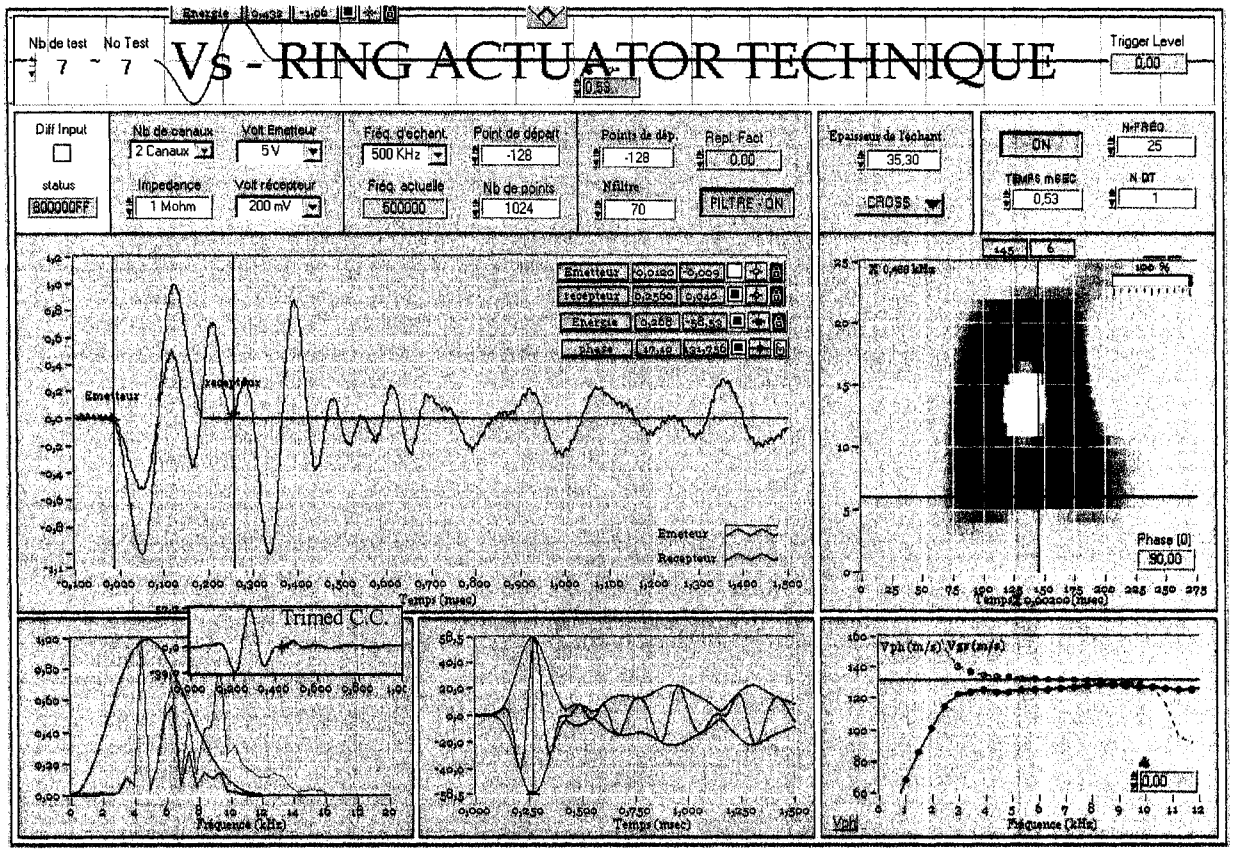

Figure 5.45 Effect of Output Signal Trimming on C.C. Function and W.V. Analysis.

Another important finding was reached during pulse testing using Setup 7. A very thin layer of non-organic silt was added at the top and bottom surfaces of the sample in order to check the quality of coupling (interaction) at the contact surfaces between the soil and the device. Surprisingly, the quality of the received signal becomes much better. Figure 5.47 displays the results of a pulse test on dry Ottawa sand sample in Proctor mold under a pressure of 28.6 kPa (γ_d = 1.73 , e = 0.53). The s-wave is clearly distinguished from the other components of the output signal. This confirms the importance of having a good coupling between the soil and the test device.

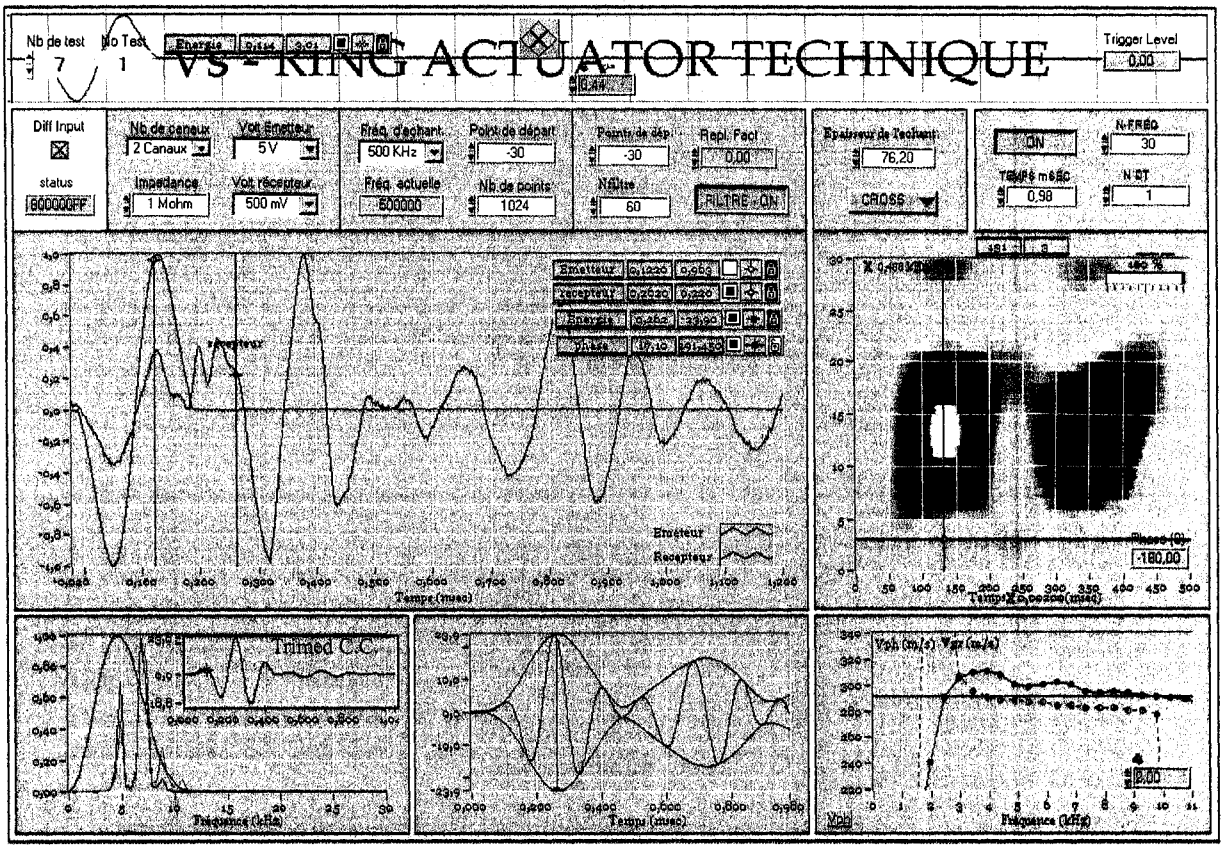

Figure 5.46 Trimming Effect on Dispersion Curves of Phase and Group Velocities.

5.7.8 Setup 8

This setup was made for increasing the contact between the inner-stone and the soil. A good contact is vital in obtaining a dominant and clear shear wave component, especially at low stresses. The commercially sold sand-porous-stones are relatively smooth. Therefore, a thin layer (0.6mm thickness) of siliceous sand grains was glued to the split porous stone on the soil side. A 0.6mm-thick aluminium disc was added on the outer porous stone in order to have an even surface at soil side. This disc extended over the piezoelectric ring trying to reduce the amplitude of the compression wave by having indirect contact between the soil and the ring. Table 5.7 summarizes the elements of this setup and Figure 5.48 presents a drawing of the emitter unit. Figure 5.49 displays a photo for this setup installed in the top cap and base pedestal of a large oedometer cell. The pulse tests showed that the radial resonant frequency of this setup is 17 kHz, the same as Setup 7.

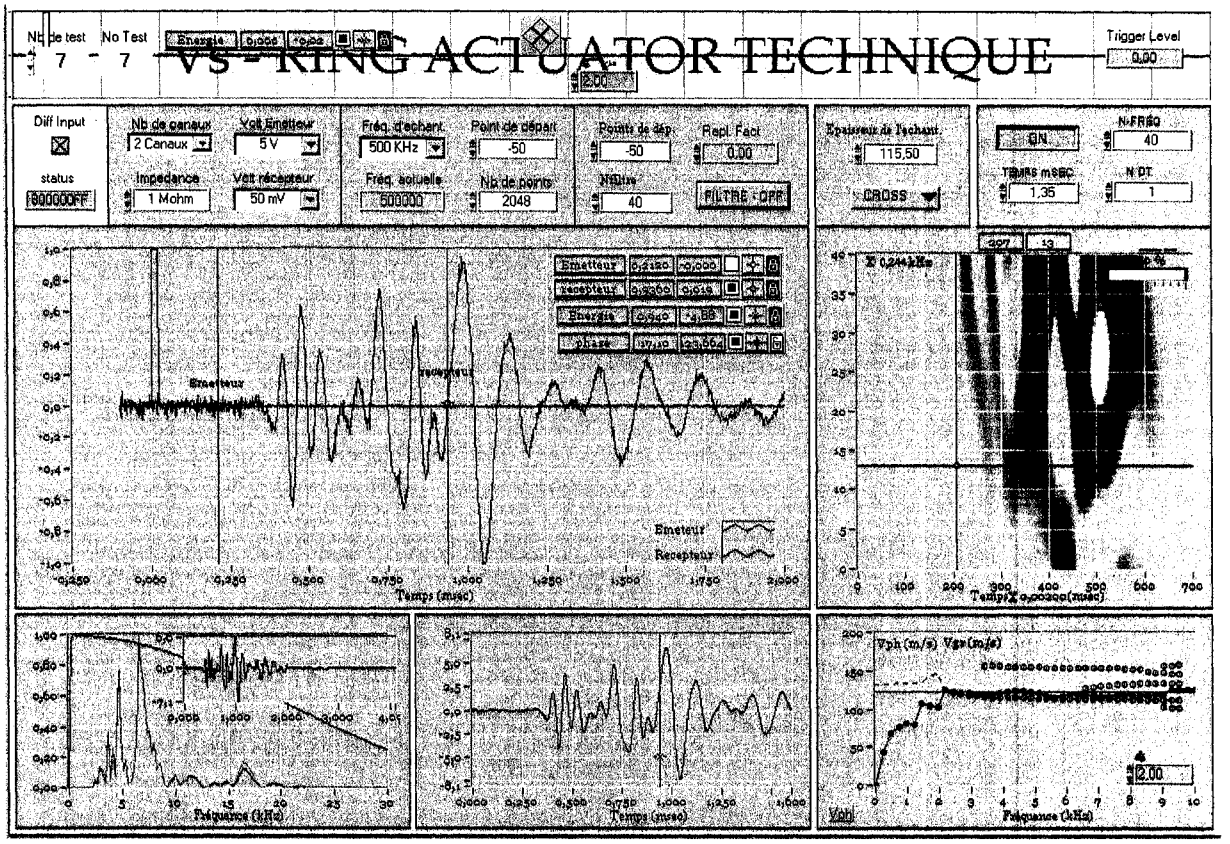

Figure 5.47 A Very Thin Layer of Silt at each Cap Enhances Interaction.

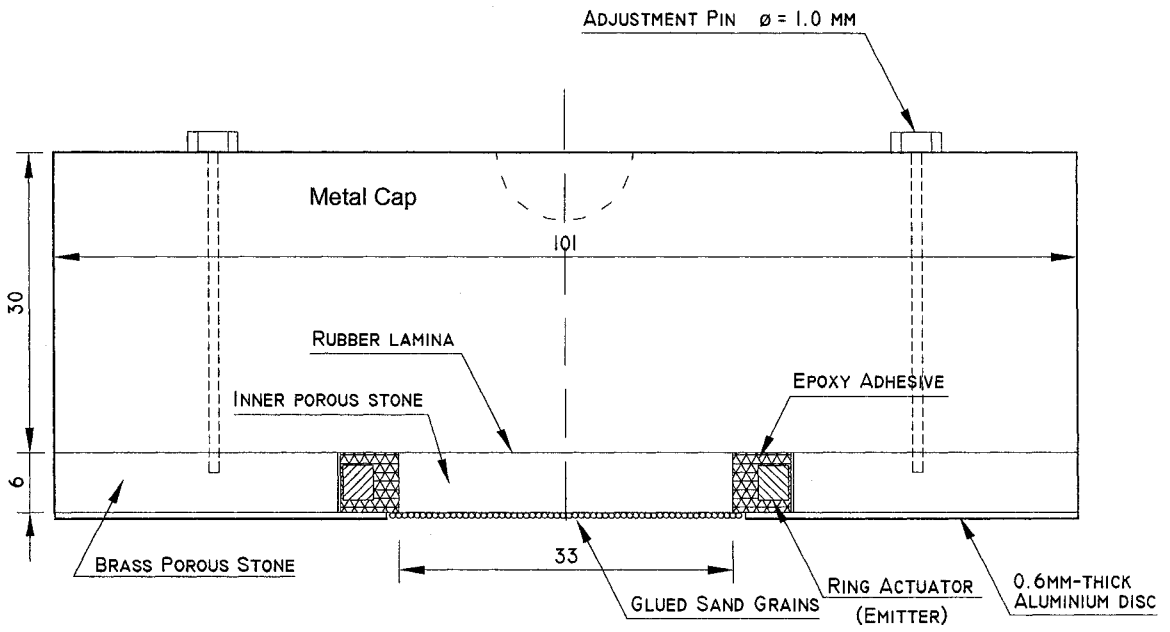

Figure 5.48 A Drawing for the Emitter Unit of Setup 8.

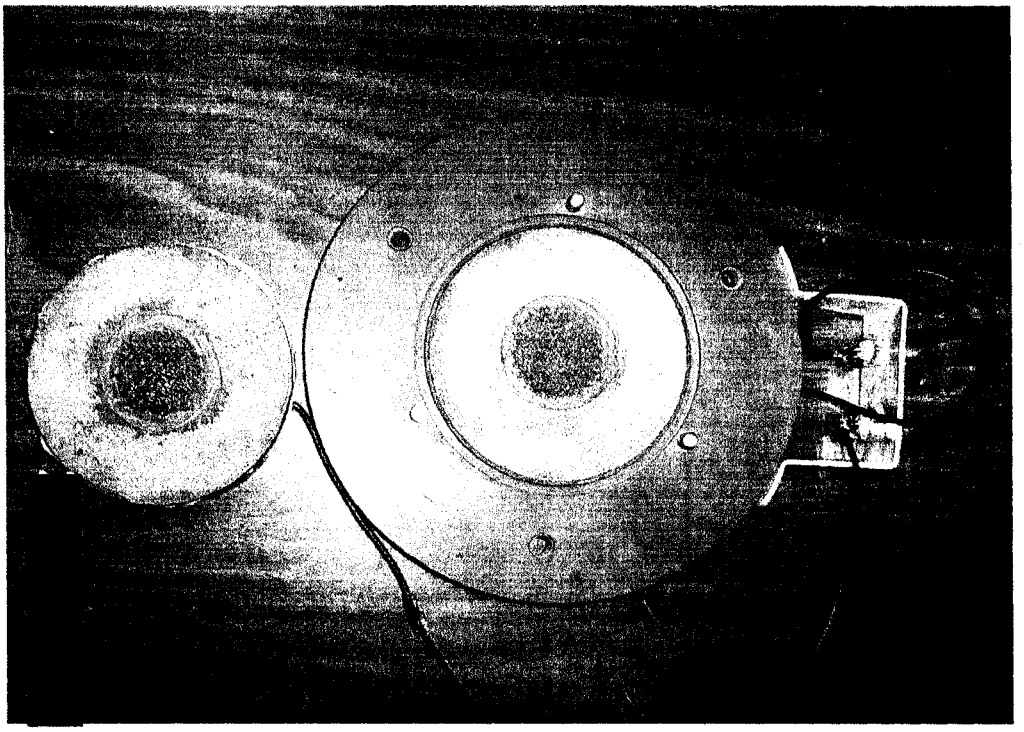

Figure 5.49 A Photo for Setup 8 (without the Outer Aluminum Disc); the Sand Grains Cover the Porous Stone and Hides the Cuts.

When testing began using Setup 8, ambiguous results were obtained. Later on, it was found that coarse sand grains makes uneven contact surface, irregularities, which produce non uniform signal at variable elevations within soil. Therefore, this thin layer was remade using uniform Ottawa sand. Then, this setup has functioned very well. This depicts the importance of having shear excitation over an even surface. Figure 5.50 displays a pulse test result on dry Ottawa sand sample of 95-mm-length under a pressure of 798 kPa. The second arrival of shear wave is clearly recorded on the received signal log. Another test was carried out on a Magog-Lake silt sample of a length equals to 76.0mm using Setup 8 (Figure 5.51). The compression and shear wave velocities of this soil are low. This allowed a complete separation of the two components. The C.C function is giving two maximum points, one at compression wave arrival and the other at shear wave arrival. The other components are small. Also, the Wigner-Ville analysis is clear for each of the compression and shear waves and is compatible with the theoretical trend. The dispersion of waves is clear. The phase/group velocity increases by decreasing frequency. The compression and shear wave velocities are 88 m/s and 50 m/s, respectively. Generally, it is evident that the ring actuators setup is functioning very well.

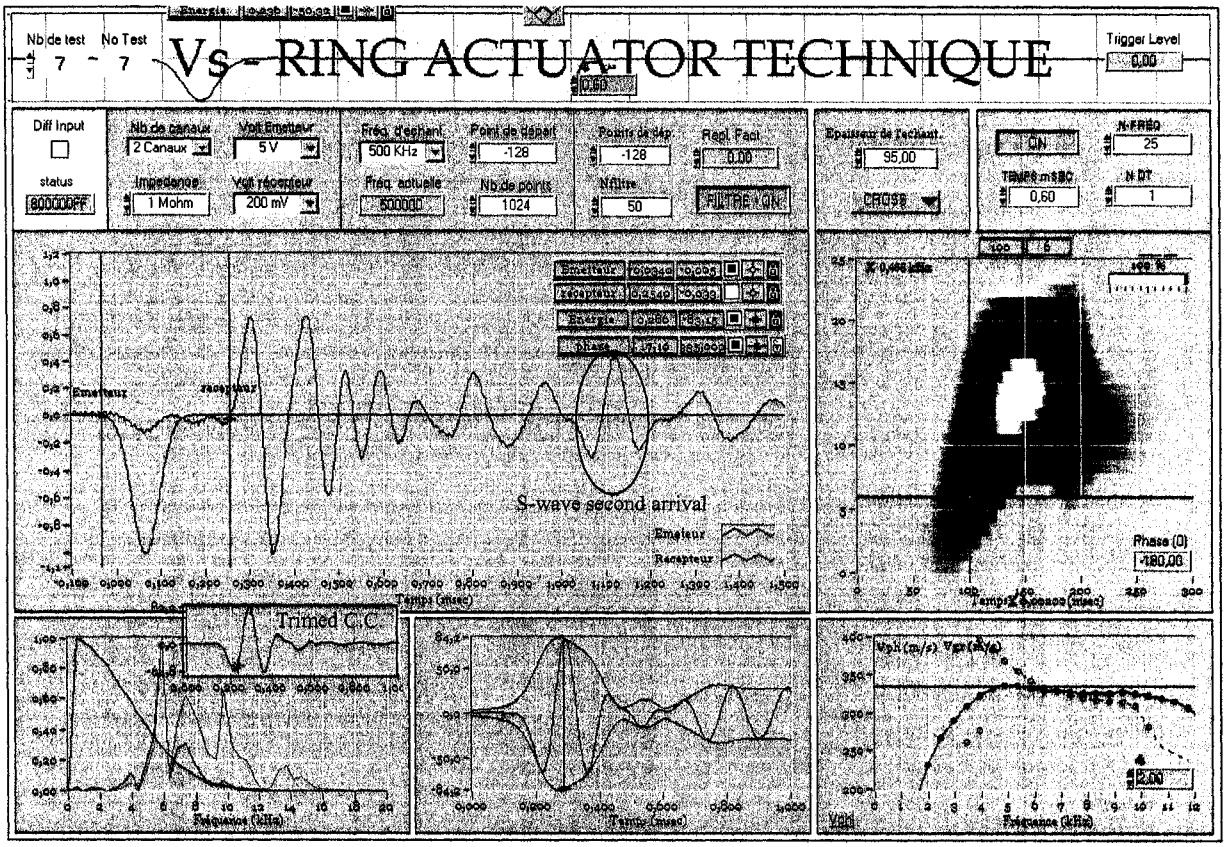

Figure 5.50 The Second Arrival of S-Wave is Clearly Recorded Using Ring Actuators.

5.8 Optimizing the Peripheral Electronic Equipments

The experimental testing program of this research has been started by using the equipments which were available in our laboratory, which had been used with bender elements tests. To carry out preliminary tests, a HP 35653A 50 kHz source module was used as a power source. This module is able to apply only triangular and rectangular signals and sweep sine waves. Its maximum voltage is ±10 Volts. The HP356518 module was used as interface/signal processor (Oscilloscope). Early in this research it was decided to replace the HP signal source by a more advanced computer card so that a sine-wave input could be used to trigger the emitter. A "Gage CG1100" generator computer card was installed on the data-acquisition computer. This card provides customized signals with amplitudes up to ±5 Volts. Therefore, the output of this card had to be amplified using a power amplifier. This issue is analyzed here to help in choosing the suitable amplifiers.

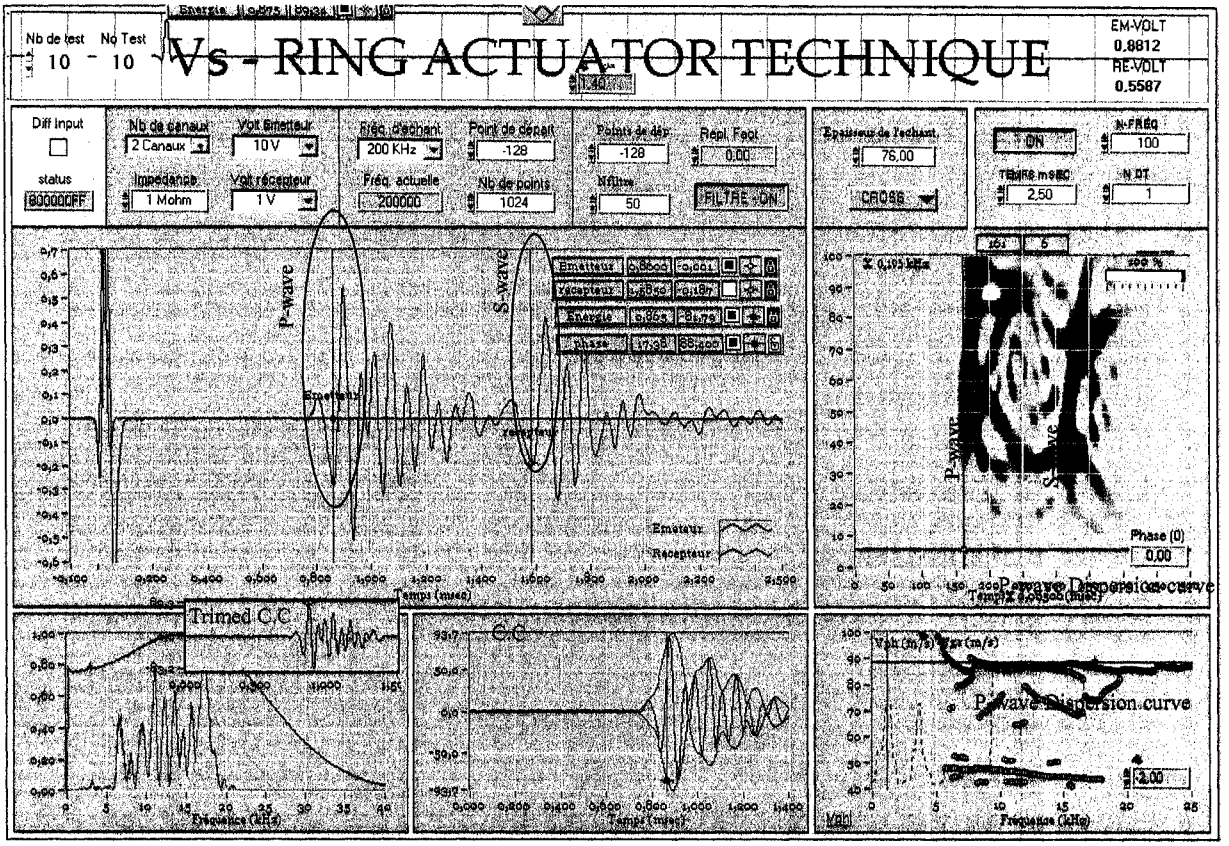

Figure 5.51 Very Clear Separation between P- & S-Waves when Testing Weak Samples.

A piezo-actuator can reach its nominal displacement in approximately 1/3 of the period of the resonant frequency, provided the controller can deliver the necessary current. This requires an amplifier with sufficient output current and low rise time. Such rapid expansion may cause significant overshoot. The following equation represents this characteristic.

$$T_{\min} = \frac{1}{3 f_o} \tag{5.11}$$

where T_{min} is the minimum rise time of a piezo-actuator [s] and f_o is the resonant frequency of the device [Hz]. If the resonant frequency of Setup 8 (17 kHz) is substituted in the previous equation, the minimum rise time for the required amplifier should be 19.6μs. Therefore, the chosen power amplifier had a minimum rise time of up to 0.120μs ($50V_{p\text{-}p}$ square wave). Similarly, the current amplifier had a rise time 15μs (for a gain of $10^6 - 10^4$ V/A).

The following equations describe the relationship between amplifier output current, voltage and operating frequency. They help in determining the minimum specifications of an amplifier to suit a piezoelectric device in dynamic operation. The long-term average current required for sinusoidal operation is

$$I_a \approx f\,C\,U_{pp} \tag{5.12}$$

The peak current required for sinusoidal operation is

$$I_{max} \approx \pi\, f\,C\,U_{pp} \tag{5.13}$$

The maximum operating frequency with triangular waveform, as a function of the amplifier output current limit is

$$f_{max} = \frac{i_{max}}{2\,C U_{pp}} \tag{5.14}$$

where: I_a = average amplifier source/sink current [A], I_{max} = peak amplifier source/sink current [A], f_{max} = maximum operating frequency [Hz], C = piezo actuator capacitance [Farad (As/V)], $U_{p\text{-}p}$ = peak-to-peak drive voltage [V], and f = operating frequency [Hz]. When the values of the different parameters in Equation 5.14 are substituted (200Volts input and 1 Volt output, Fr = 17 kHz and capacitance as in Table 5.2), the maximum current needed to operate the piezoelectric devices is 25.5 milli-Amperes for the emitter unit and 0.19 milli-Amperes for the receiver. Krohn-Hite DCA-10 Direct-Coupled Amplifier was used as power amplifier [Figure 5.52(a)]. It provides DC to 1MHz frequency range, ± 1dB frequency response, and 20dB variable voltage gain. The Krohn-Hite DCA10 is an Amplifier that delivers 10 watts continuously (20 watts peak) from dc to 1MHz, and 20 Watts continuously at DC, with extremely low harmonic distortion (0.1%) and flat frequency response. Input and output, independently, may be either direct coupled, or capacitor coupled with input cut-off at 1Hz and output cut-off at 30Hz with a 600-ohm resistive load. Therefore, this amplifier is quiet well suitable for operating piezoelectric elements.

The Krohn-Hite DCA-10 amplifier gives a maximum output voltage of 140 Volts. Therefore, it was decided to increase the input voltage on soil samples in order to put more energetic waves into soil. Hence, the output signal may not need to be amplified using the current amplifier. Thus, a new power amplifier was bought for his purpose [Figure 5.52(b)]. The Krohn-Hite 7602M is a wideband power amplifier that offers extended output power and voltage capabilities, low distortion (<0.01%), and versatility. It has a voltage gain of up to

42dB. This amplifier provides a differential output and is able to deliver 34 watts of continuous power (68 watts at dc) and 282V rms (800Vp-p). It can also provide plus and minus dc voltages simultaneously (DC offset = ±200V). Also, it measures the largest peak voltage independent of polarity with a 1 second time constant. Its accuracy is ±0.5V (at 1 kHz), with a frequency response of ±2% at 10Hz to 100 kHz and 5% to 1MHz.

For the preliminary tests, a small current amplifier was used to magnify the output voltage. It was manufactured in our workshop for a gain rage of 0-44 with input equals 10 kOhms and output of 50 Ohms. After carrying out many tests using this amplifier, it has showed malfunctioning behaviour by distorting the output signals. Therefore, another sophisticated current amplifier was bought to replace the previous one. The new amplifier "Keithley 427 Current Amplifier" is used in some tests when pre-amplification was necessary, and it proved to be efficient and helpful in signal filtering. It provides high speed combined with low noise and selectable gain, current suppression, and rise time. This amplifier has a range of 10^4 to 10^{11} volts/ampere (10^{-13} ampere resolution to 10^{-3} ampere full output), output ±10 volts at up to 3 milli-Amperes, and rise time 10% to 90% adjustable in 1x and 3.3x steps, with a minimum rise time of 15μs.

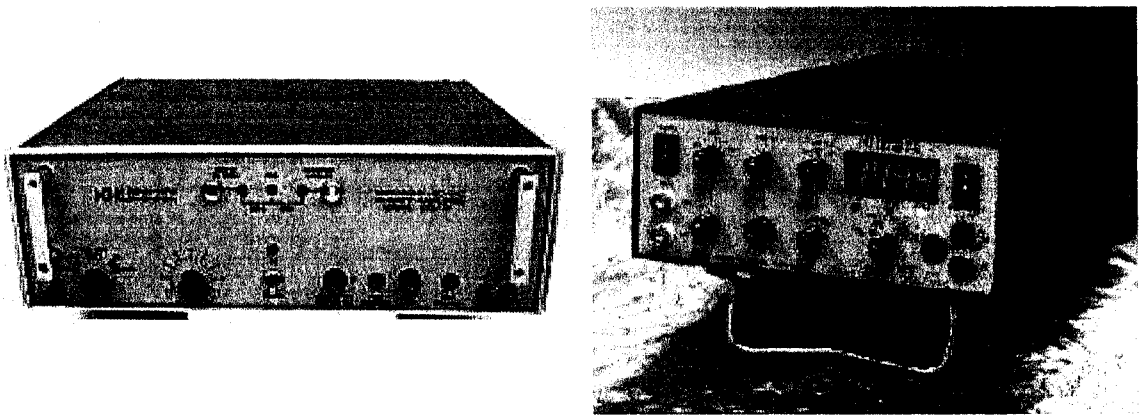

a) Krohn-Hite DCA-10 b) Krohn-Hite 7602M

Figure 5.52 The Used Power Amplifiers during this Study

The Gage oscilloscope card was installed on the data acquisition computer to monitor and record the input and output signals. A special program (software) was made by Dr. M. Karray using LabVIEW© software in order to control these devices and plot the test data. Also, this program is tailored to make some analyses to the acquired data. This software was

used to carry out all pulse tests in this study. It is capable of computing the cross-correlation function, the cross-correlation energy, the Wigner-Ville energy analysis, the dispersion curves for phase and group velocities versus frequency, and the frequency domain for the input and output signals. Figure 5.31 shows an example of the screen output from this program. At some stages of laboratory testing, this software was further adopted to trim the secondary waves of the output signal (like compression wave and reflected waves) for better analysis of shear wave data (Figure 5.51).

5.9 Accuracy and Time Delay of the New Setup

Some pulse tests were carried out on Plexiglass cylinders in order to check the accuracy of measurements using piezoelectric rings. The cylinders had a diameter of 40mm and variable lengths of 68mm, 93.2mm and 101.7mm. Setup No. 7 was used to carry out these tests under small stresses (<100 kPa). It is noticeable that the diameter of the cylinders is less than the inner diameter of the rings. Therefore, the compression wave, which is emitted by the ring, is not transmitted to the cylinder. The inner stone does not emit a compression wave. Hence, only the shear wave is transmitted to the cylinder. Figures 5.53, 5.54 and 5.55 show the signals received for different shape input waves. The shear wave arrives at the same time for the different input shapes for each sample length. The arrival times give shear wave velocities varying from 1412 to 1426m/s. Plexiglass is known to have a shear wave velocity of 1420m/s (Table 5.10). Figure 5.56 represents the relationship between the cylinder's length and the shear wave arrival time. A linear relationship is obtained as expected, and it extrapolates to zero when the sample's length becomes zero (passes by the graph's origin).

Table 5.10 Density and Elastic Waves Velocity of Three Materials.

Material	Density (kg/m^3)	Wave Velocity		
		Longitudinal (V_p)	Shear (V_s)	Rayleigh (V_R)
Plexiglass	1200	2713	1420	1285
Silica	2150	5968	3764	3409
Stainless steel	7800	5840	3130	2830

After Doghmane, A. and Hadjoub. Z. (1997)

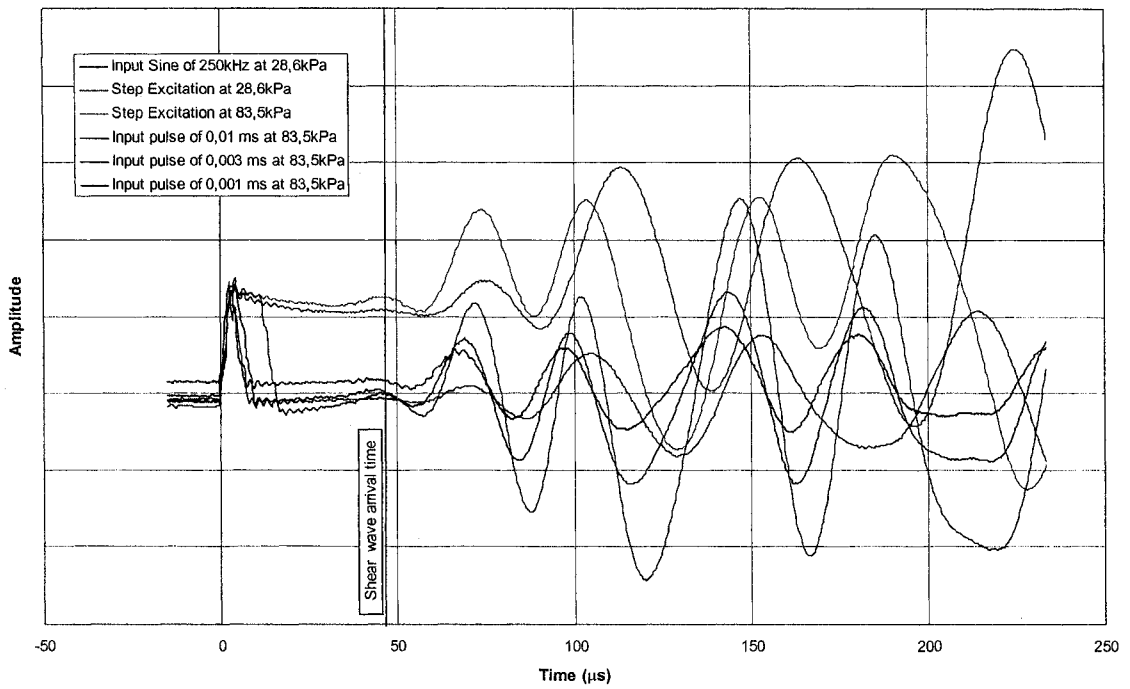

Figure 5.53 Calibration Results for the Ring Actuators Setup Using a Plexiglass Cylinder of 68-mm-Length.

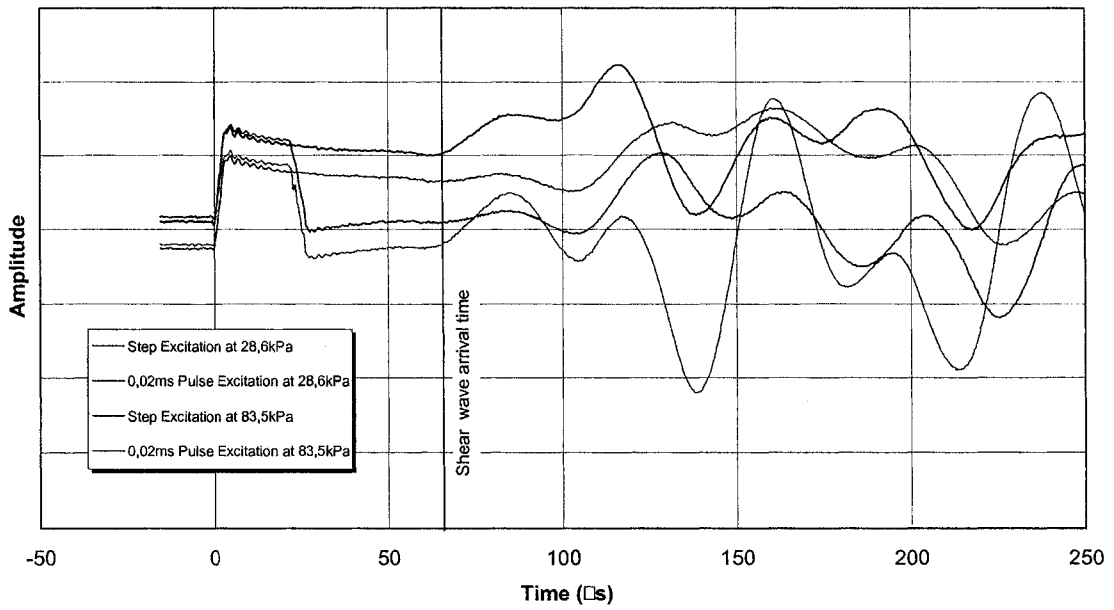

Figure 5.54 Output Signals for Pulse Tests by Ring Actuators on a Plexiglass Cylinder of 93.2-mm-Length.

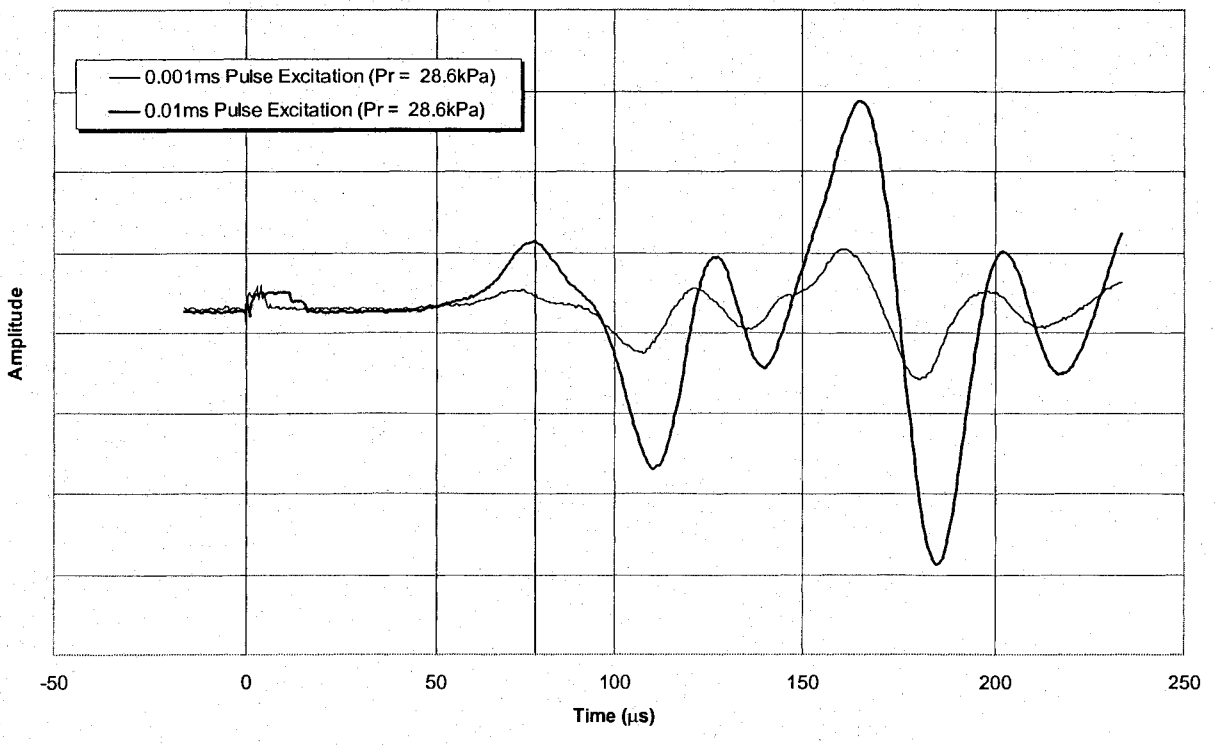

Figure 5.55 Output Signals for Pulse Tests by Ring Actuators on a Plexiglass Cylinder of 101.7-mm-Length.

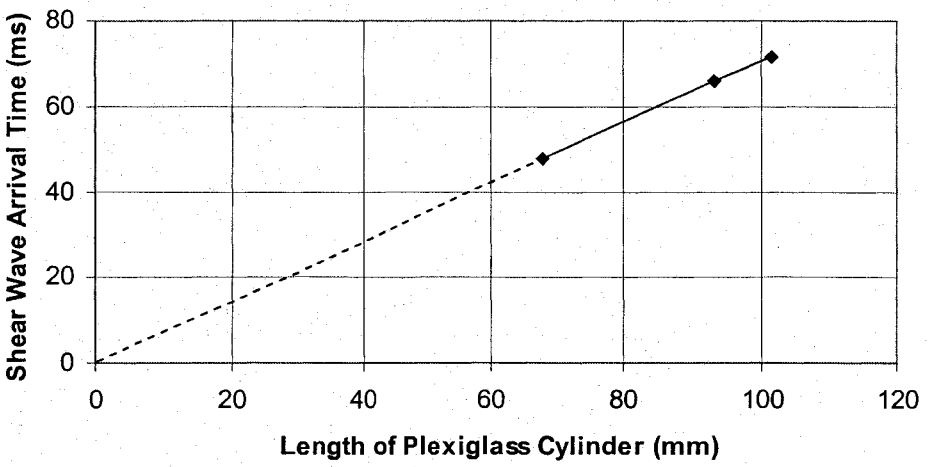

Figure 5.56 Pulse Tests Result on Plexiglass Cylinders of Variable Lengths.

The time delay of the different setups was measured by putting the emitter and receiver units in direct contact under very small pressure. It decreases by increasing the resonant frequency of the setup, and varied from 20μs to 44μs. This time delay is so small compared to the measured arrival times.

5.10 Conclusions

Piezoelectric ring actuators are employed in a new device (ring actuators setup) for the first time in geotechnical engineering instead of the commonly used bender elements. The design of this device was optimized based on numerical simulations and laboratory test results that were carried out in this research. The development of this device was challenging and eight piezoelectric setups were built. Each setup has some improvement to its precedent. The ring actuators setup overcomes the problems of wave reflections at boundaries, sample disturbance, weak shear coupling between soil and device (interaction) as well as fixation problems, low resonant frequency and limited input voltage of the existing devices. The main characteristics of ring actuators setup can be summarized in these points: Thin device, no penetration into soil is required, high energy input over a large area, and high quality output without signal stacking, amplification or conditioning. It can be used to carry out measurements under very low to very high pressures using relatively low input voltages.

When building a ring actuators setup, the following points should be considered. The area of excitation should be optimized to suit the specimen dimensions and its properties. Good contact between the piezoelectric device and soil is very important. The emitter and receiver excitation surfaces should be even and sufficiently rough while their back surfaces should be even and very smooth. Centering the setup components in the horizontal and vertical directions is important. An inner stone that easily reacts to the piezoelectric ring and soil is highly preferable. Applying lateral confinement or torsion stresses on the piezoelectric unit should be avoided. A testing device of high resonant frequency is highly recommended. Grounding the piezoelectric setup and the metallic parts of the apparatus is crucial. Several equations were introduced in this research for designing ring actuators setup and choosing its peripheral electronic equipments. The ring actuators setup has been mounted in specially designed base platen and top cap of some laboratory setups. The accuracy of this piezoelectric setup was checked using Plexiglass samples. The peripheral devices of this setup were optimized during this research.

Chapter 6 EXPERIMENTAL TESTS AND RESULTS

6.1 Introduction

This chapter introduces some laboratory test results on different soil types using piezoelectric ring actuators setups which were built in this study. These tests are to further prove the suitability and accuracy of this setup to carry out pulse tests. Some tests are carried out to investigate the compaction curve in terms of V_s and w_c. Other tests are carried out to investigate the relationship between V_s and basic soil parameters. The tests were carried out in an oedometer cell, Proctor mold and other Plexiglass molds of different heights under variable pressures and at different water contents. The effect of applying certain input wave shapes on the clarity of the output signals is investigated. This chapter introduces two ideas; compaction control using shear wave velocity and correlating V_s to usual soil parameters.

6.2 Effect of Input Wave Shape

The effect of the input wave shape on the output signal was investigated in this study. Figure 6.1 shows a phenomenon that was realized during a test on dry standard Ottawa sand sample (C-109) in the oedometer cell using Setup 7. The sample was tested with a sine wave of 1.5 kHz frequency under a pressure of 28.6 kPa. The grain size distribution of Ottawa sand (C-109) is shown in Figure 5.9. Also, Table 5.5 presents the grain size characteristics of this sand and the other used soil types in this study. It is seen that the input sine-shape emits two false peaks at receiver; the 1st peak corresponds to the beginning of the signal and the 2nd peak to the end of the signal (i.e. a peak for each sharp edge within the input wave). This means that the sine wave input may not be suitable at very low frequencies. Other input-wave shapes were used in this study for comparison.

The input-wave shapes for pulse tests were modified by adding smooth transition zones at the beginning and end of the input signal. These new modified shapes produce signals of narrow frequency domain without extra components coming from the sudden start/end of the input voltage. They also reduce the amplitude of the compression wave. Two types of these shapes (smoothed-edges sine and smoothed-edges half-sine) are shown on Figure 6.2 (c & d) together with a half-sine and sine input. The output signals of some pulse

tests on medium dense Ottawa sand (C-109) sample in a Plexiglass mold of a diameter of 100.9mm and length of 95mm using these different input shapes are displayed on the same figure. The arrival time of the shear wave is almost the same for all input shapes. The modified input shapes give a dominant shear wave component with lesser secondary waves. Other modified input wave shapes were also used [versed-sine (bell-shape) and the winged-sine]. The excitation function for the versed-sine is as follow:

$$f(t) = c(1 - \cos\frac{2\pi t}{T}) \tag{6.1}$$

where c is the amplitude constant and T is the period of the input. The excitation function for the winged-sine is

$$f(t) = c\left\lfloor 2^{(a(t-b)^2)} \right\rfloor \sin(kt) \tag{6.2}$$

The equation for the wavelet form is

$$f(t) = c\left\lfloor 2^{(a(t-b)^2)} \right\rfloor \tag{6.3}$$

where a, b, k are constants which control the shape and frequency of the input signal and c is the amplitude constant.

Figures 6.3 and 6.4 introduce these input shapes and their output signals from pulse tests on Magog-Lake Silt (Test 50; Setup 8). It can be realized that the versed-sine and the winged-sine shapes are more suitable for pulse tests. Thus, it was decided in this research to essentially use these modified input-wave shapes with the other known shapes.

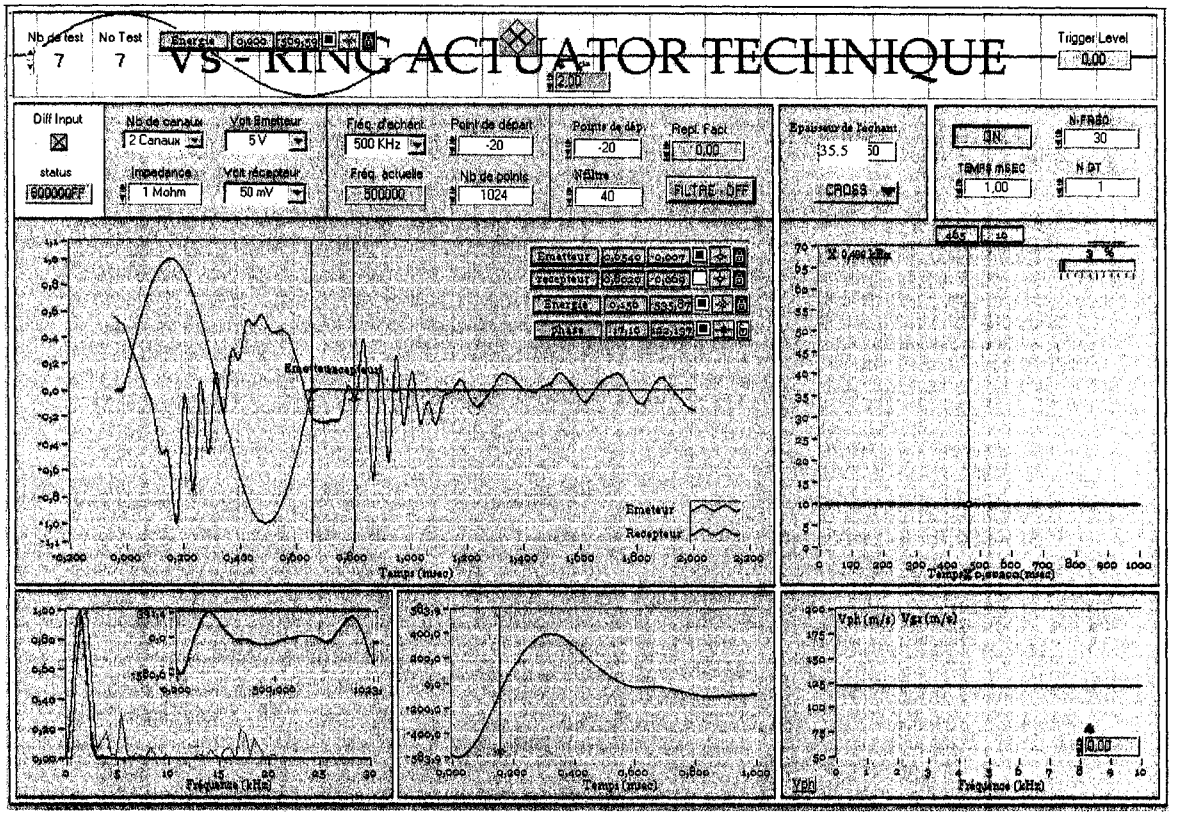

Figure 6.1 Pulse Test on Dry Ottawa Sand Sample in the Oedometer Cell.

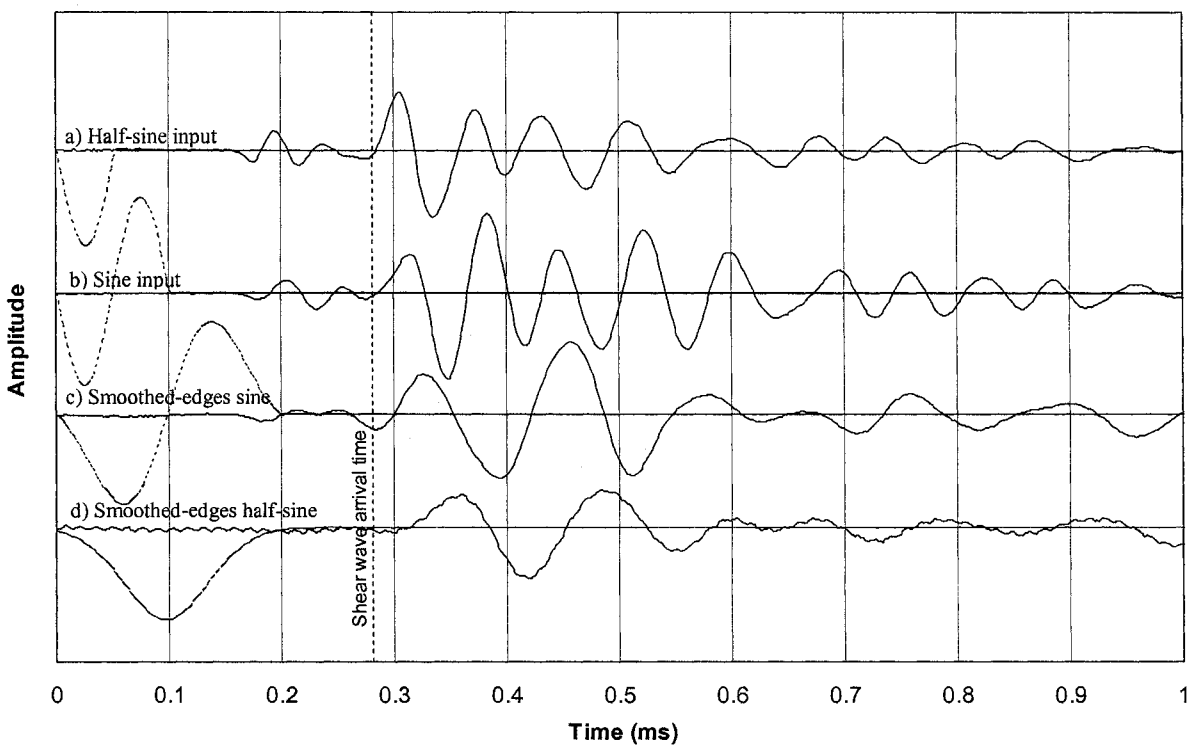

Figure 6.2 Ottawa Sand Sample Tested by Different Input Shapes; Test 48; Setup 8.

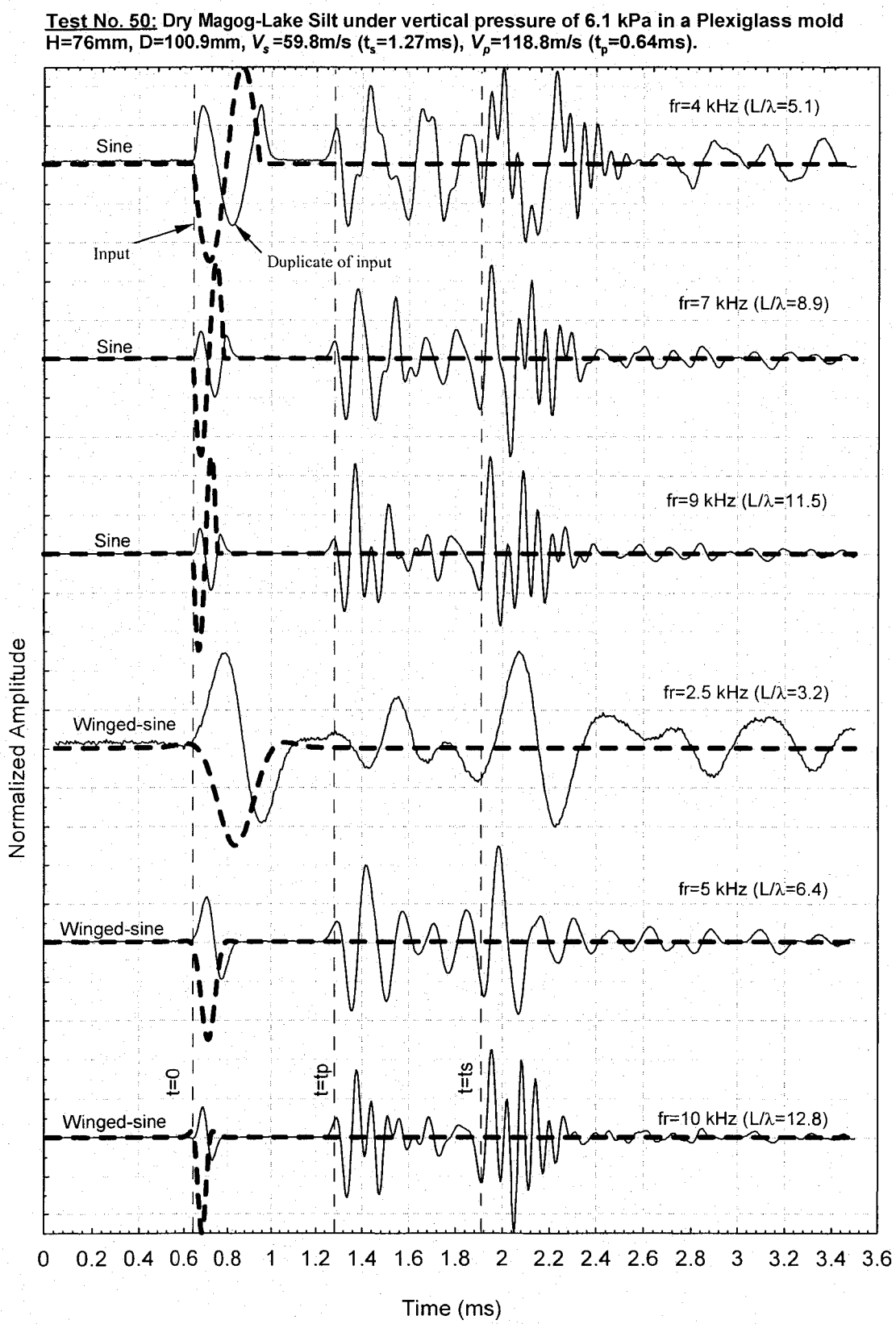

Figure 6.3 Sine Input versus Versed-Sine Shapes for Pulse Tests; Setup 8.

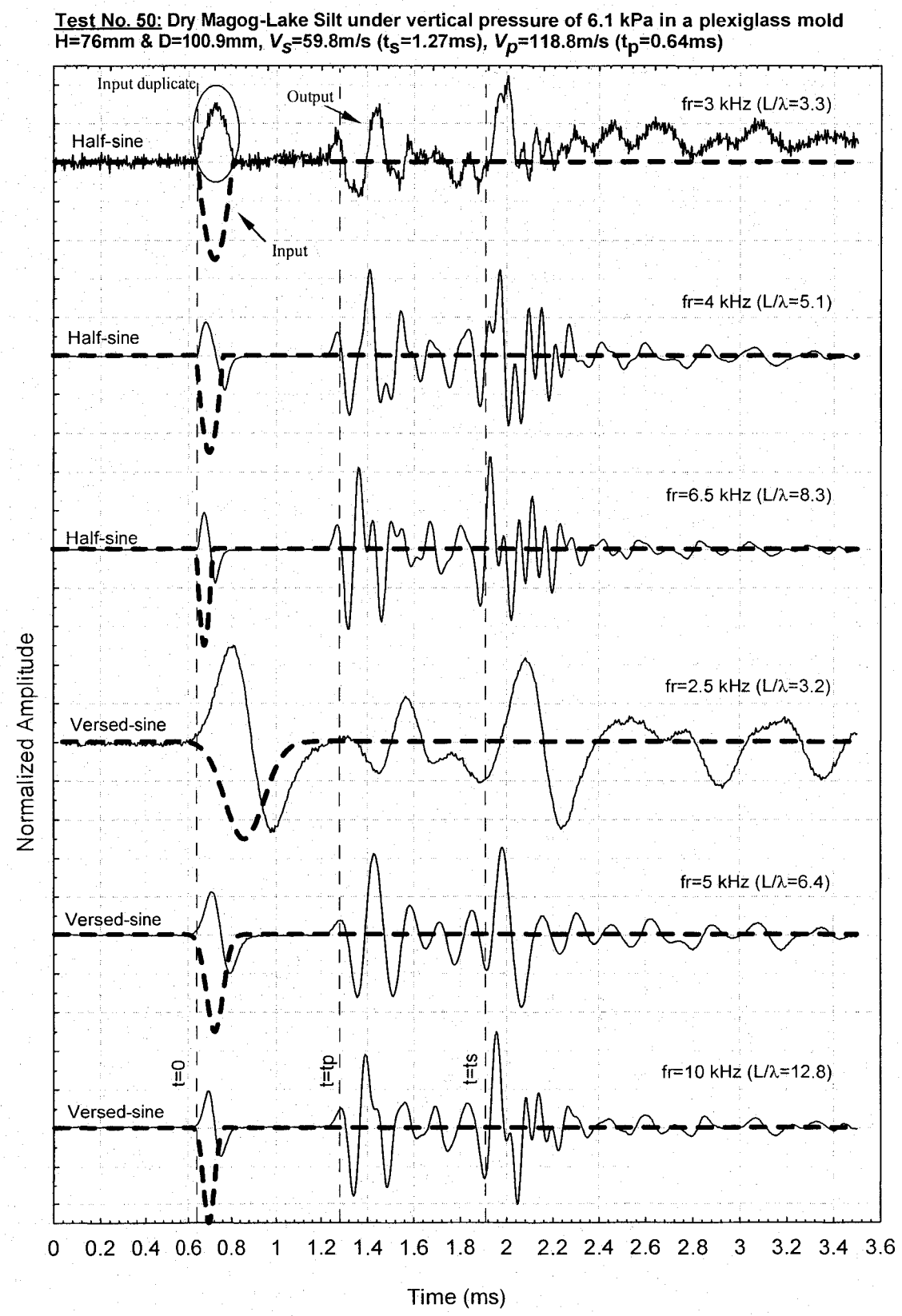

Figure 6.4: Sine Input versus Winged-Sine Shapes for Pulse Tests; Setup 8.

6.3 Tests in Oedometer Ring and Plexiglass Molds

The different developed setups were used to perform pulse tests on some soil samples in a large oedometric ring (H=35.3mm) and in two plexiglass molds (H=76.2mm & 95mm). These three setups have an internal diameter of 100.9mm (Table 5.6). Table 6.1 presents the different carried out experimental tests using these setups. These tests are to demonstrate the functionality of the built piezoelectric setups and provide some data for establishing correlations between some soil parameters and shear wave velocity. In addition, they can be used to support deriving a general equation for V_s. The input and output signals for these tests and their analyses are given in Appendix C.

Table 6.1 The Carried out Tests in the Large Oedometer Ring and in Plexiglass Molds.

Test No.	Laboratory Setup	Piezo-electric Setup	Soil Type	Specific Gravity (G_s)	Water Content (W_c)	Initial Voids Ratio
47	A	7	Standard Ottawa Sand (C-109)	2.65	0	0.69
41	D	7	Standard Ottawa Sand (C-109)	2.65	0	0.53
46	D	8	Standard Ottawa Sand (C-109)	2.65	0	0.53
3	A	4	Milby Sand	2.65	0	0.375
40	C	7	Standard Ottawa Sand (C-109)	2.65	0	0.53

A compressibility test was carried out on the standard Ottawa sand (C-109) in the large oedometer cell (Setup A: Table 5.6). This sand has maximum and minimum voids ratios of 0.78 and 0.48, respectively. The sample was prepared by hand tamping and had an initial voids ratio of 0.69 and a dry unit weight of 1.57 t/m^3, giving a relative density of 30 %. Figure 6.5 introduces the one dimensional deformation curve of this test (Test 47). The setting pressure of all carried out tests is 6.13 kPa. The pulse velocity tests by piezoelectric rings were carried out at each stress increment of the test using Setup 7 (Appendix C introduces some of

the output signals and their interpretations). The pulse test is repeated at least three times with different input frequencies and/or input shape in order to obtain different sets of results. These results are analyzed using Wigner-Ville Analysis methods as well as by C.C., energy-rise time, phase velocity, group velocity methods in order to confirm that the shear wave on the output signal is correctly chosen, especially in the cases where there is an ambiguity in the test result. Figure 6.6 presents the variation of shear wave velocity of the loose Ottawa sand (C-109) with the applied vertical stress. The empirical equations of each of Hardin and Richart (1963), Hardin and Black (1968), Jamiolkowski et al. (1991) and Robertson (1995) were used to estimate the shear wave velocity. Robertson equation is based on isotropic triaxial tests on Ottawa sand (C-109). These equations employ the average effective stress (σ'_m) in computing V_s. Therefore, the angle of internal friction of loose Ottawa sand (ϕ = 33°) was used to calculate the horizontal confinement stress on soil at rest (K_o = 1-sinϕ). Figure 6.7 presents the relationship between shear wave velocity of the loose Ottawa sand (C-109) and average stress.

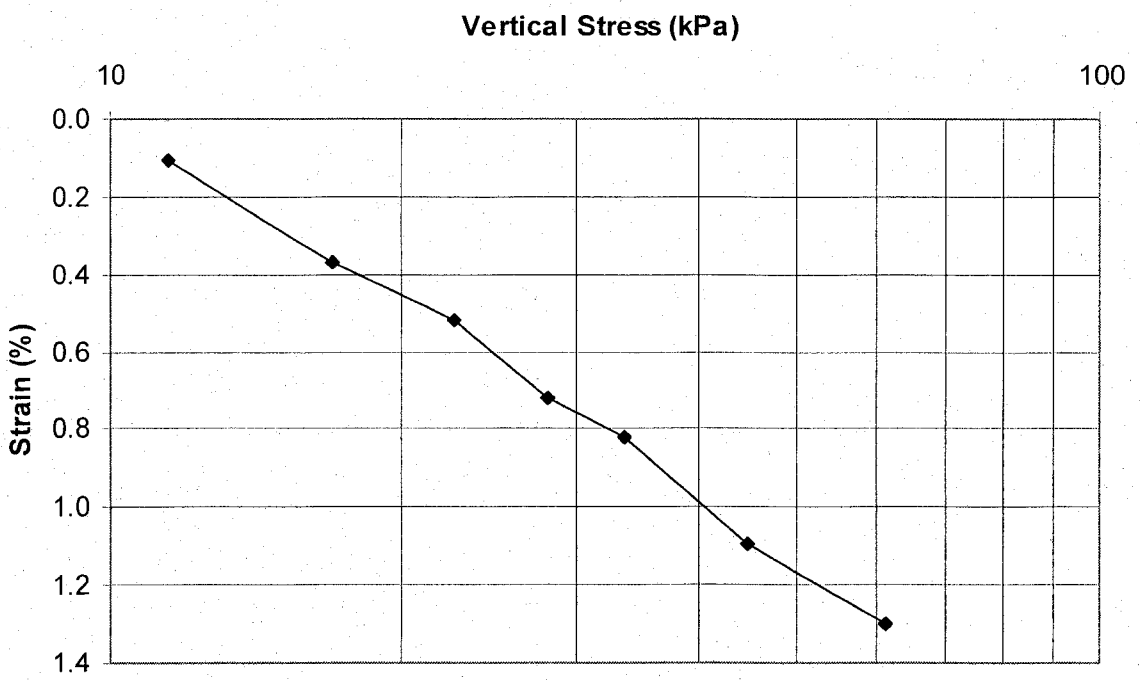

Figure 6.5 Stress-Strain Relationship for Loose Ottawa Sand (C-109); Test 47.

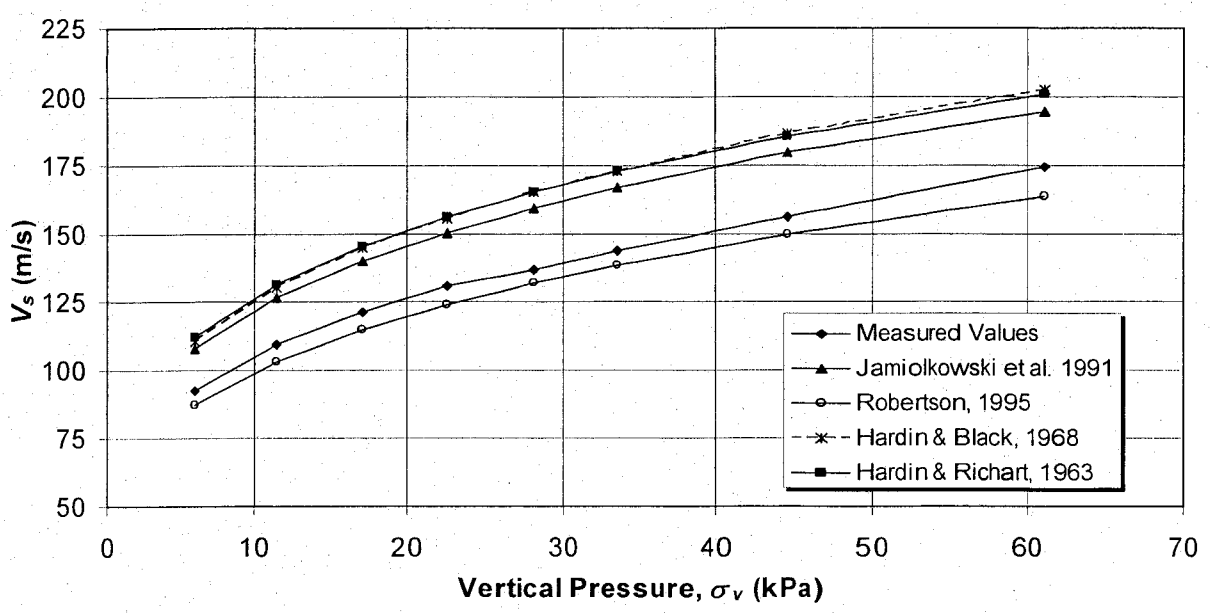

Figure 6.6 Variation of V_s with Vertical Stress for Loose Ottawa Sand (C-109) (Setup 7, Test-47, L_s = 35.3mm, D_r = 30%, e = 0.69, γ_d = 1.57).

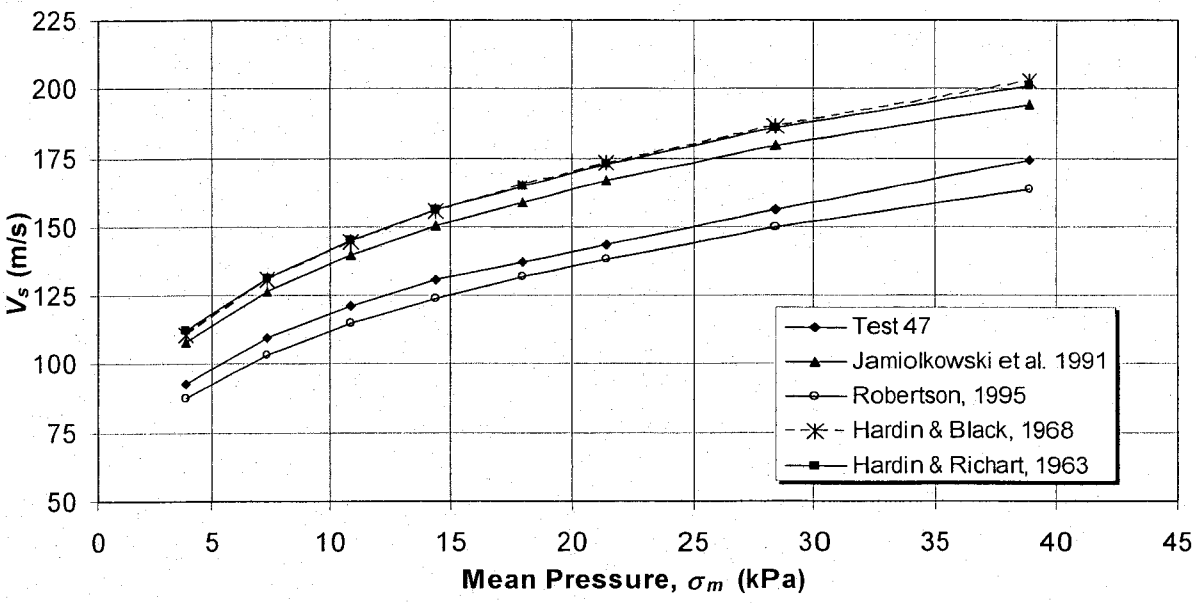

Figure 6.7 Variation of V_s with Average Stress for Loose Ottawa Sand (Test-47).

It can be realized that the results obtained in this study are close to Robertson's results while the other equations give higher V_s values. This is due to the fact that Robertson equation was obtained based on pulse tests on the same material (Ottawa sand). This somehow confirms the effect of grain size distribution and grains characteristics on V_s. The compression

wave velocity (V_p) was also measured in the carried out pulse tests. Figure 6.8 display the variation of compression wave velocity of the loose Ottawa sand (C-109) with the applied vertical stress. The p-wave velocity slightly depends on stress. Figure 6.9 presents the correlation equation between V_p and the vertical stress. The vertical stress exponent is 0.095 for the p-wave relationship while it is 0.27 for the s-wave relationship (Figure 6.10). The obtained stress-exponent for V_s relationship (0.27) is similar to Robertson et al. (1995) value (0.26). Figure 6.11 introduces the relationship between the average-stress normalized shear wave velocity (V_{s1}) and voids ratio (e). The stress exponent, n, was taken 0.25 for calculating the normalized V_s-values [$V_{s1} = V_s\ (P_a / \sigma_m')^n$]. The figure shows that V_{s1} increases slightly with decreasing voids ratio. It can be realized that the friction on the oedometer ring sides does not significantly affect the stresses on the soil as the obtained curve is almost parallel to Robertson curve. This can be explained considering that the soil is fairly loose and the applied stresses are small as well as the ratio of the height to diameter (H/D) of the sample is small (0.35).

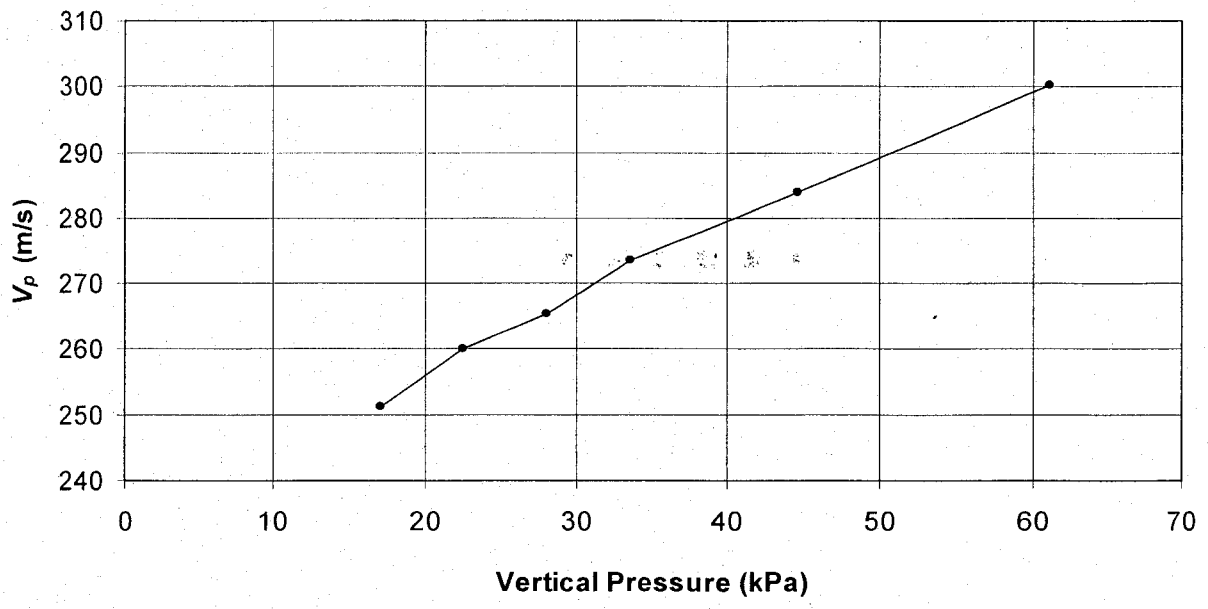

Figure 6.8 Variation of V_p with Vertical Stress for Loose Ottawa Sand (C-109); Test 47.

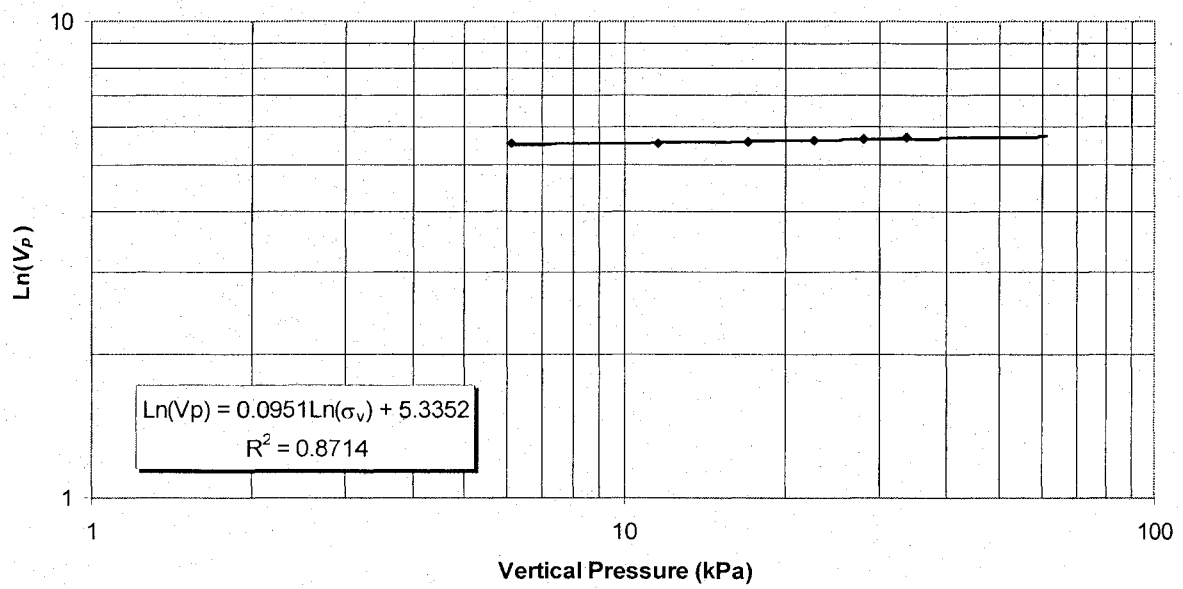

Figure 6.9 Relationship between V_p and Vertical Stress for Loose Ottawa Sand (C-109); Test 47.

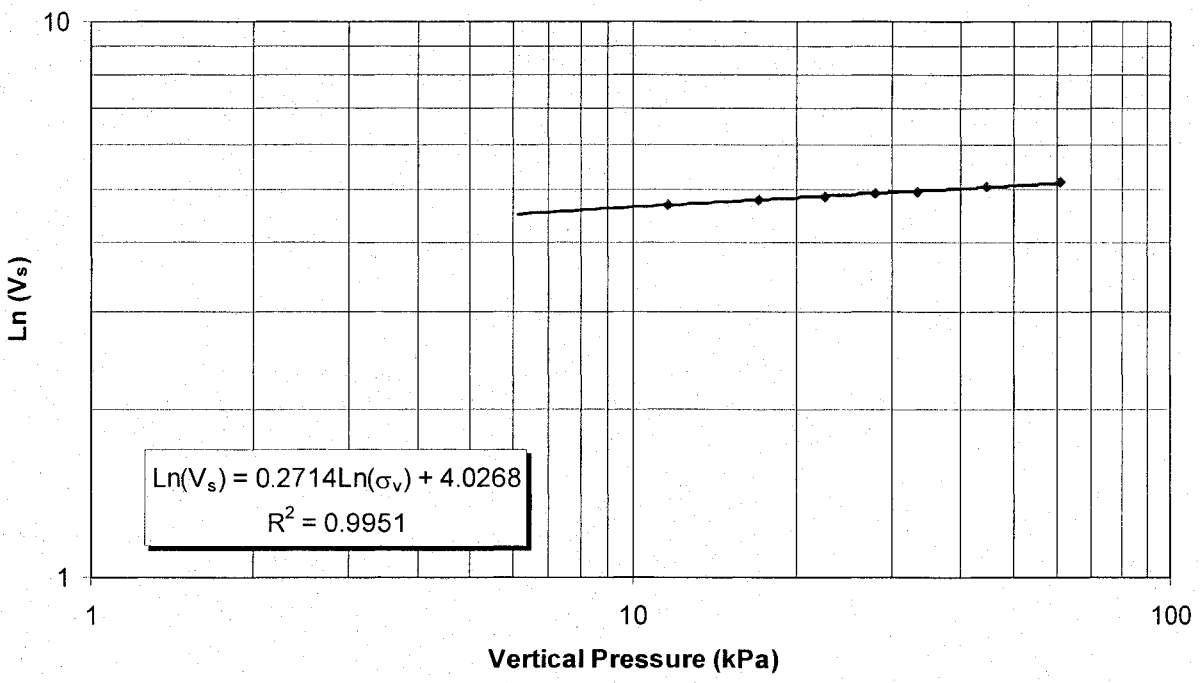

Figure 6.10 Relationship between V_s and Vertical Pressure for Loose Ottawa Sand (C-109); Test 47.

The shear wave velocity depends on the average stress (or at least on the stresses in the propagation and polarization directions; vertical and horizontal). Figure 6.12 presents the relationship between 'the normalized shear wave velocity using vertical stress', V_{s1}, and voids ratio. It can be seen that the normalized V_s values are smaller than the V_{s1} values normalized with respect to average stress. The difference is about 10% for the carried out tests and about 12 % for the estimated values according to Robertson's equation. This minor difference is attributed to the difference in the stress exponent, n, between Robertson's equation and the equation for obtained values (0.26 and 0.27, respectively). The Poisson's ratio was calculated from V_s and V_p values using theory of elasticity. Figure 6.13 displays the variation of Poisson's ratio with the applied pressure. The Poisson's ratio decreases with the increase of vertical stress in the oedometer cell where lateral stresses are at rest condition. The V_p measurement and the subsequently calculated Poisson's ratio are helpful in checking the accuracy of the calculated V_s values.

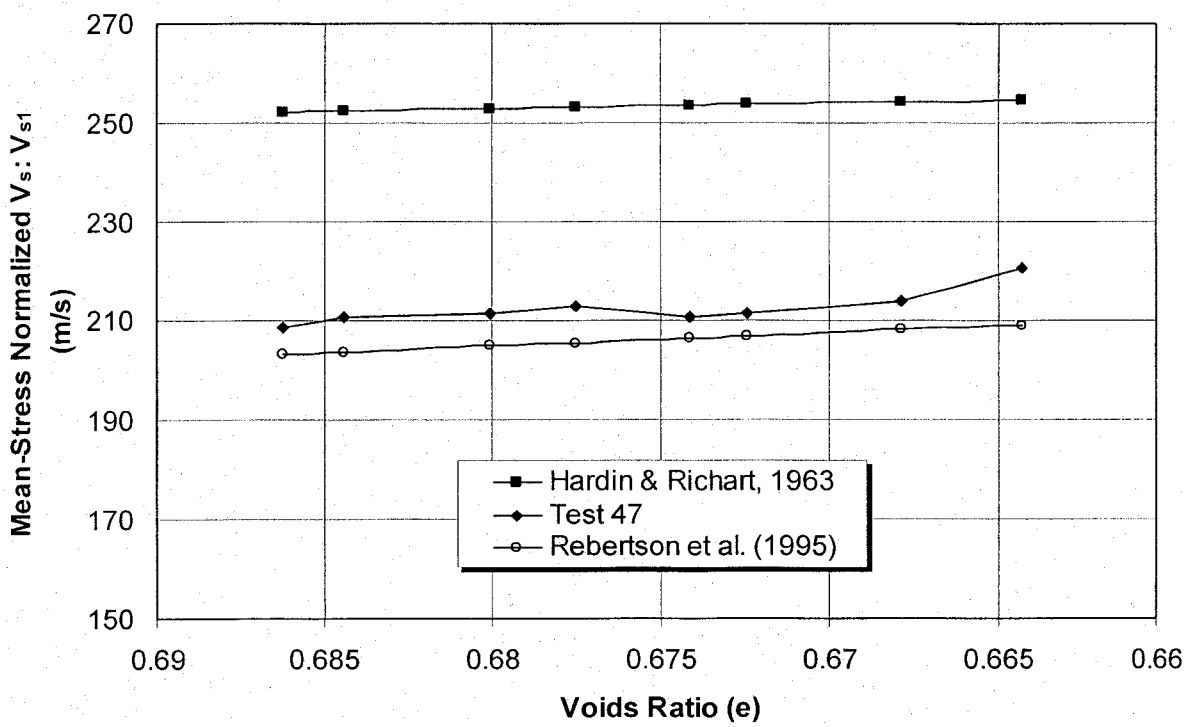

Figure 6.11 Relationship between V_{s1} and Voids Ratio for Loose Ottawa Sand (C-109); Test 47.

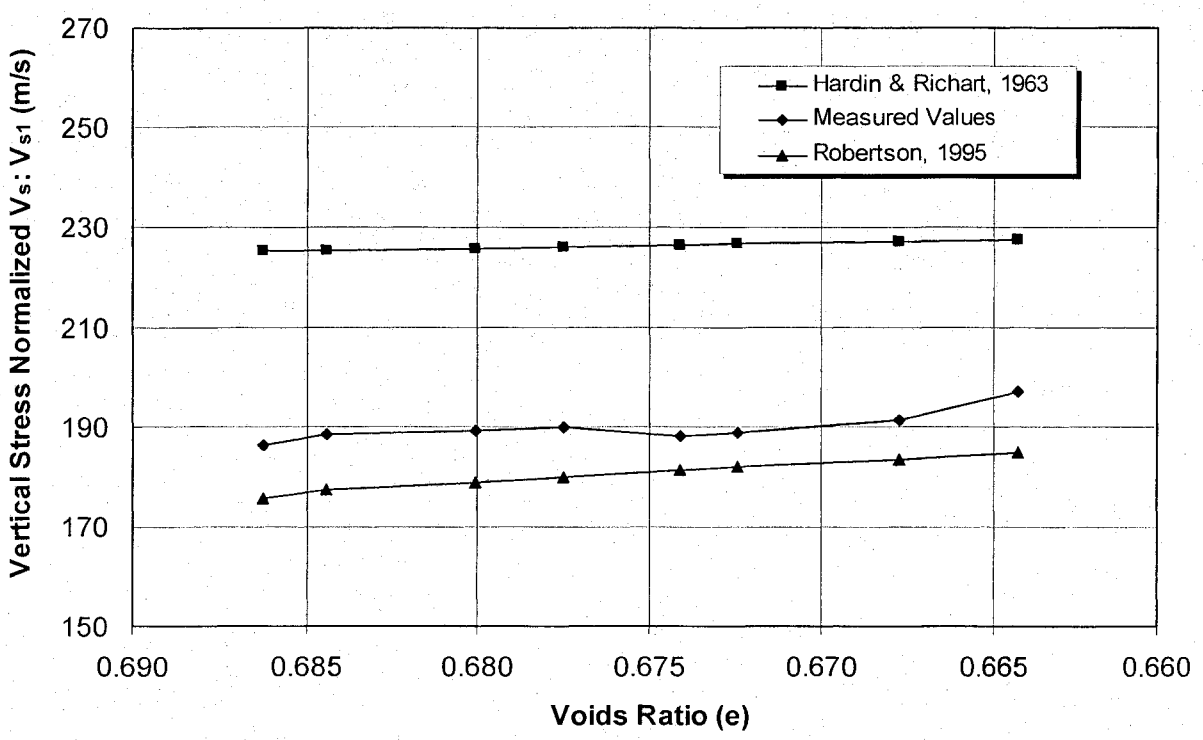

Figure 6.12 Relationship between V_{s1} and Voids Ratio for Loose Ottawa Sand (C-109); Test 47.

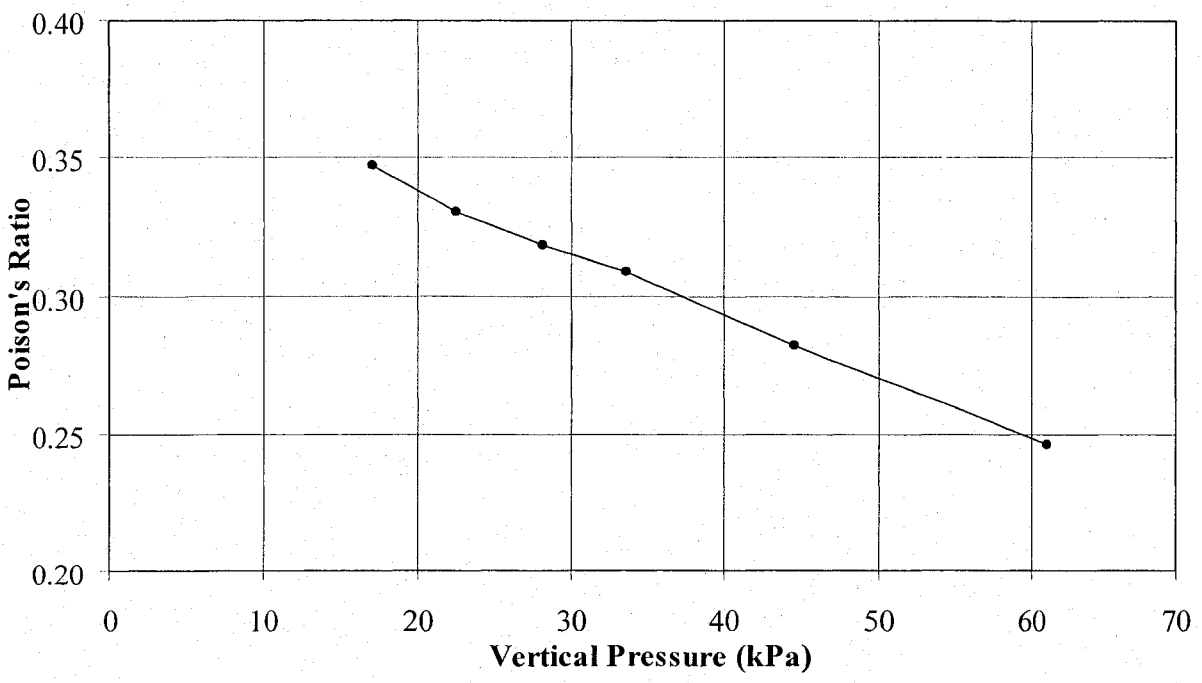

Figure 6.13 Relationship between Poisson's Ratio and Vertical Pressure for Loose Ottawa Sand (C-109); Test 47.

Other series of pulse tests were carried out in a Plexiglass mold of 95mm-length and 100.9mm-diameter (Table 6.1). Tests 41 and 46 were carried out on two dry samples of Ottawa sand (C-109) at the same initial density (e = 0.53, γ_d = 1.73; D_r = 83%). The applied stress range in these two tests is much higher than that in Test 47. Test 41 was performed using Setup No. 7 while Test 46 was performed using Setup No. 8. The screen display from the pulse test interpretation software for the carried out pulse tests in Test 46 are presented in Appendix C. The results of Test 41 and Test 46 are shown in Figure 6.14. Although each test was carried out with a different setup, the measured V_s values are practically identical. This shows the compatibility of the measurements by piezoelectric ring actuators. Hence, the following analysis will be carried out only on results of Test 46.

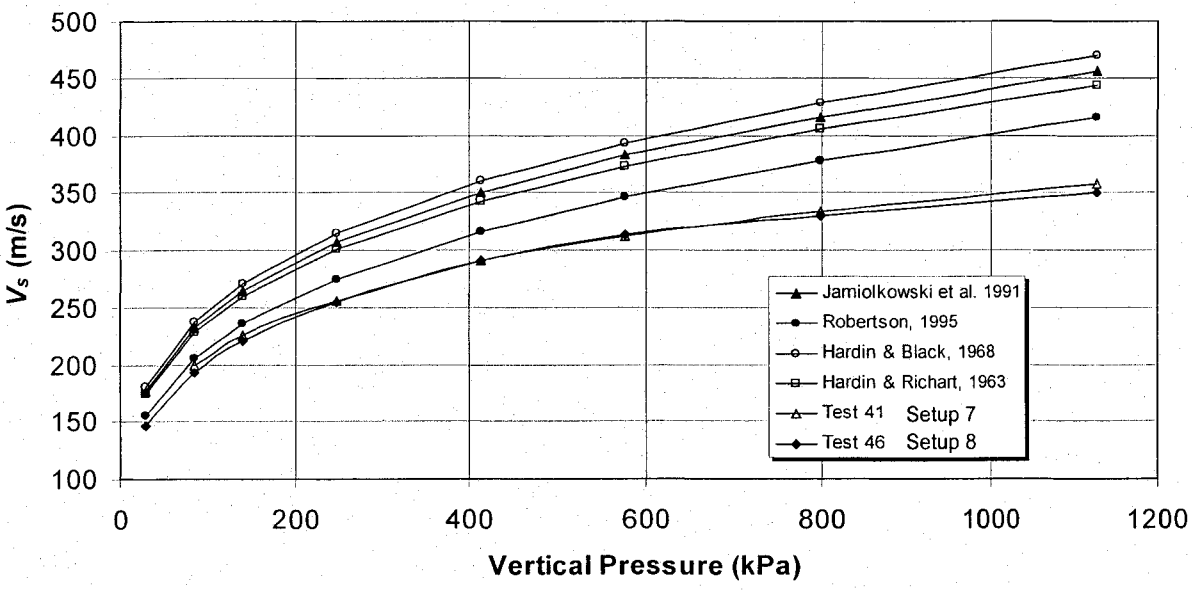

Figure 6.14 Ottawa Sand (C-109) (Test-46, Setup 8, L_s = 95mm, D_r = 83%, e = 0.53, γ_d = 1.73 t/m^3).

It can be realized on this test that the measured values diverge from the estimated values by Robertson equation by increasing the vertical stress. The difference between the measured and estimated values is 6.5% at the end of Test 47 (at a pressure of 61.1 kPa) while it is 19% at the end of Test 46 (at a pressure of 1128 kPa). This is due to the friction between the soil and the mold sides which is more pronounced in Test 46 as the mold is much longer. The friction reduces the stresses transmitted to soil and consequently it reduces the measured V_s. Figure 6.15 displays the variation of "the shear wave velocity normalized to the vertical stress" with

the applied pressure. It can be seen that this relationship is almost horizontal (no dependency) except at high stresses where the friction stresses affect the measured V_s. The same effect exists on the relationship between the voids ratio and V_s (Figure 6.16). When the normalized V_s values (V_{s1}) are drawn against the voids ratio, a slight increase of V_{s1} by decreasing the voids ratio is recorded for the small voids ratio change during the test (Figure 6.17).

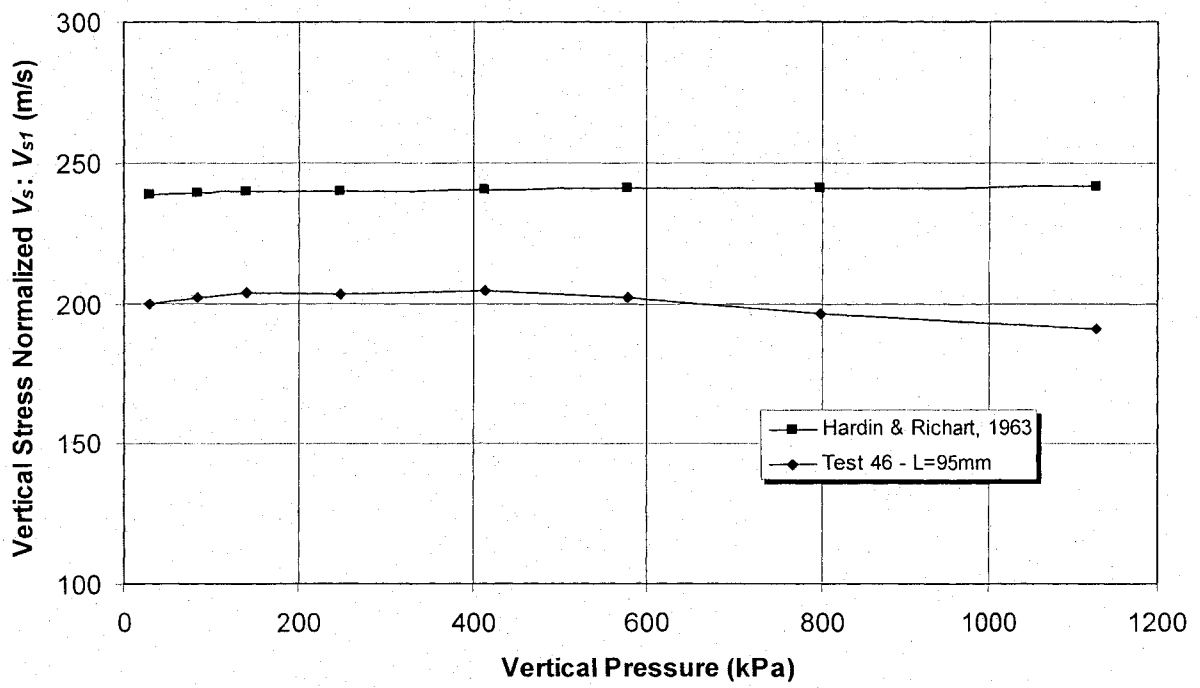

Figure 6.15 Normalized V_s for Ottawa Sand (C-109) (Test-46, L_s = 95mm, D_r = 83%, e = 0.53, γ_d = 1.73).

Figure 6.18 introduces the deformation curve of a compressibility test on a dense air-dried Milby sand sample in an oedometer cell of 35.3mm-height (Test 3). The sample was prepared by hand tamping and had an initial voids ratio of 0.375 and a dry unit weight of 1.928 t/m^3. The piezoelectric ring actuators Setup No. 4 was used to carry out this test (Chapter 6). The grain size distribution of Milby sand is shown on Figure 5.9 and its grain size characteristics are found in Table 5.5. The pulse velocity tests were carried out at each stress increment. This test is repeated at almost same conditions and the same V_s-values were obtained (Figure 6.19) under the different pressures. The compression wave velocity was measured in each test (Figure 6.20).

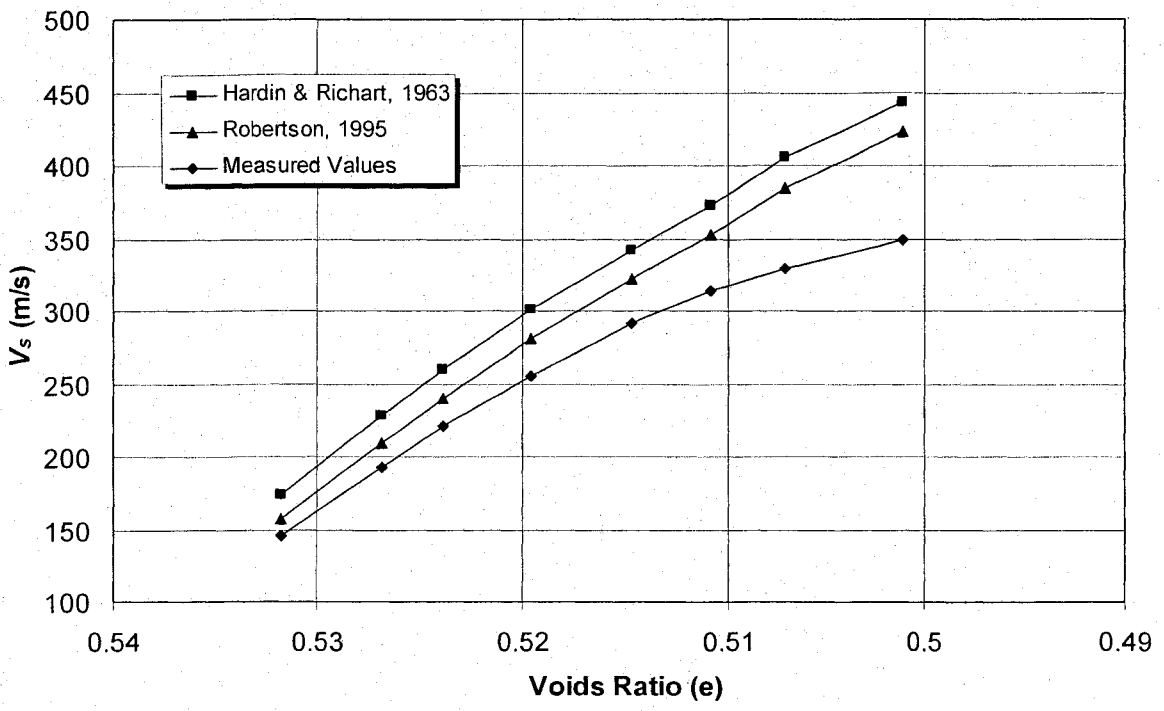

Figure 6.16 Variation of V_s with Voids Ratio for Ottawa Sand (C-109) (Test-46, L_s = 95mm, D_r = 83%, e = 0.53, γ_d = 1.73).

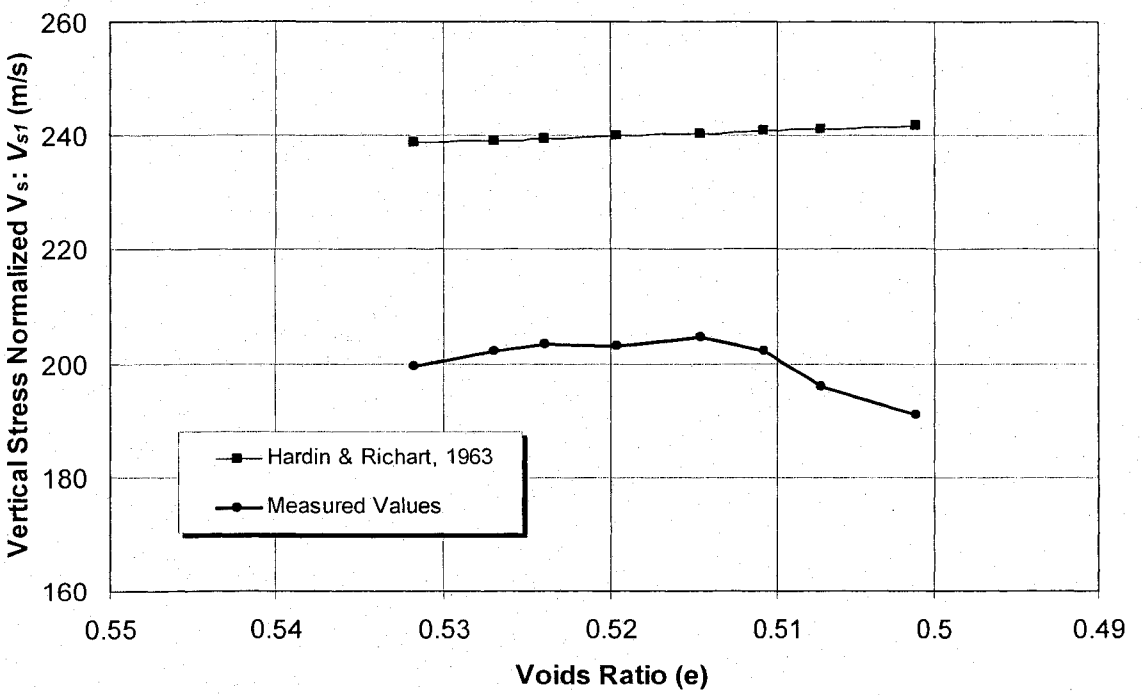

Figure 6.17 V_{s1} versus Voids Ratio for Ottawa Sand (Test-46, L_s = 95mm, D_r = 83%, e = 0.53, γ_d = 1.73).

The relation between the shear wave velocity and vertical applied pressure take the shape of a logarithmic curve. When this relationship is drawn between the vertical stress to the power of 0.25 and V_s, it becomes a strait line (Figure 6.21). These results agree well with the empirical equations for estimating V_s for sands which commonly assume n value equals 0.25. The Poisson's ratio could be calculated from V_s and V_p values using theory of elasticity. Figure 6.22 displays variation of Poisson's ratio with the applied pressure. Poisson's ratio decreases by increasing the vertical stress at rest condition ($K = K_o$). The values of Poisson's ratio at unloading condition are smaller than those at loading condition due to the increase of soil stiffness. The Poisson's ratio values reflect the condition of lateral stresses on the cell's wall.

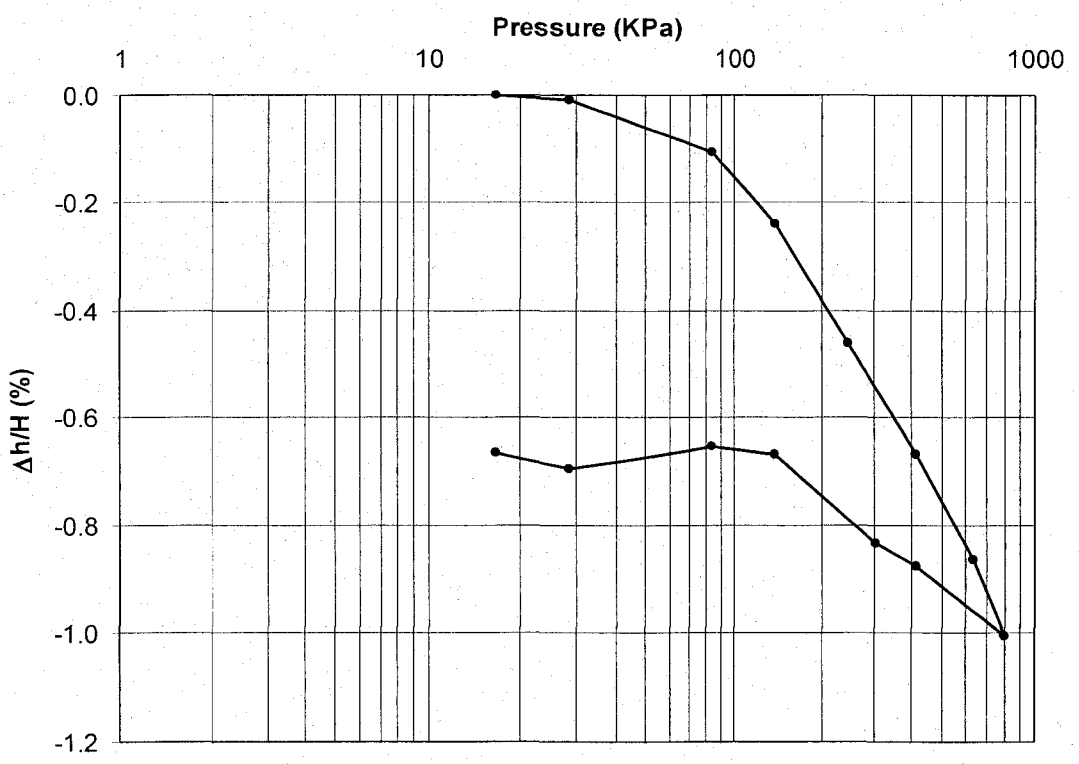

Figure 6.18 The Deformation Curve of Milby Sand in an Oedometer Ring (Test 3).

The elastic shear and Young's moduli were calculated for Test 3 and were drawn against the voids ratio (Figure 6.23). The small strain Young's Modulus (E_o) is calculated using the shear wave velocity and Poisson's Ratio. It can be realized that the variation of voids ratio is small as the initial dry density of the sample is high. This is also revealed from Figure

6.18 (the vertical strains are small). The Young's modulus is more than double of the shear modulus. The wave velocities of soil in unloading portion of the test are higher than those in the loading phase. This is due to the lower voids ratio of soil in the unloading phase which is attributed to the unrecoverable strains in soil. The soil ceases to retrieve the volumetric deformations at a vertical stress of about 100 kPa. The side friction between the soil and the cell wall controls this phenomenon.

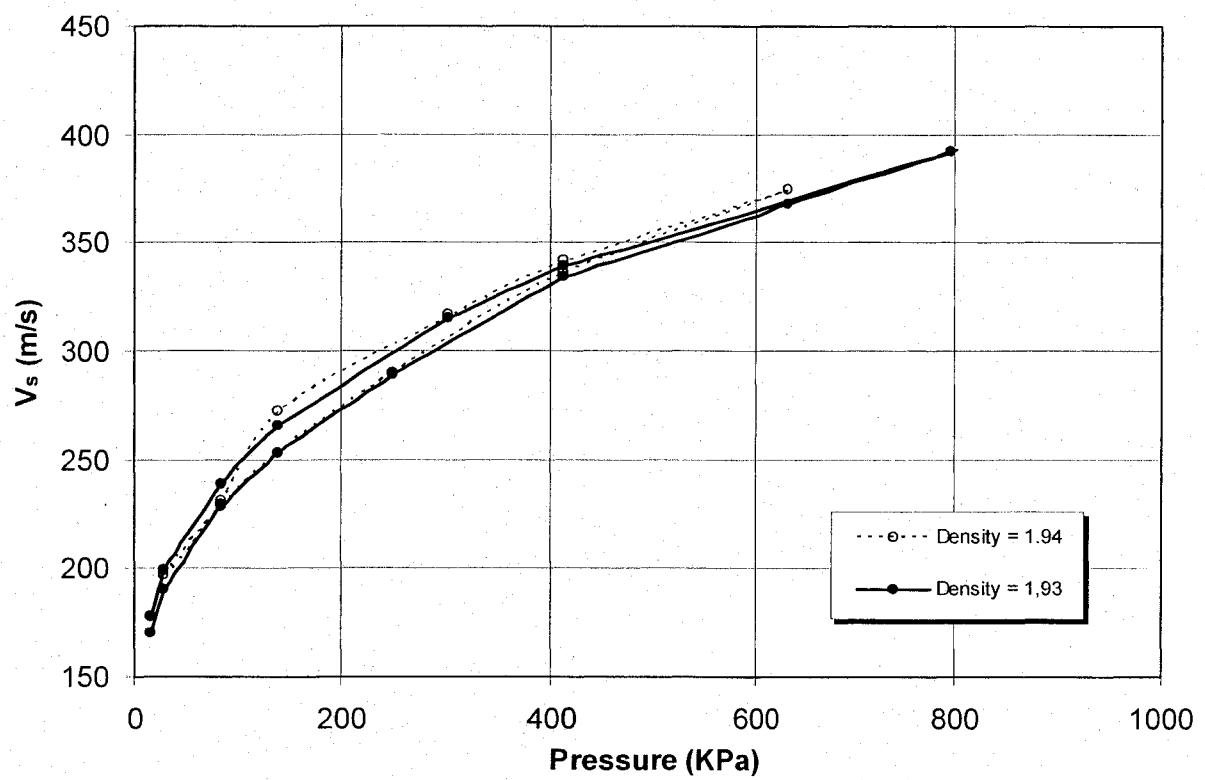

Figure 6.19 Repeated Test Using Setup 4 for a Dry Milby Sand Sample in Oedometer Cell Showing the Variation of V_s with Vertical Stress (Test 3).

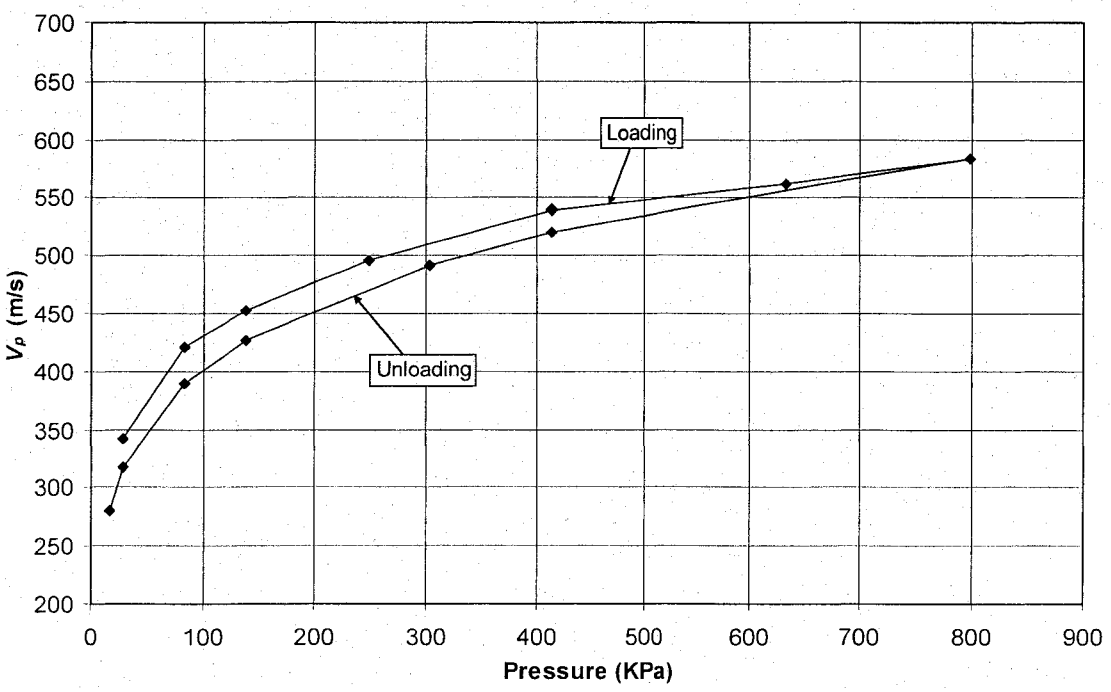

Figure 6.20 Variation of V_p with Vertical Stress for Milby Sand in Oedometer Cell.

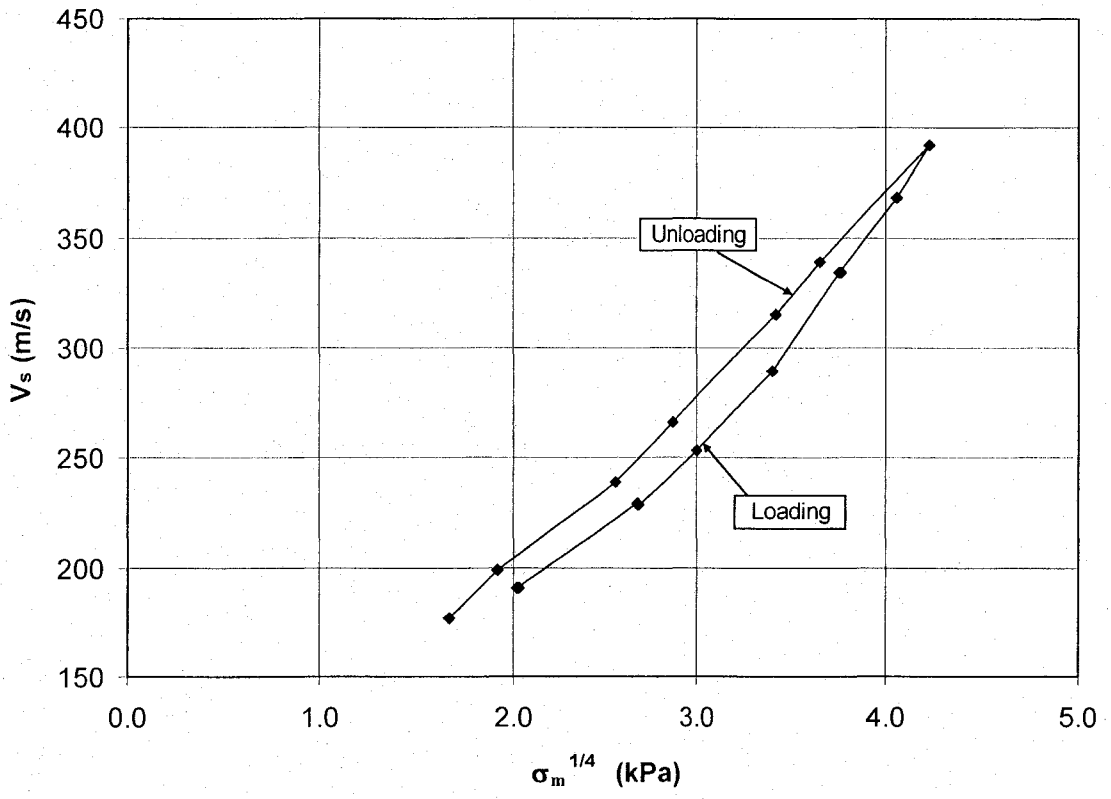

Figure 6.21 Variation of V_s with $\sigma_v^{0.25}$ for Milby Sand (Test 3).

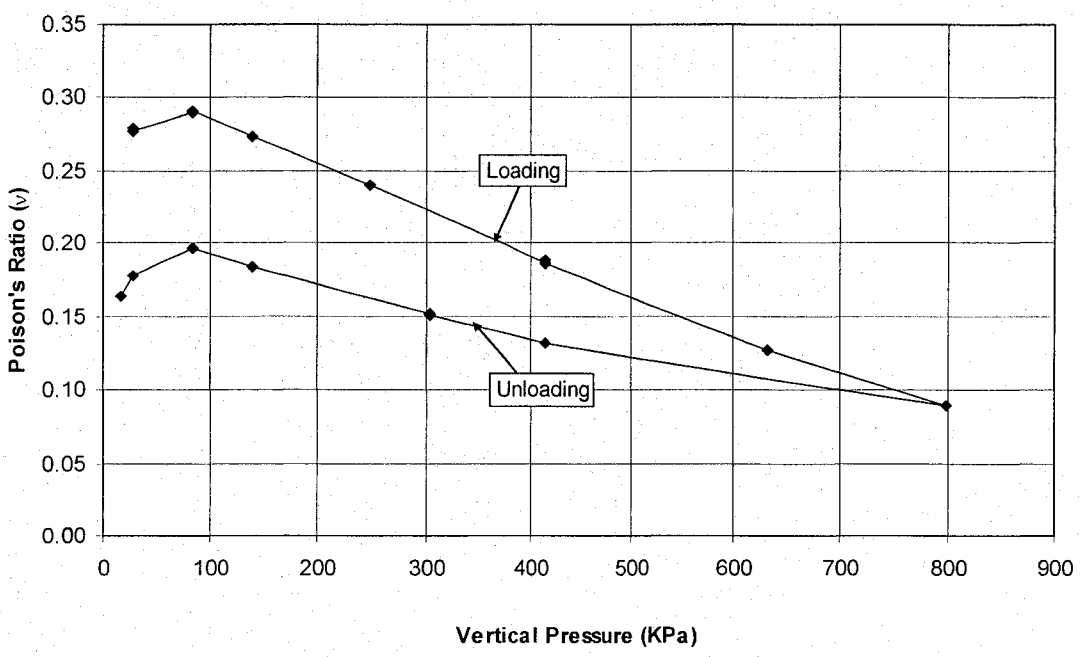

Figure 6.22Variation of Poisson's Ratio with Vertical Stress for Milby Sand.

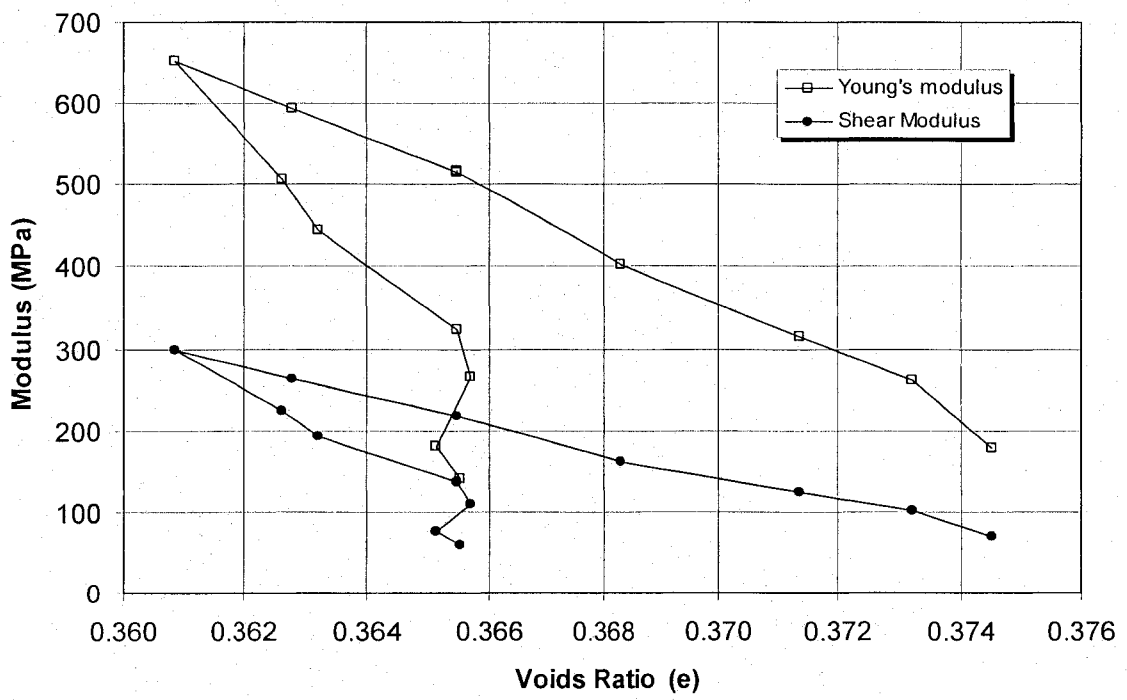

Figure 6.23 Relationship between Elastic Modulus and Voids ratio for Ottawa Sand (Test No. 3).

Pulse tests were carried out during a compressibility test on the standard Ottawa sand (C-109). The grain size distribution curves of the tested sands are displayed on Figures 5.9 and 5.10. Test 40 was carried out using Setup 7 in a Plexiglass mold of 76.2mm-length (Table 6.1). The soil had a dry density of 1.73 (W_c = 0, D_r = 83%, e = 0.53). This test is quite useful as it introduces a third mold height so that the side friction is deeply investigated. Figure 6.24 shows the pulse tests results with the estimated values using some empirical equations. The relationship between the voids ratio and V_s is plotted on Figure 6.25 with the calculated values from both Hardin and Richart (1963) and Robertson (1995) equations. The obtained results agree well with the estimated values. If the measured values are compared to those of Test 46 which has the same relative density (Figure 6.16), it shows that Test 40 gives higher V_s values than Test 46. The difference between the two tests is the sample height; the sample height in Test 40 is 76.2mm while it is 95mm in test 46. This difference can be understood by examining the deformation curves for Tests 46 and 40 (Figure 6.26). The soil in the shorter mold deformed more than the soil in the other mold. This is attributed to the side friction between soil and mold. Hence, the soil in the shorter mold (Test 40) experienced more stresses than the soil in Test 46. Consequently, V_s values of Test 40 are higher than those of Test 46. Moreover, the estimated shear wave velocities for Test 40 are higher than those for Test 46 at the same voids ratio (Figures 6.25 & 6.16). This can be explained considering that, at a certain

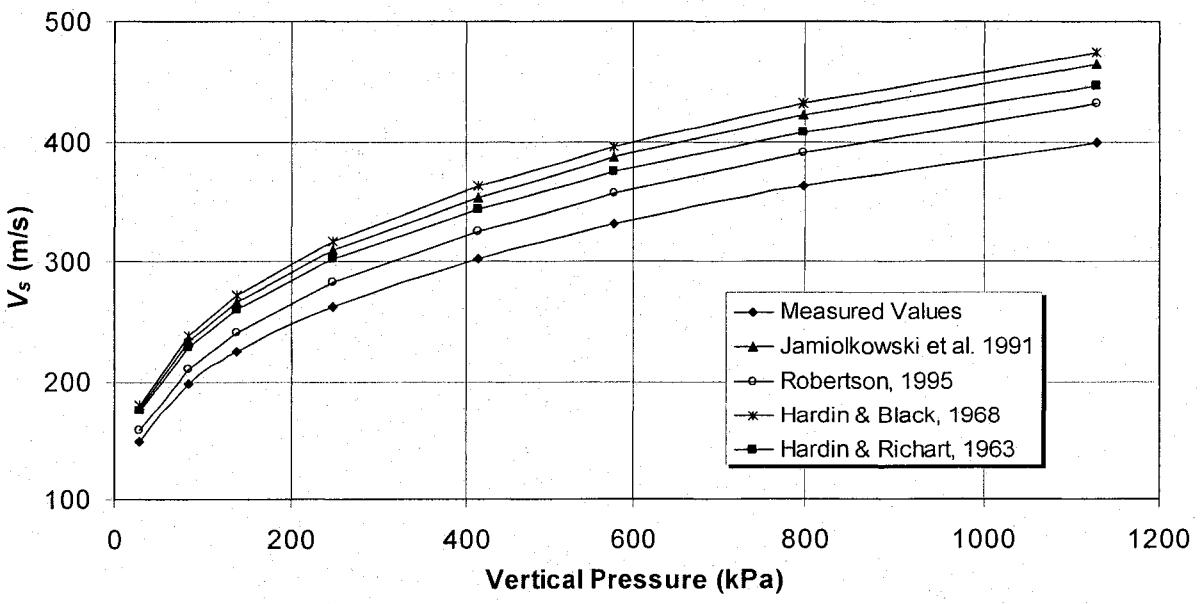

Figure 6.24 Variation of V_s with Vertical Pressure for Dense Ottawa Sand in Test 40.

voids ratio, the actual stresses on soil differ from test to another depending on the test conditions. The estimated V_s value depends primarily on voids ratio and mean effective stress. On the other hand, at a certain stress condition the V_s varies according to voids ratio. In other words, many combinations of the average stress and voids ratio may result in the same V_s value. Therefore, the comparison between results should be carried out in terms of the normalized shear wave velocity (V_{s1}) and voids ratio. Figure 6.27 displays the relationship between V_{s1} and voids ratio for results of Test 40 as well as for the estimated V_s values from some empirical equations. The shear wave velocity is normalized to the vertical stress. The normalized velocity (V_{s1}) increases by increasing the dry density of soil (decreasing voids ratio). Figure 6.28 presents the relationship between voids ratio and the average-stress normalized shear wave velocity (V_{s1}). The vertical-stress normalized shear wave velocity is lower than the average-stress normalized velocity by about 13%. The estimated V_{s1} values using Hardin and Richart (1963) and Robertson (1995) equations are higher.

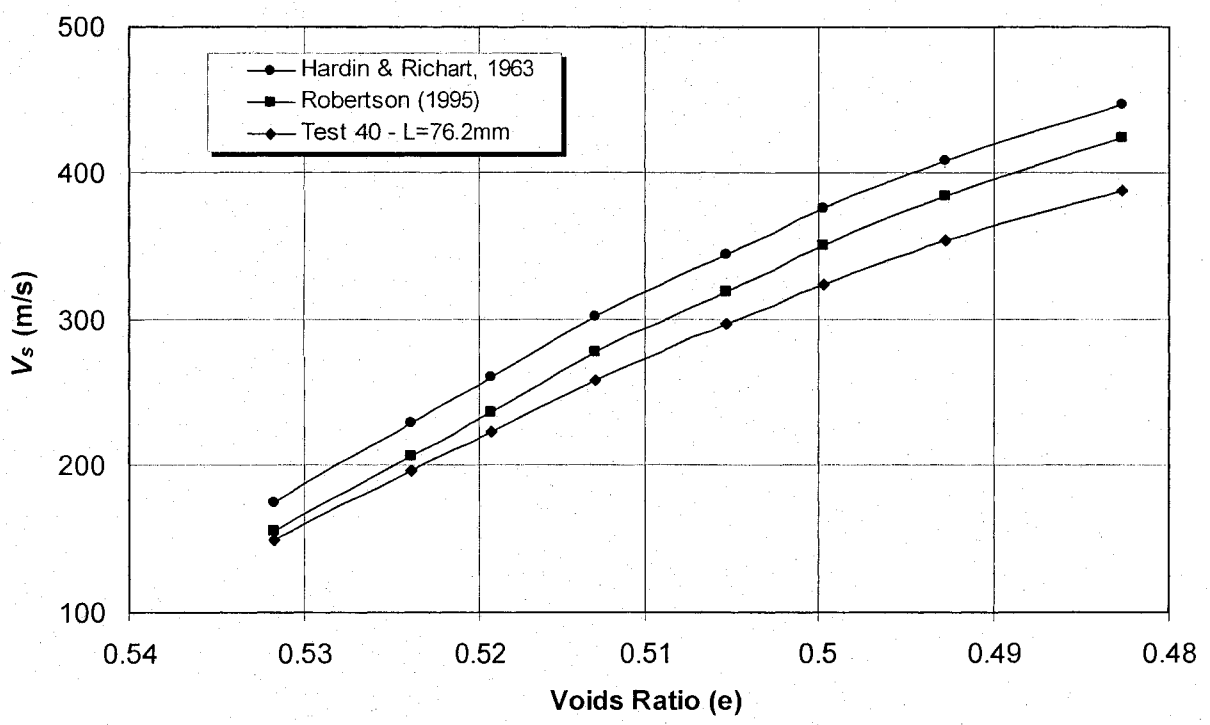

Figure 6.25 Variation of V_s with Voids Ratio in Test 40.

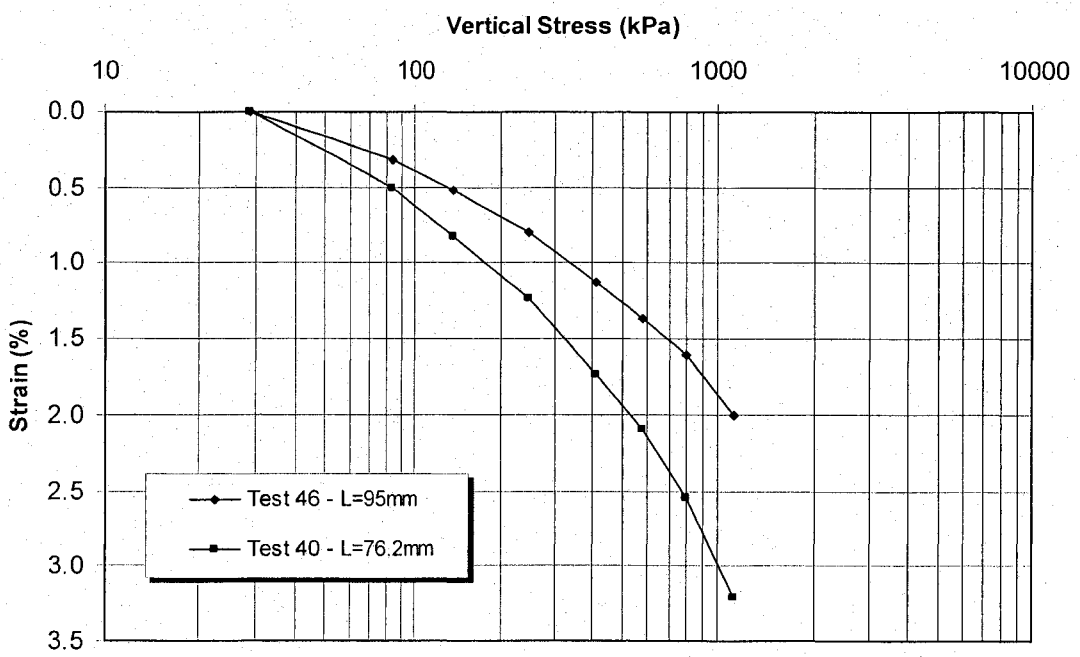

Figure 6.26 One-Dimensional Deformation Curves for Tests 46 and 40.

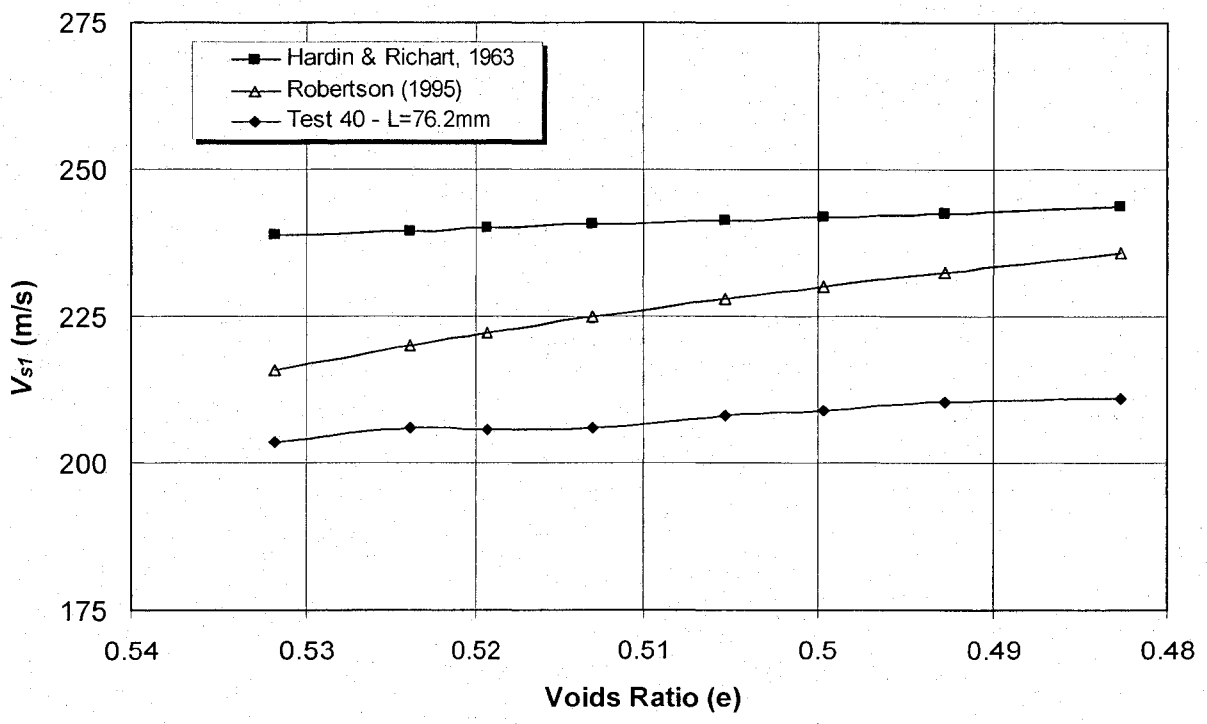

Figure 6.27 Relationship between V_{s1} and Voids Ratio for Results of Test 40.

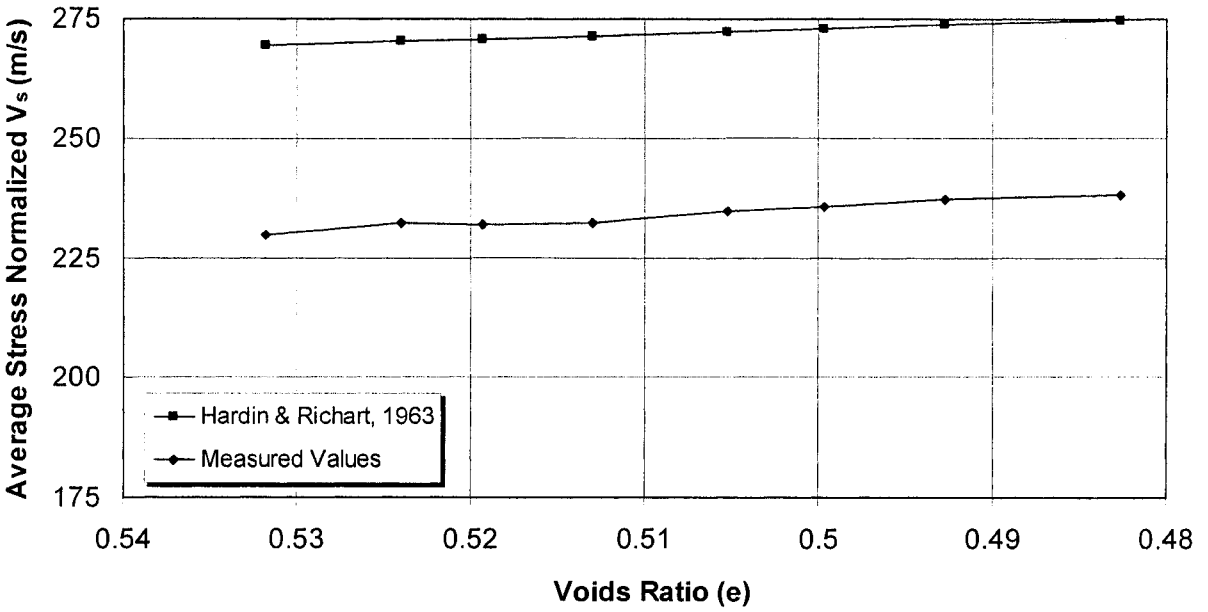

Figure 6.28 Relationship between Average Stress Normalized V_s and Voids Ratio for Results of Test 40.

6.4 Soil Compaction and Shear Wave Velocity

Some tests were carried out in this study to investigate characteristics of the compaction curve in terms of shear wave velocity and water content. Initially, two "compressibility and pulse" tests were carried out with Setup 7 (Tests 42 & 43) on dry LG4 and one test with Setup 8 (Test 49) on partially saturated LG4 in order to show the effect of density and suction forces on shear wave velocity. Then two complete Proctor compaction tests were carried out on two different soil types where the shear wave velocity was measured for each Proctor-sample at three different pressures. Table 6.2 summarizes these tests. The input and output signals for these tests and their analyses are given in Appendix C. The grain size distribution of LG4 till (silty sand) is shown on Figure 5.10. The soil sample of Test 49 had a water content of 5.0%. It was prepared according to the procedures of the modified Proctor Test (D=101.5mm & L=115.5mm). The two samples of Tests 43 and 42 were prepared by hand tamping in two Plexiglass molds of 100.9mm-diameter. The samples lengths were 95-mm and 76.2-mm, respectively. The dry densities of the samples were comparable (2.03, 1.984 & 1.98 t/m^3 for Tests 49, 43 & 42, respectively). Figure 6.29 presents the one dimensional stress-strain relationship for the three samples. The deformation of the soil sample increases with the

decrease of sample's length. A smaller compressibility is observed for the partially saturated sample (Test 49) due to suction.

Table 6.2 The Carried out Ring Actuators Pulse Tests on Compacted Soils.

Test No.	Laboratory Setup	Piezo-electric Setup	Soil Type	Specific Gravity (G_s)	Water Content (W_c)	Initial Voids Ratio
49	B	8	LG4 till	2.69	5.0	0.33
43	D	7	LG4 till	2.69	0	0.335
42	C	7	LG4 till	2.69	0	0.34
59	B	4–8	LG4 till	2.69	1.3 – 7.6	0.275 – 0.36
56	B	4	Concrete Sand	2.65	4.7 – 15.6	0.42 – 0.47

The variations of V_s with the applied pressure for the three tests are shown in Figure 6.30. As expected, the velocity increases with increasing applied pressure. The V_s-variation with pressure takes the same trend for the three samples. The partially saturated sample in Test 49 had V_s values higher than the dry samples. The difference between V_s values in Test 49 and those in Test 42 varies from 82% at the lowest pressure (29 kPa) to 26% at the highest applied pressure (798 kPa). This variation depends on soil suction, applied stresses and voids ratio. The V_s-increase is higher at low pressures than at high pressures. It is believed that the suction forces are much higher than the actual stresses at low pressures and the voids ratio is high while at high pressures, the suction stresses are lower than (or comparable to) the actual stresses on soil.

The variation of V_{s1} with vertical pressure and voids ratio for the three LG4 till samples in Tests 42, 43 & 49 are presented in Figures 6.31 & 6.32. There is a slight increase of V_{s1} with the vertical pressure. This attributed to the decrease in voids ratio during loading. The normalized velocity (V_{s1}) increase with decreasing voids ratio. The decrease of voids ratio for the partially saturated soil is much less than that for the dry samples for the same pressure-variation. The normalized shear wave velocity (V_{s1}) for this sample is much higher than the other two samples, especially at low stresses. The measured V_s values for a partially saturated soil are higher than those for a soil without suction.

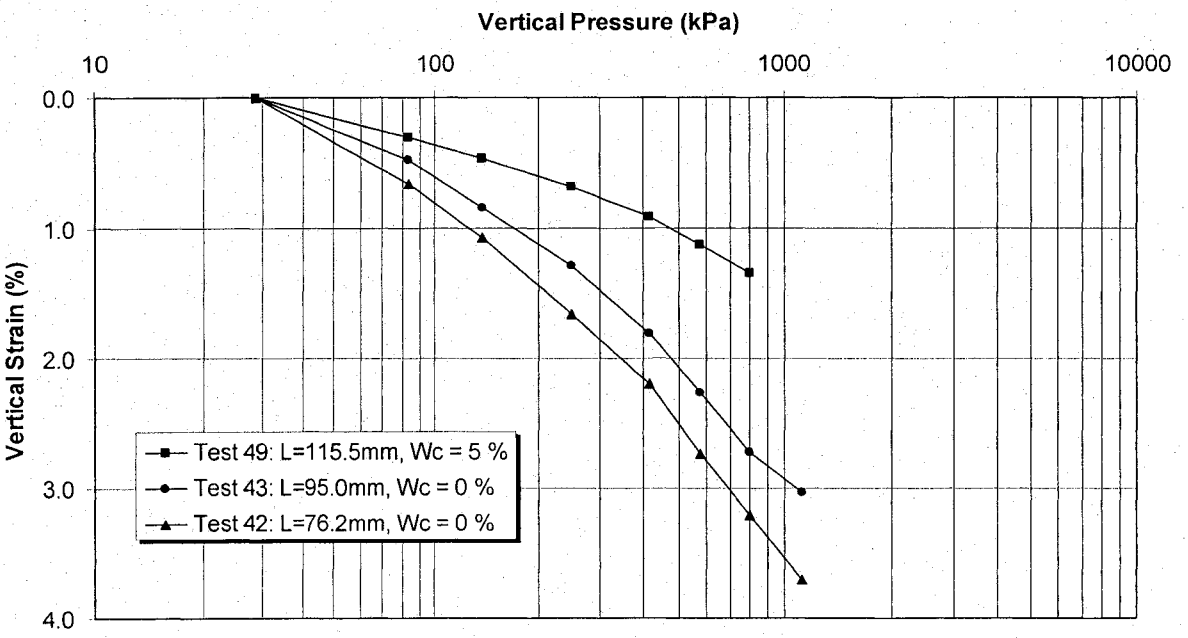

Figure 6.29 Stress-Strain Relationships for LG4 Till in Tests 49, 43 & 42.

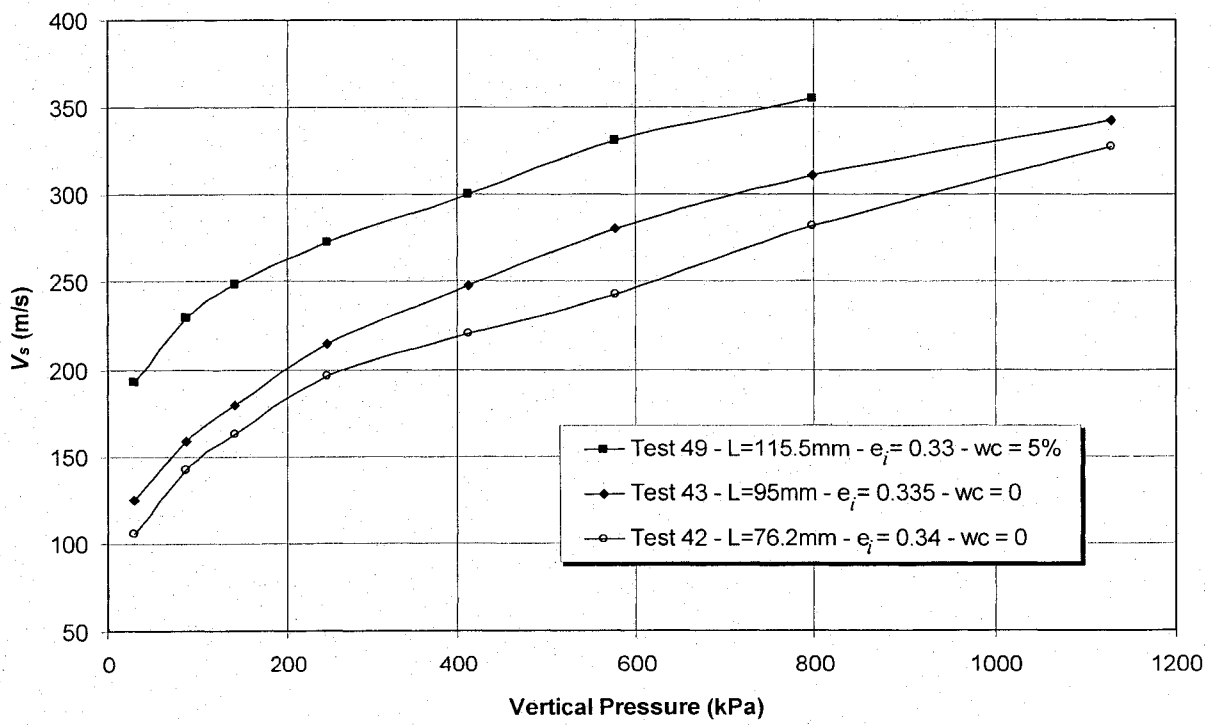

Figure 6.30 Relationships between V_s and Vertical Pressure for LG4 Till Samples.

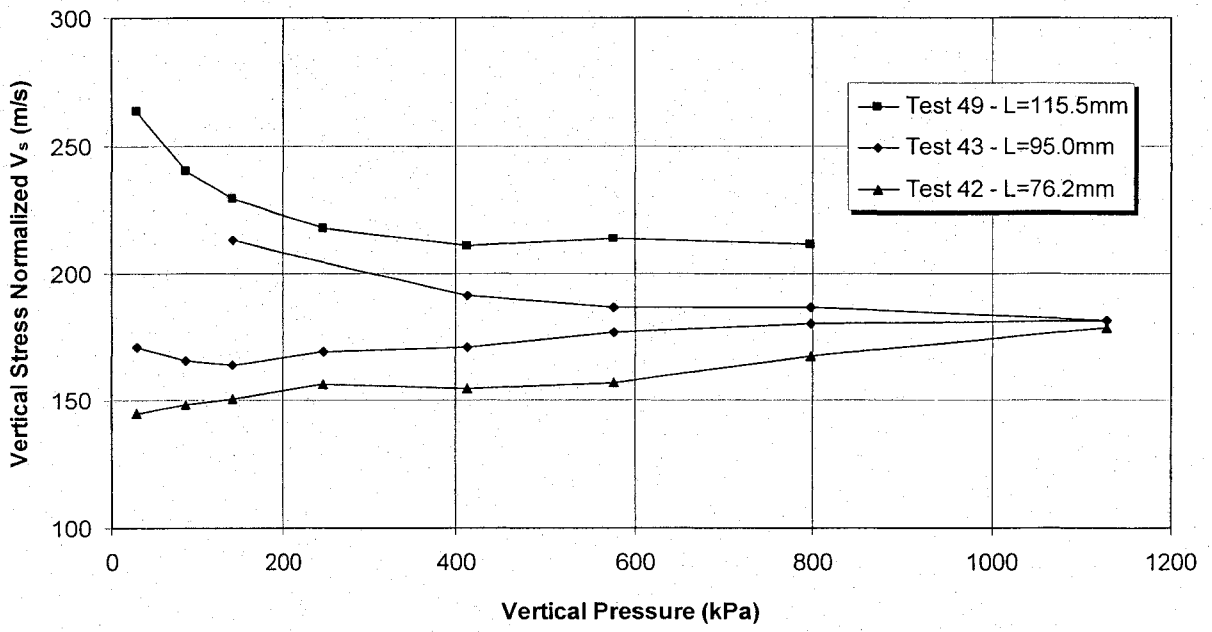

Figure 6.31 Variation of V_{s1} with Vertical Pressure for Proctor Samples of LG4 Till (Tests 42, 43 and 49).

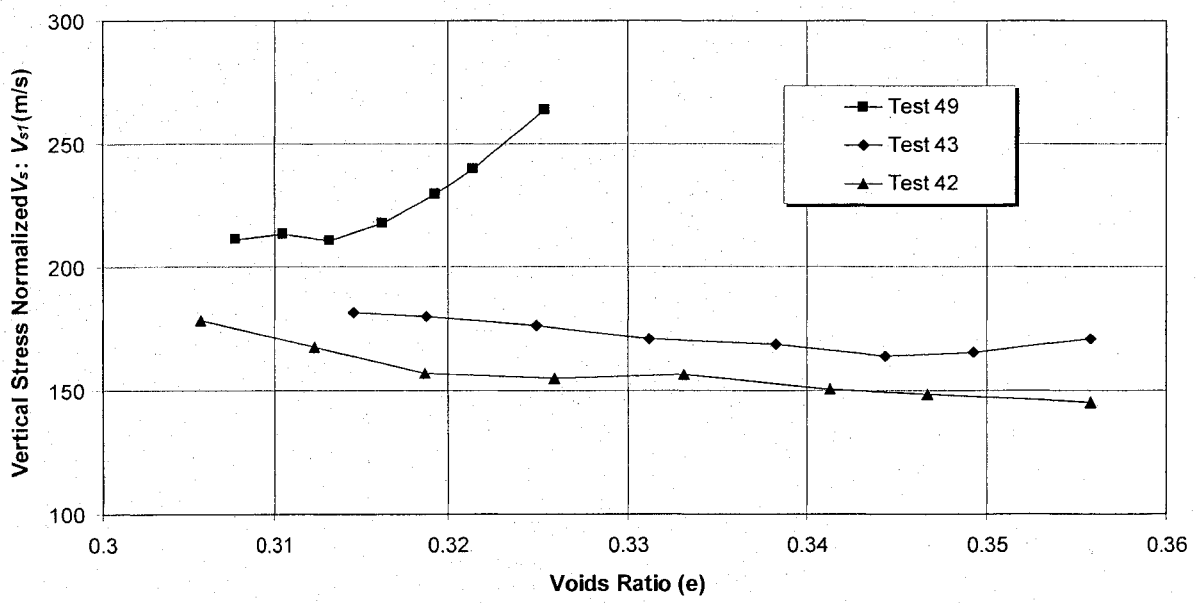

Figure 6.32 Variation of V_{s1} with Voids Ratio for LG4 Till Proctor Samples in Tests 42, 43 and 49.

A complete standard Proctor Test was carried out on LG4 (Test 59) and the pulse tests were carried out on each sample at three different vertical stresses. Figure 6.33 presents the Proctor curves as well as the zero-air voids line. Eleven samples were prepared to draw this

relationship. The degree of saturation was calculated for each sample and is written on the Figure 6.33. The optimum compaction water content for LG4 is 6.25% which corresponds to a maximum dry density of 2.08 t/m^3 (G_s of LG4 equals 2.65). Setups 4 to 8 were used to measure the shear wave velocities in this test. The variation of shear wave velocity with water content is plotted on Figure 6.34. The optimum water content which corresponds to the highest shear wave velocity is 5.5%. Hence, the V_s optimum water content is less than the density optimum water content. It can be realized that the dry-of-optimum side is having higher shear wave velocities than the wet-of-optimum side. There is a steep decrease in V_s behind the optimum water content. This means that compaction of soil at the dry-of-optimum side is better than the wet-of-optimum side. The V_s values at unloading are higher than at loading due to the decrease in voids ratio and the unreleased stresses after unloading. The shear modulus of soil was calculated and plotted against water content (Figure 6.35).

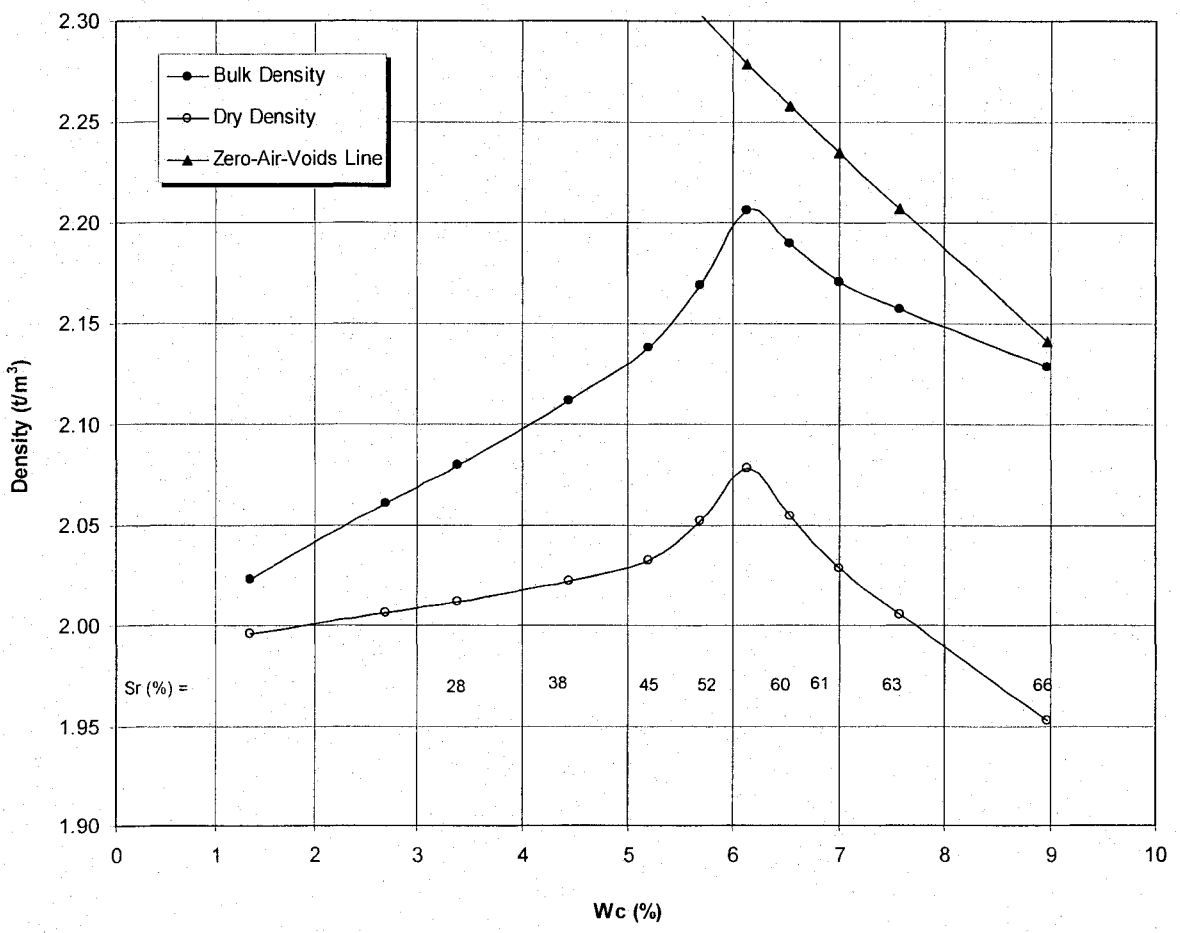

Figure 6.33 Standard Proctor Compaction Curves for LG4 Till.

The bulk unit weight of soil introduces a small difference in the shape of this relationship compared to V_s-W_c relationship. The variation of shear wave velocity with the applied pressure is shown in Figure 6.36 for each sample of the Proctor test. The trend of variation is the same for the eleven samples. As expected, the velocity increases by increasing the applied pressure. The variations of V_s with voids ratio at the different vertical stresses are presented in Figure 6.37. It can be seen that the maximum shear wave velocity is not at the minimum voids ratios. The normalized shear wave velocity to vertical stress is drawn against the water content (Figure 6.38). At the two lower pressures (11.63 & 33.63 kPa), V_{s1}-values are almost identical. At a pressure of 61.13 kPa, the normalized velocities are less than the normalized velocities at lower pressures. It is believed that the side friction between soil and mold causes this difference. Hence, measurements in Proctor Mold should be carried out at very low pressures (not exceeding about 35kPa for LG4). This means that side friction is more

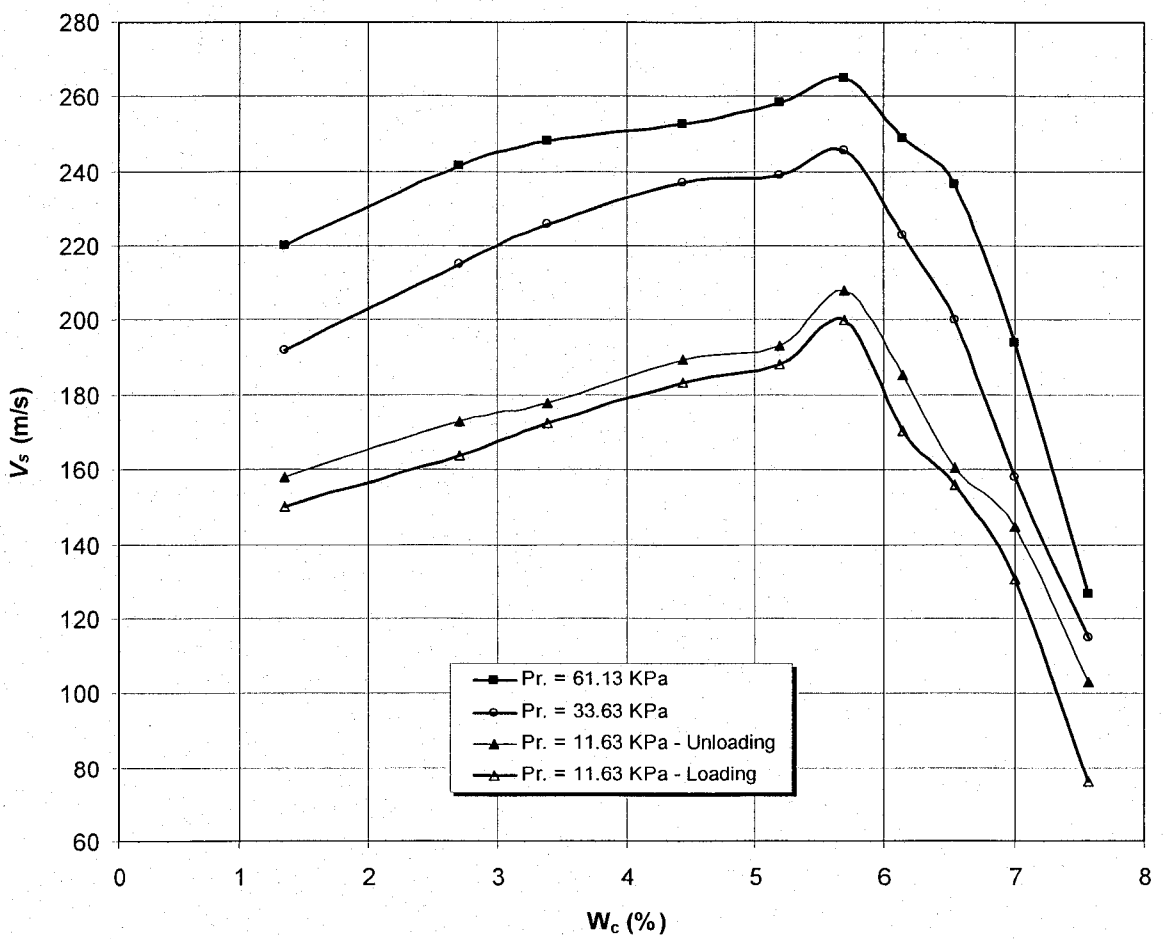

Figure 6.34 V_s - Compaction Curve for LG4 Till at Three Different Pressures.

mobilized when increasing the vertical pressure. Hence, the soil in the mold experience less stresses than the theoretically imposed pressures. Consequently, the measured V_s values are lower than expected, especially at high pressures. The loss in V_s increases by increasing the applied pressure. The pressures used in calculating V_{s1} are the theoretical stresses while the actual stresses are smaller. Therefore, the normalized V_s values decrease with increasing vertical pressure in the Proctor mold.

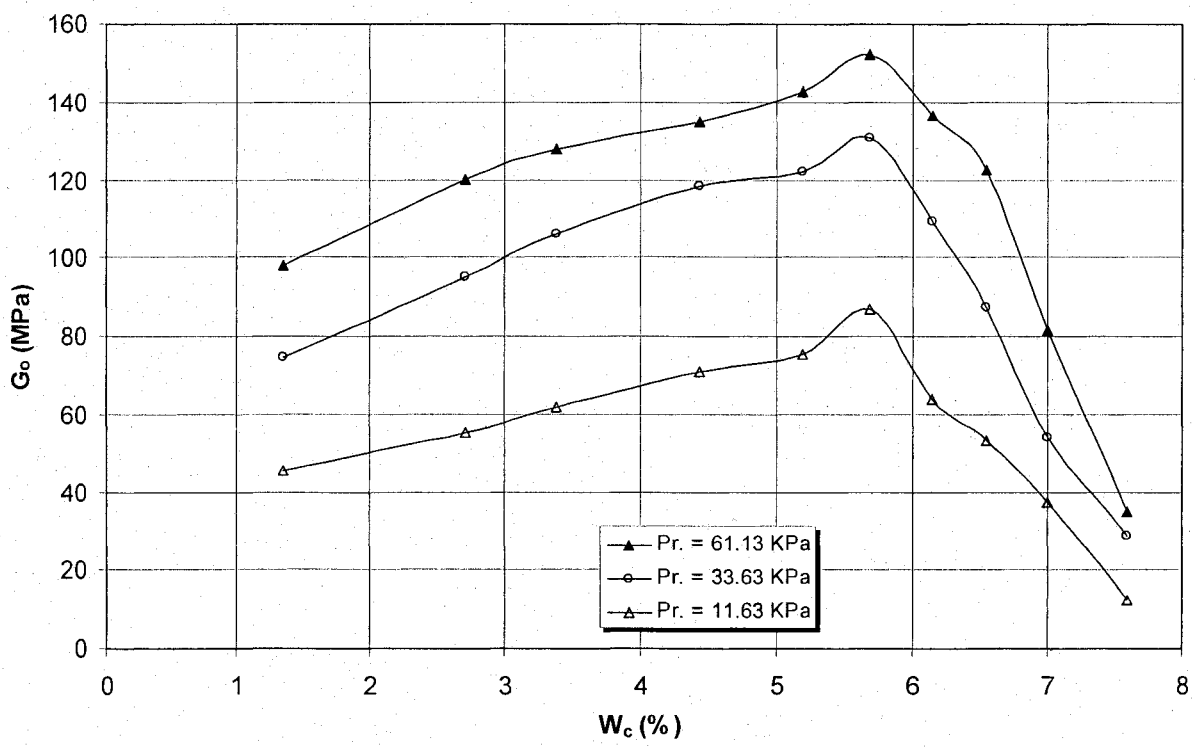

Figure 6.35 Elastic Shear Modulus of Compacted LG4 Till.

A second standard Proctor test was carried out on the concrete sand (Test 56). The shear wave velocity was measured for each compacted sample using Setup 4. The compaction curve is plotted on Figure 6.39. The optimum dry density is 1.87 t/m^3 at a water content of 11%. The measured V_s values under pressures of 11.63 & 33.61 kPa are plotted against water content in Figure 6.40. This relationship takes a bell shape around a centre water content of 10%. At lower water contents, V_s increases with decreasing water content (left part of the curve). The optimum water content for elastic shear rigidity (10%) is less than the optimum water content for density (12%). A small

increase in the applied stresses considerably increases the shear rigidity of the sand. This is attributed to the very low initial stresses applied on the soil sample.

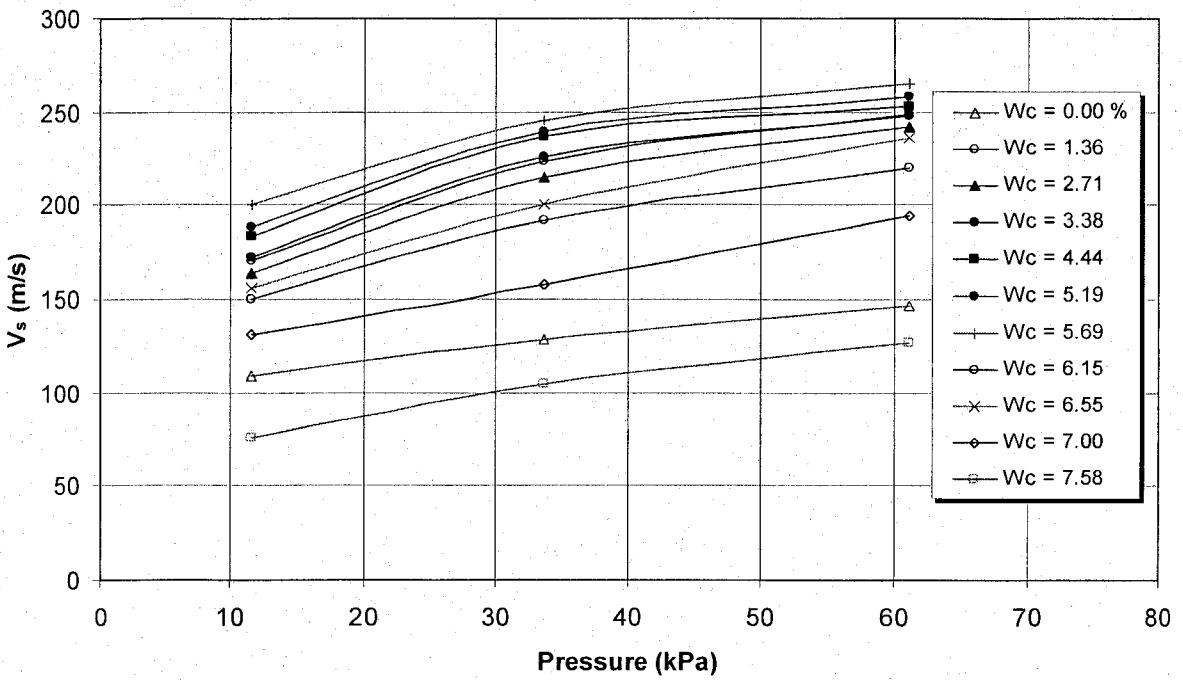

Figure 6.36 V_s versus Applied Pressure for Compacted LG4 Till Samples.

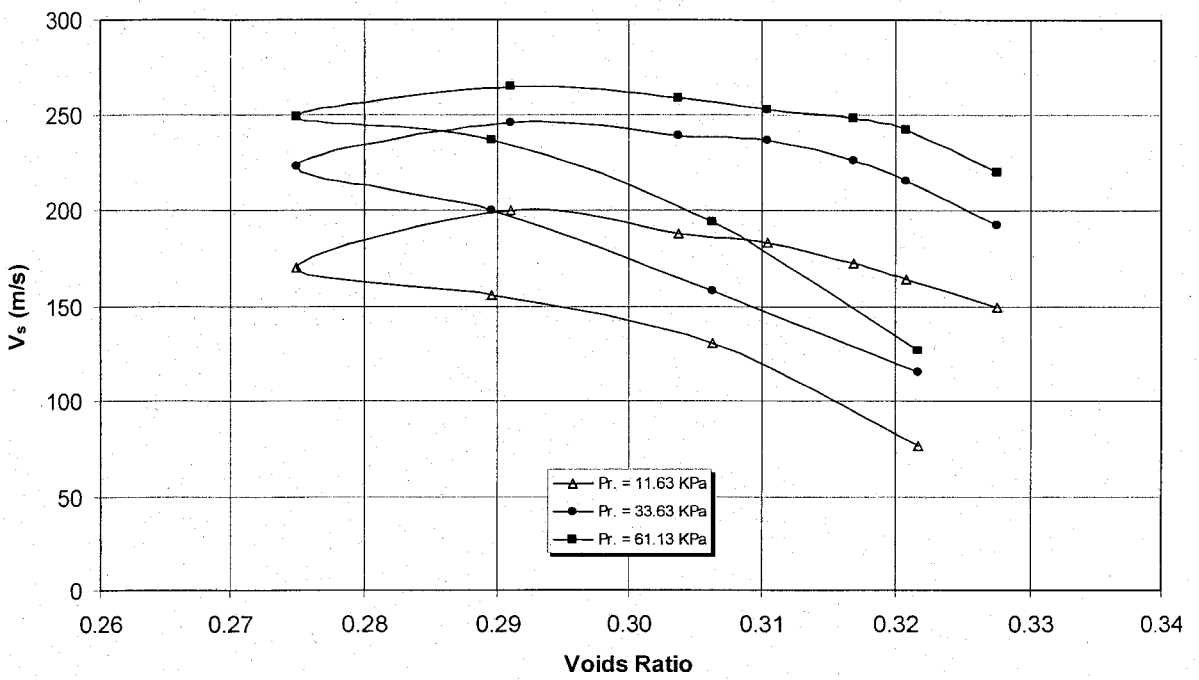

Figure 6.37 Variation of V_s with Voids Ratio for LG4 Till Samples under Different Pressures.

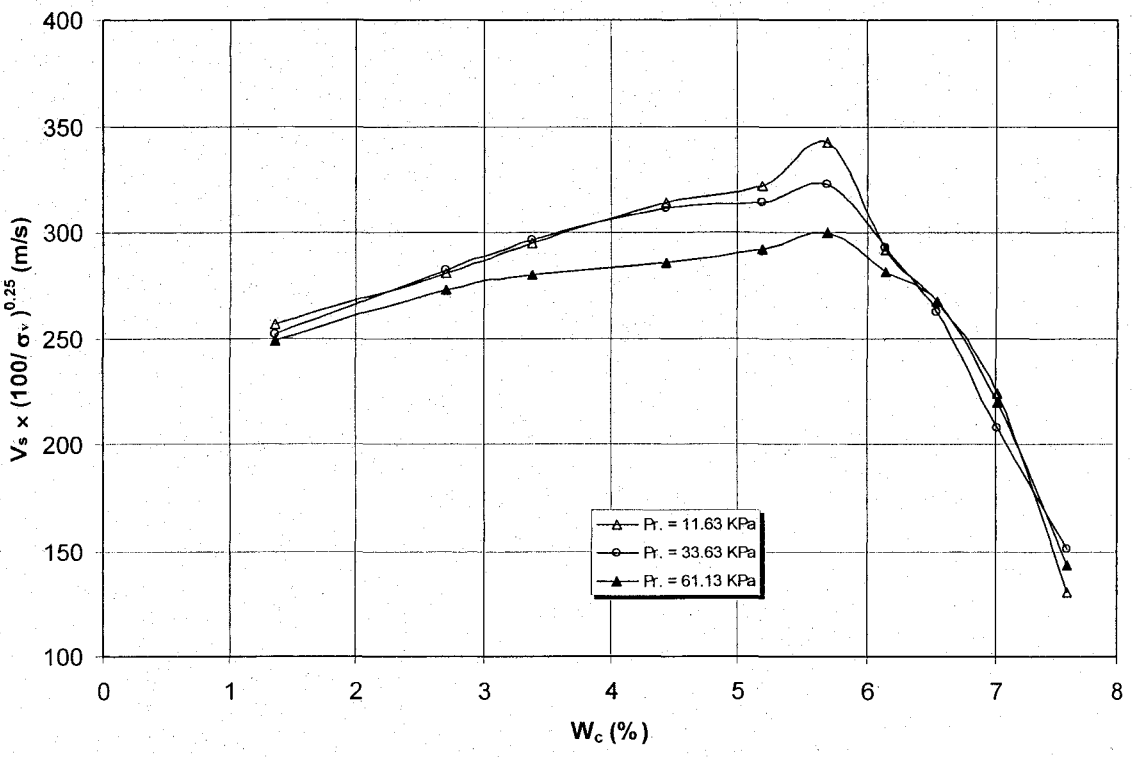

Figure 6.38 Variation of V_{s1} with Water Content for LG4 Till Samples in Proctor Mold.

Comparing the compaction curves, in terms of shear wave velocity, for the LG4 till and the concrete sand, shows that the suction stresses effects are more pronounced for the concrete sand than for the LG4 till. The maximum suction degree of saturation ($S_{opt.}$ %) depends on soil grains size and grading. For sands, it decreases by increasing the diameter of the finest 10% of the soil (D_{10}). The maximum suction water content of sands varies from 3% to 10%. The degree of saturation of the concrete sand is 26.5% at the lowest mixing water content, 4.7 %, in the test (Figure 6.40). The measured V_s values increases by decreasing the water content, in spite of the dry density decrease. Hence, the maximum suction should occur at water content lower than 4.7%. For the concrete sand, D_{10} equals 0.17mm. Thus putting this value in Equation 2.62 (Wu et al., 1984) gives $S_{opt.}$ of 6.5 % < 26.5%. For the LG4 soil, the maximum-suction degree of saturation ($S_{opt.}$ %) is calculated according to Equation 2.62 and found equals 14.8% (i.e. w_c = 1.81%). Within the compaction test range, the V_s-optimum water-content for LG4 is 5.5% (S_r = 59%). The γ_d-optimum water-content for the two tested soils is close to the V_s-optimum water-content within the common water content range for Proctor test.

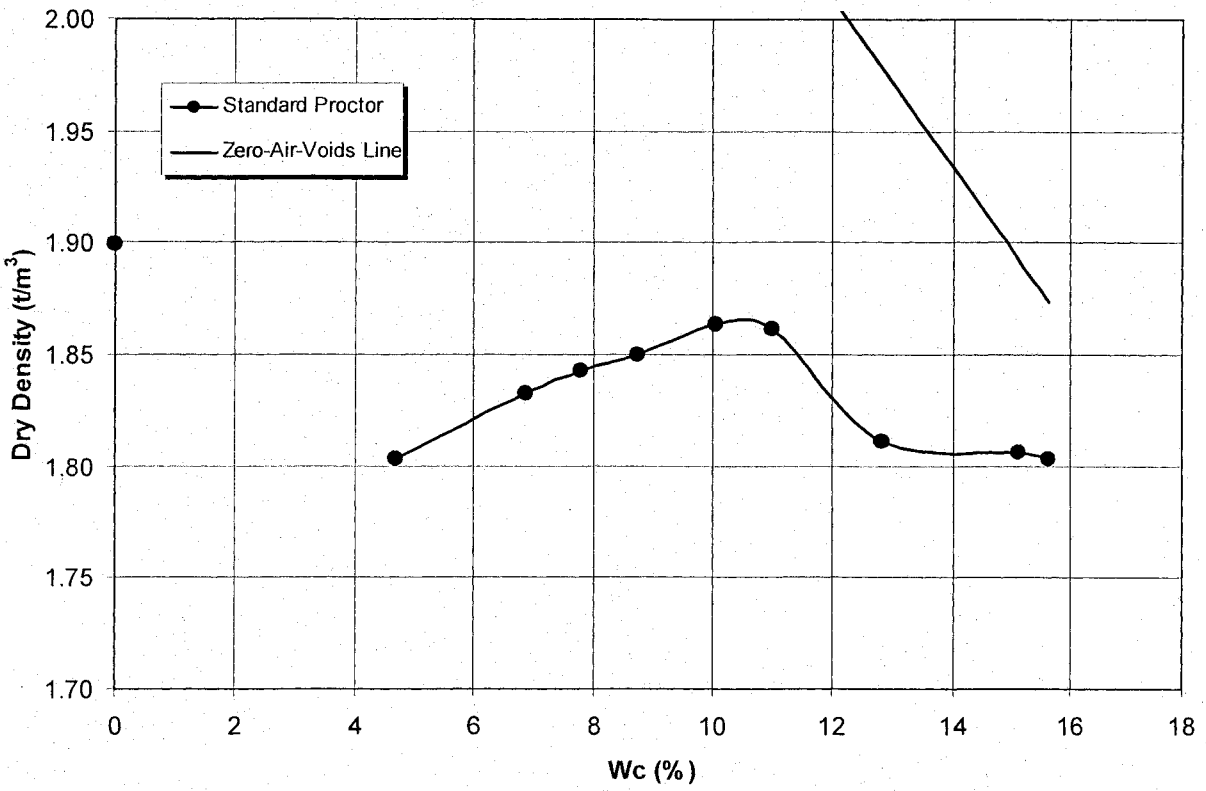

Figure 6.39 Standard Proctor Test for Concrete Sand.

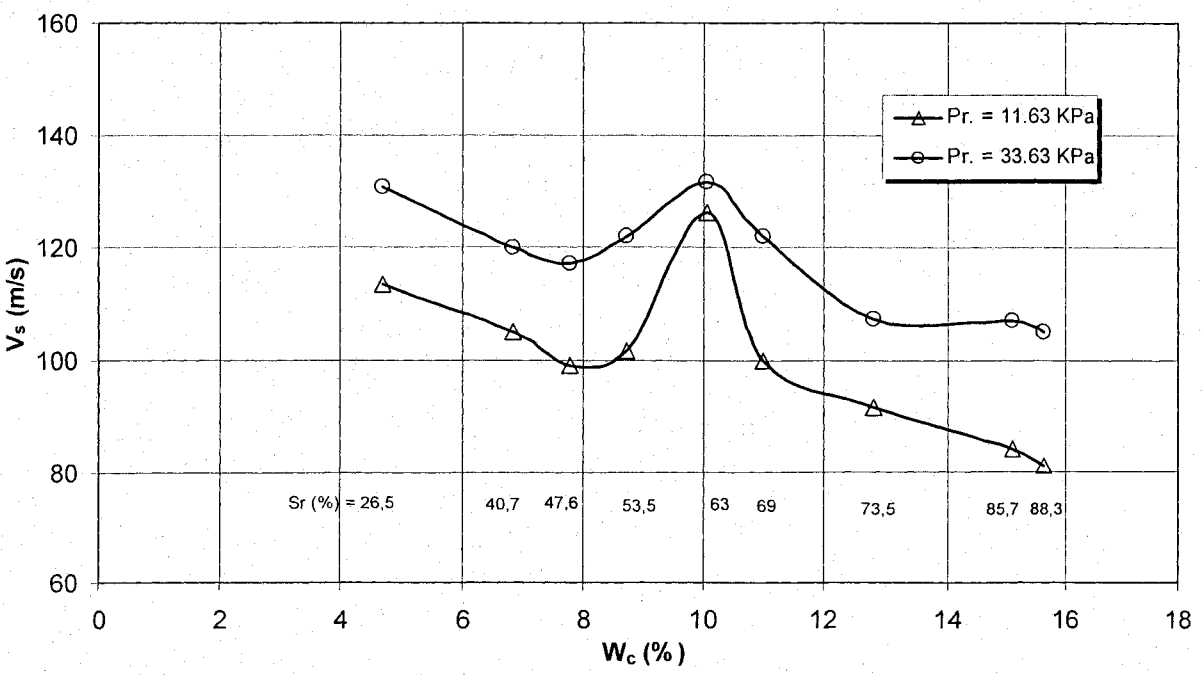

Figure 6.40 Shearing Rings Test on the Concrete Sand in Proctor Mold.

6.5 Summary

The developed ring actuators setups were used to test many soil types of different lengths under variable pressures in several laboratory setups. Some parametric studies were carried out to show the effect of input-wave frequency, input-wave voltage, input-wave shape, sample length, applied pressure, and interaction between soil and device. Many relationships between V_s or V_p and soil indices were drawn. The obtained pulse test results were compared to the estimated values using some empirical equations. The measured V_s values are in a good agreement with the previous results for the standard Ottawa sand. The obtained results demonstrate the suitability and capability of the ring actuators to measure shear and compression wave velocities of soil under the different conditions. The elastic Poisson's ratio could be calculated. The smooth-edged input-wave shapes such as winged-sine, versed-sine and wavelet are helpful in clarifying the s-wave component and reducing the secondary waves. There is a considerable difference between V_{s1} normalized to vertical stress and V_{s1} normalized to average stress. Friction between soil and mold sides affects the measured V_s values, especially in long molds at high pressures.

The V_s-w_c compaction curve was drawn for two soil types. The soil grading affect the shear wave velocity and the optimum water content for maximum shear rigidity. The partially saturated samples have considerably higher V_s values than dry samples. The water content at state of maximum-suction is significantly less than the optimum water content for soil compaction (normally out of the Proctor test w_c-range). The V_s-w_c relationship takes the form of the common bell-shape curve of the γ_d-w_c relationship, except that the dry-of-optimum side is relatively higher. The difference in V_s values between partially saturated (w_c = 5%) and dry of LG4 samples varied from 82% at the lowest applied pressure (29 kPa) to 26% at the highest pressure (798 kPa). This variation depends on each of soil suction, applied stresses and the value of voids ratio. Finally, detailed studies are needed to clearly investigate the compaction curves of soil in terms of water content and shear wave velocity. Many soil types of different grading should be tested for obtaining broad data base. However, promising results could be obtained in this study.

(Blank)

Chapter 7 CORRELATING SHEAR WAVE VELOCITY TO IN SITU TESTS INDICES AT PERIBONKA DAM

7.1 Introduction

This chapter presents interpretations and analyses for the field and laboratory tests of the Péribonka dam in order to examine the correlations between each of CPTu and SPT indices and in-situ V_s measurements. The field tests were performed for evaluating the efficiency and adequateness of the vibro-floatation compaction for the foundation (natural) soil and the lower embankment materials of the dam. The compaction was carried out to reduce the liquefaction potential under earthquake loads. Only the test data before compaction are studied in this study. The geophysical surveys (5 lines) were carried out using MASW (Modal Analysis of Surface Waves) method. The study resulted in deriving new relationships for sandy and gravelly soils. These correlations are useful for soil characterization not only at this site but at any other site of similar soil compositions. The obtained correlations were also compared to some of the existing equations in this domain. Estimating the relative density of the soil at site was useful in verifying the data base of the correlations. Therefore, Appendix A presents the existing correlations between shear wave velocity (or elastic shear modulus) and SPT and CPT tests indices. Also, Appendix B introduces the correlations for estimating relative density of soil using penetration test indices.

7.2 Site Description

The Peribonka dam is located at kilometre 151.8 of the Péribonka river, immediately in the upstream of its junction with the Manouane river, north of Lac Saint-Jean in Quebec. It is a dam of 80-m height, by 700-m length. The water head is estimated at 70-m. This dam is to generate about 2.2TWh per year. The construction of the dam began in April 2004 and will spread out until the autumn of 2008. The lower part of the dam is constructed by pouring a fill material in the river until reaching the platform level (180.00). The fill depth (from platform elevation to the riverbed) is about 10m. Then, the fill as well as the natural soil at the site are

compacted by vibrofloatation. Figure 7.1 shows a cross section of the dam where the compaction platform is indicated. The bedrock depth varies from zero to 113m. The vibrofloatation compaction depth varied from a few meters to about 55m.

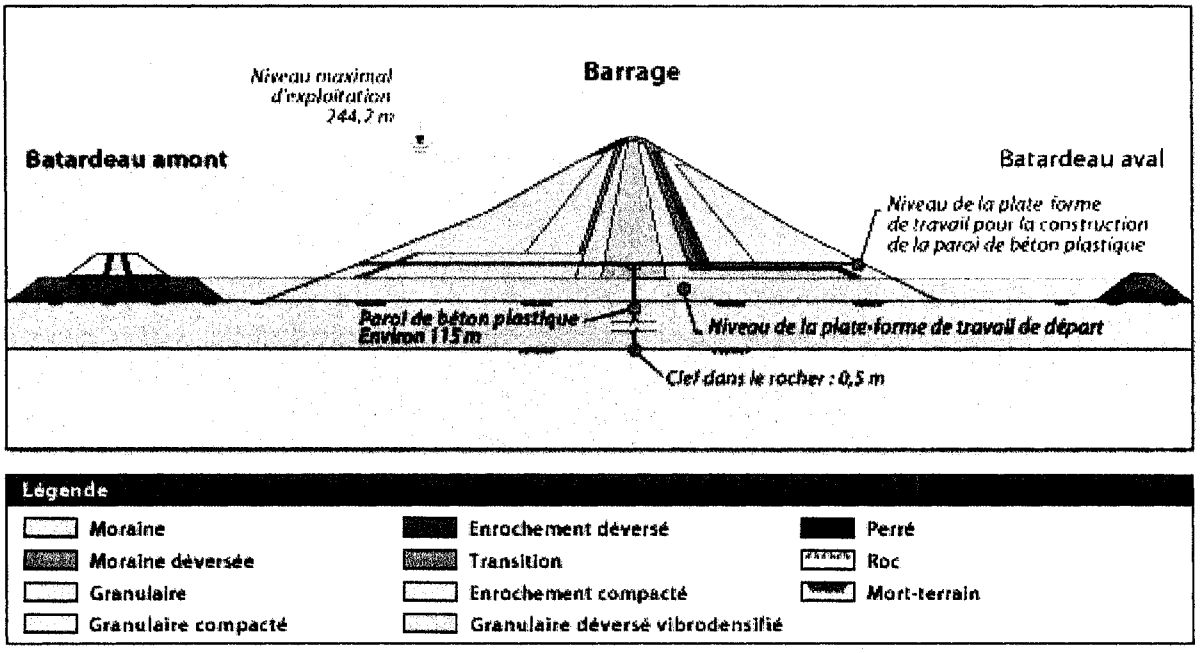

Figure 7.1 The Different Sections of the Dam (after Hydro-Quebec).

7.3 The Fill Soil and its Laboratory Tests

The grain size distribution curves of some samples from the fill material are displayed on Figure 7.2. Most of the fill soil is of a material labelled with H. Generally, the fill can be classified as "Sand and Gravel with traces of silt". Maximum and minimum density tests were carried out on some samples of the fill according to ASTM. The results are displayed in Figure 7.3. It can be seen that the maximum and minimum densities vary with soil grading. The average maximum and minimum densities are 2200 and 1900 kg/m^3, respectively. The specific gravity of fill was taken as 2.67. Hence, the average maximum and minimum voids ratio (e_{max} & e_{min}) could be calculated as 0.4 and 0.2, respectively. Figure 7.4 display the variation of maximum and minimum voids ratio with soil type. Also, the saturated density was computed (Figure 7.5). These results are useful in calculating the elastic shear modulus of soil and soil settlement due to compaction.

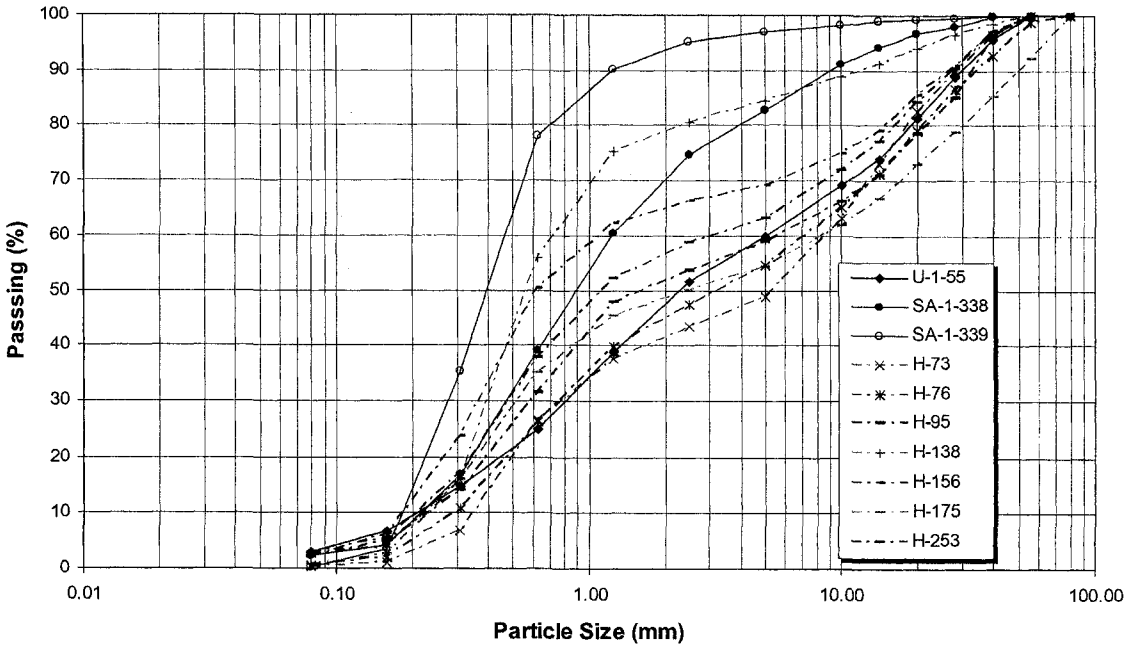

Figure 7.2 Grading of the Fill Materials.

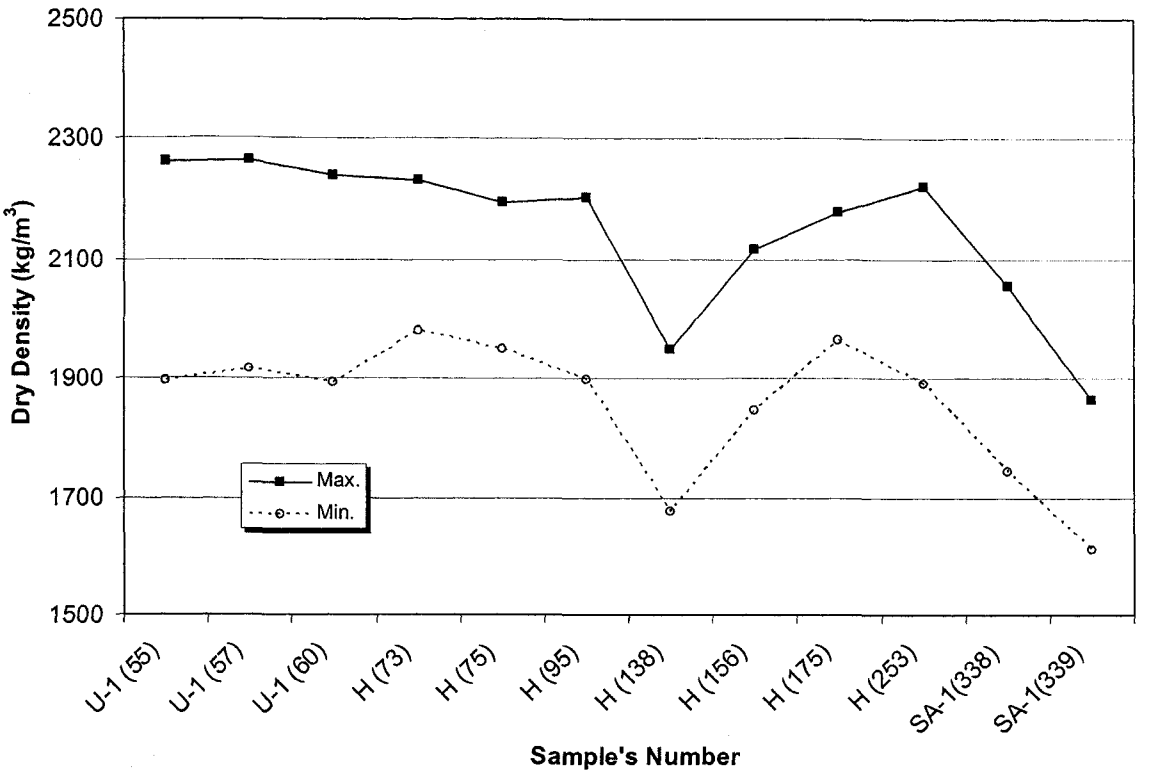

Figure 7.3 The Maximum and Minimum Densities of the Fill Materials.

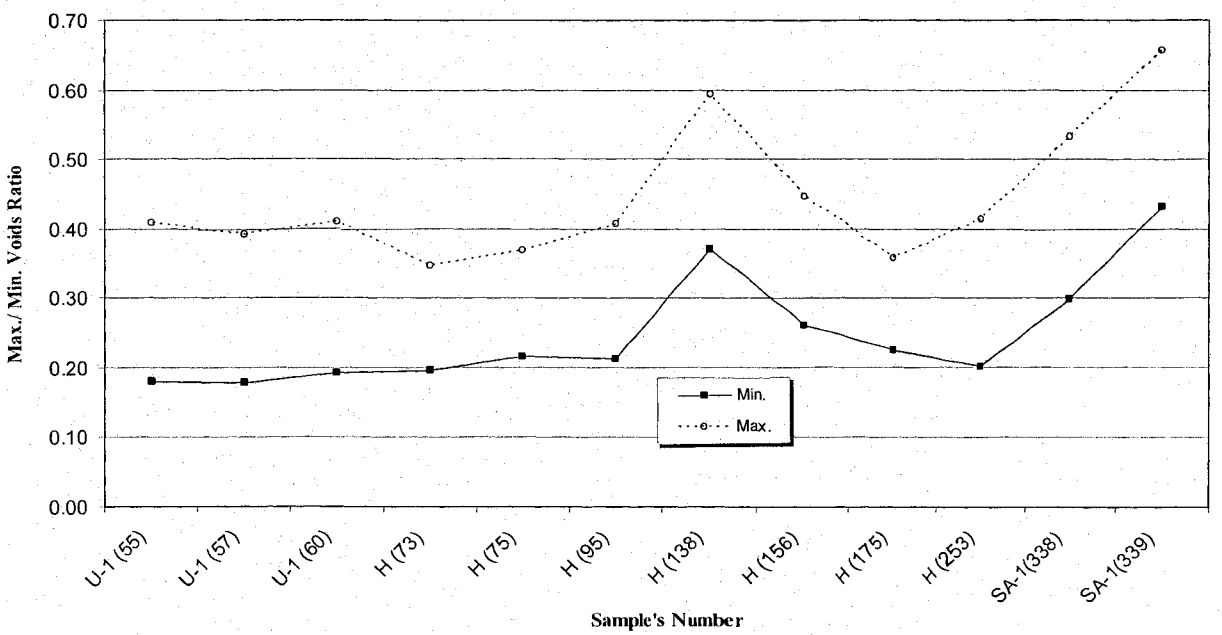

Figure 7.4 The Maximum and Minimum Voids Ratio of the Fill Materials.

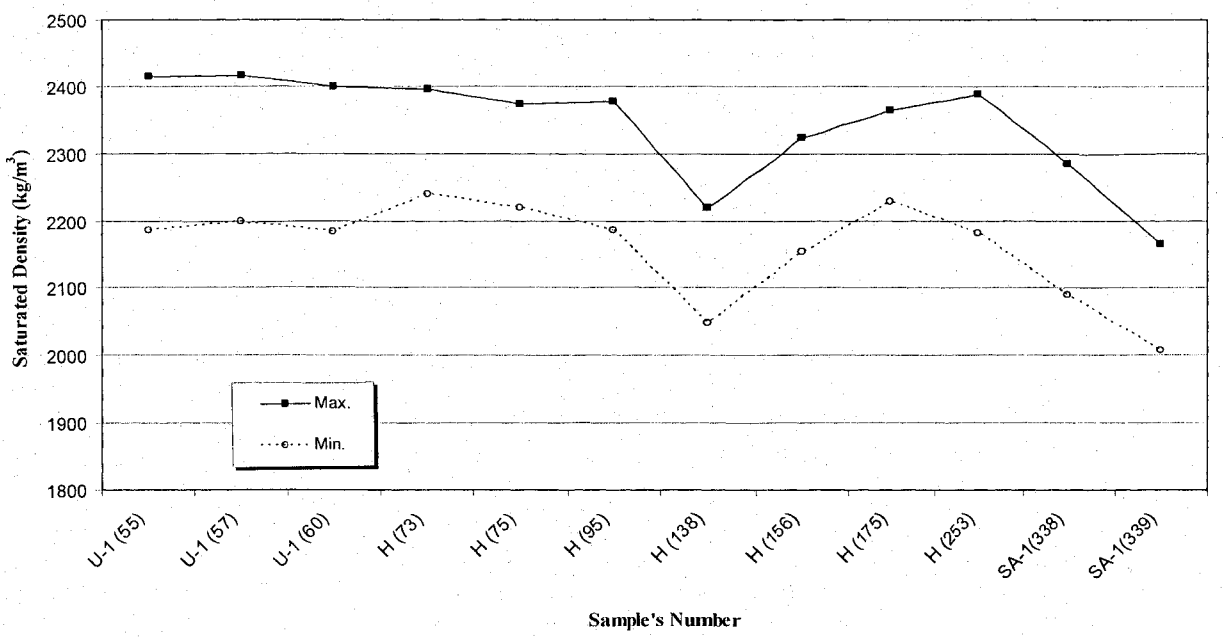

Figure 7.5 Variation of Saturated Density with Soil Type.

Considering the many laboratory tests, it is useful to study the relationship between the maximum and minimum voids ratio (e_{max} & e_{min}) and soil grading. Figure 7.6 presents the variation of e_{max} and e_{min} with the uniformity coefficient of soil. The maximum and minimum

voids ratio (e_{max}, e_{min}) decreases with the increase of uniformity coefficient up to about 10, then the relationship is constant. Also, the voids ratio range (e_{max} - e_{min}) is nearly constant. This means that soil with large grain size variations have similar maximum and minimum voids ratio to well graded soils. The relationship between each of e_{max} and e_{min} and the coefficient of curvature takes the same trend of the previously existing relationship (Figure 7.7). The effect of soil grading on e_{max} and e_{min} can be drawn in terms of the average particle size (D_{50}). Figure 7.8 shows that granular soils of D_{50} higher than about 1.0mm would have similar maximum and minimum voids ratio.

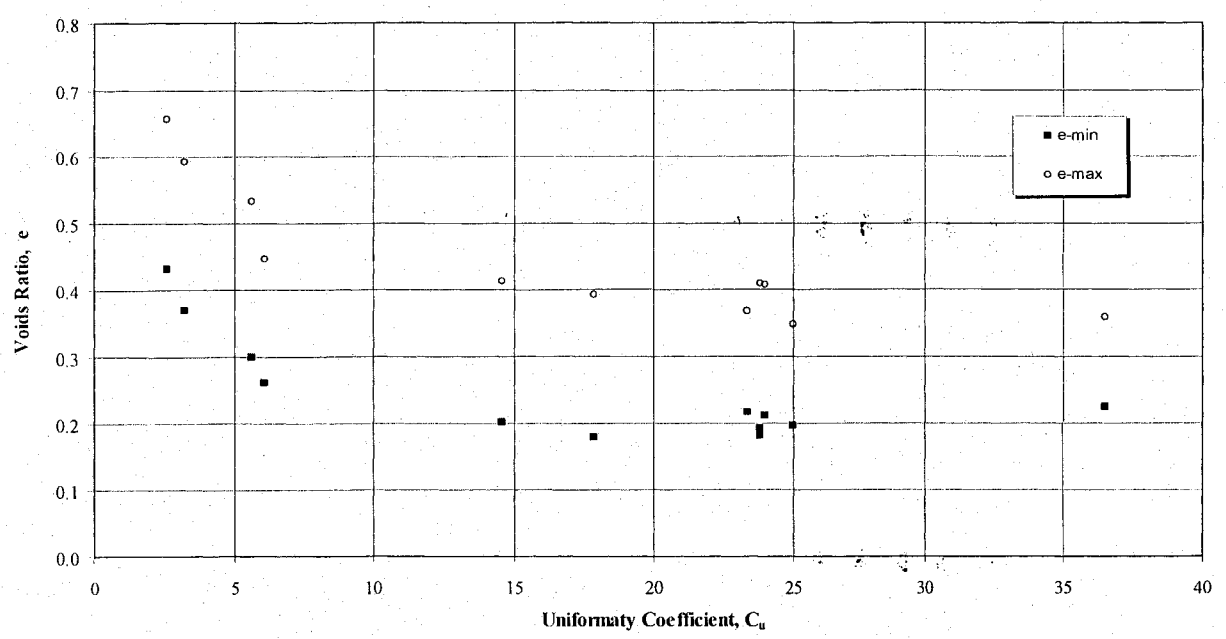

Figure 7.6 Variation of e_{max} and e_{min} with Uniformity Coefficient.

7.4 The Data Base for the Correlations

Many boreholes, Standard Penetration Tests (SPT), Piezo-Cone Penetration Tests (CPTu), Seismic-Piezo-Cone Penetration Tests SCPTu were carried out before and after the compaction to characterize the soil and evaluate the efficiency of the compaction process. Also, geophysical surveys for measuring shear wave velocity of the soil by Modal Analysis of Surface Waves (MASW) Method were carried out for the same purpose. This method gives the variation of V_s with depth all over the survey line. Figure 7.9 shows the locations of the main MASW lines at the dam site (5 V_s-geophysical survey lines). Figure 7.10 shows the locations of the boreholes carried out before and after the compaction.

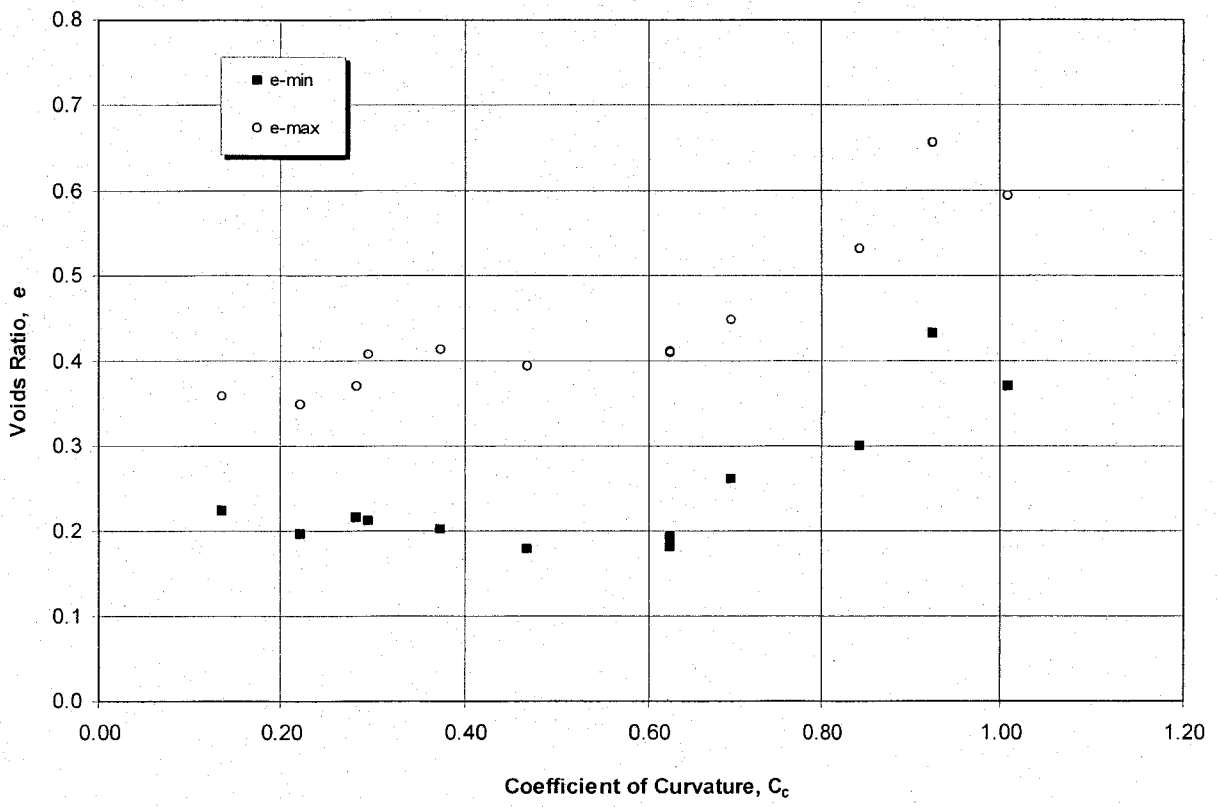

Figure 7.7 Variation of e_{max} and e_{min} with Coefficient of Curvature.

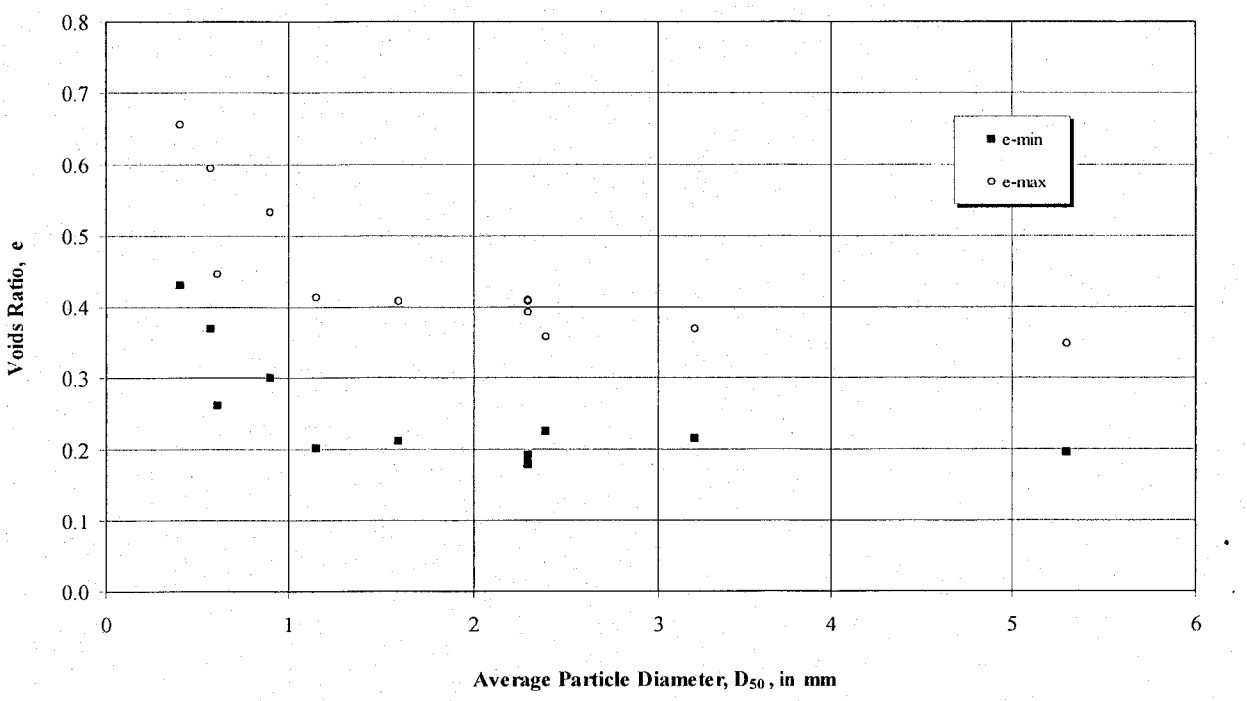

Figure 7.8 Variation of e_{max} and e_{min} with D_{50}.

Also, the cone penetration tests within 10m from the MASW lines are also displayed on Figure 7.10. Table 7.1 presents the coordinates of each Cone Penetration Test, its distance (PM) from the start point of the MASW line, its distance to the line, its elevation, its depth, the fill depth at its location, and the coordinates of the start point of each line. However, only CPTs at a distance of 3.5m or less from surface wave lines were considered for the correlations. The boreholes were used to draw two geologic cross-sections parallel to the dam axe (Figures 7.11 and 7.12). The natural soil at the dam site varies from sand to 'gravel and boulders'. Figures 7.13 –7.16 display the results of CPT and MASW investigations (profiles). For each depth interval (of constant V_s) on the MASW V_s-profile, the average value of the normalized cone index (q_{c1N}) was calculated and plotted on these figures. Table 7.2 presents the data pairs (V_{s1} and q_{c1N} points) for the correlations.

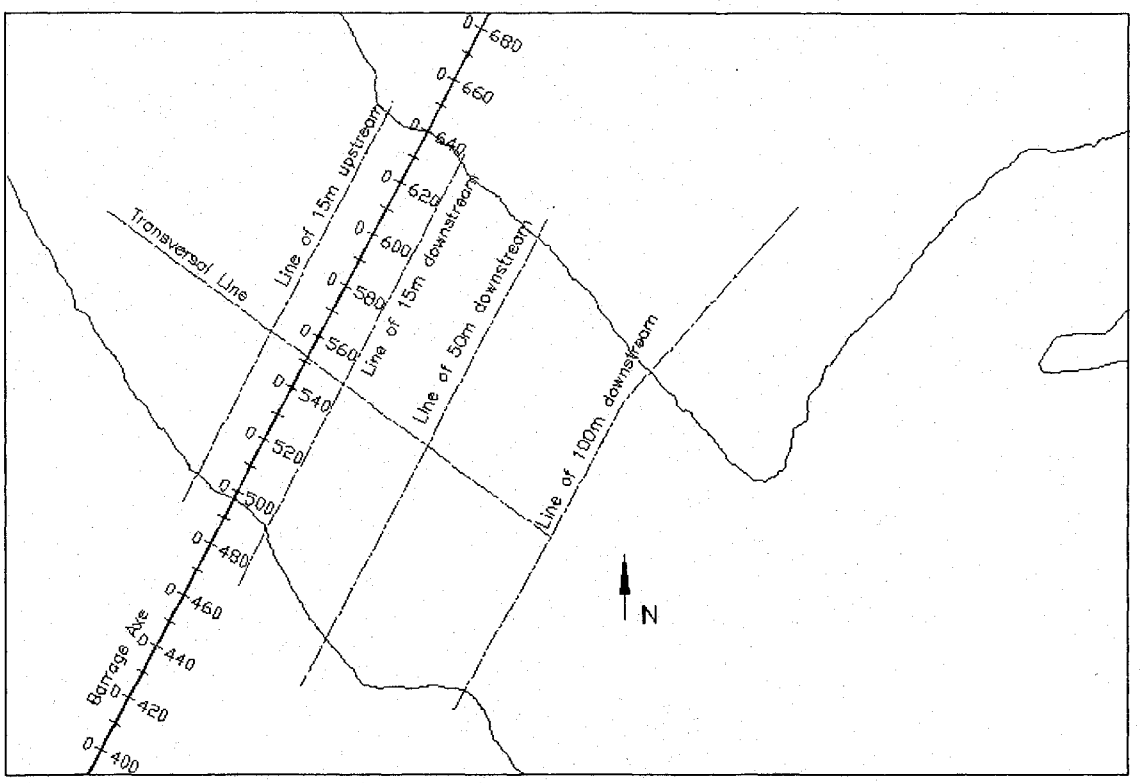

Figure 7.9 Locations of MASW Lines at Peribonka Dam Site.

7.5 Treatment of Test Data

The anomalous values of the CPT were excluded from the data base of the correlations. These abnormalities may be attributed to pushing a stone ahead of the cone. The abnormalities could

be assessed by computing the relative density of soil based on q_c. When the estimated D_r is too high (> 100), this reflects a problem in carrying out the test. Also, the soil type index, I_c, was used to check the soil classification (to check if there is gravel in the soil) in order to verify the CPT results.

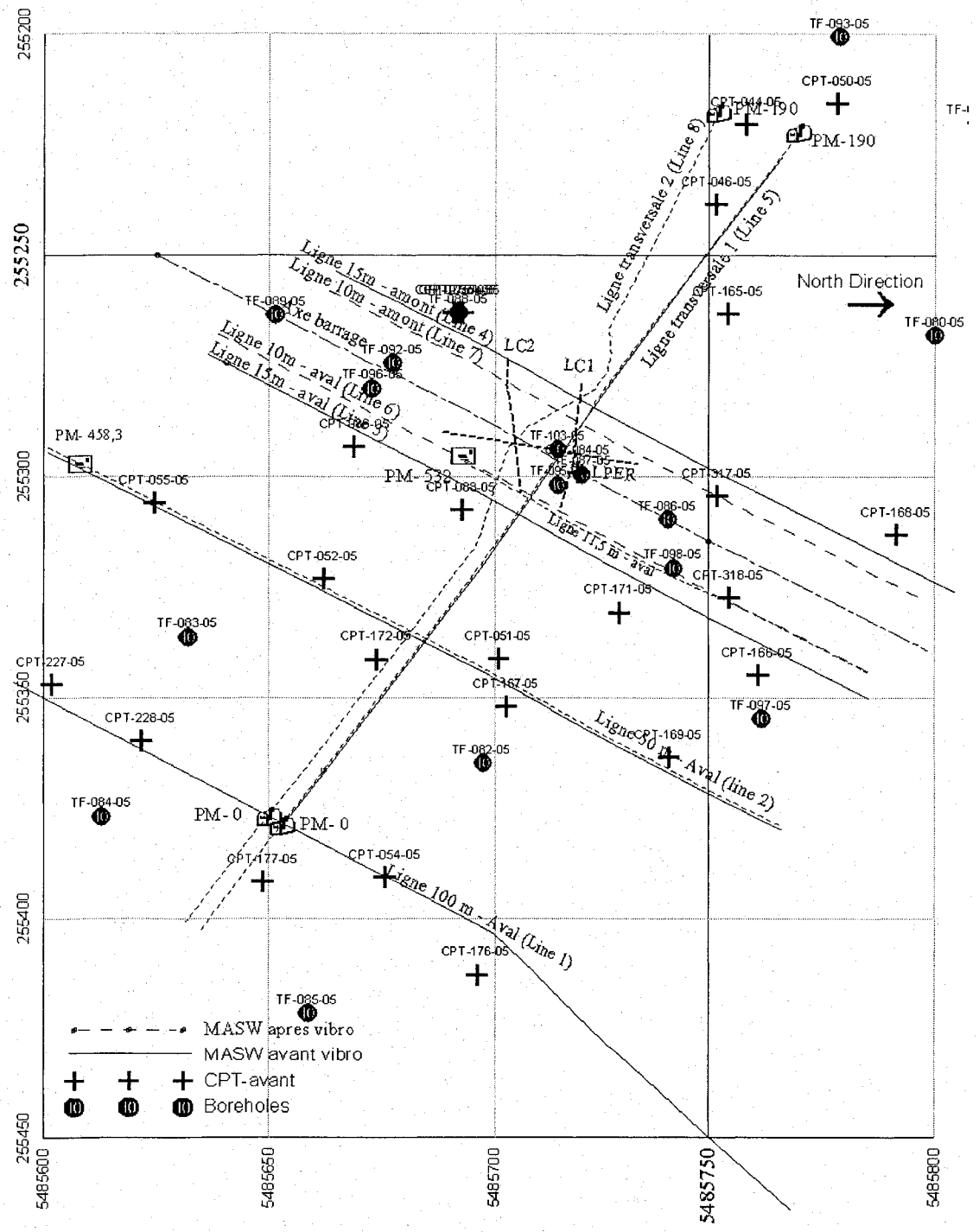

Figure 7.10 Locations of the Field Tests, Boreholes and V_s-Geophysical Survey Lines.

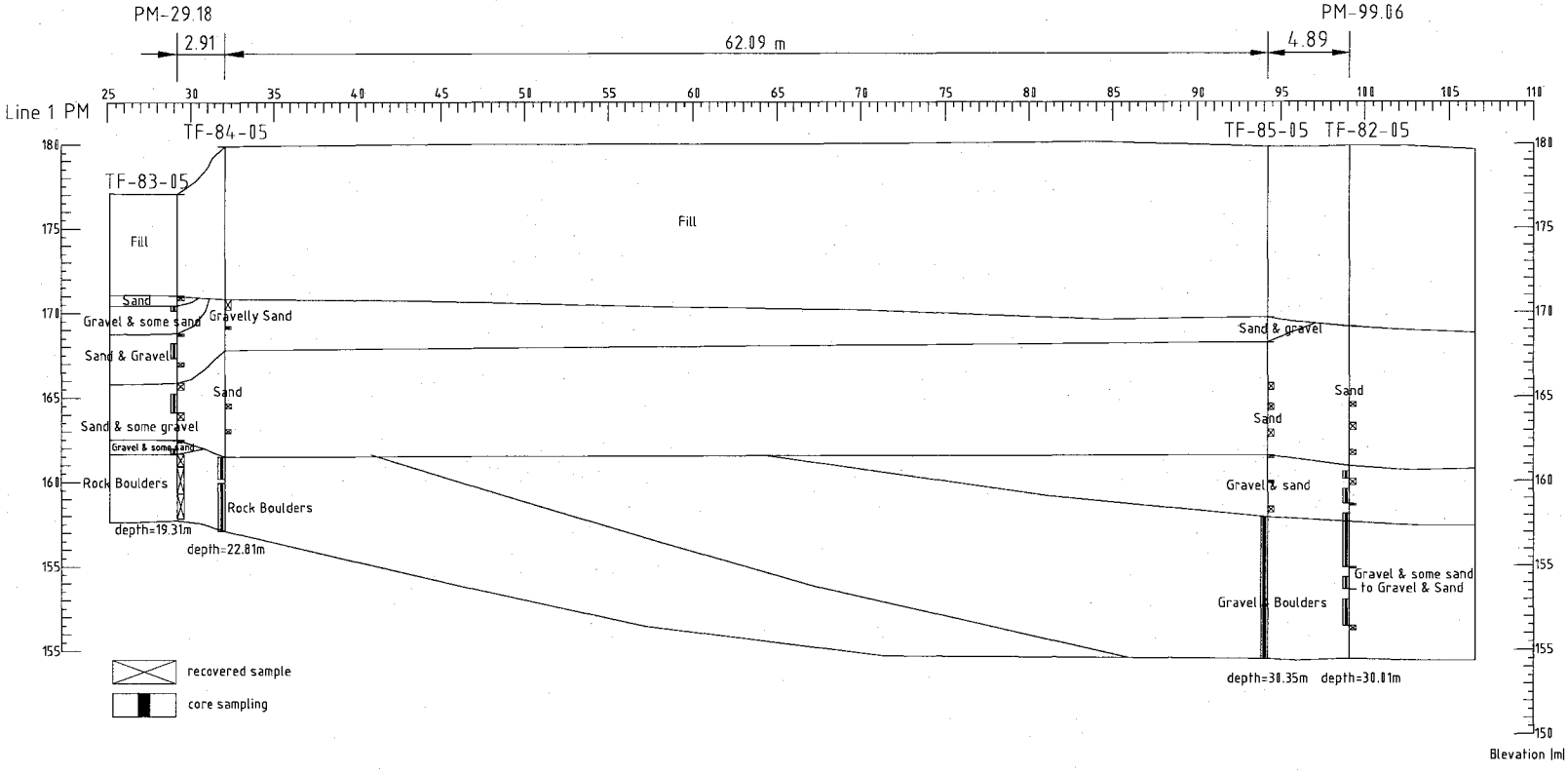

Figure 7.11 Geologic Cross Section at Lines 1 and 2.

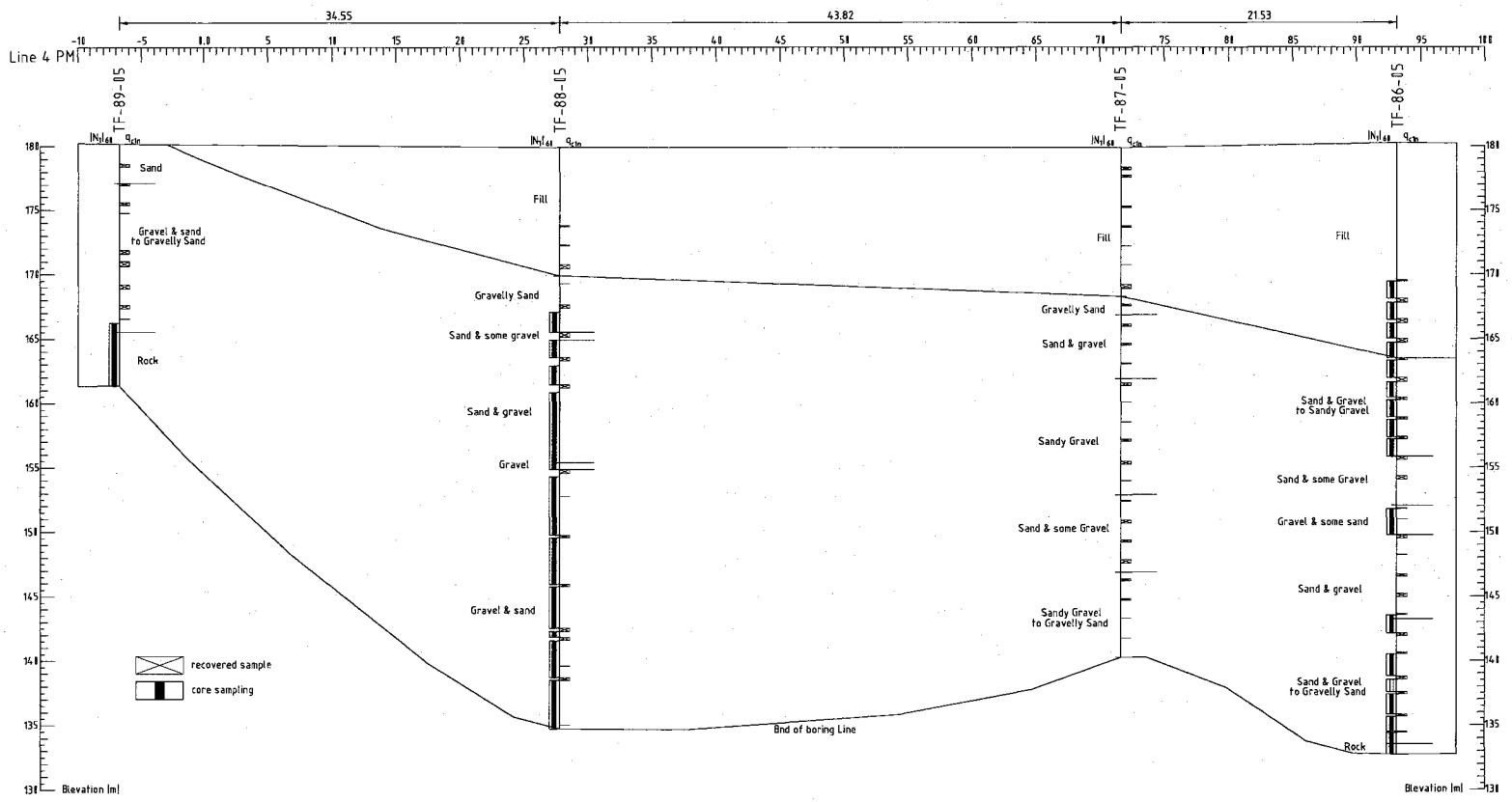

Figure 7.12 Geologic Cross Section at Lines 3 and 4.

Table 7.1 Before-Compaction CPT within 10-m from the MASW Lines.

Line No. & beginning corr.		NO SONDAGE Avant Vibro	CPT EST	CPT NORD	Closest point on MASW Line EST	Closest point on MASW Line NORD	Distance from Line (m)	PM (m)	CPT Depth (m)	Fill Depth (m)	CPT Elevat. (m)
Line 1	100m-Aval	CPT-227-05	255347	5485601,8	255349,85	5485599,8	3,48	7,40	4,50	6,50	180,00
255346,31	5485593,3	CPT-228-05	255359,7	5485621,7	255361,09	5485620,7	1,71	31,13	15,70	12,00	180,00
		CPT-054-05	255390,696	5485675,55	255390,61	5485675,6	0,10	93,47	15,70	10,00	175,20
		CPT-176-05	255412,7	5485695,71	255406,23	5485702,6	9,45	124,65	23,35	8,00	180
Line 2	50m-Aval	CPT-055-05	255305,967	5485624,68	255305,89	5485624,8	0,14	18,61	13,55	7,50	179,80
255297,28	5485608,3	CPT-052-05	255323,038	5485661,81	255324,67	5485660,9	1,87	59,30	9,55	10,00	179,80
		CPT-051-05	255341,12	5485700,89	255344,33	5485698,8	3,83	102,00	20,90	11,50	179,80
		CPT-167-05	255351,927	5485702,71	255347,91	5485705,8	5,07	109,86	11,23-15,00	10,50	180,01
		CPT-169-05	255363,3	5485741,1	255365,51	5485739,7	2,62	148,06	25,65	8,00	180
Line 3	15m-Aval	CPT-086-05	255293,1	5485668,7	255290,19	5485670,6	3,48	38,76	16,60	10,00	179,82
255272,13	5485636,3	CPT-088-05	255307,5	5485692,3	255303,26	5485695,6	5,37	66,97	3,55	11,75	179,80
		CPT-171-05	255330,6	5485729,6	255323,3	5485734,2	8,63	110,47	19,35	9,60	179,80
		CPT-318-05	255327,29	5485754,68	255332,17	5485751,4	5,88	129,82	9,60	8,50	179,80
		CPT-166-05	255344,8	5485760,9	255339,14	5485764,7	6,82	144,83	19,90	8,25	179,8
Line 4	15m-Amount	CPT-075A-05	255263	5485691,5	255266	5485688,3	4,39	26,46	17,55	7,25	179,90
255253,84	5485664,8	CPT-075B-05	255263	5485692,5	255266,38	5485689,1	4,79	27,34	15,40	7,50	179,90
		CPT-075C-05	255263	5485690,5	255266,84	5485689,9	3,89	28,27	15,15	7,50	179,90
		CPT-317-05	255304,28	5485752,02	255300,59	5485754,9	4,68	101,51	18,65	11,20	179,90
		CPT-168-05	255313	5485791,4	255317,92	5485788,4	5,76	139,22	9,10	9,50	179,9
Line 5	Transverse	CPT-177-05	255391,57	5485648,69	255389,55	5485646,3	3,13	-13,81	12,80	11,50	180,00
255378,42	5485652,9	CPT-172-05	255341,2	5485673,63	255344,71	5485678,5	6,00	42,33	12,15	11,50	179,90
		CPT-084-05	255299	5485720	255295,68	5485714,6	6,34	103,21	17,75	11,50	179,90
		CPT-165-05	255263,2	5485754,3	255256,59	5485743,4	12,75	151,77	18,35	(11,5)	179,90
		CPT-046-05	255238,414	5485751,82	255241,08	5485754,9	4,08	171,07	15,50	(11,5)	179,80
		CPT-044-05	255220,205	5485758,32	255225,77	5485766	9,49	189,98	14,35	(11,5)	179,74
		CPT-050-05	255215,494	5485778,23	255213,77	5485774,5	4,11	204,69	13,25	(11,5)	179,8

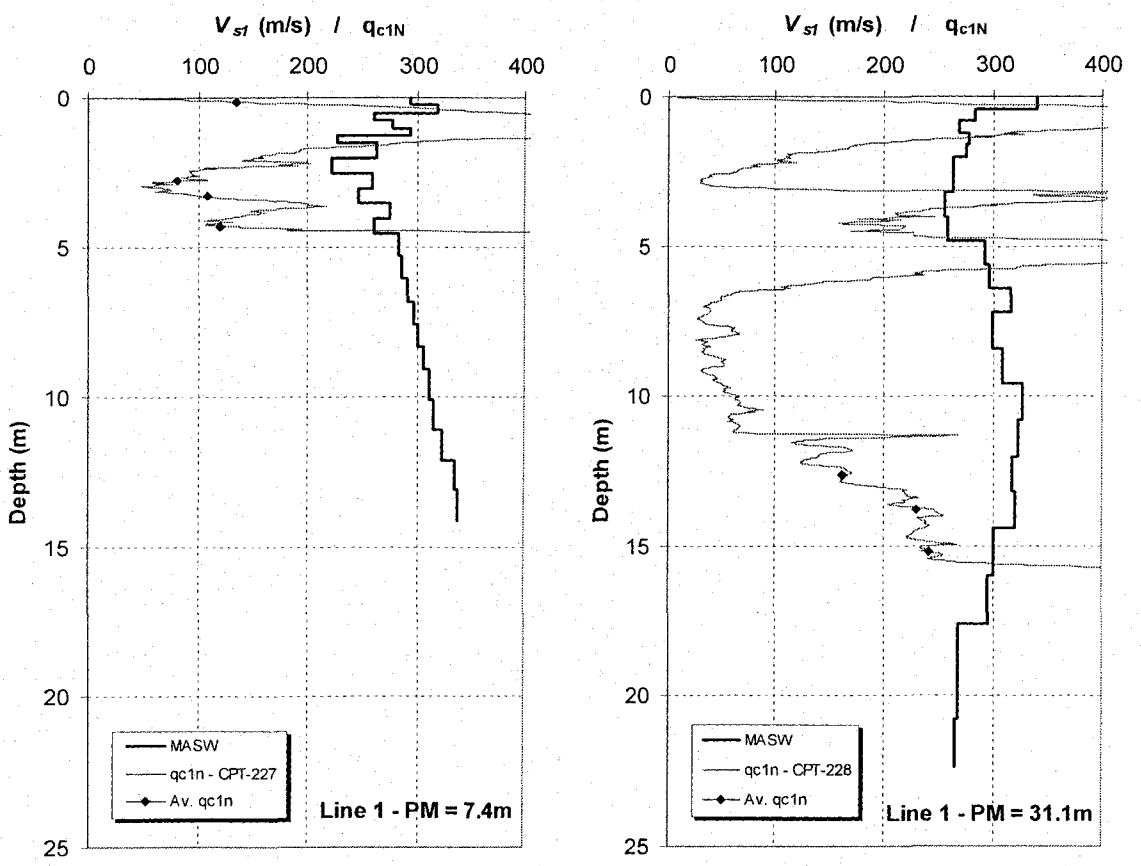

Figure 7.13 V_{s1} and q_{c1N} Profiles (CPT 227 & CPT 228).

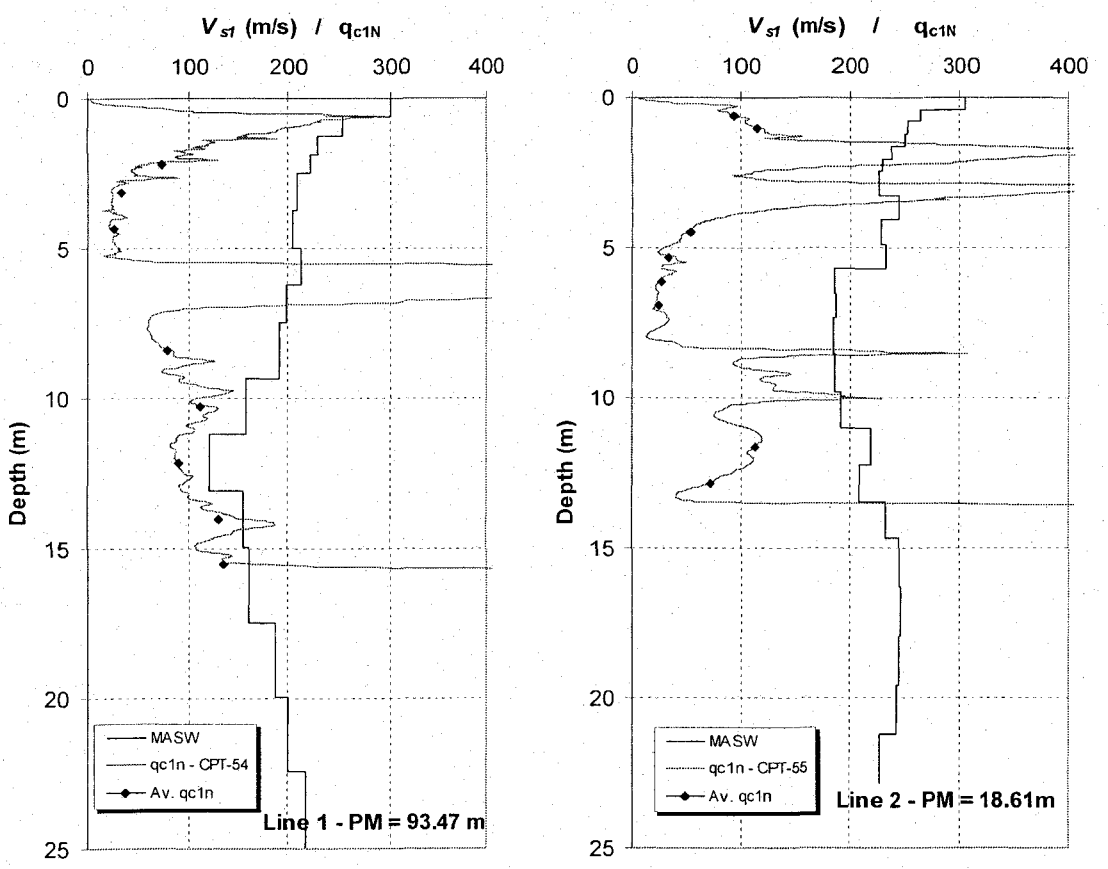

Figure 7.14 V_{s1} and q_{c1N} Profiles (CPT 54 & CPT 55).

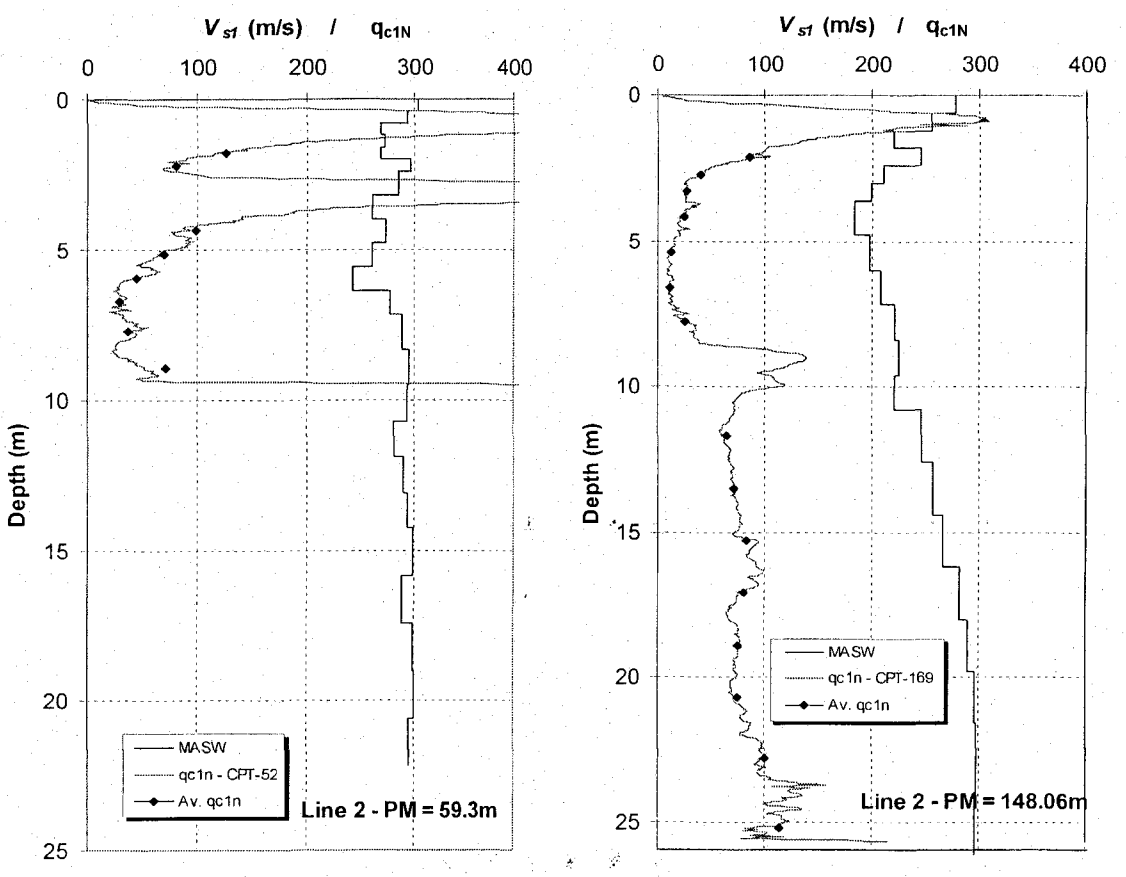

Figure 7.15 V_{s1} and q_{c1N} Profiles (CPT 62 & CPT 169).

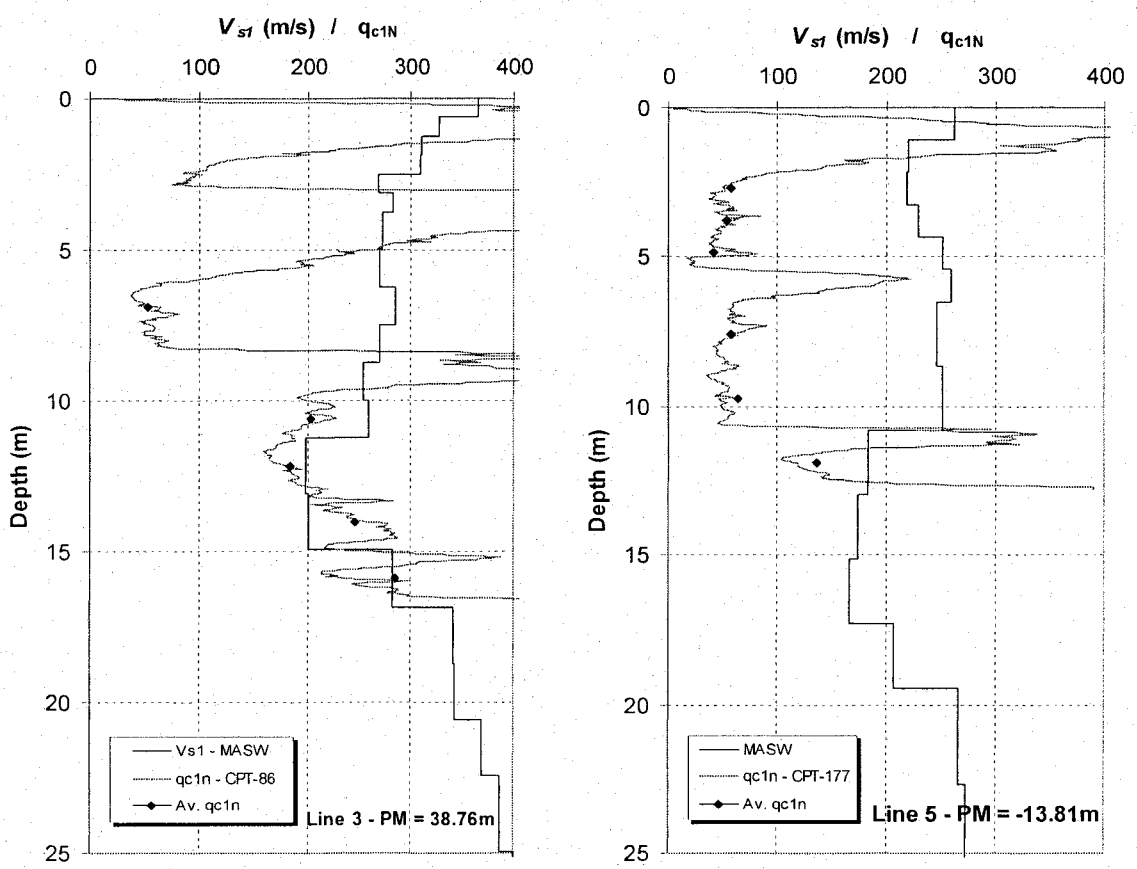

Figure 7.16 V_{s1} and q_{c1N} Profiles (CPT 86 & CPT 177).

Table 7.2 CPT and MASW Data Base at Peribonka Dam.

Line No.	PM (m)	CPT No.	Distace (m)	Depth (m)	Fill materials		Foundation Soil	
					q_{c1N}	V_{s1}	q_{c1N}	V_{s1}
1	7.4	227	3.48	0.13	135.21	294.49		
				2.77	80.62	259.89		
				3.28	108.50	247.59		
				4.28	119.77	261.40		
1	31.13	228	1.71	12.60			161.67	317.81
				13.80			230.71	319.84
				15.20			241.21	301.28
1	93.47	54	0.1	2.18	73.07	221.46		
				3.12	34.05	209.03		
				4.36	26.27	203.81		
				8.42	78.98	191.71		
				10.29			112.31	156.90
				12.16			90.97	120.06
				14.03			130.22	155.19
				15.50			135.07	160.83
2	18.61	55	0.14	0.61	95.65	264.07		
				1.02	114.65	251.72		
				4.49	55.12	228.00		
				5.30	33.47	230.79		
				6.12	27.92	186.12		
				6.94	24.62	186.67		
				11.63			113.40	219.27
				12.85			72.81	209.78
2	59.3	52	1.87	1.78	126.96	268.48		
				2.18	80.65	296.42		
				4.36	99.28	272.77		
				5.15	70.16	260.22		
				5.94	45.78	241.30		
				6.73	30.46	277.62		
				7.72	37.63	288.42		
				8.91	71.33	294.84		
2	148.06	169	2.62	2.10	86.50	245.58		
				2.70	39.87	211.19		
				3.30	26.79	199.92		
				4.20	25.24	183.42		
				5.40	13.60	197.58		
				6.60	12.11	209.07		
				7.80	26.00	222.14		
				11.70			65.67	245.93
				13.50			72.08	256.81
				15.30			83.53	266.38
				17.10			80.56	280.84
				18.90			74.95	289.34
				20.70			75.14	295.43
				22.80			100.43	296.71
				25.20			110.00	295.27
3	38.76	86	3.48	6.86	53.16	285.20		
				10.61			203.01	258.64
				12.17			182.64	197.89
				14.04			246.01	200.45
				15.91			284.57	282.24
5	-13.81	177	3.13	2.70	57.91	218.99		
				3.78	53.13	229.66		
				4.86	42.41	251.42		
				7.56	57.33	246.28		
				9.72	64.86	251.34		
				11.88			136.33	184.10

As an illustration for the different steps of data processing needed to include a test result in the data base of the correlations, CPT-55 is taken as an example (Figure 7.14). CPT-55 extend to a depth of 13.55m and is located at a distance of 0.14m from the Line 2 (PM=18.61m). The fill depth at CPT-55 location is 7.5m. Borehole TF-83-05 is the nearest borehole to the CPT location. Hence, the SPT results of this borehole are correlated to CPT-55 results. Also, the MASW V_s-profile at PM 18.61 is the nearest to CPT-55. The results of these three tests are considered one set of data. The MASW profile is an average of three profiles over a distance of four meters. The SPT number, $(N_1)_{60}$, is the corrected value for energy and overburden stress. The normalized CPT index is defined as:

$$q_{c1N} = \frac{q_c}{P_a} \cdot \left(\frac{P_a}{\sigma_v'} \right)^n \tag{7.1}$$

and the 'soil behaviour type index' (I_c) is

$$I_c = \left[(3.47 - \log Q)^2 + (1.22 + \log F)^2 \right]^{0.5} \tag{7.2}$$

where

$$Q = \frac{q_c - \sigma_v'}{P_a} \cdot \left(\frac{P_a}{\sigma_v'} \right)^n \tag{7.3}$$

and

$$F = \frac{f_s}{q_c - \sigma_v} .100 \tag{7.4}$$

where q_c is the cone resistance, σ'_v is the effective overburden pressure, P_a is the atmospheric pressure and f_s is the measured cone sleeve friction in the same units as q_c.

Figure 7.17(a, b) shows the estimation of relative density (D_r) and V_s based on CPT results using different existing correlations. The measured in situ V_s values by MASW are also plotted on Figure 7.17(b). It is realized that the estimated relative density values (Appendix B) are higher than 100% at depths 1.00-4.00m and 8.00-10.50m. This may happen due to a stone being pushed ahead of the cone. Also, the estimated V_s values are high at these depths. Comparing the different estimated profiles to the measured V_s profile depicts that the measured q_c values at the pre-mentioned depths are higher than the normal values considering

that the fill depth at CPT-55 location is 7.5m. Figure 7.18(a) displays the measured V_{s1} and q_{c1N} profiles at CPT-55 location. The two profiles are not matching each other at depths 1.00-4.00m and 8.00-10.50m. Hence, the data points at these depths were excluded from the data base of the correlations. Figure 7.14 displays the measured V_{s1} and q_{c1N} profiles at CPT-55 location and the average q_{c1N} values considered for the proposed correlations (after removing abnormal q_{c1N} values). Figure 7.18(b) presents the estimated relative density (D_r) values based on SPT number at location of CPT-55.

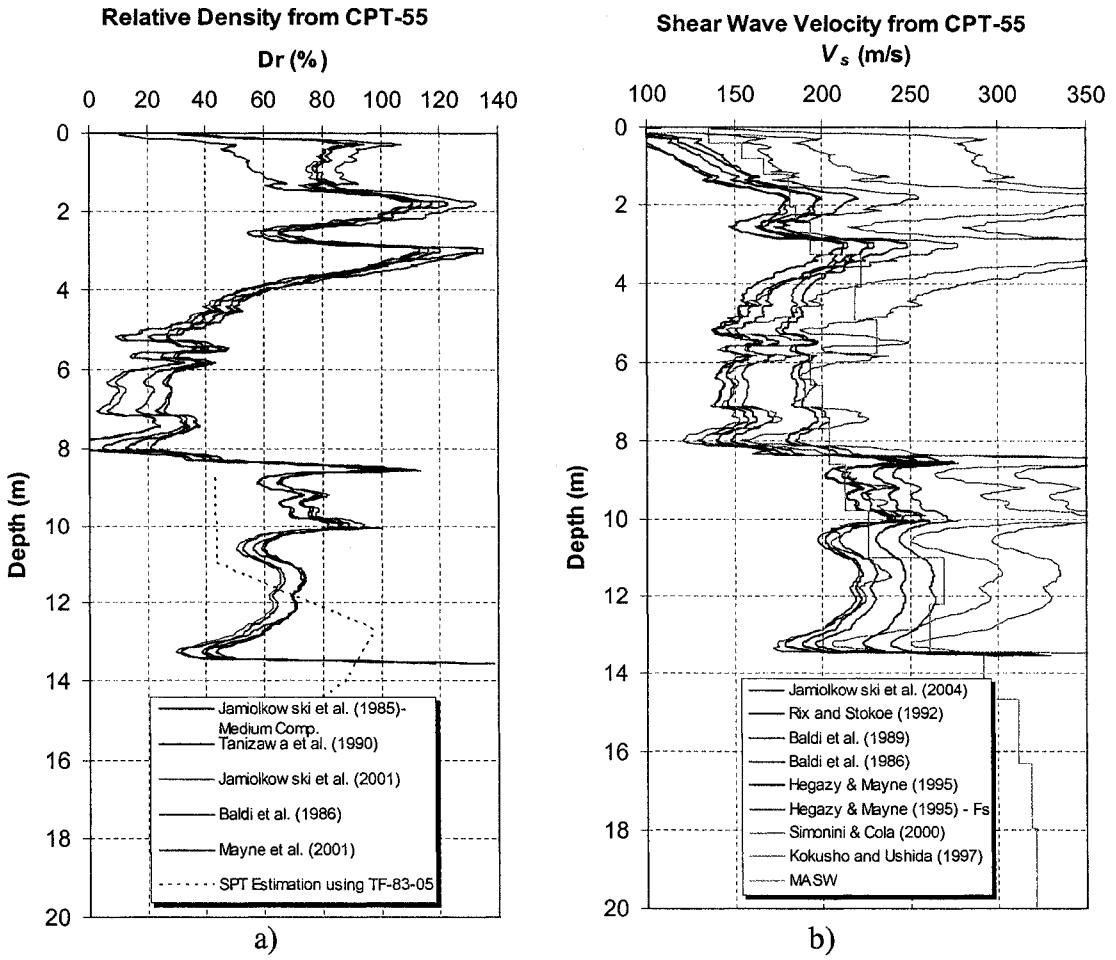

Figure 7.17 Estimation of D_r and V_s Based on CPT Results, and the Measured V_s-Profile by MASW.

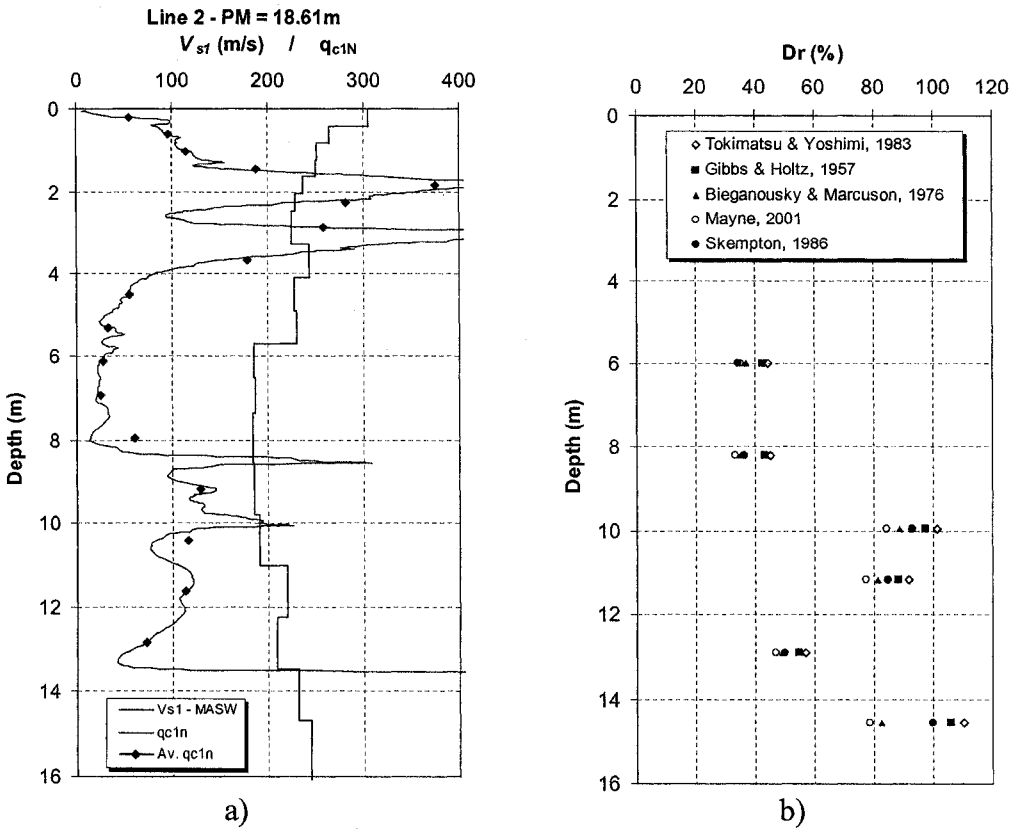

Figure 7.18 a) Profiles of V_{s1} & q_{c1N} at Location of CPT-55, b) Estimated Relative Density based on SPT.

The friction ratio (R_f or F %), the generated water pore pressure (U_2), the soil behaviour type index (I_c), OCR, K_o and voids ratio were calculated based on CPT results, and plotted against depth (Figures 7.19 and 7.20). In addition, the measured V_s-profiles were used to estimate the voids ratio using some empirical equations [Figure 7.20 (d, e)]. These graphs were used to verify of soil classification and to assess its state in order to double-check the accuracy of CPT and SPT results so that they may be reliably excluded/included in the data base. Figure 7.20 (d, e) reflects that the voids ratio differs according to soil type for the same V_s or V_{s1} value. Globally, the voids ratio of sands is higher than that of gravelly soils at the same relative density.

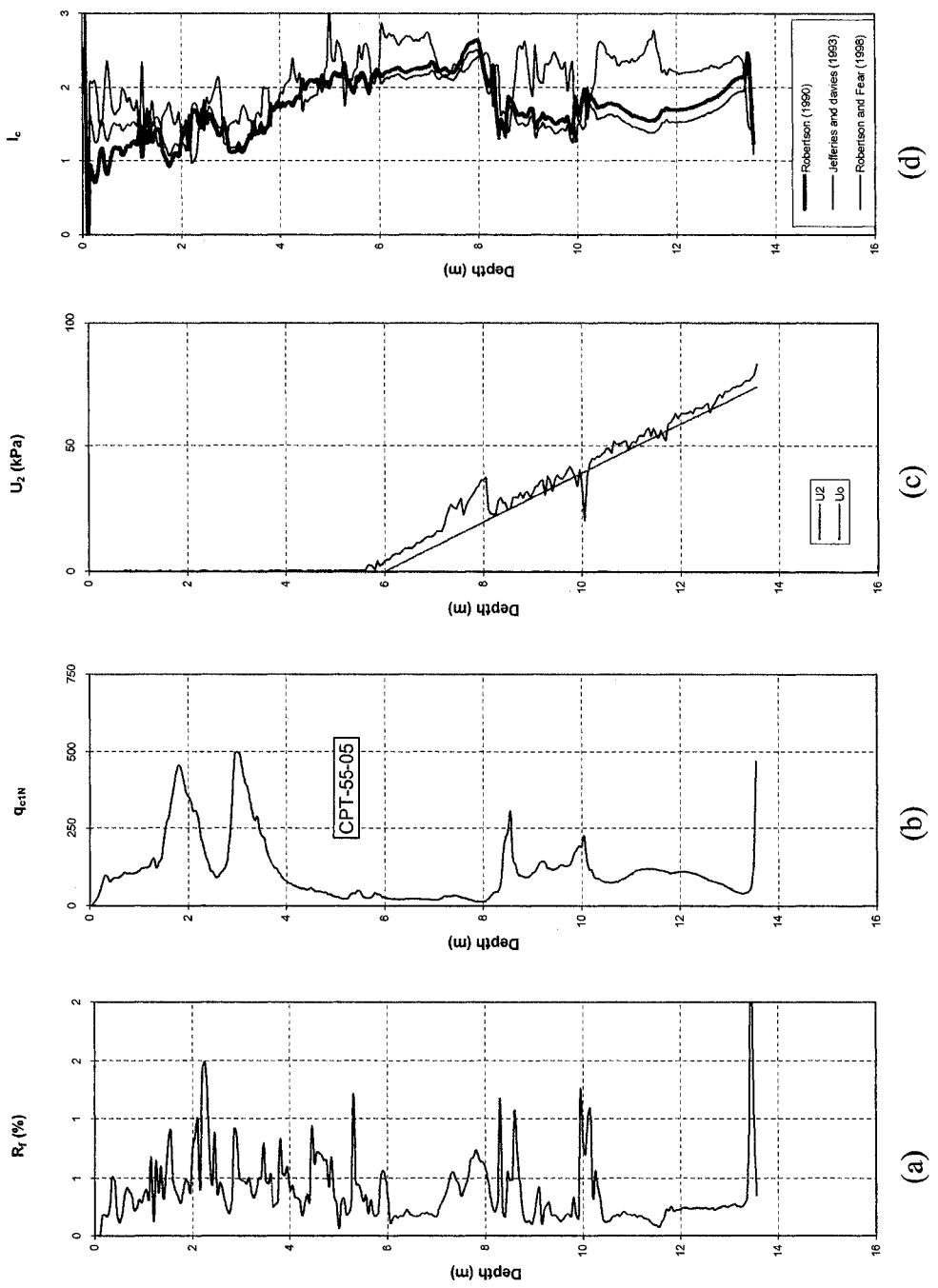

Figure 7.19 Test Results and Estimation of Friction Ratio (R_f) and Material Index (I_c) for CPT-55.

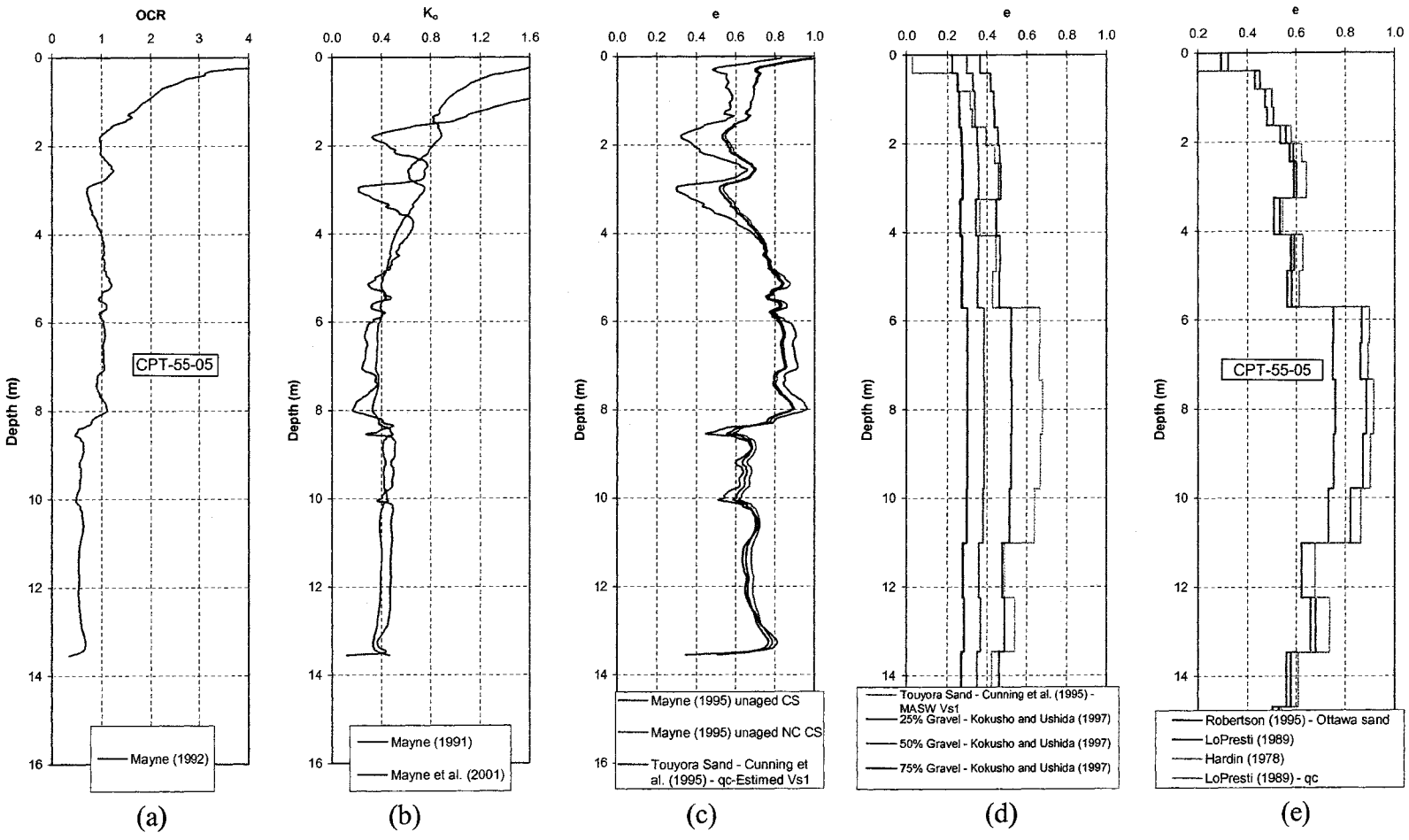

Figure 7.20 Calculation of OCR, K_0 and Voids Ratio (e) Based on CPT and V_s Profiles.

7.6 Voids Ratio and Shear Wave Velocity for Different Soil Gradiations

Figure 7.21 displays the different voids ratio functions [*f(e)*] used in estimating V_s. The empirical equations for shear wave velocity (V_s) are mainly a function in average stress and f(e). It can be seen that these functions differ from each other, especially at voids ratio range of 0.1–0.4. This is possible due to the fact that these equations were based on test results on different soil types. The voids ratio of soil can be estimated from the normalized shear wave velocity (V_{s1}) using some of the existing empirical equations. Figure 7.22 displays the estimated voids ratio versus V_{s1} using different equations for different soil types. The estimated voids ratio values of sands are quite different for those of gravely sands. For the same V_{s1} value, the voids ratio decrease with increasing gravel content. At V_{s1} equals 200 m/s, the variation in voids ratio between the different soil types reaches 0.5. Also, for the same voids ratio, a gravely soil have higher normalized V_{s1} value than a sandy soil.

The fill material of the lower enbankment of the dam (Gravel and Sand) has an average uniformity coefficient of 24. When using Kokusho and Yoshida (1997) correlations (Equation 2.47) to estimate the maximum normalized value of shear wave velocity [V_{s1}^{max}] for the fill at its densest state (at D_r = 100%), a value of 403 m/s is obtained. Entering this value in Figure 7.21, we get a corresponding voids ratio value of 0.2 which is the obtained value from laboratory minimum density test (Figure 7.6). This confirms the compatibility of laboratory results with Kokusho and Yoshida (1997) results. Also, it confirms the suitability of Kokusho and Yoshida (1997) equations to estimate V_{s1} for gravely soils.

These results reflect that the voids ratio functions for sands are not suitable to be used for gravely sands or gravels due to the difference in the voids ratio range between the two types of soils. Also, the voids ratio of gravely soils may not be estimated from the V_s-empirical equations for sands. The constants of these empirical equations (e.g. C_g, n_a, n_b & a_g) should be different from soil type to another due to particle size and grading difference. It is well known in liquefaction studies that there is a correction to V_s-values of soils that contain portion of fines in order to calculate the V_s-value for clean sand. In the same way, there should be a correction for gravel content so that a V_s-value of a gravely soil is compared to another value for clean sand.

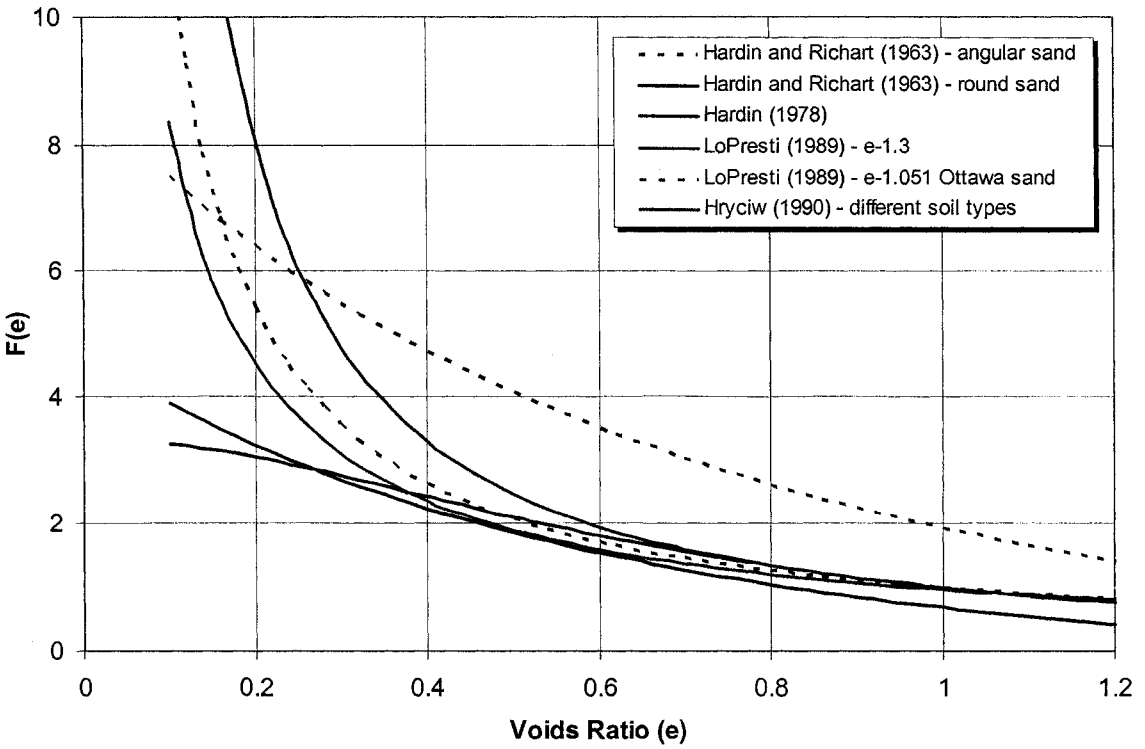

Figure 7.21 Different Voids Ratio Functions.

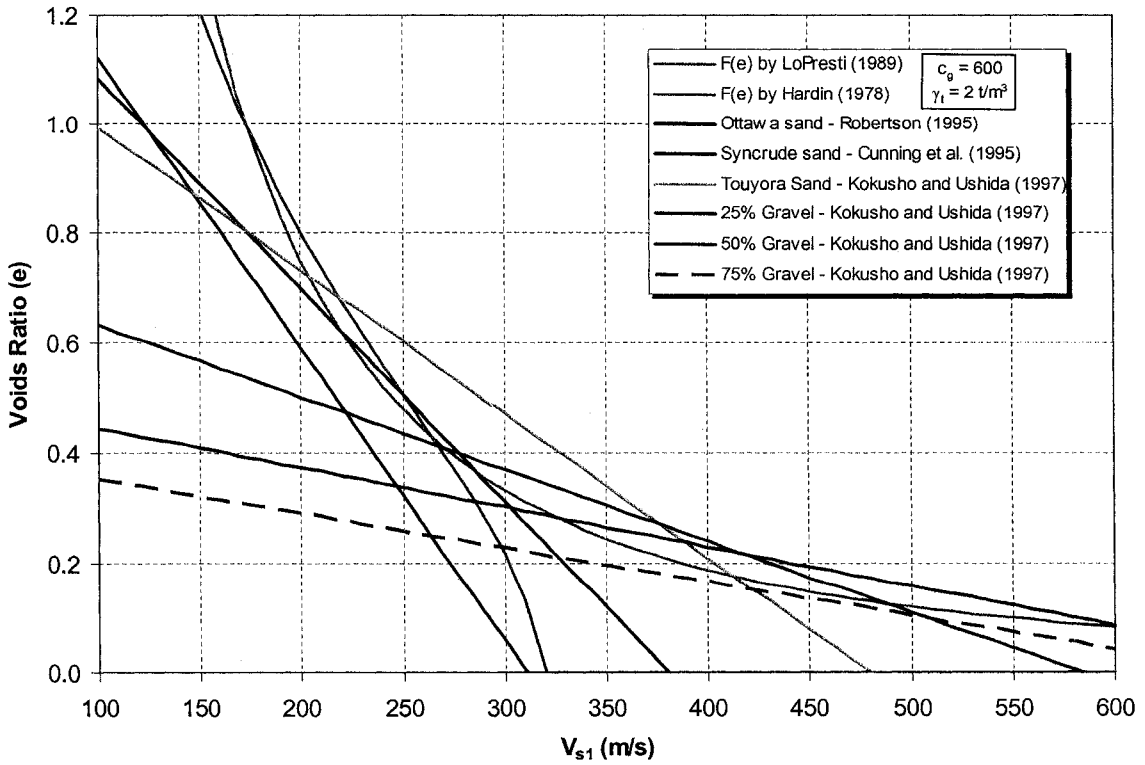

Figure 7.22 Estimating Voids Ratio from V_{s1} for Different Soil Types.

7.7 Correlating V_s to Penetration Tests Indices

The verified data base of Peribonca dam project was used to investigate the relationships between V_{s1} and each of q_{c1N} and $(N_1)_{60}$ for the different soil types at the site. These relationships are useful for soil characterization at other sites of similar soil composition. These relationships are important as the currently existing correlations of this type were derived based on tests on sands only (Appendix A).

7.7.1 Relationship between V_{s1} and q_{c1}

The data pairs for the V_{s1} – q_{c1N} relationship are presented in Table 7.2. Figure 7.23 displays this relationship using all these points (without excluding abnormalities). It can be seen that the points are scattered. Nevertheless, there is some agreement with the existing correlations. Three existing correlations for sands are illustrated on the same Figure [Robertson et al. (1992), Fear and Robertson (1995) and Andrus et al. (2003)]. Another relationship implied from the liquefaction charts is also displayed. For the same Cyclic Resistance Ratio (CRR) value, the corresponding V_{s1} and q_{c1N} were extracted from each of q_{c1N}–CRR and V_{s1}–CRR liquefaction curves [Youd et al. (2001), Kayen et al. (2004), Andrus et al. (2003), and Andrus and Stokoe (2000)]. Hence, a relationship between V_{s1} and q_{c1N} could be drawn and is called "CRR Liquefaction Criteria".

The data points in the natural soil underneath the dam were separated from the points in the fill soil. This should help in clarifying the relationship as there is big difference in soil grading between the two layers. Figure 7.24 shows only the data point in the fill layer (lower embankment of the dam). The scatter of this relationship has become lesser than in Figure 7.23. The normalized shear wave velocity increases with increasing q_{c1N}. In order to enhance this relationship, the data points at the depths where V_{s1} and q_{c1N} values are incompatible were excluded (where there are abnormal values in q_{c1N} profile). Hence, the relationship between V_{s1} and q_{c1N} for the fill soil of the dam (Sand and Gravel) is shown in Figure 7.25 (abnormal values excluded). The relationship has become more defined. It is clear that all the data points are located above the curves of the existing relationships (Appendix A). This reflects the

difference in each of V_{s1} and q_{c1N} between the fill soil (Sand and Gravel) and the tested sands in literature. A further step was taken for the analysis of the data base. The abnormal points were adjusted to match the general trend of the q_c profile. Soil classification, soil state, soil behaviour index (I_c), and friction ratio (F) were employed as a guide in this adjustment. Figure 7.26 display the data base points after making the adjustment for q_c profile. The points in this graph take the same trend of the data points in Figure 7.25. There is little divergence between the points because the fill soil is inhomogeneous. The normalized shear wave velocity increases by increasing q_{c1N}. The trend line of this relationship is parallel and higher of Robertson's relationship for Alaska sand. This depicts that gravelly sands have higher shear rigidity than sandy soils. The relationship between q_{c1N} and V_{s1} takes the shape of a power curve. The regression equation of this relationship is as follows

$$V_{s1} = 118.9(q_{c1N})^{0.174} \qquad (R^2 = 0.49) \qquad (7.5)$$

This equation is similar to the existing empirical equations for sands except that the multiplier of this equation is lower and q_{c1N}-exponent is less. Figure 7.27 presents the same set of data in Figure 7.25 but the points at shallow depths (d<1.5m) are separated from deeper points. The points at shallow depths are located at the upper zone of the graph. This is attributed to their very low stresses that give high V_{s1} values after normalization of V_s to stress.

Figure 7.28 displays the relationship between V_{s1} and q_{c1N} for the natural soil underneath the dam. There is relatively large scatter in the data. This is attributed to the heterogeneity of the natural soil (Figures 7.11 and 7.12). Also, the V_s measured by MASW takes into account the grain size of soil as a mass while the CPT is local measurement. If a stone is pushed ahead of a CPT, this will result in abnormal q_c values and the test result is not representative to soil condition. In the other hand, MASW gives V_s values which are affected by the surrounding soil (i.e. existence of stones would be positively reflected in V_s profile). However the data points in this study are located around the curves of the existing correlations as expected according to soil type.

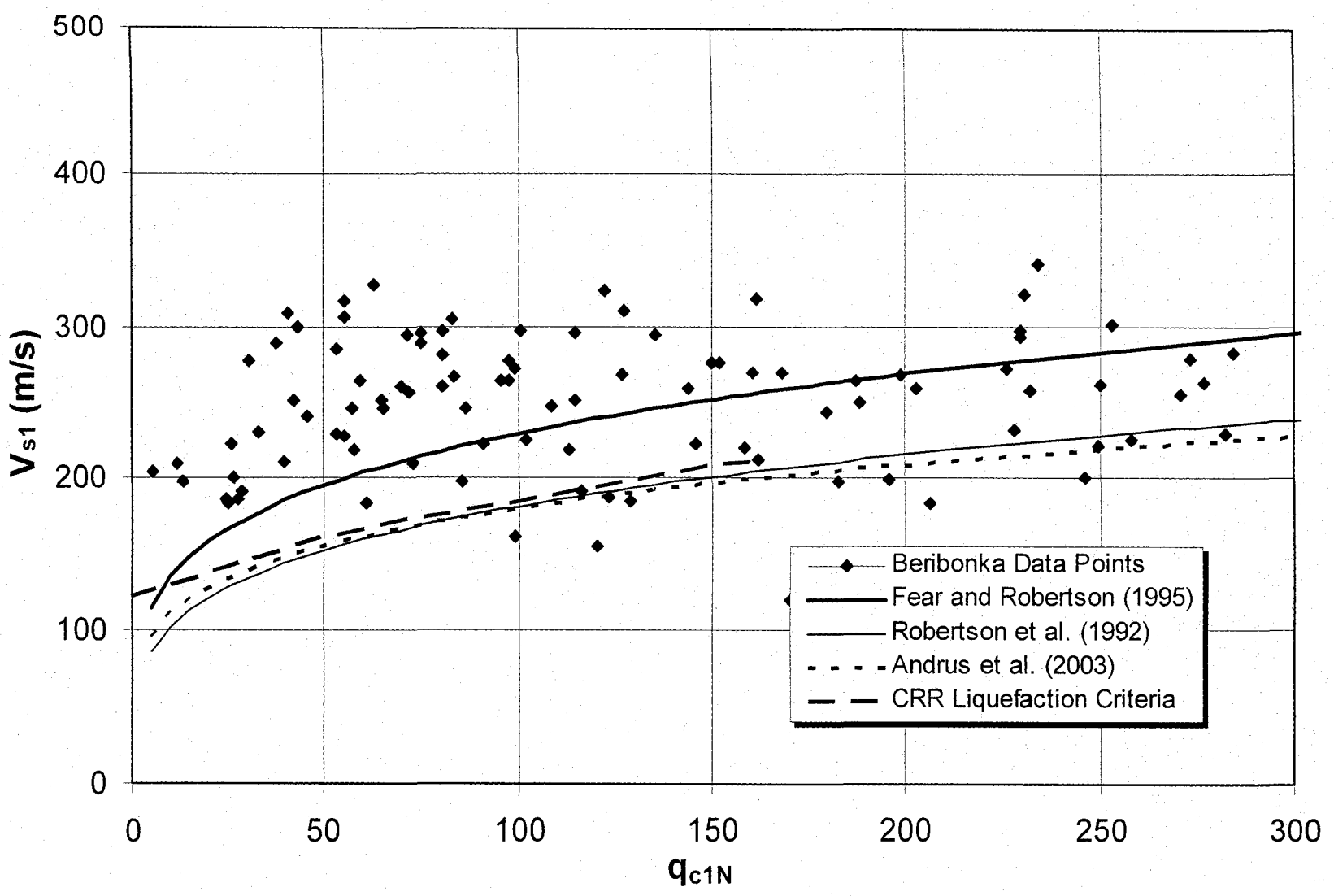

Figure 7.23 All $V_{s1} - q_{c1N}$ Points of Peribonka Dam Data Base.

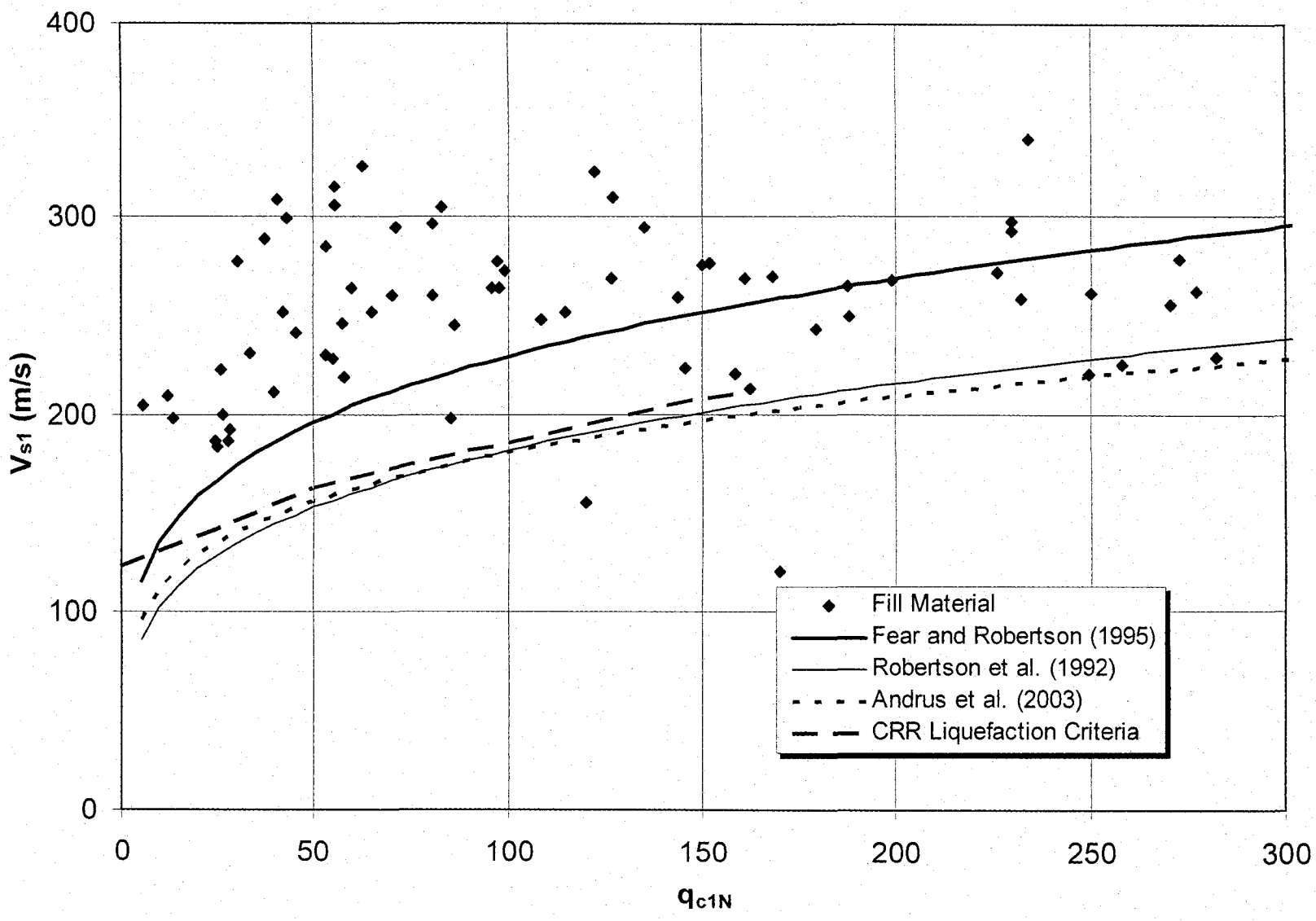

Figure 7.24 The Data Points in the Fill Soil.

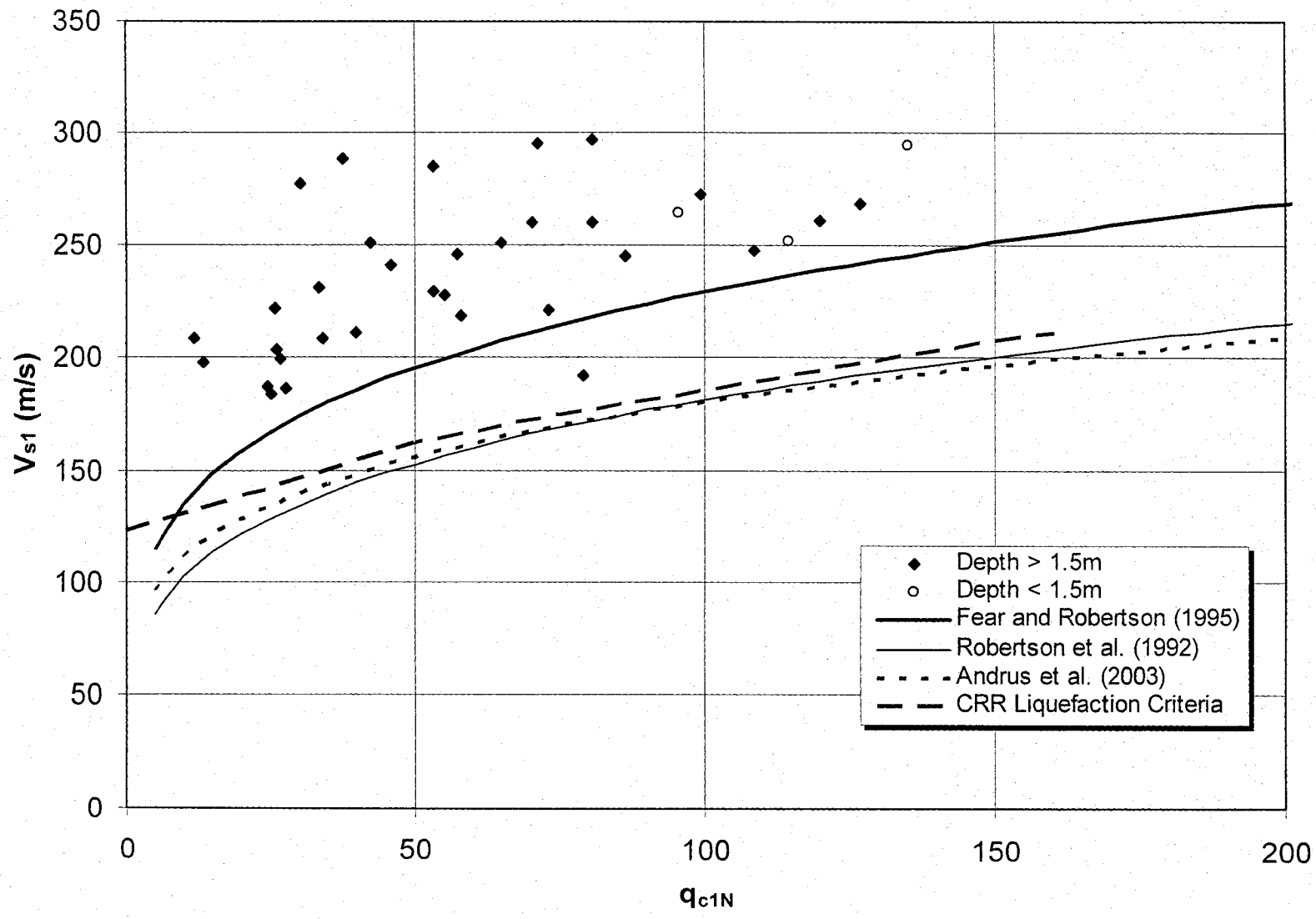

Figure 7.25 Data Points in the Fill Soil Excluding Abnormal Values.

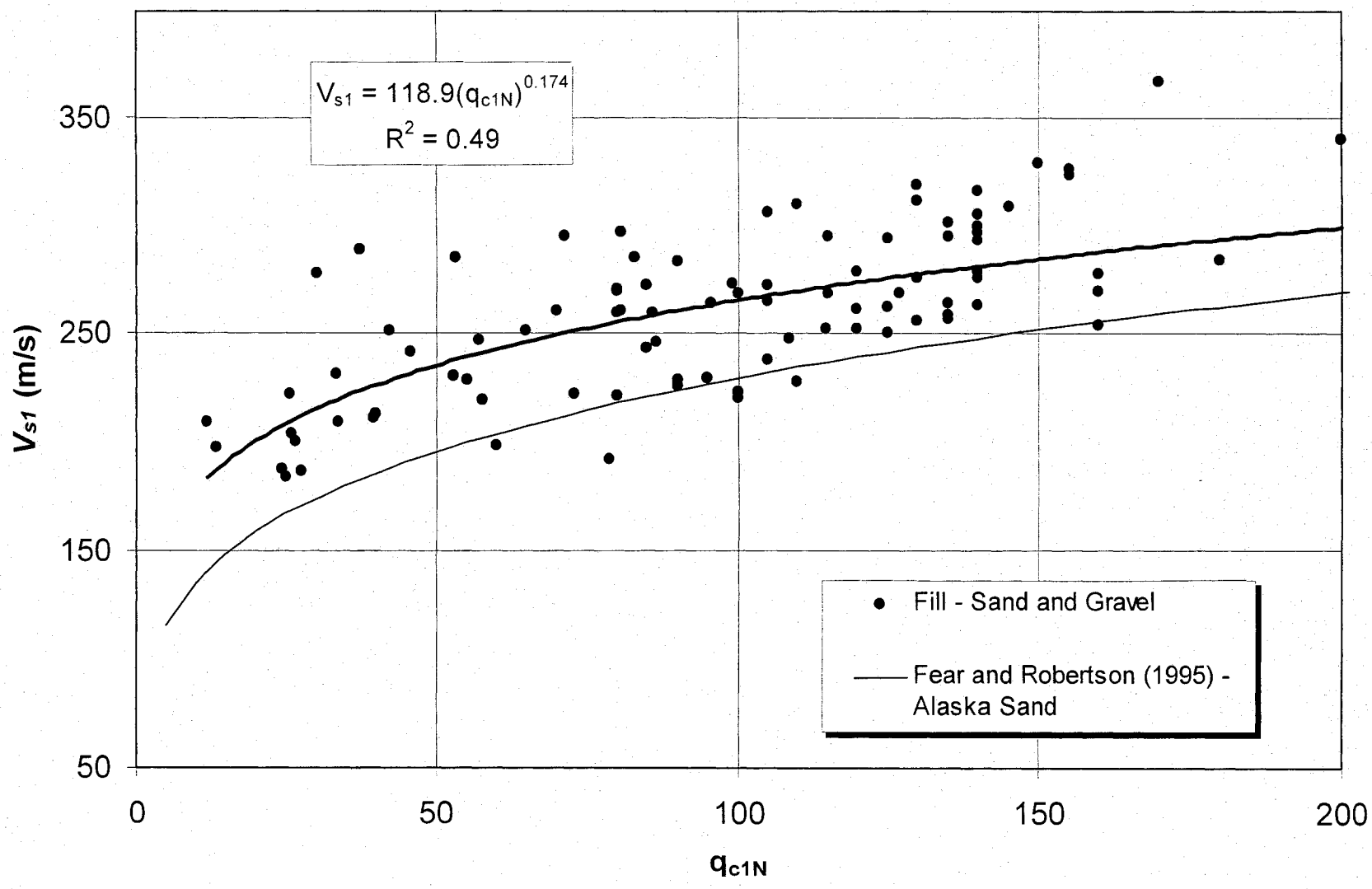

Figure 7.26 The Relationship between V_{s1} and q_{c1N} for the Fill Soil (abnormal q_c values corrected).

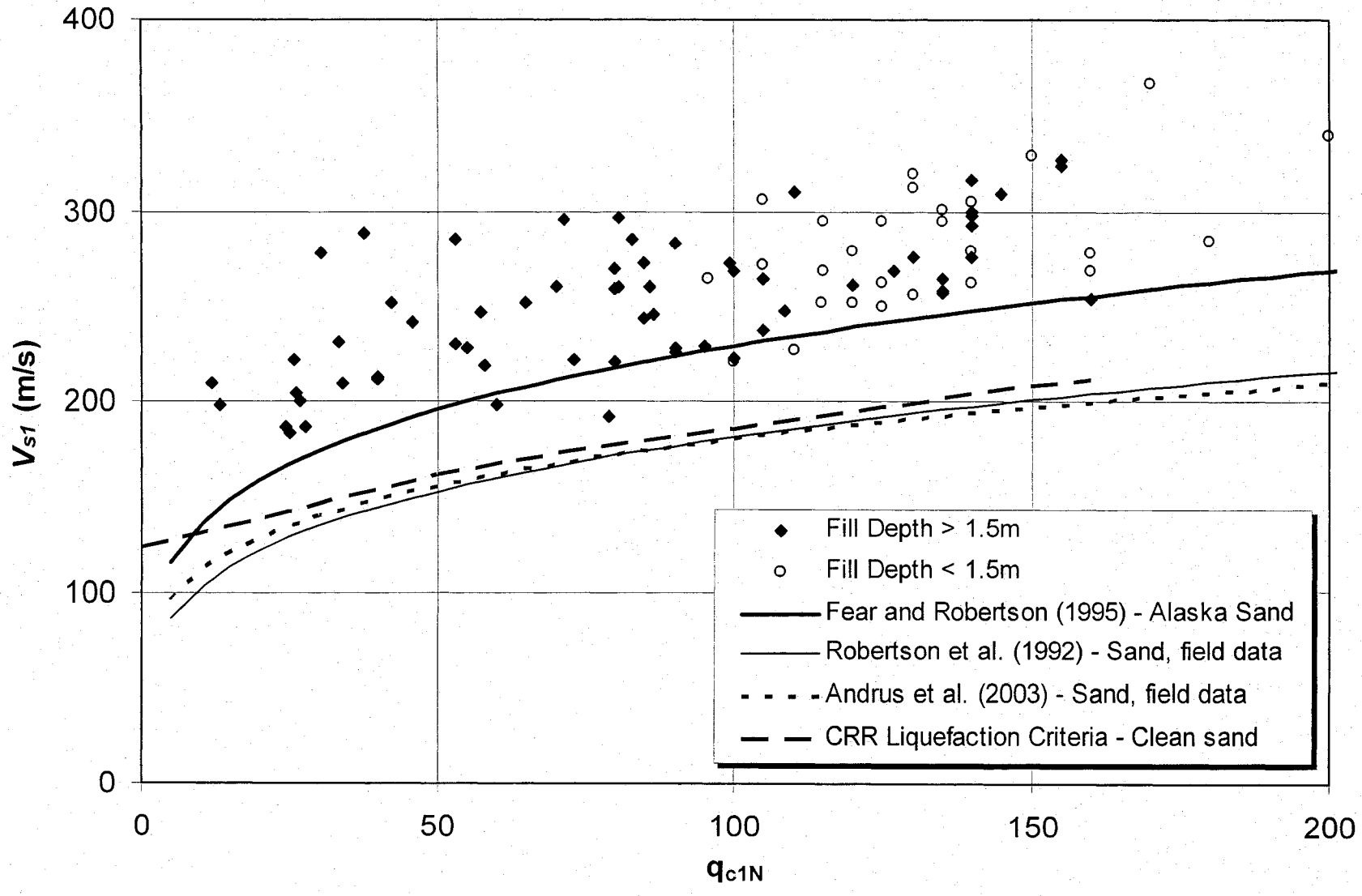

Figure 7.27 Comparison between the Obtained Results in the Fill of the Dam before Compaction and some Existing V_{s1} – q_{c1N} Correlations (V_s & q_c Profiles are within 3.5m apart).

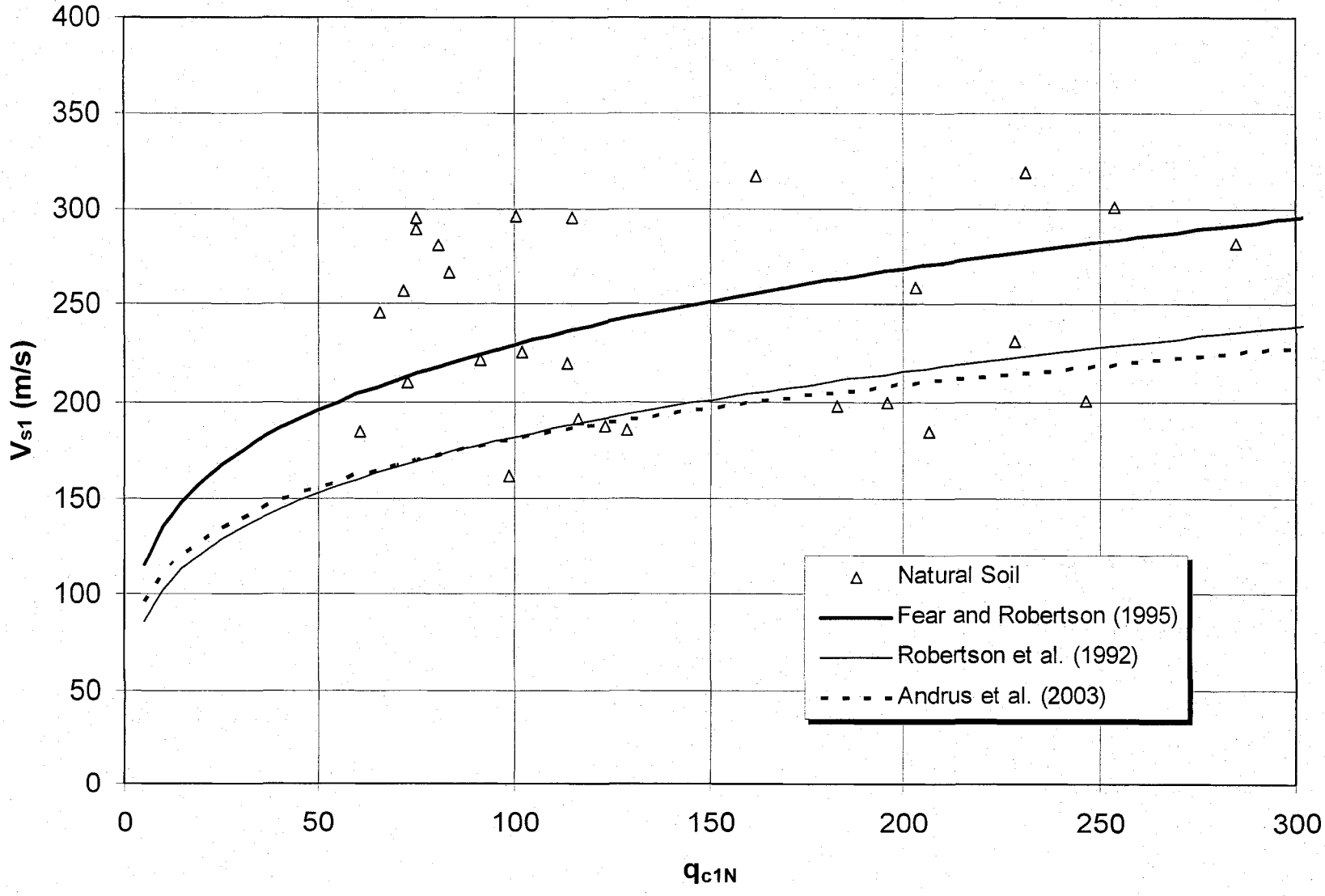

Figure 7.28 Comparison between the Obtained Results in the Natural Soil before Compaction and some Existing $V_{s1} - q_{c1N}$ Correlations (V_s & q_c profiles are within 3.5m apart).

7.7.2 Relationship between V_{s1} and $(N_1)_{60}$

Few standard penetration tests (SPT) were carried out in the fill layer. Hence, a V_{s1}-$(N_1)_{60}$ correlation for the fill soil was not possible. Figure 7.29 displays the relationship between V_{s1} and $(N_1)_{60}$ for the natural soil underneath the dam. A good trend is observed although of the data scattering. The points scattering is normal in this type of relationships due to many reasons such as the distance between V_s and SPT locations, and the fundamental differences between the two tests. The obtained regression equation of V_{s1}-$(N_1)_{60}$ relationship is

$$V_{s1} = 81.4\left[(N_1)_{60}\right]^{0.31} \qquad (R^2 = 0.55) \qquad (7.6)$$

The normalized shear wave velocity increases with the increase of the penetration resistance.

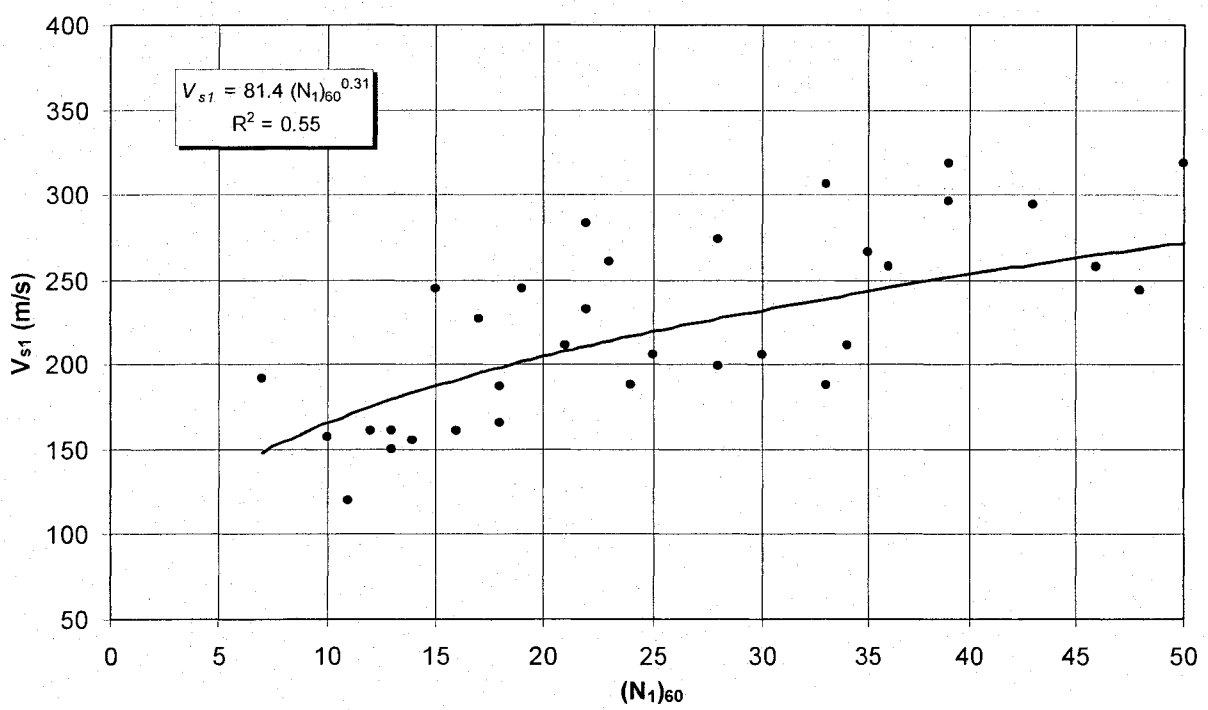

Figure 7.29 The Relationship between V_{s1} and $(N_1)_{60}$ for the Natural Soil.

This relationship is similar to Fear and Robertson (1995) correlation for Alaska sand. The multiplier in the two equations is almost the same. But the exponent of $(N_1)_{60}$ in this study is higher than the exponent in Fear and Robertson (1995) Equation. This difference is believed to be resulting from the grain size differences between the two soil types. The measured V_s

values by MASW are affected by soil grain size and grading while the SPT may not capture the effect of surrounding inclusions of gravel/couples/boulders. Figure 7.30 presents the same data points in Figure 7.29 but the soil classification of each point is illustrated. The soil classification agrees quite well with the measured values of V_{s1} and q_{c1N}. The soil of large grains size has higher shear rigidity than soil of small grains size.

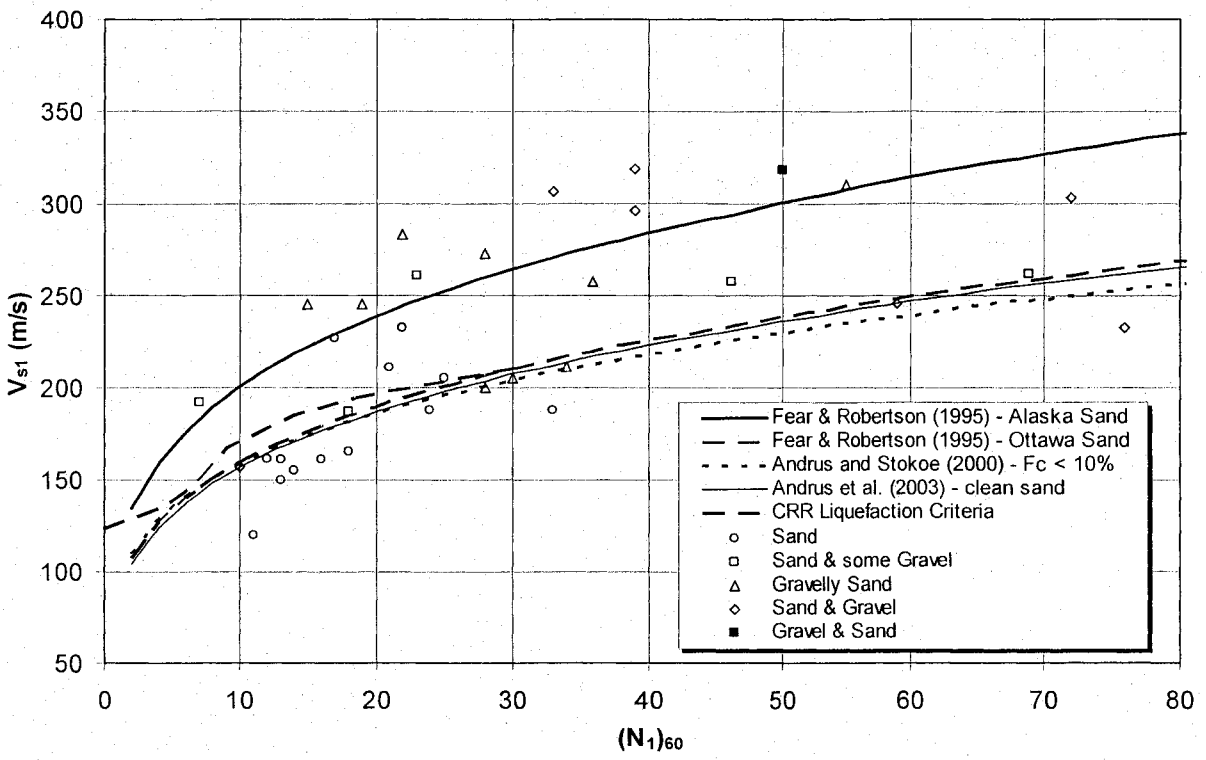

Figure 7.30 Comparison between the Obtained Results and the Existing $V_{s1} - (N_1)_{60}$ Relationships.

7.8 Conclusions

This chapter has shown that V_{s1} values for gravelly sands are higher than those for sands. The grading characteristics of soil control its rigidity. Hence, the shear wave velocity increases with the increase of grains size of soil. Also, the void ratio of gravely soils may not be

estimated from the V_s-empirical equations for sands. Several correlations between each of CPTu and SPT indices and the in-situ V_s-measurements could be reached for sandy and gravelly soils. These correlations are useful for soil characterization not only at Peribonka site, but at other sites of similar soil composition. It may be used for roughly estimating soil properties for geotechnical design.

Chapter 8 CONCLUSION AND RECOMMENDATIONS

8.1 Introduction

Numerical simulations and laboratory tests were carried out to demonstrate the problems of pulse velocity tests and their interpretation difficulties (especially by bender elements). Also, some analytical models were studied to investigate interference of waves in different laboratory setups due to reflections at sample's boundaries. The near-field phenomenon was also studied and its controlling parameters were stated and their effects on test results were were quantified. In addition, new modes of shearing excitations for pulse tests were introduced and analyzed in this research. Plane radial shearing is found to be the best mode for pulse tests. Hence, it was taken as a base for a new piezoelectric device for carrying out pulse tests. The first piezoelectric ring actuators setup, which works in this mode, was built in a team effort (Gamal-El-Dean, D. R., Ethier, Y., Lefebvre, G. A., and Karray, M).

The piezoelectric ring actuators setup was also developed in this study in a collaborative research. The development stages of this new device and the different findings during these stages were presented. Eight different piezoelectric setups were built in this study and their peripheral equipments were optimized. Many laboratory pulse tests were carried out on different soil types using these piezoelectric setups, and several relationships were obtained. Also, the compaction curve in terms of water content and V_s was studied for two soil types. In addition, two new interpretation techniques for pulse tests were introduced and evaluated in this research (Wigner-Ville Energy Analysis and Energy-Rise Methods) in a collaborative research. Nevertheless, based on the gained experience during this study, a new criterion for carrying out pulse tests and interpreting the results in time domain was presented. Wigner-Ville Energy Analysis Method was used to interpret the pulse tests of this study (the other existing methods were also used for comparison).

Finally, a detailed analysis was performed for the in situ and laboratory tests at Peribonka dam site. Several relationships between V_s and each of the SPT and CPT indices for gravelly sands were obtained. Thus, this research has shed the light on pulse velocity tests, their piezoelectric testing devices, the interpretation methods, V_s-compaction curves, and soil characterization using shear waves. The finding of this research underpins carrying out further studies in these promising domains.

8.2 Output of the Study

A simple method for pulse tests interpretation in time domain was introduced in this research (Chapter 3) in a team effort. This method is called Energy-Rise Method because it uses energy of the cross-correlation function to determine the characteristic shear wave velocity. It gave the most accurate interpretation results for the carried out simulations among the four other commonly used techniques. Also, in the light of this research results, a new criterion for carrying out and interpreting pulse tests using the conventional interpretation methods was established (Chapter 4). Moreover, some new input wave shapes were introduced and used in this research. The smooth-edged input-wave shapes such as winged-sine or versed-sine are better than the sine wave in clarifying the s-wave component and reducing the secondary waves.

The dispersive nature of pulse tests was proven numerically and in laboratory during this research. Hence, the shear wave velocity from pulse tests should be interpreted in the frequency domain. This fact renders the simple methods of interpretation inaccurate. Based on these findings, a new interpretation technique for pulse tests using Wigner-Ville Transform (Wigner-Ville Energy Analysis Method) is developed and introduced (Chapter 4). It is capable of separating the different components of the output signal in frequency domain. This helps in differentiating between reflected and base waves, if any. This new technique determines the characteristic velocity of soil considering the dispersivity of pulse tests. The currently existing interpretation techniques do not take into account this important fact.

The reason of "near-field effect" in pulse tests could be uncovered in this study. Numerical simulations and laboratory experiments were used to demonstrate these findings. The parameters that control this phenomenon could be stated and their effects on the test results were quantified. It was proved in this research that near-field phenomenon is due to reflected waves. However, measurement in the near-field may also affected by coupling of the p- and s-waves.

A new setup for pulse velocity tests was introduced and developed in this research (Chapter 5) in a collaborative research. The ring actuators setup overcomes many problems related to soil testing using the other existing devices; namely, wave reflections at boundaries (end-caps & sides), sample disturbance, weak shear coupling between soil and device (interaction) as well as the fixation problems, low resonant frequency and limited input voltage of the existing devices. It is an accurate and versatile device compared to the existing devices such as bender elements. The output signals of this device are of high quality without the need of signal stacking, amplification or conditioning. It was designed to function in plane radial shearing excitation which is completely different from the other modes of the currently existing devices. The excitation and recieption areas of this setup are large which make it more robust. As a pioneer characteristic of this device, it takes into account the soil anisotropy in the three dimensions (soil as a mass) rather than 1-plane measurements by the other devices.

The new device was implemented in pedestals and top caps that were used with an oedometer cell, a Proctor mold and other fabricated molds. The accuracy of this device was checked by carrying out pulse tests on samples of standard Ottawa sand and Plexiglass. Also, many experimental results and relationships were obtained using this device. It is capable of measuring V_s and V_p under very low to very high stresses using relatively low input voltages. The new setup is capable of eliminating secondary waves in output signals, under certain conditions, so that only the shear wave and its second arrival are recorded. This device is thin compared to other devices and transfers its moving energy by friction without penetration into the soil sample. It delivers high energy to the soil over a large area even at low confining stresses as opposed to shear plates. The difficulties encountered during the development

process of the ring actuators setup and how they were solved, the different ideas and the findings during this stage are documented in Chapter 5. Some recommendations are given in Section 8.4 for building this device or similar actuators.

8.3 Conclusions and Recommendations

The main conclusions of this research are summarized in the following points.

- Pulse tests numerical simulations by finite difference dynamic analysis code is a robust way for investigating wave transmission characteristics, and the parameters that affect the interpretation process of received signals as well as for studying new pulse testing devices/techniques.
- The numerical simulations confirmed the existence of interpretation difficulties for shear-wave velocity measurements by bender elements. It is difficult to specify the correct arrival time based on the time domain record. Shear wave velocity determination should be carried out in the frequency domain in order to obtain the characteristic velocity of soil. The currently existing interpretation techniques may give erroneous results, and are not accurate enough for precise measurements. Generally, time domain methods should be used with caution or for situation where relative or approximate measurements are needed. The cross-correlation (C.C) technique may give highly erroneous results at some conditions. Therefore it has to be used with caution and preferably in parallel with other methods of interpretation.

- Bender elements dimensions compared to the soil dimensions is very important in avoiding the interference between the base waves and the reflected waves. Generally speaking, the emitter geometry and its radiation angle as well as sample dimensions and properties control whether waves-coupling due to reflections is possible or not.
- The optimum frequency of excitation depends on soil rigidity and dimensions, type of transducer, and resonant frequencies of the different components of the system. Therefore, many input frequencies should be tried beginning at very low frequencies up to the resonant frequency of the system. Also, different input shapes should be tried. The smooth-edged input-wave shapes such as winged-sine, versed-sine and wavelet are helpful in clarifying the s-wave component and reducing the secondary waves. Usually, the

highest input wave frequency that does not create resonance in the system gives the most reliable signal for interpretation.

- The plane radial shearing mode of excitation for pulse tests is the best suitable mode among all other existing modes including the bending mode of the bender elements. All-base plane shearing eliminates reflections of waves at end caps and cancels the side reflected waves. It can be used to measure the shear wave velocity in the time domain with reasonable accuracy without side reflections. Even pure shearing excitation produces a compression wave within soil. An Actuator element that mainly produces shear displacements will also generate small compressive displacements. These displacements travel in soil as a compression wave. This wave may create other reflected waves that might interfere with the base shear wave.
- Any traveling wave with a curved front creates reflected waves when it encounters a free or a fixed boundary. The energy of the reflected wave depends on the rigidity of the boundary. Numerical simulations have shown that reflection of waves at sample's boundaries play a major role in the ambiguity and difficulty of wave interpretation. The geometrical conditions of the sample and its properties (especially Poisson's ratio), the system damping ratio as well as the input frequency control this effect. The applied stresses participate in magnifying or reducing waves-reflection effect as it controls the wave length (λ) of the probing signal. Also, the analytical studies in this research have shown that the sample and piezoelectric device dimensions and Poisson's ratio play an important role in drawing the shape of the output signal due to reflection of waves. Thus, the shape of the output signal depends on the sample's dimensions and properties, the input waveform, input frequency, input voltage, 'geometry and rigidity' of the piezoelectric device and its degree of fixation as well as on noise and interference. Therefore, the different possibilities of wave reflection that may cause waves coupling/interference should be checked for the testing apparatus considering the dimensions and specifications of the piezoelectric device. The reflected waves should not greatly interfere with the base shear wave. Otherwise, the practitioner should consider these interferences in the measurements. It is recommended to make the input frequency higher than 1.5 kHz so that noise effect can be eliminated in pulse tests.

- The near-field effect does not only depend on the sample length to input wave length ratio (L/λ). It also depends on the Poisson's ratio, the sample's geometry (the dimension perpendicular to the wave propagation direction; i.e. the diameter for a cylindrical sample) and "system damping ratio". All these parameters contribute to near-field effect and determine whether it may affect/rule the measurement accuracy or not. Pulse test measurements should be carried out after the compression and shear waves become well separated.

- It is recommended to understand the output signals of pulse tests by characterizing each wave within the received signal (the different components of the signal) in order to reliably identify the s-wave. Eliminating the secondary waves in the output signal is quite helpful in interpreting the results. Trimming the output signals to remove the secondary components so that the shear wave may be exclusively analyzed using Wigner-Ville Energy Analysis method is a useful process in obtaining clear results when there is no overlap between the different components of the signal. Obtaining shear wave dispersion curves similar to the theoretical trends is a good indication of the quality of output signal. Overlapping of secondary waves may create a major component on the output signal of an energy that may exceed the s-wave amplitude.
- The pulse test results have demonstrated the suitability and capability of the ring actuators to accurately measure shear and compression wave velocities of soil under the different conditions. It has been proven that friction between soil and mold sides affects the measured V_s values, especially at high pressures. Pulse test measurements in Proctor mold should be carried out at very low pressures (not exceeding about 35kPa for LG4 till).

- The V_s–w_c compaction curve was drawn for two soil types (Chapter 6). The V_s–w_c relationship takes the form of the common bell-shape curve of the γ_d-w_c relationship, except that the dry-of-optimum side is relatively higher. The difference in V_s values between partially saturated (w_c = 5%) and dry of LG4 till samples varied from 82% at the lowest applied pressure (29 kPa) to 26% at the highest pressure (798 kPa). This variation depends on soil suction, applied stresses and the value of voids ratio.

- The maximum suction degree of saturation ($S_{opt.}$ %) depends on soil grains size and grading. The water content at this state is much less than the optimum water content for maximum density (normally out of the proctor test w_c-range). Within the water-content range for Proctor test, the optimum water content for V_s is slightly less than the density optimum water content. The dry-of-optimum side is having higher shear wave velocities than the wet-of-optimum side. This means that compaction of soil at the dry-of-optimum side is better than the wet-of-optimum side because the compacted soil will be more rigid.

- The data analyses for Peribonka dam resulted in establishing some equations and correlations for sandy gravels (Chapter 7). The grain size analysis of the fill materials have shown that soils of D_{50} greater than about 1.0-mm would have similar maximum and minimum voids ratio. Also, a soil with very wide grain size variations would have similar maximum and minimum voids ratio to well graded soils.
- For the same V_{s1} value, the voids ratio decrease by increasing the gravel content. The voids ratio functions [*f(e)*] for sands are quite different for those of gravely sands or gravels. For example, at V_{s1} equals 200 m/s the variation in voids ratio between the different soil types is up to 0.5. Also, for the same voids ratio, a gravely soil have higher normalized V_{s1} value than a sandy soil.
- The measured V_{s1}-values for the dam fill materials (gravel and sand) are higher than the estimated values using the existing V_{s1}–q_{c1N} correlations for sands. Kokusho and Yoshida (1997) test results on gravelly sands are in excellent agreement with the laboratory and in situ test results for Peribonka dam. Their empirical equations may be used to estimate V_{s1} for gravely soils.

- In this study, a correlation equation was derived between V_{s1} and q_{c1N} for the embankment material of the dam (Equation 7.5). The relationship takes the same trend of the existing empirical equations for sands (power curve), except that the multiplier of the equation is lower and q_{c1N}-exponent is less.
- A good trend is obtained for the relationship between V_{s1} and $(N_1)_{60}$ for the natural soil underneath the dam. A correlation equation was derived between these two parameters (Equation 7.6). This obtained equation is similar to Fear and Robertson (1995) correlation

for Alaska sand. The multiplier in the two equations is almost the same. But the exponent of $(N_1)_{60}$ in this study is higher which can be attributed to the difference in soil type and gradation.

- Many combinations of stress and voids ratio may result in the same V_s value. Therefore, the comparison between results should be carried out in terms of the normalized shear wave velocity (V_{s1}) and voids ratio. The voids ratio functions for sands are not suitable to be used for gravely sands or gravels due to the difference in the voids ratio range between the two types of soils. Also, the voids ratio of gravely soils may not be estimated from the V_s-empirical equations for sands.

8.4 Recommendations for Building Ring Actuators Setup

The development stages of ring actuators setup were useful in reaching important findings for building robust setups. The following sentences summarize these findings. The good contact between piezoelectric device and soil is important in pulse tests. The emitter and receiver excitation surfaces should be even and sufficiently rough. The area of excitation for ring actuators pulse tests should be optimized to suit the specimen dimensions and properties. The back surface of the ring actuator unit should be even and very smooth to facilitate its reaction. Also, it is recommended to avoid applying lateral confinement or torsion stresses on the piezoelectric unit which may restrain its deformations. Centering the rings with their inner stones in the horizontal and vertical directions is necessary to achieve the desired performance of the setup. An inner stone that easily react to the piezoelectric ring and soil is highly desirable in building a robust ring-actuators setup. A piezoelectric setup of high resonant frequency is highly preferred in soil testing, especially at high pressures or when testing stiff soils. Grounding the piezoelectric setup and the metallic parts of the apparatus is vital in eliminating electromagnetic waves in the output signals. Several equations are given in Chapter 5 for designing a piezoelectric ring actuator setup and choosing its peripheral electronic equipments. The specifications of the electronic equipments are essential for accurate and proper measurements.

8.5 Further Research

This section proposes some points that may be investigated in order to advance the research in the domain of this study. As a simplified method for interpretation of pulse tests, the Energy-Rise-Time method should be further investigated to interpret pulse tests on many soil types at different conditions. Further work may be carried out to investigate the effect soil heterogeneity and layering on the measured shear wave velocity using ring actuator. The new setup should be installed and used in other laboratory setups (triaxial and direct shear) which will result in obtaining important results. Correlating V_s to usual soil parameters using this robust device is a very useful research topic for many geotechnical applications. Investigating the laboratory compaction curves in terms of water-content and shear-wave velocity for different soil types would be another important application. It is recommended to measure the suction pressure of the compacted soil (in Proctor mold) as well as the lateral pressures on the mold in order to calculate the actual stresses on soil. The results of these investigations may be used to interpret the geophysical measurements for controlling compaction works. A general equation for estimating V_s for all soil types can be developed based on laboratory studies. This equation should take into account the effect of soil grading characteristics which is not considered in the currently existing equations.

(Blank)

REFERENCES

Abbiss, C. P. (1981), Shear Wave Measurements of the Elasticity of the Ground, Geotechnique, Vol. 31, No. 1, pp. 91-104.

Andrus, R. D., Zhang, J., Ellis, B. S. and Juang, C. H. (2003), Guide for Estimating the Dynamic Properties of South Carolina Soils for Ground Response Analysis, Clemson University, Civil Engineering Department, Clemson, SC 29634-0911.

Andrus, R.D. and Stokoe II, K.H. (2000), Liquefaction resistance of soils from shear wave Velocity, ASCE J. Geotech. Geoenviron. Eng., 126(11), pp. 1015–25.

Arroyo, M., Muir Wood, D., Greening, P.D., Medina, L., and Roi, J. (2006), Effects of Sample Size on Bender-Based Axial G_0 Measurements, Geotechnique, Vol. 56, No. 1, pp. 39-52.

Arulnathan, R., et al. (2000), New Tool for Shear Wave Velocity Measurements in Model Tests. ASTM Geotechnical Testing Journal, GTJODJ, Vol. 23, No. 4, pp. 444-453.

Arulnathan, R., Boulanger, R. W. and Riemer, M. F. (1998), ASTM Geotechnical Testing Journal, GTJODJ, Vol. 21, No. 2, pp. 120-131.

Atkinson, J. H. & Little, J. A. (1988), Undrained triaxial strength and stress-strain characteristics of a glacial till soil, Can. Geotech. J. 25, No.3, 428-439.

Baldi, G., Bellotti, R., Ghionna, V., Jamiolkwski, M and Pasqualini, E. (1986), Interpretation of CPTs and CPTUs, 2nd Part: Drained penetration of sands, 4th Int. Geotechnical Seminar, Field Instrumentation and In-Situ Measurments, Nanyang Technological Institute, Singapore, pp. 143-156.

Baldi, G., Belloti, R., Ghiona, V. N., Jamiolkowski, M. and Pasqualini (1989), Interpretation of CPT's and CPTU's: 2nd Part; Drained penetration of sands, Field Instrumentation and In Situ Measurments, 12th Int. Conf. on Soil Mechanics and Foundation Engineering, Rio de Janeiro.

Been, K. and Jefferies, M. G. (1985), A State Parameter for Sands, Geotechnique, Vol. 35, No.2, pp. 95-112.

Bellotti, R., Jamiolkowski, M., Lo Presti, D.C.F. & O'Neill, D.A. (1996) Anisotropy of Small Strain Stiffness in Ticino Sand, Geotechnique, Vol. 46, No.1, pp. 115-131.

Bellotti, R. et al. (1997), Stiffness of Toyoura Sand from Dilatometer Tests, Journal of Geotechnical and Geoenvironmental Engineering Division, ASCE, Vol. 123, No. 9, pp. 836-846.

Blewett, J., Blewett, I. J., Woodward, P.K. (1999), Measurement of Shear-Wave Velocity Using Phase-Sensitive Detection Techniques, Canadian Geotech. J., Vol. 36, No. 5, pp. 934-939.

Blewett, J., Blewett, I. J., and Woodward, P. K., 2000, Phase and Amplitude Responses Associated with the Measurement of Shear-Wave Velocity in Sand by Bender Elements, Canadian Geotechnical Journal, Vol. 37, pp. 1348–1357.

Bieganousky, W. A., and E. F. Marcuson, III. (1976), Liquefaction Potential of Dams and Foundations: Report 1--Laboratory Standard Penetration Test on Reid Bedford Model and Ottawa Sands, Report S-76-2. Waterways Experiment Station.

Bodare, A. and Massarsch, K. R. (1984), Determination of Shear Wave Velocity by Different Cross Hole Methods, Proc. 8th World Conf. on Earthquake Engineering, July 21 - 28, 7 p.

Boulanger et al. (1998), Dynamic Properties of Sherman Island Peat, J. of Geotech. and Geoenvironmental Engrg., ASCE, Vol. 124, No. 1, pp.12-20.

Brignoli, E. & Gotti, M. (1992), Misure di velocita di onde di taglio laboratorio con l'impiego di trasduttori piezoelettrici, Rivista Italiana di Geotecnica, 26–16.

Brignoli, E. M., Goti, and Stokoe, II (1996), Measurement of Shear Waves in Laboratory Specimens by Means of Piezoelectric Transducers, ASTM Geotech. Testing J., Vol. 19, No. 4, pp. 384-397.

Burland, J. B. (1989), Small Is Beautiful-The Stiffness of Soils at Small Strains, Canadian Geotech. J., Vol. 26, pp. 499-516.

Burns, S. E. and Mayne, P. (1996), Small and High-Strain Soil Properties Using the Seismic Piezocone, Transportation Research Record 1548, National Acad. Press, Washington, pp. 81-88.

Cho, G. C. and Santamarina, J. C. (2001), Unsaturated Particulate Materials—Particle-Level Studies,

Journal of Geotechnical and Geoenvironmental Engineering, ASCE, Vol. 127, No. 1, pp. 84-96.
Clariá Jr., J. J. and Rinaldi, V. A. (2007), Shear Wave Velocity of a Compacted Clayey Silt, ASTM Geotechnical Testing Journal, Vol. 30, No. 5.
Cubrinovski, M. and Ishihara, K. (1999), Empirical Correlation between SPT N-value and Relative Density for Sandy Soils, Soils and Foundations, Vol. 39, No. 5, pp. 61-71.
Cundall, P. A. and O. D. L. Strack (1983), Modelling of Microscopic Mechanisms in Granular Material. In Mechanics of Granular Materials: New Models and Constitutive Relations, J. T. Jenkinsand M. Satake, Amsterdam, Elsevier: 137-149.
Cunning, J.C., Robertson, P.K., and Sego, D.C. (1995), Shear Wave Velocity to Evaluate in-Situ State of Cohesionless Soils, Canadian Geotechnical Journal, Vol. 32, pp. 848-858.
Das, B. M. (1994), Fundamentals of Soil Dynamics, New York, Elsvier.
Doghmane, A. and Hadjoub, Z. (1997), J. Phys. D 30, 2777.
Duffy, J. and R. Mindlin (1957), Stress-strain relations for a simple model of a granular medium. J. Appl. Mech. 24(4), 585 - 593.
Dyvik, R. Madshus, C. (1985), Lab Measurements of G_{max} Using Bender Elements, Proc. ASCE Annual Convention, Advances in the Art of Testing Soils under Cyclic Conditions, Detroit, Michigan, pp. 186-196.
Fear, C.E., and Robertson, P.K. (1995), Estimation of the undrained shear strength of sand: a theoretical framework, Canadian Geotechnical Journal, 32, pp. 859-870.
Gibbs, H.J. and Holtz, W.G. (1957), "Research On Determining the Density of Sands by Spoon Penetration Testing", Proc. 4th Int. Conf. Soil Mech. and Found. Eng., London, Vol. 1, pp. 35-39.
Girsang, C. H. (2001), A Numerical Investigation of the Seismic Response of the Aggregate Pier Foundation System, Ph.D. thesis, Virginia Polytechnic Institute and State University, Blacksburg.
Giunta, G. (1993), Stiffness of Sands in Monotonic Tortional Shear, thesis, Politecnico di Torino, Italy.
Goodman, N.R. (1960), Measuring Amplitude and Phase. J. Franklin Inst., Vol. 270, pp. 437-450.
Greening, P. D. and Nash, D. F. T. (2002), Frequency Domain Determination of G_0 Using Bender Elements, ASTM Geotechnical Testing Journal, Vol. 27, No. 3, Paper ID GTJ11192, pp 1-7.
Hall, J. R., Jr. and Richart, F. E. (1963), ''Dissipation of Elastic Wave Energy in Granular Soils'', Journal of the Soil Mechanics and Foundations Division, ASCE, Vol. 89, No. SM6, pp. 27-56.
Hardcastle, J. H. and Sharma, S. (1998), Shear Modulus and Damping of Unsaturated Loess, Proc. of Geotechnical Earthquake Engineering and Soil Dynamics III Conference, Seattle, Washington, August 3-6, pp. 178-188.
Hardin, B. O. (1987), 1-D Strain in Normally Consolidated Cohesionless Soils, Journal of the Geotechnical Engineering Division, ASCE, Vol. 113, No. 12, pp. 1449-1467.
Hardin, B. O. (1965), ''Dynamic Versus Static Shear Modulus of Dry Sand'', Materials Research & Standards, ASTM, Vol. 5, No. 5, pp. 232-335.
Hardin, B. O., Black, W. L. (1968), Vibration Modulus of Normally Consolidated Clay, J. of the Soil Mechanics and Foundations Div., ASCE, Vol. 94, No. 2, pp. 353-369.
Hardin, B. O. (1980), 'Anisotropic Shear Modulus Due to Stress Anisotropy, Discussion, J. of the Geotechnical Engineering Div., ASCE, Vol. 106, GT8, pp. 956-958.
Hardin, B. O. (1978), The Nature of Stress-Strain Behavior for soils, Proc. of ASCE Geotechnical Enginering Division Speciality Conference on Earthquake Engineering and Soil Dynamics, June 19-21, Pasadena, CA, Vol. 1, pp. 3-90.
Hardin, B. O. and Blanford, G. E. (1989), Elasticity of Particulate Materials, Journal of the Geotechnical Engineering Division, ASCE, Vol. 115, No. 6, pp. 788-805.
Hardin, P. O. and Richart, F. E. (1963), ''Elastic Wave Velocities in Granular Soils'', J. of the Soil Mechanics and Foundations Div., ASCE, Vol. 89, No. SM1, pp. 33-65.
Hardy, S. (2003), The Implementation and Application of Dynamic Finite Element Analysis to Geotechnical Problems, Ph.D. thesis, Imperial College of Science, Univ. of London, p. 320.
Hatanaka, M. and Feng, L. (2006), Estimating Relative Density of Sandy Soils, Soils and Foundation

J., Vol.46 No.3 (2006.6), pp. 299-314.
Havelock, T.H. (1914), The Propagation of Disturbances in Dispersive Media Cambridge, C.U.P.
Hegazy, Y.A. and Mayne, P.W. (1995), Statistical Correlations Between V_s and CPT Data for Different Soil Types, Proc. Int. Symp. on Cone Penetration Testing (CPT'95), Vol. 2, Linköping, Swedish Geotechnical Society, pp. 173-178.
Houlsby, G.T. and Wroth, C.P. (1991), The Variation of the Shear Modulus of a Clay with Pressure and Overconsolidation Ratio, Soils and Foundations, Vol. 31, No. 3, pp 138-143.
Hryciw, R. D. (1990), Small-Strain-Shear Modulus of Soil by Dilatometer, Journal of Geotechnical Engineering Division, ASCE, Vol. 116, No. 11, pp. 1700-1716.
Hryciw, R. D. and Thomann, T. G. (1993), Stress-History-Based Model for G_e of Cohesionless Soils, J. of the Geotechnical Engineering Div., ASCE, Vol. 119, No. 7, pp. 1073-1093.
Imai, T. and Tonouchi, K. (1982), Correlation of N Value with S-Wave Velocity and Shear Modulus, Proc. 2nd European Symposium on Penetration Testing, Amsterdam, 24-27 May, pp. 67-72.
Imai, T. and Yokota, K. (1982) Relationships between N Value and Dynamic soil Properties, Proc. 2nd European Symposium on Penetration Testing, Amsterdam, 24-27 May, pp. 73-78.
Isenhower, W. M. (1979), Torsional Simple Shear/Resonant Column Properties of San Francisco Bay Mud, Austin, Univ. of Texas, M.S. Thesis, 307p.
Ismail, M. A. & Rammah, K. I. (2006), A New Setup for Measuring during Laboratory Compaction, ASTM Geotech. Testing J., Vol. 29, Issue 4, pp. 1-9.
Ismail, M. A. & Rammah, K. I. (2005), Shear-plate transducers as a possible alternative to bender elements for measuring G_{max}, Geotechnique 55, No.5, 403-407.
Iwasaki, T., and Tatsuoka, F. (1977), Effect of Grain Size and Grading on Dynamic Shear Moduli of Sands, Soils and Found., Tokyo, 17(3), 19–35.
Iwasaki, T., Tatsuoka, F. and Takagi, Y. (1978), Shear Moduli of Sands under Cyclic Torsional Shear Loading, Soils and foundations,Vol.18, No.1, pp.39-56.
Jamiolkowski, M. B., (2004), Soil properties evaluation from static cone penetration test, private communication with Correia, A., Viana da Fonseca, A., and Gambin, M. (2004)
Jamiolkowski et al. (1985), 11th ICSMFE (4), San Francisco, pp. 1891-1896.
Jamiolkowski, M., Lancellotta, R., and Lo Presti, D. C. F. (1995), Remarks on Stiffness at Small Strains of Six Italian Clays, Proc. Int. Symp. of Pre-failure Deformation of Geomaterials, Sapporo, September 12-14, 1994, Edited by Shibuya, Mitachi & Miura, pp. 817-836.
Jamiolkowski, M., Leroueil, S., and Lo Presti, D. C. F. (1991), Theme lecture: Design Parameters from Theory to Practice, Proc. Geo-Coast'91, Int. Conf. on Geotech. Engineering for Coastal Development: Theory and Practice on Soft Ground, Yokohama, Japan, Sept. 3-6, pp. 1–41.
Jovicić, V., Coop. M. R. and Simić, M. (1996), Objective Criteria for Determining G_{max} from Bender Element Tests, Technical Note, Geotechnique, Vol. 46, No. 2, pp. 357-362.
Karray, M. (1999), Ph.D. thesis, Université de Sherbrooke, Sherbrooke, Quebec
Kawaguchi, T., Mitachi, T. and Shibuya, S. (2001), Evaluation of Shear Wave Travel Time in Laboratory Bender Element Test, the XVth International Conference on Soil Mechanics and Geotechnical Engineering, Istanbul, August 27-31, pp. 155-158.
Kokusho, T. and Yoshida, Y. (1997), SPT N-Value and S-Wave Velocity for Gravelly Soils with Different Grain Size Distribution, Soils and Foundations, Vol. 37, No. 4, pp. 105-113.
Kokusho, T., Yoshida, Y., and Eashi, Y. (1983), Evaluation of Seismic Stability of Dense Sand Layer (Part 2) - evaluation method by standard penetration test, Electric Power Central Research Institute, Japan, Report 383026 (In Japanese).
Kuhlemeyer, R.L. and Lysmer, J. (1973), Finite Element Method Accuracy for Wave Propagation Problems, Journal of Soil Mechanics and Foundations Division, ASCE, 99(SM5), pp.421-427.
Lade, P. V. and Nelson, R. B. (1987), Modeling the Elastic Behaviour of Granular Materials, Int. J. of Numerical and Analytical Methods in Geomechanics, Vol. 11, pp. 521-542.
Lawrence, F.V., Jr. (1963), Propagation of Ultrasonic Waves Through Sand. Research Report R63-8, Massachusetts Institute of Technology, Cambridge, MA.

Lawrence, F. V., Jr., (1965), Ultrasonic Shear Wave Velocities in Sand and Clay, Report R65-05 by M.I.T., Dept. of Civil Eng. to U. S. Army Engineer Waterways Experiment Station.
Lee, J.S. and Santamarina, J.C. (2005), P-wave Reflection Imaging, ASTM Geotechnical Testing J., vol. 28, pp. 197-206.
Lings, M. L., Greening, P. D. (2001), A Novel Bender/Extender Element for Soil Testing, Technical Note, Geotechnique, Vol. 51, No. 8, pp. 713-717.
Lo Presti D. C. F. (1996), personal communications with Salgado, Bandini and Karim (2000).
Lo Presti, D.C.F. (1987), Mechanical behaviour of Ticino sand from resonant-column tests, Ph.D. Thesis, Department of Structural Engineering, Politecnico di Torino, Italia.
Lo Presti, D. C. F. (1987), Proprietà Dinamiche dei Terreni, XIV Conferenza Geotecnica di Torino, Dept. of Structural Engineering, Politecnico di Torino.
Mancuso, C., Simonelli, A. L., Vinale, F. (1989), Numerical Analysis of In Situ S-Wave Measurements, Proc. of 12th Int. Conf. Soil Mech., Rio de Janeiro3, pp. 277-280.
Mancuso, C. and Vinale, F. (1988), Propagaziane delle Onde Simiche: Teoria e Misura in Sito, Atti Del Convegno DelGruppo Nazionale Di Coordinamento Per Gli Gtudi Di Ingegnaria Geotecnica, Monselice, pp. 115–138.
Mayne, P. (2001), In-Situ 2001, International Conference on In-Situ Measurement of Soil Properties & Case Histories, Bali, Indonesia, (Keynote Lecture).
Mayne, P.W. and Kulhawy, F.H. (1982), K_o-OCR Relationships in Soil, Journal of the Geotechnical Engineering Division, ASCE, Vol. 108, GT6, pp. 851-872.
Mayne, P.M., Schneider, J. A. and Martin, G. K. (1999), Small-and Large-Strain Soil Properties from Seismic Flat Dilatometer Tests, Pre-failure Deformation Characteristics of Geomaterials, Jamiolkowski, M., Lancellotta, R., and Lo Presti, D. C. F. (Editors), Balkema, pp. 419-426.
Meyerhof G.G. (1957), Discussion on Soil Properties and their Measurement, Session 2, Proc. 4th ICSMFE, Vol. III, 110.
Mohsin, A.M. and Airey, D.W. (2003), Automating G_{max} Measurement in Triaxial Tests, 3rd International Symp. on the Deformation Characteristics of Geomaterials ISLYON, Lyon, 73-80.
Nakagawa, K., Soga, K. and Mitchell, J. K. (1996), Pulse Transmission System for Measuring Wave Propagation in Soils, Journal of Geotechnical Engineering, Vol. 122, No. 4, pp. 302-308.
Ni, S-H. (1987), Dynamic Properties of Sand Under True Triaxial Stress States from Resonant Column/Torsion Shear Tests, PhD thesis, University of Texas at Austin.
Ohta, Y. and Goto, N. (1978a), Empirical Shear Wave Velocity Equations in Terms of Characteristic Soil Indexes, Journal of Earthquake Engineering and Structural Dynamics, Vol. 6, pp. 167-187.
Ohta, Y. and Goto, N. (1978b), Physical Background of the Statistically Obtained S-wave Velocity Equation in Terms of Soil Indexes, Butsuri-Tanko (Geophysical Exploration), (in Japanese; translated by Y. Yamamoto), Vol. 31, No. 1, pp. 8-17.
Peck, R.B., Bazaraa, A. R. S. (1969), Discussion of "Settlement of Spread Footings on Sands", Journal of Soil Mechanics and Foundation Engineering, ASCE, Vol. 95, No. SM3, pp. 905-909.
Peelamedu, S. M., Barnett, A. R., Dukkipati, R. V. and Naganathan, N. G. (2003), Finite Element Approach to Model and Analyze Piezoelectric Actuators, Mechanical, Industrial and Manufacturing Engineering Department, The University of Toledo, OH 43606.
Petrakis, E., Dobry, R. and Ng, T.-T. (1989), Small Strain Response of Random Arrays of Elastic Spheres Using a Nonlinear Distinct Element Procedure, Int. Symposium on Wave Propagation in Granular Media, Annual Winter Meeting of ASME, San Francisco, CA, AMD Vol. 101, 17-27.
Piratheepan, P., and Andrus, R. D. (2002), Estimating Shear-Wave Velocity from SPT and CPT Data, final report to U.S. Geological Survey, Award Number 01HQR0007, Clemson University, Clemson, SC.
Qian, X., Gray, D. H., and Woods, R. D. (1994), Voids and Granulometry: Effects on Shear Modulus of Unsaturated Sands, J. Geotech. Engrg., ASCE, Vol. 119, No. 2, pp. 295–314.
Richart et al. (1970), Vibration of Soils and Foundations, Civil Eng. & Mechanics Series, Prentice

Hall, Englewood Cliffs, N.J., 414p.
Rinaldi, V. A., Santamarina, J. C., and Redolfi, E., 1998, Characterization of Collapsible Soils with Combined Geophysical and Penetration Testing, Symposium In-Situ Characterization of Soils, Atlanta, GA, 1998.
Rix, G. J., and K. H. Stokoe, II, (1991), Correlation of Initial Tangent Moduli and Cone Penetration Resistance, Calibration Chamber Testing, A.B. Huang, Ed., Elsevier, 351-362.
Robertson, P. K. and Campanella, R. G. (1983), Interpretation of Cone Penetration Test. Part I: Sand, Canadian Geotech. J., Vol. 20, No. 4, pp. 718-733.
Robertson, P. K. et al. (1995), Shear-Wave Velocity to Evaluate In-Situ State of Ottawa Sand, J. of Geotechnical Engineering Div., ASCE, Vol. 121, No. 3, pp. 262-273.
Robertson, P. K., D. J. Woeller, W. D. L. Finn (1992), Seismic Cone Penetration Test for Evaluating Liquefaction under Seismic Loading, Canadian Geotechnical Journal, Vol. 29, pp. 686-695.
Roesler, S.K. (1979), Anisotropic shear modulus due to stress anisotropy, Journal of the Geotechnical Engineering Division, ASCE, 105(GT7), pp. 871–880.
Roscoe, K.R., Schofield, A.N., and Wroth, C.P. (1958), On the Yielding of Soils, Géotechnique, Vol. 8, pp. 22–53.
Sachse, W. and Pao, Y.-H. (1978), On the Determination of Phase and Group Velocities of Dispersive Waves in Solids, Journal of Applied Physics, Vol. 49, No. 8, pp. 4320-4327.
Salem, H. S. (2000), Poisson's Ratio and the Porosity of Surface Soils and Shallow Sediments, Determined from Seismic Compressional and Shear Wave Velocities, Technical Note, Geotechnique, Vol. 50, No. 4, 461-463.
Sanchez-Salinero, I., Roesset, J. M., and Stokoe, K. H. (1986) Analytical studies of body wave propagation and attenuation, Report GR 86-15, Civil Engr. Dept, Univ. of Texas at Austin, TX.
Santamarina, J.C. and Fam, M.A. (1997), Interpretation of bender element tests (discussion), Géotechnique, 47(4), pp. 873–877.
Santamarina, J. C. and Fam, M. (1995), Changes in Dielectric Permittivity and Shear Wave Velocity during Concentration Diffusion, Canadian Geotechnical Journal, l32(4), pp. 647-659.
Santamarina JC, Klein KA, Fam MA. (2001), Soils and Waves, John Wiley, New York.
Salgado, R., Bandini, P. and Karim, A. (2000), Shear Strength and Stiffness of Silty Sand, J. of Geotechnical and Geoenvironmental Engineering Div., ASCE, Vol. 126, No. 5, pp. 451-462.
Schmertmann (1978), Report TS-78-209, FHWA, Washington, DC, 145 p.
Schmertmann, J. H. (1985), "Stress Ratio Effects on Shear Modulus of Dry Sands", Discussion, Journal of Geotechnical Engineering, ASCE, Vol. 111, GT September, pp. 1153-1154.
Seed, H. B., Idriss, I. M. and Arango, I. (1983), Evaluation of Liquefaction Potential Using Field Performance Data, Journal of Geotechnical Engineering, ASCE, Vol. 109, No. 3, pp. 458-483.
Seed, H. B. et al. (1986), Moduli and Damping Factors for Dynamic Analyses of Cohesionless Soils, Journal of Geotechnical Engineering, ASCE, Vol. 112, No. 11, pp. 1016-1032.
Shibuya, S. (2000), TC29 Report, Proc. of 2nd Int. Sym. on Pre-failure Deformation of Geomaterials, Tonino, Vol 2, Palkema.
Shirley, D. J., Anderson, A. L. (1975), In situ measurement of marine sediment acoustical properties during coring in deep water, IEEE Trans on Geoscience and Electronics, GE-13(4), pp.163-169.
Shirley, D.J., and Hampton, L.D. 1978. Shear wave measurements in laboratory sediments. Journal of the Acoustical Society of America, 63(2): 607–613.
Simonini, P. and Cola, S. (2000), Use of Piezocone to Predict Maximum Stiffness of Venetian Soils, J. of Geotechnical and Geoenvironmental Engineering Div., ASCE, Vol. 127, No. 4, pp. 297-313.
Skempton, A. W. (1986), Standard Penetration Test Procedures and the effects in Sands of Overburden Pressure, Relative Density, Particle Size, Aging and Overconsolidation, Geotechnique, (36)3, 425-447.
Sykora, D. W. and Koester, J. P. (1988), Correlations between Dynamic Shear Resistance and Standard Penetration Resistance in Soils, Proc. of the specialty conference on Earthquake Engineering and Soil Dynamics, II-Recent Advances in Ground-Motion Evaluation, ASCE, Utah,

USA, pp. 389-405.
Sykora, D. W. and Stokoe, D. H., II (1983), Correlations of In situe measurement in sand with shear wave velocity, Geotechnical Engieering Report, GR83-33, The University of Texas at Austin, Austin, TX.
Tanaka, H. and Tanaka, M. (1998) Characterization of Sandy Soils Using CPT and DMT, Soils and Foundations, Vol. 38, No. 3, pp. 55-65.
Tanizawa, F., Tatsuoka, F., Teachavorasinskun, S., Iwasaki, K. and Zhou, S. (1990), On Correlation among cone resistance and shear modulus and angle of shear resistance of Toyoura sand, Proc. of 25th Japan National Conf. on SMFE, pp. 141-144, (in Japanese).
Tatsuoka, F. (1985), Stress Ratio Effects on Shear Modulus of Dry Sands, Discussion, Journal of Geotechnical Engineering, ASCE, Vol. 111, GT September, pp. 1155-1157.
Tatsuoka, F. and Shibuya, S. (1991), Deformation characteristics of soils and rocks from field and laboratory tests, Keynote Lecture for Session No.1, Proc. of the 9th Asian Regional Conf. on SMFE, Bangkok, Vol. II, pp.101-170.
Teachavorasinskun, S. (1989), Stress-strain and strength characteristics of granular materials in simple shear, Master of Engineering thesis, University of Tokyo.
Thomann, T. G. and Hryciw, R. D. (1990), Laboratory Measurement of Small Strain Shear Modulus Under Ko Conditions, ASTM Geotechnical Testing Journal, Volume 13, Number 2, 97-105.
Tokimatsu, K. and Yoshimi, Y. (1983), Empirical Correlation of Soil Liquefaction Based on SPT N-Value and Fines Content, Soils and Foundations, JSSMFE, 23(4), 56-74.
Viggiani, G. and Atkinson, J. H. (1995), Interpretation of Bender Element Tests, Technical Note, Geotechnique, Vol. 45, No. 1, pp. 149-154.
Vaghela, J.G. & Stokoe II, K.H. (1995), Small Strain Dynamic Properties of Soils from Free-Free Resonant Column Testing, Geotech. Engineering J. GT95-1, The University of Texas at Austin.
Tanner, W. M. (2004), Travel Time Tomographic Imaging of the Distribution of the Effective Stress in Clean Sand Under a Model Footing, Master Thesis, Louisiana State University, U.S.A.
Wang et al. (2007), Measurement Biases in the Bender Element Test, J. of Geotechnical and Geoenvironmental Engineering, ASCE, Vol. 133, No. 5, pp. 564-574.
Whitman, R. V. (1954), The Behaviour of Soils Under Dynamic Loadings, Final Report on Laboratory Studies, Aug. MIT Dept. of Civil and Sanitary Eng. Soil Mechanics Lab.
Wroth, C. P. and Houlsby, G. T. (1985), Soil mechanics-property characterisation, and analysis procedures, Proc. 11th Conf Soil Mech., San Francisco 1,1-55.
Wu, Z. H., Xie, D. Y., Yu, X. F., Li, Q. Y., and Chen, X. Y., 1987, Dynamic Characteristics of Intact Loess, Engineering Aspects of Soil Erosion, Dispersive Clays and Loess, Geotechnical Special Publication No. 10, ASCE C.W. Lovell and R. L.Wiltshire, Eds., pp. 148–167.
Yoshida, Y., Motonori, I., and Kokusho, T. (1988), Empirical Formulas of SPT Blow-Counts for Gravelly Soils, In Proc. of the 1st International Symposium on Penetration Testing (ISOPT-1, 1988), Orlando, Fla, A.A. Balkema, Rotterdam, pp. 381–387.
Yu, P. and Richart, F. E., Jr. (1984), "Stress Ratio Effects on Shear Modulus of Dry Sands", Journal of Geotechnical Engineering, ASCE, Vol. 110, No. 3, pp. 331-345.
Yu, P. and Richart, F. E., Jr. (1985), Stress Ratio Effects on Shear Modulus of Dry Sands, Closure, Journal of Geotechnical Engineering, ASCE, Vol. 111, GT September, pp. 1157-1159.
Youd, T.L., et al. (2001), Liquefaction Resistance of Soils: Summary report from the 1996 NCEER and 1998 NCEER/NSF workshops on evaluation of liquefaction resistance of soils, Journal of geotechnical and geoenvironmental engineering, Vol. 127, No. 10, pp. 817-833.
Zeng, X. and Ni, B. (1998), Measurement of G_{max} Under Anisotropic Loading Condition Using Bender Elements, Proc. of Geotechnical Earthquake Engineering and Soil Dynamics III Conference , Seattle, Washington, pp. 189-200.

Appendix A Correlations between Shear Wave Velocity (or Elastic shear Modulus) and in Situ Tests Indices

A.1 V_s or G_o Correlations to SPT Index

Since the appearance of penetration tests, engineers have been attempting to use their results to assess the deformation characteristics of soils and settlement of structures. A large amount of experimental data has shown that G_o for granular soils is mostly a function of the effective stress and void ratio. On the other hand, the same basic variables (D_r and σ') influence penetration tests indices. Therefore, many correlations between V_s or small-strain shear modulus (G_o) and penetration resistance have been deducted. They reflect the high potential of employing V_s in conventional geotechnical engineering. The next subsections introduce the existing correlations in this domain.

A.1.1 Ohta and Goto (1978)

An investigation by Ohta and Goto (1978a) to systematize empirical equations for the shear wave velocity of soils was made in terms of four characteristic indexes. The adopted indexes are the N-value of the Standard Penetration Test, soil depth (H), geological age (epoch, E) and soil type (F). Six soil types (Clay, fine sand, medium sand, coarse sand, sand & gravel and gravel) of two ages (alluvium and diluvium) were employed in the study. Alluvium soil is a river deposit while diluvium soil is a sedimentary coarse superficial deposit of glacial and fluvio-glacial origin laid down during the ice age. Fifteen sets of empirical equations to estimate shear wave velocity were obtained by combining the above four indexes (Table A.1). All of these sets were derived by use of about 300 data points. Variables and combinations of variables were examined by Ohta and Goto (1978) to determine their effect on V_s predictions and also to determine which combinations of variables produced the most accurate results (highest correlation coefficients). The best equation was found to be the one which included all the indexes (equation XV: Table A.1), and its correlation coefficient is 0.86. The empirical equation relating the standard penetration N-value solely to the shear wave velocity provided a correlation coefficient of only 0.72, and is one of the lowest ranking among the 15 sets of equations. Later, Ohta and Goto (1978b) narrowed the soil divisions to three groups (clays, sands and gravels). This simplification produced only slightly lower correlation coefficients for correlations involving soil-type divisions. As mentioned before, V_s and SPT N-value is mostly a function of the effective stress and the relative density (void ratio). This might explain the good performance of the Ohta & Goto (1978) formulas (or other similar) which

relate the SPT number, N, and shear wave velocity, V_s. Seed et al. (1986), Jamiolkowski et al. (1988) and Baldi et al. (1988a) demonstrated that Ohta and Goto (1978) formula provides a reliable estimate of V_s limited to cohesionless Holocene deposits (<10,000 years).

A.1.2 Imai and Tonouchi (1982)

Imai and Tonouchi (1982) gathered results of field and laboratory tests for about 250 sites of alluvial, diluvial and tertiary deposits in Japan using 386 boreholes that gave 1654 data points of different geological ages. This database was used to study the relationships between SPT number (N-value) and each of compression wave velocity, V_p, shear wave velocity, V_s, and dynamic shear modulus, G_d, for the aforementioned soils. Figure A.1 shows Imai and Tonouchi (1982) data arranged according to soil type and geological age in statistical plot. This figure shows that V_s varies around a certain value according to soil type while there is no clear distinguishing differences for V_p between different soil types. This confirms that V_s is a characteristic soil property.

Table A.1 V_s Empirical Equations in Four Characteristic Indexes (Ohta & Goto, 1978)

No.	Concerned index	Equation	Probable error (%)	Correlation coefficient
I	Soil type	$Vs' = 169{\cdot}7 \begin{pmatrix} 1{\cdot}000 \\ 1{\cdot}359 \\ 1{\cdot}375 \\ 1{\cdot}470 \\ 1{\cdot}949 \\ 2{\cdot}398 \end{pmatrix}_F$ (m/sec)	36·3	0·463
II	Geological epoch	$Vs' = 172{\cdot}9 \begin{pmatrix} 1{\cdot}000 \\ 1{\cdot}923 \end{pmatrix}_E$	31·5	0·621
III	Depth	$Vs' = 92{\cdot}12H^{0{\cdot}339}$	29·6	0·670
IV	Geological epoch Soil type	$Vs' = 145{\cdot}1 \begin{pmatrix} 1{\cdot}000 \\ 1{\cdot}753 \end{pmatrix}_E \begin{pmatrix} 1{\cdot}000 \\ 1{\cdot}230 \\ 1{\cdot}318 \\ 1{\cdot}445 \\ 1{\cdot}566 \\ 1{\cdot}828 \end{pmatrix}_F$	28·5	0·696
V	N-value	$Vs' = 85{\cdot}34N^{0{\cdot}348}$	27·4	0·719
VI	N-value Soil type	$Vs' = 85{\cdot}60N^{0{\cdot}346} \begin{pmatrix} 1{\cdot}000 \\ 1{\cdot}053 \\ 0{\cdot}950 \\ 0{\cdot}936 \\ 1{\cdot}048 \\ 1{\cdot}222 \end{pmatrix}_F$	27·2	0·726
VII	Depth Soil type	$Vs' = 78{\cdot}98H^{0{\cdot}312} \begin{pmatrix} 1{\cdot}000 \\ 1{\cdot}260 \\ 1{\cdot}282 \\ 1{\cdot}422 \\ 1{\cdot}641 \\ 2{\cdot}255 \end{pmatrix}_F$	25·2	0·765
VIII	Depth Geological epoch	$Vs' = 97{\cdot}28H^{0{\cdot}351} \begin{pmatrix} 1{\cdot}000 \\ 1{\cdot}542 \end{pmatrix}_E$	25·1	0·767
IX	N-value Geological epoch	$Vs' = 92{\cdot}18N^{0{\cdot}346} \begin{pmatrix} 1{\cdot}000 \\ 1{\cdot}456 \end{pmatrix}_E$	24·2	0·784
X	N-value Geological epoch Soil type	$Vs' = 93{\cdot}10N^{0{\cdot}340} \begin{pmatrix} 1{\cdot}000 \\ 1{\cdot}448 \end{pmatrix}_E \begin{pmatrix} 1{\cdot}000 \\ 1{\cdot}056 \\ 1{\cdot}013 \\ 1{\cdot}039 \\ 1{\cdot}069 \\ 1{\cdot}221 \end{pmatrix}_F$	24·0	0·787
XI	N-value Depth	$Vs' = 61{\cdot}62N^{0{\cdot}264}H^{0{\cdot}222}$	22·1	0·820
XII	Depth Geological Soil type	$Vs' = 84{\cdot}36H^{0{\cdot}346} \begin{pmatrix} 1{\cdot}000 \\ 1{\cdot}435 \end{pmatrix}_E \begin{pmatrix} 1{\cdot}000 \\ 1{\cdot}202 \\ 1{\cdot}261 \\ 1{\cdot}412 \\ 1{\cdot}482 \\ 1{\cdot}927 \end{pmatrix}_F$	22·0	0·822
XIII	N-value Depth Soil type	$Vs' = 62{\cdot}14N^{0{\cdot}319}H^{0{\cdot}330} \begin{pmatrix} 1{\cdot}000 \\ 1{\cdot}091 \\ 1{\cdot}029 \\ 1{\cdot}073 \\ 1{\cdot}151 \\ 1{\cdot}485 \end{pmatrix}_F$	21·5	0·830
XIV	N-value Depth Geological epoch	$Vs' = 68{\cdot}44N^{0{\cdot}208}H^{0{\cdot}188} \begin{pmatrix} 1{\cdot}000 \\ 1{\cdot}308 \end{pmatrix}_E$	20·3	0·848
XV	N-value Depth Geological epoch Soil type	$Vs' = 68{\cdot}79N^{0{\cdot}171}H^{0{\cdot}199} \begin{pmatrix} 1{\cdot}000 \\ 1{\cdot}303 \end{pmatrix}_E \begin{pmatrix} 1{\cdot}000 \\ 1{\cdot}086 \\ 1{\cdot}066 \\ 1{\cdot}135 \\ 1{\cdot}153 \\ 1{\cdot}448 \end{pmatrix}_F$	19·7	0·856

Note :

$$\begin{pmatrix} alluvium \\ diluvium \end{pmatrix}_E \quad \begin{pmatrix} clay \\ fine-sand \\ medium-sand \\ coarse-sand \\ sand\ \&\ gravel \\ gravel \end{pmatrix}_F$$

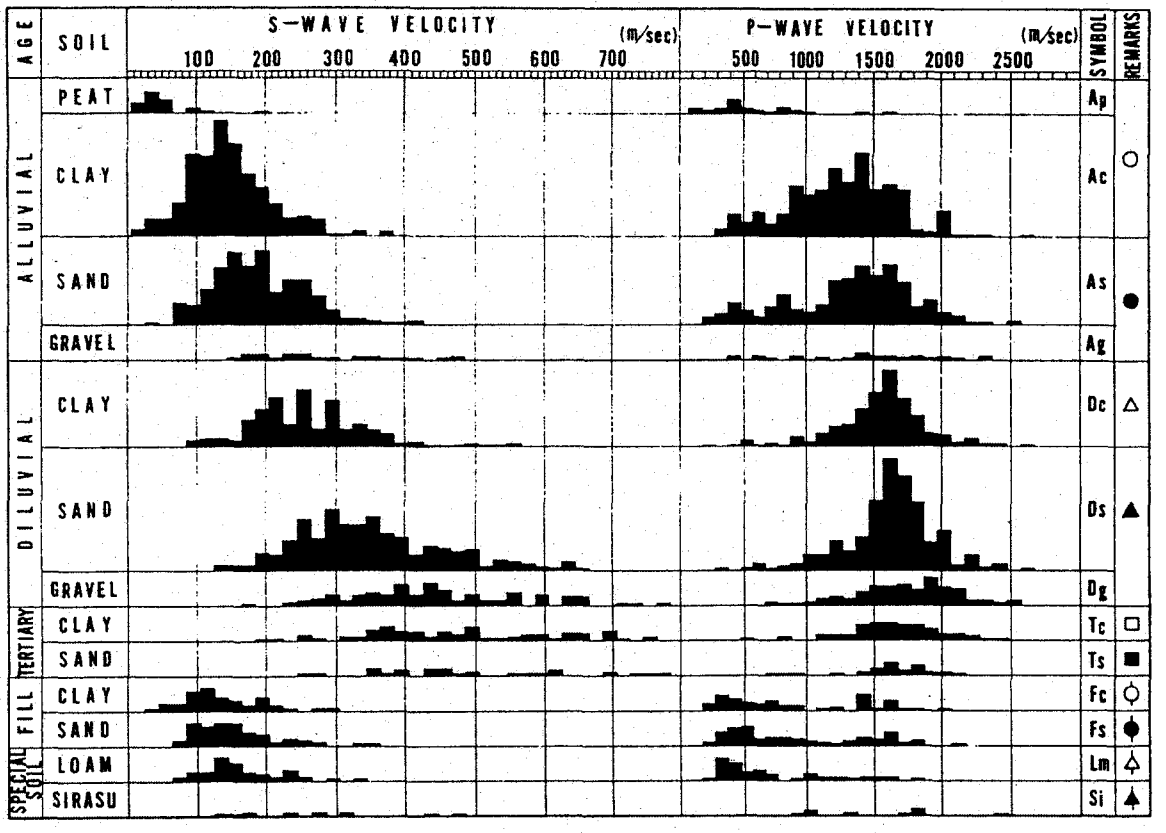

Figure A.1 Distribution of V_s and V_p (Imai and Tonouchi, 1982).

Figure A.2 depicts the variation of elastic wave velocities (V_p and V_s) versus N. It can be seen that there is a direct relationship between V_s and N regardless of whether the ground is alluvial, diluvial or tertiary. In order to examine the relationship between V_s and N in detail, data was arranged separately for geology and soil type (Figure A.3). It can be seen from the figure that there are somewhat different tendencies according to geology. For the same N value, shear wave velocity is greatest in tertiary (11-26.5milion Year) layers, less in diluvial layers and least in alluvial layers (notations definition are in Figure A.1). Also, shear wave velocities are higher in clayey than in sandy soil for the same N value. Furthermore, Figure A.4 summarizes the distribution ranges for each classification.

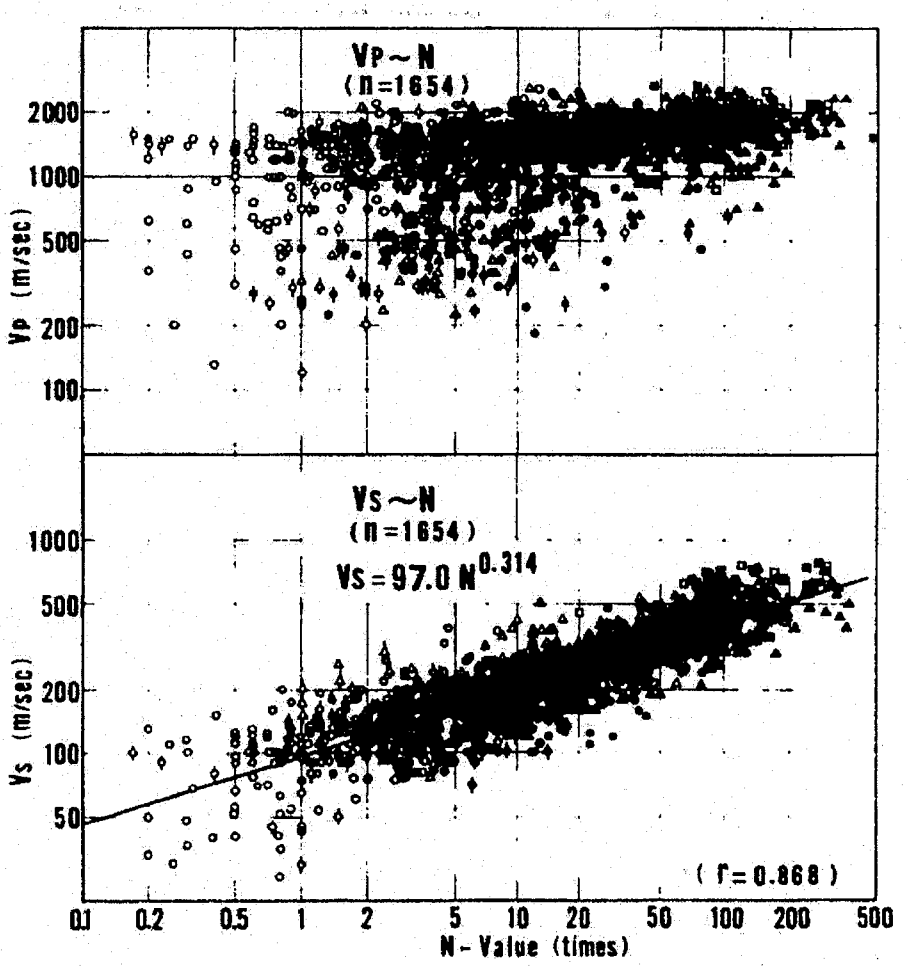

Figure A.2 Relationships of V_p and V_s to N Value (Imai and Tonouchi, 1982).

Disregarding the above distinctions between categories, the overall curve in the graph of Figure A.4 represents the following experimental formula, derived from the 1654 points of data available:

$$V_s = 97N^{0.314} \tag{A.1}$$

Imai and Tonouchi (1982) also studied the correlation between the dynamic shear modulus, G_o, and N (Figure A.5). Disregarding the differences for various categories, the formula for the data as a whole is:

$$G_o = 144N^{0.68} \tag{A.2}$$

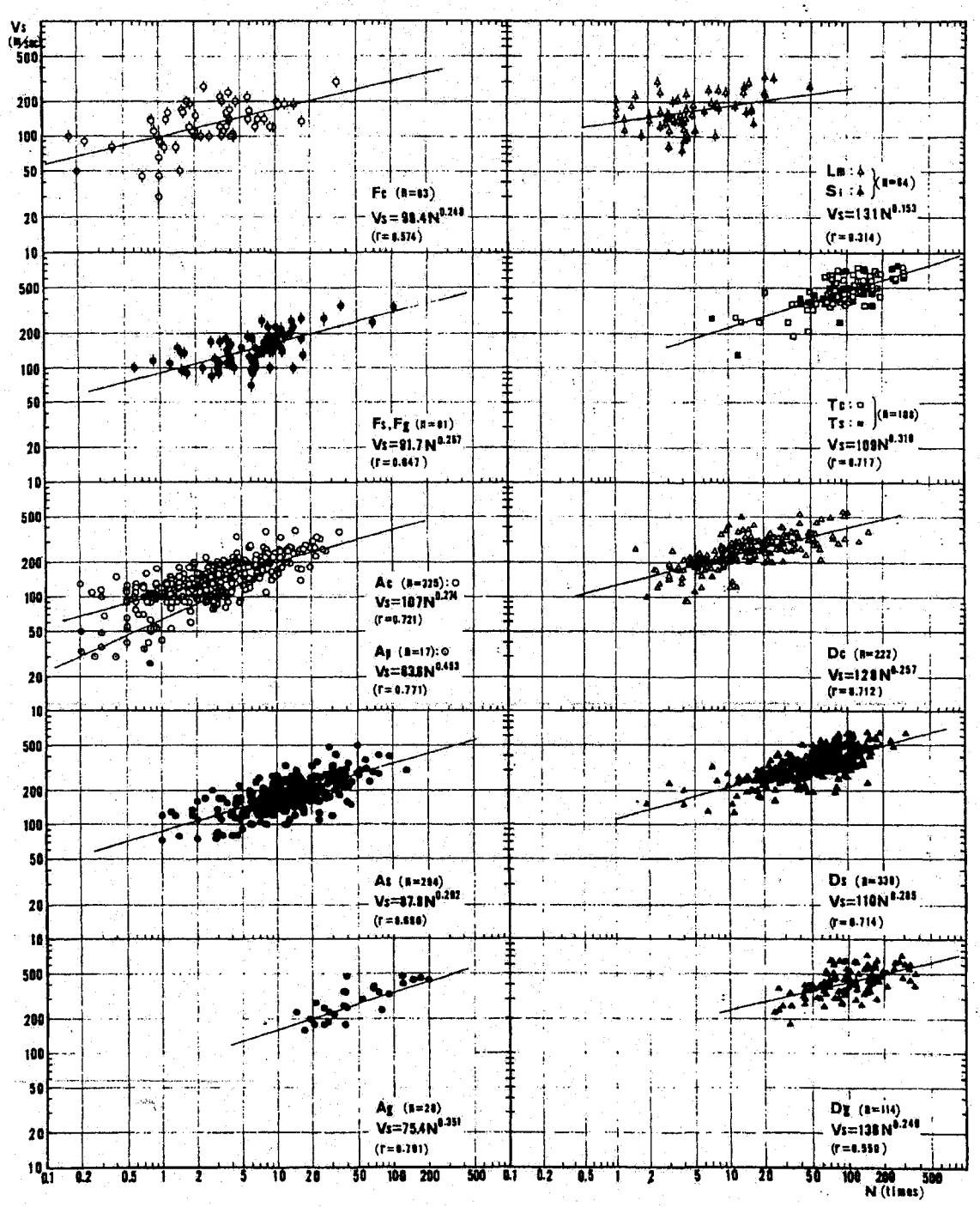

Figure A.3 SPT N-Value versus Shear Wave Velocity for Different Soil Types (Imai and Tonouchi, 1982).

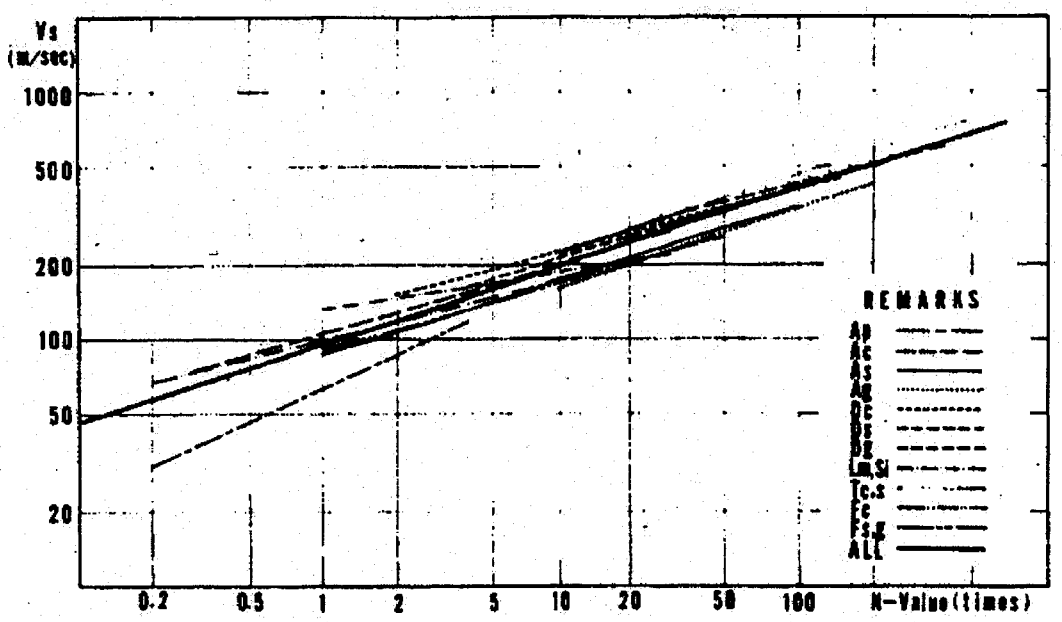

Figure A.4 Summarized Relationships of V_s to N (Imai and Tonouchi, 1982).

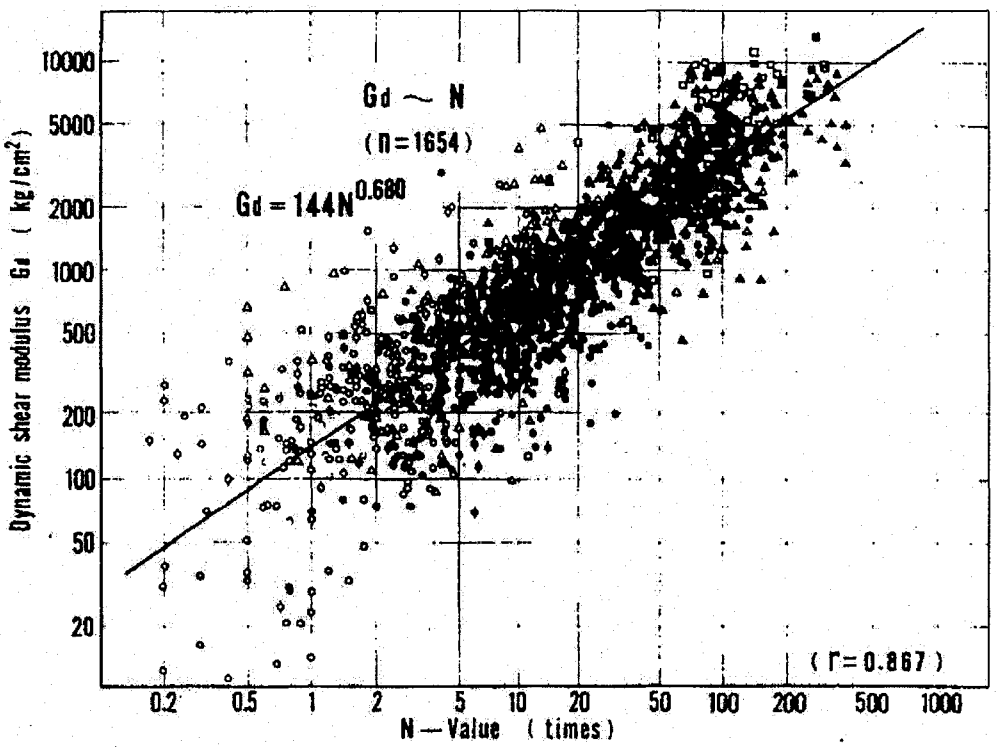

Figure A.5 Relationship between Dynamic Shear Modulus and SPT Blow Counts N (Imai and Tonouchi, 1982).

A.1.3 Imai and Yokota (1982)

Imai and Yokota (1982) used results of geophysical survey tests and laboratory resonant column tests to investigate the relation between the SPT blow count (N) and elastic shear modulus (G_o). Geophysical survey tests were conducted by downhole method in order to measure P- and S-waves velocity, therefore the authors called it PS logging. G_o value obtained from PS logging corresponds to location where resonant column test was carried out. The following two correlations were concluded for sandy soils:

$$G_{RC} = 167 N^{0.38} \quad \text{(A.3)}$$

$$G_{PS} = 168 N^{0.51} \quad \text{(A.4)}$$

Figure A.6 shows the relationships of shear modulus from resonant column (G_{RC}) under shear strain equal to 10^{-6} and elastic shear modulus obtained from PS logging (G_{PS}) to N-value. This figure depicts a good correlation between N and G_o especially for sandy soil.

A.1.4 Seed, Idriss and Arango (1983)

Based on resonant column and cyclic torsional tests result, Seed, Idriss and Arango (1983) developed the following two equations for sands and silty sands:

$$G_{max} = 65 \text{ N} \quad \text{(tsf)} \quad \text{(A.5)}$$

and

$$V_s = 185 \text{ N}^{0.5} \text{ (fps)} \quad \text{(A.6)}$$

The previous V_s-equation was developed based on Equation A.5 and theory of elasticity ($G_{max} = \rho V_s^2$) after substituting the soil unit weight equals to 120 Ib/ft^3.

A.1.5 Other Correlations

Table A.2 summarizes results of the previously mentioned studies for G_o / V_s and in situ tests indices of soil as well as some other recent correlations. The recent relationships were derived between the normalized shear wave velocity (V_{s1}) and the normalized penetration resistance index.

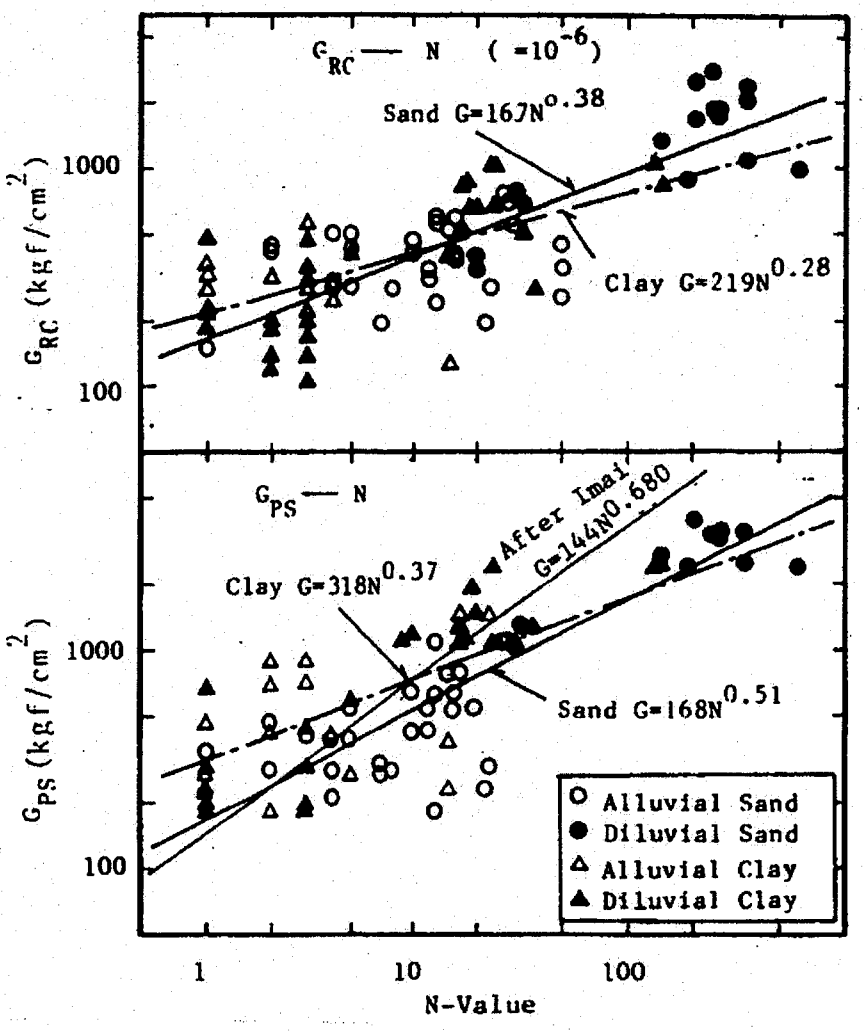

Figure A.6 Relationship between Small Strain Shear Modulus and SPT Number (Imai and Yokota, 1982).

Table A.2 Correlations for Estimating Shear Wave Velocity from SPT Number.

Source	Formula	Material tested / Particle size	Basis of Formula	Notes
Ohta and Goto (1978)	$V_s = \begin{bmatrix} 62.14 & \text{clay} \\ 67.79 & \text{fine sand} \\ 63.94 & \text{medium sand} \\ 66.68 & \text{coarse sand} \\ 71.52 & \text{sand and gravel} \\ 92.28 & \text{gravel} \end{bmatrix} N^{0.31} H^{0.23}$	all types of soils	Field SPT results (300 data points; r^2=0.83)	Probable error = 21.5%
Imai and Tonouchi (1982)	$V_s = 97\ N^{0.314}$ $G_d = 144\ N^{0.68}$	all types of soils	Field SPT results (1654 data sets; r^2=0.868)	
Imai and Yokota (1982)	$G_{PS} = 168\ N^{0.51}$ $G_{RC} = 167\ N^{0.38}$	Different types of sands	results of geophysical survey (PS) tests	
Seed, Idriss and Arango (1983)	$V_s = 185\ N^{0.5}$ (fps) $G_{max} = 65$ N (tsf)	sands and silty sands	resonant column and cyclic torsional tests	Unit weight taken 1.922 t/m^3 for getting V_s
Sykora and Stokoe (1983)	$V_S = 106\ .68\ N^{0.27}$ m/s		n = 229 & r^2 = 0.84	

Table A.2 Correlations for Estimating Shear Wave Velocity from SPT Number (cont.).

Source	Formula	Material tested / Particle size	Basis of Formula	Notes
Seed et al. (1986)	$G_{max} = 1000\left[35(N_{60})^{0.34}\right](\sigma'_v)^{0.4}$ $G_{max} = 1000\left[20(N_{1,60})^{1/3}\right](\sigma'_m)^{1/2}$	Granular soils (Holocene sands)		G_{max} & σ'_m in lb/ft^2
Yoshida et al. (1988)	$V_s = 49\,N_j^{0.25}(\sigma'_v)^{0.14}$ $V_s = 56\,N_j^{0.25}(\sigma'_v)^{0.14}$	- Fine Holocene sand - Coarse to Fine Holocene sand		V_S in m/s $\sigma'v$ in kPa
Fear and Robertson (1995)	$V_{s1} = 89.8(N_1)_{60}^{0.25}$ $V_{s1} = 113\,(N_1)_{60}^{0.25}$	- Ottawa sand - Alaska sand (FC = 30 %)		V_{S1} in m/s
Kokusho and Yoshida (1997)	$V_S = \left[V_{s1}^{min} + \left(V_{s1}^{max} - V_{s1}^{min}\right)D_r\right](\sigma'_h\sigma'_v / P_a^2)^m$ $V_{s1}^{max} = 420\,U_c/(U_c + 1)$ $V_{s1}^{min} = 120$ m/s , $m = 0.12\,(D_r)^{-0.2}$ $N = 5.8(42.6U_c^{0.46}/5.8)^{D'_r}(\sigma_m / P_a)^{nD'_r}$ $D_r^* = \log(e_{max}/e)/\log(e_{max}/e_{min})$ $nD_r^* = 0.27\,(D_r^*)^{-0.4}$	Five gravelly sands (gravel = 0, 25, 50 & 75%)	Laboratory measurements in a large cylindrical container	- Probable error= ± 20% - N can be used to estimate D_r.

Table A.2 Correlations for Estimating Shear Wave Velocity from SPT Number (cont.).

Source	Formula	Material tested / Particle size	Basis of Formula	Notes
Andrus and Stokoe (2000)	$V_{s1} = 93.2(N_1)_{60}^{0.231}$	FC < 10 % & nonplastic	Holocene sands	V_{S1} in m/s
Piratheepan and Andrus (2002)	$V_s = 66.7 N_{60}^{0.248} Z^{0.138}$ $V_s = 72.3 N_{60}^{0.228} Z^{0.152}$ $V_s = 72.9 N_{60}^{0.224} Z^{0.130}$ $V_{s1} = 95.5(N_1)_{60}^{0.226}$ $V_{s1} = 103(N_1)_{60}^{0.205}$ $V_{s1} = 102(N_1)_{60}^{0.205}$	FC<10 % FC=10-35 % FC<40 % FC<10 % FC=10-35 % FC<40 %	Holocene sands	V_S and V_{S1} in m/s Z in m
Andrus et al. (2003)	$(V_{s1})_{cs} = 87.7 (N_1)_{60\text{-}cs}^{0.253}$	Holocene sands	Sites in California, Japan and Canada. V_s from crosshole, downhole, or seismic CPT tests techniques	Data corrected for fines content to get the clean sand (cs) values.

A.2 Correlations between V_s or G_o and CPT Index

A.2.1 Baldi et al. (1986)

In the past, correlations between the cone tip resistance (q_t or q_c) of the cone penetration test (CPT) and the maximum shear stiffness for granular soils were developed. Other correlations applicable to all soil types have been proposed. Baldi et al. (1986) carried out some laboratory cone tests on Ticino sand (medium to coarse sands) using a calibration chamber setup. They have employed the regression analysis on the results of 127 resonant column tests (Lo Presti, 1987) performed on both NC and OC specimens of Ticino sand in order to introduce the following correlation for estimating V_s from CPT test for both NC and OC clean Ticino sand:

$$G_o = 44.4 q_c \left(\sigma_o^{'}\right)^{-0.12} \exp(-1.92 D_r) \qquad \text{(A.7)}$$

where σ'_o is the effective mean stress in kPa and the relative density, D_r, as a fraction of unity. Table A.3 summarizes result of Baldi et al. (1986) study as well as the other existing studies for correlating V_s to CPT index. Some of these studies are presented in the following sections.

A.2.2 Baldi et al. (1989)

Baldi et al. (1989) gathered many experimental and field data besides carrying out in situ and laboratory tests on each of Ticino, Hokksund and Po river predominantly silica sands. Baldi et al. (1989) introduced the following correlation for clean quartz sands:

$$V_s = 277 (q_t)^{0.13} \left(\sigma_{vo}^{'}\right)^{0.27} \qquad \text{(A.8)}$$

where V_s in m/sec, q_t in MPa and σ'_{vo} is the effective overburden stress in MPa. Figure A.7 shows the variation of the measured V_s with the calculated values. The measured V_s values have a good agreement with those inferred from CPT using Equation A.8. Baldi et al. (1989) also performed resonant column tests for measuring G_o of samples extracted from sites where CPT was conducted. G_o was measured at octahedral shear strain (γ_{oct}) of 10^{-5}. Thus they could relate G_o to q_c considering the over consolidation ratio of soil as shown in Figure A.8. This figure gives a tentative correlation between G_o and q_c for uncemented predominantly silica sands.

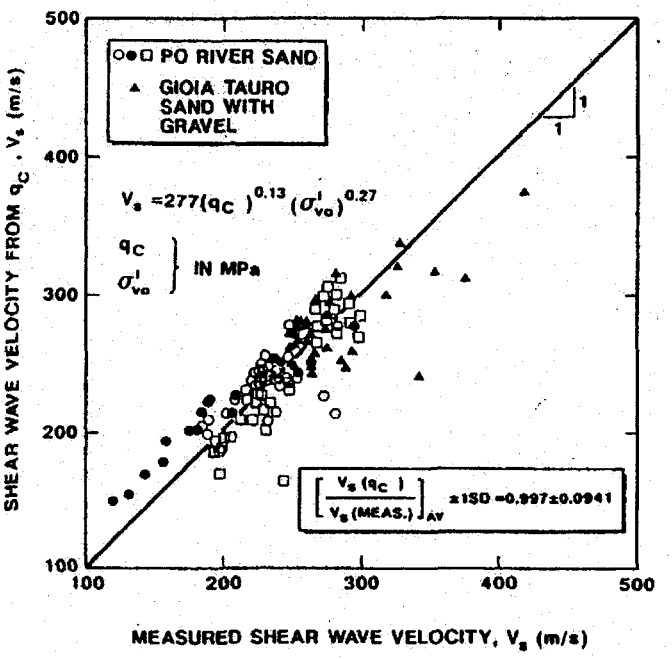

Figure A.7 Measured and Predicted Vs for Silica Sands (Baldi et al., 1989).

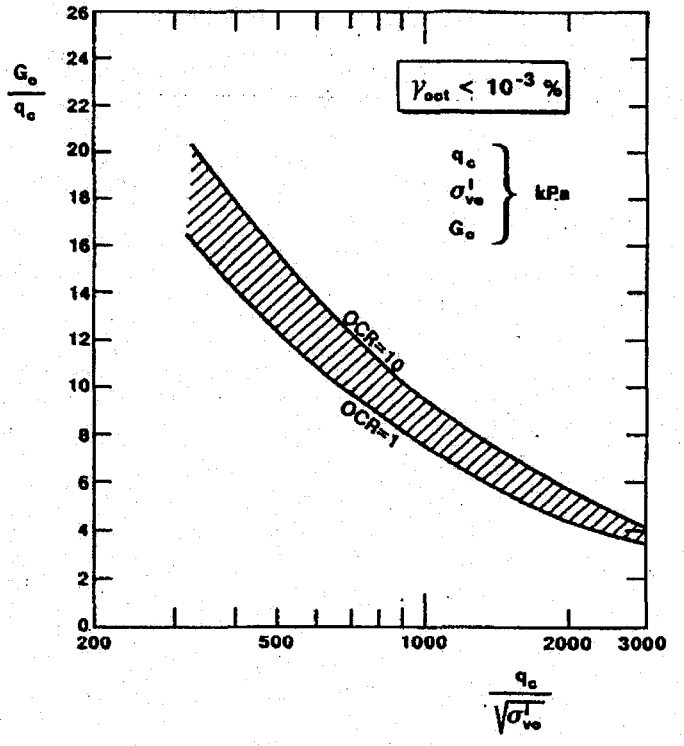

Figure A.8 Relationship between Small Strain Shear Modulus and CPT Tip Resistance for Silica Sands (Baldi et al., 1989).

A.2.3 Rix and Stokoe (1991)

Further work was performed by Rix and Stokoe (1991) in calibration chambers with two other types of sands. One sand was washed mortar sand and the other was imported from the Heber Road Research Site in California. Based on their work, they developed a correlation to directly determine the shear modulus (G_{max}) of sand from piezocone testing, as shown in the following equation.

$$\left(\frac{G_o}{q_c}\right)_{av.} = 1634\left(\frac{q_c}{\sqrt{\sigma'_{vo}}}\right)^{-0.75} \qquad \left(\text{Range} = \text{Average} \pm \frac{\text{Average}}{2}\right) \qquad \text{(A.9)}$$

where G_o, σ'_{vo} and q_c are in kPa.

The shear wave velocity, V_s, is then calculated using the following equation

$$V_s = \sqrt{\frac{G_{max}}{(\gamma/g)}} \qquad \text{(A.10)}$$

where, G_{max} in Pa, γ in KN/m^3 and g = 98.1 m/s^2 and V_s in m/s.

A.2.4 Hegazy and Mayne (1995)

Cone penetration data and V_s data were collected from 61 sites worldwide (24 sands, 36 clays & 1 mine tailing). The shear wave velocity data were measured using different in situ techniques including seismic cone, cross-hole, down-hole and spectral analysis of surface wave tests. Simple and multiple regression analyses were performed by Hegazy and Mayne (1995) with V_s and three independent parameters including q_c, f_s and σ'_{vo} collected from 24 different sand sites. The regression showed that q_c and σ'_{vo} are the most significant parameters. The following two equations were introduced for *sands*.

$$V_s = 13.18 q_c^{0.192} \sigma'^{0.179}_{vo} \qquad (r^2 = 0.684, \text{number of points (n)} = 133) \qquad \text{(A.11)}$$

where V_s in m/s and σ'_{vo} and q_c are in kPa.

$$V_s = 12.02 q_c^{0.319} f_s^{-0.0466} \qquad (r^2 = 0.574, n = 92) \qquad \text{(A.12)}$$

where f_s is the sleeve friction, f_s, σ'_{vo} and q_c are in kPa and V_s in m/s.

Also, Hegazy and Mayne (1995) compiled together data from 61 sites including clays, sands, intermediate soil types and mine tailings for obtaining a general equation for all soil types. Three independent parameters including q_c, f_s and σ'_{vo} were considered for all soil types. The

authors reported that f_s and σ'_{vo} are almost equally important in the regression process. They have proposed the following equation:

$$V_s = (10.1Logq_c - 11.4)^{1.67}(100 f_s / q_c)^{0.3} \qquad (r^2 = 0.695, n = 323) \qquad (A.13)$$

This equation was cross-checked for a mine tailing site and indicates a good agreement between the measured in-situ and estimated values of V_s except at shallow depths (d<8m). Finally, the authors concluded that the most reliable method to obtain the shear wave velocity of soil is the direct in situ measurement, as the statistical regression formulations can not explain all the variability associated with natural soil deposits.

A.2.5 Kokusho and Yoshida (1997)

Based on laboratory test results on sandy and gravelly soils with widely varying grain size distribution (Figure 2.23), Kokusho and Yoshida (1997) introduced the following relationship for estimating SPT N-value at energy ratio of 75% taking the lower normalized value of N, N_1, equals to 5.8.

$$N = 5.8(42.6U_c^{0.46} / 5.8)^{D_r^*}(\sigma_m / P_o)^{n(D_r^*)} \qquad (A.14)$$

Where D^*_r is the logarithmic relative density $[\log(e_{max}/e)/\log(e_{max}/e_{min})]$ and $n(D^*_r)$ is a constant depends on relative density and can be determined approximately from

$$n(D^*_r) = 0.27/(D^*_r)^{0.4} \qquad (A.15)$$

Based on the authors two empirical equations for estimating N and V_s (Equation A.14 and Equation 2.51), Kokusho and Yoshida (1997) have drawn a relationship between SPT N-value and V_s, both normalized with respect to effective stress (Figure A.9). The results seem consistent with Ohta and Goto (1978) correlations which were based on field data.

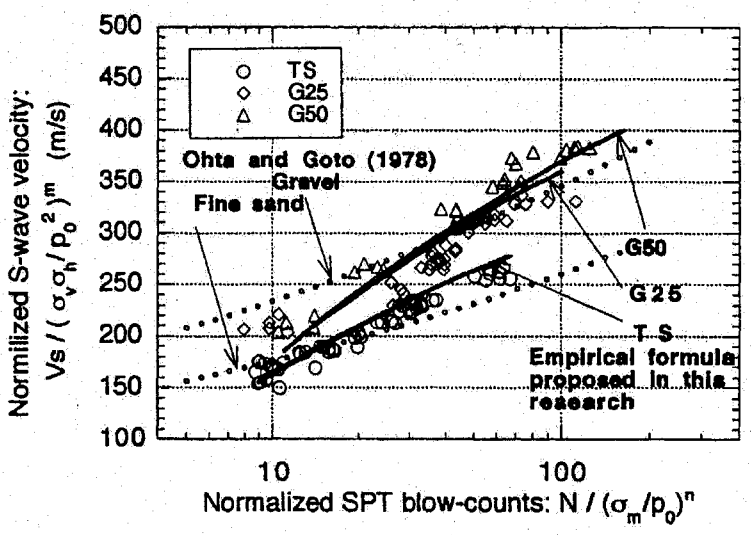

Figure A.9 Normalized Shear Wave Velocity versus Normalized SPT N-Value (Kokusho and Yoshida, 1997).

A.2.6 Simonini and Cola (2000)

Simonini and Cola (2000) used results of cross-hole test, Seismic CPT and laboratory tests to relate G_{max} to q_c for Venice city soil (interbeded sands, silts and silty clay sediments). Figure A.10 shows the results which were formulated as follows:

$$G_{\max} = 42.9(q_c)^{0.51} \qquad (r^2 = 0.483) \qquad \text{(A.16)}$$

$$G_{\max} = 32.9(q_c)^{0.48} e^{-1.23} \qquad (r^2 = 0.568) \qquad \text{(A.17)}$$

$$G_{\max} = 21.5(q_c)^{0.79}(1+B_q)^{4.59} \qquad (r^2 = 0.628) \qquad \text{(A.18)}$$

where G_{max} and q_c in MPa, B_q equals $\Delta u/q_c$, and Δu is the excess of pore water pressure due to cone penetration in the soil. $\Delta u/q_c$ is a function of soil type, its structural condition and the over consolidation ratio. Equation A.17 uses a void ratio exponential function which has improved the correlation. Differently, Equation A.18 uses a function in B_q to substitute the void ratio effect; a more improvement of the correlation is obtained.

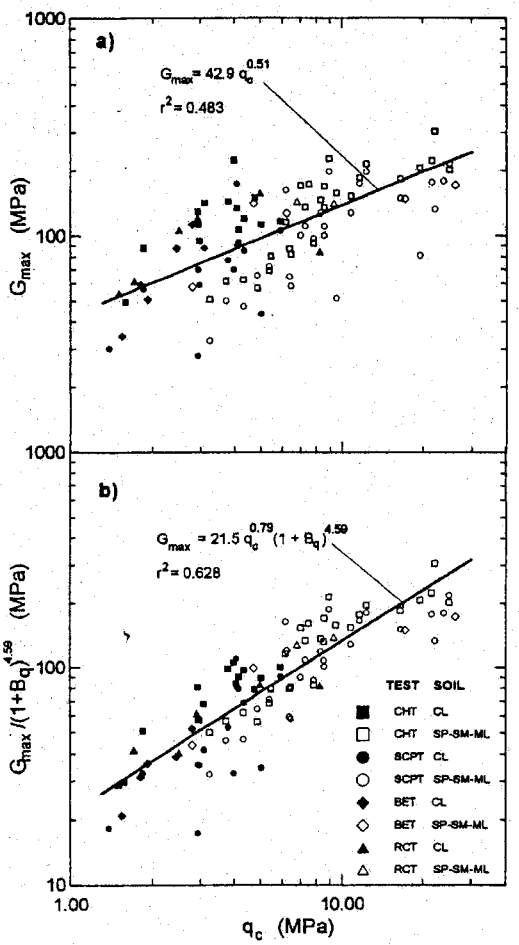

Figure A.10 G_{max} to q_c for Venice City Soil (Simonini and Cola, 2000).

A.2.7 Jamiolkowski et al. (2004)

Jamiolkowski et al. (2004) derived the following correlation for estimating the shear modulus of soil from the cone test index. It takes a ratio form.

$$\frac{G_o}{q_c} = 144.04\left(\frac{q_c}{\sqrt{\sigma'_{vo} P_a}}\right)^{-0.631} \tag{A.19}$$

This equation is based on field tests result on sand and gravel of Pleistocene age at Messina straits.

A.2.8 Other Studies

Table A.3 briefly introduces the currently existing equations between V_s and q_c for granular soil. The studies of each of Robertson et al. (1992), Andrus, Piratheepan, and Juang (2002), and Andrus et al. (2003) are summarized in this table.

Table A.3 Existing Correlations for Estimating Shear Wave Velocity from Cone Penetration Test Results.

Source	Formula	Material tested / Particle size	Basis of Formula	Notes
Baldi et al. (1986)	$G_o = 44.4 q_c (\sigma'_o)^{-0.12} \exp(-1.92 D_r)$ σ'_o in kPa & D_r as a ratio	Ticino sand (medium to coarse sands)	Cone tests in a calibration chamber	Based on resonant column tests on Ticino sand by Lo Presti (1987)
Baldi et al. (1989)	$V_s = 277(q_t)^{0.13}(\sigma'_{vo})^{0.27}$ V_s in m/s, q_t & σ'_{vo} in MPa	uncemented Ticino, Hokksund and Po river sands	experimental and field data records and some in situ and laboratory tests	good agreement with seismic cone and cross-hole field tests
Rix and Stokoe (1991)	$\left(\frac{G_o}{q_c}\right)_{av.} = 1634\left(\frac{q_c}{\sqrt{\sigma'_{vo}}}\right)^{-0.75}$ Range = Average $\pm \frac{\text{Average}}{2}$ G_o, σ'_{vo} and q_c are in kPa	Washed mortar sand and sand from Heber Road Research Site in California.	Cone tests in a calibration chamber	
Robertson et al. (1992)	$V_{s1} = 102 q_{c1}^{0.25}$		Field measurements	q_{c1} in MPa & V_s in m/s
Fear and Robertson (1995)	$V_{s1} = 135 q_{c1}^{0.23}$	Alaska sand (tailings composed of large amount of carbonate shell material, FC=30%)	Field measurements	q_{c1} in MPa & V_s in m/s

Table A.3 Existing Correlations for Estimating Shear Wave Velocity from Cone Penetration Test Results (cont.).

Source	Formula	Material tested / Particle size	Basis of Formula	Notes
Hegazy and Mayne (1995)	$V_s = 13.18 q_c^{0.192} \sigma_{vo}'^{0.179}$ for sands ($r^2 = 0.684$, n = 133) $V_s = 12.02 q_c^{0.319} f_s^{-0.0466}$ ($r^2 = 0.574$, n = 92) for sands $V_s = (10.1 Log q_c - 11.4)^{1.67} (100 f_s / q_c)^{0.3}$ ($r^2 = 0.695$, n = 323) for all soil types V_s in m/s and σ'_{vo} and q_c are in kPa	24 different sand sites 24 different sand sites 61 different sites (24 sands, 36 clays & 1 mine tailing)	Field measurements (seismic cone, cross-hole, down-hole and spectral analysis of surface wave tests)	
Simonini and Cola (2000)	$G_{max} = 42.9(q_c)^{0.51}$ ($r^2 = 0.483$) $G_{max} = 32.9(q_c)^{0.48} e^{-1.23}$ ($r^2 = 0.568$) $G_{max} = 21.5(q_c)^{0.79}(1 + B_q)^{4.59}$ $B_q = \Delta u / q_c$ ($r^2 = 0.628$)	Venice city soil (interbeded sands, silts and silty clay sediments)	cross-hole test, Seismic CPT and laboratory tests	

Table A.3 Existing Correlations for Estimating Shear Wave Velocity from Cone Penetration Test Results (cont.).

Source	Formula	Material tested / Particle size	Basis of Formula	Notes
Andrus, Piratheepan, and Juang (2002)	$V_s = 26.3 q_c^{0.199} f_s^{0.003}\ ASF$ ($r^2 = 0.61$) $V_s = 4.63 q_c^{0.342} I_c^{0.688} Z^{0.092}\ ASF$ where V_S is in m/s, q_c & f_s in kPa, *ASF* is an age scaling factor and *Ic* = soil behaviour type index $V_{s1} = 77.4 q_{c1n}^{0.178}\ ASF$ ($r^2 = 0.60$) For Holocene sands (<10,000 years), ASF=1.00 & for Pleistocene (10,000 to 1.5 million years) ASF=1.44 & 1.41 for Eq. 1 & 2, respectively	Holocene sands (SW, SP, SP-SM, SM)	Data compiled from primarily sites in California, Japan and Canada. V_s from crosshole, downhole, or seismic CPT tests techniques	
Andrus et al. (2003)	$(V_{s1})_{cs} = 67.6\ (q_{c1n})_{cs}^{0.213}$	Holocene sands	Data compiled from primarily sites in California, Japan and Canada. V_s from crosshole, downhole, or seismic CPT tests techniques	Data corrected for fines content to get the clean sand (cs) values.
Jamiolkowski et al. (2004)	$\frac{G_o}{q_c} = 144.04\left(\frac{q_c}{\sqrt{\sigma'_{vo} P_a}}\right)^{-0.631}$	Sand and gravel of Pleistocene age at Messina straits	Field tests result	

A.3 Conclusions

The correlations between the small-strain indexes (G_{max} or V_s) and penetration resistance are important for several aspects: 1) the geotechnical indexes of in situ tests are widely used for assessing soil state and for design purposes, and there are huge experience in design and analysis using these indexes. Thus the correlations between in situ tests indexes and V_s may be used as a link to interpret soil properties by traditional methods. 2) As a new application, currently the value of shear wave velocity itself can not recall to the mind (of most engineers) the state or strength of soil like the common test indexes such as N. 3) An index like q_c, which might be estimated from q_c-V_s correlations, represent the ultimate shearing resistance of soil under a small circular footing (projected area of the cone) which can be adopted using modulus deterioration forms in order to predict the small-and-large-strain soil behaviour. Therefore correlating V_s to other soil indices such as N, q_c, E_d (dilatometer modulus) is useful and attractive. By calculating these indices based on V_s measurements, the soil properties may be evaluated using the well established interpretation methods for in situ tests.

(Blank)

Appendix B Correlations for Estimating Relative Density of Soil from Penetration Test Indices

B.1 Correlations for Estimating Relative Density from SPT

There are some empirical correlations between relative density and the Standard Penetration Test index [N_{60} or $N_{1(60)}$] which dates back to 1957. The effective vertical overburden stress (σ'_v) where the SPT were carried out affects this relationship, therefore it was necessary to included σ'_v for N_{60} equations while not necessary in $N_{1(60)}$ because $N_{1(60)}$ is 'N_{60} normalized for the overburden stress'. These equations are introduced in this section because some of them are used in the analysis of Peribonca dam in situ tests. Table B.2 summarizes the existing correlations for estimating relative density of soil from SPT indices.

B.1.1 Meyerhof (1957)

Meyerhof (1957) derived an equation for estimating the relative density based on test results on saturated clean coarse sands.

$$D_r = 21\sqrt{\frac{N}{0.7 + (\sigma'_v / 98)}} \qquad \text{(B.1)}$$

Where N is the SPT blow count number (N_{60}) and σ'_v is the effective vertical overburden pressure in kPa. This equation gives too low relative density values for $\sigma'_v > 150$ kPa. Also, it is preferred to be used for estimating relative density of medium to dense soils ($D_r > 50\%$).

B.1.2 Gibbs and Holtz (1957)

Gibbs and Holtz (1957) derived an equation for estimating the relative density based on the test results on normally consolidated sands.

$$D_r = \sqrt{\frac{N}{17 + 12\sigma'_v}} \qquad \text{(B.2)}$$

Where N is the SPT blowcount number and σ'_v is the effective vertical overburden pressure in ksf (klb/f^2).

B.1.3 Peck and Bazaraa (1969)

Peck and Bazaraa (1969) derived two equations for estimating the relative density based on test results on coarse sands.

$$D_r = \sqrt{\frac{N}{22 + 0.773\sigma'_v}} \qquad \sigma'_v < 75 \text{ kPa} \qquad \text{(B.3)}$$

$$D_r = \sqrt{\frac{N}{66 + 0.193\sigma'_v}} \qquad \sigma'_v \geq 75 \text{ kPa} \qquad \text{(B.4)}$$

where N is the SPT blowcount number and σ'_v is the effective vertical overburden pressure in kPa.

B.1.4 Bieganousky and Marcuson (1976)

Bieganousky and Marcuson (1976) derived the first equation that takes into account the soil grading effect for estimating the relative density. Also, it uses $(N_1)_{60}$ instead of the commonly used N value.

$$D_r = \sqrt{\frac{(N_1)_{60}}{60 + 25 \log D_{50}}} \qquad \text{(B.5)}$$

Where, D_{50} is in mm and $(N_1)_{60}$ is the normalized SPT N value for rod energy of 60% as follows:

$$(N_1)_{60} = N_{60}\left(\frac{98}{\sigma'_v}\right)^{0.5} \qquad \text{(B.6)}$$

B.1.5 Kokusho et al. (1983)

Kokusho et al. (1983) have suggested a correlation for estimating the relative density of granular soils based on test results on dense Tonegawa sand (medium to fine sand of D_{50} = 0.32mm; $D_r > 60\%$).

$$D_r = 36\left(\frac{N}{\sigma'_v/98 + 1.5}\right)^{0.37} \qquad \text{(B.7)}$$

where σ'_v is in kPa.

B.1.6 Tokimatsu and Yoshimi (1983)

Tokimatsu and Yoshimi (1983) proposed an empirical correlation for estimating the relative density of sandy soils based on SPT N value. This equation is a modification of Meyerhof (1957) equation. It adds a term for taking into account the effect of fines content on Dr-N-σ'_v relationship.

$$D_r = 21\sqrt{\frac{N}{0.7 + (\sigma'_v/98)}} + \frac{\Delta N_F}{1.7} \qquad \text{(B.8)}$$

where, ΔN_F is calculated based on the fines content of the soil as in Table B.1.

Table B.1 Corrections of N According to Fines Content.

F_c (%)	ΔN_F
0 - 5	0
5 - 10	1.2 (F_c - 5)
10 - 20	6 + 0.2 (F_c - 10)
20 -	8 + 0.1 (F_c - 20)

B.1.7 Skempton (1986)

Based on test results for normally consolidated sands, Skempton (1986) derived the following equation:

$$D_r = \sqrt{\frac{(N_1)_{60}}{C}} \tag{B.9}$$

Where C is a constant depends on the density state of soil (C = 58, 60 & 65 for dense, medium dense and loose sands, respectively).

B.1.8 Cubrinovski and Ishihara (1999)

Cubrinovski and Ishihara (1999) derived an equation for estimating the relative density of normally consolidated deposits of all soil types based on SPT N value. It does not take into account the horizontal stress effect (or OCR) as well as soil fabric. The SPT rod energy for their data base is 78% (78% of the maximum free-fall energy).

$$D_r = \sqrt{\frac{N(e_{max} - e_{min})^{1.7}}{9}\left(\frac{98}{\sigma'_v}\right)^{0.5}} \tag{B.10}$$

where σ'_v is in kPa and D_r as a ratio.

Also, Cubrinovski and Ishihara (1999) proposed an equation for estimating the voids ratio range of soil based on its average diameter.

$$e_{max} - e_{min} = 0.23 + (0.06 / D_{50}) \tag{B.11}$$

where, D_{50} is in mm.

B.1.9 Hatanaka and Feng (2006)

Hatanaka and Feng (2006) have proposed a set of two equations for estimating the relative density of granular soils based on field test results for fine to medium sands of D_{50}<1mm and $D_{max} \leq 4.75$mm with fines content (F_c) less than 20%. The different soil gradations are based on high quality undisturbed samples extracted by the freezing technique.

$$D_r = 1.55N_1 + 40 \qquad N_1 \leq 25 \qquad \text{(B.12)}$$

$$D_r = 0.84N_1 + 57.8 \qquad 25 < N_1 \leq 50 \qquad \text{(B.13)}$$

where, if $15\% \leq F_c \leq 20\%$, $N_1 = (N+12.9) \times (98/\sigma'_v)^{0.5}$.

Table B.2 Correlations for Estimating Relative Density from SPT N-Value.

Source	Formula	Material tested / Particle size	Basis of Formula	Notes
Gibbs and Holtz (1957)	$D_r = \sqrt{\frac{N}{17 + 12\,\sigma'_v}}$	Normally consolidated sands (fine and coarse)	Series of model ground tests on coarse sand σ'_v in ksf	Other curves were drawn by the author for fine sand and air-dry/partially wetted sand
Meyerhof (1957)	$D_r = 21\sqrt{\frac{N}{0.7 + (\sigma'_v / 98)}}$	For saturated clean coarse sands D_{50}=1.4mm ($D_r \geq 50\%$)	equation based on Gibbs and Holtz (1957) results	σ'_v in kPa Low estimate of D_r for σ'_v > 150 kPa Preferred for $D_r \geq 50\%$
Peck and Bazaraa (1969)	$D_r = \sqrt{\frac{N}{22 + 0.773\,\sigma'_v}}$ $\sigma'_v < 75$ kPa $D_r = \sqrt{\frac{N}{66 + 0.193\,\sigma'_v}}$ $\sigma'_v \geq 75$ kPa	Coarse Sands	Field and laboratory results	σ'_v = vertical effective stress in kPa
Tokimatsu and Yoshimi (1983)	$D_r = 21\sqrt{\frac{N}{0.7 + (\sigma'_v / 98)}} + \frac{\Delta N_F}{1.7}$	Sandy soils with fines content; no clear limitation of the equation application		Modification of Meyerhof (1957) equation ΔN_f is a function of the fines content, but yet to be proven

Table B.2 Correlations for Estimating Relative Density from SPT N-Value (cont.).

Source	Formula	Material tested / Particle size	Basis of Formula	Notes
Kokusho et al. (1983)	$D_r = 36\left(\frac{N}{\sigma'_v/98 + 1.5}\right)^{0.37}$	Dense medium to fine sand of D_{50}=0.32mm (D_r>60%); fines content (F_c) = 4 %	Series of SPT using model ground in laboratory	σ'_v =42-156 kPa
Skempton (1986)	$D_r = \sqrt{\frac{(N_1)_{60}}{C}}$ C = 58, 60 & 65 for dense, medium dense and loose sands, respectively	Medium dense fine sand, NC dense coarse sand & OC fine sand	Field data	30% ≤ D_r ≤ 90%
Skempton (1986)	$D_r = \sqrt{\frac{N}{a\sigma'_v + b}}$ If sand is over-consolidated, increase b by a factor C_f: $C_f = \frac{1 + K_o}{1 + 2K_{onc}}$ where $K_o \approx (1 - \sin\varphi')\, OCR^{\sin\varphi'}$ $K_{onc} \approx (1 - \sin\varphi')$	Normally Consolidated Sands	Field data	a = 0.3 (mean value) b = 30 (mean value)

Table B.2 Correlations for Estimating Relative Density from SPT N-Value (cont.).

Source	Formula	Material tested / Particle size	Basis of Formula	Notes
Cubrinovski and Ishihara (1999)	$D_r = \sqrt{\frac{N\,(e_{max} - e_{min})^{1.7}}{9}\left(\frac{98}{\sigma'_v}\right)^{0.5}}$ $e_{max} - e_{min} = 0.23 + (0.06 / D_{50})$	Normally consolidated deposits of all soil types	Data base of in situ SPT for different soil types	Not considering soil fabric and σ'_h. Rod energy = 78%
Mayne (2001)	$D_r = \sqrt{\frac{(N_1)_{60}}{C_p C_A C_{OCR}}}$ $C_P = 60 + 25 \log D_{50}$ $C_A = 1.2 + 0.05 \log(t/100)$ $C_{OCR} = OCR^{0.18}$ or $D_r = 12.2 + 0.75 \left[\begin{array}{l} 222\ N + 2311 \\ -\ 711\ OCR \\ -\ 779\ (\sigma'_v / Pa) \\ -\ 50\ C_u^2 \end{array}\right]^{0.5}$	Normally consolidated and over-consolidated fine to medium fine sands.	Field and laboratory data	
Hatanaka and Feng (2006)	$D_r = 1.55\ N_1 + 40$ For $N_1 \leq 25$ $D_r = 0.84\ N_1 + 57.8$ $25 < N_1 \leq 50$	Fine to medium sands, D_{50}<1mm & $D_{max} \leq$ 4.75mm	Field test results (73 high quality undisturbed samples extracted by freezing for comparing D_r values)	Estimation error = ± 10% The fines content (F_c) < 20%

B.2 Correlations for Estimating Relative Density from CPT

There are some equations for estimating relative density based on Cone Penetration Test (CPT) which were developed primarily for clean sands based on Calibration Chamber (CC) test results. The following sections present the currently existing equations for CPT-D_r relationships and Table B.3 introduces a summary of these studies.

B.2.1 Jamiolkowski et al. (1985)

Based on Calibration Chamber data, Jamiolkowski et al. (1985) introduced an empirical equation for estimating the relative density of normally consolidated, uncemented, unaged sands using cone penetration test results. These data were corrected using field test results in order to cancel the effect of walls flexibility of the calibration chamber.

$$D_r^2 = \frac{1}{305 Q_c OCR^{0.18}} \frac{q_c / P_a}{(\sigma'_{vo} / P_a)^{0.5}} \tag{B.14}$$

where Q_c is a compressibility factor (0.91 for high, 1.0 for medium, and 1.09 for low).

The over consolidation factor in this equation ($OCR^{0.18}$) was evaluated to be 2.3, 5.1, and 10.1 using the mean OCR values for low, medium, and high OCR data, respectively. The majority of natural sands are likely to be of medium to high compressibility and low to medium OCR.

Jamiolkowski et al. (1985) empirical equation for estimating relative density also can be written as follows:

$$D_r = -85 + 66 \log\left(\frac{q_c}{(\sigma'_{vo})^{0.5}}\right) \quad \text{for high compressibility sand,} \tag{B.15a}$$

$$D_r = -98 + 66 \log\left(\frac{q_c}{(\sigma'_{vo})^{0.5}}\right) \quad \text{for medium compressibility sand, and} \tag{B.15b}$$

$$D_r = -111 + 66 \log\left(\frac{q_c}{(\sigma'_{vo})^{0.5}}\right) \quad \text{for low compressibility sand.} \tag{B.15c}$$

where σ'_{vo} is in t/m^2.

Such correlations are applicable to normally consolidated (NC), fine to medium, unaged, uncemented, clean sands.

B.2.2 Baldi et al. (1986)

Based on large calibration chamber test results on Ticino and Hokksund sands (medium to coarse sands) Baldi et al. (1986) determined different constants for the empirical equation made by Schmertman (1976) depending on test and soil conditions

$$D_r(\%) = \frac{100}{C_2}\ln\left[\frac{q_c}{C_0(\sigma'_v)^{C_1}}\right] \quad \text{(B.16)}$$

where σ'_v and q_t is in kPa.

The constants (C_0, C_1 & C_2) depend on soil type, stress history, boundary conditions referring to stresses and strains existing during Calibration Chamber (CC) tests and water content and degree of saturation. For normally consolidated (NC) Ticino sand, the constants were C_0 = 157, C_1 = 0.55, and C_2 = 2.41.

B.2.3 Tanizawa et al. (1990)

Tanizawa et al. (1990) proposed a similar equation to Jamiolkowski et al. (1985) correlation in order to predict the relative density (D_r) from CPT for Toyoura sand (after Tanaka and Tanaka, 1998). Toyoura sand is medium quartz sand (30% fine sand) of D_{50} equals 0.22 mm; U_c = 1.31.

$$D_r(\%) = -85.1 + 76\log\left(\frac{q_t}{(\sigma'_{vo})^{0.5}}\right) \quad \text{(B.17)}$$

where σ'_{vo} and q_t is in kgf/cm^2.

B.2.4 Jamiolkowski et al. (2001)

Based on Schmertman (1976) empirical equation, Jamiolkowski et al. (2001) developed the following equation using the Calibration Chamber test results on three types of sands (Ticino, Hokksund and Toyoura sands)

$$D_r(\%) = \frac{100}{C_2}\ln\left[\frac{q_c/P_a}{C_0(\sigma'_{vo}/P_a)^{C_1}}\right] \quad \text{(B.18)}$$

where P_a, σ'_{vo} and q_c are in kPa.

For Ticino sand (medium to coarse sand; D_{50} = 0.60 mm; U_c = 1.3), C_0 = 17.74, C_1 = 0.55, and C_2 = 2.9 (r^2 = 0.81, n = 305). Hokksund sand is a medium sand (23% coarse sand) of D_{50} = 0.45 mm; U_c = 1.91. For the three tested sands, C_0 = 17.68, C_1 = 0.50, and C_2 = 3.1 (r^2 = 0.79, n = 180).

Table B.3 Correlations for Estimating Relative Density from Cone Penetration Test Results.

Source	Formula	Material tested / Particle size	Basis of Formula	Notes
Jamiolkowski et al. (1985)	$D_r^2 = \frac{1}{305 Q_c OCR^{0.18}} \frac{q_c / P_a}{(\sigma'_{vo} / P_a)^{0.5}}$ Q_c = (0.91 for high, 1.0 for medium, and 1.09 for low compressibility)	normally consolidated, uncemented, unaged, fine to medium, sands	Calibration Chamber data, corrected for boundary conditions using field test results	
Baldi et al. (1986)	$D_r(\%) = \frac{100}{C_2} \ln\left[\frac{q_c}{C_0(\sigma'_v)^{C_1}}\right]$ For NC Ticino sand C_0 = 157, C_1 = 0.55, and C_2 = 2.41(r^2 = 0.92, n = 102) For NC Hokksund sand C_0 = 86, C_1 = 0.53, and C_2 = 3.29 (r^2 = 0.96, n = 20)	Ticino sand (medium to coarse sand; D_{50} = 0.60 mm; U_c = 1.3) and Hokksund sand (medium sand (23% coarse sand) of D_{50} = 0.45 mm; U_c = 1.91)	large calibration chambers test results	Based on Schmertman (1976) Equation

Table B.3 Correlations for Estimating Relative Density from Cone Penetration Test Results (cont.).

Source	Formula	Material tested / Particle size	Basis of Formula	Notes
Tanizawa (1990)	$D_r(\%) = -85.1 + 76\log(\frac{q_t}{(\sigma'_{vo})^{0.5}})$	Toyoura sand (medium quartz sand (30% fine sand) of D_{50} = 0.22 mm; U_c = 1.31)		
Jamiolkowski et al. (2001)	$D_r(\%) = \frac{100}{C_2}\ln\left[\frac{q_c / P_a}{C_0(\sigma'_{vo} / P_a)^{C_1}}\right]$ C_0 = 17.74, C_1 = 0.55 & C_2 = 2.9 (r^2 = 0.81, n = 305) for Ticino sand C_0 = 17.68, C_1 = 0.50 & C_2 = 3.1 (r^2 = 0.79, n = 180) for Ticino, Hokksund and Toyoura sands	Ticino, Hokksund and Toyoura sands	Calibration Chamber test results (D=1.2m & H=1.5m), corrected for boundary conditions using empirical equation.	

Appendix C Screen Display from the Pulse Test Interpretation Software for some carried out Ring Actuators Tests

Test 3

Pulse Tests on Milby Sand in the Oedometer Ring (Setup A)

Using the Ring Actuators Setup No. 4.

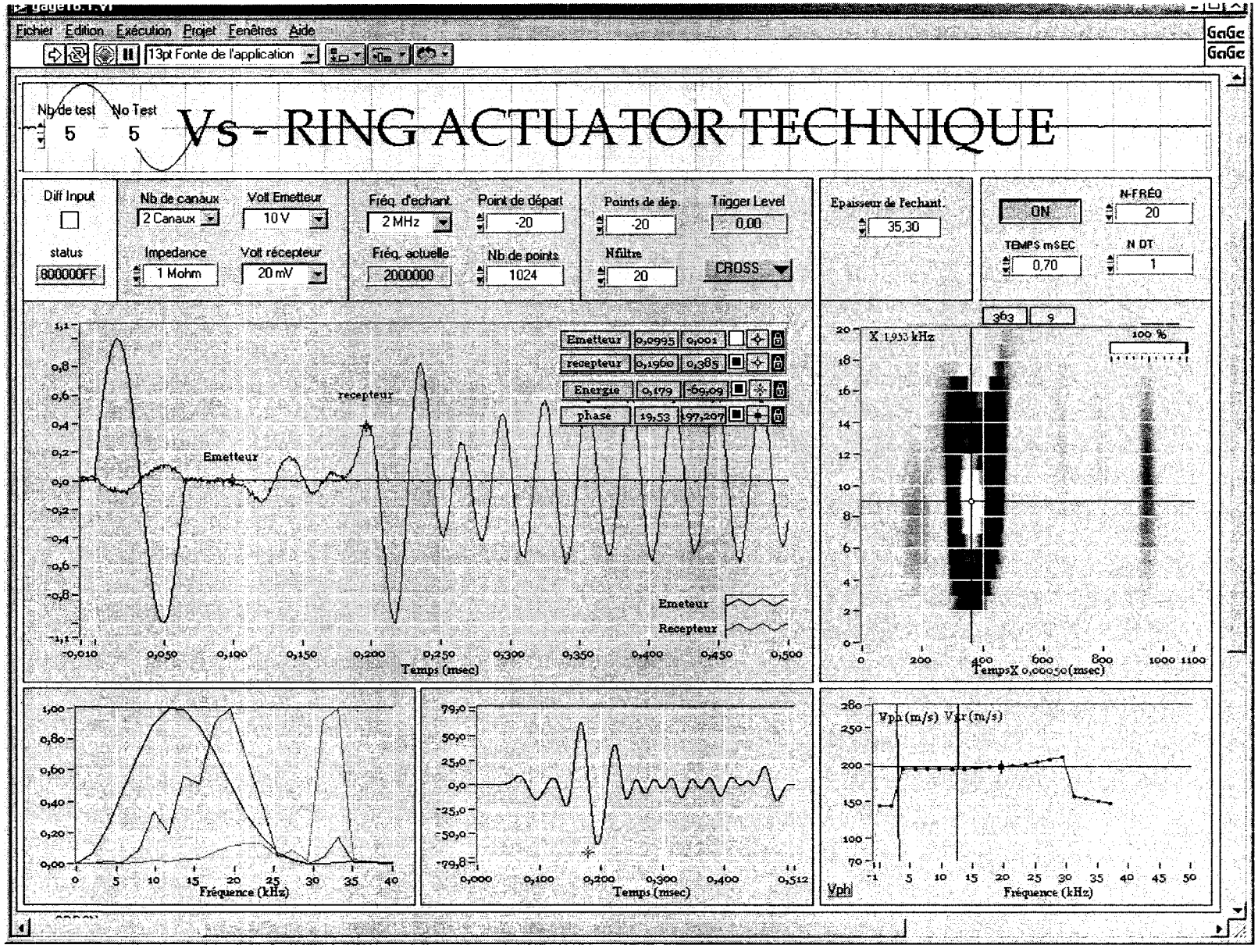

Figure C.1 Test 3(a); Sine wave input of 15 kHz, Pressure = 16.6 kPa.

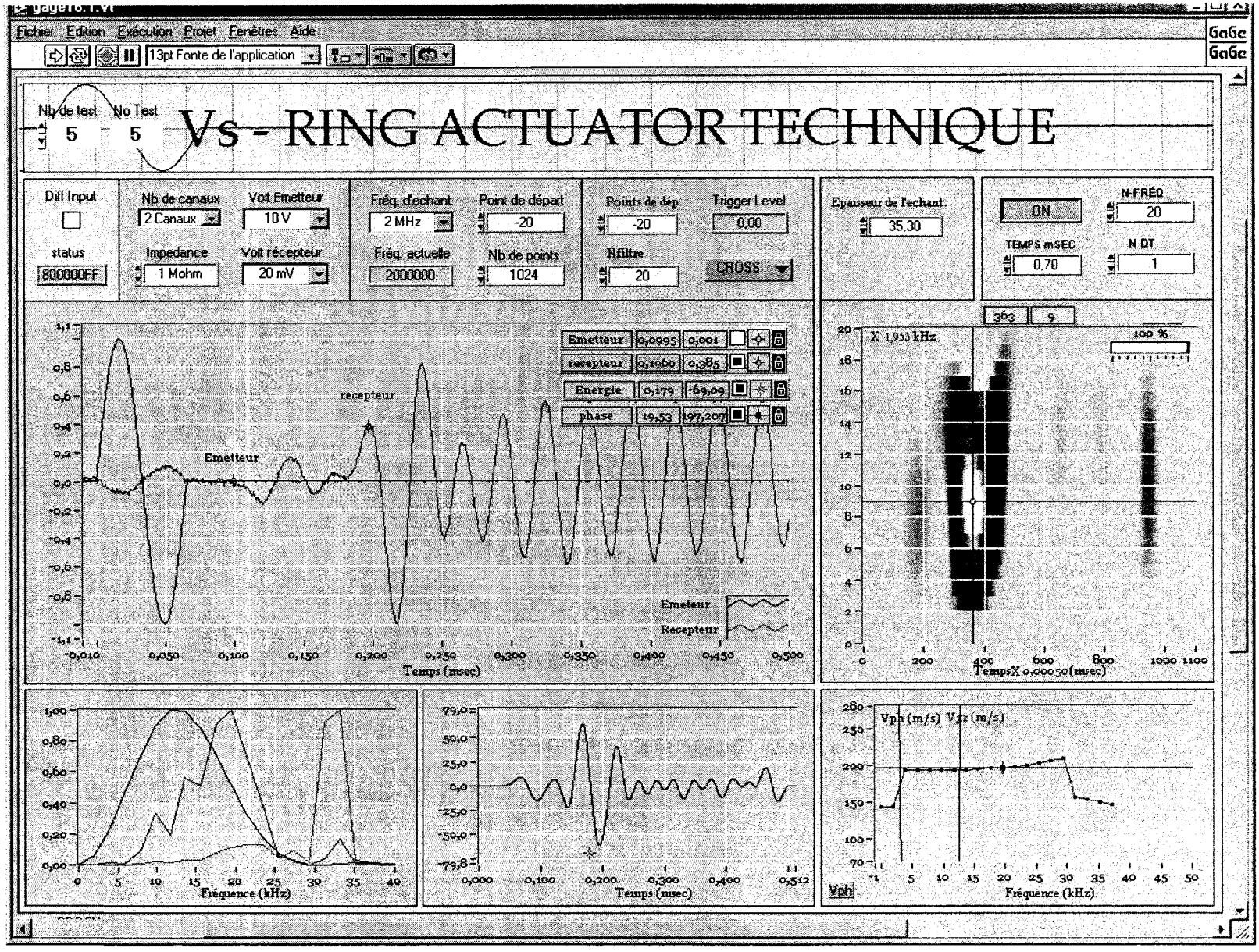

Figure C.2 Test 3(b); Sine wave input of 15 kHz, Pressure = 28.6 kPa.

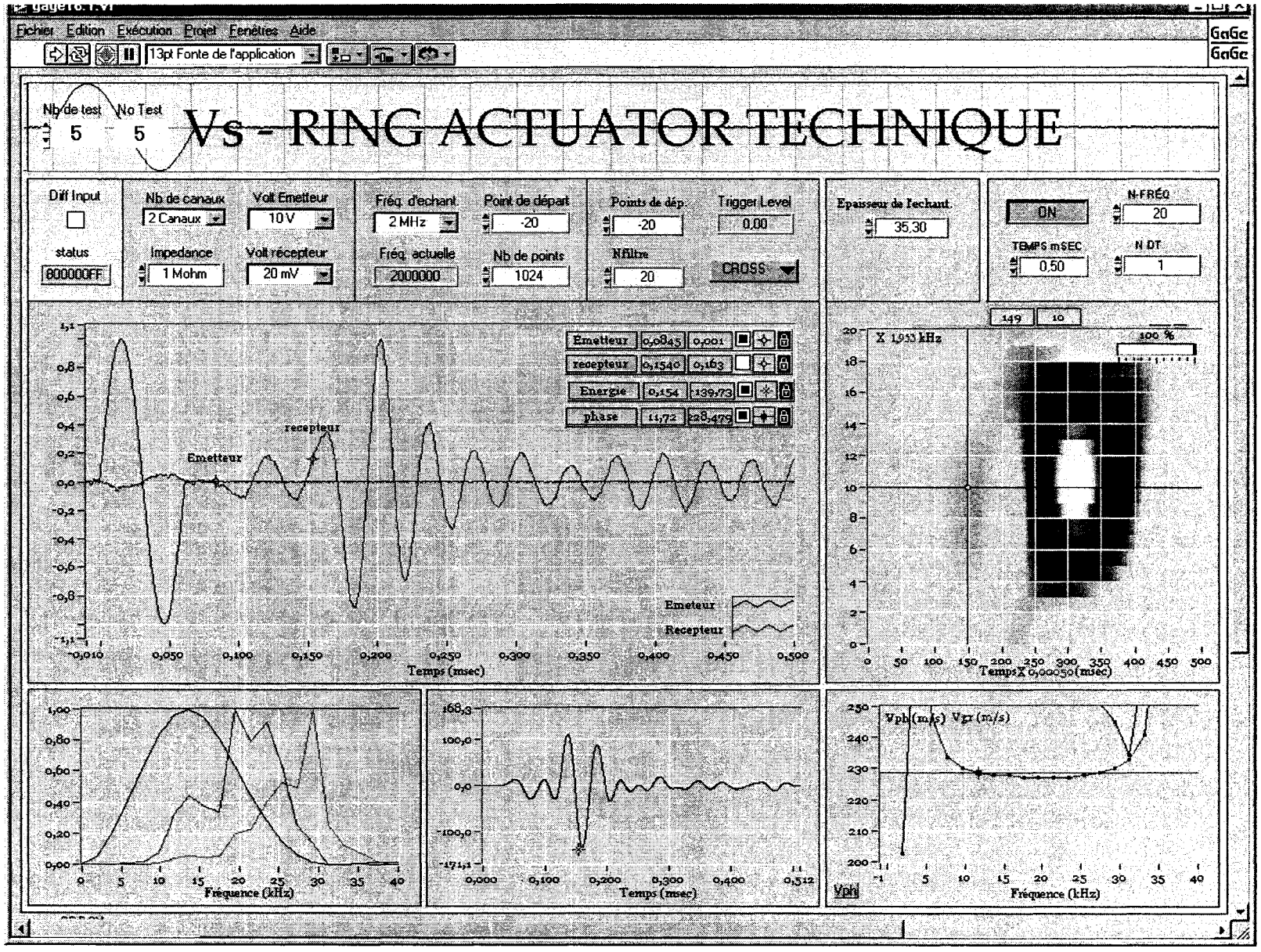

Figure C.3 Test 3(c); Sine wave input of 16 kHz, Pressure = 83.5 kPa.

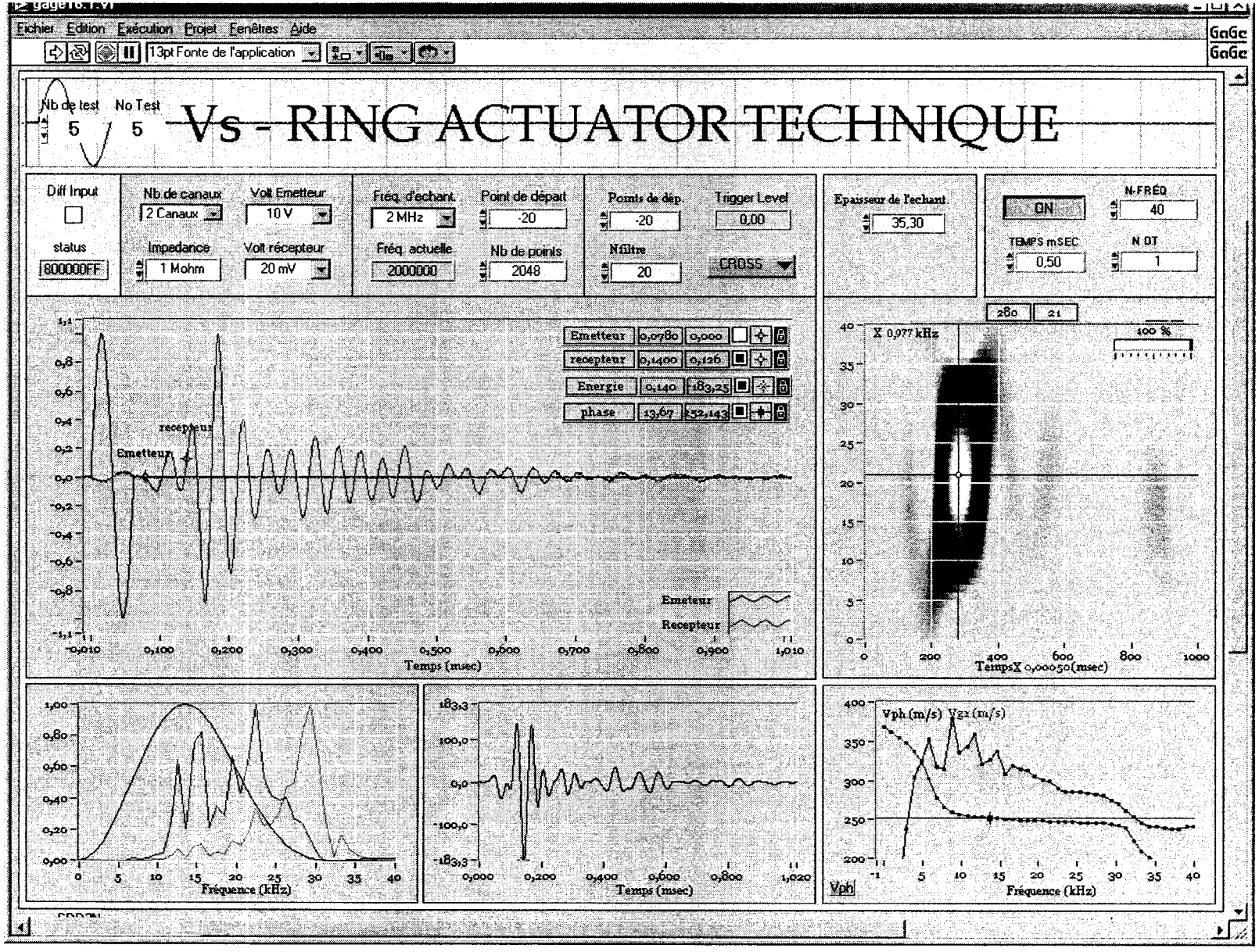

Figure C.4 Test 3(d); Sine wave input of 16 kHz, Pressure = 138.5 kPa.

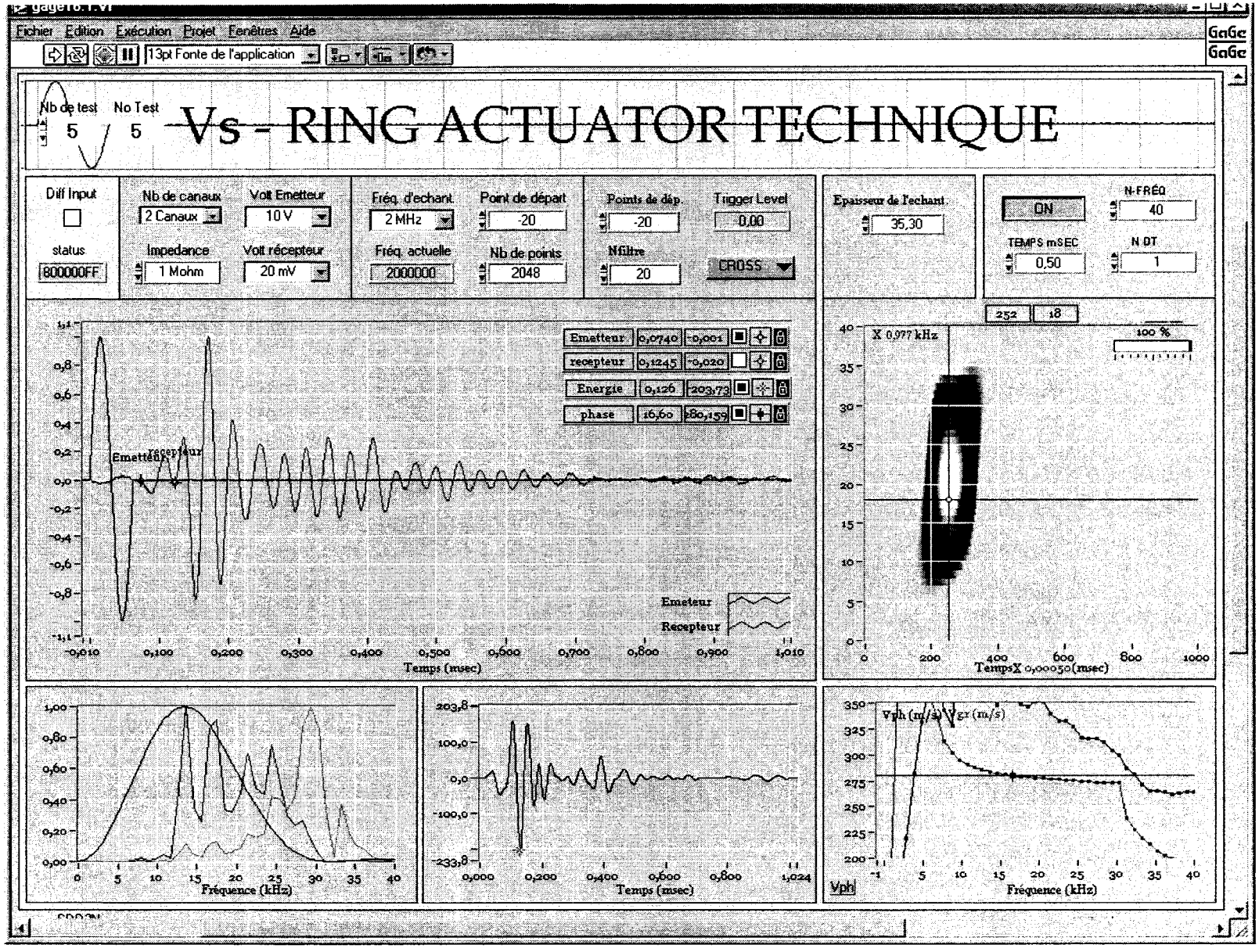

Figure C.5 Test 3(e); Sine wave input of 16 kHz, Pressure = 248.4 kPa.

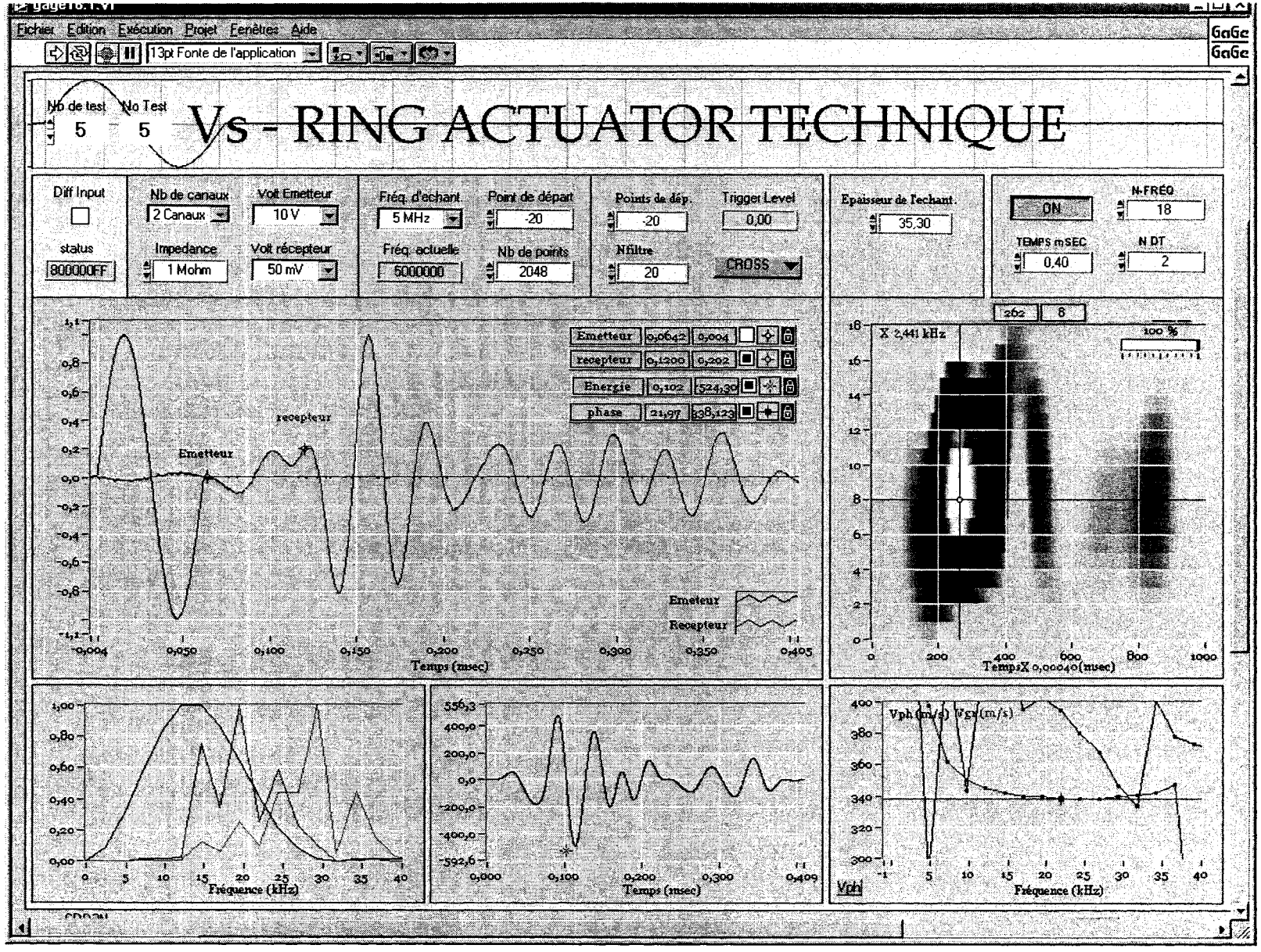

Figure C.6 Test 3(f); Sine wave input of 16 kHz, Pressure = 413.3 kPa.

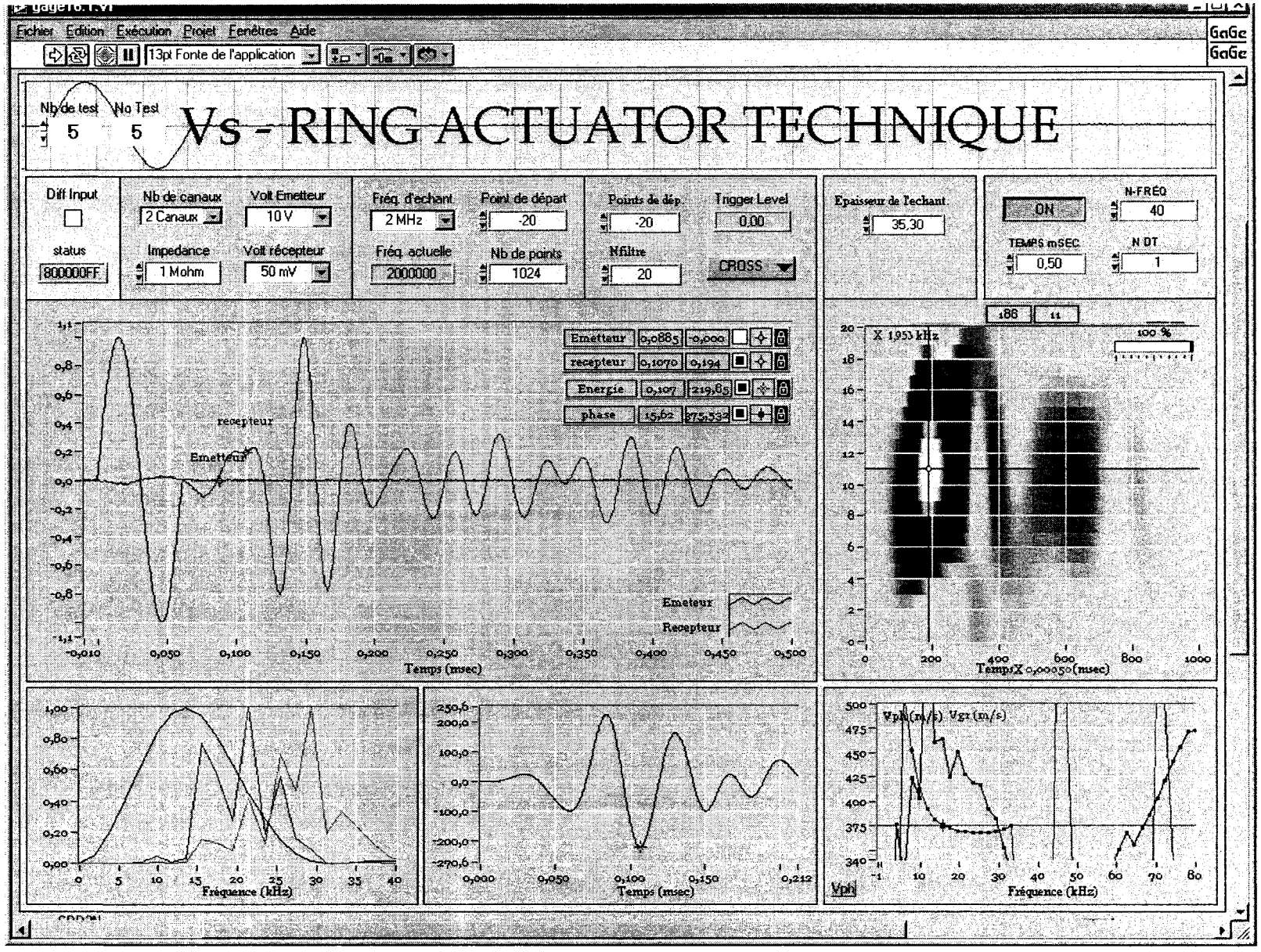

Figure C.7 Test 3(g); Sine wave input of 16 kHz, Pressure = 633.1 kPa.

Test 40

Pulse Tests on Loose Ottawa Sand (C-109) in the Short Plexiglass Mold (Setup C)

Using the Ring Actuators Setup No. 7.

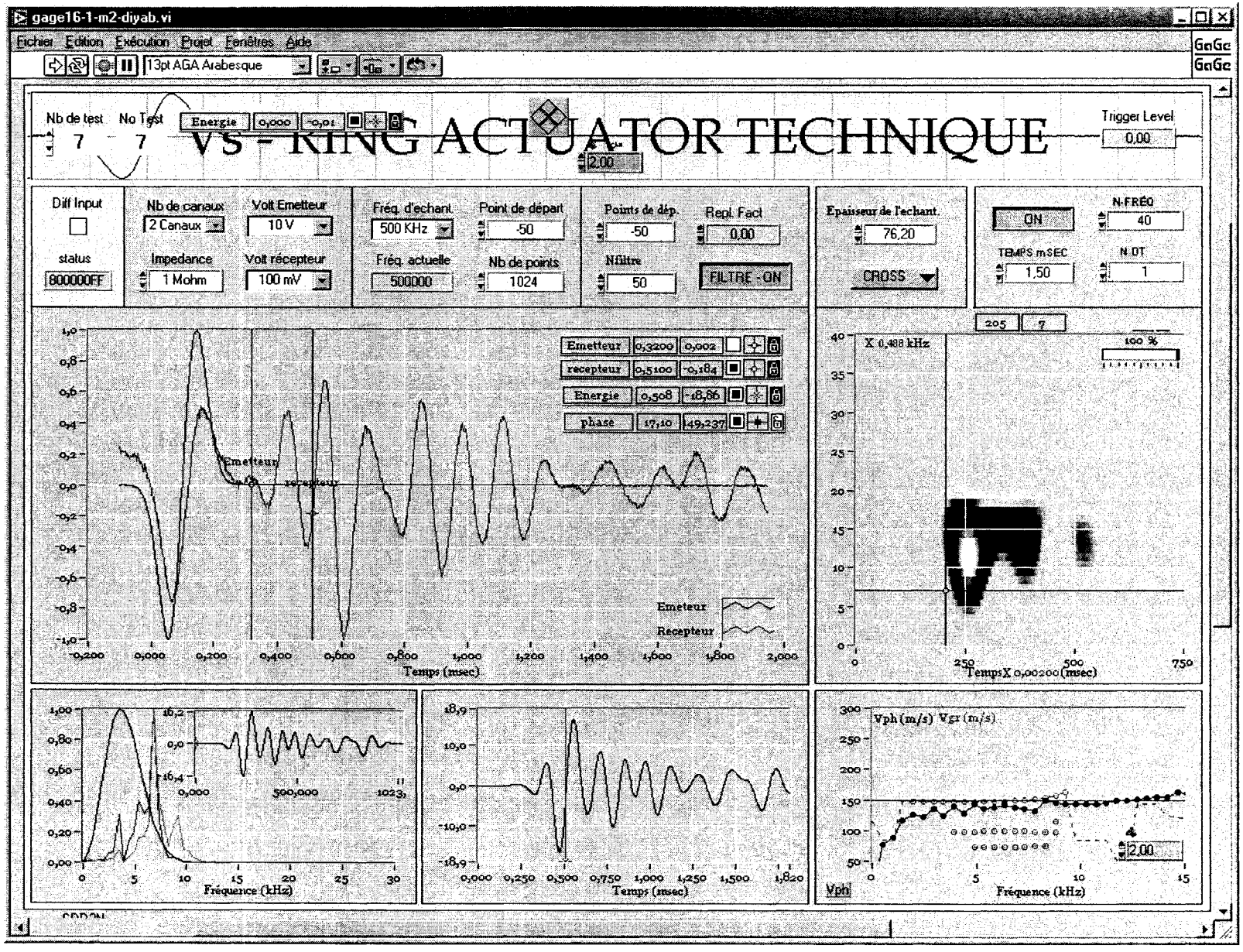

Figure C.8 Test 40(a); Sine-like input shape (wavelet), Pressure = 28.6 kPa.

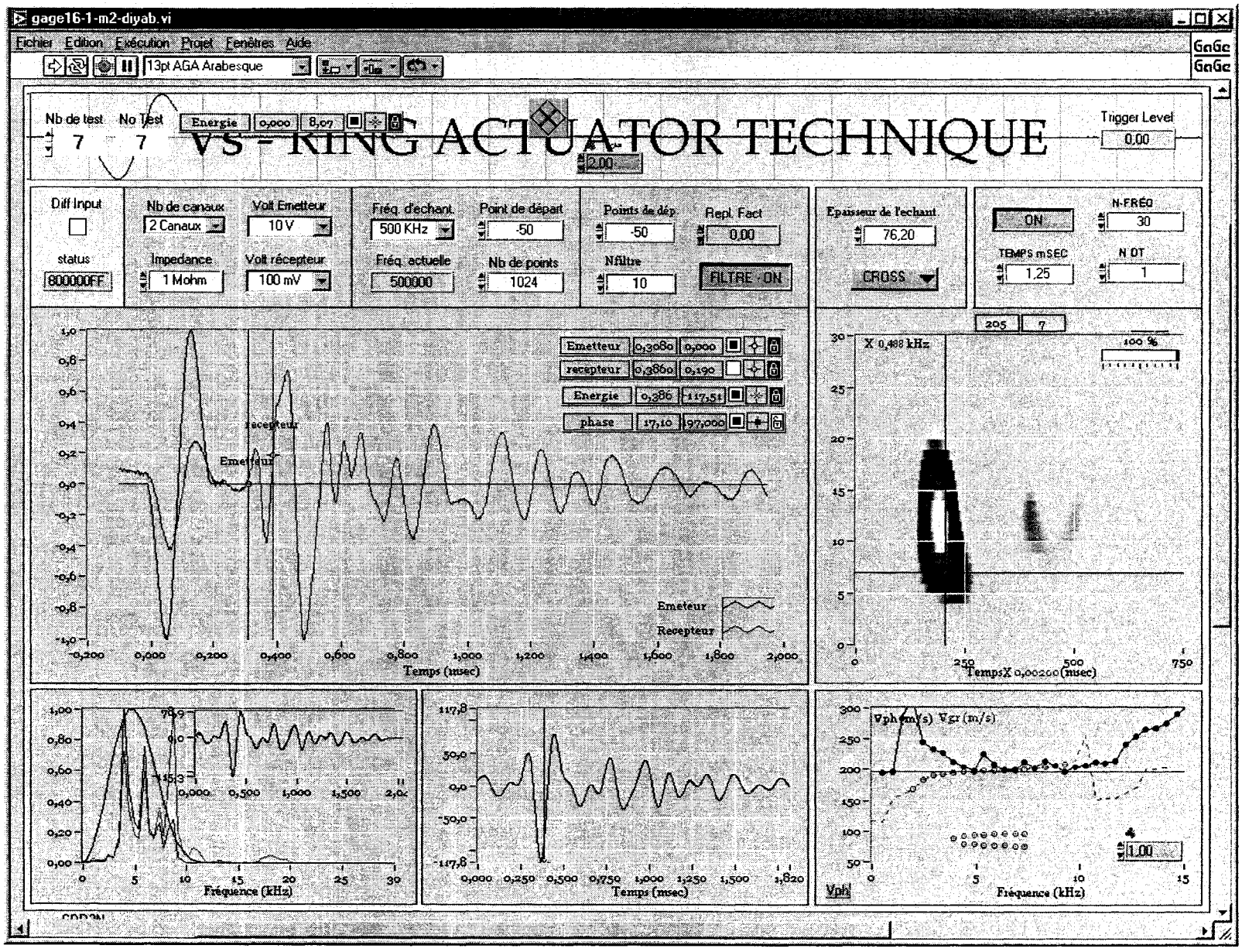

Figure C.9 Test 40(b); Sine-like input shape (wavelet), Pressure = 83.5 kPa.

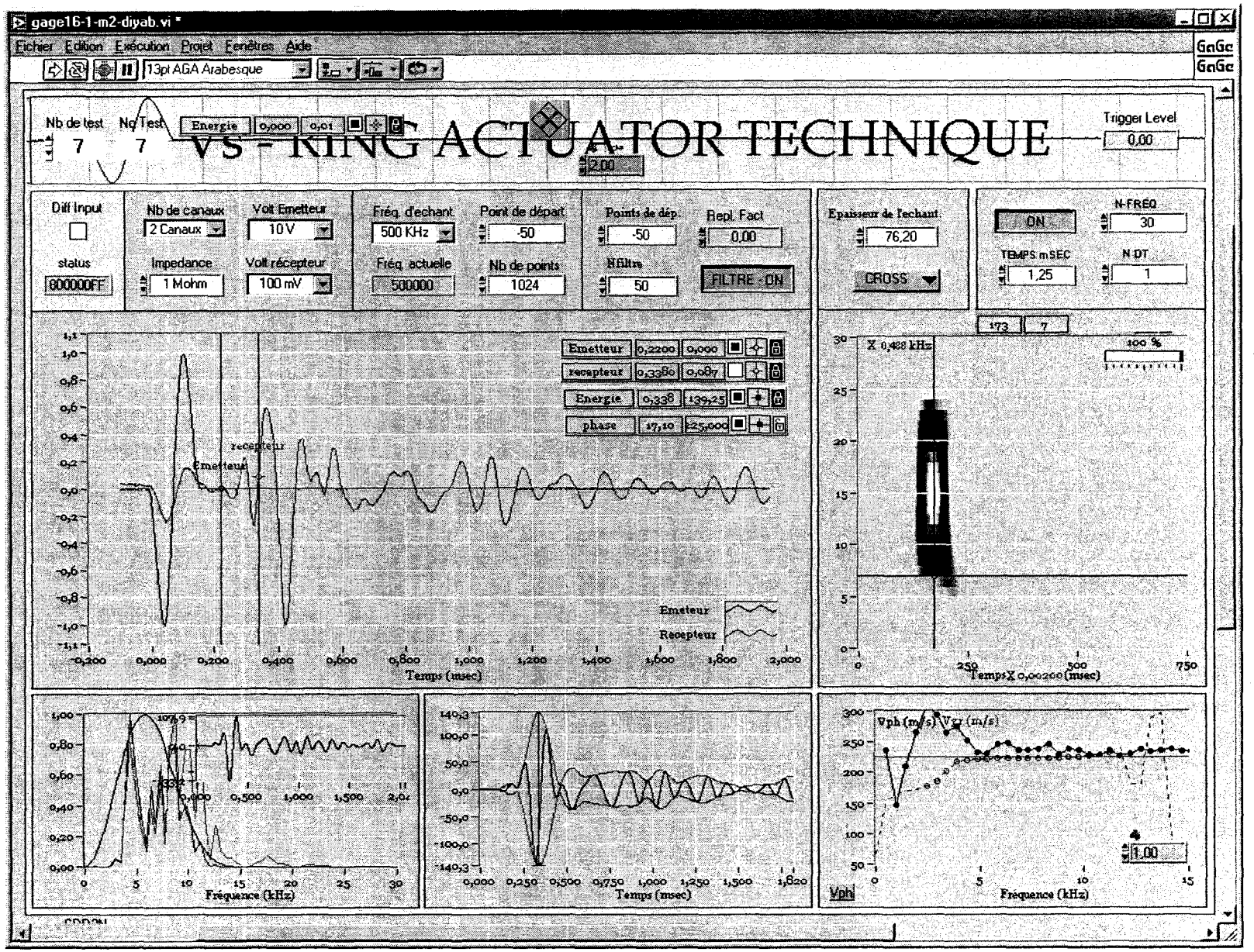

Figure C.10 Test 40(c); Sine-like input shape (wavelet), Pressure = 138.5 kPa.

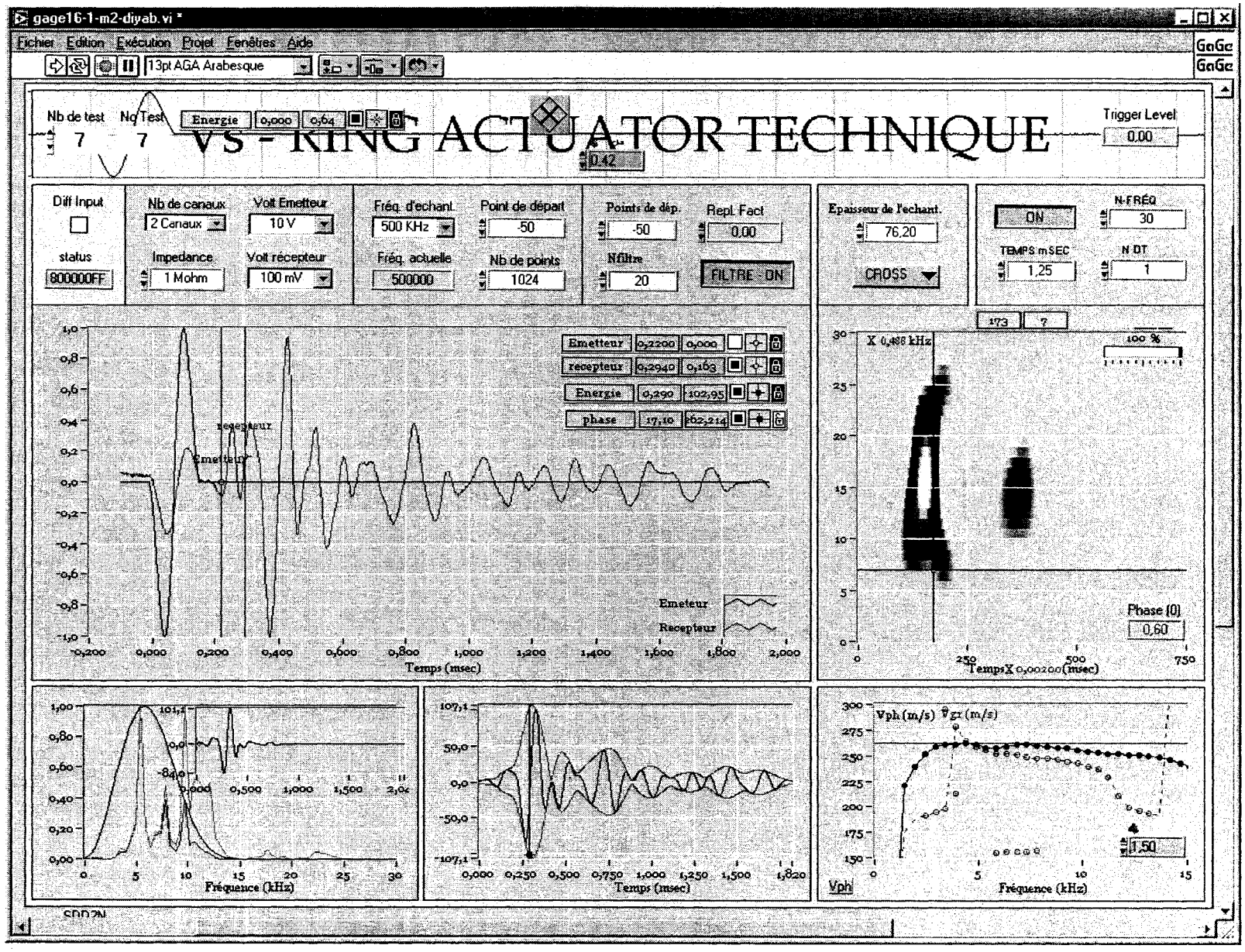

Figure C.11 Test 40(d); Sine-like input shape (wavelet), Pressure = 248.4 kPa.

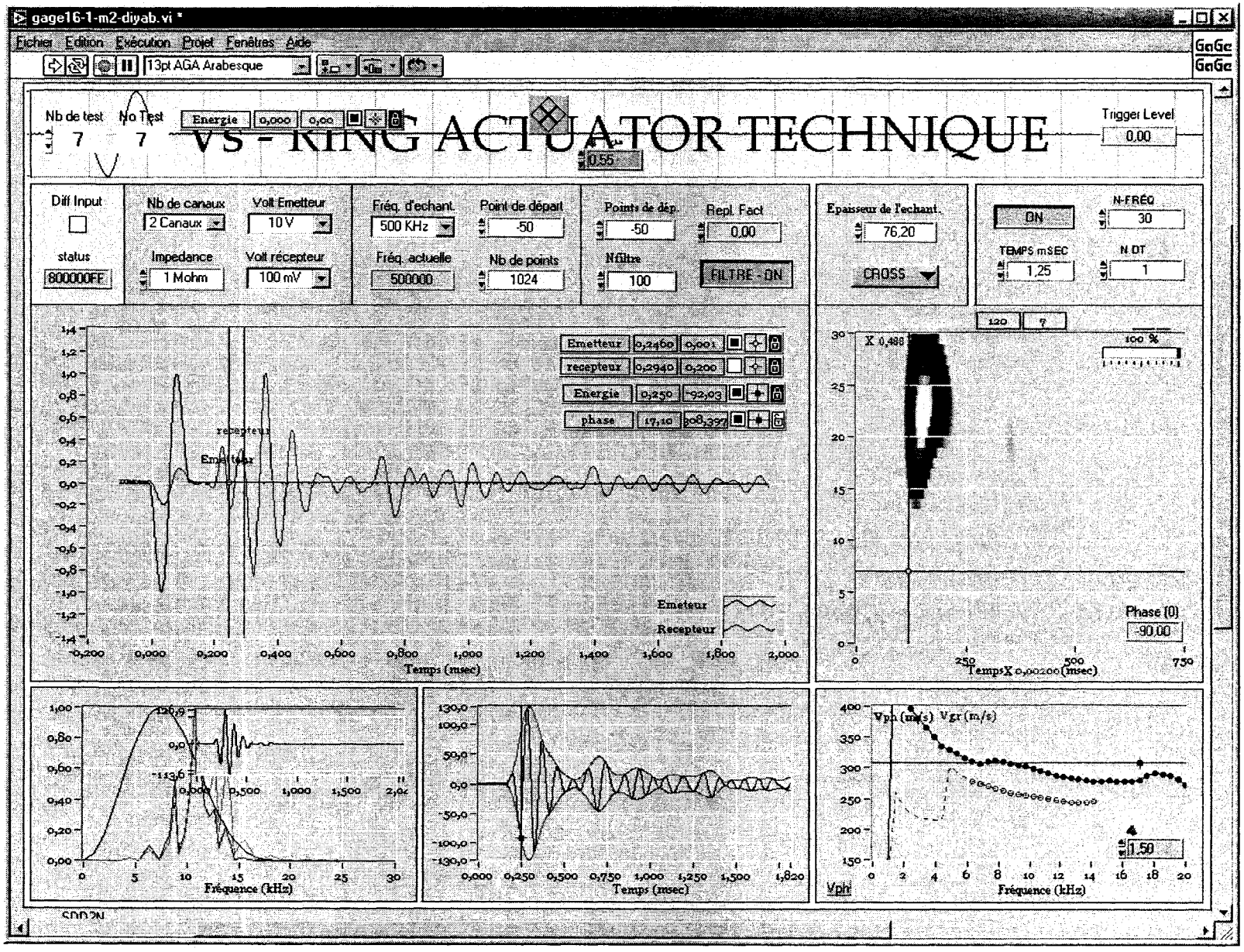

Figure C.12 Test 40(e); Sine-like input shape (wavelet), Pressure = 413.3 kPa.

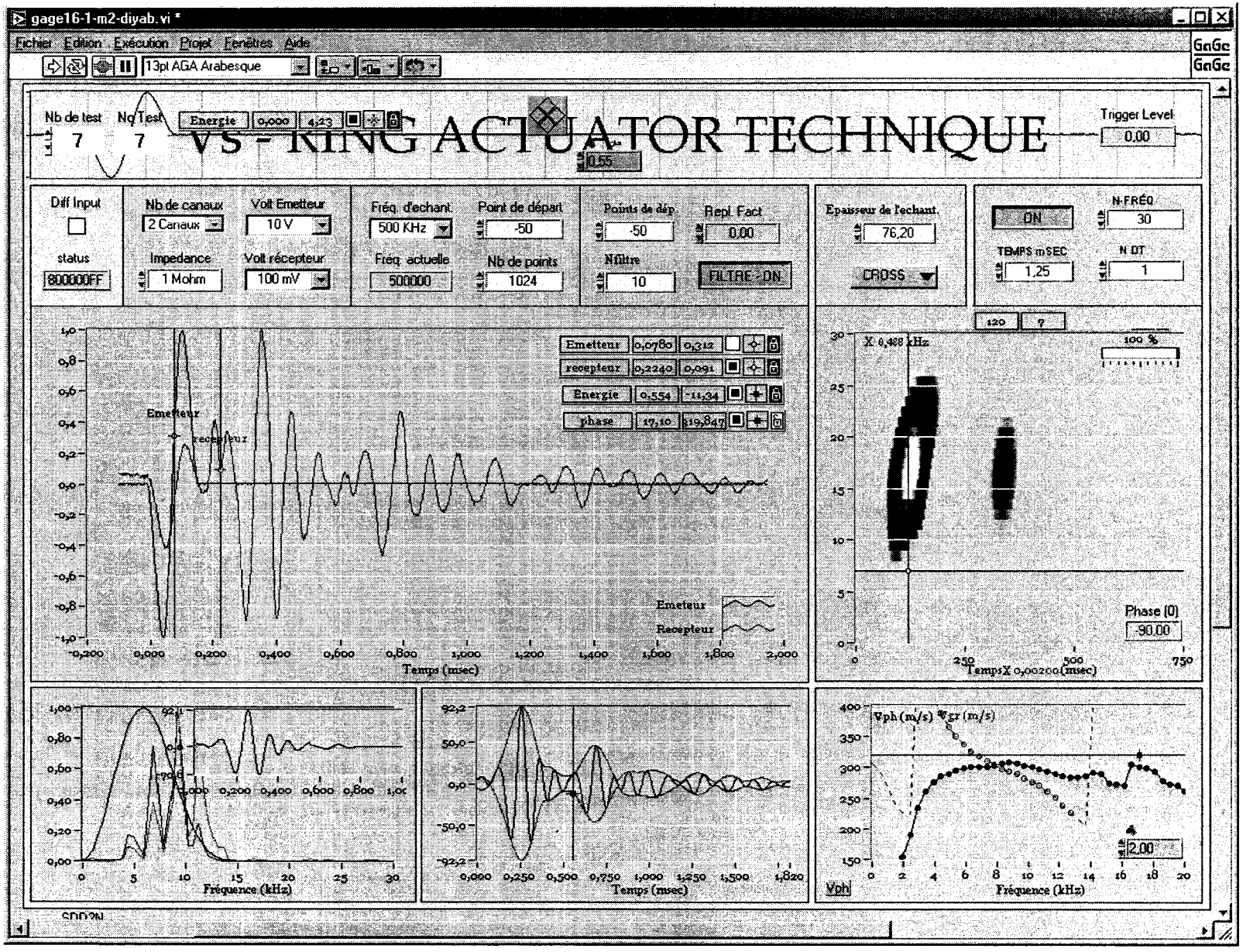

Figure C.13 Test 40(f); Sine-like input shape (wavelet), Pressure = 578.1 kPa.

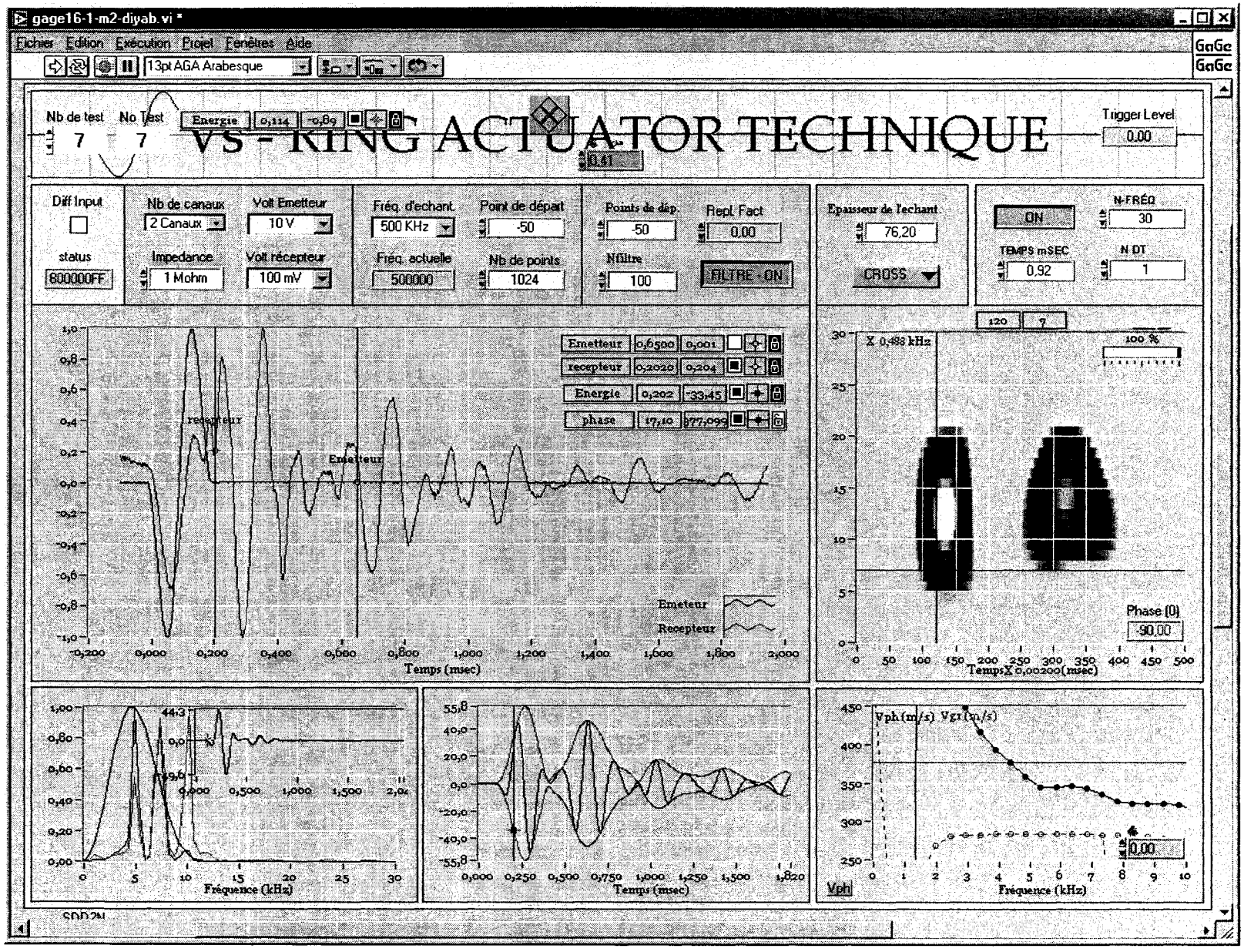

Figure C.14 Test 40(g); Sine-like input shape (wavelet), Pressure = 797.9 kPa.

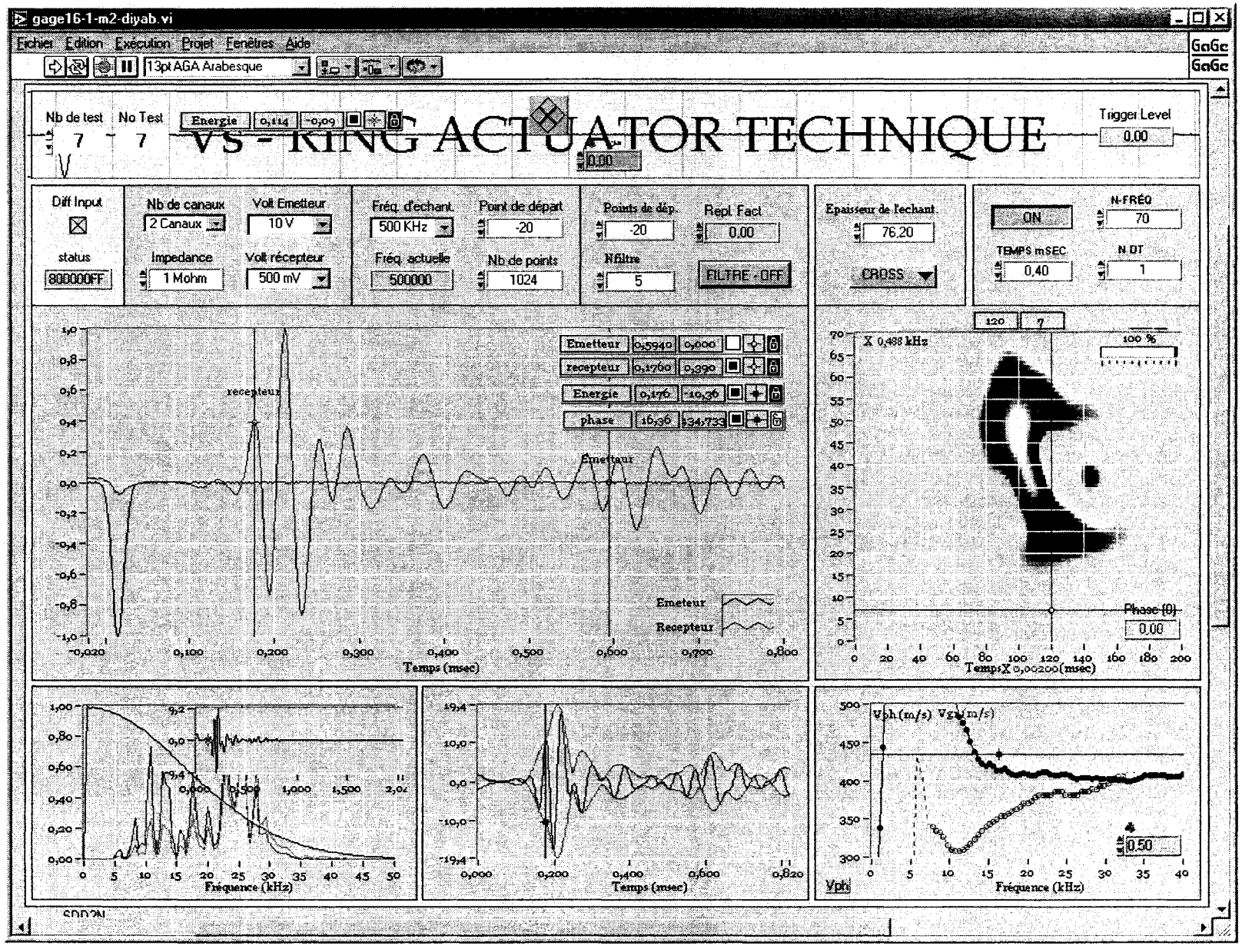

Figure C.15 Test 40(h); Versed half-sine input, Pressure = 1127.7 kPa.

Test 42

Pulse Tests on LG4 Till in the Short Plexiglass Mold (Setup C)

Using the Ring Actuators Setup No. 7.

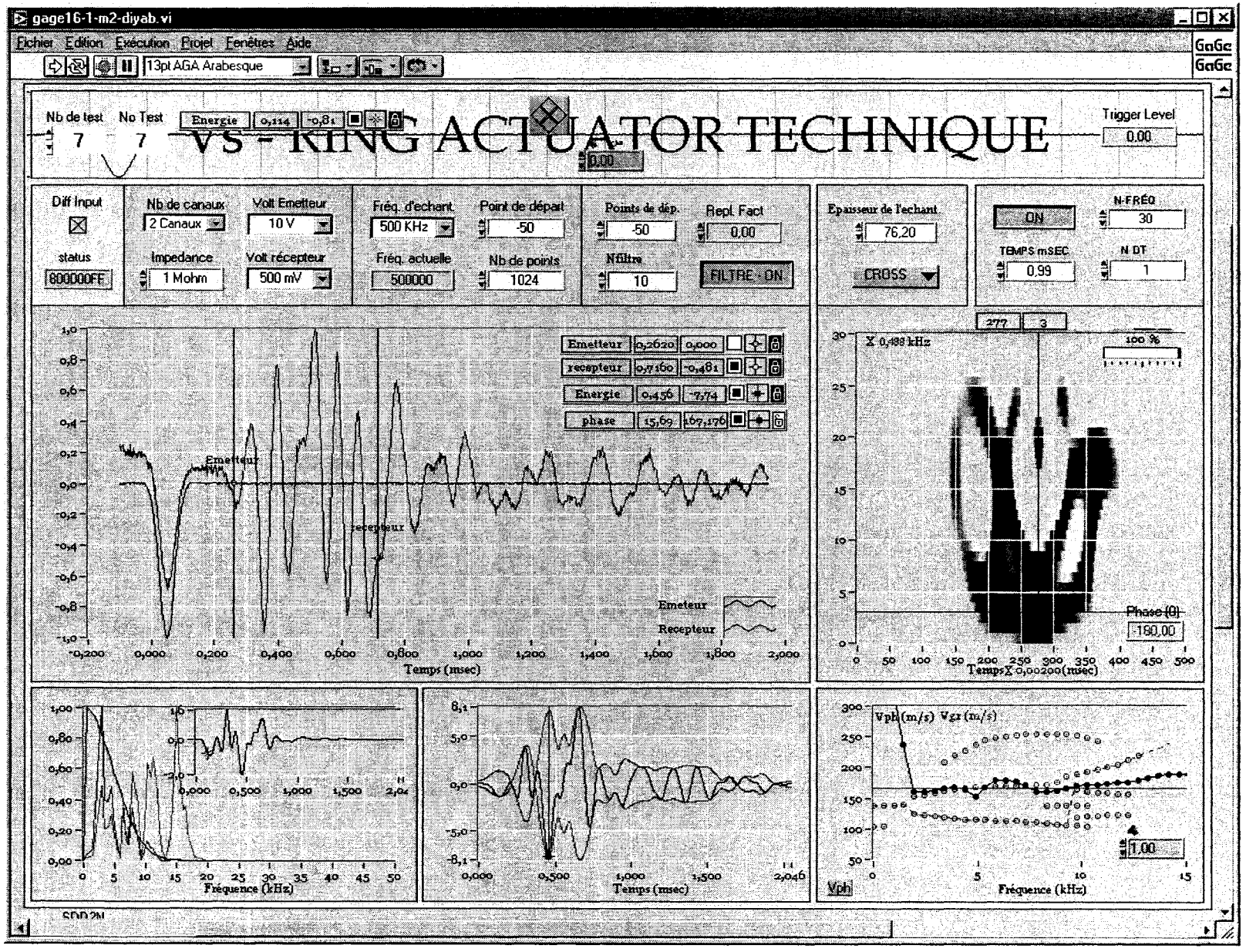

Figure C.16 Test 42(a); Versed sine input, Pressure = 28.6 kPa.

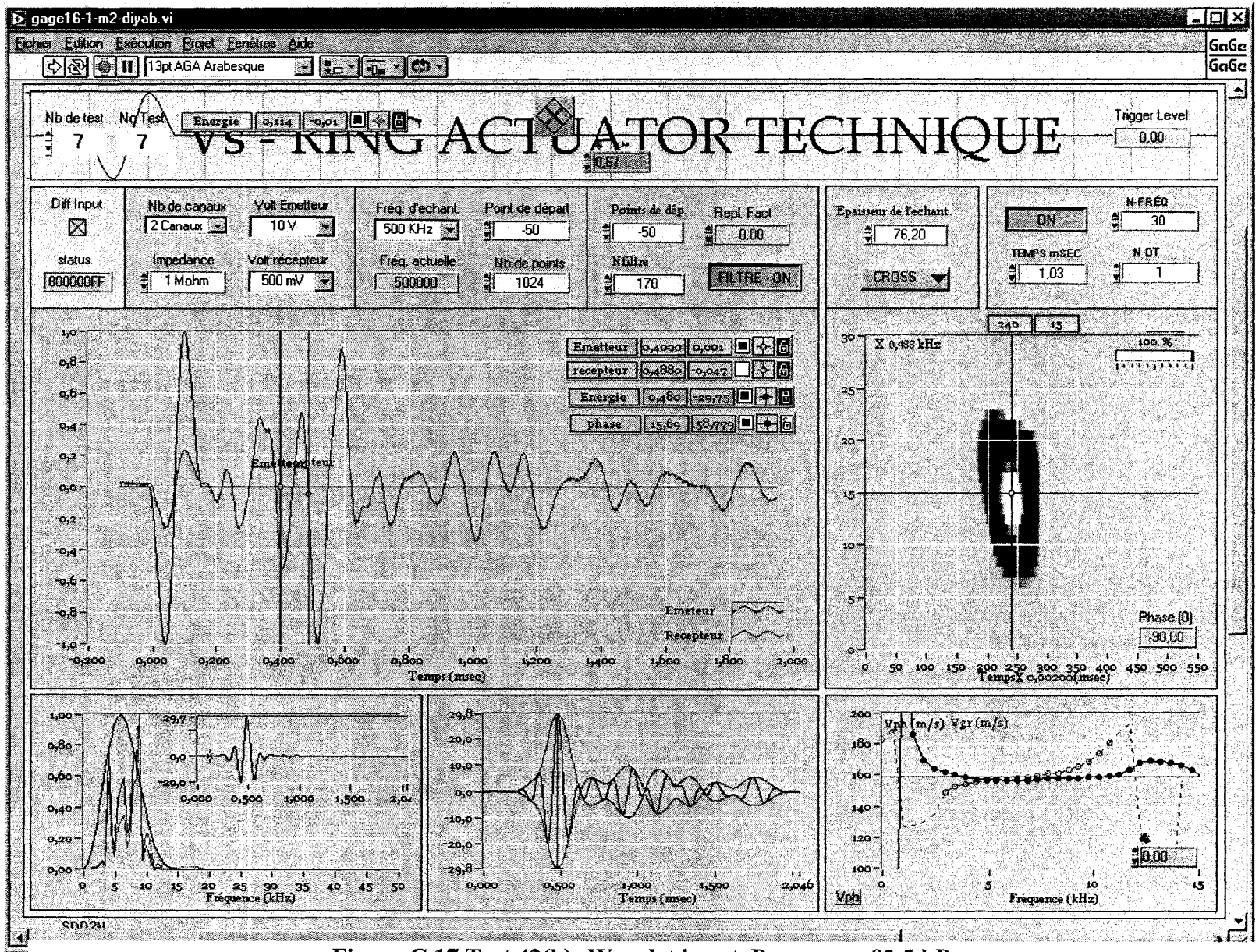

Figure C.17 Test 42(b); Wavelet input, Pressure = 83.5 kPa.

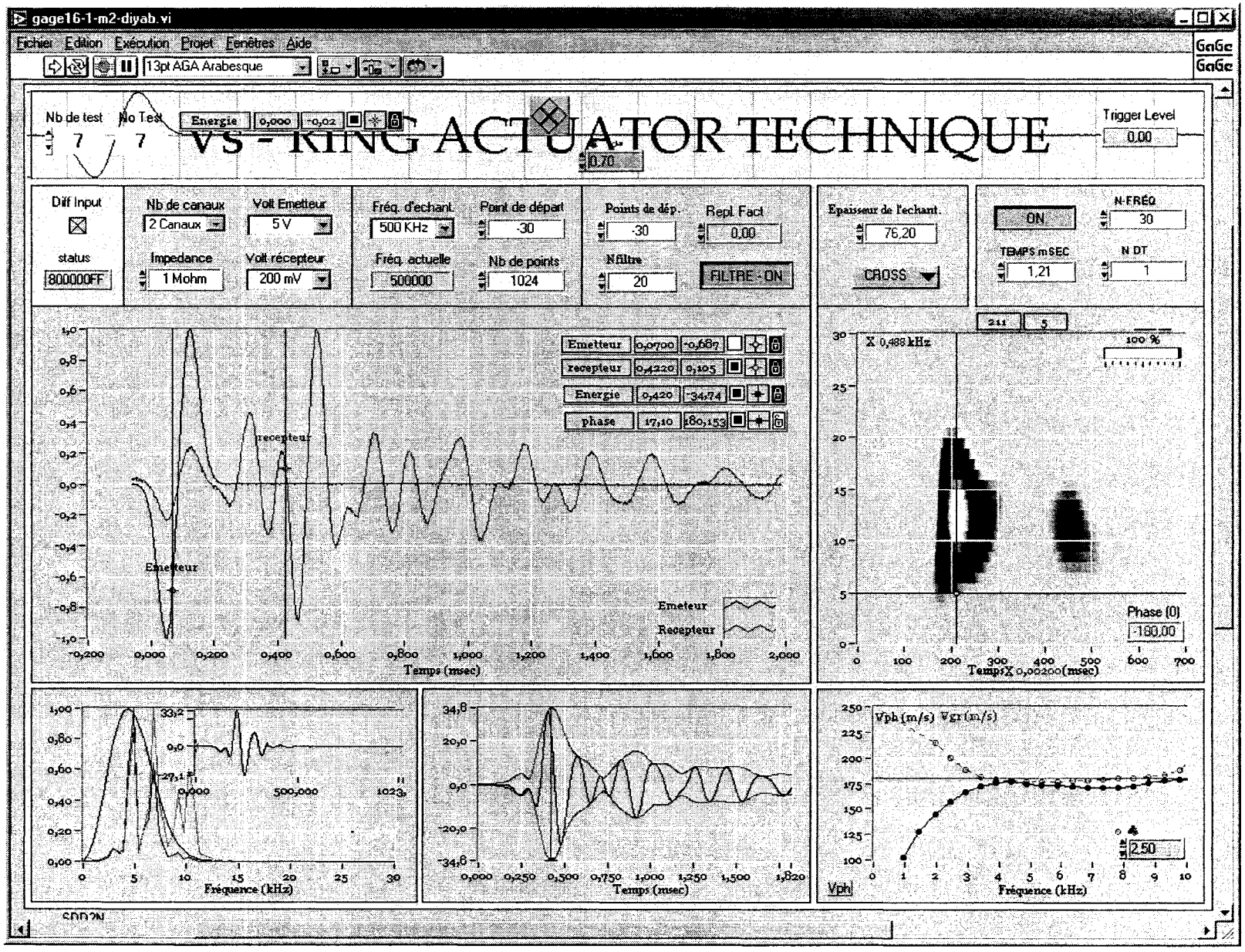

Figure C.18 Test 42(c); Versed-sine input, Pressure = 138.5 kPa.

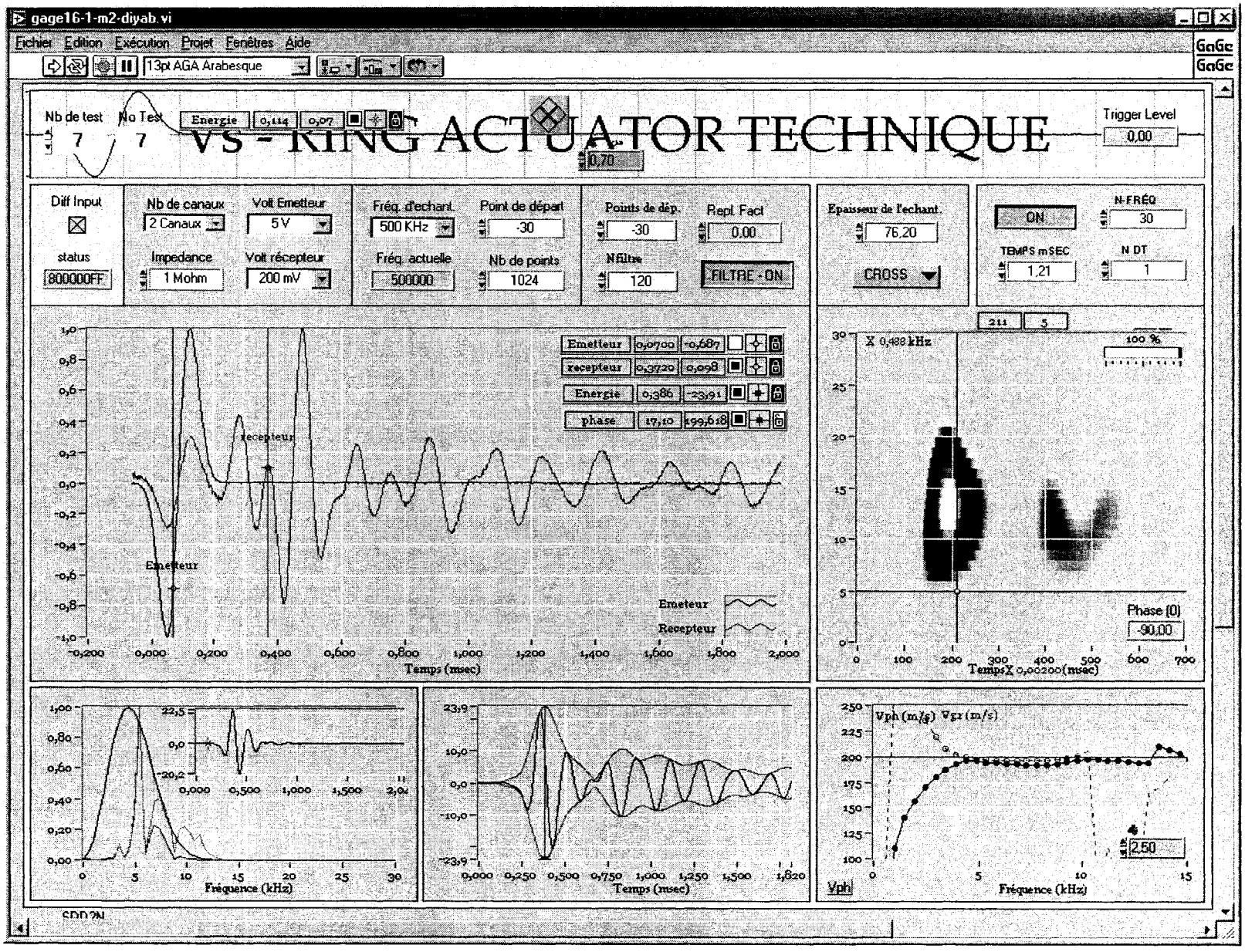

Figure C.19 Test 42(d); Wavelet input, Pressure = 248.4 kPa.

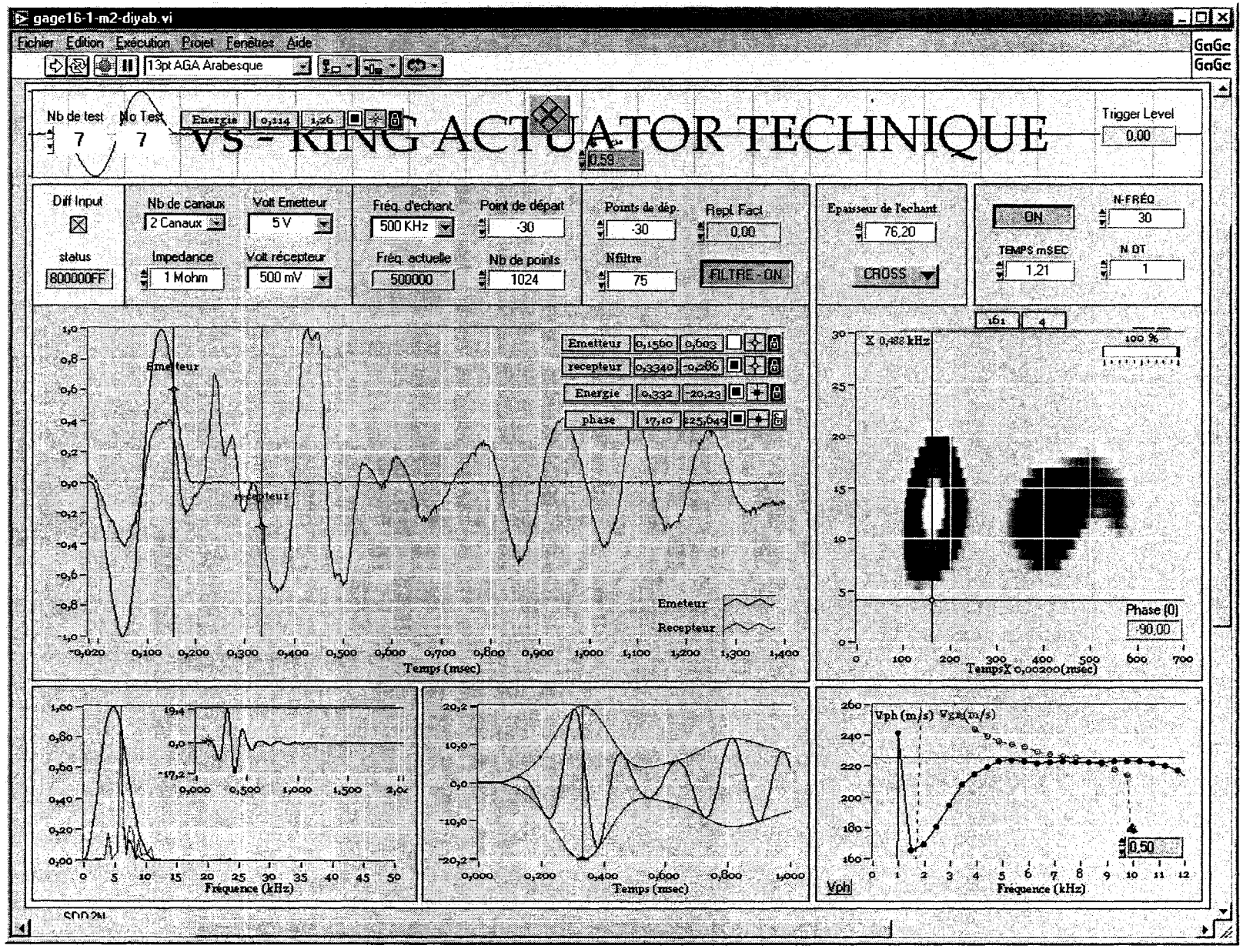

Figure C.20 Test 42(e); Wavelet input, Pressure = 413.3 kPa.

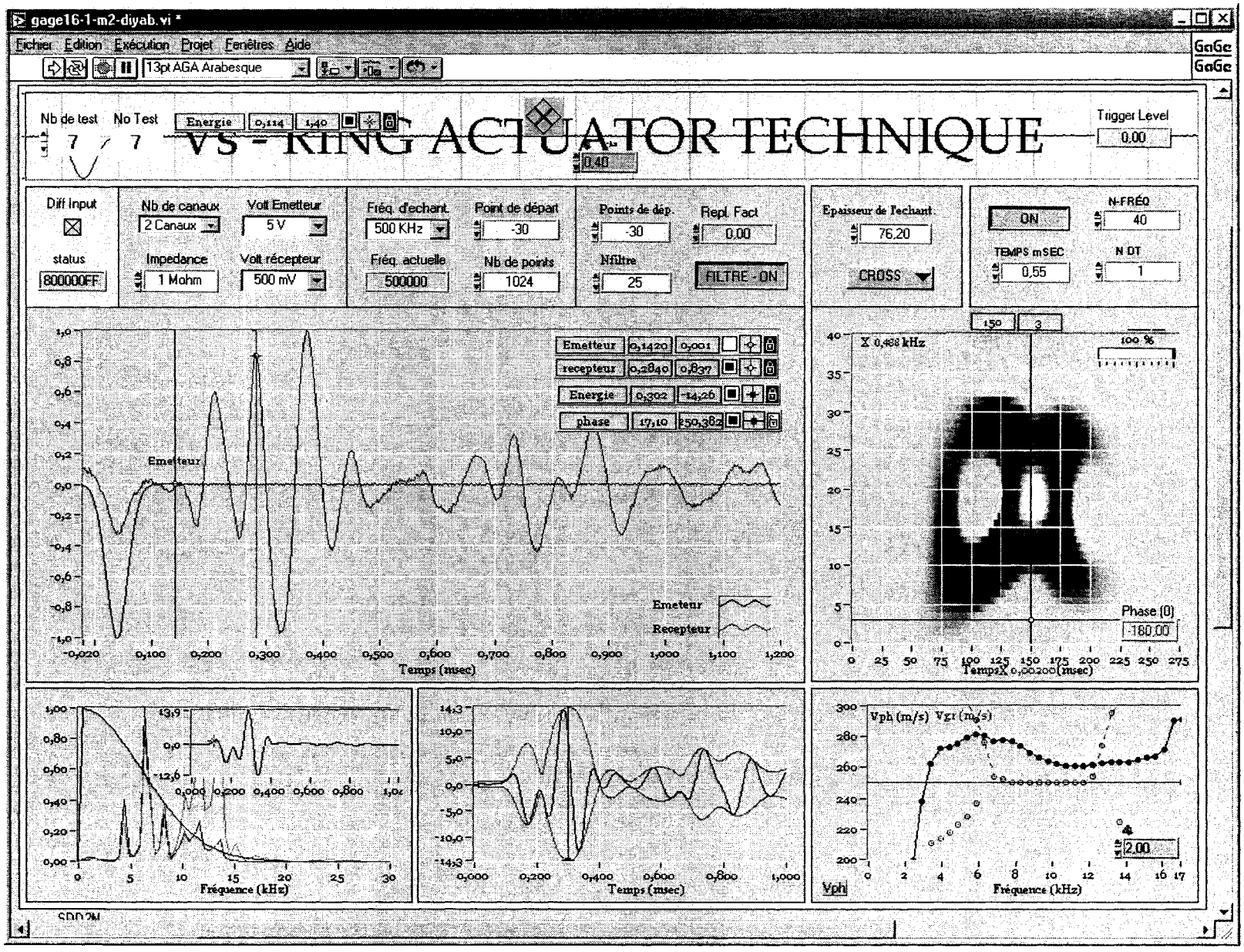

Figure C.21 Test 42(f); Versed sine input, Pressure = 578.1 kPa.

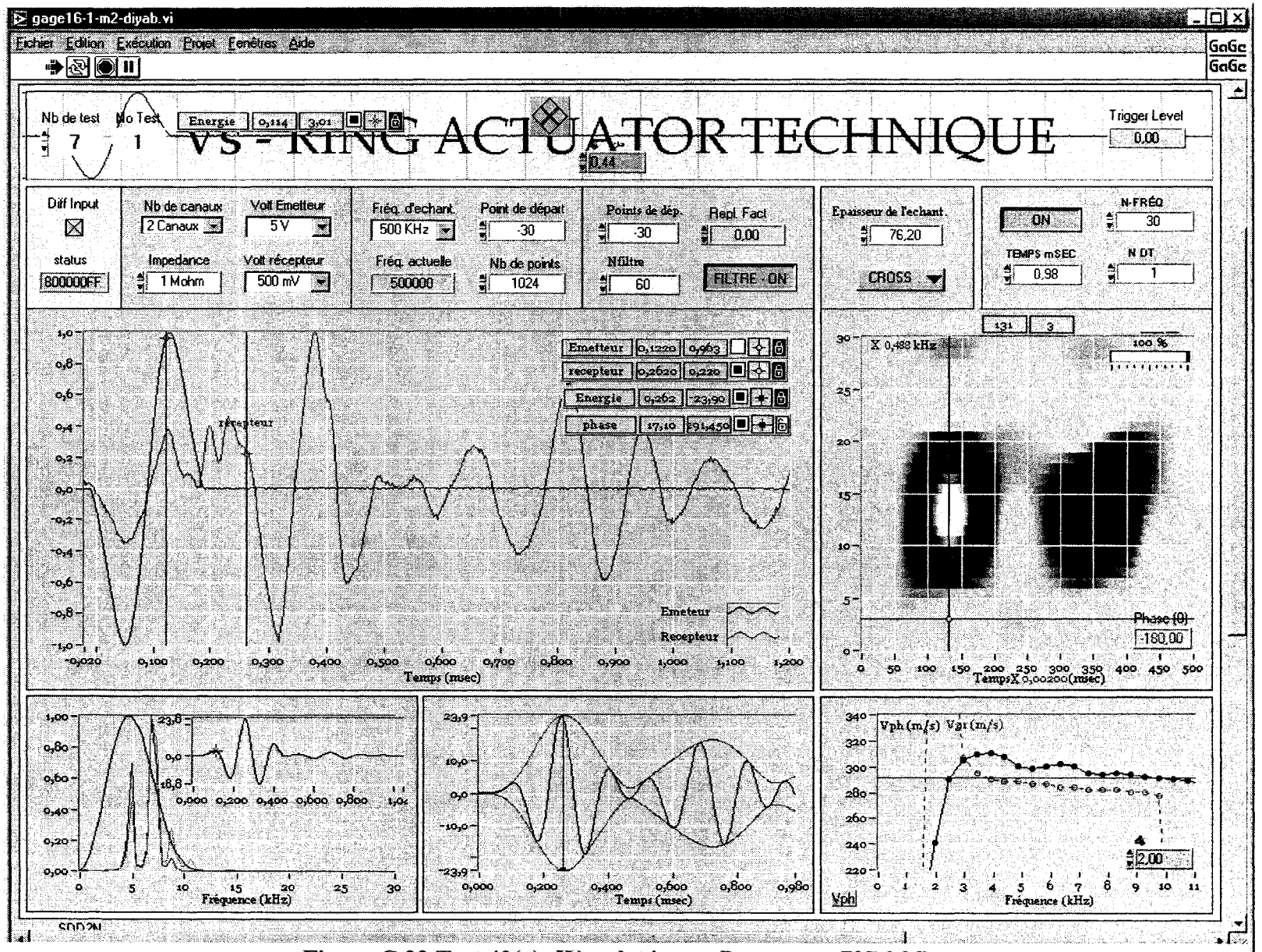

Figure C.22 Test 42(g); Wavelet input, Pressure = 797.9 kPa.

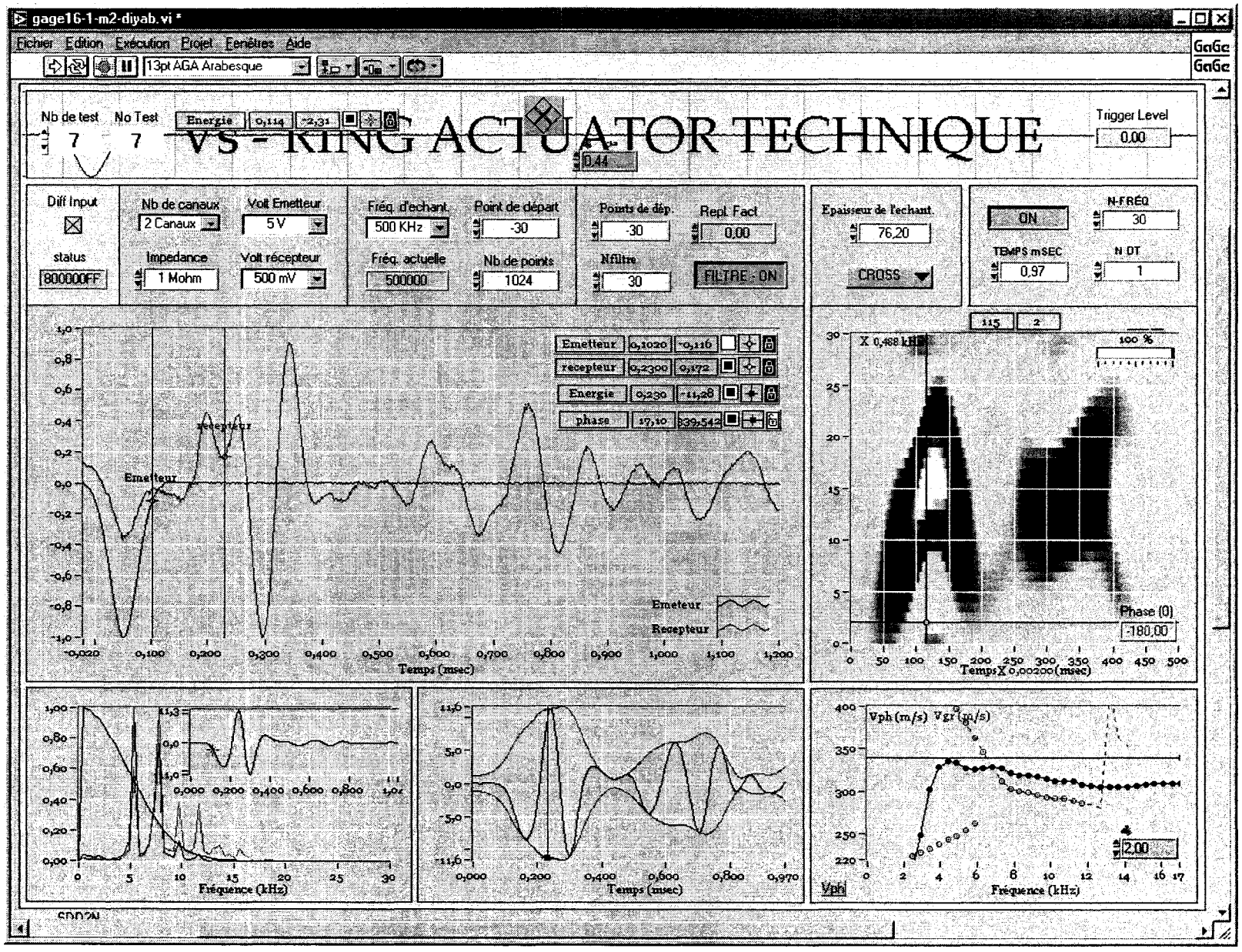

Figure C.23 Test 42(h); Versed sine input, Pressure = 1127.7 kPa.

Test 43

Pulse Tests on LG4 Till in the Medium Plexiglass Mold (Setup D)

Using the Ring Actuators Setup No. 7.

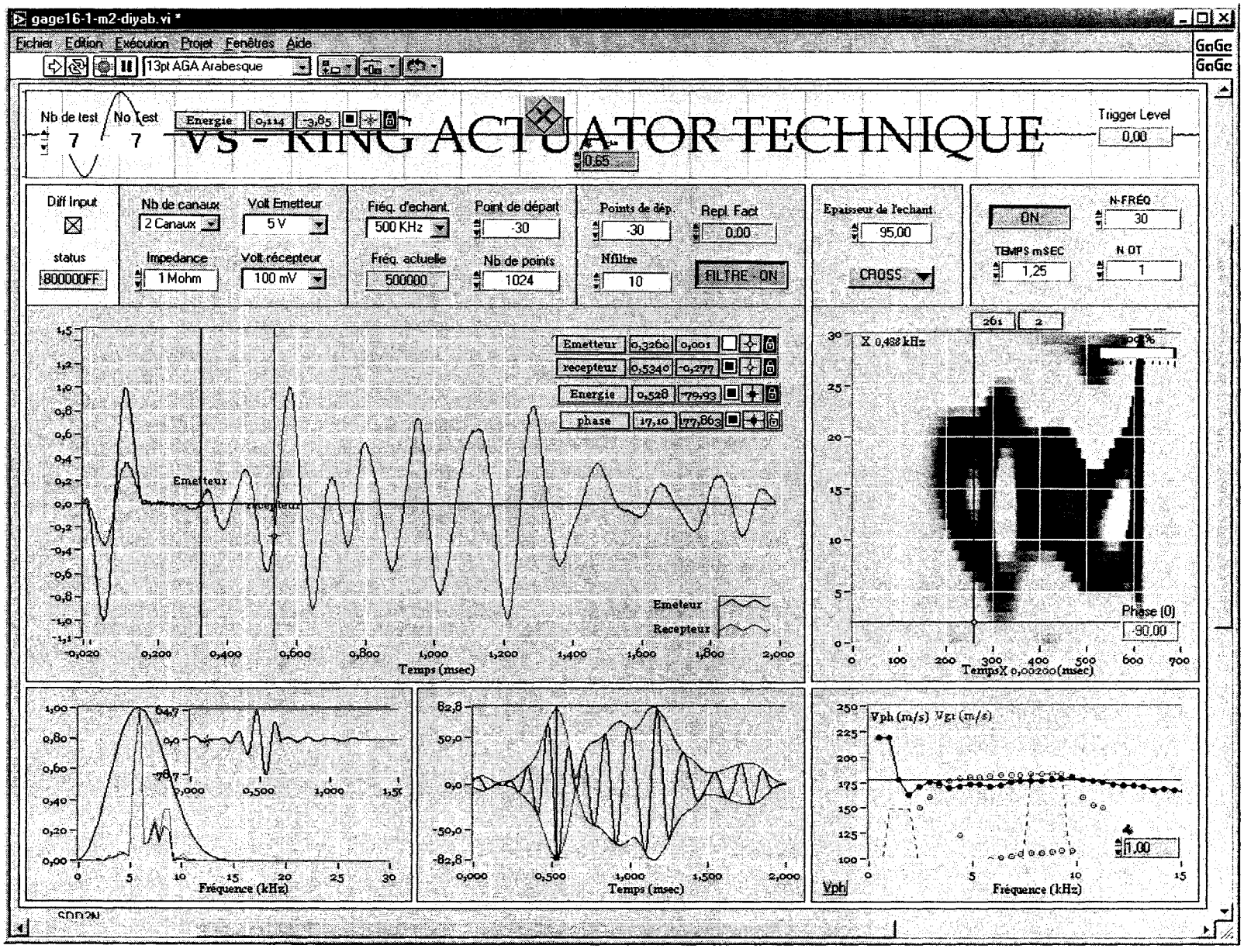

Figure C.24 Test 43(a); Versed sine input, Pressure = 28.6 kPa.

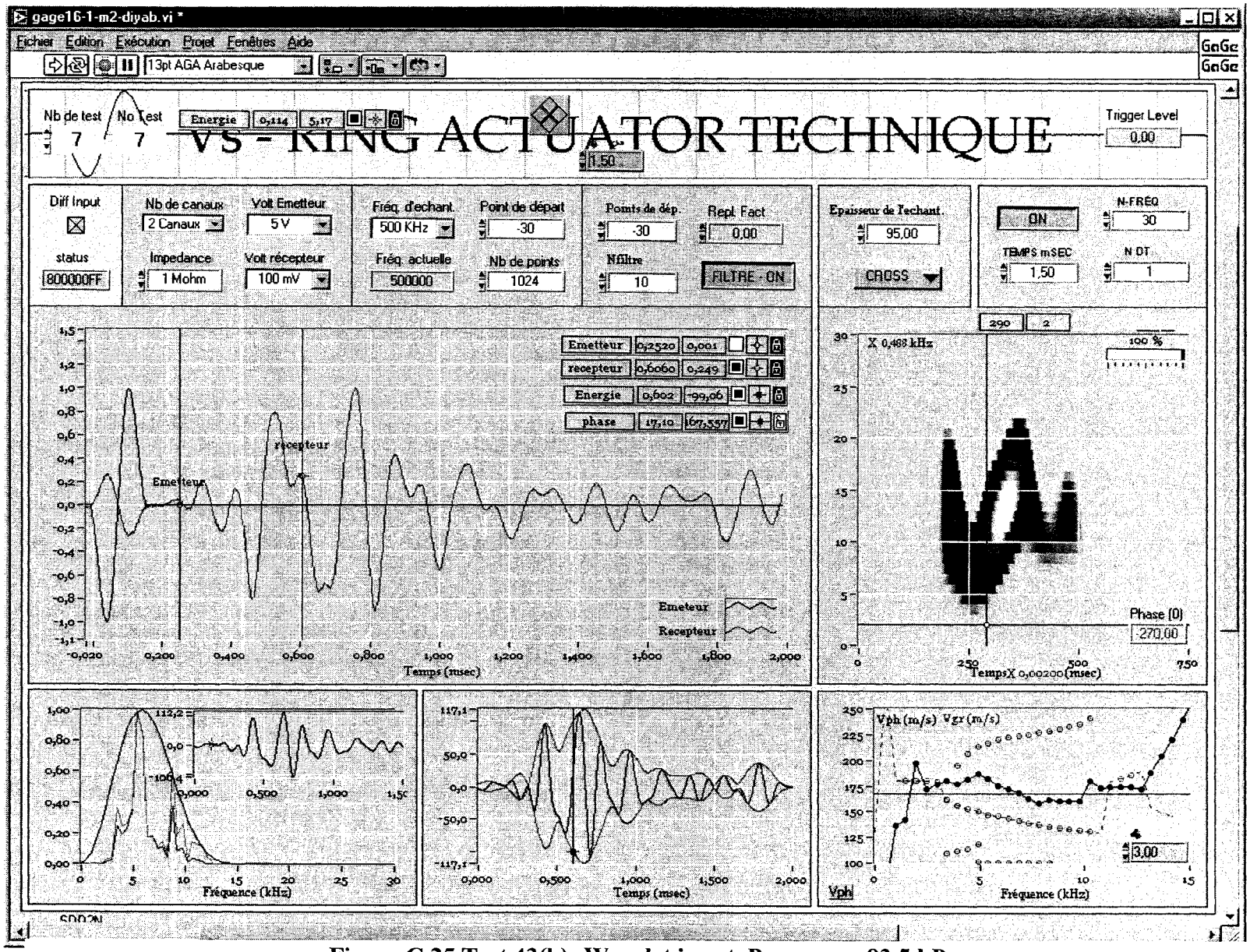

Figure C.25 Test 43(b); Wavelet input, Pressure = 83.5 kPa.

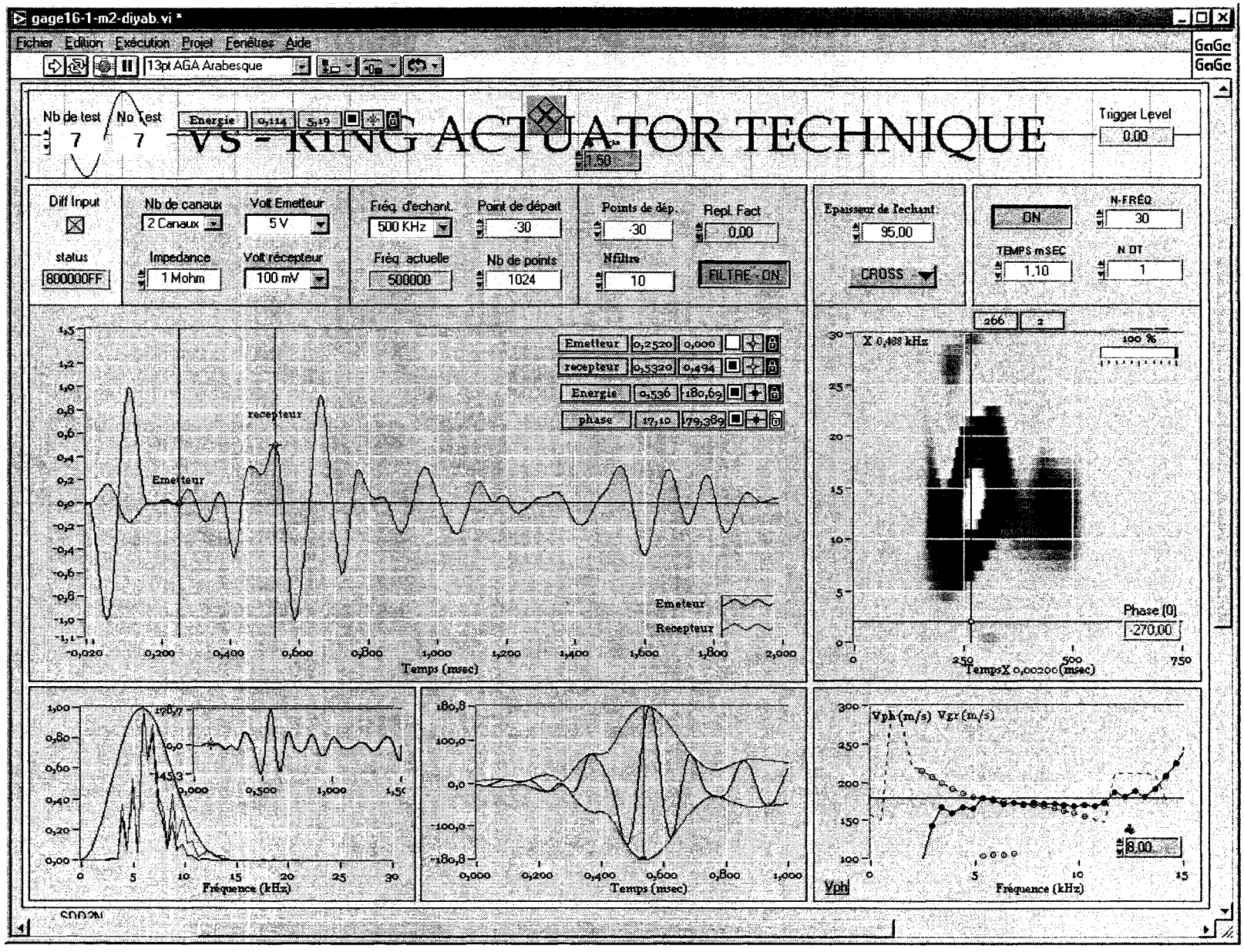

Figure C.26 Test 43(c); Versed-sine input, Pressure = 138.5 kPa.

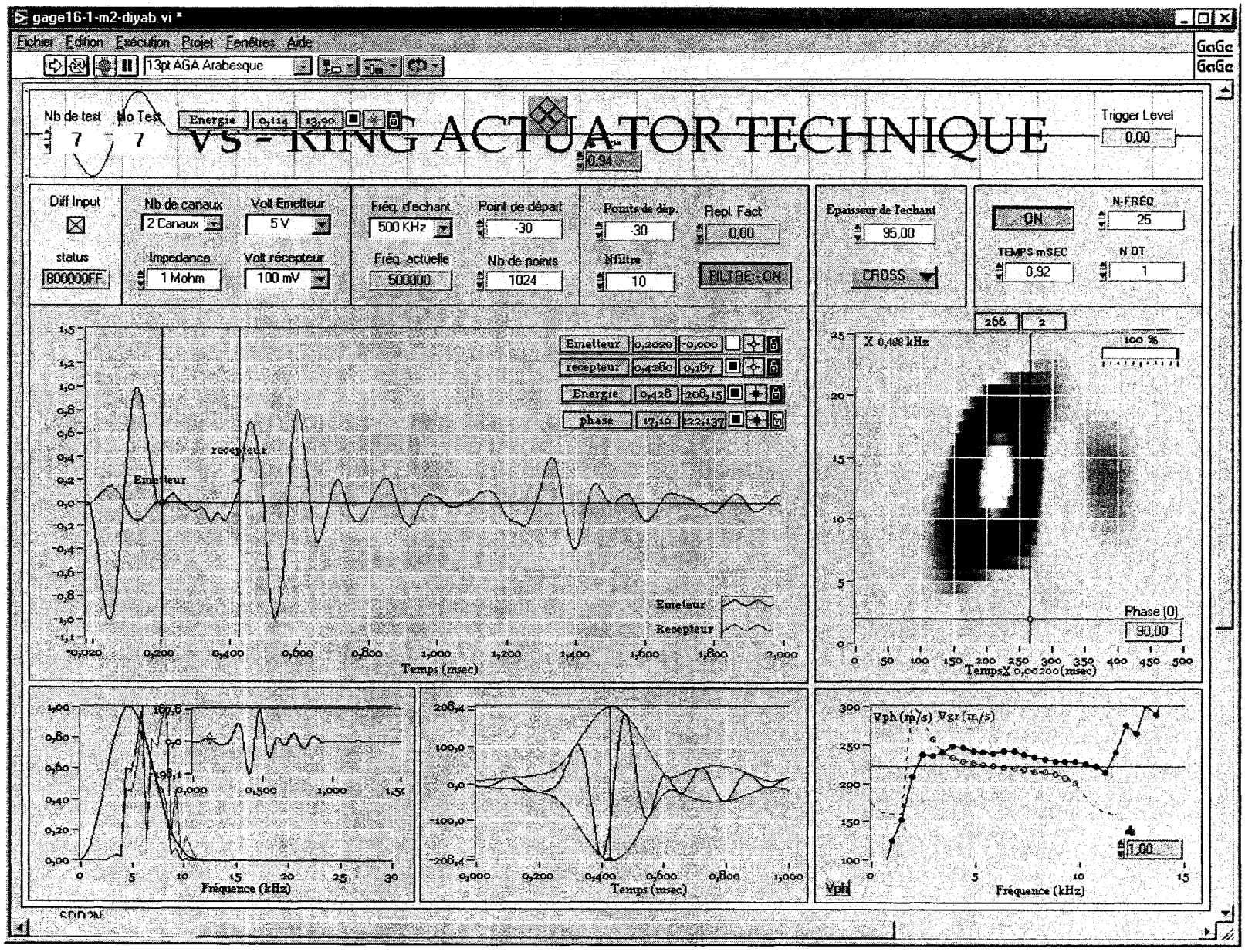

Figure C.27 Test 43(d); Wavelet input, Pressure = 248.4 kPa.

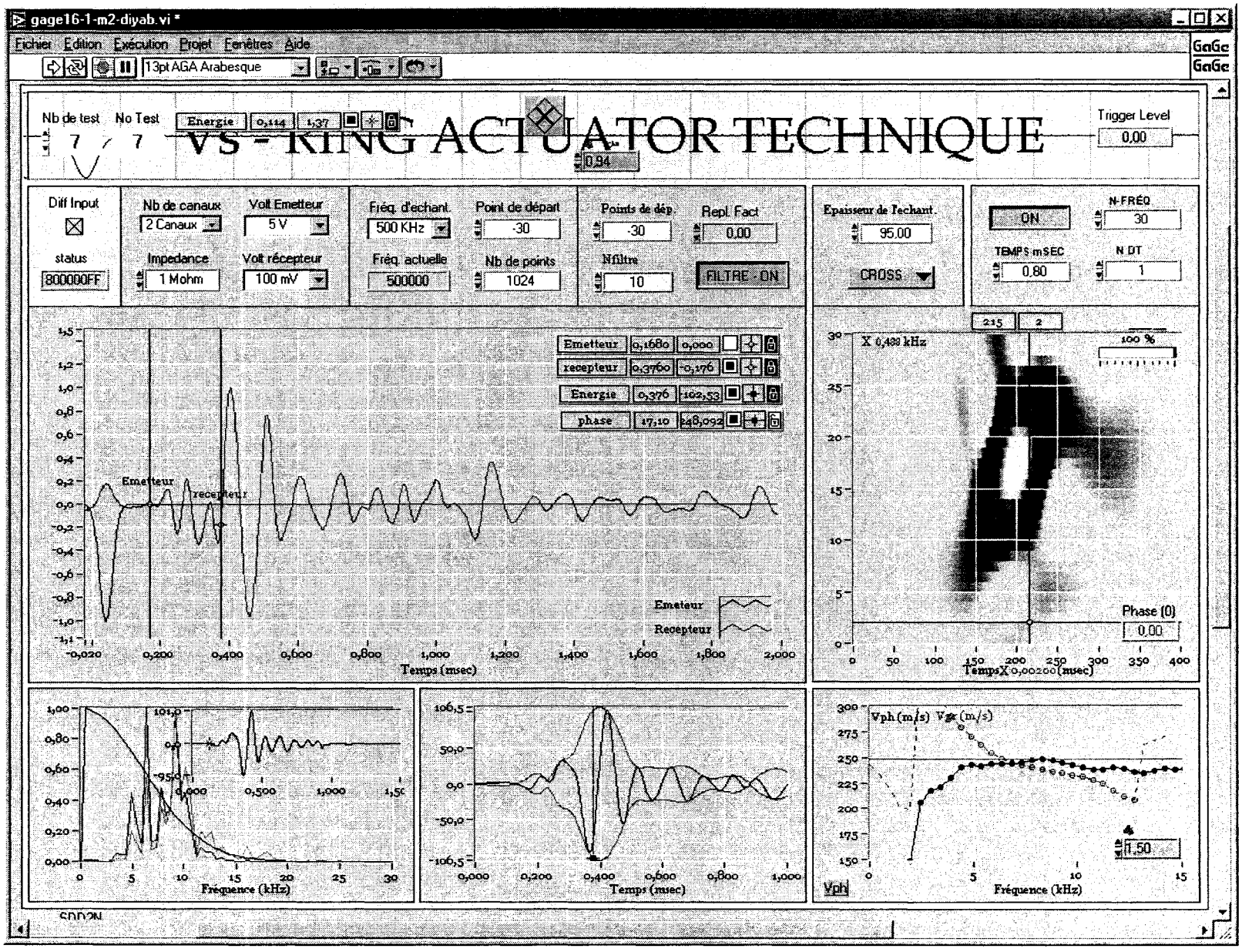

Figure C.28 Test 43(e); Versed sine input, Pressure = 413.3 kPa.

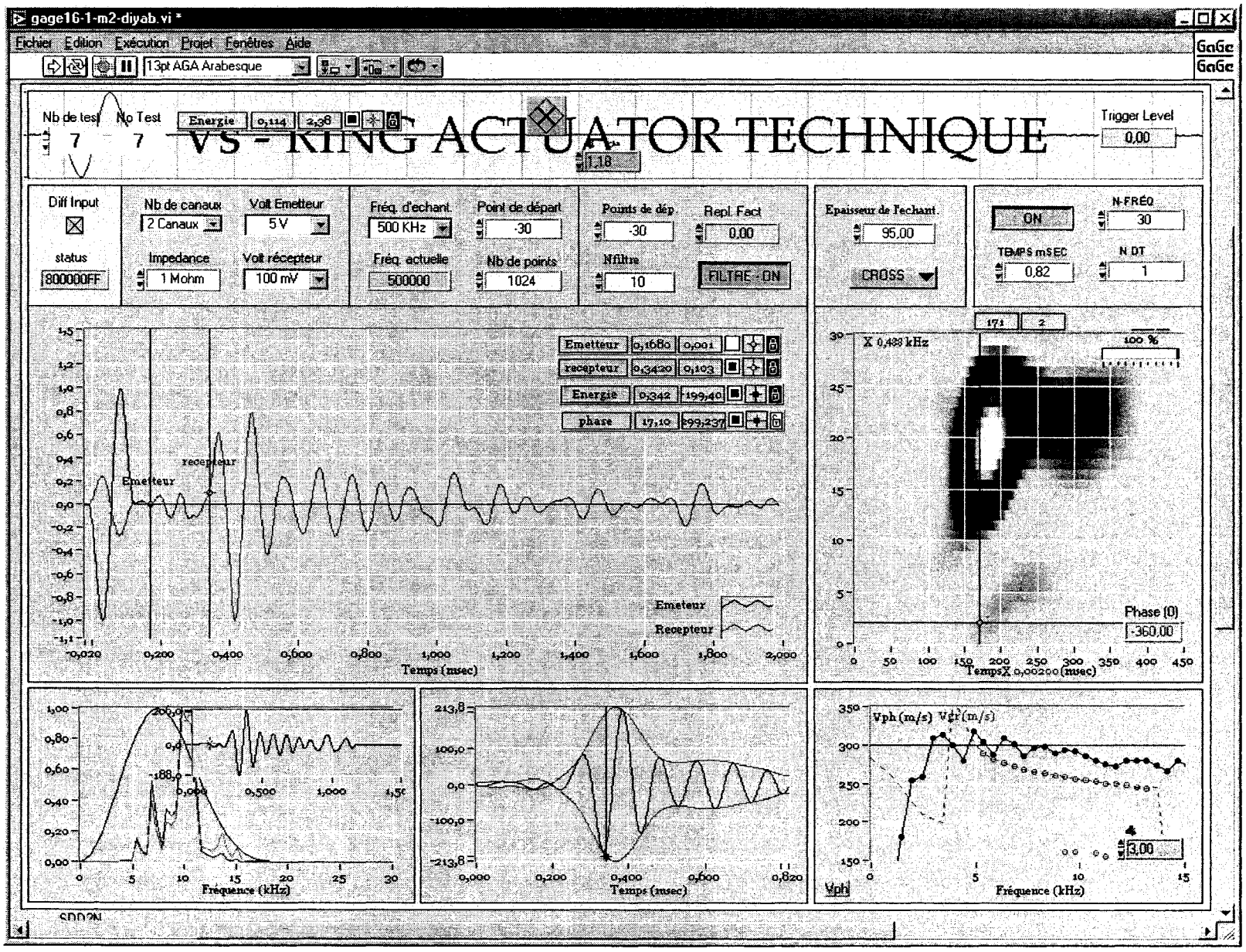

Figure C.29 Test 43(f); Versed sine input, Pressure = 578.1 kPa.

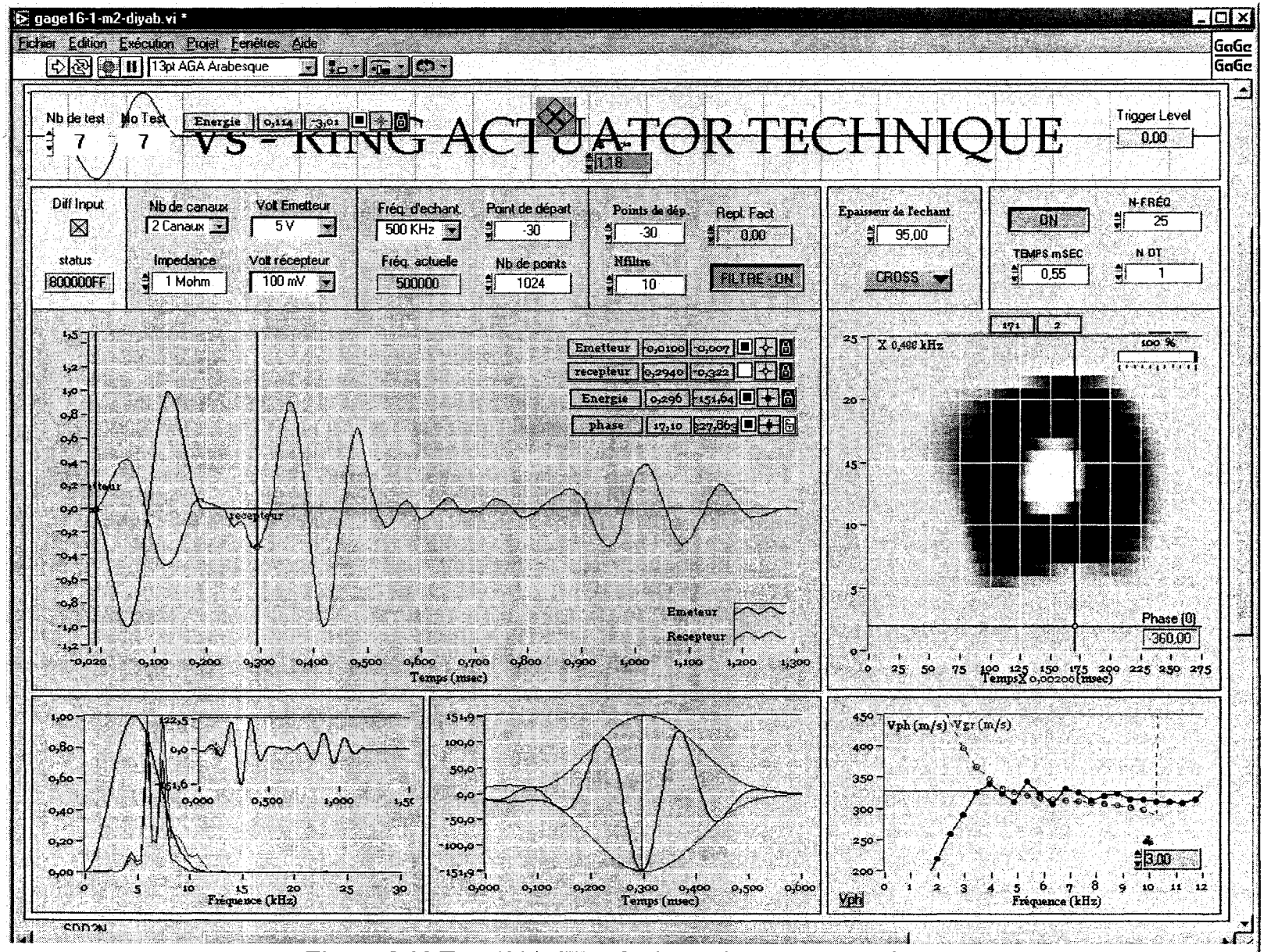

Figure C.30 Test 43(g); Wavelet input, Pressure = 797.9 kPa.

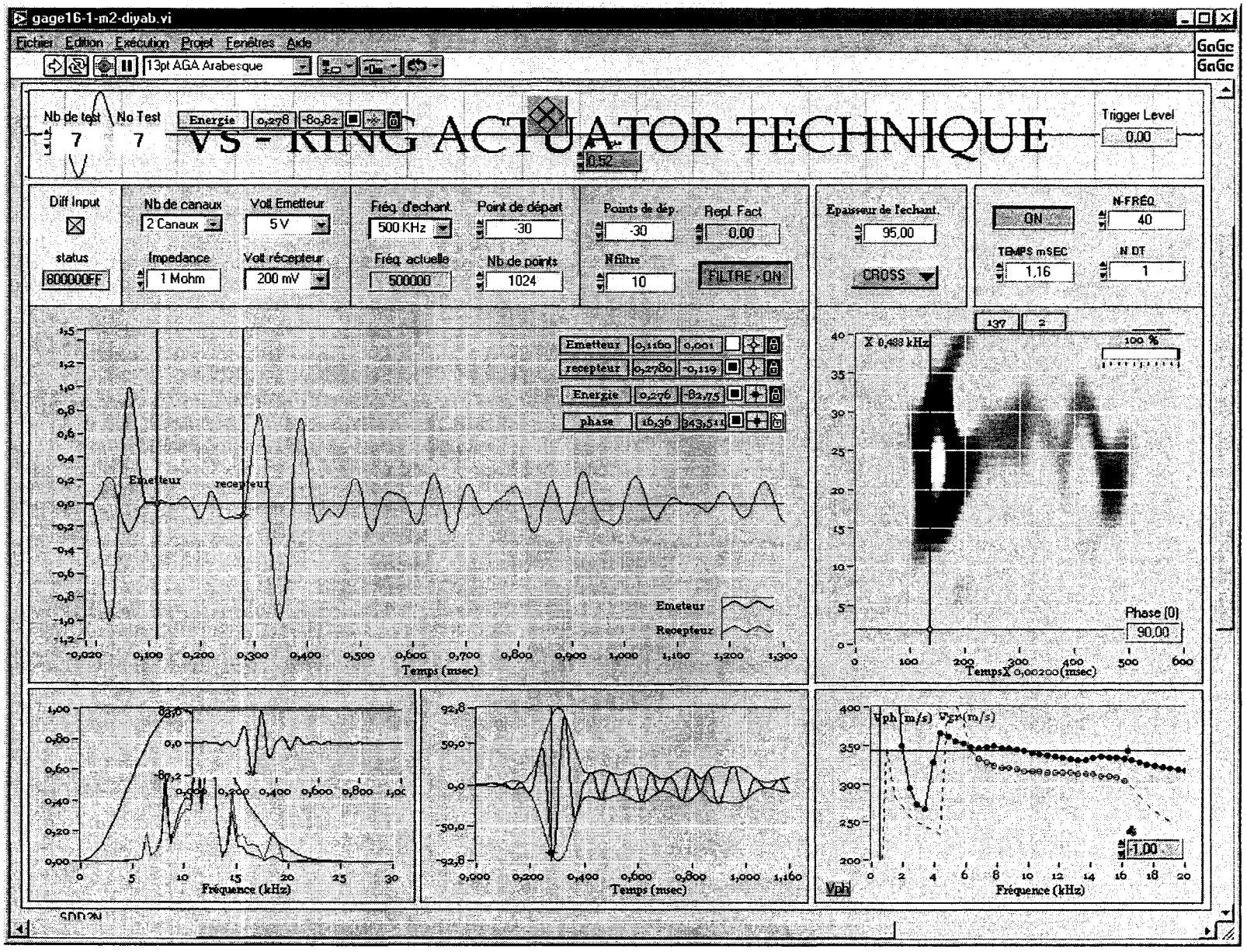

Figure C.31 Test 43(h); Versed sine input, Pressure = 1127.7 kPa.

Test 46

Pulse Tests on Dense Ottawa Sand (C-109) in the Medium Plexiglass Mold (Setup D)

Using the Ring Actuators Setup No. 8.

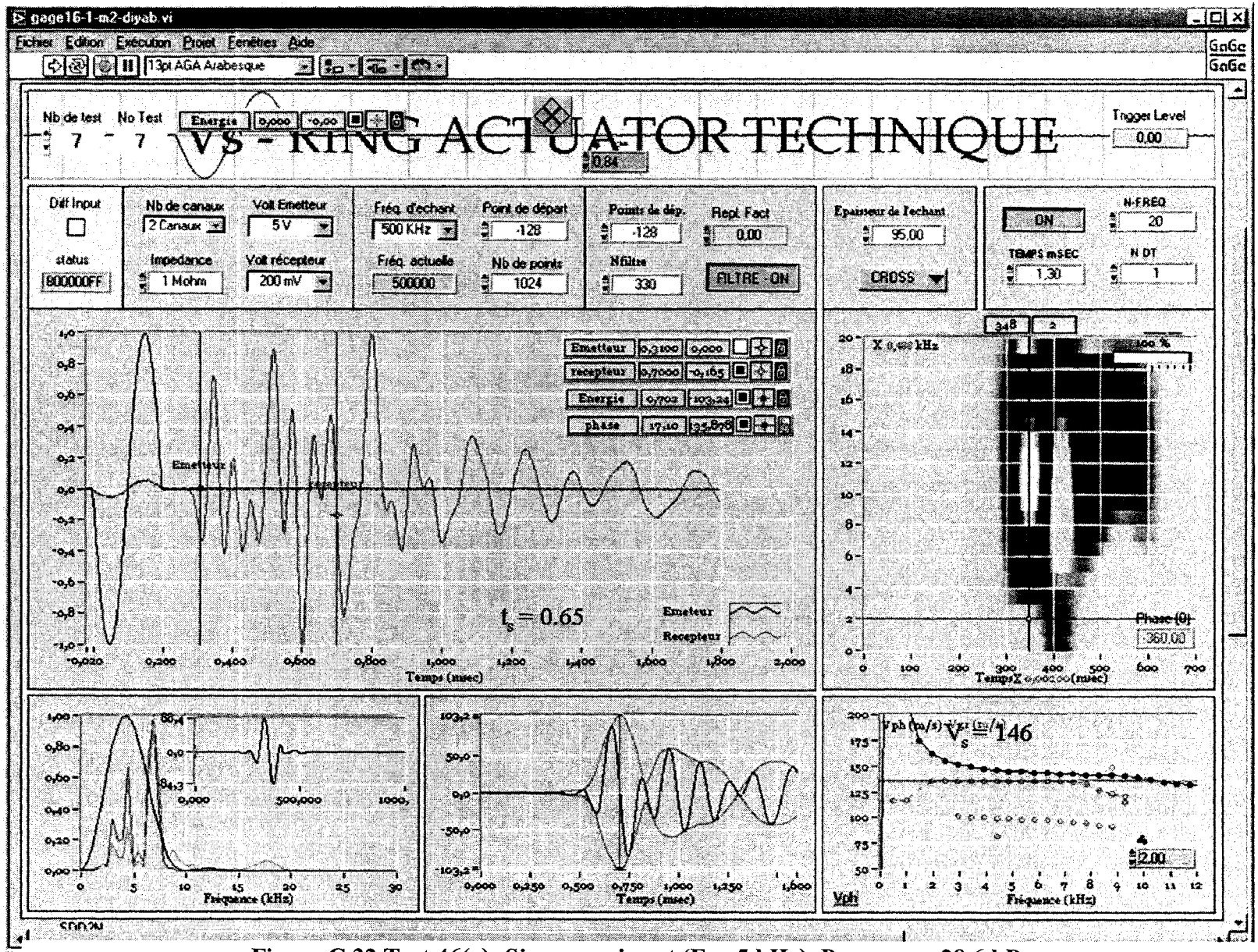

Figure C.32 Test 46(a); Sine wave input (Fr= 5 kHz), Pressure = 28.6 kPa.

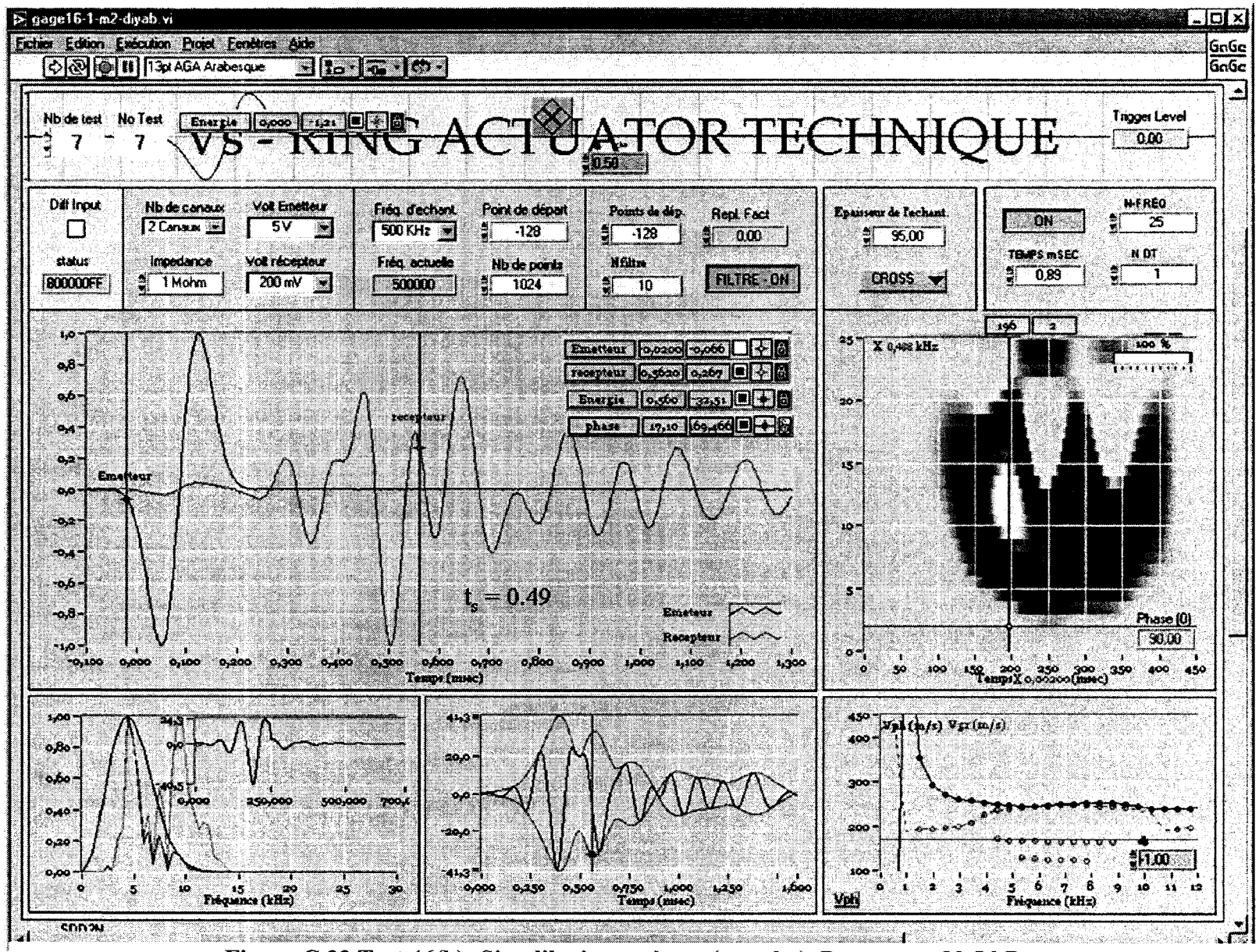

Figure C.33 Test 46(b); Sine-like input shape (wavelet), Pressure = 83.5 kPa.

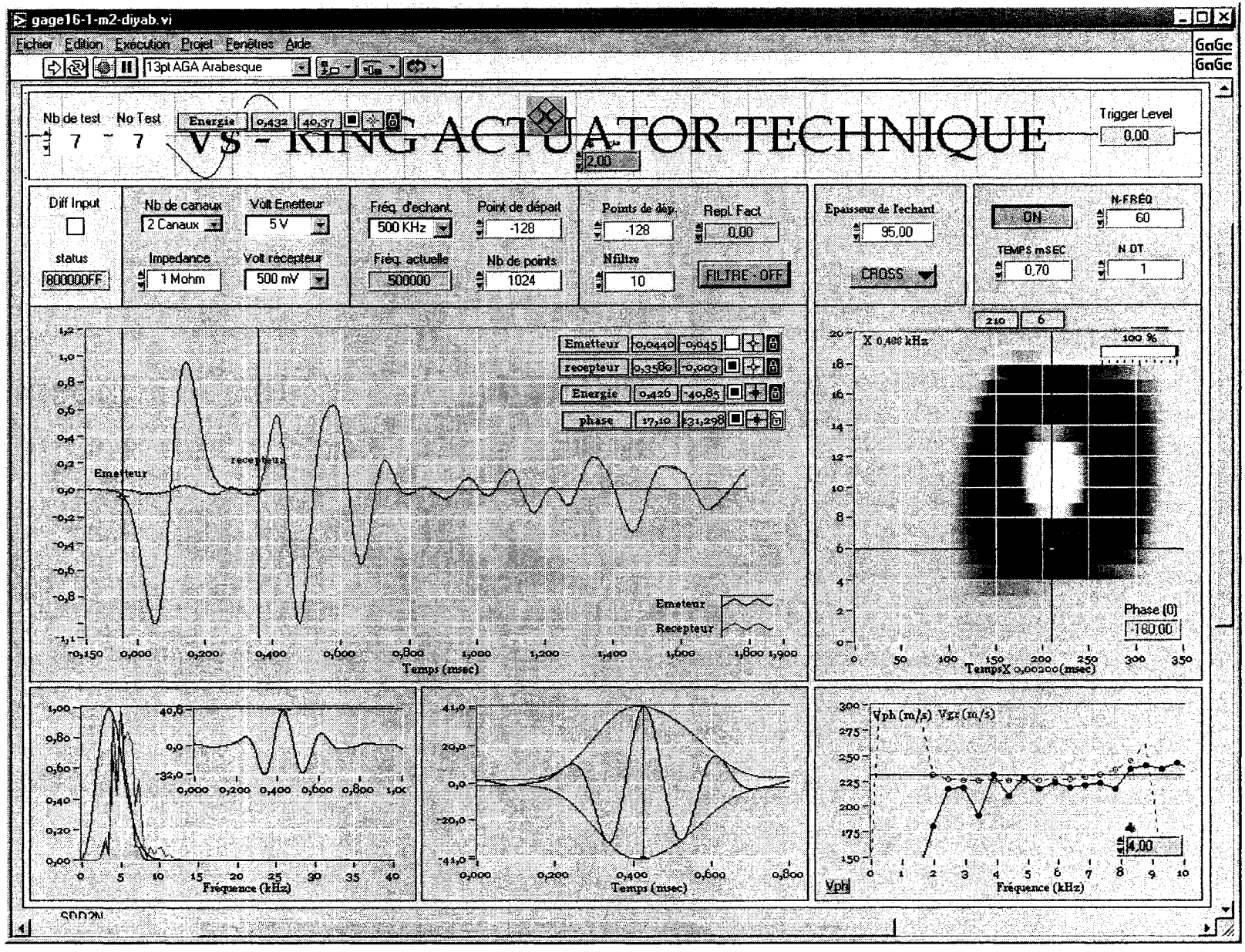

Figure C.34 Test 46(c); Versed sine input, Pressure = 138.5 kPa.

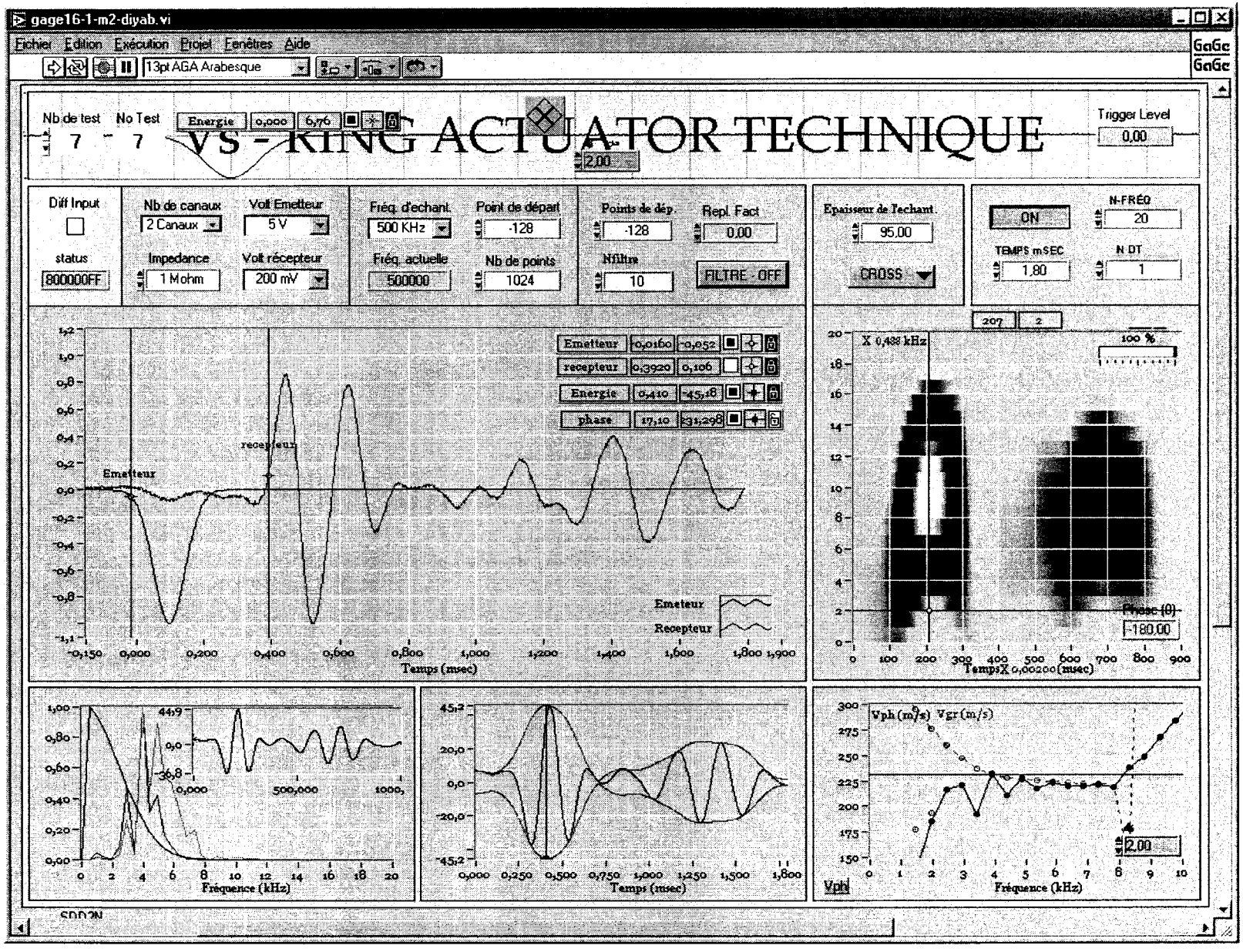

Figure C.35 Test 46(c-1); Versed half-sine input, Pressure = 138.5 kPa.

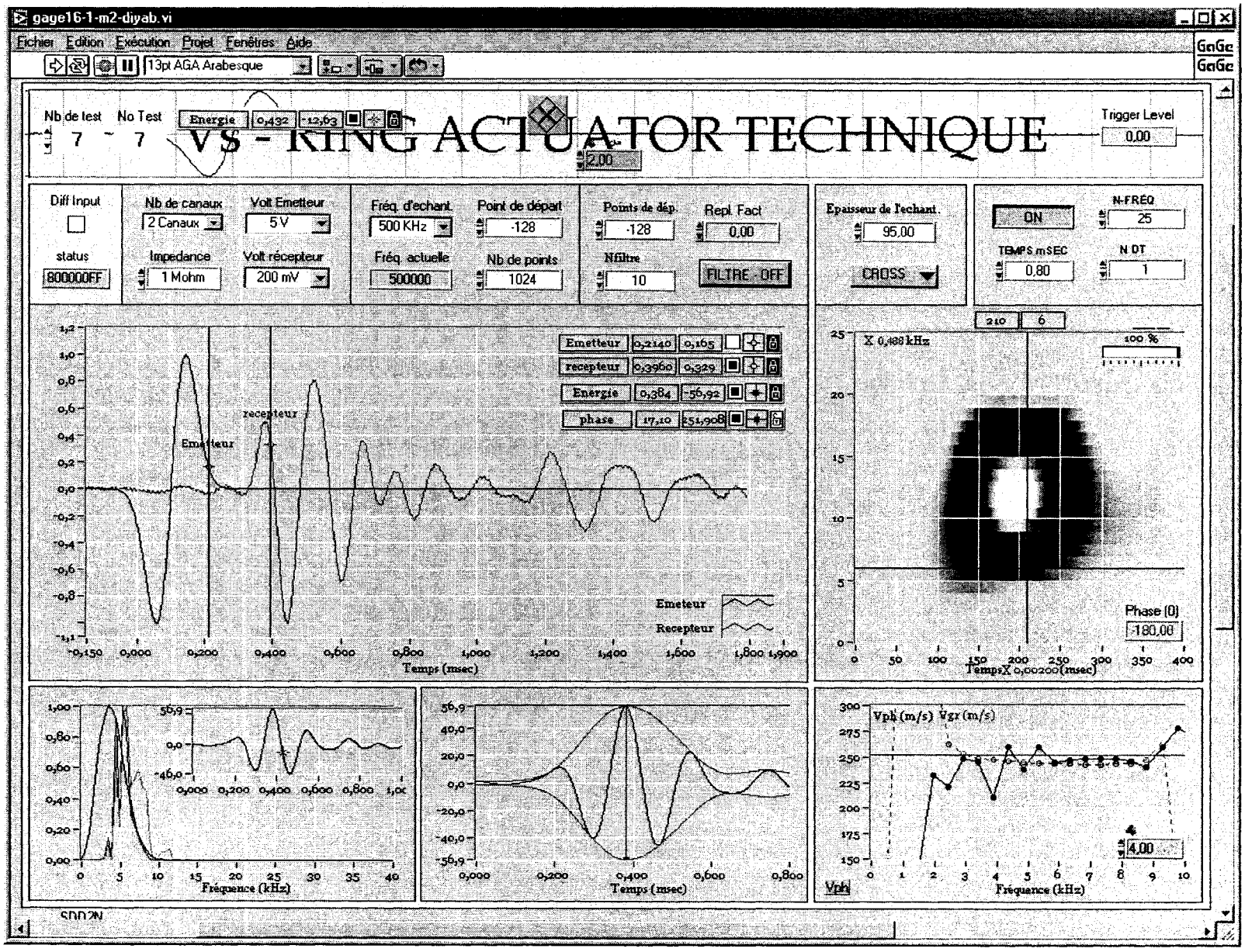

Figure C.36 Test 46(d); Versed sine input, Pressure = 248.4 kPa.

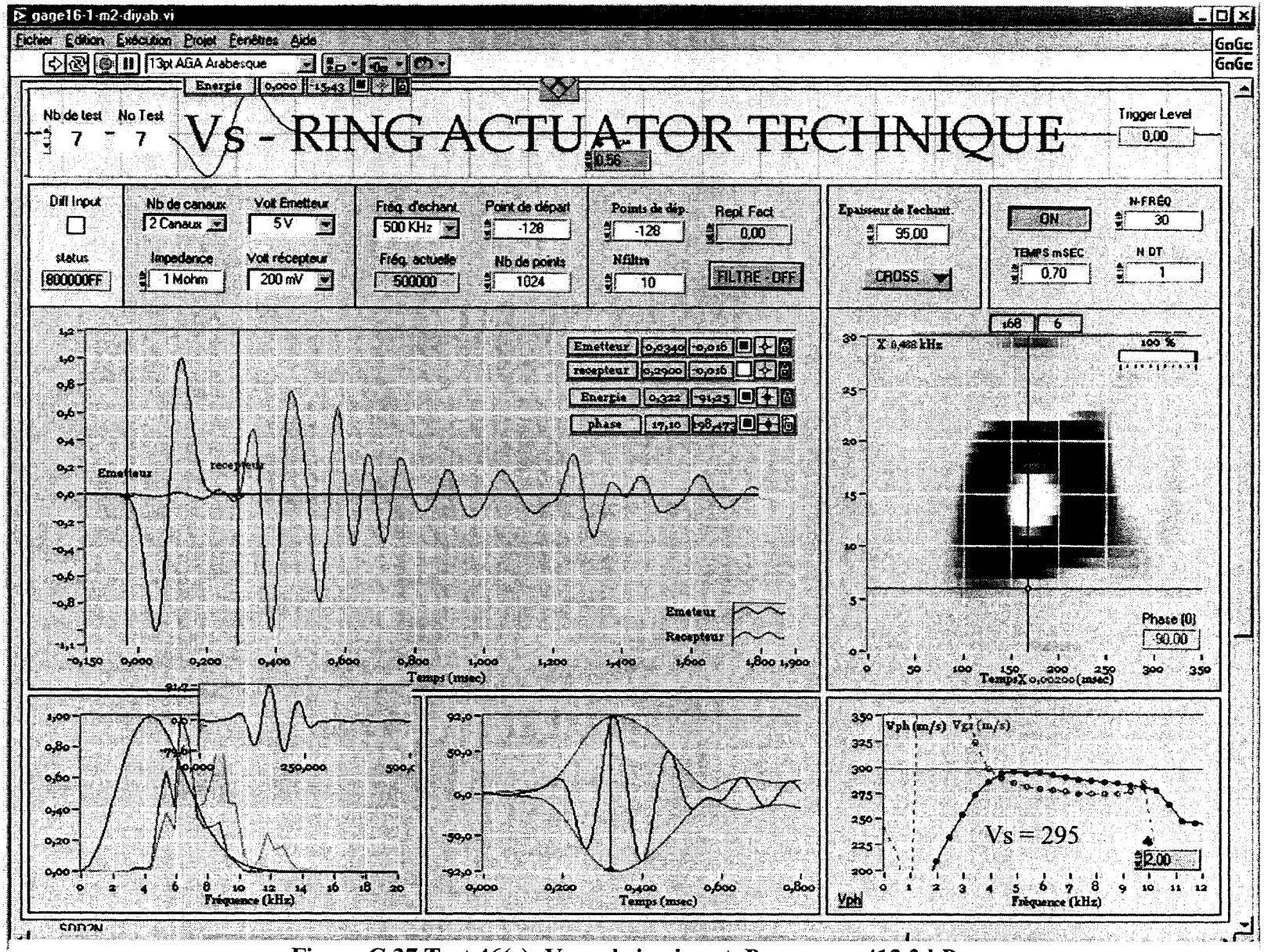

Figure C.37 Test 46(e); Versed sine input, Pressure = 413.3 kPa.

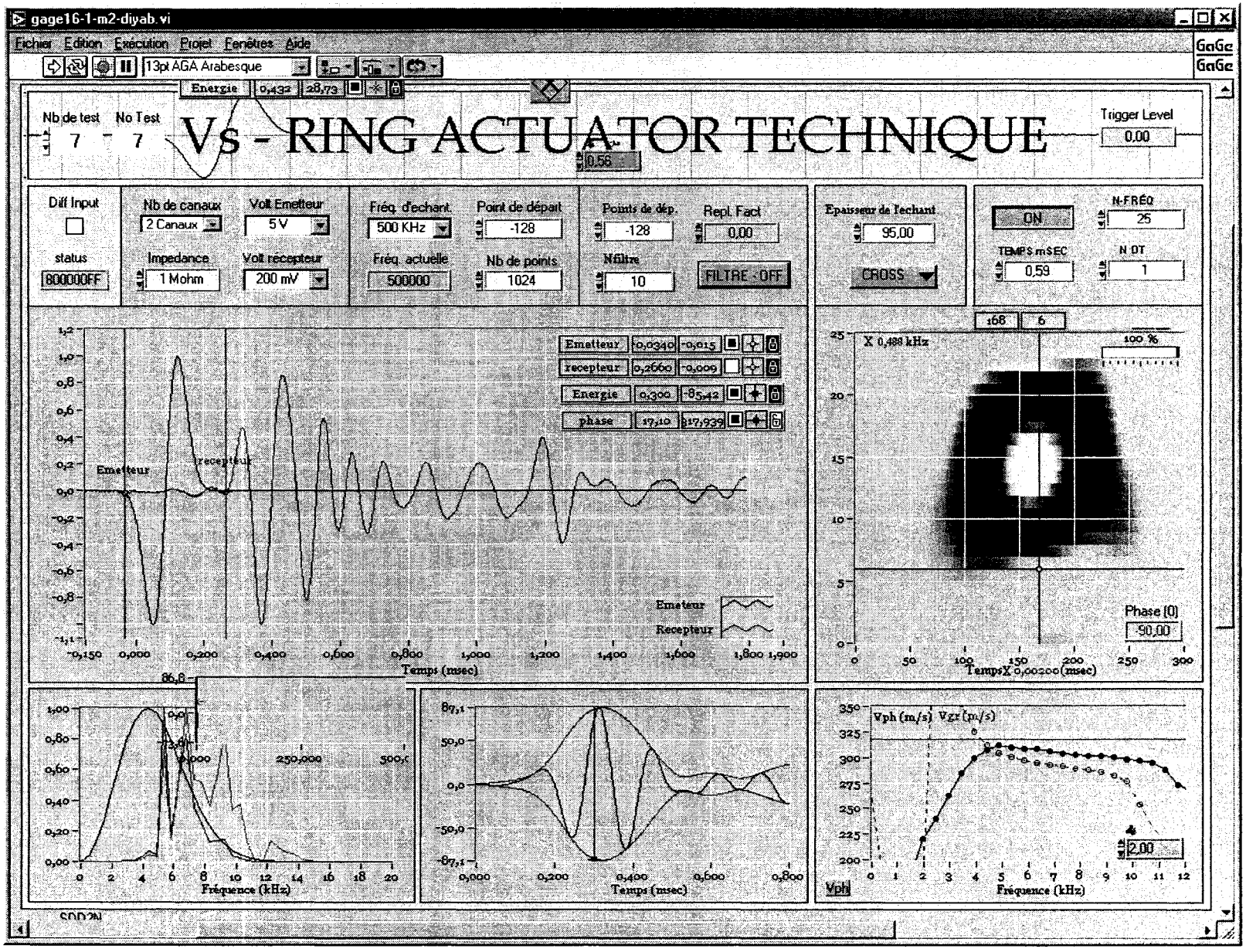

Figure C.38 Test 46(f); Versed sine input, Pressure = 578.1 kPa.

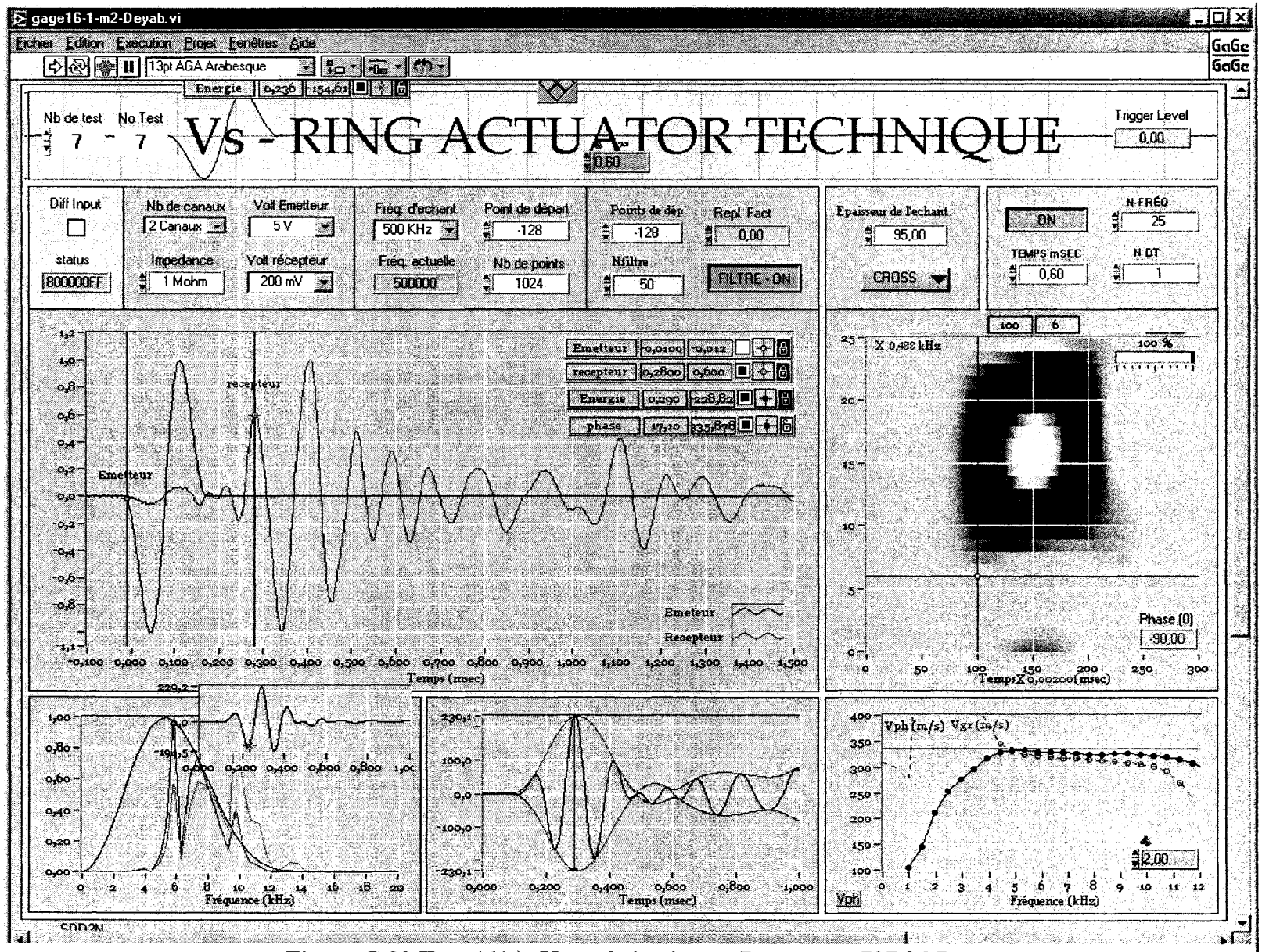

Figure C.39 Test 46(g); Versed sine input, Pressure = 797.9 kPa.

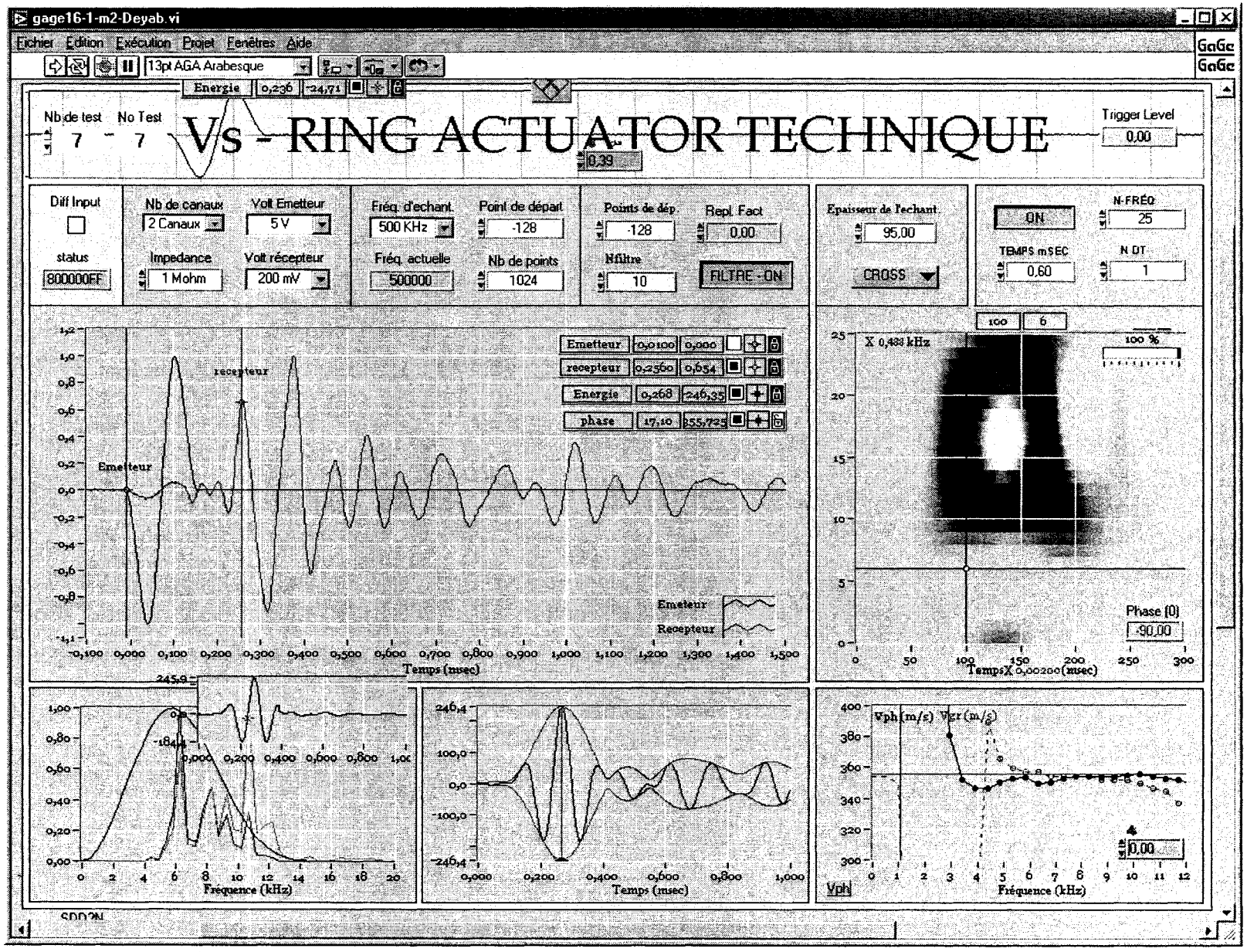

Figure C.40 Test 46(h); Sine-like input shape (wavelet), Pressure = 1127.7 kPa.

Test 47

Pulse Tests on Loose Ottawa Sand (C-109) in the Large Oedometer Ring (Setup A) Using the Ring Actuators Setup No. 7.

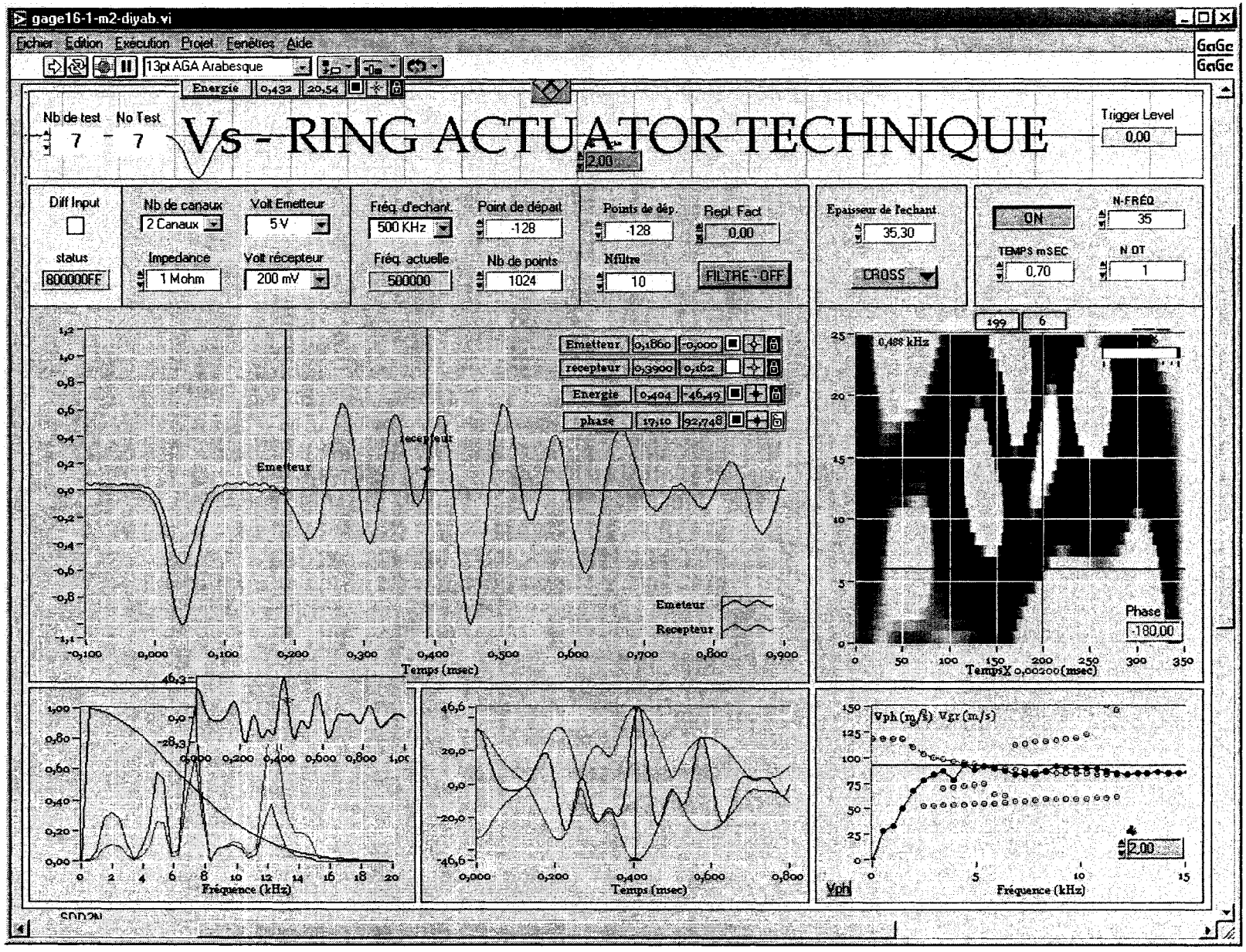

Figure C.41 Test 47(a); Versed half-sine input, Pressure = 6.1 kPa.

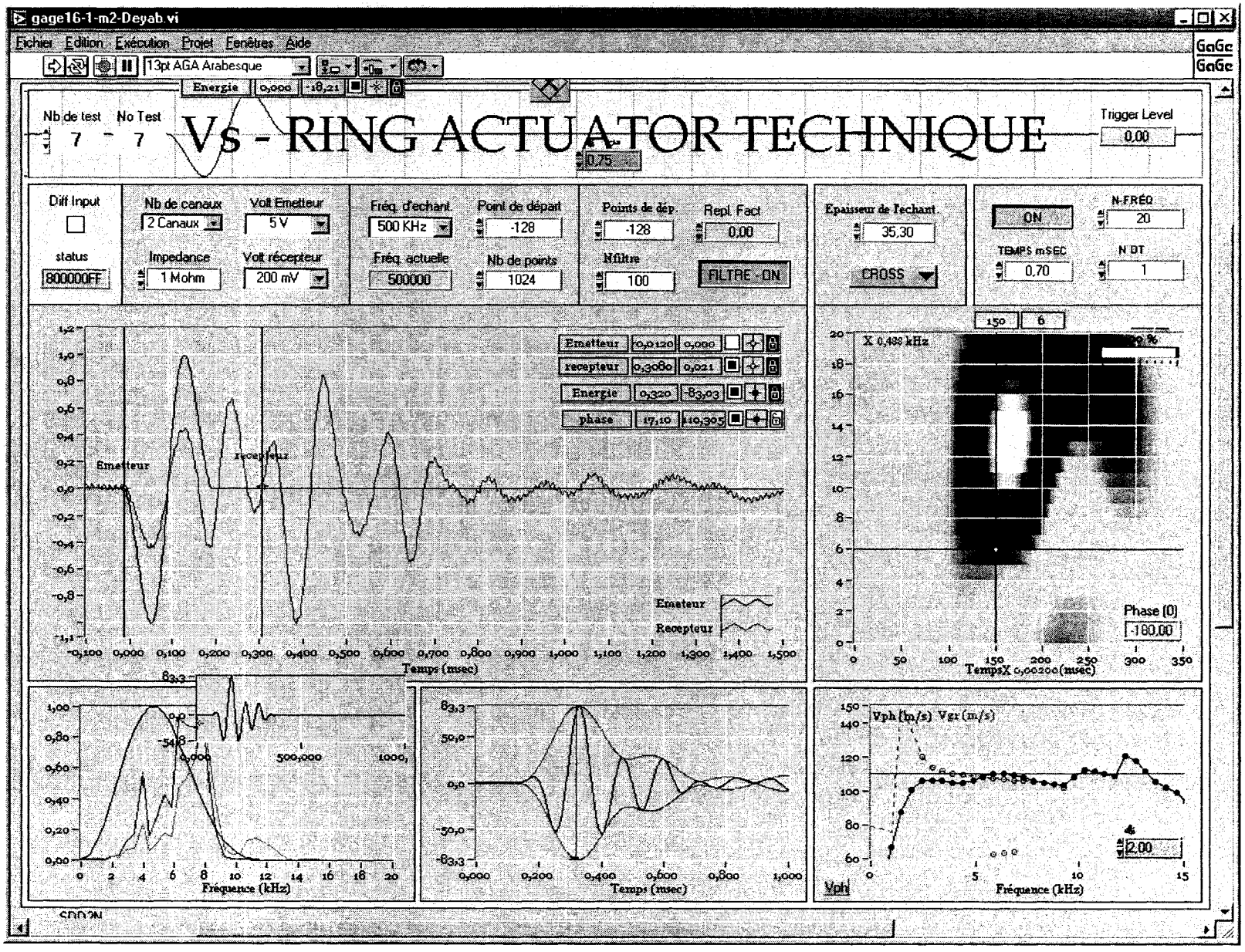

Figure C.42 Test 47(b); Sine-like input shape (wavelet), Pressure = 11.6 kPa.

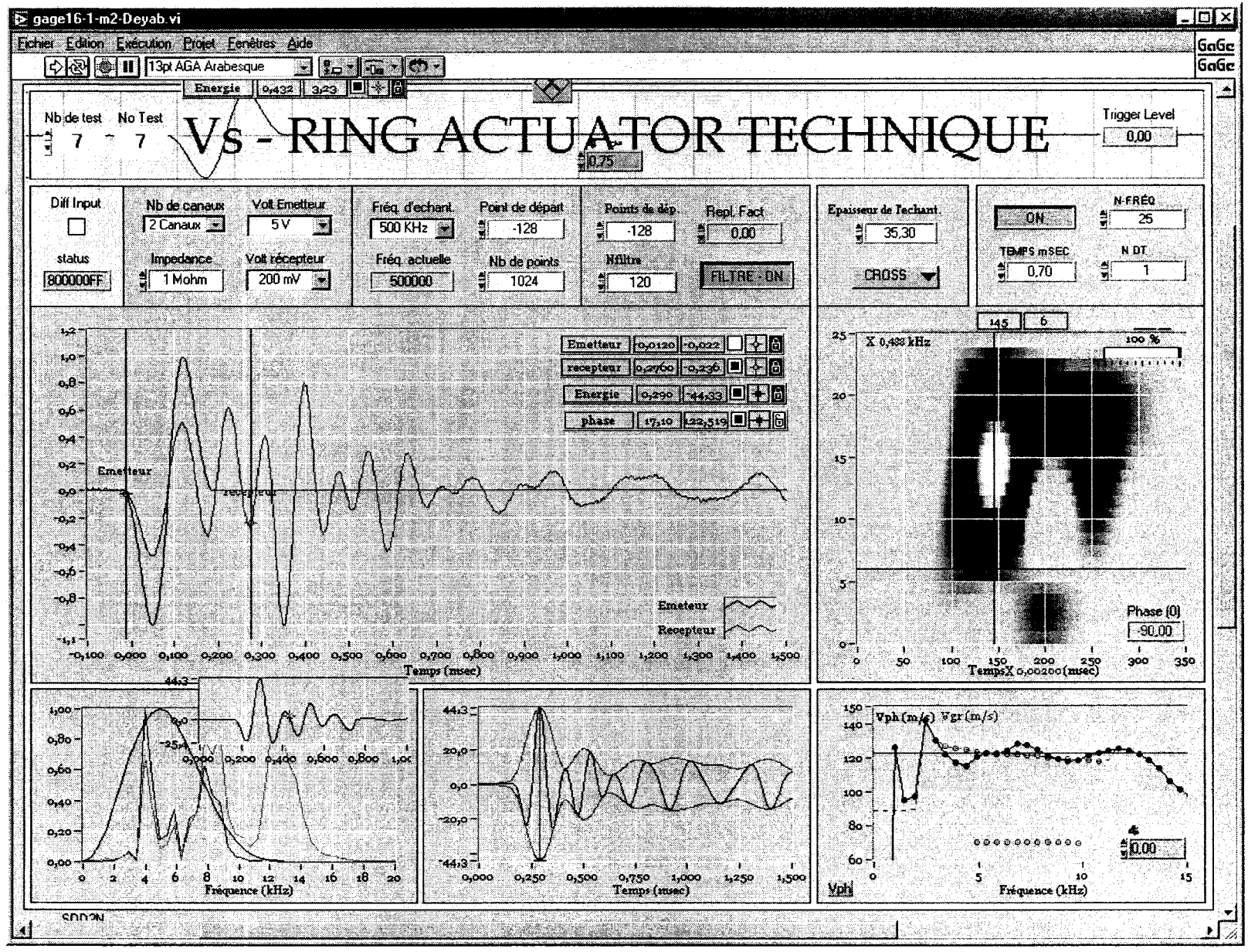

Figure C.43 Test 47(c); Sine-like input shape (wavelet), Pressure = 17.1 kPa.

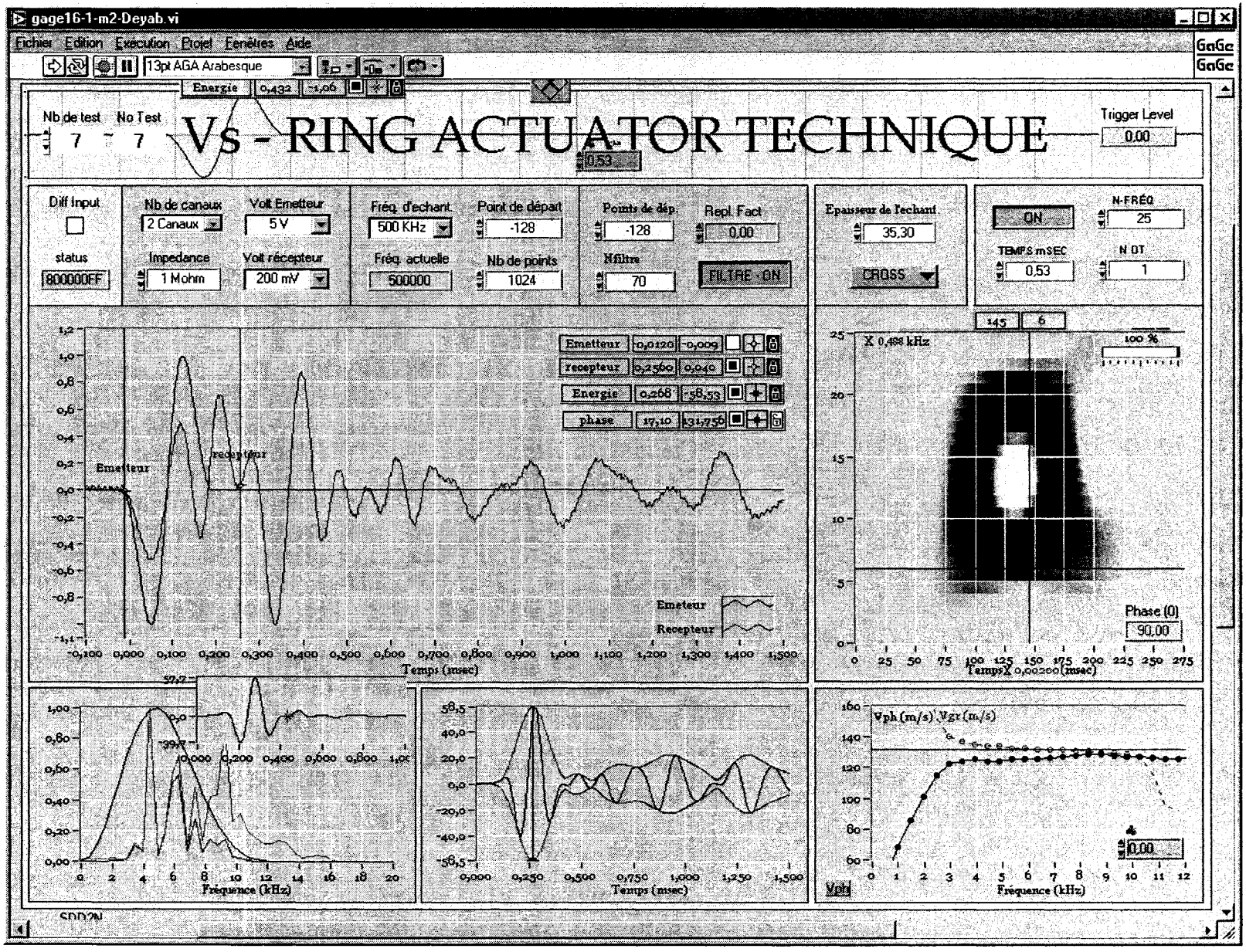

Figure C.44 Test 47(d); Sine-like input shape (wavelet), Pressure = 22.6 kPa.

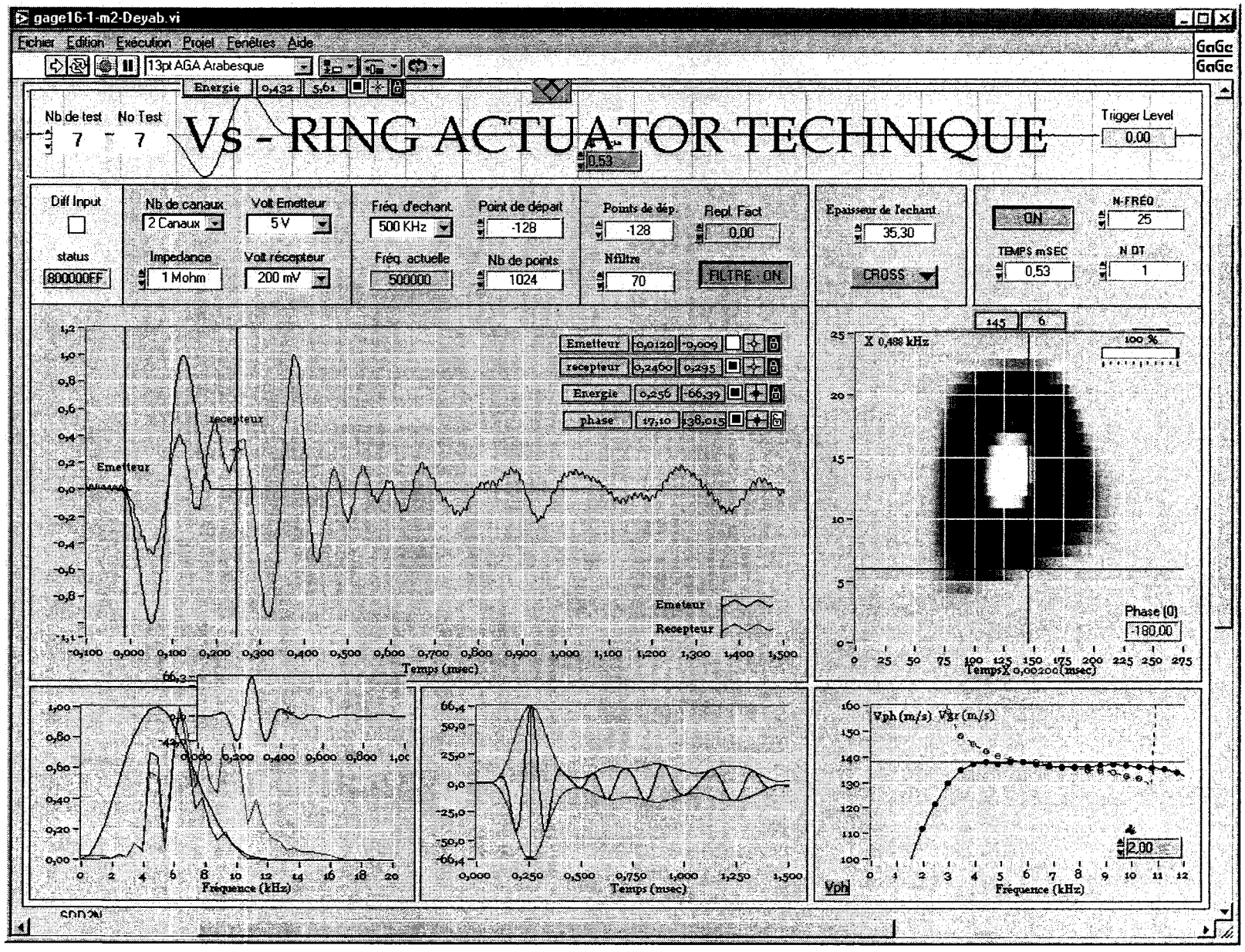

Figure C.45 Test 47(e); Sine-like input shape (wavelet), Pressure = 28.1 kPa.

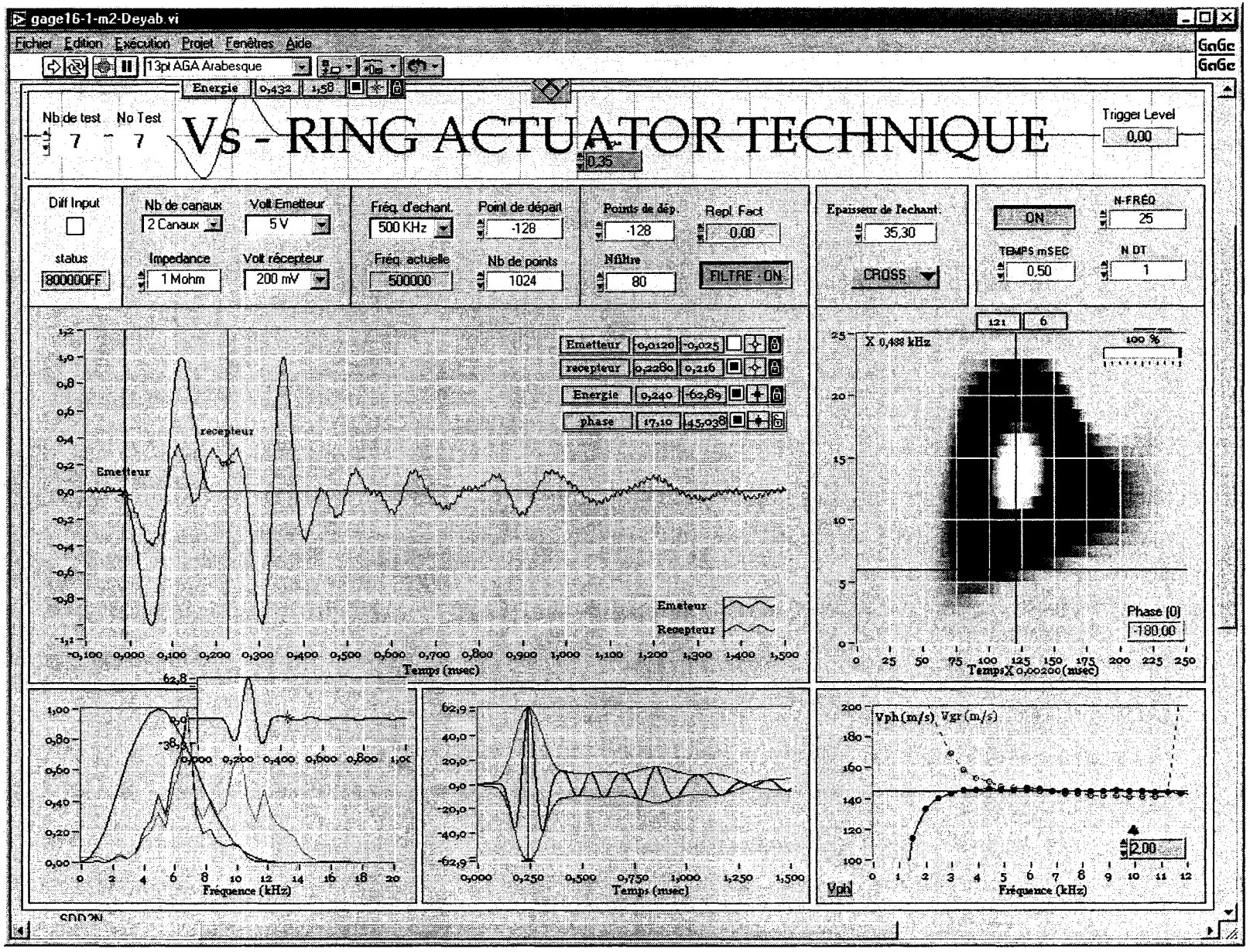

Figure C.46 Test 47(f); Sine-like input shape (wavelet), Pressure = 33.6 kPa.

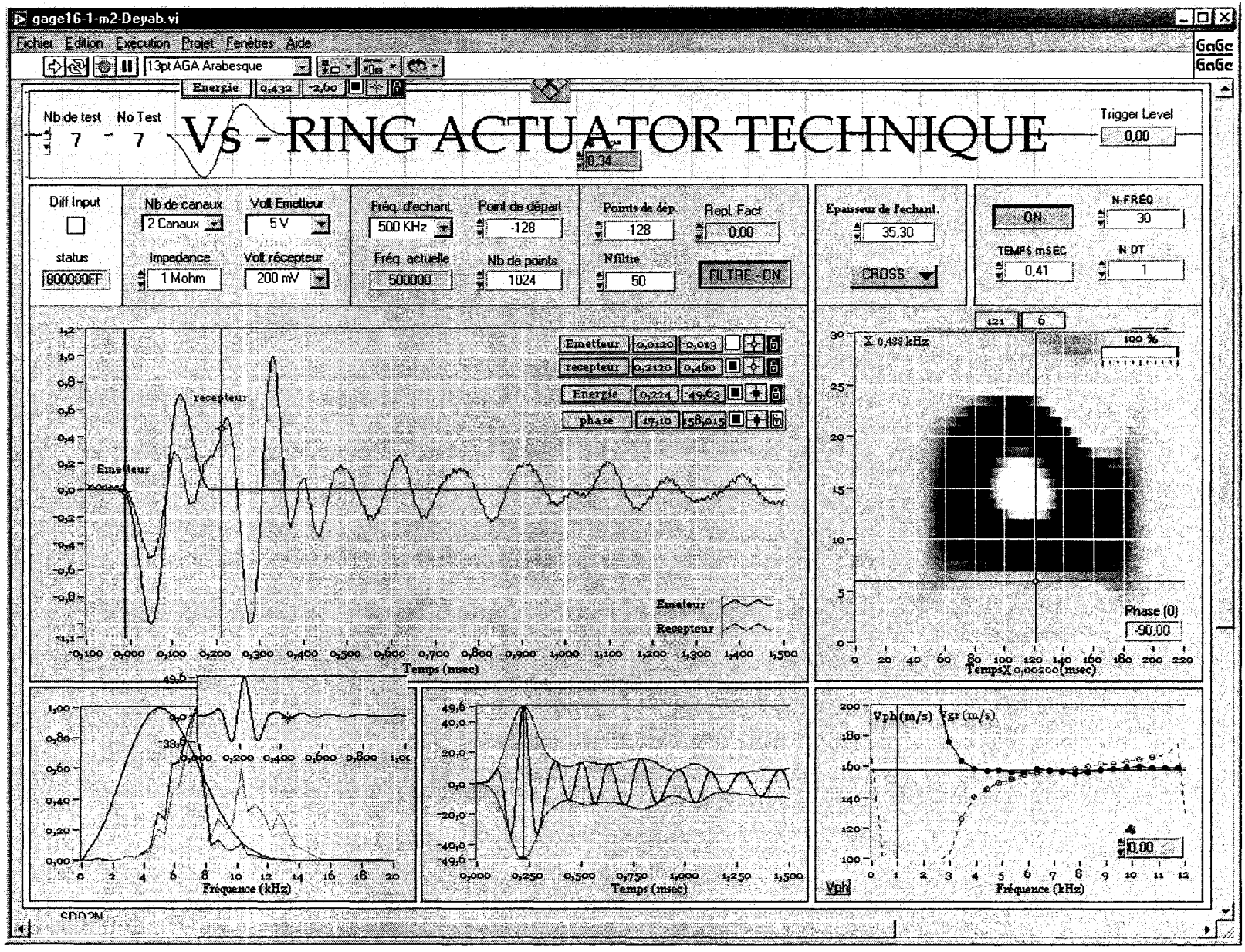

Figure C.47 Test 47(g); Sine-like input shape (wavelet), Pressure = 44.6 kPa.

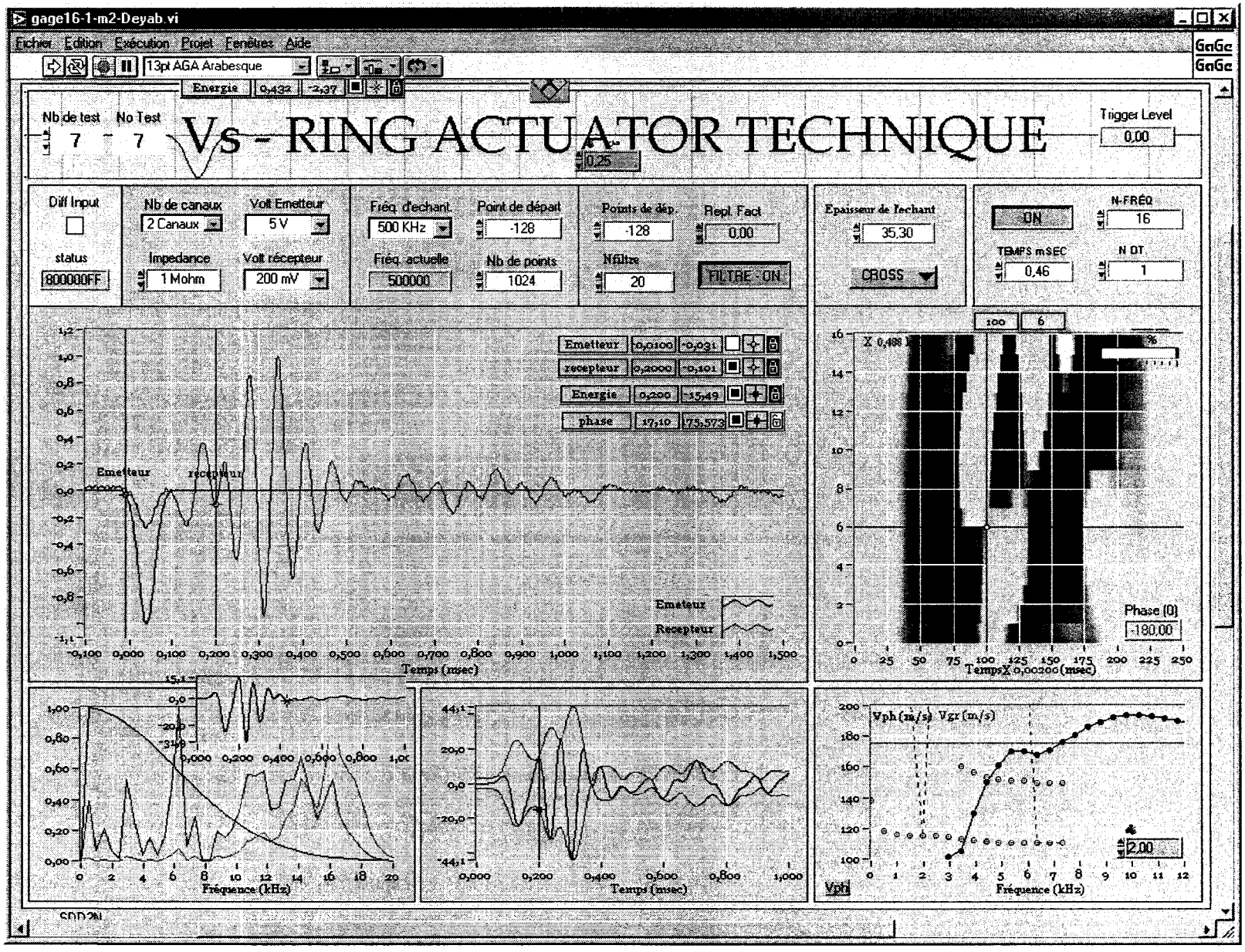

Figure C.48 Test 47(h); Versed half-sine input, Pressure = 61.1 kPa.

Test 49

Pulse Tests on Partially Saturated LG4 Till in Proctor Mold (Setup B)

Using the Ring Actuators Setup No. 8.

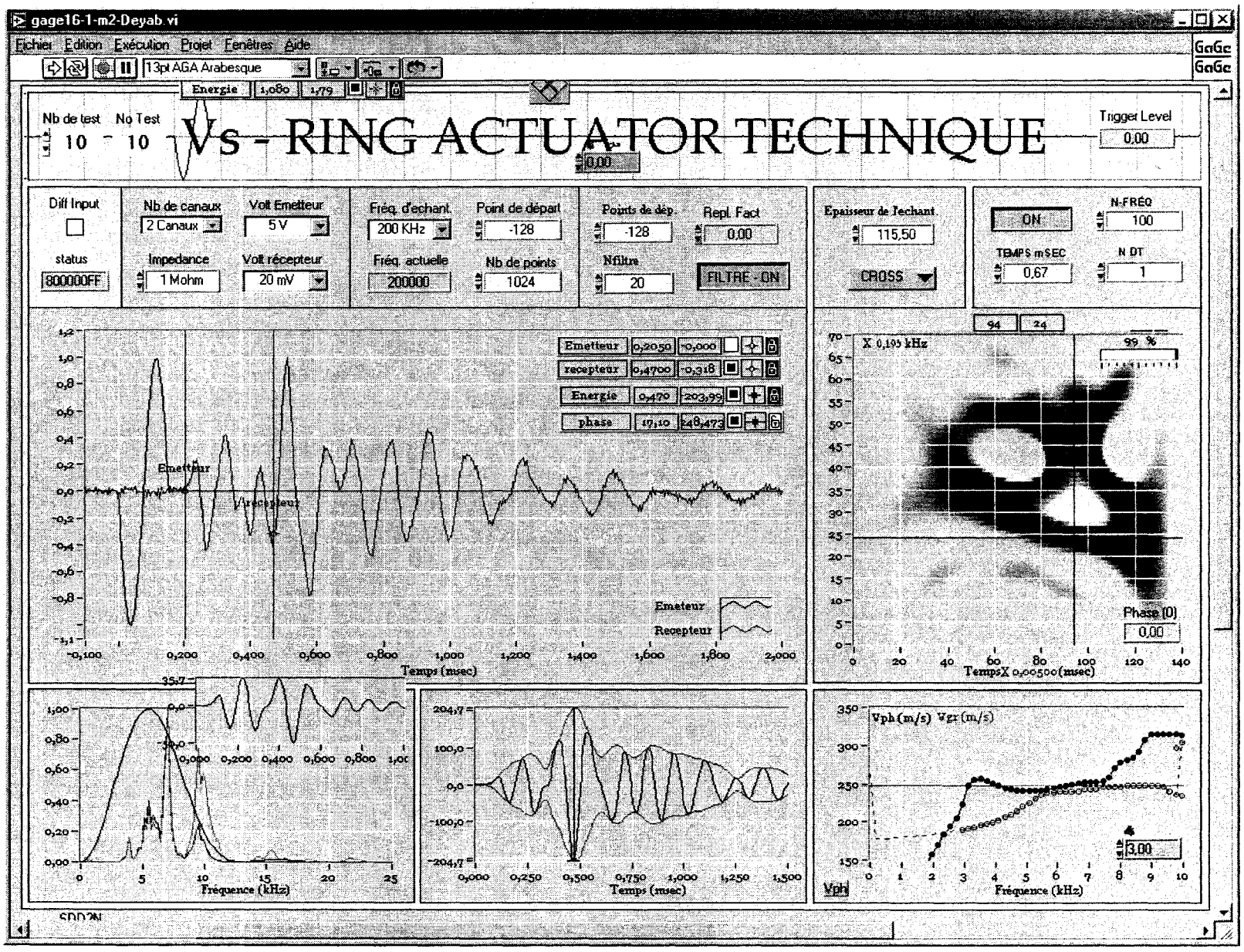

Figure C.49 Test 49(a); Sine input of 7 kHz, Pressure = 138.5 kPa.

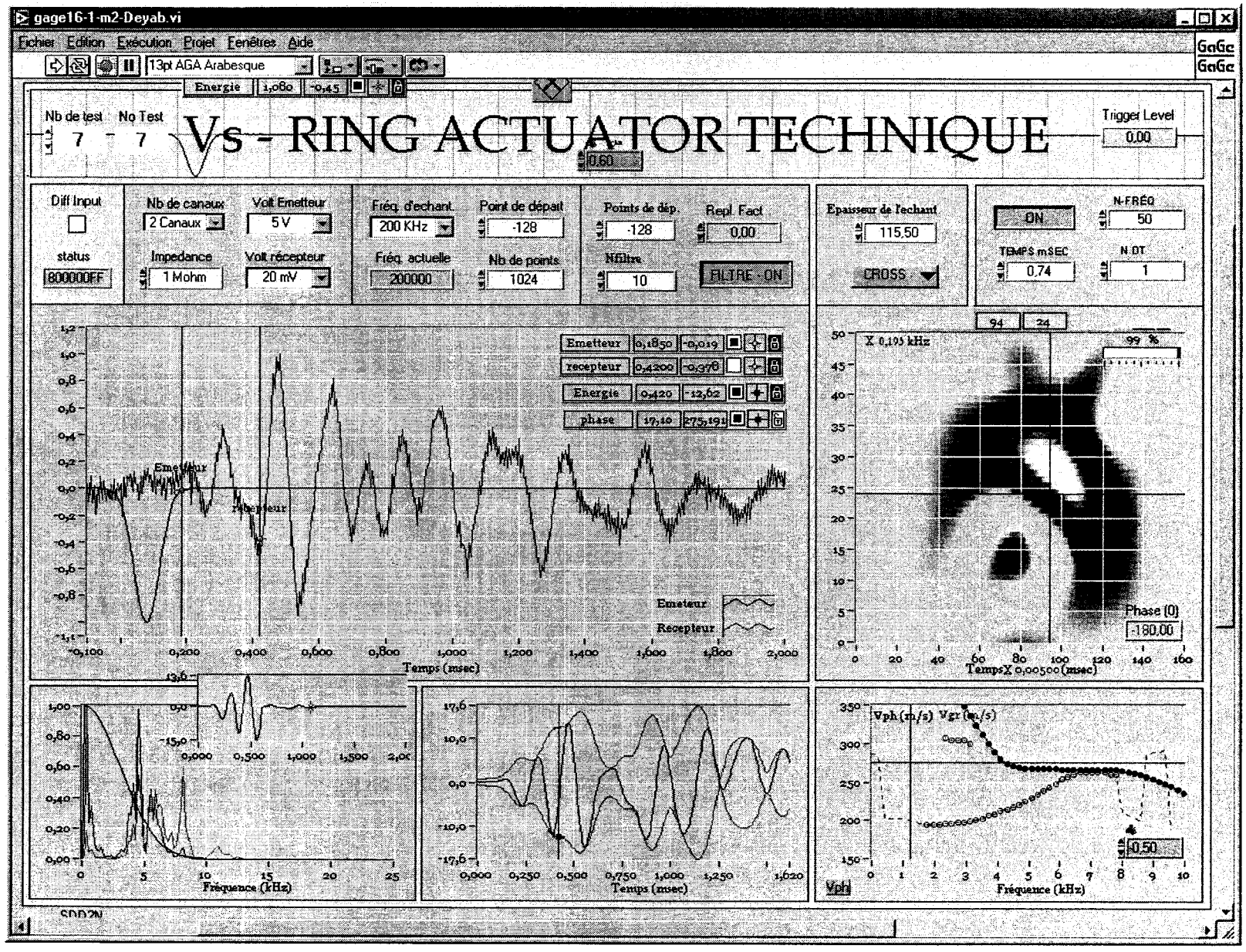

Figure C.50 Test 49(b); Versed sine input, Pressure = 248.4 kPa.

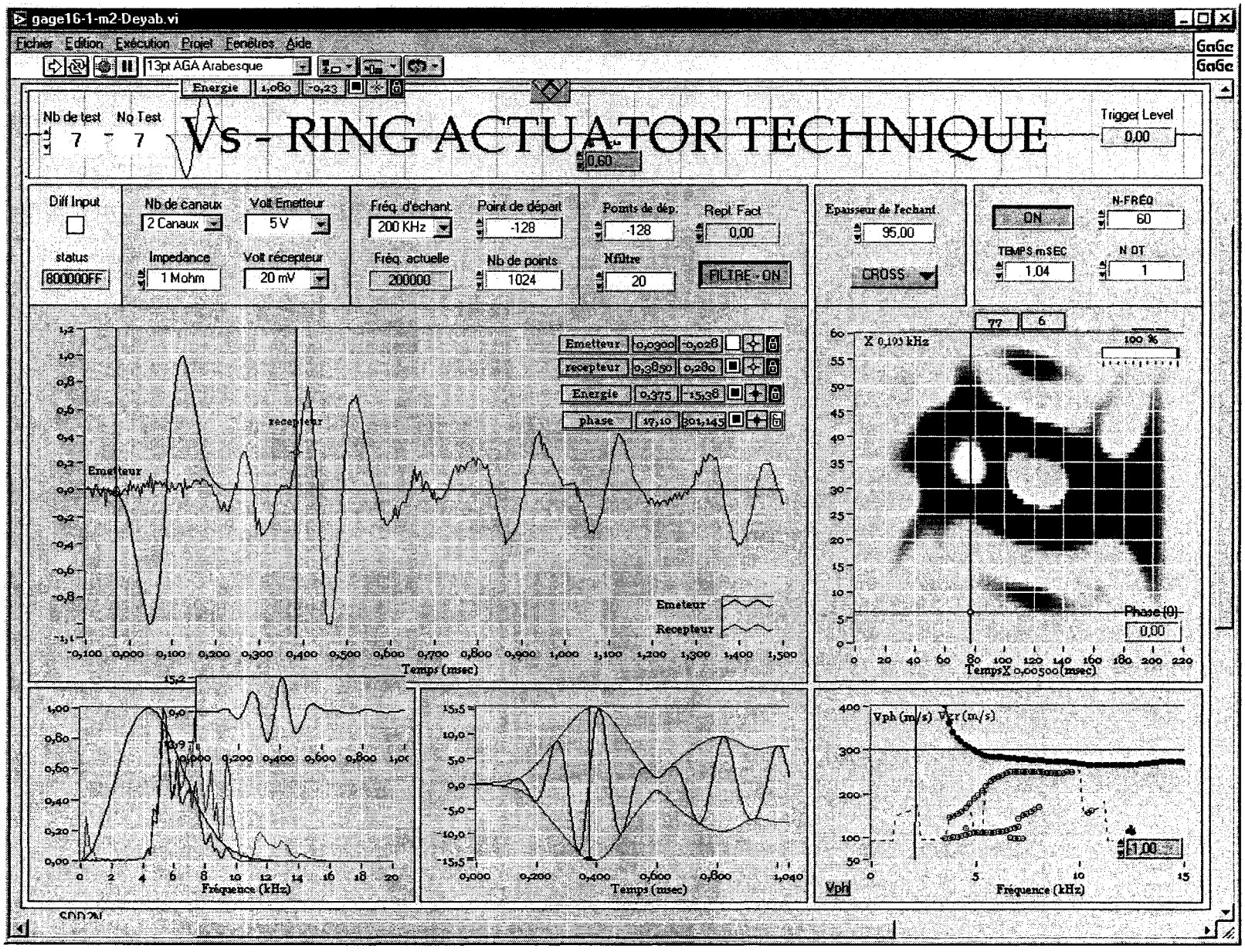

Figure C.51 Test 49(c); Versed sine input, Pressure = 413.3 kPa.

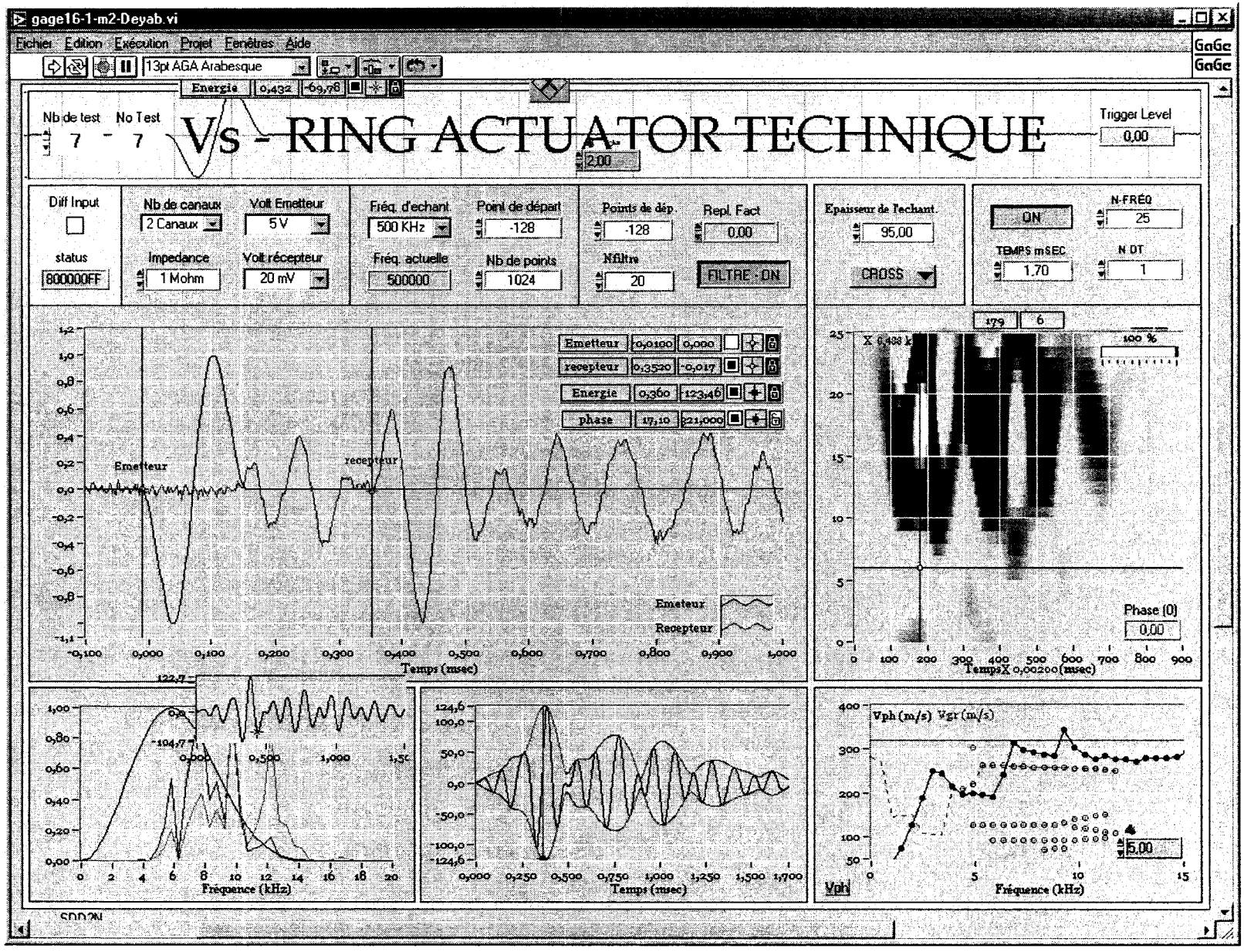

Figure C.52 Test 49(d); Versed sine input, Pressure = 578.1 kPa.

Test 56

Pulse Tests on Compacted Concrete Sand in Proctor Mold (Setup B)

Using the Ring Actuators Setup No. 4.

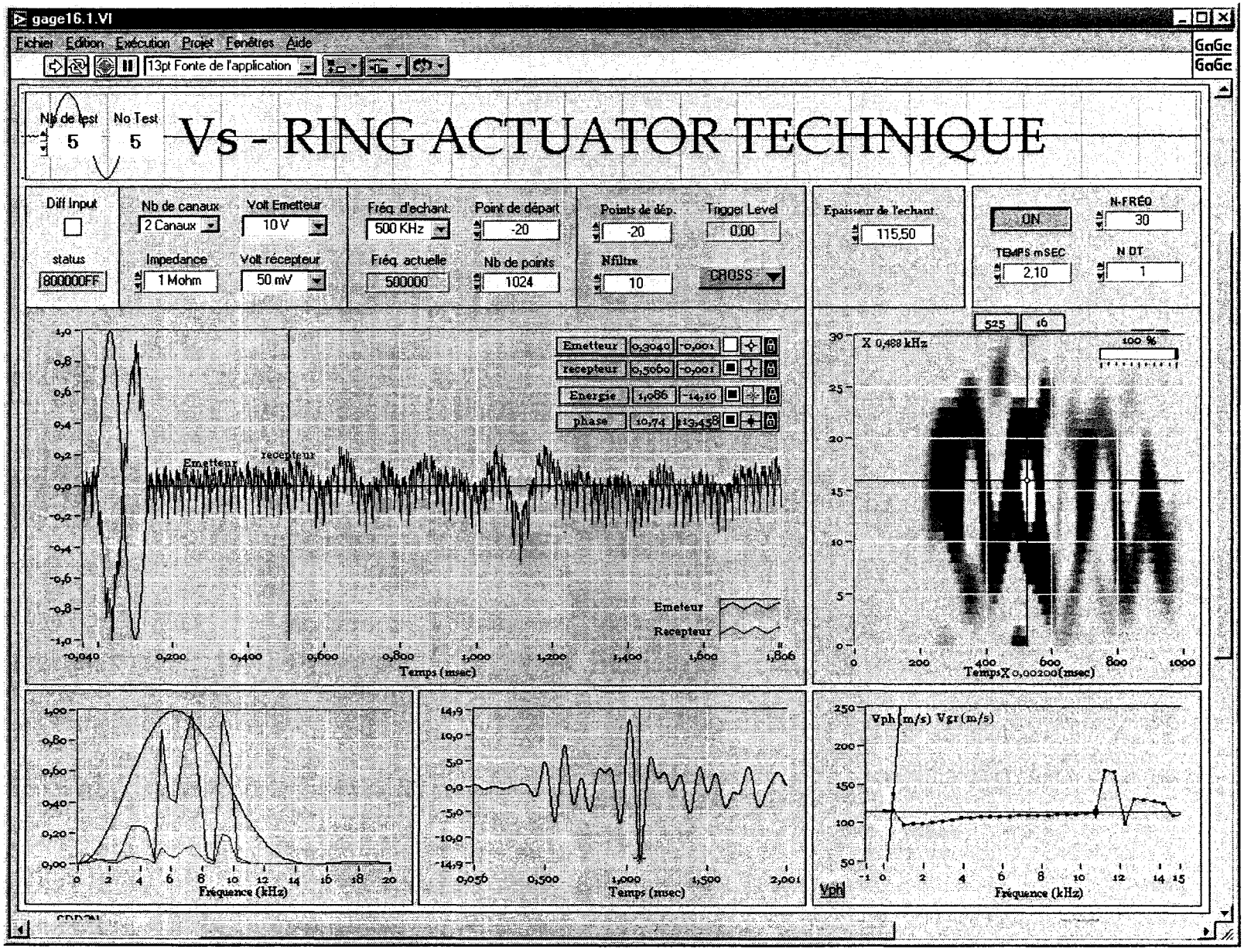

Figure C.53 Test 56(a); Sine wave input of 7.5 kHz, Pressure = 11.63 kPa, w_c = 4.7%.

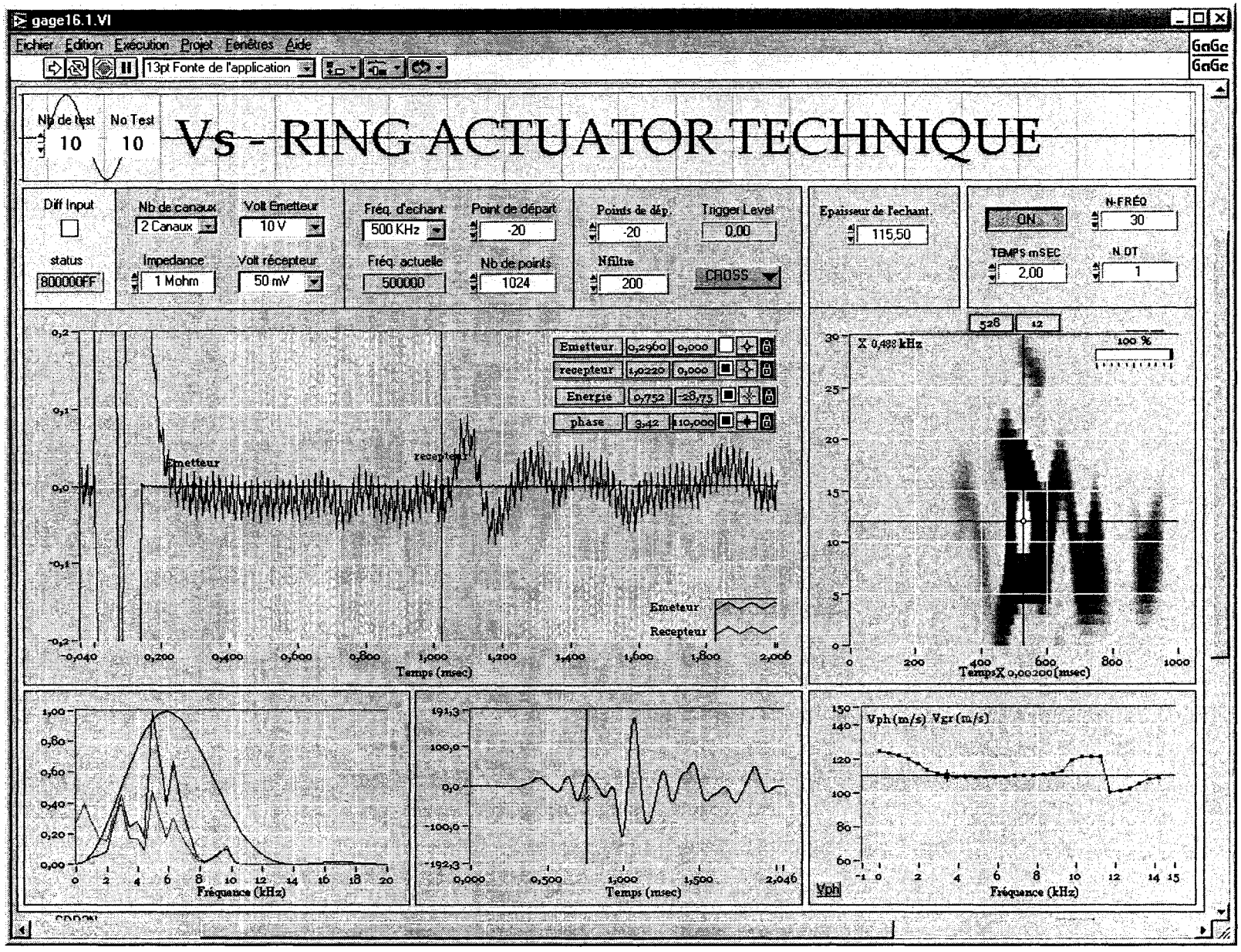

Figure C.54 Test 56(b); Sine wave input of 15 kHz, Pressure = 11.63 kPa, w_c = 6.85%.

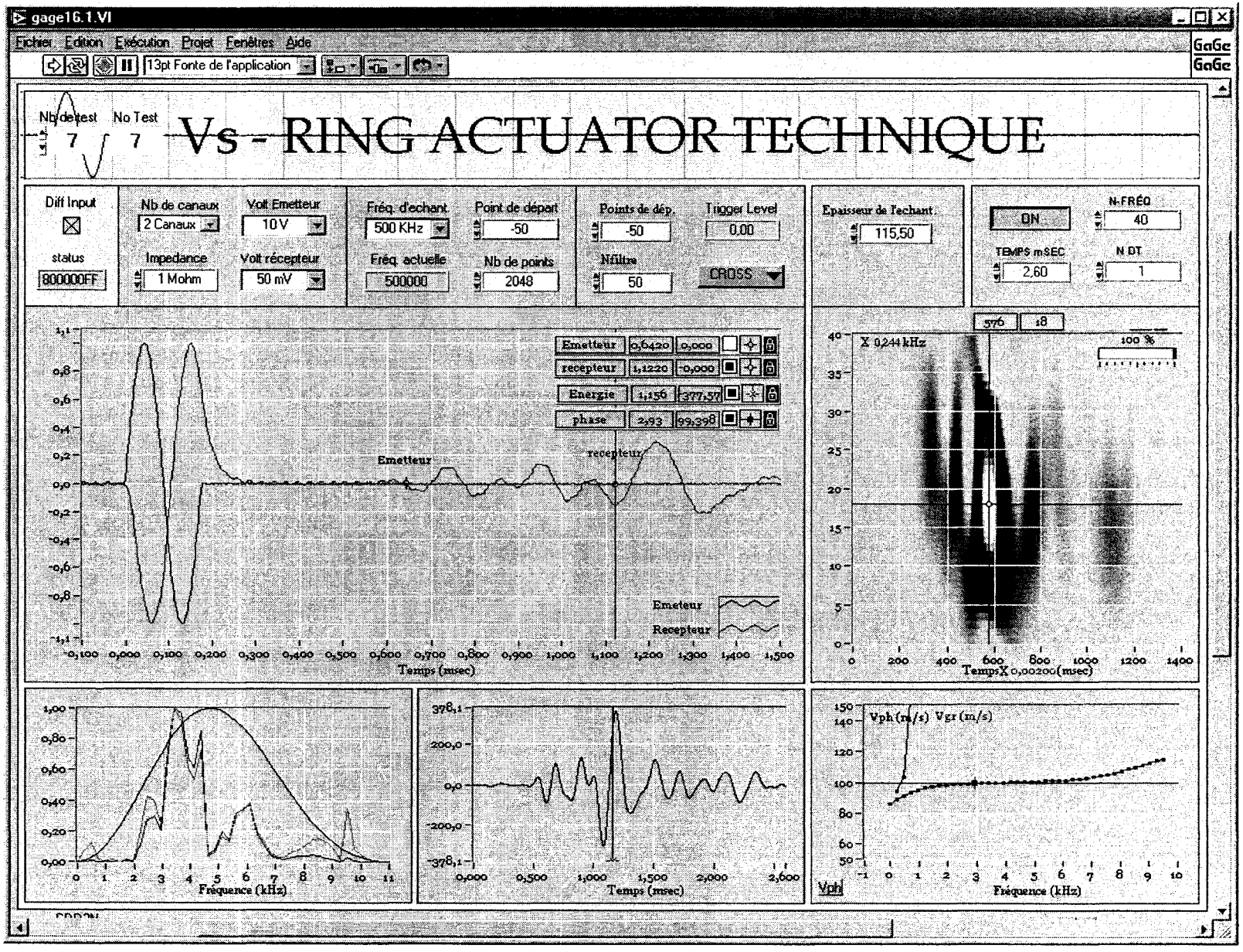

Figure C.55 Test 56(c); Sine wave input of 3.5 kHz, Pressure = 11.63 kPa, w_c = 7.8%.

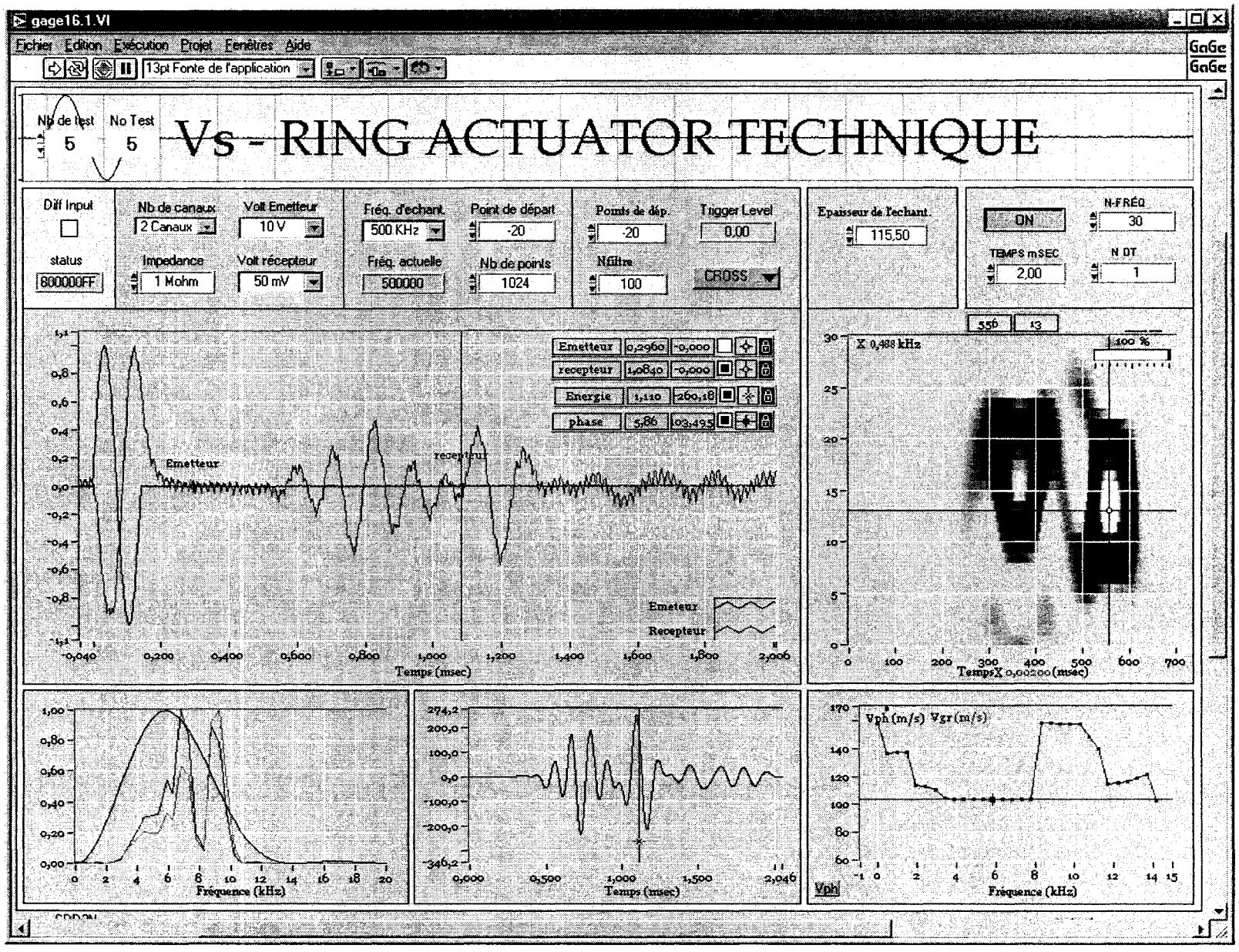

Figure C.56 Test 56(d); Sine wave input of 7 kHz, Pressure = 11.63 kPa, w_c = 8.73%.

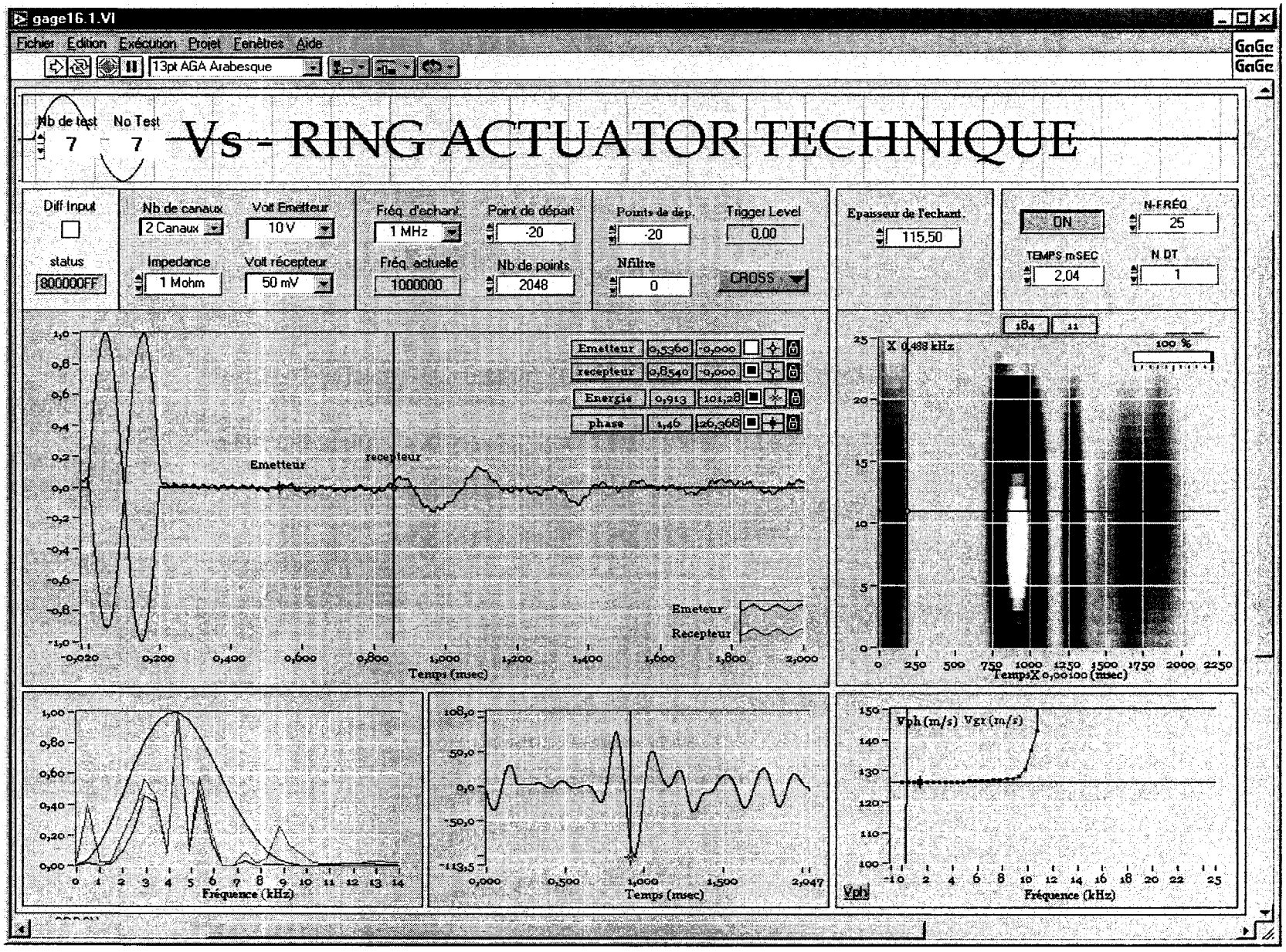

Figure C.57 Test 56(e); Sine wave input of 5 kHz, Pressure = 11.63 kPa, $w_c = 10\%$.

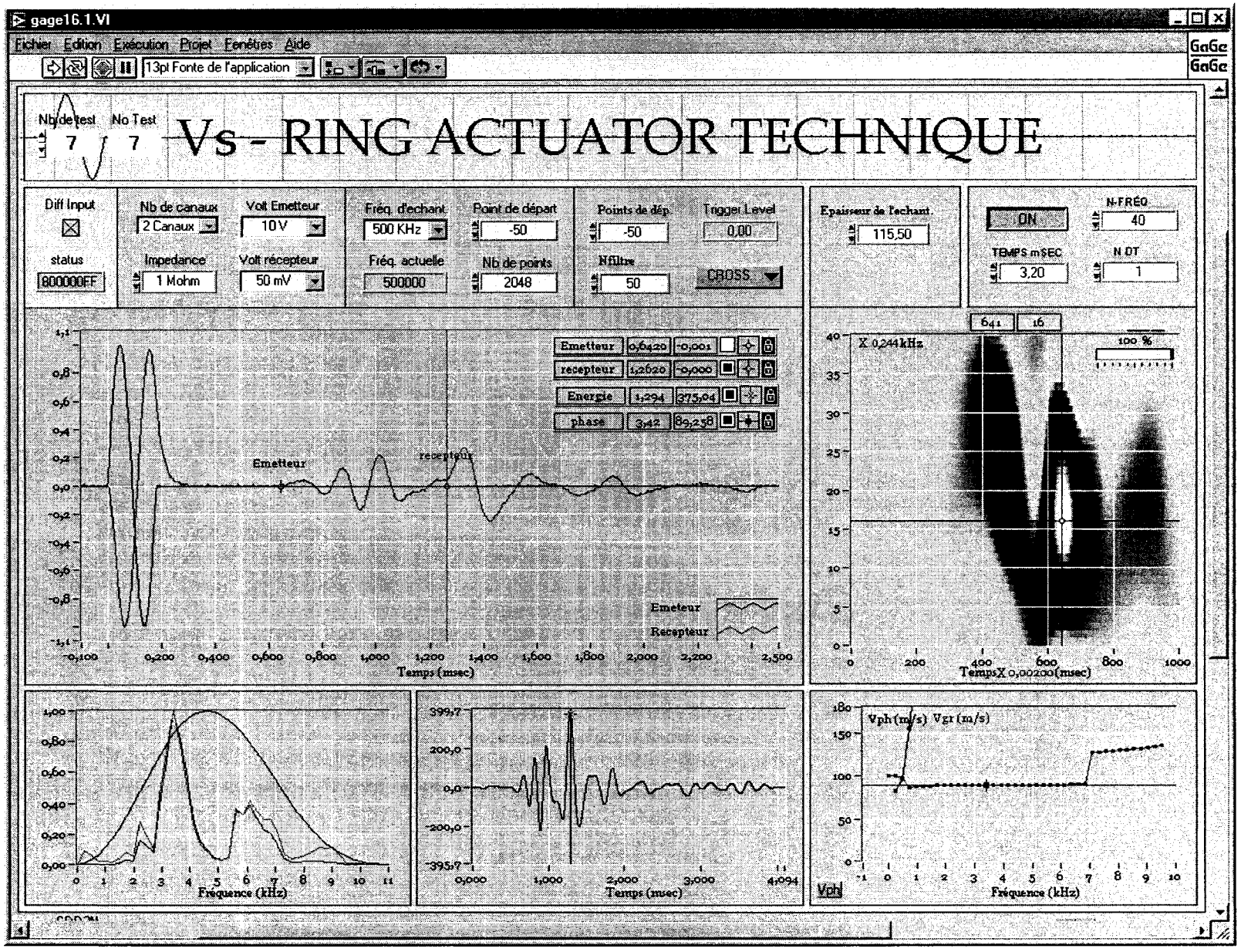

Figure C.58 Test 56(f); Sine wave input of 5.5 kHz, Pressure = 11.63 kPa, w_c = 11%.

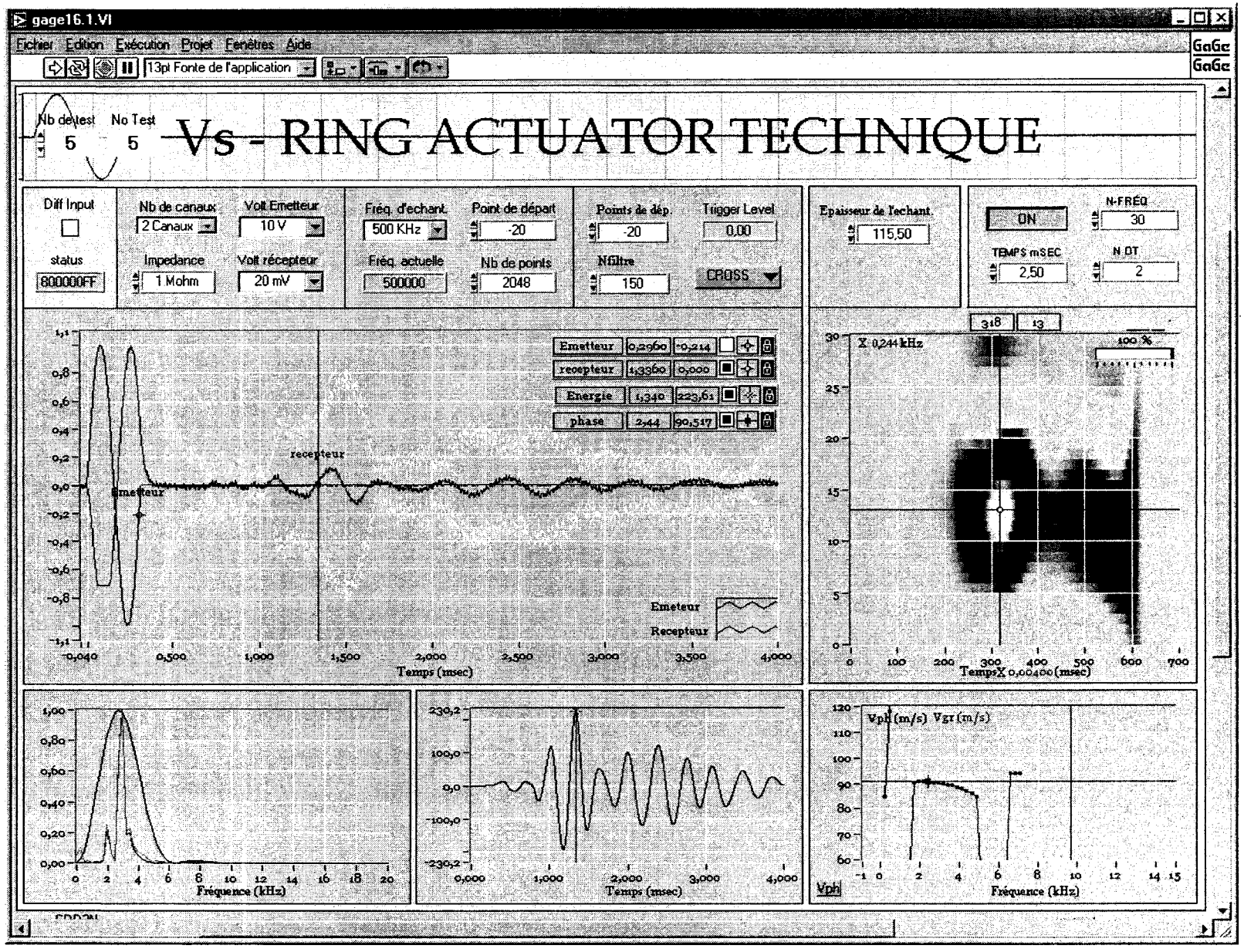

Figure C.59 Test 56(g); Sine wave input of 2 kHz, Pressure = 11.63 kPa, w_c = 12.83%.

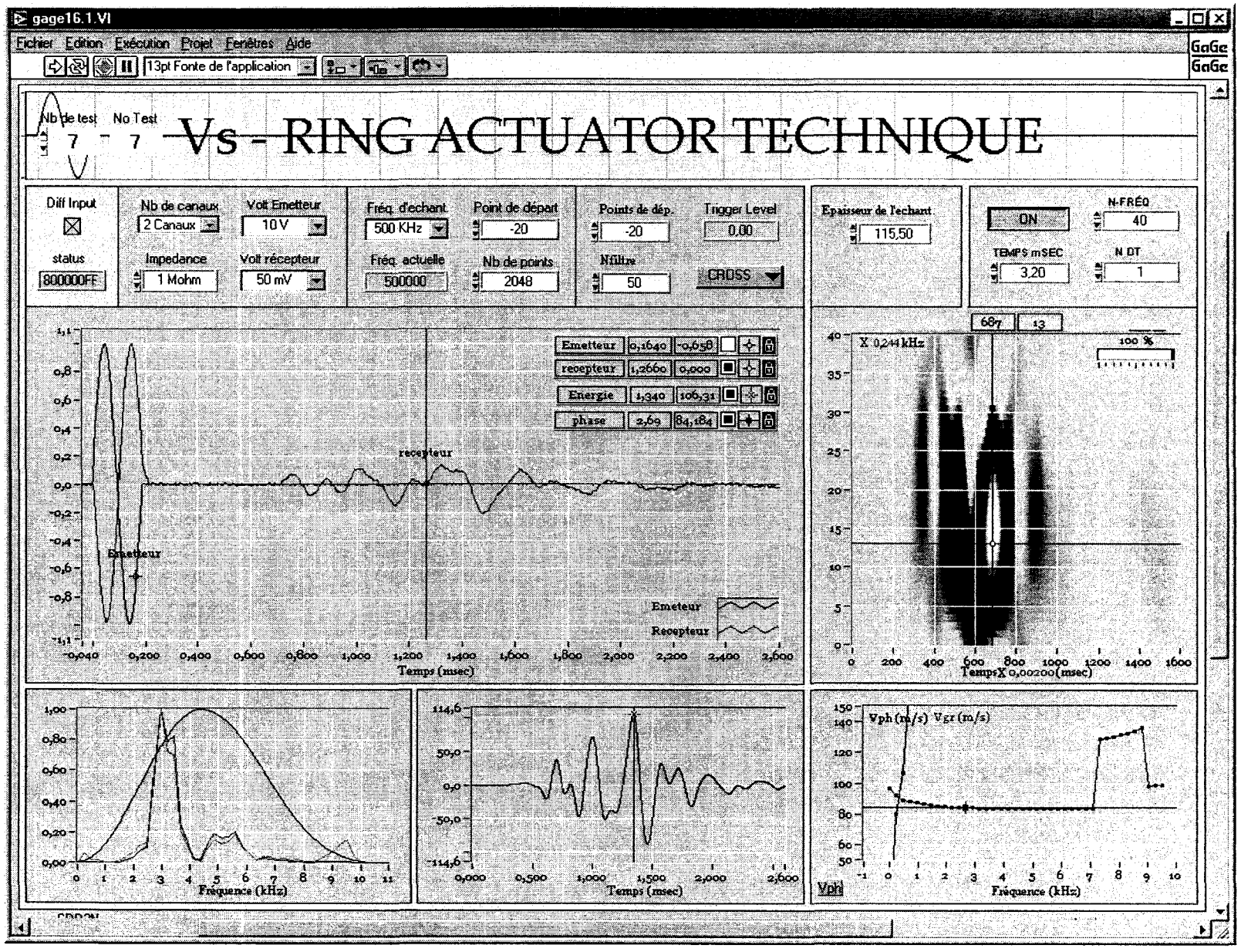

Figure C.60 Test 56(h); Sine wave input of 5.3 kHz, Pressure = 11.63 kPa, w_c = 15.1%.

Test 59

Pulse Tests on Compacted LG4 Till in Proctor Mold (Setup B)

Using the Ring Actuators Setups No. 4 – 8.

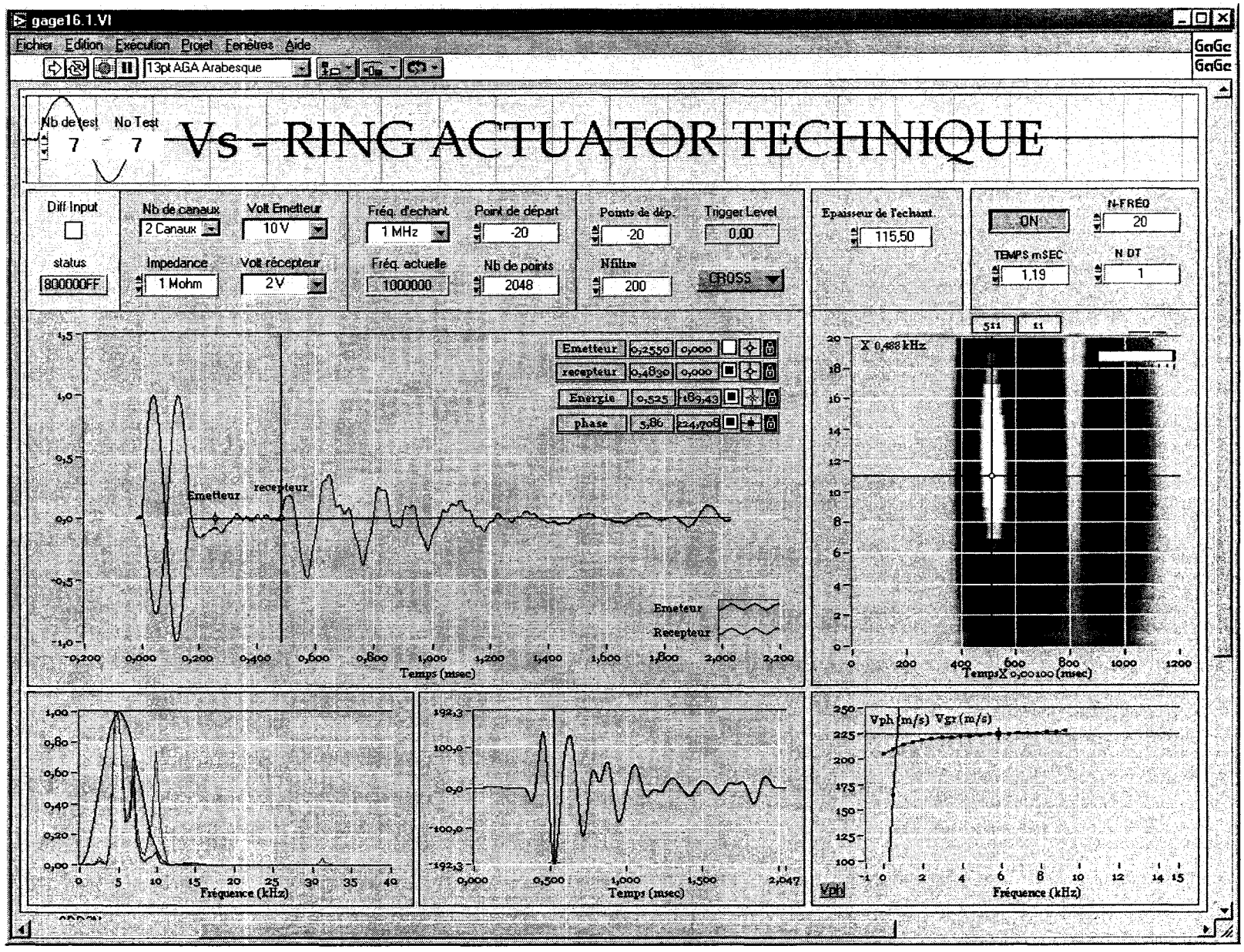

Figure C.61 Test 59(a); Sine wave input of 6 kHz, Pressure = 61.13 kPa, w_c = 1.36%.

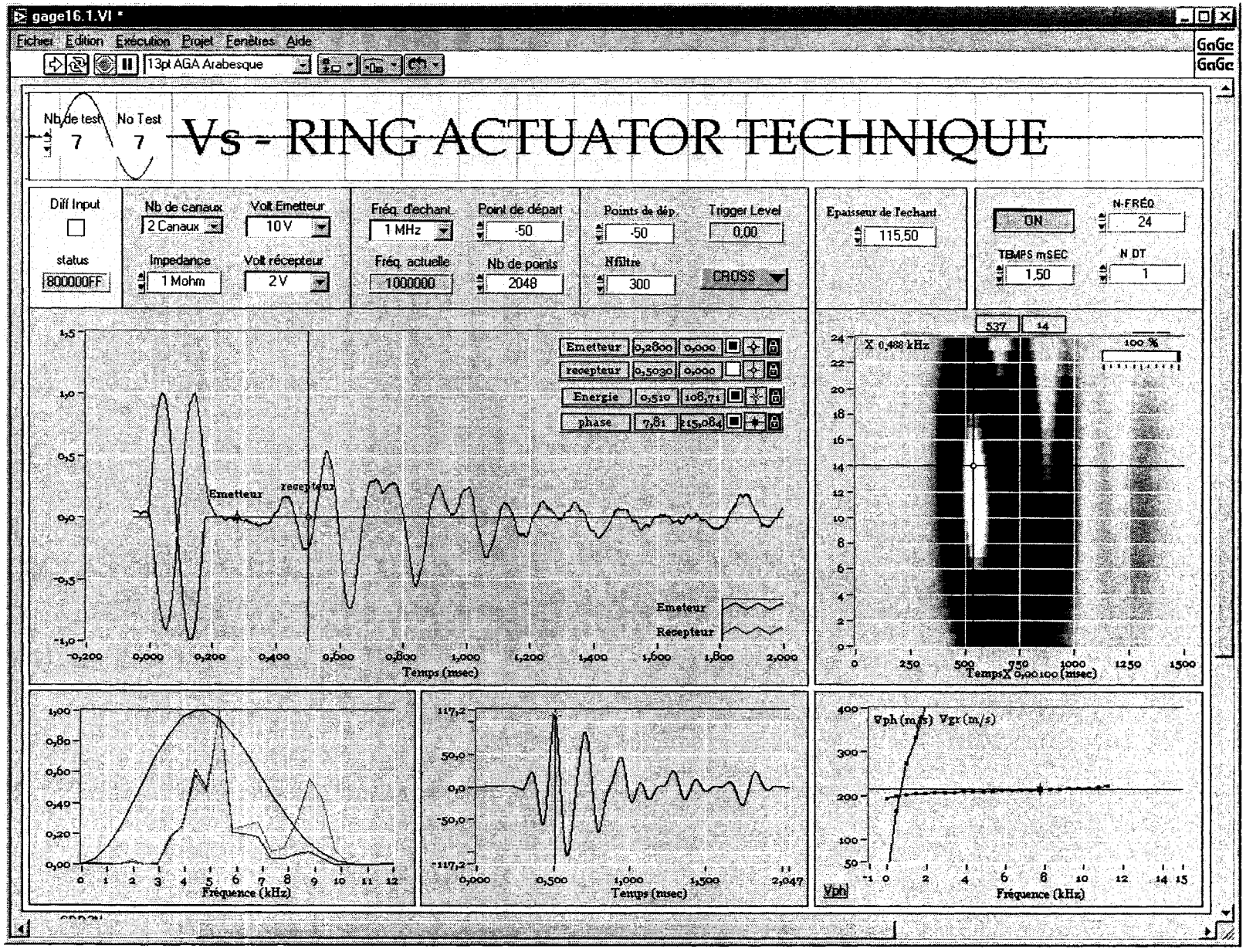

Figure C.62 Test 59(b); Sine wave input of 5.5 kHz, Pressure = 33.63 kPa, w_c = 2.7%.

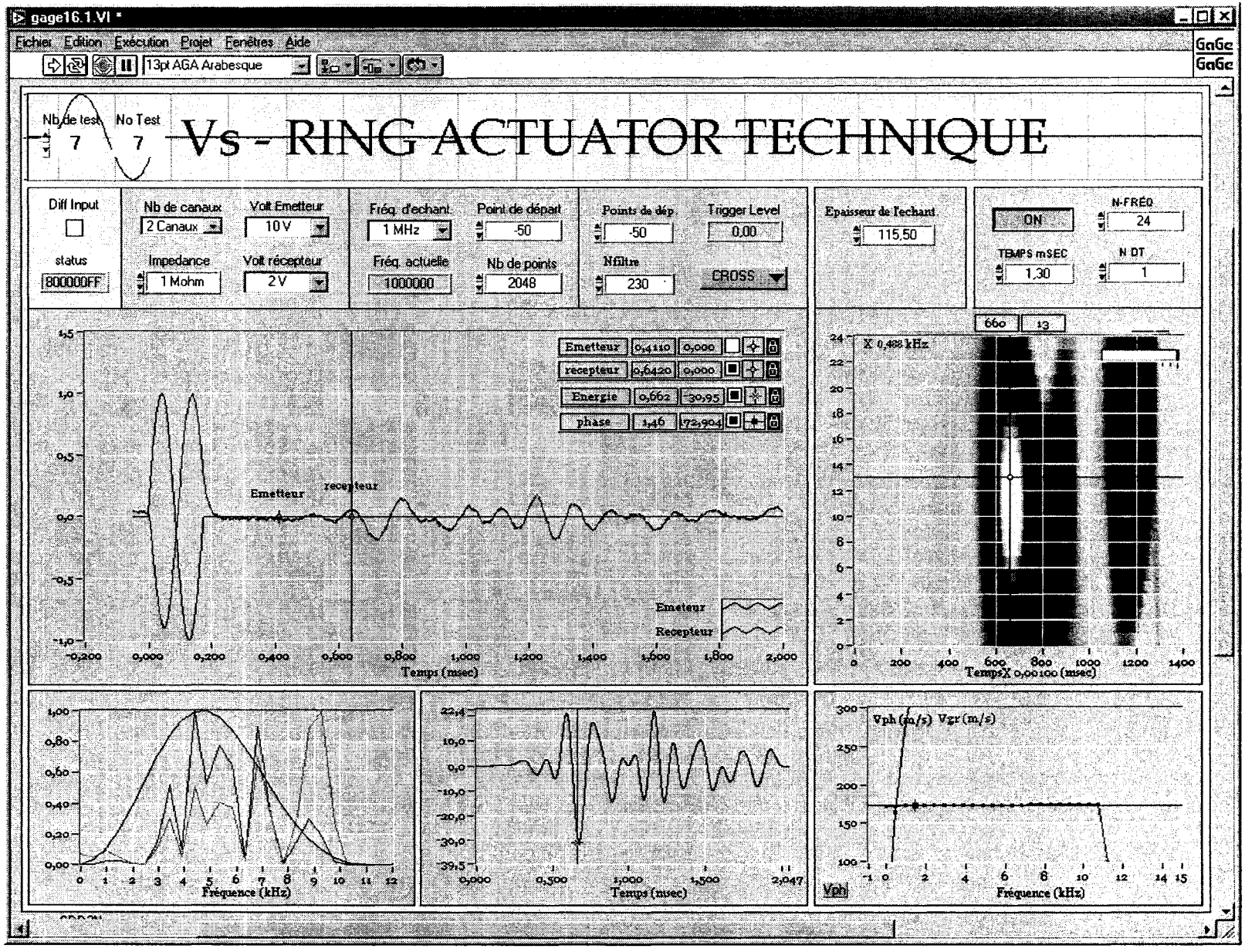

Figure C.63 Test 59(c); Sine wave input of 3.5 kHz, Pressure = 11.63 kPa, w_c = 3.4%.

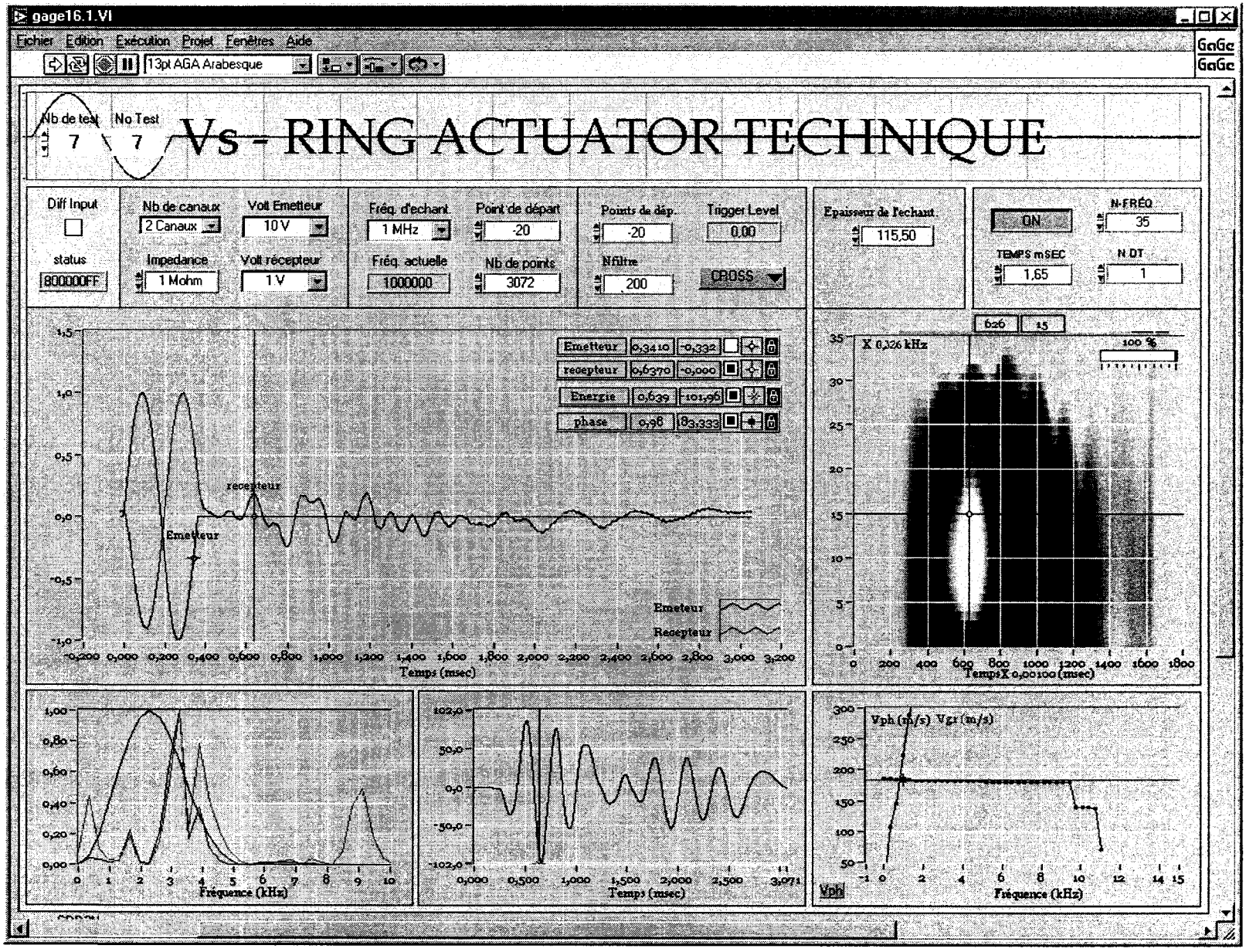

Figure C.64 Test 59(d); Sine wave input of 3.4 kHz, Pressure = 11.63 kPa, w_c = 4.44%.

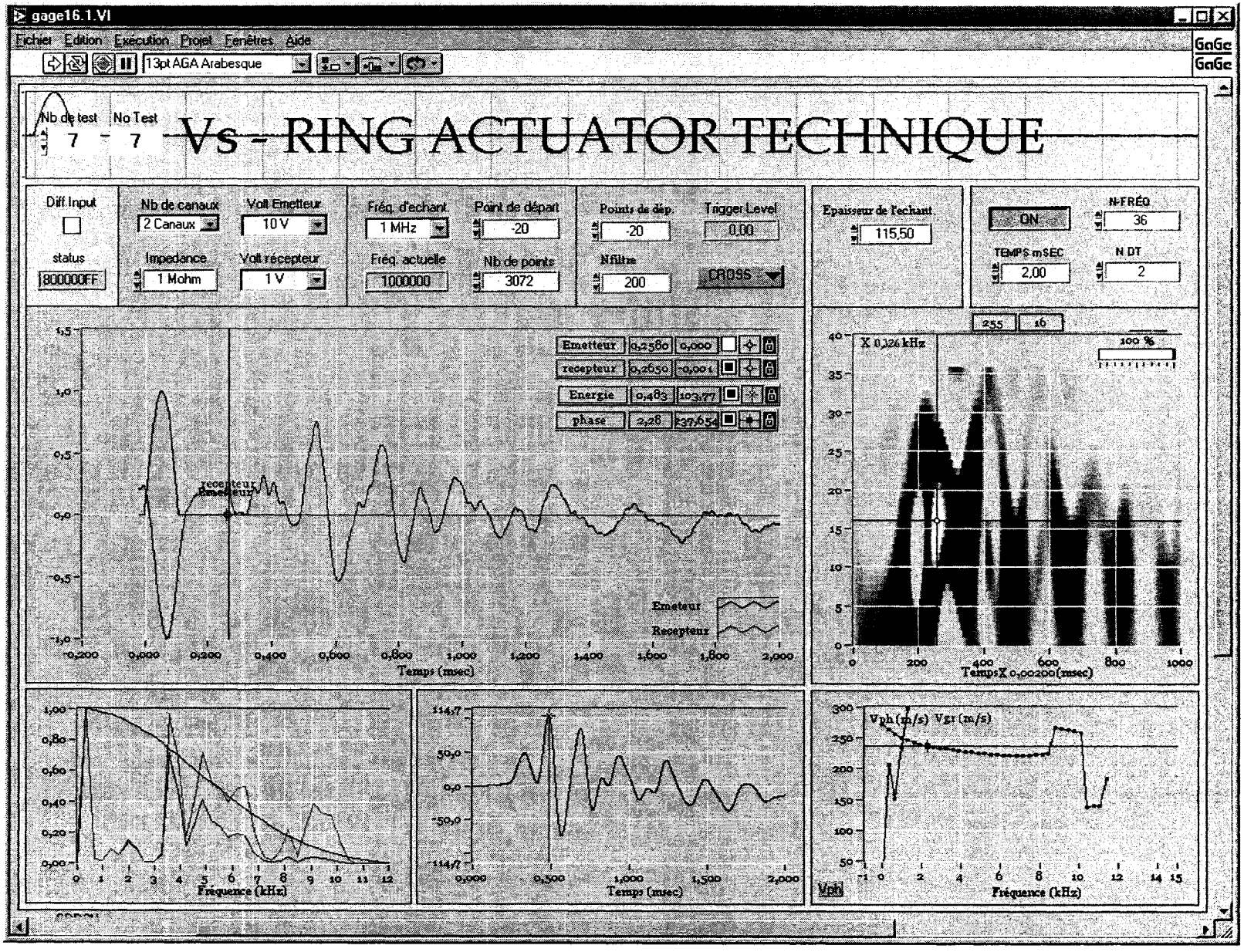

Figure C.65 Test 59(e); Sine wave input of 4.5 kHz, Pressure = 33.63 kPa, w_c = 4.44%.

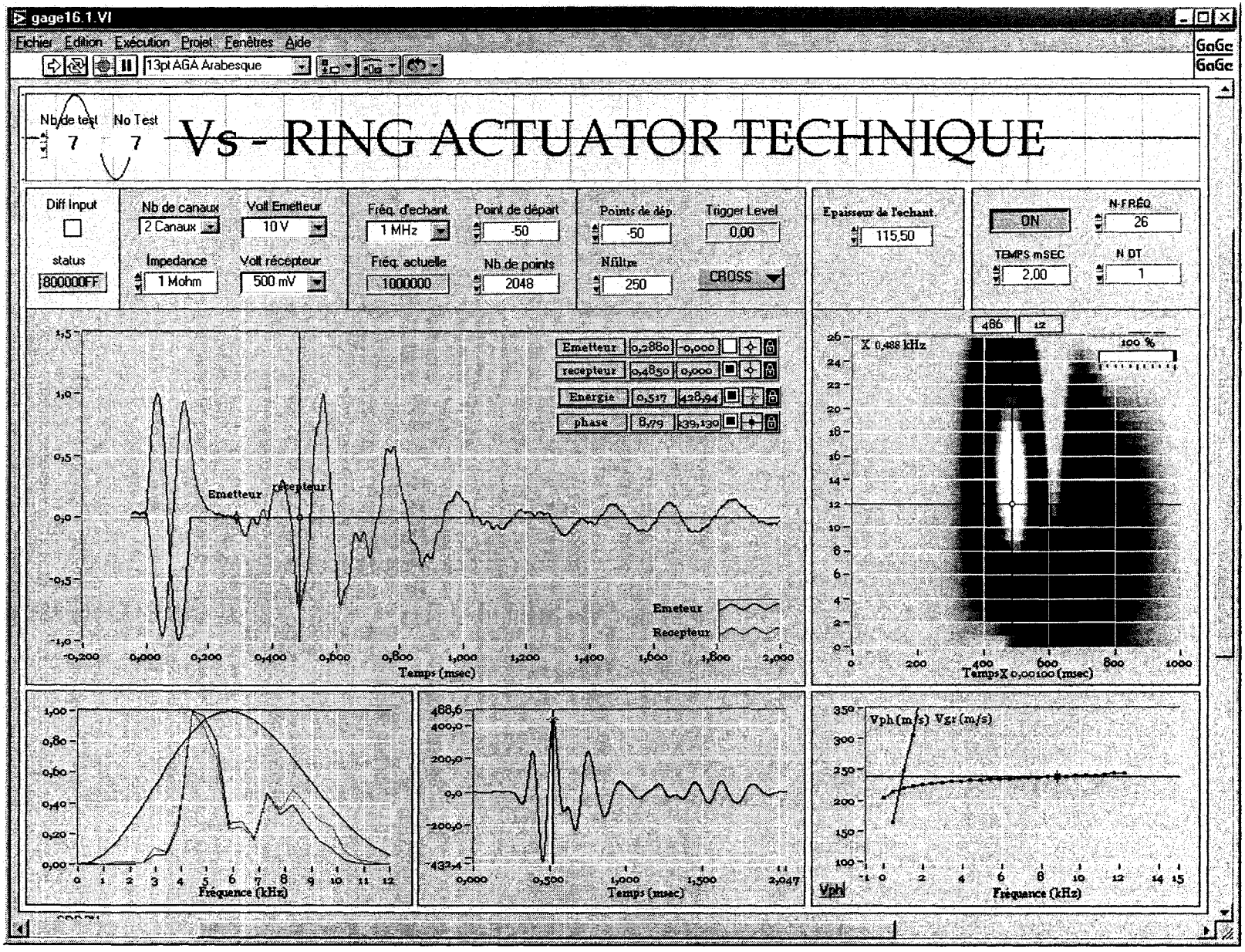

Figure C.66 Test 59(f); Sine wave input of 7 kHz, Pressure = 11.63 kPa, w_c = 5.19%.

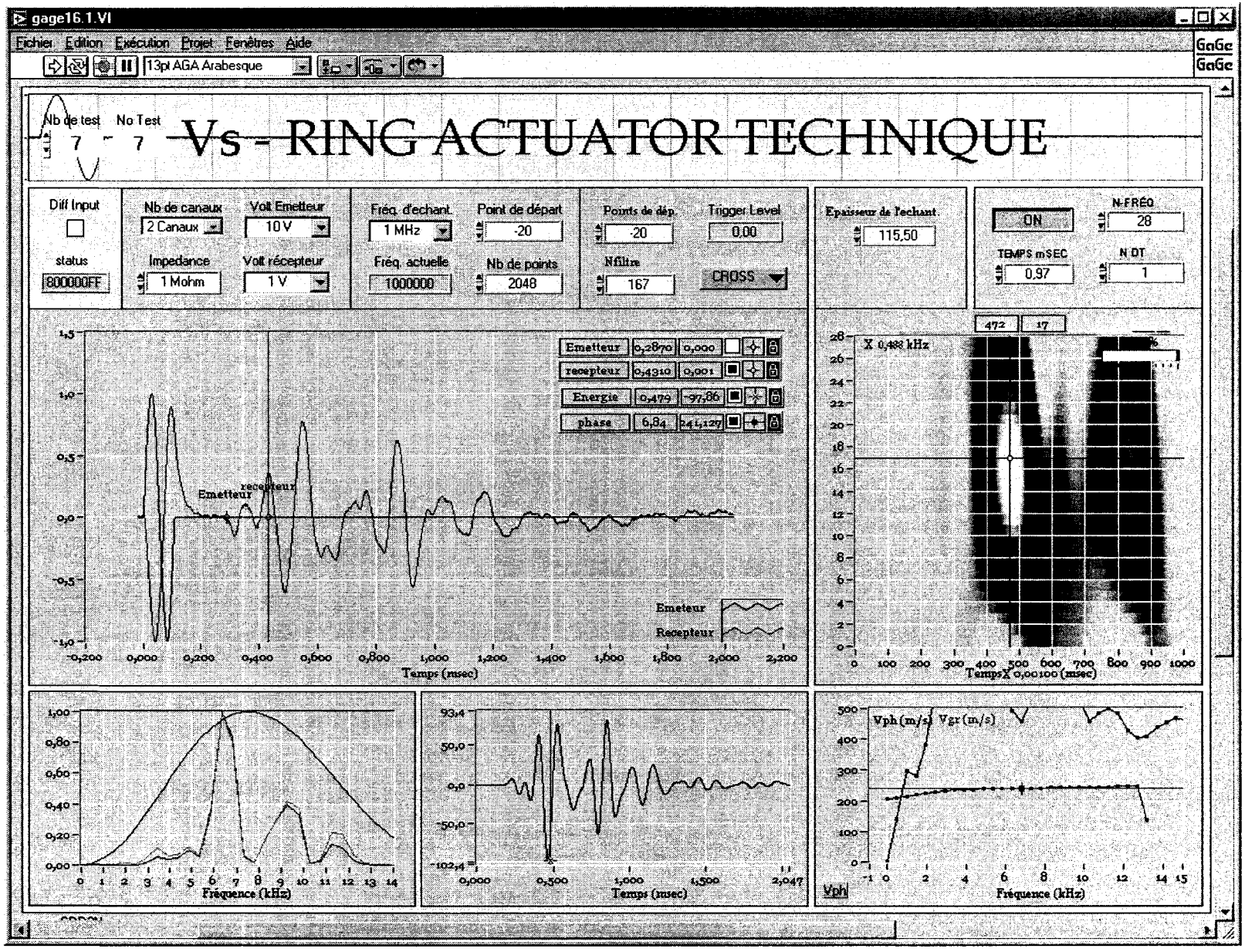

Figure C.67 Test 59(g); Sine wave input of 9 kHz, Pressure = 11.63 kPa, w_c = 5.69%.

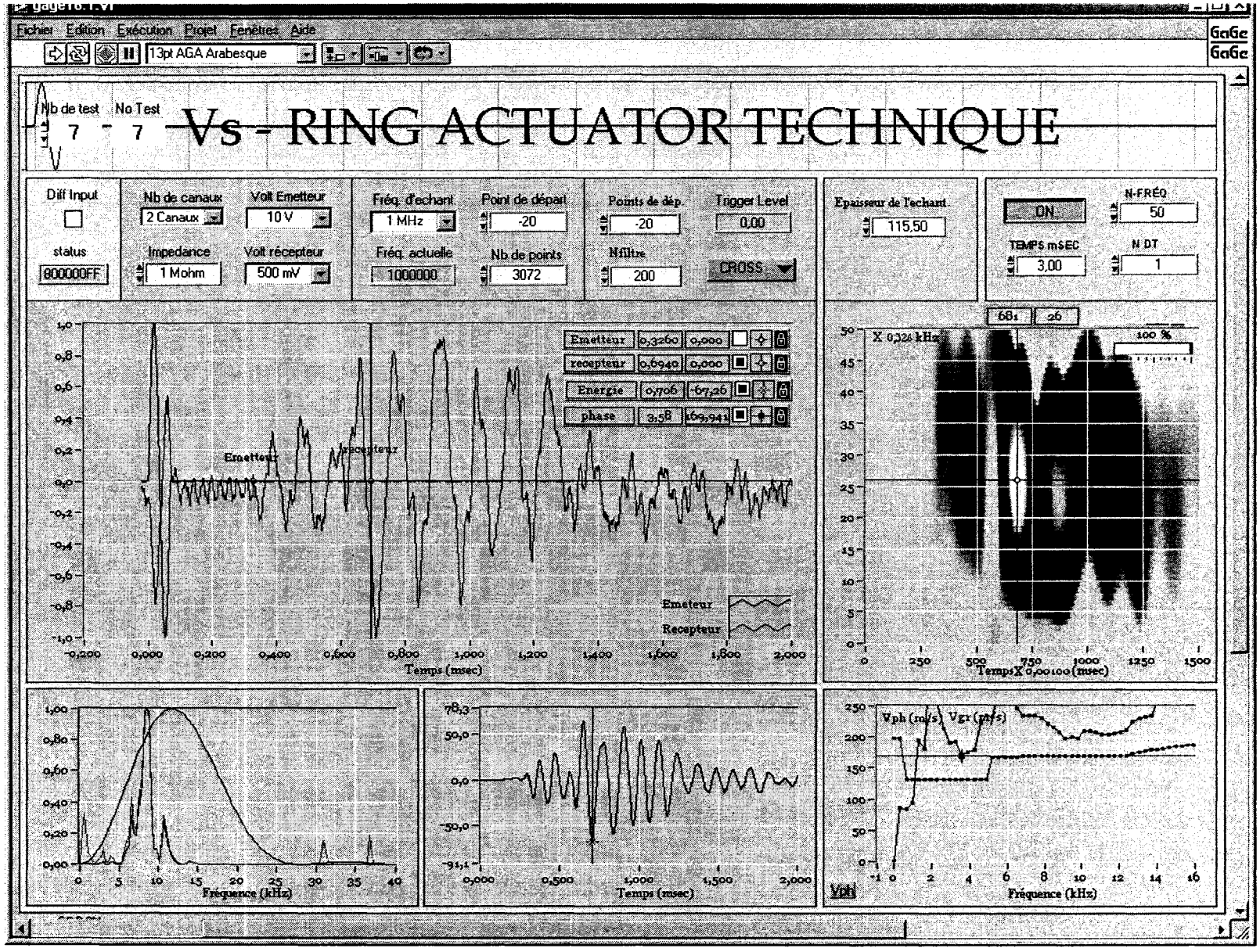

Figure C.68 Test 59(h); Sine wave input of 14 kHz, Pressure = 11.63 kPa, w_c = 6.15%.

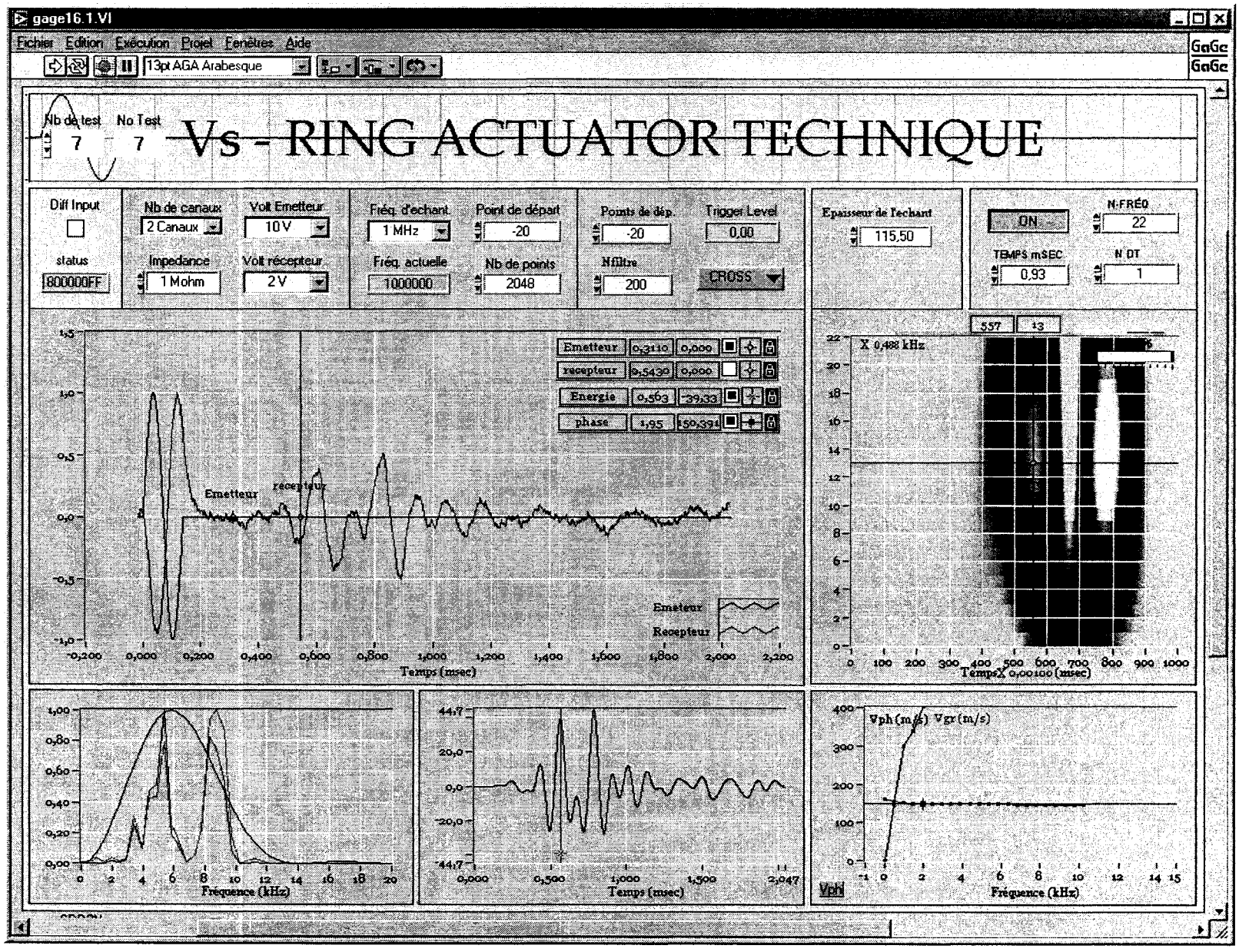

Figure C.69 Test 59(i); Sine wave input of 7 kHz, Pressure = 11.63 kPa, w_c = 6.55%.

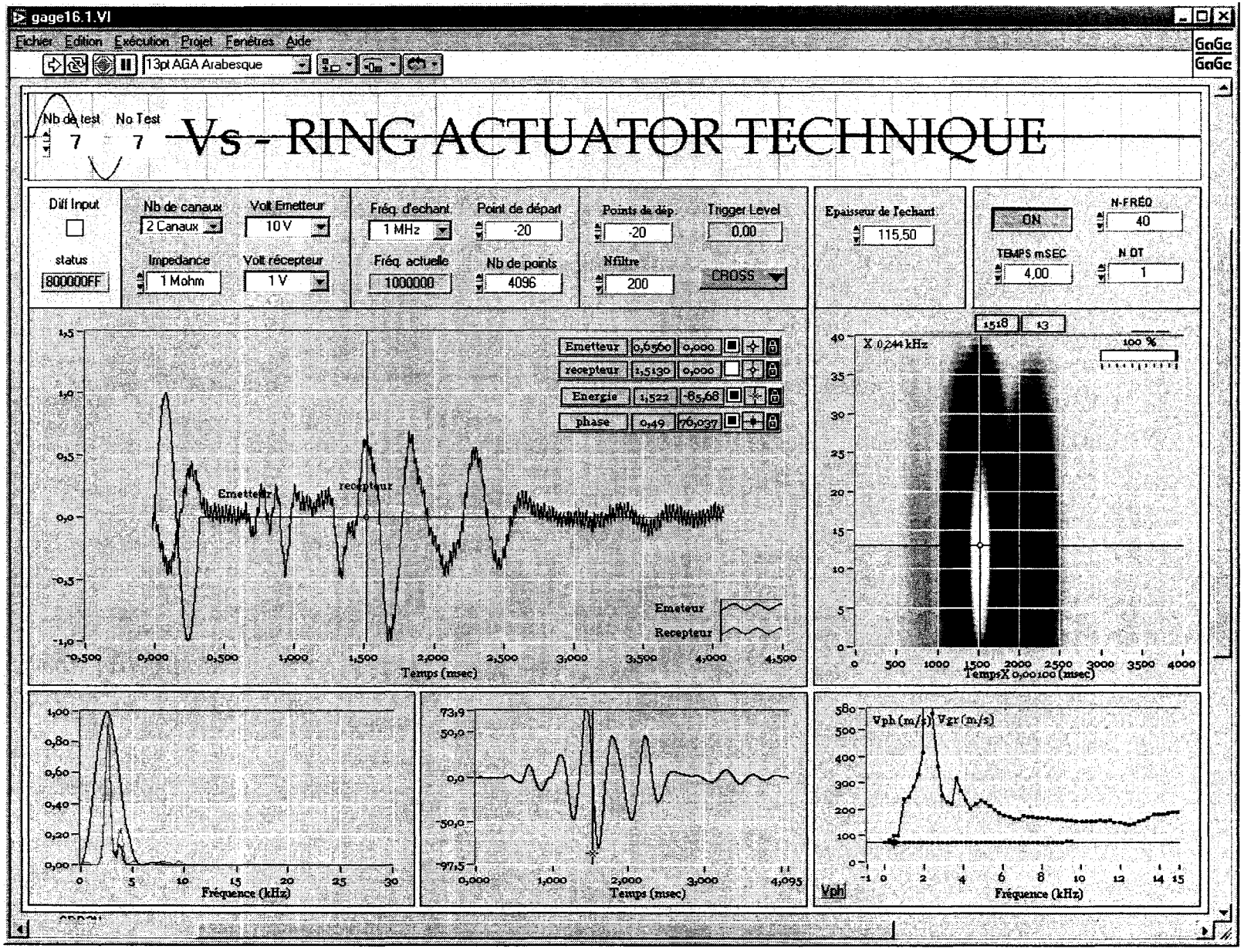

Figure C.70 Test 59(j); Sine wave input of 3 kHz, Pressure = 11.63 kPa, w_c = 7.58%.

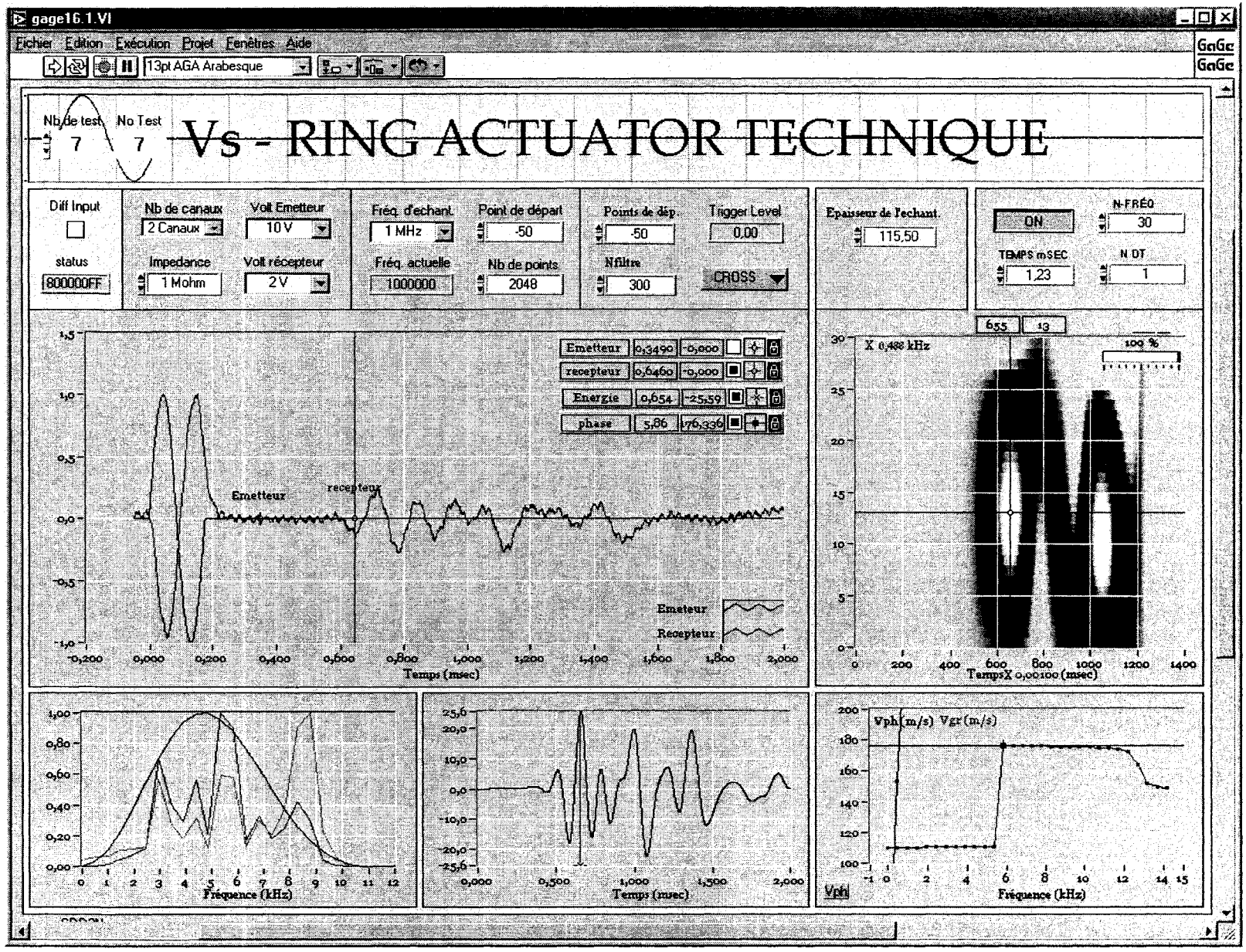

Figure C.71 Test 59(k); Sine wave input of 3.5 kHz, Pressure = 33.63 kPa, w_c = 7.58%.

ABOUT THE AUTHOR

Deyab Gamal El-Dean was born in August, 1970 in Sirs-Ellayan (Egypt). He is the eldest of the eight childrens of Ragab D. Gamal El-Dean and H. M. Shaaban. Gamal El-Dean has received his high school diploma from Sirs-Ellayan School, El-Menoufia. In 1993, he has graduated from El-Menoufia University with a first class Bachelors of Science in Civil Engineering. Then, he entered the military service in The Engineering Authority of the Armed Forces. Upon being honourably discharged from the military service with the rank of First Class Lieutenant in 1996, he worked in Vibrex Company for Tunnelling and Foundations. Then, he joined the Housing and Building National Research Center (HBNRC) in Cairo, Egypt in May 1997 where he gained strong experience in research, laboratory and in situ testing, and consultancies. He has participated in updating and derving two codes of practice for soil and rock. He has been also involved in slope stability, foundation engineering, environmental and hydrogeological studies. In addition, he extensively worked in part time basis to a major consultancy office (Hamza Associates) in structural and geotechnical engineering. In May 2001, Gamal El-Dean obtained his M.Sc. degree in Civil Engineering (Geotechnical) at Cairo University, Egypt. The thesis title was 'properties and classification of weak rocks'. Gamal El-Dean was offered a scholarship from Prof. G. Lefebvre for making his Ph.D in Quebec, Canada. He has begun his studies in Sept. 2002 at Université de Sherbrooke. Gamal El-Dean married Ms. N. Abd Alla in September, 2004 and they were blessed by two children (Sarah and Abdo-Arrahman) since then. Gamal El-Dean is a licenced professional engineer (P.Eng.) in Ontario, Canada, and is a member of several professional organizations.